Atmospheric refraction and propagation over curved surfaces

Thesis

Atmospheric Refraction and Propagation over Curved Surfaces

Thesis submitted by

Qiang Wang BSc (Hons)

for the degree of

Doctor of Philosophy

Engineering Mechanics Discipline

Faculty of Technology

The Open University

Milton Keynes MK7 6AA

England, UK

September 1997

To my husband Xian-wei Liu

EX12

RESEARCH DEGREES CENTRE

LIBRARY AUTHORISATION FORM

Please return this form to the The Research Degrees Centre with the two bound copies of your thesis to be deposited with the University Library.
All students should complete Part 1. Part 2 only applies to PhD students.

Student: QIANG WANG PI: M7190903

Degree: Ph.D.

Thesis title: Atmospheric Refraction and propagation over curved Surfaces

Part 1 Open University Library Authorisation [to be completed by all students]

I confirm that I am willing for my thesis to be made available to readers by the Open University Library, and that it may be photocopied, subject to the discretion of the Librarian.

Signed: [signature] Date: 21/01/98

Part 2 British Library Authorisation [to be completed by PhD students only]

If you want a copy of your PhD thesis to be available on loan to the British Library Thesis Service as and when it is requested, you must sign a British Library Doctoral Thesis Agreement Form. Please return it to the Research Degrees Centre with this form. The British Library will publicise the details of your thesis and may request a copy on loan from the University Library. Information on the presentation of the thesis is given in the Agreement Form.

The University has agreed that your participation in the British Library Thesis Service should be voluntary. Please tick either (a) or (b) to indicate your intentions.

[a] ☑ I am willing for the Open University to loan the British Library a copy of my thesis.
A signed Agreement Form is attached.

[b] ☐ I do not wish the Open University to loan the British Library a copy of my thesis.

Signed: [signature] Date: 21/01/98

h:\vaxm winword\res_exam exdoc\EX12

Abstract

This thesis presents theoretical and experimental investigations of atmospheric refraction and diffraction of sound over curved surfaces. The main contributions of this work are as follows:

- The development of an alternative method for calculating the influence of wind on sound propagation in the presence of a ground of finite impedance.
- The development of numerical models to calculate sound propagation due to monopole and dipole sources over cylindrical or spherical convex and concave surfaces of finite impedance.
- Laboratory measurements of sound propagation over curved surfaces and comparisons with the proposed theoretical and numerical models.
- The exploration of the theory for surface wave contributions in an upward refracting atmosphere in the light of obtained experimental data and observation of the surface waves above a convex surface.
- Experimental and theoretical investigations of the effectiveness of a barrier in the presence of sound speed gradients.

Acknowledgments

Many people deserve thanks for their supervision, assistant, and emotional support which helped make this thesis a reality.

First of all, I would like to thank Dr Kai Ming Li for his supervision and wisdom in the guidance of my research efforts, and Professor Keith Attenborough for his expert advice and word editing my thesis. Many thanks to Dr John Evans, to Simon Moss and to Dr Shahram Taherzadeh for their kind help and English correction. Much appreciation to Brendan Aengenheister, Peter Seabrook, Philip Payne and Tim Waters-Fuller for their assistance in doing experiments. I would like to acknowledge Mrs Sharon Watt, Mrs Rebecca McCormack and everyone in the Acoustics Group and Engineering Mechanics Discipline.

I would also like to acknowledge the Research Committee of the Open University for offering me an Open University Competitive Studentship. Finally, I wish to thank Dr Simon Chandler-Wide for providing a copy of his BEM program and Dau Companies Ltd. for providing the piezo-ceramic transducer discs.

Most sincere thanks to my parents for that they brought me up, to my husband for his love and encouragement, and to my son for his good wishes. I would also like to thank my mother-in-law, Tong-zhi Xia and my sister-in-law, Hua-zhen Liu for their emotional support.

Contents

List of Figures and Captions

List of Symbols

S_0	monopole source strength
S_d	dipole source strength
$2\Delta_d$	separation of two out-of-phase monopole
z_s	source height
z	receiver height
$c(z)$	sound speed
$\bar{c}(z)$	effective sound speed
c_0	$c(0)$
ω_0	source angular frequency
k_0	ω_0/c_0
$\mathbf{u}$	wind velocity vector
$\mathbf{r}$	distance vector between source and receiver
r	distance between source and receiver
R_c	radius of curvature
R_{eff}	effective radius of curvature
$H_0^1(\ )$	Hankel function of first kind and of order 0
ψ_w	angle between wind direction and horizontal direction pointing from source to receiver
$P(k_r,z)$	Fourier transform for $p(x,y,z)$

$p(x,y,z)$	Fourier transform for $P(k_r,z)$
p_1	sound pressure at 1 m in the absence of reflected wave
p_0	sound pressure at an identical field point in the absence of reflected wave
k_r	magnitude of the horizontal wave number
k_n	n th term of k_r
k_x	$x-$axis component of wave number
k_y	$y-$axis component of wave number
k_z	vertical component of
ε	azimuthal angle
t	time
ω_m	convected angular frequency
$\tilde{\Phi}$	velocity potential
$\delta(\ )$	delta function
$n_c(z)$	index of refraction in the absence of wind
k	wave number
M	Mach number
M_e	effective Mach number
κ	wave number in the presence of wind
$z_>$	$\max(z_s,z)$
$z_<$	$\min(z_s,z)$
$\xi(z)$	dimensionless scale factor
ξ_0	$\xi(k_r,0)$
$\xi_<$	$\xi(k_r,z_<)$

$\xi_>$	$\xi(k_r, z_>)$
$\overline{\xi}_0$	$\xi(k_n, 0)$
$\overline{\xi}_s$	$\xi(k_n, z_s)$
$\overline{\xi}$	$\xi(k_n, z)$
$k_<$	$k_z(z_<)$
$k_>$	$k_z(z_>)$
Ai( )	Airy function
Ai'( )	Airy function derivative
β	normalized specific admittance of the impedance ground
z_t	turning point
Γ	reflection factor
q	scaled and nondimensionalized admittance
q_n	n th term of q
l	thickness of the creeping wave
l_n	n th term of l
ψ_r	azimuthal angle of the receiver position
b_n	n th pole
τ_n	n th pole
Δ_1	error function
Δ_2	error function
a_n'	n th zero of Airy function derivative
a_n	n th zero of Airy function
q_0	effective scaled and nondimensionalized admittance

a_T	normalized sound speed gradient due to temperature
a_W	normalized wind velocity gradient
f	source frequency
dc/dz	sound speed gradient
h_n	n th mode height
$p^{(c)}$	sound pressure over a cylindrically curved surface
$p^{(b)}$	sound pressure in the presence of a bilinear sound speed profile
$p^{(s)}$	sound pressure over a spherically curved surface
ψ_s	azimuthal angle
J	Jacobian of the transformation
ψ	azimuthal angle
σ	flow resistivity
σ_e	effective flow resistivity
α_e	effective rate of change of porosity with depth
R, θ, ϕ	receiver in a spherical polar coordinate
$R_s, \theta_s \phi_s$	source in a spherical polar coordinate
P_i	amplitude of a incident wave
Θ	central angle between source and receiver above a spherical surface
$h_n(\ )$	n th spherical Bessel function
$j_n(\ )$	n th spherical Bessel function
$h_n'(\ )$	n th derivative of spherical Bessel function
$j_n'(\ )$	n th derivative of spherical Bessel function
$P_n(\ )$	Legendre polynomial of degree n

$J_v(\ )$	Bessel function of first kind of order v
$G_{\beta_c}(\ )$	sound pressure above a plane of homogenous admittance β_c without a barrier
$G(\ )$	sound pressure in the presence of a barrier
γ	contour of cross section of a cylinder
EA	excess attenuation
TL	transmission loss
IL	insertion loss
$v(\ )$	Fock function
$w_1(\ )$	Fock function
$w_2(\ )$	Fock function
Φ_g	knife-edge diffraction
Ψ_g	Fock's background
d	shortest distance between source and receiver
d_1	distance to reflection point
d_2	distance from reflection point
d_r	reflected wave
θ_0	angle of incidence above a curved surface
Q	complex spherical wave reflection coefficient
R_p	plane wave reflection coefficient
$F(\ )$	boundary loss factor
w	numerical distance
p_r	reflected wave
p_d	sound pressure due to a dipole source

p_v	sound pressure due to a vertical dipole source
p_h	sound pressure due to a horizontal dipole source
ψ_d	polar angle of dipole moment vector
γ_d	azimuthal angle of dipole moment vector
φ	$\arg(q)$
φ_z	$\pi/2 - \arg(q)$
$\mathrm{IL}_{\mathrm{total}}$	total insertion loss
$\mathrm{IL}_{\mathrm{barrier}}$	barrier insertion loss

Chapter 1

Introduction and literature review

Atmospheric refraction has been the subject of extensive research in the past five decades [4-7, 39, 76, 77]. Recent studies on the diffraction of sound over curved surfaces and its analogy to atmospheric refraction over flat ground surfaces have led to various solutions to the problem of predicting the effects of temperature and wind velocity gradients in the presence of flat ground surfaces [3, 8, 15, 19]. Despite the substantial progress in these areas, there remain many problems that are not well understood, such as: the effect of wind velocity on sound propagation, the diffraction of sound due to dipole sources, the existence of surface waves above a curved finite impedance surface, and the influence of sound speed gradients on the effectiveness of a noise barrier.

This thesis is divided into eight chapters. Following a brief introduction, this first chapter continues with a literature review. The literature review is split into five parts corresponding to the various topics in the thesis.

Chapter 2 is devoted to a theoretical study of sound propagation outdoors in the presence of vector wind velocity and sound speed gradients. The proposed numerical model differs from the conventional approach in which the effect of wind is replaced by an effective sound speed gradient.

Chapter 3 and Chapter 4 describe respectively the theory and experimental investigations on diffraction of sound by convex surfaces. The theory is based on the residue series solution for a monopole source with a bilinear profile [3, 15]. It is extended to deal with propagation in an exponential profile, to dipole fields, and to propagation in three dimensions over spherical and cylindrical convex surfaces. Laboratory experiments have been conducted to validate the theoretical expressions derived in Chapter 3 for both monopole and dipole sources.

Theory and laboratory experiments on diffraction of sound by concave surfaces are reported in Chapter 5. The theory is based on the normal mode solution for a monopole source in a bilinear profile above finite impedance ground [9]. It is extended to deal with propagation in an exponential profile, to dipole fields, and to propagation in three dimensions over spherical and cylindrical concave surfaces. Laboratory experiments have been used to validate the theoretical expressions for both monopole and dipole sources.

In Chapter 6, the theory for the role of the surface wave pole in an upward refracting atmosphere suggested by Raspet *et al* [8] is explored and re-interpreted in the light of experimental data that has been obtained. Experimental evidence of the existence of the surface waves above a convex finite impedance surface is also shown in this chapter.

Chapter 7 discusses the effectiveness of a barrier in the presence of positive and negative sound speed gradients. A series of indoor experimental measurements have been performed to investigate the diffraction of sound from a barrier on the top of a convex or concave surface. Firstly, the boundary element method is used to compare with the experimental data on barrier performance over curved surfaces; secondly, it is used to predict the effectiveness of a barrier in the presence of both positive and negative sound speed

gradients, up to a range of the order of 100 m, in comparison with that in the absence of the sound speed gradient.

Chapter 8 summarizes the conclusions of Chapters 2-7 and presents some recommendations for future work.

1.1 Sound propagation outdoors in the presence of wind

Investigations of the effects of atmospheric temperature and wind on sound propagation may be traced back to around 1700 [78-82]. These early investigations have been followed by many extensive research projects. For the last fifty years, increased concern over outdoor sound propagation in a refracting atmosphere has led to significant advances, which have been summarized by Ingard [87], Delany [88], Piercy *at al* [89], Attenborough [55], L'Esperance *et al* [90] and Embleton [91].

Sound speed in the atmosphere depends on the temperature, and if the temperature varies with height in the medium, sound rays follow curved paths rather than straight lines. The radius of curvature of ray paths at any point is inversely proportional to the sound speed gradient at this point [79, 80]. If the temperature decreases with height above the ground, as is usually the case during the daytime, the sound rays will be refracted upward, and an observer at some distance from the source may be in a kind of acoustic shadow zone. At night, the ground usually cools by radiation faster than the atmosphere. There is generally an inversion of temperature gradient, and the sound rays will be bent downwards.

Wind speed increases with height above the ground. A sound ray propagating in the air will bend downwards along the downwind direction and bend upwards in the upwind direction. The radius of curvature of the rays is inversely proportional to the wind velocity gradient.

The vertical gradients of temperature and of wind velocity can be strong in the first few meters above the ground. In the vicinity of the ground, the variation of average wind velocity and that of average temperature with height for a large flat area appear similar in trend. Because of this, in a combined field of temperature and wind velocity gradients, a heuristic approximation has been used to replace the separate temperature and wind velocity profiles with an effective sound speed profile in the direction of propagation [3, 5, 92, 93].

There have been many attempts to model the effect of wind on sound propagation outdoors. Most of the previous attempts have used ray approximations [6, 7, 96-98], high-frequency asymptotic approximations [36, 99], and the fast field program (FFP) [1, 4, 100-102]. All of these have used the effective sound speed profile to approximate the effect of wind velocity gradients.

However, the use of the effective sound speed profile may cause errors since in fact the wind velocity profile is different from the temperature profile, although the effects of wind and temperature gradients appear similar in some aspects. Temperature is a scalar quantity, the refraction of sound produced by lapse or inversion conditions is therefore the same in all horizontal directions. In the simple case of a linear sound speed profile caused by a temperature gradient, the sound rays will be circular with constant radius [32]. Wind, however, produces refraction that is non-uniform in direction according to the vector component in the direction of propagation. Thus the refraction produced by the wind is zero when the sound propagates directly cross-wind, and increases progressively as the direction of propagation approaches the wind direction. In the simple case of a linear sound speed induced by the wind velocity gradient, the rays are assumed to be curved cylindrically [32].

In practice, wind speed gradients play at least as important a role as temperature gradients, as has been demonstrated in experimental investigations [103-104]. During daylight hours, sound propagation is usually affected by the wind velocity gradients. It is interesting therefore to examine the effect of wind on sound propagation outdoors.

Instead of using the effective sound-speed profile, Nijis and Wapenaar [112] developed a numerical model, in terms of a two-dimensional inverse Fourier transform, for studying sound propagation in an atmosphere including the effects of wind and temperature gradients. Their model assumes that the winds are horizontal and that the properties of the media only vary with altitude. They also assume that a one-dimensional Fourier transform will give correct results for propagation in the spatial direction corresponding to the wave number component in the presence of wind. Nijis and Wapenaar's implementation has caused some further discussions [94-95].

Many researchers have used the fast field program (FFP) [101, 109-111] or the chirp $z-$transform fast field program (CFFP) [93] to study the problem of sound propagation in an inhomogeneous medium with an arbitrary vector wind profile. The FFP and CFFP were developed for evaluation of the far-field sound pressure due to a point monopole source embedded in a medium with a vertically stratified effective sound-speed profile. Wilson [1] has modified the wave equation and allowed the FFP to compute the sound field in a stratified, moving medium. The computational method involves a 2-D FFP of horizontal wave-number spectrum rather than the previous 1-D FFPs. However, the maximum range of the calculations is limited by the computation time and memory requirement. Li *et al* [2] have developed a new CFFP-type program designated CFFPW that allows vector wind to be taken into account rather than the use of the effective sound-speed model in the conventional CFFP.

To address the effect of wind gradients separately from that of temperature gradients on sound propagation, a numerical approach that involves the evaluation of an inverse Fourier integral by the calculation of residues [58] can be developed. The residue theorem has been used in obtaining analytical solutions for a stationary stratified medium [3, 8]. The solution is known as the residue series solution in an upward refracting medium [3, 5, 8], and the normal mode solution in a downward refracting medium [9]. Pierce [3] has derived the solution for upward refraction above a complex impedance plane in terms of the residue series solution. Berry and Daigle [15] have improved Pierce's residue series solution to achieve greater accuracy. Raspet *et al* [9] have derived the normal mode solution from the residue series for downward refraction above a complex impedance ground surface.

For sound propagation above an impedance ground in a refracting medium in the absence of wind, all these numerical models and computational codes should reduce to agree with the benchmark cases [10].

1.2 Diffraction by convex surfaces

The effects of temperature and wind velocity gradients, ignoring atmospheric turbulence, and the effects of ground terrain appear to be two separate topics. However, each of their effects on the sound field when treated separately is similar. The effects of temperature and wind velocity gradients can be deduced by analogy with propagation over certain equivalent ground shapes, and vice versa [13, 32]. There is a good analogy between propagation in a non-refracting medium having straight ray paths over a convex surface and propagation in an upward refracting atmosphere having concave curved ray paths over a flat ground [14, 45]. Many features of the sound field in an upward refracting medium can be studied under laboratory conditions over a carefully constructed convex surface. The

diffraction of sound in a manner that simulates sound propagation outdoors in an upward refracting medium due to a temperature or wind velocity gradient offers an interesting problem for study.

There has been considerable research into diffraction of electromagnetic waves by convex cylinders [21, 105, 106]. The diffraction of sound by convex surfaces, with a radius of curvature much larger than a wavelength, has been treated in great detail since the initial work of Fock [48] for electromagnetic waves and subsequent works in acoustics by Pierce [3] and others [15, 19, 20]. In recent years a substantial effort has been made in order to develop asymptotic solutions for propagation over arbitrarily but sufficiently smooth convex surfaces [107]. There are two particular types of convex surface, that of a sphere and that of a long circular cylinder, that simulate sound propagation over a flat ground with a sound speed gradient caused by temperature and sound propagation over a flat ground with a sound speed gradient due to wind velocity, respectively.

Berry and Daigle [15] have proposed that the sound field above a cylindrical surface with no refraction is analogous (*cf.* Figure 3.1) to the sound field above a flat ground with the so-called bilinear sound speed gradient, described by Equation (1) in References [18]. They have improved Pierce's residue series solution [3] and derived a residue series solution that enables the prediction of the sound field in the regions including the penumbra, the insonified area and the shadow zone. The numerical predictions of Berry and Daigle's adaptation [15] agree well with their experimental measurements deep in the shadow zone, but the agreement is less satisfactory in the vicinity of the shadow boundary.

Di and Gilbert [85] have indicated that a stricter analogy exists between a cylindrical surface above which there is no refraction and a flat ground with the sound speed gradient

varying with height according to an exponential profile rather than a bilinear profile. This is expected to lead to the residue series solution for an exponential profile.

Pierce [26] divided the space external to a convex surface into a number of distinct regions (*cf.* Figure 1.1). These include an outer region in which the solution is adequately described by geometrical acoustics, an inner region that is in the immediate vicinity of the surface, and other regions as shown in Figure 1.1. The so-called geometrical acoustics solution for plane waves above a convex surface is described as a superposition of an incident and a reflected ray (*cf.* Figure 1.2). The geometrical acoustics solution for a point source radiating over a curved surface of finite impedance follows the same approach as that used to derive the geometrical acoustics solution for a plane incident wave [26, 29].

Pierce [26] suggested use of the matched asymptotic expansions (MAE) method for the inner region problems. The use of the MAE has proved useful in predicting the sound field in the penumbra region behind a convex cylinder [19, 20], but the MAE theory is restricted to the propagation of plane waves.

It has been shown [3] that the residue series solution developed for the case of a stratified atmosphere is valid for propagation above a curved surface, with approximations consistent with those applicable to a stratified atmosphere, if the vertical distances are interpreted as heights transverse to the curved surface, the horizontal distance is interpreted as the arc length along the curved surface, and the radius of curvature is interpreted as the radius of the curved surface.

The fast field program (FFP) [10] was developed for the prediction of underwater sound propagation [118-120] and has been adapted to model propagation in a stratified atmosphere [93, 101, 109]. Therefore, by means of the analogy described earlier, FFP can be used to predict the diffraction of sound by a convex surface.

An alternative approach for modelling sound propagation over a curved surface is to use Green's function techniques to develop an integral equation with the air-ground surface as the domain of integration [25, 108]. This integral equation is solved by the boundary element method (BEM). The use of the BEM has proved powerful in predicting the sound field diffracted by a barrier on a flat surface [24, 52]. In the BEM method, a curved surface may be modelled as a sequence of barriers [24].

To simulate the sound speed gradient induced by a temperature gradient, a spherical surface may be considered [32]. The geometrical solution for scattering of sound by a spherical surface is well-known [22, 106]. Following the procedures described by Jones [22] using the asymptotic approximations [106] for the Legendre polynomials, a factor connecting the sound field above a large spherical surface and that above a long cylindrical surface may be found [22].

Usually most theories available for predicting sound propagation over curved surfaces are expressed in terms of sound radiation from a point monopole source or for a plane incident wave. In practice, however, many noise sources are directional. For example, source descriptions in terms of dipoles are also useful [148, 149].

It appears difficult to extend the current MAE theory to allow the prediction of the sound field due to a dipole source. However, it is possible to extend the residue series solution for a monopole source to the residue series solution for dipole sources.

As well as the theoretical studies that have been pursued in this field, experimental investigations into sound propagation over convex cylinders have made considerable progress during the last twelve years [15, 20, 29, 32, 113, 104].

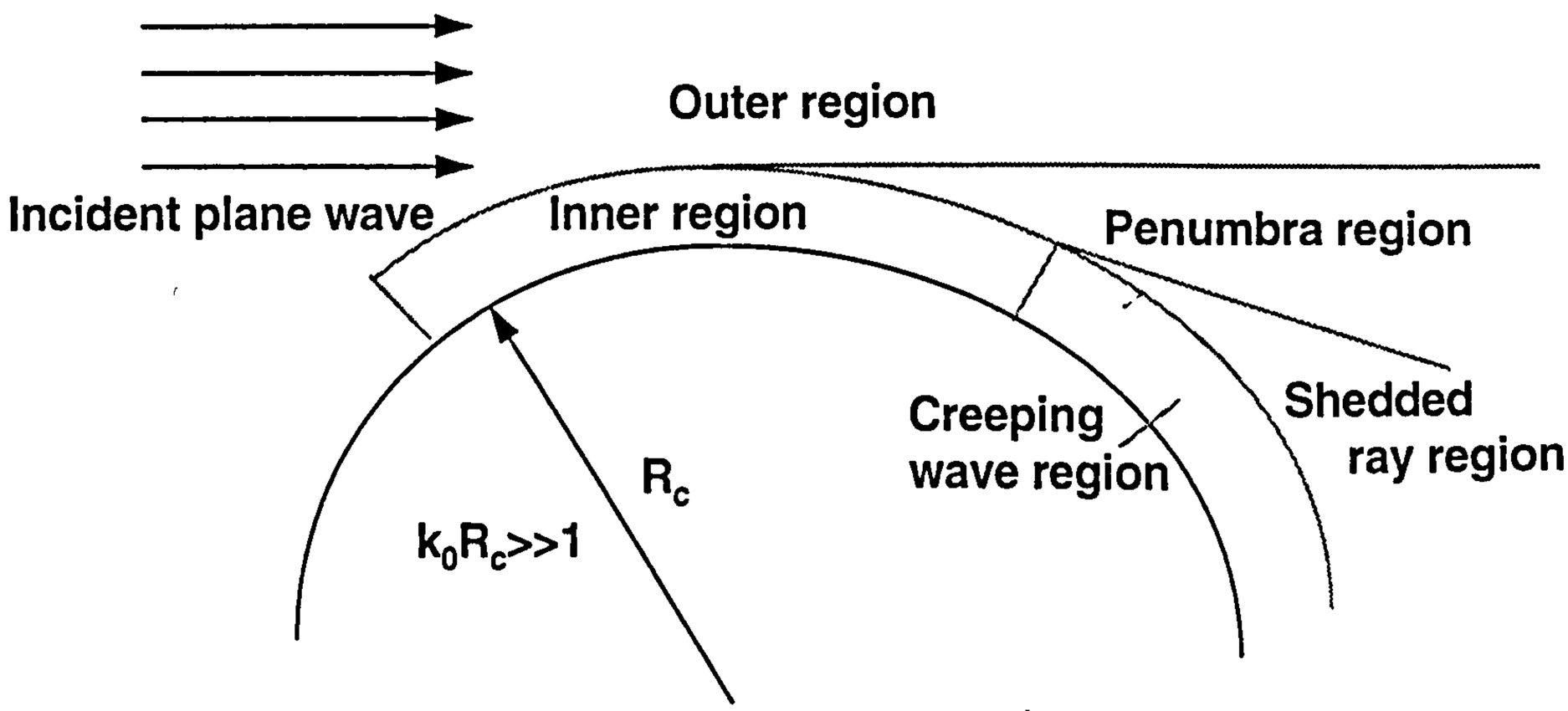

Figure 1.1 Different wave propagation regimes in the vicinity of the apex of a curved surface when a plane wave is incident from the left.

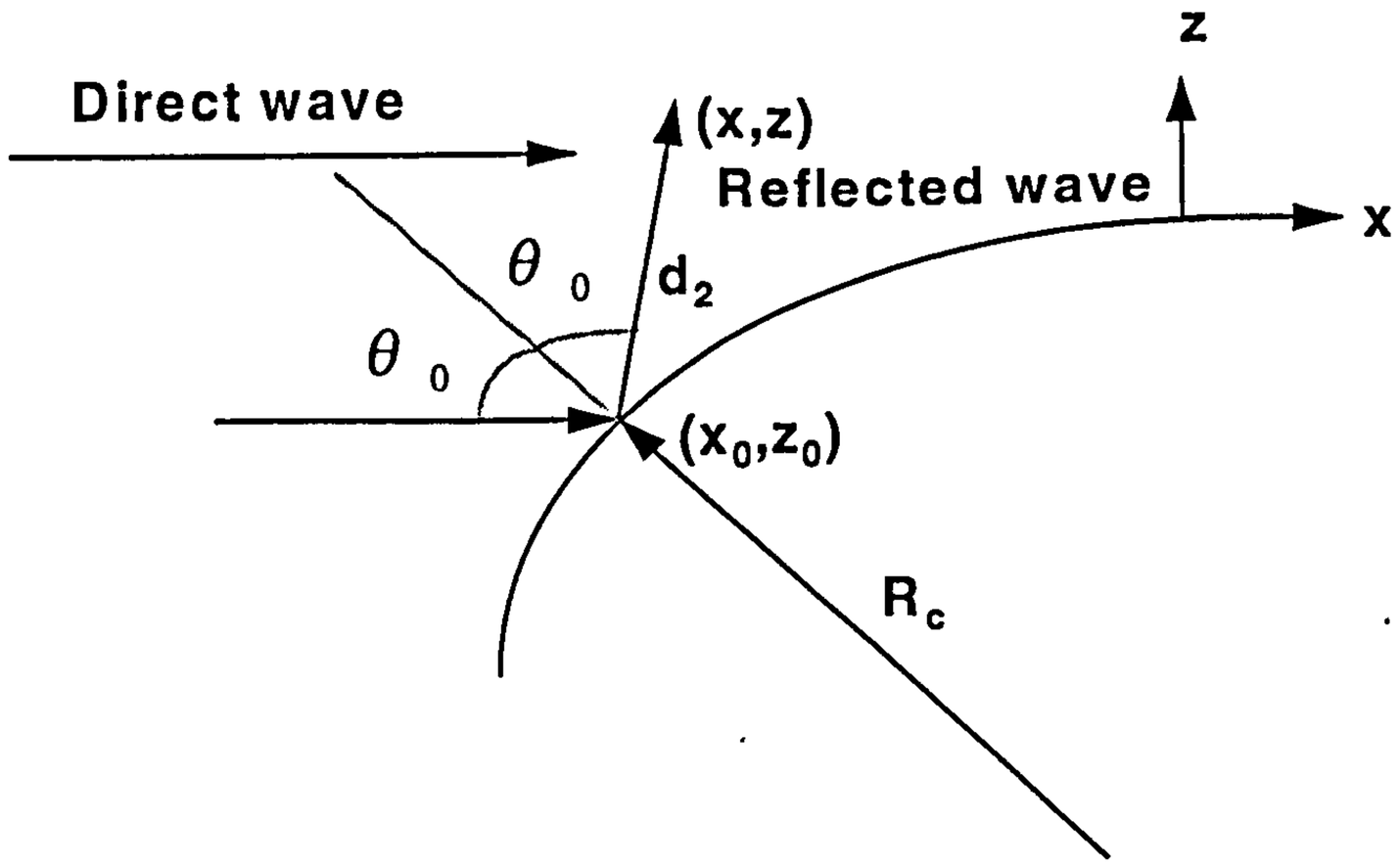

Figure 1.2 Illustration of the geometrical acoustics solution for the sound field in the illuminated region above a curved surface.

Almgren [32] used a curved ground scale model to simulate the effect of refraction due to a sound speed gradient on outdoor sound propagation. He measured the sound pressure relative to free field from a spark source above a convex cylinder that was constructed by a 4 mm thick Perspex sheet with an actual radius of curvature of 6.8 m [115, 116]. As he used a scale factor of 1:100, this radius of curvature corresponds to a constant sound speed gradient of $-0.5\ s^{-1}$ in full-scale. Almgren reported good agreement between the ray-theoretical study and his measurement results.

Berry and Daigle [15] conducted a series of laboratory experiments of the diffraction of sound by rigid and finite impedance convex surfaces. The rigid convex surface was the cross section of a cylinder of radius 5 m, built by overlaying sheets of 0.25 in. masonite on a curved support structure. The finite impedance convex surface was obtained by covering the rigid surface with felt. The measurements were made in the frequency range between 0.3 and 10 kHz at receivers placed in all of the area within, and above, the shadow zone, for various source heights. Their measurements were compared to predictions of the residue series solution or of the geometrical acoustics solution. Berry and Daigle found that deep within the shadow zone, the residue series solution predictions and the measurements agreed typically within 0.5 dB. The same agreement is obtained between the measurements and the geometrical acoustics solution well above the shadow boundary. However, they reported that in the intermediate region the residue series solution does not converge at any frequency when ten terms are calculated. In the vicinity of the shadow boundary, predictions from the residue series solution were found to differ from the measurements by 2-5 dB.

Berthelot [19] suggested use of the shortest distance between the source and the receiver, d, instead of the arc distance along the surface boundary from the source to the receiver,

r, in the residue series calculation that involves a Hankel function $H_0^1(k_n r)$, where k_n is the horizontal wave number of n th term. He demonstrated that the residue series solution for a bilinear profile with his interpretation of d yields better agreement with Berry and Daigle's measurements [15] in the penumbra region behind a long cylinder, in comparison with those using r. However, there is no rigorous justification for this modification [19]. It is expected that use of the residue series solution for an exponential profile might solve this problem because of the stricter analogy [85] that exists between propagation over a cylindrical surface and propagation in an exponential sound speed profile.

Kearns [29], Chambers [113], Berthelot and Zhou [20] used a convex surface formed from a section of plywood with a radius of curvature of approximately 2.5 m to investigate diffraction of sound. A surface with smaller finite impedance was obtained by covering the plywood with carpet. Both surfaces were described by the Delany and Bazley model [34] with flow resistivity of 80 MPa s m^{-2} for bare plywood and 1.6 kPa s m^{-2} for the carpet-covered surface. Their data were compared with predictions from the MAE theory and from the geometrical acoustics solution.

Berthelot and Zhou [20] found an interesting phenomenon in the penumbra region. The excess attenuation shows dips, which are equivalent to their peaks, at 10 kHz along the line of sight behind the apex of the carpet-covered convex surface. There are small discrepancies between the MAE calculations and the measurements. They mentioned that the cause of this phenomenon is not well understood. In Chapter 4, we investigate this phenomenon and show that the discrepancies increase as the scaled and nondimensionalized admittance, q, becomes larger.

1.3 Diffraction by concave surfaces

The diffraction of sound in a way that simulates sound propagation outdoors in a downward refracting medium due to a temperature or wind velocity gradient is also an interesting topic. There is a similar acoustic analogy for propagation above a concave surface to that described in Chapter 1.2 above a convex surface [45]. The analogy exists between propagation in a non-refracting medium having straight ray paths over a concave surface and propagation in a downward refracting atmosphere having convex curved ray paths over a flat ground [14, 45]. To validate the relevant theories relating the sound propagation in a downward refracting atmosphere, it is convenient to make measurements in the analogous configuration using laboratory conditions and studying propagation over a concave surface.

The FFP [101, 109-111] and the BEM [24, 52] have been used to predict sound propagation in a downward refracting medium [9, 10], and, therefore, they can be adapted to predict the diffraction of sound by a concave surface.

Rasmussen [6] has derived equations for sound pressure in terms of the Fock functions [48]. Raspet *et al* [9] follow the notation used by Berry and Daigle [15] for upward refraction. They have evaluated the sound pressure wave equation using the normal mode method, which resolves the propagating wave into discrete modes, for sound propagation in a downward refracting atmosphere above a complex impedance ground surface. The normal mode method has been used to predict low-frequency sound propagation from explosions [121] and from wind turbines [122]. In the normal mode method, the residue of the integrand is calculated at each pole of the integral, and the results summed to form the normal mode solution [9, 10]. According to Berry and Daigle's analogy [15], the sound

field above a concave surface with no refraction is analogous (*cf.* Figure 3.2) to the sound field above a flat ground with a positive bilinear sound speed gradient. Strictly the analogy is between propagation over a cylindrical concave surface above which there is no refraction and propagation over a flat ground with the sound speed gradient varying with height according to an exponential profile rather than a bilinear profile [85]. The normal mode solution is relatively robust [123], and it has the potential advantage of being able to predict propagation in various sound speed profiles [35]. The normal mode solution for a bilinear profile derived by Raspet *et al* [9] can be extended to the normal mode solution for an exponential profile. The resulting normal mode solution may be used to predict diffraction of sound by a cylindrical concave surface that simulates sound propagation in a downward refracting medium ignoring atmospheric turbulence.

During recent decades, much less attention has been paid to the diffraction of sound by a concave surface than to diffraction by a convex surface. Almgren [32] found that it is reasonable to simulate the influence of a positive and constant sound speed gradient on downward sound propagation by a concave surface. This method was validated by a ray-theoretical study and by experiments over a rigid (but with finite impedance) concave surface. The experiments were conducted above a cylindrical concave surface which was constructed from a 4 mm thick Perspex sheet with an inverted radius of curvature of 38 m. As he used a scale factor of 1:100, this radius of curvature corresponds to a constant sound speed gradient of $0.09\ s^{-1}$ in full-scale. The experimental results were compared to the sound pressure calculated using the theories of Pridmore-Brown [77, 117], Pierce [3], and Rasmussen [49] for a temperature stratified medium. The agreement is as good for positive gradients as for negative gradients over a rigid ground. Almgren suggested that this simulation should also be valid if the surface has finite impedance.

Gabillet *et al* [46] applied the Gaussian beam approach to atmospheric sound propagation in the presence of refraction above a ground surface. Calculations obtained from the Gaussian beam solution were compared with experimental measurements made above a concave surface to simulate propagation under downward refraction in the cases of both hard and finite impedance surfaces. The experiments were made above a hard cylindrical concave surface and a cylindrical concave surface of finite impedance. The hard concave surface was constructed by laying sheets of masonite over a concave structure with a radius of curvature of 20 m to simulate propagation in the presence of a sound speed gradient of 17.15 s^{-1}. The concave surface of finite impedance was obtained by using several layers of felt to cover the hard concave surface. They claimed that satisfactory agreement between Gaussian beam theory predictions and data exists only for higher frequencies when the receiver is not too close to the ground. When the receiver is within a few wavelengths of the ground, the Gaussian beam solution is difficult. Above a hard concave surface, good agreement between theoretical predictions and data was found only beyond 2 kHz, and above an impedance concave surface, agreement was found only for frequencies higher than 6 kHz.

The diffraction of sound by a concave surface, to simulate sound propagation in a downward refracting medium due to dipole sources has not been studied previously according to literature currently available. The normal mode solutions for a monopole source are extended to dipole sources in Chapter 5.

1.4 Surface waves

The propagation of sound from a point monopole source above porous ground surfaces is often modelled by the propagation of spherical waves above a complex impedance plane.

Some of the integral solutions to this problem show a pole in the complex wave number that leads to a distinct term that possesses the properties of a surface wave.

Tolstoy [70] describes a criterion for a wave to be a true surface wave based on the limit of the upper half-space becoming incompressible, *i.e.* the speed of sound tends to infinity while the density remains constant. A true surface wave will propagate along the surface independent of the body wave in the upper half-space. Raspet and Baird [43] have applied Tolstoy's criteria [70] to spherical waves propagating above an impedance boundary in a homogeneous medium and demonstrated that a true surface wave propagates along the surface independently of the body wave.

The existence of a surface wave above a porous ground in a homogeneous medium has been generally accepted [44]. For a source located close to the ground, a surface wave only exists when the reactive component of the acoustic impedance exceeds its resistive component [44, 91]. Embleton and Daigle [124] suggested that surface waves could be explained further by considering the particle motion. The surface waves exist above an impedance surface when the surface can influence the airborne particle velocity near the ground and reduce the phase velocity of sound waves in the air at the surface. Some of the energy in the air is trapped, regardless of the curvature of the incident sound field, and remains near the surface as the wave propagates from the source to the receiver [44, 68]. Daigle [67] and Daigle *et al* [68] examined the evidence for the nature of surface waves. They indicated that the surface wave is characterized by cylindrical spreading with increasing horizontal range, and by exponential decay with increasing vertical height above the ground, and propagates at a phase speed less than the speed of sound in the air.

The surface wave over an impedance surface is a phenomenon that is special to acoustic waves. It does not exist for electromagnetic waves over ordinary ground because the electromagnetic reactance is inductive [91].

Some early studies of the fundamentals connected with acoustical surface waves were carried out by Brekhovskikh [63]. He examined the acoustic surface waves for a comb-like structure and a boundary with an elastic impedance. Ivanov-Shits and Rozhin [64] continued Brekhovskikh's work by attempting to verify experimentally the existence of the surface waves above a lattice of thin aluminum strips mounted on a rigid sheet of plywood. They measured the horizontal and vertical sound field over this comb-like structure using a battery of eleven speakers, rather than a point source that has been used in most work. Although some agreement between the measured and calculated values of the vertical attenuation and phase velocity was obtained, the experiment was not conclusive proof that the surface wave exists.

Thomasson [65] measured the vertical and horizontal attenuation of the surface wave over a rigidly backed porous layer, and used these measurements to derive values of the impedance. He showed a good agreement between the derived values of the impedance and the values measured using an impedance tube. Donato [42] studied the vertical and horizontal attenuation of the surface wave as a function of frequency by a similar method to Thomasson. His measurements were made above a square lattice of cavities constructed from overhead lighting panels mounted on a wooden board. Donato reported that the values of the impedance that were deduced from the measurements of the vertical and horizontal attenuation of the surface waves were consistent with the theoretical calculations of impedance.

The experiments conducted by Daigle [67] produced results indicative of a surface wave and showed the initial single pulse separating into two components with increasing horizontal range. This phenomenon has been confirmed by subsequent laboratory measurements above other similar model surfaces [68, 75]. Hutchinson-Howorth and Attenborough [69] performed similar experiments above a lattice-on-board surface using pulses. They reported that as the source and the receiver separation increases the surface wave arrival becomes distinct. The surface wave magnitude decreases rapidly with increasing receiver height due to the exponential decay. Daigle *et al* [44] studied the propagation of acoustical pulses generated from filtered gated sine waves above the model surface used by Donato [42]. They found good overall agreement between calculated and measured pulses despite the fact that the measured pulses do not show as much separation as expected for the idealized surface. It has been concluded [44] that the surface wave could be seen as a separate arrival from a component arriving earlier travelling at the speed of sound in air, above a porous ground in a homogeneous medium.

Acoustic surface waves along the ground have been discussed extensively for the case of a homogeneous atmosphere [40, 41, 74, 125, 126], but not for the case of a refracting medium. Raspet *et al* [8] have studied the relationship between the spherical wave analysis of sound propagation [42] in a homogeneous atmosphere and the residue series solution [3, 15] for upward refraction, and examined the behavior of the Airy function solution for upward refraction as the sound speed gradient tends to zero. They have found the relationship of this limit to Donato's formulation for the homogeneous medium and shown that in an upward refracting atmosphere, for impedance phase angle greater than $\pi/3$, there is a residue series term that becomes the surface wave pole described by Donato, and that the surface wave contribution is most important in the transition region from the illuminated area to the shadow zone.

Pierce [3] has suggested a technique of pole searching for a ground surface of complex impedance in an upward refracting medium. Raspet *et al* [8] have indicated that this technique only works well for impedance phase angles less than $\pi/3$, but not for moderately large q when the phase angle is greater than $\pi/3$, where q is the scaled and nondimensionalized admittance (*cf.* Chapter 2). They modified Pierce's technique and have proposed a new numerical scheme [8] that works for arbitrary phase and magnitude of q.

The existence of the surface wave in an upward refracting medium has been predicted by Raspet *et al* [8], but has not been observed unequivocally in propagation experiments. The lack of conclusive confirmation of surface waves in a refracting atmosphere has led to some controversy about their existence.

The acoustic analogy makes it possible to study the surface waves above a convex surface and hence to simulate sound propagation over an impedance ground in an upward refracting medium. A suitable comb-like surface has an impedance with an imaginary part that exceeds the real part. If the surface waves propagate at a velocity less than the velocity of the creeping waves, then the surface waves might be expected to show up as a separate arrival from a component arriving earlier travelling at the creeping wave speed.

Raspet *et al* [8] have assumed that a particular residue series term is a surface wave pole since it behaves in a different manner than the other residue series contributions. This assumption is checked in Chapter 6 by studying the properties of the surface waves above a convex surface.

1.5 Diffraction by a barrier in a refracting medium

Over the last half of this century, extensive research work has been carried out on sound propagation outdoors in the presence of a noise barrier, for the purpose of predicting barrier performance under a variety of conditions. From the vast literature [127-142] on predicting the diffracted sound field around a barrier, only a few studies have been concerned with estimating the performance of a barrier in a refracting medium.

Maekawa [127] investigated Kirchhoff's diffraction theory [128] and made model experiments. He proposed an empirical chart for predicting the diffraction of sound around a semi-infinite plane barrier in a free field. This method can be extended to predict the diffraction of sound around a semi-infinite barrier on the ground [135, 138, 139]. He also suggested a simple method for estimating the performance of a finite length barrier, based on the replacing an actual barrier by an equivalent thin screen with diffraction treated by the Kirchhoff approximation.

Pierce [129] developed asymptotic expressions for waves generated by a point monopole source in the vicinity of a barrier applicable at points both near and far from the shadow zone boundary of the barrier.

Sezenc [52] used the boundary element method (BEM) to study the diffraction of sound by barriers on the ground with a variety of shapes. Hothersall *et al* [24] used the BEM to predict the sound pressure behind a barrier on an impedance plane for various barrier configurations.

These treatments are restricted to propagation in a homogeneous medium with a constant sound speed profile. However, in practice gradients of temperature and wind velocity cause

the atmosphere to be inhomogeneous with a sound speed variation. In an inhomogeneous medium, sound ray paths become curved over the barrier. These curved ray paths may influence the performance of a barrier.

It is common to find that theoretical predictions of the barrier attenuation do not agree with measurements in field experiments. The discrepancies are mainly caused by the influence of atmospheric factors such as turbulence, wind and temperature gradients that have been ignored in most previous theoretical studies. De Jong and Stusnick [57] performed scale model experiments [140] in a low-speed wind tunnel to investigate the effect of the wind on the total insertion loss that is equivalent to the barrier reduction in their paper [57]. The total insertion loss of a barrier, which we denote by IL_{total}, is defined as the difference between the sound pressure level without a barrier in a homogeneous medium and the sound pressure level with a barrier in a refracting atmosphere. De Jong and Stusnick reported that in general IL_{total} increased for upwind propagation and decreased for downwind propagation. However, values of IL_{total} fluctuated significantly during the measurements due to the effects of turbulent scattering around the barrier.

Salomons [141] used the parabolic equation (PE) method to study sound diffraction by a barrier on an absorbing ground in a downwind situation with logarithmic sound speed profiles [142]. His work has shown that meteorology, apart from the effects of turbulence, often has significant effects on sound diffraction by a barrier, particularly in downwind situations. Salomons [53] also developed a new model, which is based on the theory of Pierce [3] for diffraction by a wedge in a homogeneous medium and Snell's law for atmospheric refraction, to study a noise barrier in a refracting atmosphere. He reported that for downwind propagation over a barrier on absorbing ground, *e.g.* grassland, the total insertion loss IL_{total} decreases with increasing distance behind the barrier. During

downwind propagation over a barrier on reflecting ground, however, the total insertion loss is predicted to remain constant. For upwind propagation, Salomons indicated that a noise barrier is very ineffective in the refractive shadow region. Further he found that the so-called barrier-induced wind-speed gradients have a small effect on the total insertion loss of the barrier.

The total insertion loss, IL_{total}, however, may not be a clear measure of the effectiveness of a barrier in a refracting medium because it includes meteorological effects. Gabillet *et al* [46] used a different measure, the barrier insertion loss, which we denote by $IL_{barrier}$, to characterize the effectiveness of a barrier on a curved surface that simulates propagation in a refracting medium. $IL_{barrier}$ is defined as the difference in sound pressure levels without and with a barrier. They conducted laboratory experiments above a rigid or a felt-covered concave surface, with a radius of curvature of 20 m, in the presence of a rigid thin barrier. Predictions from the Gaussian beam solution were compared with their measurements, but the results are not shown in terms of $IL_{barrier}$. Gabillet *et al* [46] reported that downward refraction does not necessarily destroy $IL_{barrier}$ when the ground surface is rigid. An explanation for this phenomenon is that the barrier may block the caustics resulting from the rays with multiple reflections near the ground. In the case where the concave surface is the felt-covered, Gabillet *et al* [46] claimed that the barrier insertion loss is negligible.

Rasmussen [54] developed a hybrid model for predictions to compare with his experimental data. The hybrid model is based on a combination of diffraction theory originating from Kouyoumjian and Pathak [143, 144] for a simple barrier in a stationary homogeneous atmosphere, and a Hankel transform [145, 146] for a point source in a layered atmosphere over an impedance ground surface. The experiments were made with a barrier placed on absorbing ground (the effective flow resistivity at the ground

$\sigma_e = 20$ kPa s m^{-2}, the effective rate of change of porosity with depth $\alpha_e = 60$ m^{-1}) under upwind and downwind conditions in a small open ended boundary layer wind tunnel with no temperature gradients. Data was obtained in a scale model using a 1:25 scaling factor and presented in terms of excess attenuation, EA, which is defined as sound pressure level relative to free field sound pressure level. Rasmussen [54] reported that this model is only useful under upwind conditions, but not under downwind conditions. For upwind propagation, the predictions of this model do not agree well with the measurements in the interference pattern, but there is a general agreement. For downwind propagation, there are considerable discrepancies between the model predictions and the measurements.

Hothersall *et al* [24] have shown that the BEM can be used to predict the sound field behind a barrier with a variety of configurations from a point source. In Chapter 7, we study the effect of a refracting medium on the performance of a barrier for various ground impedance surfaces by approximating a barrier on a curved surface by a multi-sided polygon and by using the existing BEM program.

1.6 Summary

This chapter has described the rationale for the thesis, has reviewed the existing theoretical and experimental work from the acoustical literature, and has given a brief introduction to each of the following chapters.

Chapter 2

Sound propagation outdoors in the presence of wind†

The study of sound propagation in the atmosphere remains a very challenging task even though a substantial effort has been made in this area in the last decade. Numerical methods for calculating propagation from a point monopole source over a locally reacting impedance ground in the presence of wind and temperature gradients have been developed recently [4-6]. These include a number of approximate schemes that address the effects of wind and temperature gradients by taking an effective sound speed into account. Use of an effective sound speed profile does not give an accurate representation of the propagation of sound in the presence of a wind gradient. It is possible to develop a rigorous integral formulation that includes a wind velocity profile explicitly without imposing an effective sound speed profile.

In this chapter, we propose an alternative method for calculating the effect of wind on sound propagation outdoors. It involves the evaluation of an inverse Fourier integral by contour deformation according to the residue theorem [58]. This method has been used when analytical solutions for propagation of sound in a stationary stratified medium are concerned [59]. The solution is known as the residue series solution for an upward refracting medium [3, 5, 8], or the normal mode solution for a downward refracting

† Parts of the work reported here have been published in [35].

medium [9]. This chapter offers a generalization of the previous results, and the previous theory is extended to include explicitly vector wind velocity profiles. As in previous studies, the effects of gravity, turbulence, absorption of sound, and the variation of density in the atmosphere are disregarded in this study.

2.1 The influence of wind and temperature gradients on sound propagation

To obtain insight into how wind and temperature gradients effect sound propagation separately, we begin by considering a point monopole source (strength S_0) located at $(0,0,z_s)$ above a locally reacting surface in a moving stratified medium. The mean velocity of air $\mathbf{u}(z)$, and sound speed in the absence of wind $c(z)$ only vary with the height z. These variations cause the rays initially leaving the source in nearly horizontal directions to bend upwards or downwards with a radius of curvature [3] given by

$$R_c = \bar{c}(z)/|d\bar{c}(z)/dz|_{z=0}, \tag{2.1.1}$$

where the effective sound speed, $\bar{c}(z)$, is defined as [39]

$$\bar{c}(z) = c(z) + \mathbf{u}\cdot\mathbf{r}, \tag{2.1.2}$$

where $\mathbf{u}(z) = (u_x, u_y, 0)$ is the wind velocity assuming that the velocity is negligible in the z-direction. For mathematical convenience, the vector wind velocity can be expressed in a polar form

$$u_x = u\cos\psi_w \text{ and } u_y = u\sin\psi_w, \tag{2.1.3}$$

where u and ψ_w are the magnitude and the angle between the wind direction and the horizontal direction pointing from source to receiver, respectively.

Using the continuity and momentum equations [60], and the method of Fourier transformation, the acoustic pressure can be written in an integral form [61].

Introduce a Fourier transform pair for acoustic pressure $p(x,y,z)$ and $P(k_x,k_y,z)$ where

$$p(x,y,z)=\frac{1}{(2\pi)^2}\int_{-\infty}^{\infty}\int_{-\infty}^{\infty}P(k_x,k_y,z)\exp\left[i(k_x x+k_y y)\right]dk_x dk_y, \tag{2.1.4}$$

and

$$P(k_x,k_y,z)=\frac{1}{(2\pi)^2}\int_{-\infty}^{\infty}\int_{-\infty}^{\infty}p(x,y,z)\exp\left[-i(k_x x+k_y y)\right]dxdy. \tag{2.1.5}$$

Here k_x and k_y may be considered as the horizontal components of the wave number in a cylindrical polar coordinate system and they can be expressed in polar form:

$$k_x=k_r\cos\varepsilon \text{ and } k_y=k_r\sin\varepsilon, \tag{2.1.6}$$

where ε is the azimuthal angle related to the positive x axis, see Figure 2.1, and k_r is the magnitude of the horizontal wave number. In Equation (2.1.4), time dependence $\exp(-i\omega_0 t)$, where ω_0 is the angular frequency of the source, is understood. This satisfies the inhomogeneous Helmholtz equation if the velocity potential $\tilde{\Phi}(k_r,z)$ satisfies

$$\frac{d^2\tilde{\Phi}}{dz^2}+k_z^2(k_x,k_y,z)\tilde{\Phi}=2\pi i S_0\delta(z-z_s), \tag{2.1.7}$$

where S_0 is the source strength, and

$$k_z(k_x,k_y,z)=+\sqrt{(\omega_m/c)^2-k_x^2-k_y^2}, \tag{2.1.8}$$

may be interpreted as the vertical component of the wave number. The variable

$$\omega_m\left(k_x, k_y, z\right) = \omega_0 - k_x u_x - k_y u_y, \tag{2.1.9}$$

may be interpreted as the convected angular frequency. In the transformed space, the velocity potential and acoustic pressure are related by

$$P = \rho\omega_m \tilde{\Phi}. \tag{2.1.10}$$

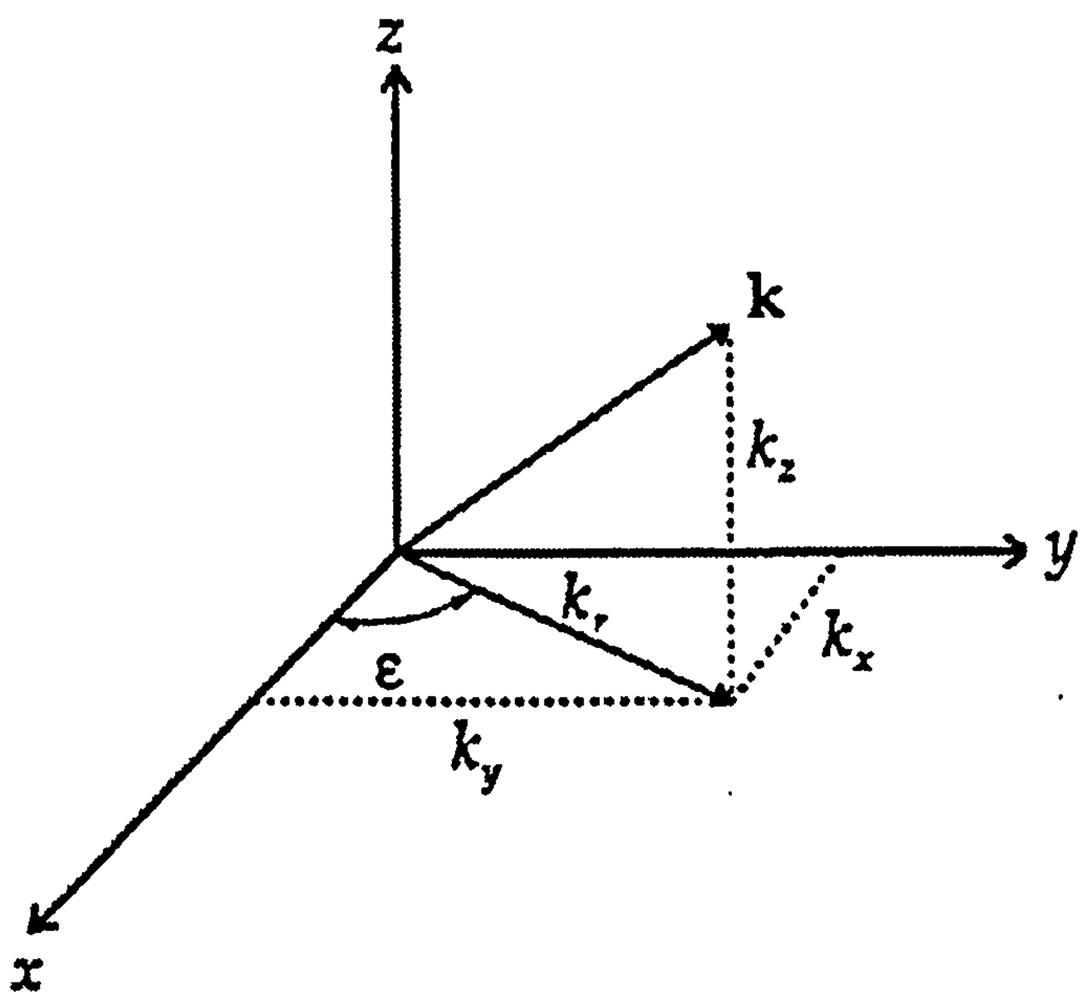

Figure 2.1 The spatial position of the propagation vector, **k** and its components.

To obtain a finite and bounded solution for the acoustic pressure, it is important to select the positive root of k_z.

Substituting Equations (2.1.3) and (2.1.6) into Equation (2.1.9), the convected angular frequency ω_m can be rewritten in the polar form as

$$\omega_m(k_r,\varepsilon,z)=\left[k_0 n_c(z)-k_r M(z)\cos(\varepsilon-\psi_w)\right]c(z) \tag{2.1.11}$$

where $k_0 \equiv k(0)=\omega_0/c_0$, $c_0 \equiv c(0)$, $M(z)=u(z)/c(z)$ is the Mach number of wind, and

$n_c(z)$ is the index of refraction in the absence of wind, defined as

$$n_c(z)=k(z)/k_0 . \tag{2.1.12}$$

Equation (2.1.8) then becomes

$$k_z(k_r,\varepsilon,z)=+\sqrt{\kappa^2(k_r,\varepsilon,z)-k_r^2} \tag{2.1.13}$$

where

$$\kappa(k_r,\varepsilon,z)=k_0 n_c(z)-k_r M(z)\cos(\varepsilon-\psi_w) \tag{2.1.14}$$

is the wave number in the presence of wind. In the absence of wind, Equation (2.1.13)

reduces to

$$k_z(k_r,\varepsilon,z)=+\sqrt{k^2(z)-k_r^2} \tag{2.1.15}$$

which is equivalent to the well-known form given in previous publications, for example, in References [4, 36].

For simplicity of the subsequent analysis, the problem is restricted so that there is only one turning point at $z=z_t$ for a given k_r in Equation (2.1.13). On the basis of ray theory, the turning point happens where the slope of a ray path is zero, and corresponds to $k_z(k_r,\varepsilon,z_t)=0$. The analytical solutions for the transformed pressure $P(k_r,\varepsilon,z)$ can be found differently for an upward refracting medium and for a downward refracting medium according to the corresponding sound speed gradient and boundary condition in each case [8, 9]. In the following sections, these two different situations will be discussed separately.

2.2 An upward refracting medium

A solution for $\tilde{\Phi}$ in Equation (2.1.7) is given by [62]

$$\tilde{\Phi}(k_r,\varepsilon,z)=\left[\frac{\xi_<\xi_>}{k_<^2k_>^2}\right]^{1/4}\left[C_1\left(\xi/k_z^2\right)^{1/4}\mathrm{Ai}(-\xi)+C_2\left(\xi/k_z^2\right)^{1/4}\mathrm{Ai}\left(-\xi e^{i2\pi/3}\right)\right] \tag{2.2.1}$$

where the subscripts < and > represent the parameters to be evaluated at heights of $z_< = \min(z,z_s)$ and $z_> = \max(z,z_s)$, and the abbreviations $\xi_< \equiv \xi(k_r,\varepsilon,z_<)$, $\xi_> \equiv \xi(k_r,\varepsilon,z_>)$, $k_< = k_z(k_r,\varepsilon,z_<)$ and $k_> = k_z(k_r,\varepsilon,z_>)$ are used; Ai( ) is the Airy function with respect to its argument; C_1 and C_2 are constants to be determined from the Sommerfeld radiation condition, the continuity of pressure at the source plane, the discontinuity of particle velocity at the source plane, and the impedance boundary condition

$$\frac{\partial P}{\partial z}+ik_0\beta P=0 \tag{2.2.2}$$

where β is the normalized specific admittance of the impedance ground. In Equation (2.2.1), the variable $\xi(k_r,\varepsilon,z)$ may be regarded as a dimensionless scale factor that characterizes the variations of wind and temperature gradients in the atmosphere defined by

$$\xi(k_r,\varepsilon,z)=\left[\frac{3}{2}\int_z^{z_t}k_z(k_r,\varepsilon,z)dz\right]^{2/3} \qquad \text{if } z>z_t \tag{2.2.3a}$$

or

$$\xi(k_r,\varepsilon,z)=-\left[\frac{3}{2}\int_z^{z_t}\sqrt{-k_z^2(k_r,\varepsilon,z)}dz\right]^{2/3} \qquad \text{if } z<z_t \tag{2.2.3b}$$

To simplify the following analyses, we adjust the source strength S_0 in Equation (2.1.7) so that the sound pressure in a homogeneous medium can be reduced to the well-known form $\exp(ik_0d)/d$ where d is the direct distance between the source and receiver. Substituting

Equation (2.2.1) into Equation (2.1.7), we obtain an approximate solution for the transformed acoustic pressure as

$$P(k_r,\varepsilon,z)=2\pi e^{i\pi/6}\frac{\omega_m(k_r,\varepsilon,z)}{\omega_m(k_r,\varepsilon,z_s)}\left[\frac{\xi_<\xi_>}{k_<k_>}\right]^{1/4}\mathrm{Ai}\left(-\xi_> e^{i2\pi/3}\right)\left[\mathrm{Ai}\left(-\xi_<\right)-\Gamma\mathrm{Ai}\left(-\xi_< e^{i2\pi/3}\right)\right], \tag{2.2.4}$$

where Γ may be considered to be the transformed reflection factor and given by

$$\Gamma=\frac{\mathrm{Ai}'(-\xi_0)-q\mathrm{Ai}(-\xi_0)}{e^{i2\pi/3}\mathrm{Ai}'\left(-\xi_0 e^{i2\pi/3}\right)-q\mathrm{Ai}'\left(-\xi_0 e^{i2\pi/3}\right)}, \tag{2.2.5}$$

where $\mathrm{Ai}'(\,)$ is the derivative of the Airy function. The subscript 0 denotes that the variable is to be evaluated at $z=0$, and q is a scaled and nondimensionalized admittance [35] defined by

$$q=ik_0\beta l \tag{2.2.6}$$

where β is the normalized specific admittance of the impedance plane, and

$$l=\left.\frac{1}{d\xi/dz}\right|_{z=0}\equiv\sqrt{\frac{\xi_0}{k_0^2-k_r^2}}, \tag{2.2.7}$$

l may be regarded as the so-called thickness of the creeping wave layer [8]. Note also that there are two other parameters, $\partial\xi_0/\partial k_r$ and $\partial q/\partial k_r$, to be determined for further calculation. They are given by

$$\frac{\partial\xi_0}{\partial k_r}=-\left(\frac{1}{\sqrt{\xi_0}}\right)\int_{z_t}^{0}\frac{k_r+M\kappa\cos(\psi_r-\psi_w)}{k_z}dz, \tag{2.2.8}$$

where ψ_r is the azimuthal angle of the receiver position, and

$$\frac{\partial q}{\partial k_r}=\left(\frac{1}{2\xi_0}\frac{\partial\xi_0}{\partial k_r}+\frac{k_r}{k_0^2-k_r^2}\right)q. \tag{2.2.9}$$

Substituting Equation (2.2.4) into Equation (2.1.4) yields the integral expression for the acoustic pressure as follows:

$$p \approx e^{i\pi/6}\sqrt{\frac{8\pi}{ir}}\int_0^{\infty}\frac{\omega_m(k_r,\varepsilon,z)}{\omega_m(k_r,\varepsilon,z_s)}\left[\frac{\xi_<\xi_>}{k_<^2k_>^2}\right]^{1/4} \times \mathrm{Ai}\left(-\xi_> e^{i2\pi/3}\right)\left[\mathrm{Ai}\left(-\xi_<\right)-\Gamma\mathrm{Ai}\left(-\xi_< e^{i2\pi/3}\right)\right]\sqrt{k_r}e^{ik_r r}dk_r \tag{2.2.10}$$

Equations (2.1.13) and (2.1.14) are used in Equations (2.2.3a) and (2.2.3b) to rewrite $\xi(k_r,\varepsilon,z)$ in the form

$$\xi(k_r,\varepsilon,z)=\left[\frac{3}{2}\int_{z_t}^{z}\sqrt{\left[k_0 n_c(z)-k_r M_e(z)\right]^2-k_r^2}\,dz\right]^{2/3} \quad \text{if } z>z_t \tag{2.2.11a}$$

or

$$\xi(k_r,\varepsilon,z)=-\left[\frac{3}{2}\int_{z}^{z_t}\sqrt{k_r^2-\left[k_0 n_c(z)-k_r M_e(z)\right]^2}\,dz\right]^{2/3} \quad \text{if } z<z_t \tag{2.2.11b}$$

where

$$M_e(z)=M(z)\cos\left(\psi_r-\psi_w\right), \tag{2.2.12}$$

is the effective Mach number. It is obvious that the effective Mach number is equal to the Mach number if the wind direction is the same as the direction of sound propagation. Furthermore, the effect of a cross-wind can be ignored because the corresponding effective Mach number $M_e(z)=0$.

2.2.1 Residue series solution

The integral Equation (2.2.10) can be evaluated by summing the contribution of the poles in the first quadrant of the complex k_r – plane [3, 8]. According to the residue theorem, it may be represented by the residue series solution

$$p(r,z)=e^{i\pi/4}\sqrt{\frac{8\pi}{r}}\sum_n\frac{\omega_m(k_n,z)}{\omega_m(k_n,z_s)}\left[\frac{\bar{\xi}_s\bar{\xi}}{\bar{k}_z^2(z_s)\bar{k}_z^2(z)}\right]^{1/4} \times\frac{\sqrt{k_n}\,\mathrm{Ai}\left(-\bar{\xi}_s e^{i2\pi/3}\right)\mathrm{Ai}\left(-\bar{\xi}e^{i2\pi/3}\right)e^{ik_n r}}{\left[\left(\bar{\xi}_0+q_n^2\right)\partial\bar{\xi}_0/\partial k_n-\partial q_n/\partial k_n\right]\left[\mathrm{Ai}\left(-\bar{\xi}_0 e^{i2\pi/3}\right)\right]^2}, \tag{2.2.13}$$

where $\bar{\xi}_0(k_n)$ are the zeros of the dispersion equation [36]

$$e^{i2\pi/3}\mathrm{Ai}'\left(-\bar{\xi}_0 e^{i2\pi/3}\right)-q_n\mathrm{Ai}\left(-\bar{\xi}_0 e^{i2\pi/3}\right)=0, \tag{2.2.14}$$

that appears in the denominator of the integrand in Equations (2.2.5), and k_n is the wave number k_r of the nth term. The overbars denote the variables to be evaluated at the pole k_n, such as $\bar{\xi}_0 \equiv \xi(k_n,0)$, $\bar{\xi}_s \equiv \xi(k_n,z_s)$, $\bar{\xi} \equiv \xi(k_n,z)$, and $\bar{k}_z \equiv k_z(k_n,z)$. The scaled and nondimensionalized admittance q_n and the thickness of creeping wave layer l_n are functions of the wave number k_n defined by

$$q_n \equiv q_n(k_n) = ik_0\beta l_n, \tag{2.2.15}$$

$$l_n \equiv l_n(k_n) = \sqrt{\bar{\xi}_0/\left(k_0^2-k_n^2\right)}. \tag{2.2.16}$$

$\partial\bar{\xi}_0/\partial\bar{k}_n$ and $\partial q_n/\partial\bar{k}_n$ in Equation (2.2.13) can be straightforwardly determined from Equations (2.2.8) and (2.2.9).

For convenience, in the following numerical analysis Equation (2.2.13) is rewritten in the form

$$p(r,z) = e^{i\pi/4}\sqrt{\frac{8\pi}{r}}\sum_n \frac{\omega_m(k_n,z)}{\omega_m(k_n,z_s)}\left[\frac{\bar{\xi}_s\bar{\xi}}{\bar{k}_z^2(z_s)\bar{k}_z^2(z)}\right]^{1/4} \times \frac{\sqrt{k_n}\,\mathrm{Ai}\left(-\bar{\xi}_s e^{i2\pi/3}\right)\mathrm{Ai}\left(-\bar{\xi}e^{i2\pi/3}\right)e^{ik_n r}}{e^{-i2\pi/3}\dfrac{\partial\bar{\xi}_0}{\partial k_n}\left\{\left[\mathrm{Ai}'(b_n)\right]^2-b_n\left[\mathrm{Ai}(b_n)\right]^2\right\}-\dfrac{\partial q_n}{\partial k_n}\left[\mathrm{Ai}(b_n)\right]^2}, \tag{2.2.17}$$

where

$$b_n = e^{i2\pi/3}\left(k_n^2-k_0^2\right)l_n^2 \tag{2.2.18}$$

are the zeros of the expression

$$\mathrm{Ai}'(b_n)+q_n e^{i\pi/3}\mathrm{Ai}(b_n)=0. \tag{2.2.19}$$

In principle, the sound field in the presence of wind can be calculated by summing the residue series terms given in Equation (2.2.17) for arbitrary wind velocity and sound speed profiles. However, closed form analytical solutions may be found only for a limited number of profiles. We shall discuss the solutions for a bilinear profile and for a linear profile in this chapter. The solution for an exponential profile will be investigated in the next chapter.

2.2.2 Numerical analysis

It should be noted that the residue series solution depends critically on the successful tracking of the poles that contribute to give the total sound field. In general, Equation (2.2.19) must be solved numerically to obtain the poles of b_n and k_n. An efficient numerical method that will work for arbitrary wind velocity and sound speed profiles is described as follows. It is convenient to introduce an error function for the dispersion Equation (2.2.19) as

$$\Delta_1(b_n) = \mathrm{Ai}'(b_n) + q_n e^{i\pi/3}\mathrm{Ai}(b_n), \tag{2.2.20}$$

and another error function to determine k_n such that

$$\Delta_2(b_n, k_n) = \bar{\xi}_0(k_n)e^{i2\pi/3} + b_n \tag{2.2.21}$$

where $\bar{\xi}_0(k_n)$ is given by Equation (2.2.11).

Extending the technique suggested by Pierce [3], we can find the poles from Equations (2.2.20) and (2.2.21) by minimizing the errors using the Newton-Raphson algorithm [16]. The first estimate used in the scheme for b_n and q_n is as follows:

$$b_n = a_n' + e^{-i\pi/6}\, q_0/a_n' \qquad \text{if } q_0 \text{ is small,} \tag{2.2.22a}$$

$$b_n = a_n + e^{2i\pi/3}/q_0 \qquad \text{if } q_0 \text{ is large,} \tag{2.2.22b}$$

where a_n' is the nth zero of the Airy function derivative, a_n is the nth zero of the Airy function [37], and

$$q_0 = \frac{ik_0\beta}{\left[2\left(|a_T|+|a_W|\right)k_0^2\right]^{1/3}}, \tag{2.2.23}$$

where a_T and a_W are the normalized sound speed gradient due to temperature and the normalized wind velocity gradient, respectively, which are defined separately by

$$a_T = \frac{1}{c(z)}\frac{dc}{dz}\bigg|_{z=0}, \tag{2.2.24}$$

and

$$a_W = \frac{1}{c(z)}\frac{du}{dz}\bigg|_{z=0}. \tag{2.2.25}$$

In the case of upward refraction, both a_T and a_W are the negative values. The scaled and nondimensionalized admittance q_n is given by

$$q_n = ik_0\beta\sqrt{\frac{b_n e^{-i2\pi/3}}{k_n^2 - k_0^2}}, \tag{2.2.26}$$

where

$$k_n = \sqrt{k_0^2 + \left[2\left(|a_T|+|a_W|\right)k_0^2\right]^{2/3} b_n e^{-i2\pi/3}}. \tag{2.2.27}$$

Substituting the trial values of b_n and q_n given by Equations (2.2.22) and (2.2.26) into Equation (2.2.20), we can find b_n by minimizing $|\Delta_1|$, as b_n are the only unknown variables in this equation. The next step is to substitute these new trial values of b_n into Equation (2.2.21) and minimize $|\Delta_2|$ to find the roots of k_n. This completes a cycle of two iterations for the determination of b_n and k_n. After running the first cycle, new values of b_n, k_n and q_n have been produced to be used as the starting values for the next cycle of iteration. The iterative process can be used repeatedly to search for the pole locations by minimizing simultaneously the magnitude of the error functions $|\Delta_1|$ and $|\Delta_2|$ until b_n, k_n and q_n converge to the required accuracy.

To ensure the successful locations of all poles, for arbitrary phase and magnitude of q_n, especially for moderately large q_n with the phase angles $[\varphi_n = \arg(q_n)]$, $\varphi_n < \pi/6$, the above method can be extended by following the numerical scheme suggested by Raspet *et al* [8]. In this case, it is found necessary to start at $b_n = a_n'$, *i.e.* $q_0 = 0$ in Equation (2.2.19) and to increase q_0 in small steps of the order of 0.01. The solutions for b_n and k_n obtained from the previous q_0 are used as the initial values in the iterative cycle for the next q_0. Until the magnitude of q_0 reaches that given in Equation (2.2.23), we can follow the method described earlier to determine the poles.

2.3 A downward refracting medium

As mentioned above, the solution for a downward refracting medium differs from that for an upward refracting medium. However, by using essentially the same technique as that used in the case of upward propagation, the analytical solution can be found in the case of downward propagation. Only the solution is presented here, the details of the analysis are omitted.

2.3.1 Normal mode solution

The solution for the transformed pressure $P(k_r,\varepsilon,z)$ in a downward refracting medium is

$$P(k_r,\varepsilon,z) = 2\pi e^{i\pi/6}\frac{\omega_m(k_r,\varepsilon,z)}{\omega_m(k_r,\varepsilon,z_s)}\left[\frac{\xi_<\xi_>}{k_<k_>}\right]^{1/4} \times \mathrm{Ai}(-\xi_>)\left[\mathrm{Ai}(-\xi_< e^{i2\pi/3}) - \Gamma\mathrm{Ai}(-\xi_<)\right] \tag{2.3.1}$$

Similarly, with some tedious analyses, substituting Equation (2.3.1) into Equation (2.1.4) yields the integral expression for the acoustic pressure as follows:

$$p \approx e^{i\pi/4}\sqrt{\frac{8\pi}{r}}\int_0^\infty \frac{\omega_m(k_r,\varepsilon,z)}{\omega_m(k_r,\varepsilon,z_s)}\left[\frac{\xi_<\xi_>}{k_<^2k_>^2}\right]^{1/4} \times \mathrm{Ai}(-\xi_>)\left[\mathrm{Ai}(-\xi_< e^{i2\pi/3}) - \Gamma\mathrm{Ai}(-\xi_<)\right]\sqrt{k_r}e^{ik_r r}dk_r \tag{2.3.2}$$

The equations above are very similar to those for the upward refracting medium except that the variables $\xi(k_r,\varepsilon,z)$ and Γ are defined differently, *i.e.*

$$\xi(k_r,\varepsilon,z) = \left[\frac{3}{2}\int_z^{z_t}\sqrt{[k_0 n_c(z) - k_r M_e(z)]^2 - k_r^2}\,dz\right]^{2/3} \quad \text{if } z < z_t \tag{2.3.3a}$$

or

$$\xi(k_r,\varepsilon,z) = -\left[\frac{3}{2}\int_{z_t}^{z}\sqrt{k_r^2 - [k_0 n_c(z) - k_r M_e(z)]^2}\,dz\right]^{2/3} \quad \text{if } z > z_t \tag{2.3.3b}$$

and

$$\Gamma = \frac{e^{i2\pi/3}\mathrm{Ai}'\left(-\xi_0 e^{i2\pi/3}\right) + q\mathrm{Ai}\left(-\xi_0 e^{i2\pi/3}\right)}{\mathrm{Ai}'\left(-\xi_0\right) + q\mathrm{Ai}'\left(-\xi_0\right)}. \tag{2.3.4}$$

In a downward refracting medium, the integral Equation (2.3.2) can be evaluated in the same manner as that used in the case of an upward refracting medium. Similarly, we can sum the contributions from the poles in the first quadrant of the complex k_r - plane for the integrand in this equation [9]. The normal mode solution is the residue series for the acoustic pressure corresponding to downward refraction:

$$p(r,z) = e^{i\pi/4}\sqrt{\frac{8\pi}{r}}\sum_n \frac{\omega_m(k_n,z)}{\omega_m(k_n,z_s)}\left[\frac{\bar{\xi}_s\bar{\xi}}{\bar{k}_z^2(z_s)\bar{k}_z^2(z)}\right]^{1/4} \times \frac{\sqrt{k_n}\,\mathrm{Ai}\left(-\bar{\xi}_s\right)\mathrm{Ai}\left(-\bar{\xi}\right)e^{ik_n r}}{\frac{\partial\bar{\xi}_0}{\partial k_n}\left\{\left[\mathrm{Ai}'(\tau_n)\right]^2 - \tau_n\left[\mathrm{Ai}(\tau_n)\right]^2\right\} + \frac{\partial q_n}{\partial k_n}\left[\mathrm{Ai}(\tau_n)\right]^2}, \tag{2.3.5}$$

where

$$\tau_n = \left(k_n^2 - k_0^2\right)/_n^2 \tag{2.3.6}$$

are the zeros of the dispersion equation

$$\mathrm{Ai}'(\tau_n) + q_n\mathrm{Ai}(\tau_n) = 0. \tag{2.3.7}$$

2.3.2 Numerical analysis

In the case of a downward refracting medium, the solutions of Equation (2.3.7) for τ_n can be found by a similar numerical method to that described earlier for the upward refraction. Accordingly, the following two error functions are introduced:

$$\Delta_1(\tau_n) = \mathrm{Ai}'(\tau_n) + q_n\mathrm{Ai}(\tau_n), \tag{2.3.8}$$

and

$$\Delta_2(\tau_n, k_n) = \bar{\xi}_0(k_n) + \tau_n, \tag{2.3.9}$$

where $\bar{\xi}_0(k_n)$ is defined by Equation (2.3.3).

Following the procedure for arbitrary phase and magnitude of q_n described earlier in the case of upward refraction, the zeros of Equation (2.3.7) as q_n increases can be traced using Newton-Raphson's method. However, the downward refracting case does not converge rapidly since most of the poles lie close to the real axis. This means that a large number of modes are required to evaluate Equation (2.3.5) accurately. The number of terms necessary for downward refraction [9] due to the presence of wind may be approximated by

$$n_{\max} \approx \frac{2fR_c}{3c_0}, \tag{2.3.10}$$

where f is the acoustic frequency and R_c is defined in Equation (2.1.1). If the gradient is truncated at a given height, the solution will not contain modes that are reflected from the gradient above this height. The height [9] corresponding to the n th mode, h_n, may be approximated by

$$h_n = \left(\frac{3\pi n}{2}\right)^{2/3} l_n . \tag{2.3.11}$$

It is found convenient to use an alternative scheme for finding τ_n, k_n and q_n. Extending the method suggested by Raspet *et al* [9], we can find the poles from Equations (2.3.8) and (2.3.9) by reducing the errors using the Newton-Raphson algorithm. Raspet *et al* [9] indicated that in the normal mode solution there is always one term, which, in the limit of large radius of curvature, approaches the form of the surface wave of the spherical wave evaluation. Since this term is only a surface wave under limited conditions, they denoted this contribution as the ground impedance mode [9]. As in the downward refraction solution, the modes of order higher than the ground impedance mode of order arise from the n th zero of the Airy function derivative to the (n -1)th zero of the Airy function as $|q_n|$ increase from zero to infinity. On the other hand, the modes of order lower than the ground

impedance mode of order arise from the n th zero of the Airy function derivative to the n th zero of the Airy function. The first estimates used for locating τ_n and q_n are as follows:

$$\tau_n = a_n' - q_0/a_n' \qquad \text{if } q_0 \text{ is small,} \qquad (2.3.12a)$$

$$\tau_n = a_m - 1/q_0 \qquad \text{if } q_0 \text{ is large} \qquad (2.3.12b)$$

where a_m is the m th zero of the Airy function, and q_0 is given by Equation (2.2.23). If n is larger than the order of the ground impedance mode, $m = n-1$. If n is smaller than the order of the ground impedance mode, $m = n$. If n is equal to the ground impedance mode, $\tau_n = q_0^2$. As the ground impedance mode arises from the first pole for $\varphi_n < 80^\circ$ [9], Equation (2.3.12b) becomes

$$\tau_1 = q_0^2,$$

$$\text{and } \tau_{n+1} = a_n - 1/q_0 . \qquad (2.3.13)$$

When $\varphi_n > 80^\circ$, the ground impedance mode arises from progressively higher mode orders. The ground impedance mode arises from the second mode when $81^\circ < \varphi_n < 83^\circ$ and from the third mode when $84^\circ < \varphi_n < 85^\circ$. When $\varphi_n = 86^\circ$, 87° and 88°, the fourth, the sixth and the ninth modes correspond to the impedance mode, respectively.

It is noted that for downward refraction, a_T and a_W are positive values in Equations (2.2.24) and (2.2.25). The admittance q_n in Equation (2.3.8) becomes

$$q_n = ik_0\beta\sqrt{\frac{\tau_n}{k_n^2 - k_0^2}}, \qquad (2.3.14)$$

where

$$k_n = \sqrt{k_0^2 + \left[2\left(|a_T| + |a_W|\right)k_0^2\right]^{2/3}\tau_n} . \qquad (2.3.15)$$

Substituting the trial values of τ_n, and q_n given by Equations (2.3.12), (2.3.13) and (2.3.14) into Equation (2.3.8), we can determine τ_n by minimizing $|\Delta_1|$, as τ_n are the only unknown variables in this equation. The next step is to substitute these new trial values of τ_n into Equation (2.3.9) and minimize $|\Delta_2|$ to find the roots of k_n. This completes a cycle of two iterations for the determination of τ_n and k_n. After running the first cycle, new values of τ_n, k_n and q_n have been produced to be used as the starting variables for the next cycle of iteration. The iterative process can be used repeatedly to search for the pole locations by minimizing simultaneously the magnitude of the error functions $|\Delta_1|$ and $|\Delta_2|$ until τ_n, k_n and q_n converge to the required accuracy.

Similarly, we can extend this method using Raspet *et al*'s numerical scheme [9] to secure the successful locations of all poles for arbitrary phase and magnitude of q_n.

2.4 A bilinear profile of sound speed in the absence of wind

Assuming a stationary medium where $M_e = 0$, the derived Equations (2.2.17) and (2.3.5) can be reduced to the results published in the literature [3, 5, 8, 9] in the special case where the sound speed gradient is described by a so-called bilinear profile

$$n_c(z) = \sqrt{1 + 2a_T z}\,. \tag{2.4.1}$$

The vertical wave number k_z given by Equation (2.1.13) becomes

$$k_z(k_r, z) = +\sqrt{k_0^2(1 + 2a_T z) - k_r^2}\,. \tag{2.4.2}$$

Substitution of Equation (2.4.2) into Equation (2.2.11) and evaluation of the integral Equation (2.2.10) leads to an explicit expression for $\bar{\xi}(z)$, *i.e.*

$$\bar{\xi}(z) = \left(k_0^2 - k_n^2\right)l^2 + z/l\,. \tag{2.4.3}$$

l , which is known as the creeping wave layer thickness in the upward refracting medium or the wave layer thickness in the downward refracting medium, becomes constant for all poles and is given by

$$l = \left(2a_T k_0^2\right)^{-1/3}. \tag{2.4.4}$$

In an upward refracting medium, the total sound field given by Equation (2.2.17) reduces to

$$p^{(b)}(r,z) = \frac{\pi e^{i\pi/6}}{l} \sum_n \sqrt{\frac{2}{\pi k_n r}} \frac{\mathrm{Ai}\left(-\overline{\xi}_s e^{i2\pi/3}\right)\mathrm{Ai}\left(-\overline{\xi} e^{i2\pi/3}\right) e^{ik_n r - i\pi/4}}{\left\{\left[\mathrm{Ai}'(b_n)\right]^2 - b_n\left[\mathrm{Ai}(b_n)\right]^2\right\}}, \tag{2.4.5}$$

where

$$b_n = e^{i2\pi/3}\left(k_n^2 - k_0^2\right)/l^2 \tag{2.4.6}$$

are the zeros of the expression

$$\mathrm{Ai}'(b_n) + q e^{i\pi/3}\mathrm{Ai}(b_n) = 0, \tag{2.4.7}$$

$$q = ik_0\beta l, \tag{2.4.8}$$

and the superscript (b) denotes the sound field due to a bilinear sound speed profile. It will be shown that this expression is analogous to Equation (6) in Reference [15].

For the downward refraction, the total sound field given by Equation (2.3.5) reduces to

$$p^{(b)}(r,z) = \frac{i\pi}{l} \sum_n \sqrt{\frac{2}{\pi k_n r}} \frac{\mathrm{Ai}\left(-\overline{\xi}_s\right)\mathrm{Ai}\left(-\overline{\xi}\right) e^{ik_n r - i\pi/4}}{\left\{\tau_n\left[\mathrm{Ai}(\tau_n)\right]^2 - \left[\mathrm{Ai}'(\tau_n)\right]^2\right\}}, \tag{2.4.9}$$

where

$$\tau_n = \left(k_n^2 - k_0^2\right)/l^2 \tag{2.4.10}$$

are the zeros of the expression

$$\mathrm{Ai}'(\tau_n) + q\mathrm{Ai}(\tau_n) = 0, \tag{2.4.11}$$

and this expression is analogous to Equation (7) in Reference [9]. In Equation (2.4.9), the expression for $\overline{\xi}(z)$ is

$$\bar{\xi}(z) = \left(k_0^2 - k_n^2\right)l^2 - z/l\,. \qquad (2.4.12)$$

2.5 A linear profile of wind velocity and sound speed

In the idealized situation where wind velocity and sound speed are assumed to vary linearly with height, the index of refraction in the absence of wind n_c and the Mach number of wind M_e are given by

$$n_c(z) = \left(1 - a_T z\right)^{-1} \qquad (2.5.1)$$

and

$$M_e = a_W z\,. \qquad (2.5.2)$$

Substituting Equation (2.5.1) and (2.5.2) into Equation (2.1.13), the vertical wave number becomes

$$k_z = +\sqrt{\left[k_0\left(1 - a_T z\right)^{-1} - k_r a_W z\right]^2 - k_r^2}\,. \qquad (2.5.3)$$

It was noted [3, 15] that a linear sound speed variation with height may be approximated by a bilinear profile if $z \ll R_c$. However, the following analyses show that analytical solutions of the present model may be found in the case where a linear profile of sound speed and wind velocity varies with height without the above approximation.

2.5.1 Comparison with benchmark cases

To validate the present calculation mode, the mode is first compared with the benchmark case 2 and case 3 [10] where the effects of wind are ignored. Equation (2.5.3) is now reduced to

$$k_z = +\sqrt{\left[k_0\left(1 - a_T z\right)^{-1}\right]^2 - k_r^2}\,. \qquad (2.5.4)$$

Substituting Equation (2.5.4) into Equation (2.2.11) [or Equation(2.3.3)], we find the closed form analytical expressions for $\overline{\xi}(z)$, $\partial\overline{\xi}_0/\partial k_n$ and $\partial q_n/\partial k_n$, which are required for the calculation of the sound pressure in Equations (2.2.17) and (2.3.5) respectively.

For upward refraction,

$$\overline{\xi}(z)=\left\{\left(\frac{3}{2a_T}\right)\left[k_0\ln\left(\frac{k_0+\sqrt{k_0^2-k_n^2(1+a_Tz)^2}}{k_n(1+a_Tz)}\right)-\sqrt{k_0^2-k_n^2(1+a_Tz)^2}\right]\right\}^{2/3}$$

$$\text{if } z>z_t, \tag{2.5.5a}$$

$$\overline{\xi}(z)=-\left\{-\left(\frac{3}{2a_T}\right)\left[\frac{\pi}{2}k_0+\sqrt{k_n^2(1+a_Tz)^2-k_0^2}+k_0\tan^{-1}\left(\frac{k_0}{\sqrt{k_n^2(1+a_Tz)^2-k_0^2}}\right)\right]\right\}^{2/3}$$

$$\text{if } z<z_t; \tag{2.5.5b}$$

for downward refraction,

$$\overline{\xi}(z)=\left\{\left(\frac{3}{2a_T}\right)\left[k_0\ln\left(\frac{k_0+\sqrt{k_0^2-k_n^2(1+a_Tz)^2}}{k_n(1+a_Tz)}\right)-\sqrt{k_0^2-k_n^2(1+a_Tz)^2}\right]\right\}^{2/3}$$

$$\text{if } z<z_t, \tag{2.5.6a}$$

$$\overline{\xi}(z)=-\left\{-\left(\frac{3}{2a_T}\right)\left[\frac{\pi}{2}k_0+\sqrt{k_n^2(1+a_Tz)^2-k_0^2}+k_0\tan^{-1}\left(\frac{k_0}{\sqrt{k_n^2(1+a_Tz)^2-k_0^2}}\right)\right]\right\}^{2/3}$$

$$\text{if } z>z_t. \tag{2.5.6b}$$

It is noted that the following expressions are the same for both upward and downward refraction in the absence of wind.

$$\frac{\partial\overline{\xi}_0}{\partial k_n}=-\left(\frac{1}{a_Tk_n}\right)\sqrt{\frac{k_0^2-k_n^2}{\overline{\xi}_0}}, \tag{2.5.7}$$

and

$$\frac{\partial q_n}{\partial k_n} = \frac{ik_0\beta}{\bar{\xi}_0}\left[k_n\left(\frac{\bar{\xi}_0}{k_0^2 - k_n^2}\right)^{2/3} - \frac{1}{2a_T k_n}\right]. \qquad (2.5.8)$$

In the benchmark cases, a four-parameter model [10] is used to characterize the ground impedance. The same parameters as the benchmark cases are chosen for calculations: $a_T = \pm 2.915\ \mathrm{m}^{-1}$, $a_W = 0$, $dc/dz = \pm 0.1\ \mathrm{s}^{-1}$, $z = 1.0$ m, $z_s = 5.0$ m, and $1/\beta$ is $38.79 + 38.41i$ and $12.81 + 11.62i$ at 10 Hz and 100 Hz, respectively. The gradients are truncated at an altitude of 1000 m. The transmission loss is defined as

$$\mathrm{TL} = 20\log(p/p_1) \qquad (2.5.9)$$

where p_1 is the acoustic pressure at a distance of 1 m from the source in the absence of the reflected wave.

The solid lines in Figures 2.2(a) and (b) show the transmission loss versus distance at 10 Hz and 100 Hz, respectively, in the upward refracting atmosphere that corresponds to the benchmark case 3. The solid lines in Figures 2.4(a) and 2.5 are analogous to those in Figures 2.2(a) and (b), but in the downward refracting medium that correspond to the benchmark case 2. In the upward refracting medium, the predictions are calculated by summing 20 terms of the residue series solution. This number of terms ensures the convergence of the solution. In the downward refracting medium, the predictions are calculated by summing the corresponding number of modes described in Equation (2.3.9).

We can see from the solid lines in Figures 2.2, 2.4(a) and 2.5 that the general behavior of these calculations and the benchmark results are very close for a medium with a linear sound speed profile.

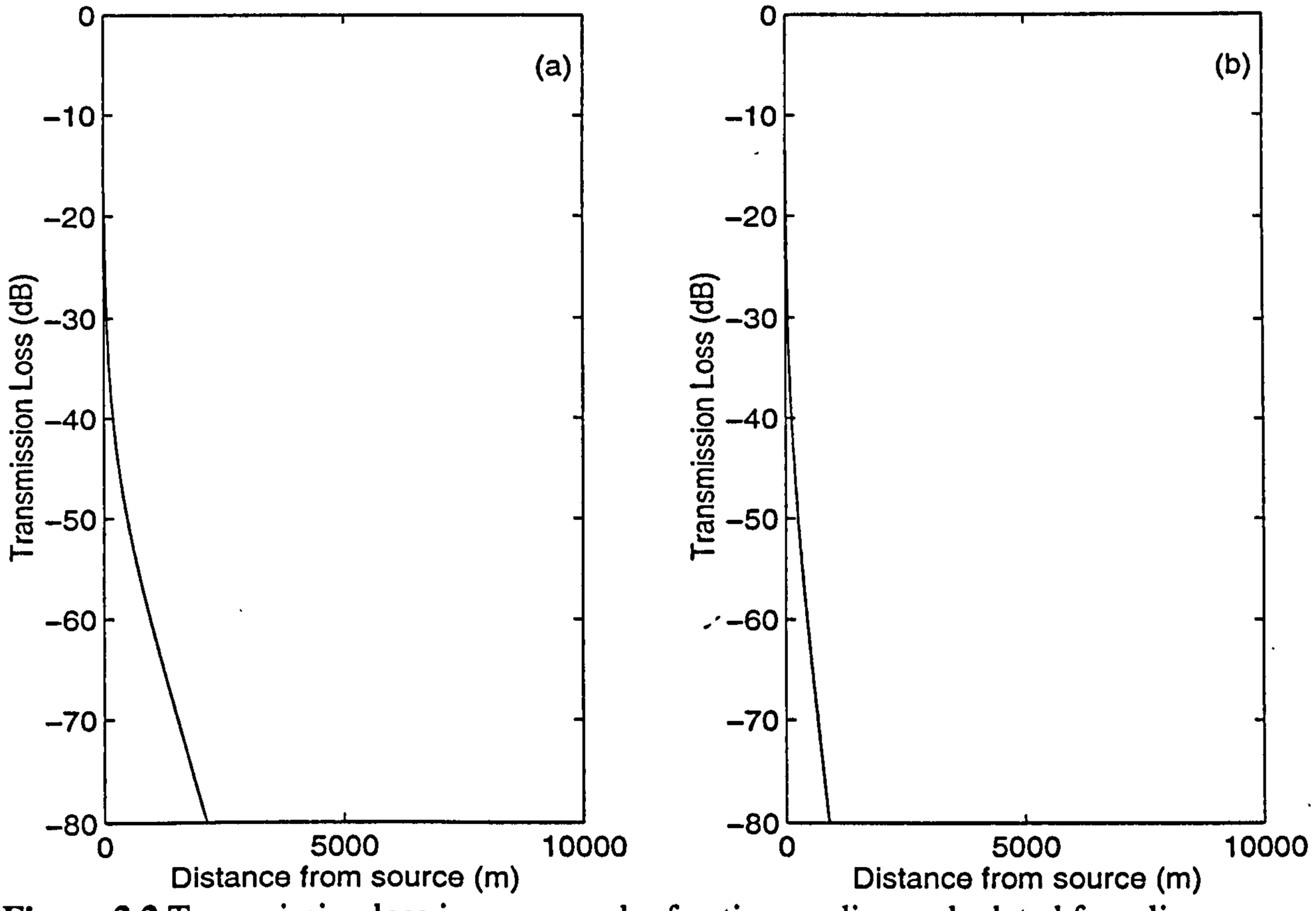

Figure 2.2 Transmission loss in an upward refracting medium calculated for a linear sound speed profile (solid lines) and a linear wind velocity gradient (dotted lines), with a constant gradient of $-0.1\ s^{-1}$, at frequencies of (a) 10 Hz and (b) 100 Hz.

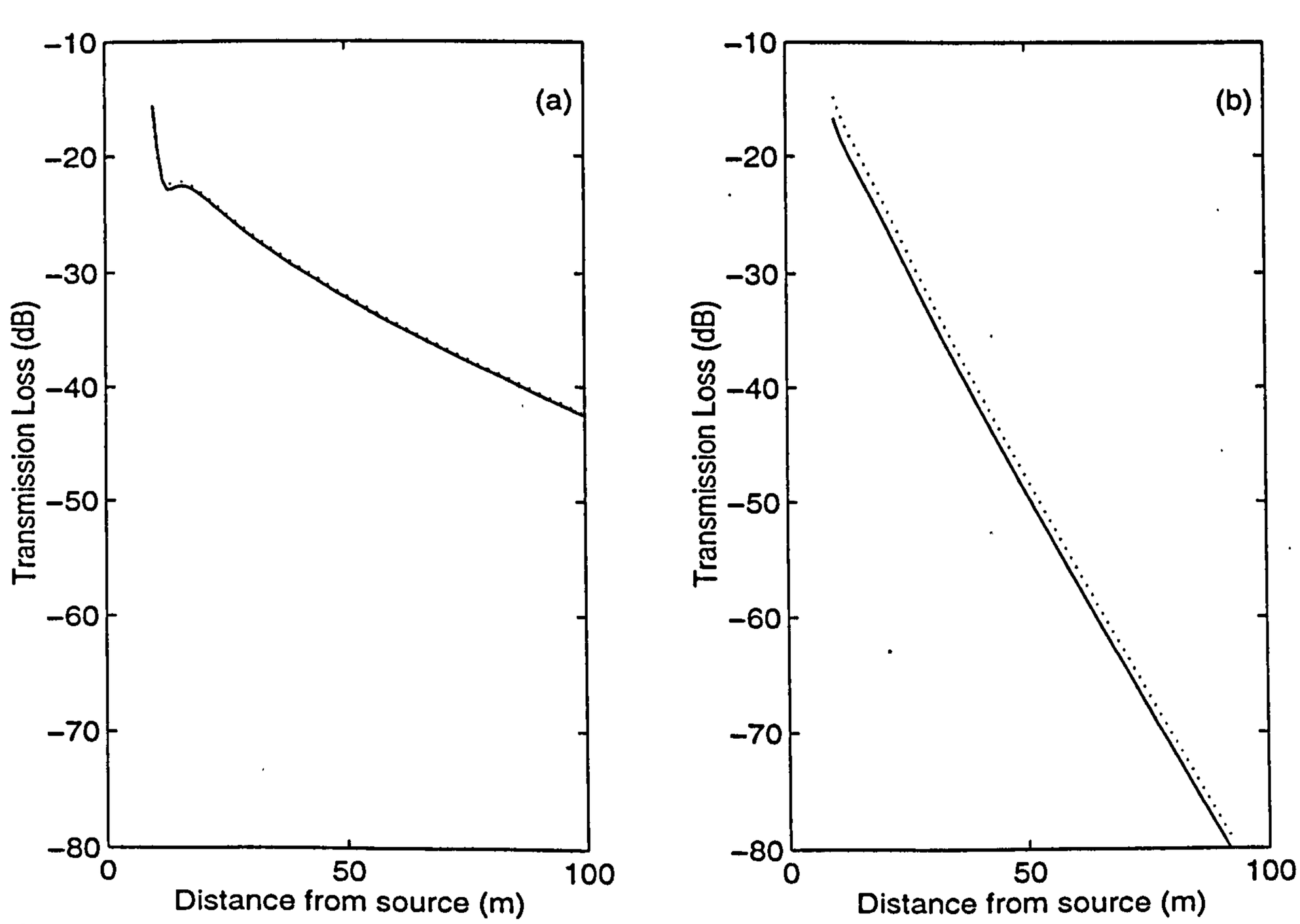

Figure 2.3 Same as **Figure 2.2** but at a source frequency of 100 Hz and with gradients of (a) $-1.0\ s^{-1}$ and (b) $-10.0\ s^{-1}$.

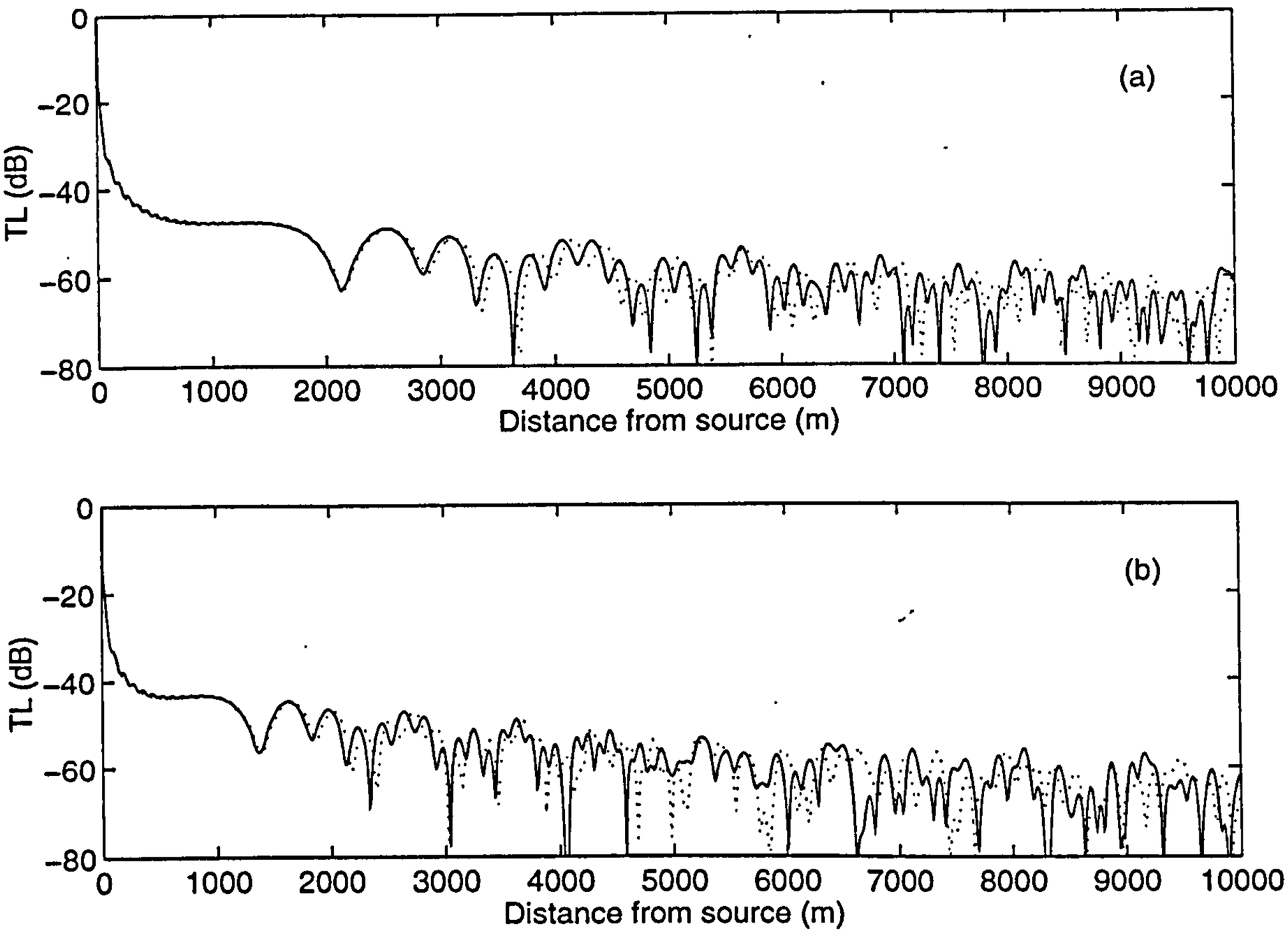

Figure 2.4 Transmission loss in a downward refracting medium calculated for a linear sound speed profile (solid lines) and a linear wind velocity gradient (dotted lines), for a frequency of 10 Hz, and with constant gradients of (a) 0.1 s^{-1} and (b) 0.2 s^{-1}. $z_s = 5.0$ m and $z = 1.0$ m..

2.5.2 Analytical results

On the basis of the success achieved in the absence of wind, a wind shear layer with constant density is now introduced to the problem. To simplify the analysis, the index of refraction is assumed to be constant, *i.e.* $n_c = 1$, and the effective wind velocity varies linearly with height, as described in Equation (2.5.2).

There are several efficient models for replacing the wind gradient by an effective sound speed. However, the present model shows an alternative way to compute the sound pressure without the usual approximation.

In this situation, Equation (2.5.3) becomes

$$k_z = +\sqrt{(k_0 - k_r a_w z)^2 - k_r^2}\,, \tag{2.5.10}$$

and there are also the closed form analytical expressions for $\bar{\xi}(z)$, $\partial\bar{\xi}_0/\partial k_n$ and $\partial q_n/\partial k_n$.

For upward refraction,

$$\bar{\xi}(z) = \left(\frac{3}{4a_w k_n}\right)^{2/3}\left\{(k_0 - a_w k_n z)\sqrt{(k_0 - a_w k_n z)^2 - k_n^2}\right.$$
$$\left. - k_n^2 \ln\left[\left(k_0 - a_w k_n z + \sqrt{(k_0 - a_w k_n z)^2 - k_n^2}\right)\Big/ k_n\right]\right\}^{2/3} \quad \text{if } z > z_t\,, \tag{2.5.11a}$$

$$\bar{\xi}(z) = -\left(\frac{3k_n}{4a_w}\right)^{2/3}\left\{\frac{\pi}{2} + \frac{(k_0 - a_w k_n z)}{k_n^2}\sqrt{k_n^2 - (k_0 - a_w k_n z)^2}\right.$$
$$\left. + \tan^{-1}\left[\left((k_0 - a_w k_n z)\sqrt{k_n^2 - (k_0 - a_w k_n z)^2}\right)\right]\right\}^{2/3} \quad \text{if } z < z_t\,; \tag{2.5.11b}$$

for downward refraction,

$$\bar{\xi}(z) = \left(\frac{3}{4a_w k_n}\right)^{2/3}\left\{(k_0 - a_w k_n z)\sqrt{(k_0 - a_w k_n z)^2 - k_n^2}\right.$$
$$\left. - k_n^2 \ln\left[\left(k_0 - a_w k_n z + \sqrt{(k_0 - a_w k_n z)^2 - k_n^2}\right)\Big/ k_n\right]\right\}^{2/3} \quad \text{if } z < z_t\,, \tag{2.5.12a}$$

$$\bar{\xi}(z) = -\left(\frac{3k_n}{4a_w}\right)^{2/3}\left\{\frac{\pi}{2} + \frac{(k_0 - a_w k_n z)}{k_n^2}\sqrt{k_n^2 - (k_0 - a_w k_n z)^2}\right.$$
$$\left. + \tan^{-1}\left[\left((k_0 - a_w k_n z)\sqrt{k_n^2 - (k_0 - a_w k_n z)^2}\right)\right]\right\}^{2/3} \quad \text{if } z > z_t\,; \tag{2.5.12b}$$

Similarly, we note that the expressions for $\partial\bar{\xi}_0/\partial k_n$ and $\partial q_n/\partial k_n$ are the same for both upward and downward refraction in the presence of a linear wind gradient.

$$\frac{\partial\bar{\xi}_0}{\partial k_n} = \frac{k_0\sqrt{k_0^2 - k_n^2} + k_n^2 \ln\left[k_0 + \sqrt{k_0^2 - k_n^2}/k_n\right]}{2a_w\sqrt{\bar{\xi}_0}\,k_n^2}\,, \tag{2.5.13}$$

and

$$\frac{\partial q_n}{\partial k_n} = ik_0\beta\left(\frac{1}{2\bar{\xi}_0}\frac{\partial\bar{\xi}_0}{\partial k_n} + \frac{k_n}{k_0^2 - k_n^2}\right)\sqrt{\frac{k_0^2 - k_n^2}{\bar{\xi}_0}}\,. \tag{2.5.14}$$

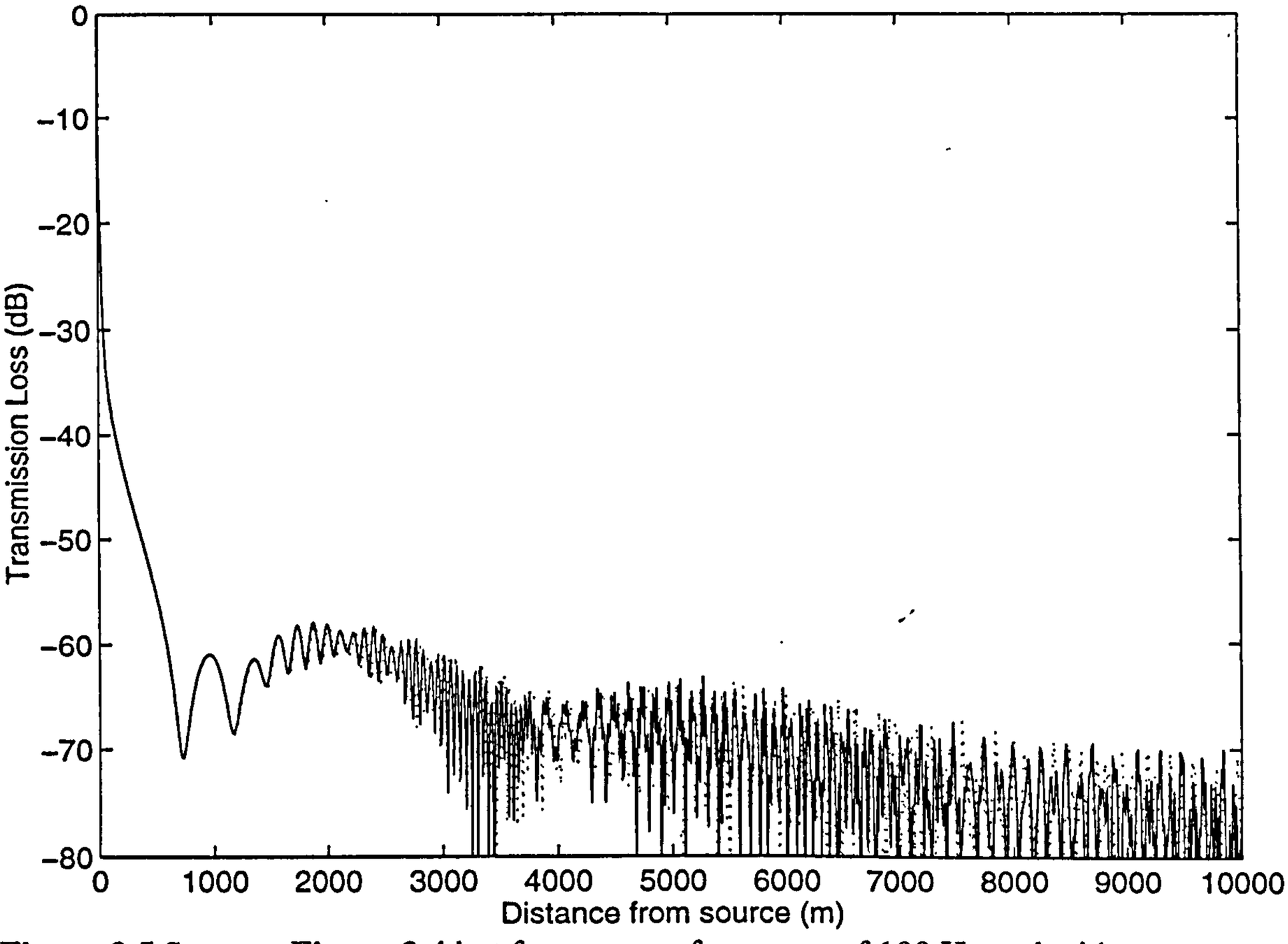

Figure 2.5 Same as **Figure 2.4** but for a source frequency of 100 Hz and with a constant gradient of 0.1 s^{-1}.

The parameters chosen for the calculations in this situation are the same as those in the windless case but $a_w = \pm 2.915\ m^{-1}$ and $a_T = 0$. The dotted lines in Figures 2.2(a) and (b) show the transmission loss versus distance at 10 Hz and 100 Hz, respectively, in the moving upward refracting medium with a constant wind velocity gradient. The dotted lines in Figures 2.4(a) and 2.5 are the same as those in Figures 2.2(a) and (b) but in the downward refracting medium.

These figures distinguish between the effects of temperature and wind gradients on the propagation of sound. If an effective sound speed gradient is used to replace a wind velocity gradient in Figures 2.2 and 2.3, we can consider that the solid lines in these figures display the results of applying an effective sound speed gradient. In an upward refracting medium, there is little difference in the predictions between using effective sound speed

and wind velocity gradients. In Figure 2.2, the two predictions displayed by the solid lines and the dotted lines are indistinguishable. As the sound speed gradient is increased, the differences between these two predictions become larger. Figures 2.3(a) and (b) show the two predictions in the cases where the sound speed gradients are assumed to be 1.0 s^{-1} and 10 s^{-1}, respectively. It can been seen that there are no significant errors from using an effective sound speed profile instead of a wind velocity profile, provided that the sound speed gradient is weak.

However, a different situation is predicted for the downward refracting medium. In a downward refracting atmosphere, the discrepancy between the use of wind velocity gradients and the customary effective sound speed profile approach increases rapidly as the sound speed gradient, the acoustic frequency and the range increase. Even in the case of a weak gradient, $dc/dz = 0.1\ s^{-1}$, as shown in Figure 2.4(a), there is a visible shift in the interference patterns starting at a distance about 2500 m from the source, although there are no appreciable differences in the magnitude of the transmission loss predictions. Increasing the gradient to $dc/dz = 0.2\ s^{-1}$, we can find from the solid line in Figure 2.4(b) that the obvious shift starts at a distance of about 1500 m from the source.

This phenomenon may be explained more clearly by plotting the differences in the pole k_n locations versus frequency for the first six poles, where the differences are calculated as the pole locations due to the effective sound speed gradient minus the pole locations due to the wind velocity gradient. The real and imaginary parts of differences are shown in Figures 2.6 (a) and (b) respectively. It is noted that the use of an effective sound speed profile underpredicts the real part of k_n and overpredicts the imaginary part of k_n, especially for high modes.

Furthermore, we can show the predicted transmission loss versus frequency in Figure 2.7.

In this analysis, Attenborough's two-parameter model [11],

$$\beta = \left\{ 0.436\sqrt{\frac{\sigma_e}{f}} + \left[0.436\sqrt{\frac{\sigma_e}{f}} + 19.48\frac{\alpha_e}{f} \right] i \right\}^{-1}, \qquad (2.5.15)$$

is used to provide a value for the ground impedance. The effective flow resistivity at the ground surface, σ_e, and the effective rate of change of porosity with depth, α_e, are 100 kPa s m^{-2} and 100 m^{-1}, respectively. These values of parameters, which are typical of many types of outdoor ground surface [12], correspond to a relatively hard ground.

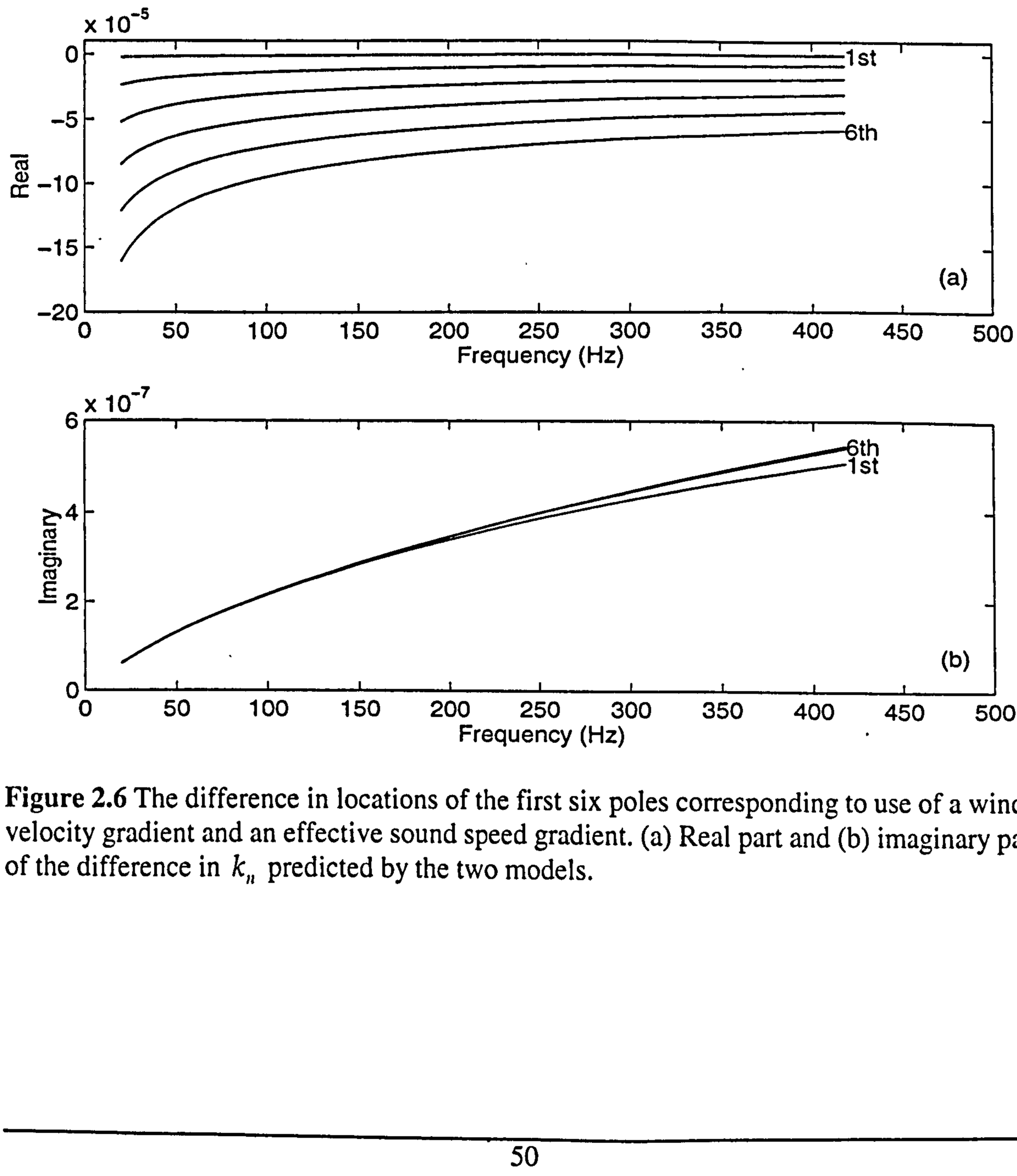

Figure 2.6 The difference in locations of the first six poles corresponding to use of a wind velocity gradient and an effective sound speed gradient. (a) Real part and (b) imaginary part of the difference in k_n predicted by the two models.

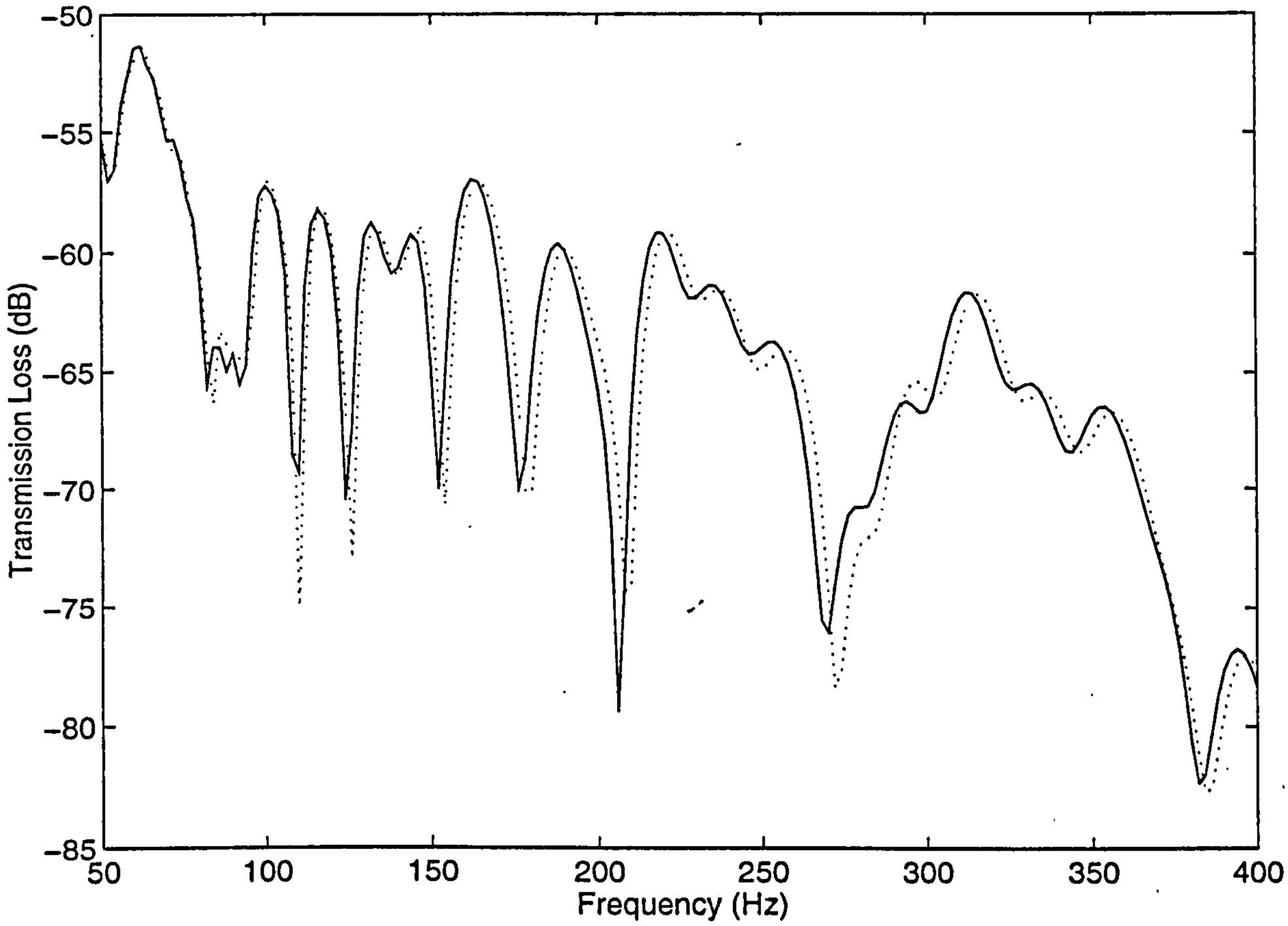

Figure 2.7 Transmission loss versus frequency calculated with a gradient of 0.1 s^{-1}, $z_s = 5.0$ m, $z = 1.0$ m, $r = 3000$ m, $\sigma_e = 100$ kPa s m^{-2} and $\alpha_e = 100$ m^{-1}. Dotted line: prediction for a wind velocity gradient, and solid line: prediction for an effective sound speed gradient.

A source height of 5.0 m, receiver height of 1.0 m and range of 3000 m are selected for the calculations. In this example, 20 modes are used for all frequencies. The gradient of the profile is $0.1\,s^{-1}$ and it is truncated at 65.7 m for 400 Hz. It is again found that the use of an effective sound speed gradient becomes progressively less satisfactory as the frequency increases.

2.5.3 Comparison with Li *et al*

In this section, the model will be compared with the chirp fast-field program (CFFPW) developed by Li *et al* [2]. The parameters, which include the gradients, the source and receiver heights, and the values of the admittance, chosen to take the same values as the

benchmark cases, are used for the calculations except the gradients are truncated at an altitude of 200 m.

In Figure 2.8, the dotted line represents the prediction of the transmission loss using the wind velocity gradient for downward refraction. The frequency is 10 Hz and $1/\beta$ is $38.79 + 38.41i$. The truncated gradient implies that there are only three dominant modes of propagation. In this model, the ambient temperature is constant and the wind velocity increases linearly with height from 0 ms^{-1} at the ground to 20 ms^{-1} at 200 m above the ground. The solid line in this figure represents the prediction of the effective sound speed model. The two predictions agree closely up to a range of about 4000 m. The difference between the two predictions only appears as a shift in the interference pattern, apparently due to the difference in phase speeds between the two methods. In Figure 2.9 the same values of parameters as in Figure 2.8 are used except that the frequency is increased to 100 Hz and $1/\beta$ is $12.81 + 11.62i$. We note from this figure that the agreement becomes worse at longer distances. Although the envelopes of the solutions are similar, the details of the curves differ from each other.

Li *et al* developed the fast field program designated CFFPW for numerical computation of anisotropic sound propagation through an atmosphere with a wind velocity gradient. The two groups of comparison obtained from the CFFPW using a linear wind profile and the conventional CFFP using an effective sound speed profile, have been demonstrated in Figures 5 and 6 of Reference [12]. Comparing Figures 2.8 and 2.9 with Figures 5 and 6 in Reference [12], we can find that they agree very closely, considering the approximations inherent in each solution.

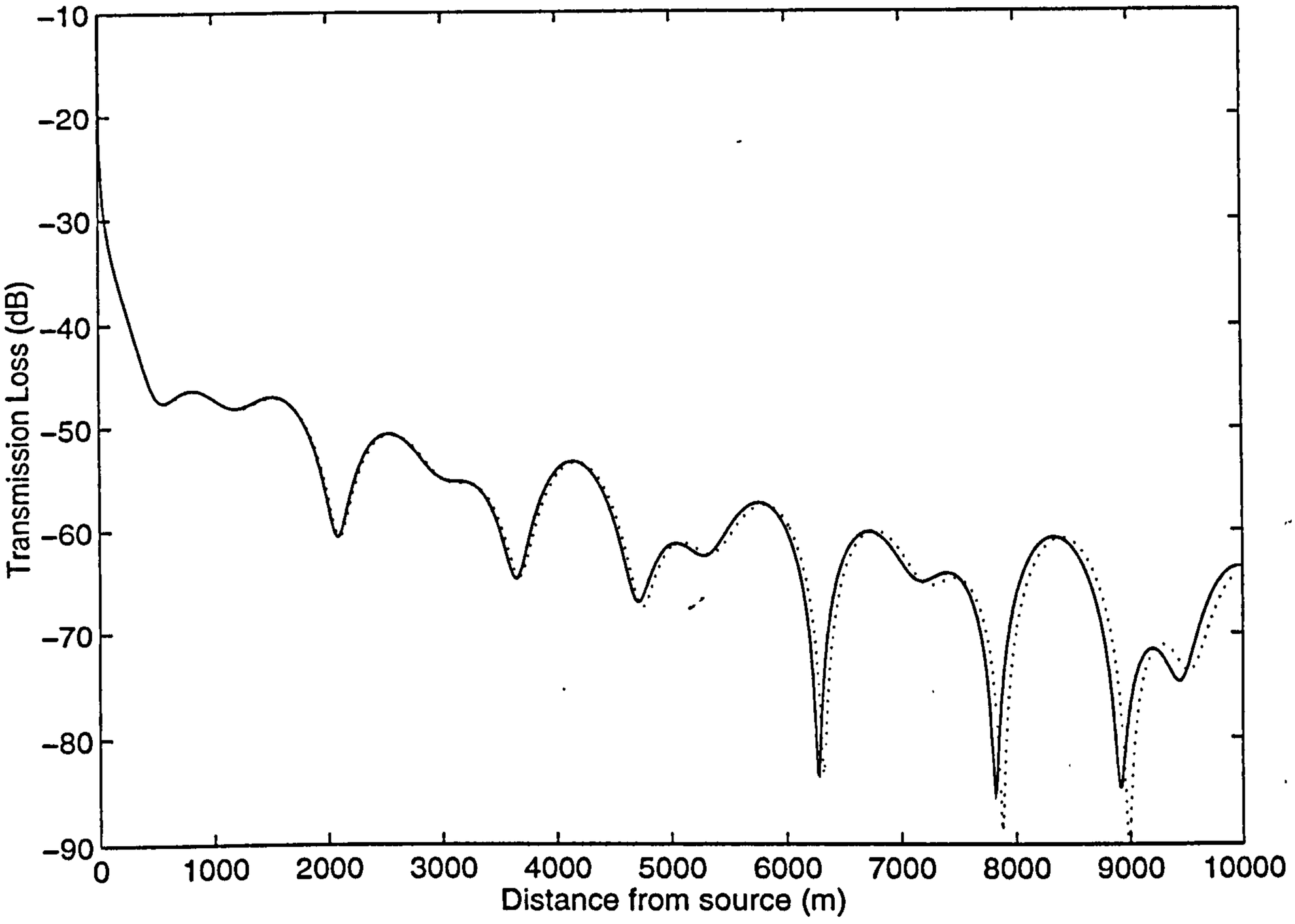

Figure 2.8 Same as **Figure 2.4(a)**, but with the gradient truncated at a height of 200 m above the ground.

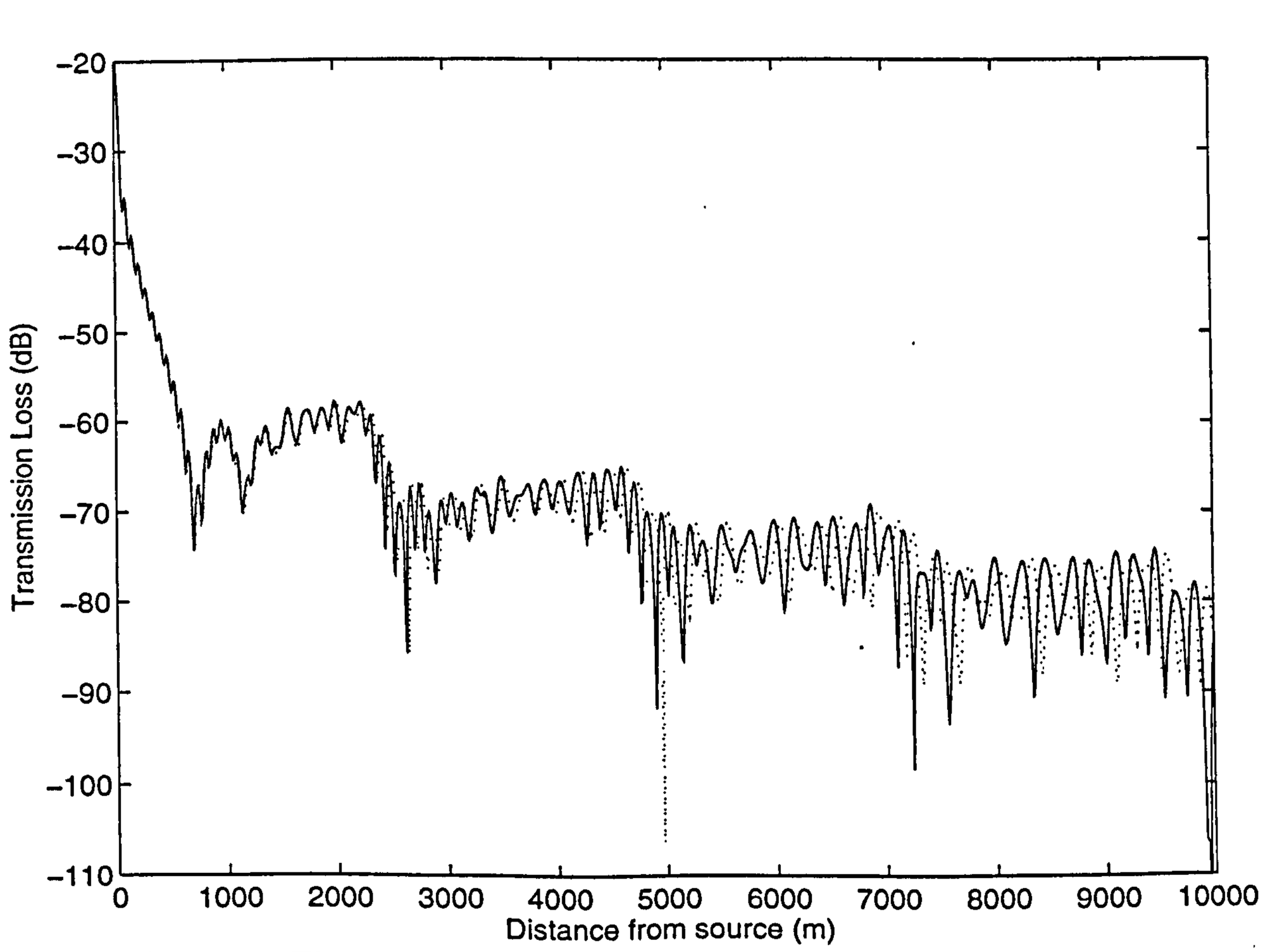

Figure 2.9 Same as **Figure 2.8** but for a frequency of 100 Hz.

2.5.4 Comparison with Raspet *et al*

Raspet *et al* [8] performed calculations of surface wave and residue series contributions in an upward refracting atmosphere in the absence of wind. To highlight the effect of the surface wave contribution in the presence of wind, the sound field for an impedance phase angle, $\varphi_z = 75^\circ$ ($\varphi_z = \pi/2 - \varphi$, *i.e.* $\varphi = 15^\circ$) is shown in Figure 2.10. Detailed discussions of the surface wave will be presented in Chapter 6. The values of parameters used in this figure are identical to those given in Figure 5(c) of Reference [8]. The solid lines in Figure 2.10 represent the predictions using the effective sound speed gradient, which correspond to the results of Raspet *et al* [8]. The dotted lines represent the predictions using the wind velocity gradient. In Figure 2.10, the first term containing the surface wave contribution is the dominant term in the total sound field at close range out to 27 m, whereas the second term, which is an ordinary residue series term, becomes dominant deep within the shadow zone. It is seen from this figure that the prediction of the surface wave contribution by using an effective sound speed gradient is sufficiently accurate at short range but it becomes less accurate deep in the shadow zone. On the other hand, although the agreement between these two predicted contributions becomes worse due to higher order terms at greater distances, the predicted contribution due to the dominant ordinary residue term is adequate for most practical ranges of interest. Consequently, as shown in Figure 2.10 and the earlier plots, it is adequate to replace the wind velocity profile with an effective sound speed profile when predicting the total sound field for upward refraction.

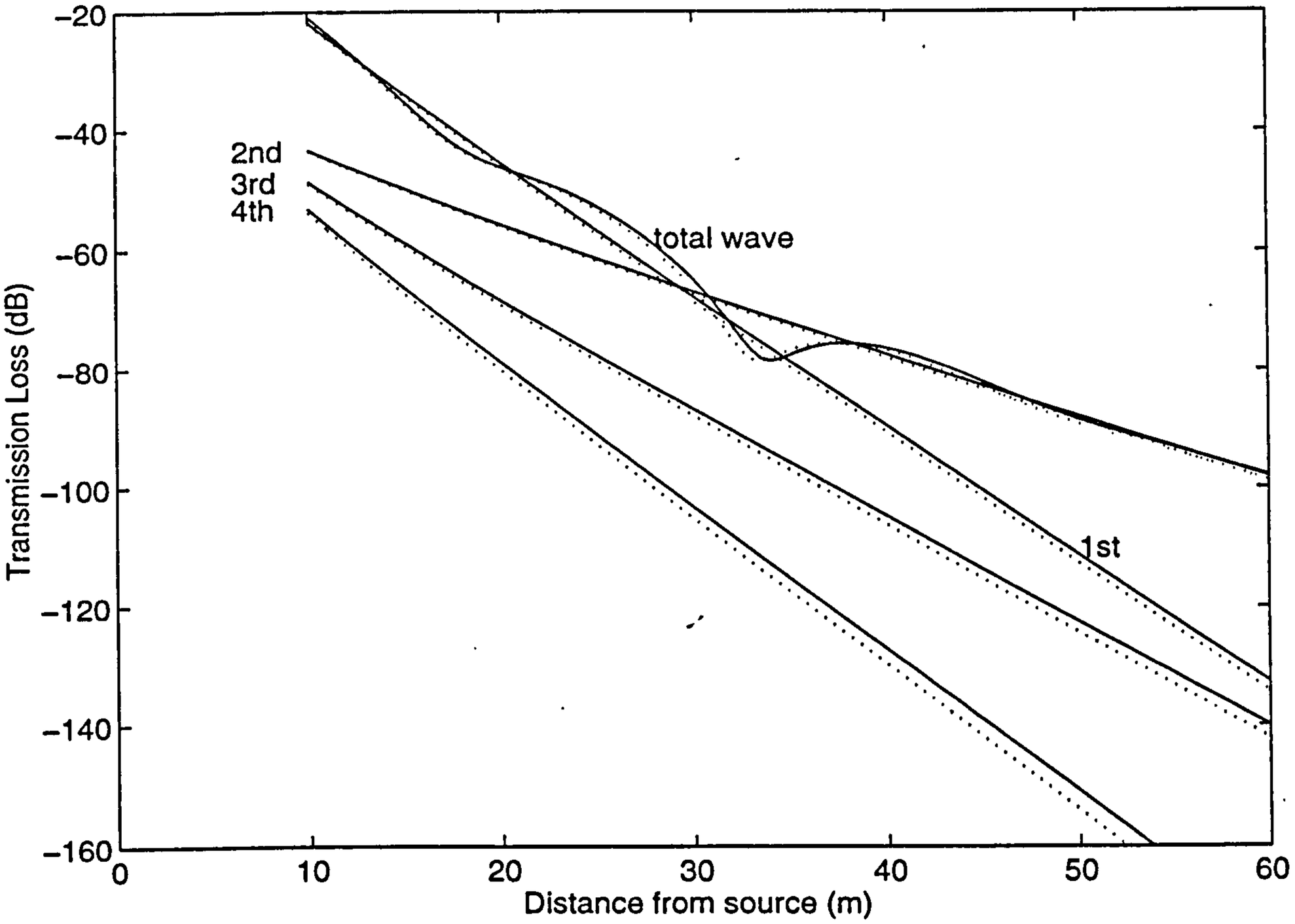

Figure 2.10 Transmission loss predicted for a frequency of 500 Hz in an upward refracting medium with $|q| = 3.0$ and $\varphi = 15^\circ$ by using a wind velocity gradient (dotted lines) and an effective sound speed gradient (solid lines), with constant gradients of $-2.1\ s^{-1}$, and $z_s = z = 0.1$ m.

2.6 Summary

In this chapter, numerical models for the propagation of sound outdoors in the presence of temperature and wind velocity gradients have been examined. The present approach is in contrast to the conventional approaches in which the effect of wind is replaced by the use of an effective sound speed gradient. Analytical expressions have been derived for a stratified upward or downward refracting medium with arbitrary vector wind and temperature profiles. The expressions for a bilinear profile of sound speed and for a linear profile of wind velocity and sound speed have been discussed in detail.

In an upward refracting medium, it has been demonstrated that the use of an effective sound speed gradient is adequate for predicting the sound field at most practical ranges of interest. On the other hand, in a downward refracting medium, it has been found that the use of an effective sound speed gradient is adequate for predicting the sound field only at short distances, low frequencies and weak gradients. This mainly results from the difference in phase between modes of using effective sound speed profile and wind velocity profile, which increase with range, frequency and gradient.

Chapter 3

Theories for sound propagation over convex surfaces[†]

The study of sound propagation in an upward refracting medium outdoors is very difficult because of the impossiblity of controlling and monitoring the complexity of the atmosphere. However, it has been found that it is possible to simulate curved ray paths over a flat ground by curving the ground beneath a homogeneous atmosphere [3, 13, 14]. This means that we can understand more about upward refraction of sound in the atmosphere by studying the diffraction of sound by a convex surface indoors. There has been considerable progress in constructing asymptotic solutions for propagation over smooth convex surfaces [83], however, further development of the theory is needed to give insight into the intriguing physical phenomenon of sound diffraction by convex surfaces.

There is a general belief [32] that if the refraction of sound waves is caused by a temperature gradient, then the analogous problem should be modelled by a ground with a spherical curvature, and if the sound speed gradient is dominated by a wind velocity gradient, it is proper to use a cylindrically curved surface to model the ground. We shall consider two types of convex surfaces: a sphere and a long circular cylinder. The use of Matched Asymptotic Expansions (MAE) has been proved useful in predicting the sound field in the penumbra region [19, 20, 26], but the MAE theory is restricted to the

[†] Parts of the work reported in this chapter were presented in References [18, 38].

propagation of plane waves. It appears difficult to extend the current MAE theory to allow for the prediction of the sound field due to a dipole source. Therefore, we shall follow the approach of the residue series solution together with a conformal transformation [84].

Berry and Daigle [15] have proposed that the sound field above a large cylinder with no refraction is analogous to the sound field above a flat ground where the sound speed varies with height according to the so-called bilinear profile (*cf.* Chapter 2.4). They derived a residue series solution that enables prediction of the sound field in the penumbra and shadow zone. The theoretical results agree well with their experimental measurements deep in the shadow zone but the agreement is less satisfactory in the vicinity of the shadow boundary.

Di and Gilbert [85] have indicated that a stricter analogy exists between propagation over a cylindrical surface and propagation over a plane under an exponential sound speed profile. Recent calculations using an FFP for an exponential profile have confirmed this [86].

In the illuminated regions over a convex surface, where a direct wave and a reflected wave can be identified, the use of a geometrical acoustics solution has been suggested [3, 15, 26] to predict the sound field. Berry and Daigle [15] extended the geometrical acoustics solution for a plane wave derived by Pierce [3, 26] to the case of a point monopole source. They have shown that their data measured at locations considerably above the shadow boundary agree with the predictions from the geometrical acoustics solution for a point monopole source. However, they reported that the residue series solution did not converge at any frequency in this region. We shall demonstrate that the geometrical acoustics solution works well also in the illuminated region in the vicinity of the source, where the residue series solution is not valid. In the region well above the shadow boundary, we shall show that the residue series solution can converge at any frequency or geometry with a

great number of terms, however, there appear large discrepancies between the residue series calculations and the measurements.

In this chapter, we extend the analogy to dipole sources, and to three dimensions over spherical and cylindrical convex surfaces. Sound propagation over flat impedance ground in the presence of a temperature or wind velocity gradient is studied further by using appropriate convex surfaces above which there is no refraction. The theories developed in the previous chapter are applicable to the problems that appear in this chapter as the sound speed gradient is used regardless of atmospheric turbulence and absorption.

3.1 Acoustic analogy to propagation over a convex surface

The simulation is based on the acoustic analogy between curved ray paths above flat ground and propagation above a curved surface without refraction. Many problems of refraction in the atmosphere can be therefore studied accurately by making measurements over curved surfaces in the laboratory.

3.1.1 Berry and Daigle's analogy

Berry and Daigle [15, 17] have proposed that the straight line sound propagation above a cylindrically curved surface with no refraction is analogous to propagation along the curved ray path above a plane boundary with a bilinear profile of sound speed. The profile is given by

$$c(z)=\frac{c_0}{\sqrt{1+2z/R_c}}\approx c_0\left(1-\frac{z}{R_c}+\frac{2z^2}{3R_c^2}-\cdots\right). \tag{3.1.1}$$

In this analogy, as illustrated in Figure 3.1, the vertical heights of source and receiver, z_s and z, are interpreted as the heights transverse to the curved surface. The horizontal distance from the source to receiver, r, is interpreted as the arc length along the curved

surface, and the radius of ray curvature of a curved ray path, R_c, becomes the radius of the convex cylinder. Hereafter, this analogy is called the B-D analogy.

3.1.2 Di and Gilbert's analogy

Di and Gilbert have shown [85] that the equivalent sound speed profile is exponential rather than bilinear (or linear) when considering propagation above a cylindrical convex surface. They suggested that there should be an exact analogy between propagation over a cylindrical convex surface under a constant sound speed profile and propagation over a plane boundary under an upward refracting sound speed profile. The profile is given by

$$c(z) = c_0 \exp(-z/R_c) \approx c_0\left(1 - \frac{z}{R_c} + \frac{z^2}{2R_c^2} - \cdots\right), \tag{3.1.2}$$

where

$$z = R_c \log\left(\frac{R_c + h}{R_c}\right), \tag{3.1.3}$$

with h being interpreted as the perpendicular distance from the curved surface at a receiver position. Hereafter, this analogy is called the D-G analogy.

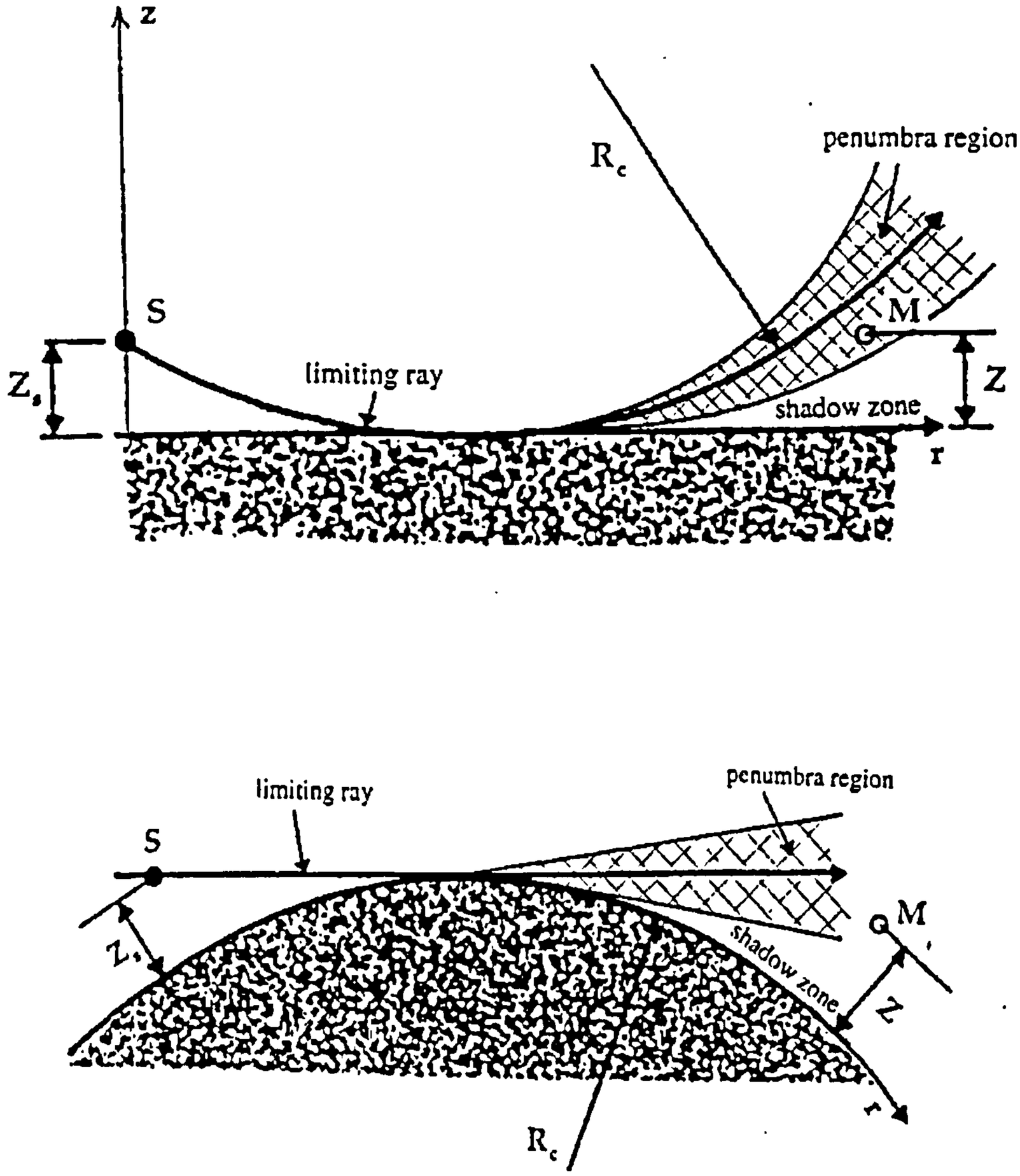

Figure 3.1 Sketch showing the analogy between propagation along a curved ray path above a plane boundary and straight line propagation above a convex surface.

3.2 Berry and Daigle's residue series solution

Using the B-D analogy, Berry and Daigle extended Pierce's procedure and derived the residue series solution for the sound field in an upward refracting medium, which is valid in the penumbra region, beyond and within the shadow zone. The acoustic pressure [15] is given by

$$p^{(b)}(r,z)=\frac{\pi e^{i\pi/6}}{l}\sum_n H_0^1(k_n r)\frac{\mathrm{Ai}\left[b_n-(z_s/l)e^{2i\pi/3}\right]\mathrm{Ai}\left[b_n-(z/l)e^{2i\pi/3}\right]}{\left[\mathrm{Ai}'(b_n)\right]^2-b_n\left[\mathrm{Ai}(b_n)\right]^2}, \qquad (3.2.1)$$

where

$$l=\left(\frac{R_c}{2k_0^2}\right)^{1/3}, \qquad (3.2.2)$$

$$b_n=\tau_n e^{2i\pi/3} \qquad (3.2.3)$$

are the zeros of

$$\mathrm{Ai}'(b_n)+qe^{i\pi/3}\mathrm{Ai}(b_n)=0. \qquad (3.2.4)$$

For a large argument, the Hankel function in Equation (3.2.1) can be approximated by its asymptotic form and Equation (3.2.1) becomes

$$p^{(b)}(r,z)=\frac{\pi e^{-i\pi/12}}{l}\sum_n\sqrt{\frac{2}{\pi k_n r}}\frac{\mathrm{Ai}\left[b_n-(z_s/l)e^{i2\pi/3}\right]\mathrm{Ai}\left[b_n-(z/l)e^{i2\pi/3}\right]e^{ik_n r}}{\left[\mathrm{Ai}'(b_n)\right]^2-b_n\left[\mathrm{Ai}(b_n)\right]^2}, \qquad (3.2.5)$$

which is identical to Equation (2.4.5).

The scaled and nondimensionalized admittance q determines the pole locations. If its phase angle [$\varphi=\arg(q)$], $\varphi>\pi/6$, all the poles lie between the zeros of the Airy function derivative and the zeros of the Airy function, and a technique suggested by Pierce [3] using the Newton-Raphson method can be used to search for the poles, starting with the trial solutions given by

$b_n=a_n'+qe^{-2i\pi/3}/a_n'$ if $|q|$ is small, (3.2.6a)

$b_n=a_n+e^{2i\pi/3}/q$ if $|q|$ is large. (3.2.6b)

In the case where $\varphi<\pi/6$, there is always a pole that contains the surface wave contribution. It was shown [8] that Pierce's technique does not work for large $|q|$. Raspet *et al* [8] developed a numerical scheme to ensure the successful locations of all poles.

However, running this scheme is not convenient if there is a large number of q as a function of frequency to be calculated. An alternative method that will work for arbitrary phase and large $|q|$ starts with the trial solutions given by

$$b_n = a_m + e^{2i\pi/3}/q \qquad \text{if } |q| \text{ is large,} \tag{3.2.7}$$

where $m = n-1$ if n is larger than the order of the term in which the surface wave contribution includes, or $m = n$ if n is smaller than the order of that term. There is a justification for the use of this method in Figures 3.2(a) and (b). These two figures show the behavior of τ_n as $|q|$ increases from 0 to 20 with $\varphi = 10°$, calculated by Pierce's technique and the Raspet *et al* scheme, respectively. The circles are the zeros of $\mathrm{Ai}'\left(\tau_n e^{i2\pi/3}\right)$. The first term contains the so-called surface wave contribution [8]. Comparing these two figures, it is noted that if $|q|$ is small, the corresponding locations of all the poles are the same; if $|q|$ is large, the corresponding locations of all terms except the first are the same, they originate from the n th zeros of the Airy function derivative to the $(n-1)$ th zeros of the Airy function, as $|q|$ increases to 20. Only for the special case where the pole, such as the first term, includes the surface wave contribution, it is necessary to find the locations of this pole by the Raspet *et al* scheme.

There is no convergent result given by Berry and Daigle's residue series solution in which they sum no more than 20 terms above the shadow boundary, and there is a large discrepancy between the predictions and their measurements in the penumbra region [15]. However, it is possible to show that the residue series will converge up to any frequency above the limiting ray if sufficient terms are included. For example, with 30 terms, the series converges to 10 kHz for the geometry given by Figure 6 in Reference [15], see Figure 3.3. In this figure, the solid line represents the prediction using the residue series solution and the circles represent the measured results obtained by Berry and Daigle. It can

be shown that about 60 terms are necessary to converge up to 20 kHz for this geometry. We note that the residue series is a poorly convergent sum of many small terms in the region above the limiting ray. Furthermore, there are discrepancies between the prediction and the measurement, which will be discussed in Chapter 3.8 and Chapter 4.2.

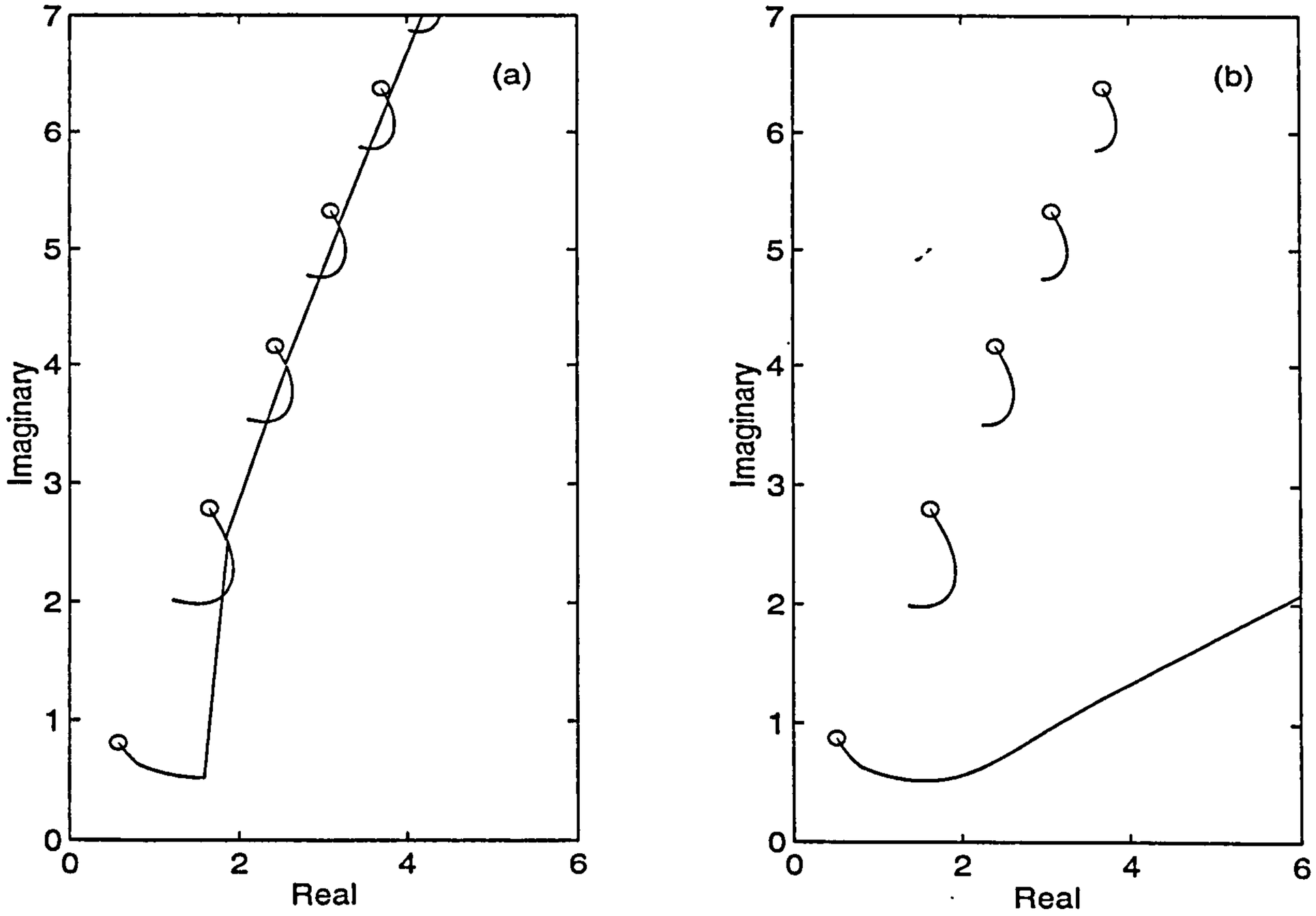

Figure 3.2 Behavior of the τ_n as $|q|$ varies from 0 to 20 with $\varphi = 10°$. Circles: the zeros of the Airy function. (a) calculation obtained from Pierce's technique, (b) calculation obtained from the Raspet *et al* scheme.

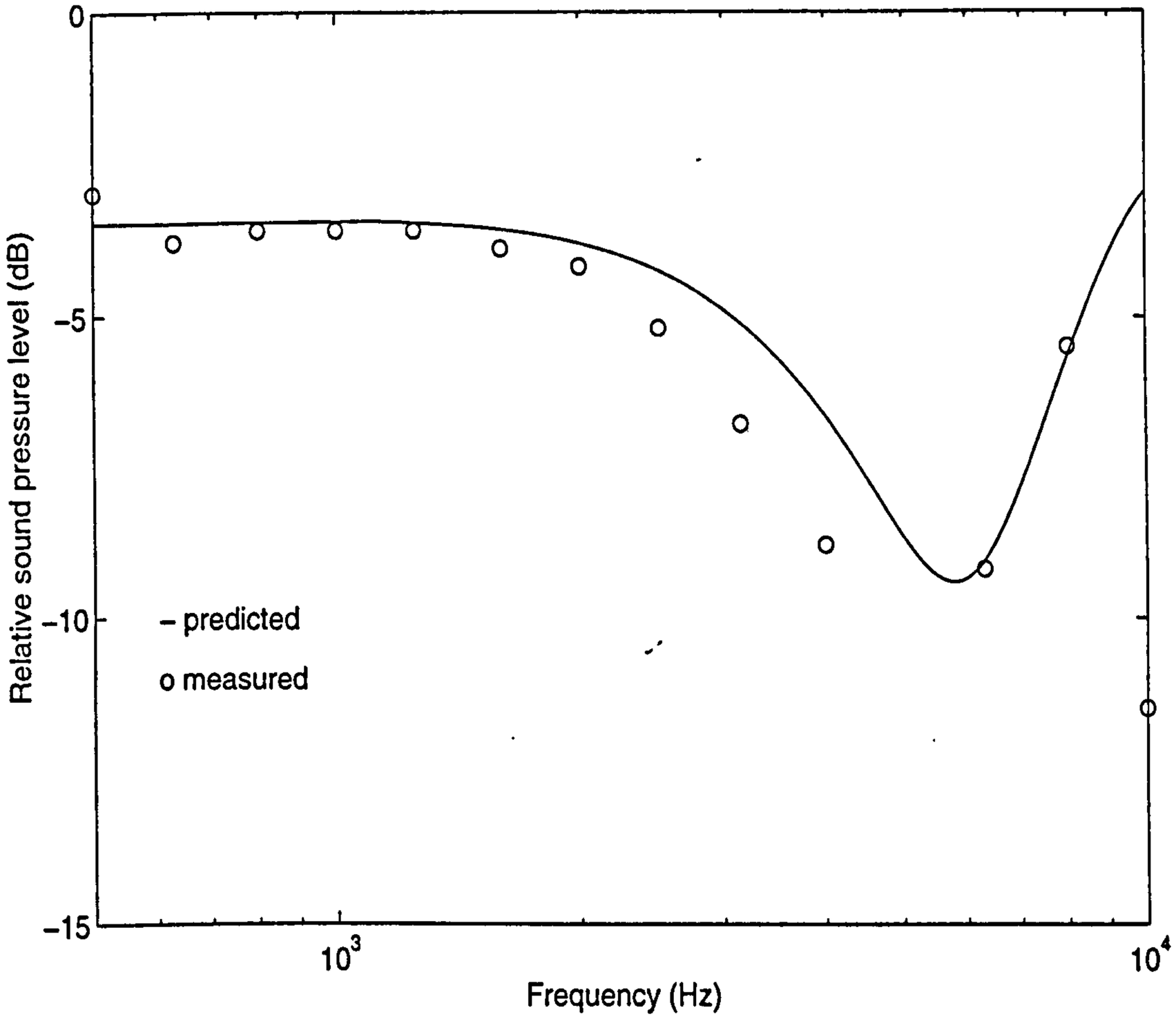

Figure 3.3 Measured and predicted results obtained with the source above a rigid convex surface, $R_c = 5.0$ m, $z_s = 0.43$ m, $z = 0.93$ m and $r = 3.65$ m.

3.3 Sound field diffracted by a cylindrical surface

Using the D-G analogy with a conformal transformation [85], the theory developed for the case of a stratified atmosphere is directly applicable to modelling the sound above a cylindrical convex surface. Using polar coordinates (r, ψ_s) (see Figure 3.4), the acoustic pressure defined in Equation (2.1.4) may be recast in term of $P(k_r, \psi, z)$

$$p^{(c)}(r,z) = \int_{-\pi}^{\pi}\int_{0}^{\infty} k_r P(k_r,\psi,z)\exp\left[ik_r r\cos(\psi-\psi_s)\right]dk_r d\psi\,, \tag{3.3.1}$$

where the superscript (c) denotes the sound field over a long cylinder, and $P(k_r, \psi, z)$ satisfies

$$\frac{d^2P(k_r,\psi,z)}{dz^2} + k_z^2(k_r,\psi,z)P(k_r,\psi,z) = -J\delta(z-z_s)\,, \tag{3.3.2}$$

where J is the Jacobian of the transformation given by

$$J = \exp(2z/R_c), \tag{3.3.3}$$

and

$$k_z(k_r,\psi,z) = +\sqrt{(k_0^2 - k_r^2\sin^2\psi)\exp(2z/R_c) - k_r^2\cos^2\psi}\,. \tag{3.3.4}$$

In the above equations, ψ is the azimuthal angle in the plane of constant z.

An analytical solution for $P(k_r,\psi,z)$ can be found in this case [85]. Substituting the expression for $P(k_r,\psi,z)$ into Equation (3.3.1), the sound pressure behind a long cylinder can be written as a sum of residue series:

$$p^{(c)}(r,\psi,z) = e^{i\pi/4}\sqrt{\frac{8\pi}{r}}\sum_n\left[\frac{\bar{\xi}_s\bar{\xi}}{\bar{k}_z^2(z_s)\bar{k}_z^2(z)}\right]^{1/4} \times \frac{\sqrt{k_n}\,\mathrm{Ai}\left(-\bar{\xi}_s e^{i2\pi/3}\right)\mathrm{Ai}\left(-\bar{\xi}e^{i2\pi/3}\right)e^{ik_n r}}{e^{-i2\pi/3}\dfrac{\partial\bar{\xi}_0}{\partial k_n}\left\{\left[\mathrm{Ai}'(b_n)\right]^2 - b_n\left[\mathrm{Ai}(b_n)\right]^2\right\} - \dfrac{\partial q_n}{\partial k_n}\left[\mathrm{Ai}(b_n)\right]^2} \tag{3.3.5}$$

where

$$\bar{\xi}(z) = \left\{\frac{3}{2}k_n R_c\cos\psi\left[\frac{\bar{k}_z(z)}{k_n\cos\psi} - \tan^{-1}\left(\frac{\bar{k}_z(z)}{k_n\cos\psi}\right)\right]\right\}^{2/3} \qquad \text{if } z < z_t, \tag{3.3.6a}$$

$$\bar{\xi}(z) = -\left\{\frac{3}{2}k_n R_c\cos\psi\left[-\frac{\sqrt{-\bar{k}_z^2(z)}}{k_n\cos\psi} + \tanh^{-1}\left(\frac{\sqrt{-\bar{k}_z^2(z)}}{k_n\cos\psi}\right)\right]\right\}^{2/3} \qquad \text{if } z > z_t, \tag{3.3.6b}$$

$$\bar{\xi}_0 = \left\{\frac{3}{2}k_n R_c\cos\psi\left[\frac{\sqrt{k_0^2 - k_n^2}}{k_n\cos\psi} - \tan^{-1}\left(\frac{\sqrt{k_0^2 - k_n^2}}{k_n\cos\psi}\right)\right]\right\}^{2/3}, \tag{3.3.7}$$

and

$$\frac{\partial\bar{\xi}_0}{\partial k_n} = -\frac{R_c}{\sqrt{\bar{\xi}_0}}\sec\psi\tan^{-1}\left(\frac{\sqrt{k_0^2 - k_n^2}}{k_n\cos\psi}\right). \tag{3.3.8}$$

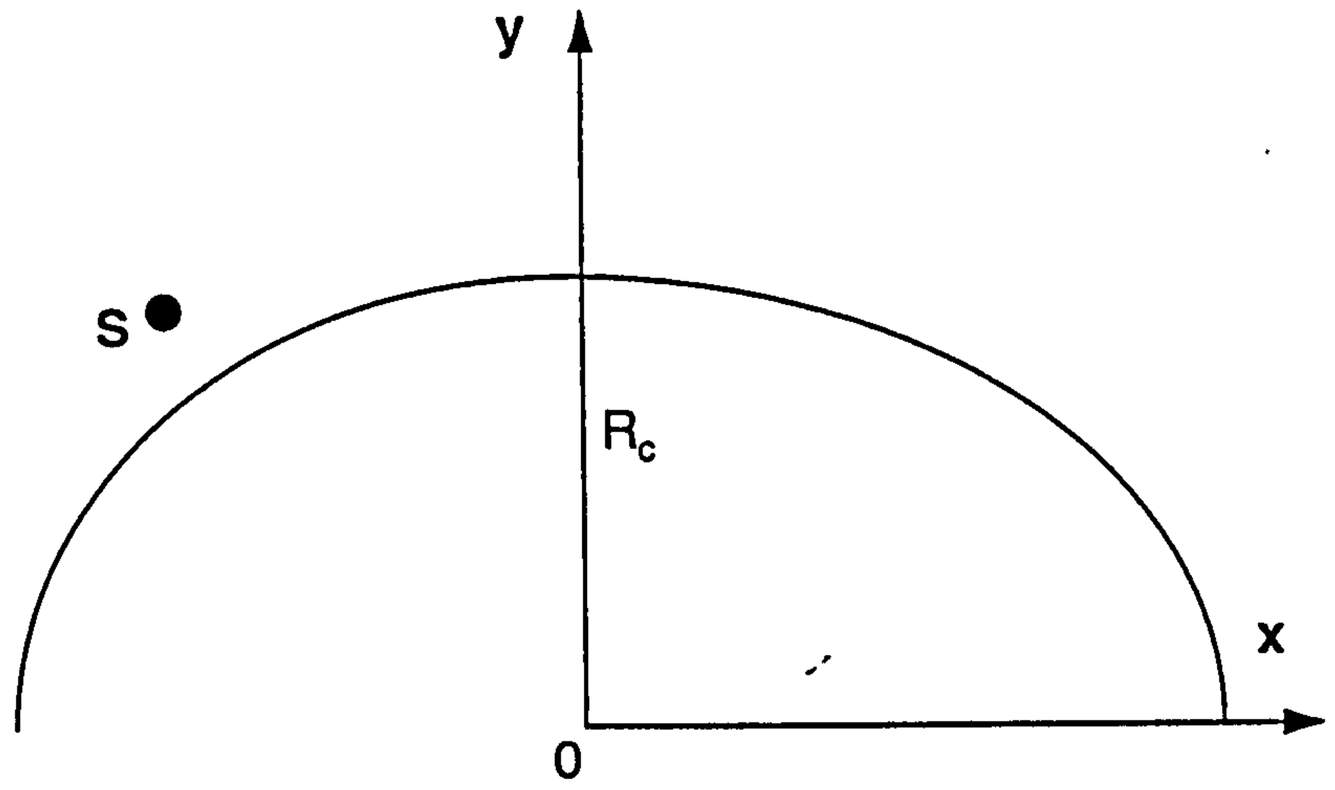

(a)

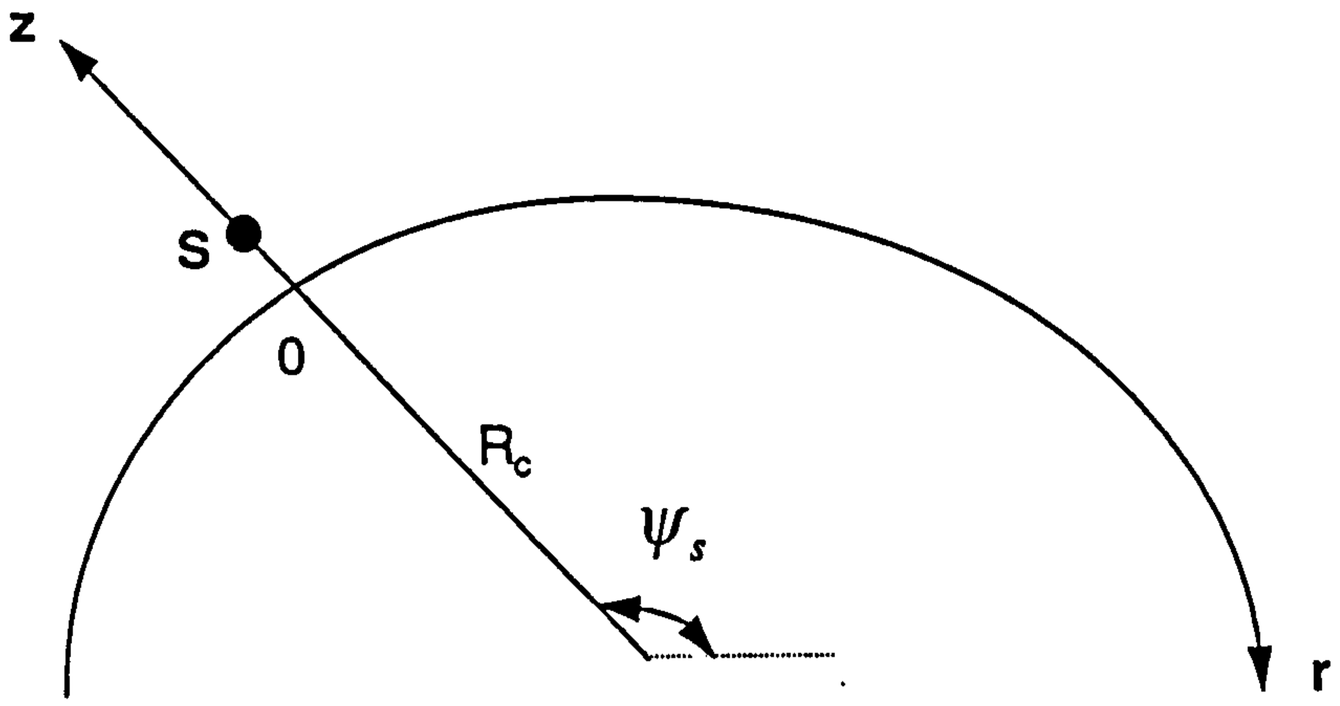

(b)

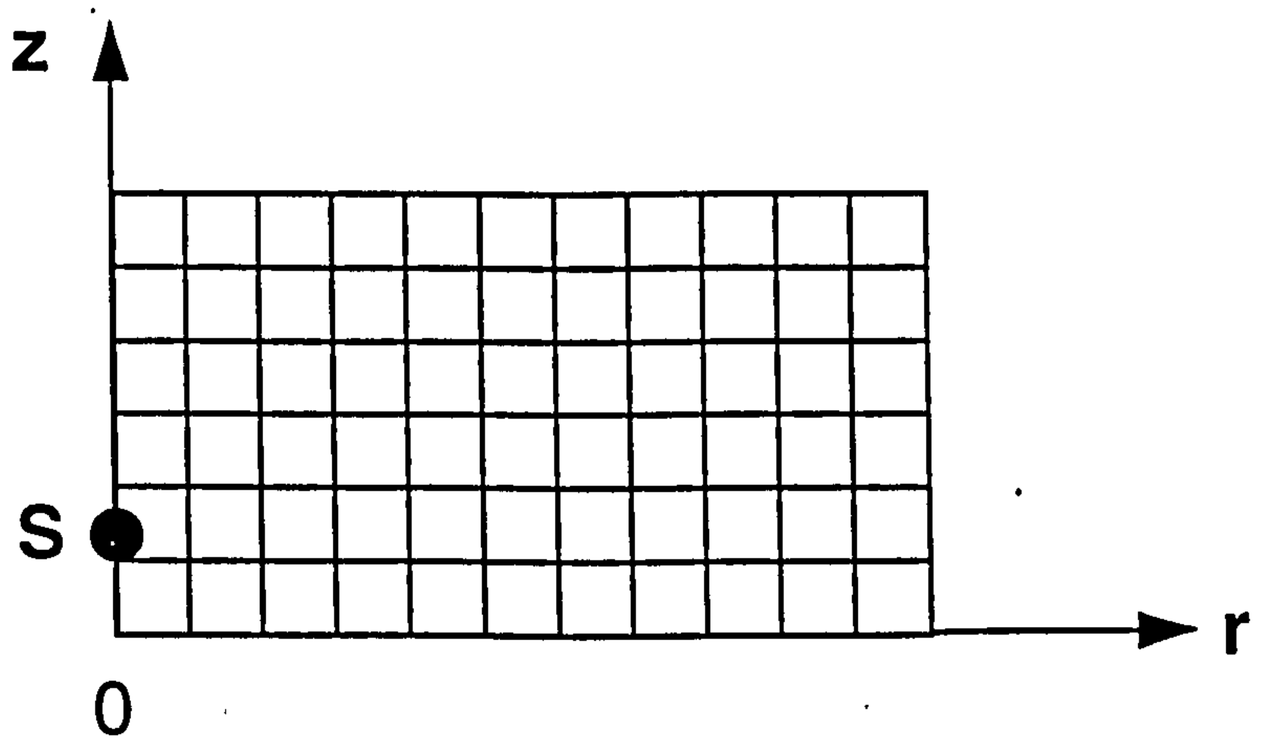

(c)

Figure 3.4 Illustration of conformal mapping for a single convex surface. (a) physical coordinate system (x, y). (b) transformed coordinate system (r, z) in the physical domain. (c) transformed coordinate system in the transformed domain.

Variables b_n and q_n have been defined in Equations (2.2.22) to (2.2.26). The poles of b_n and k_n can be solved using the numerical method described in Chapter 2.2.2.

3.3.1 Comparison to Berry and Daigle's data and bilinear profile predictions

With the conformal transformation, the residue series solution given by Equation (3.3.5) is consistent with an exponential profile. Near the surface in the shadow zone, this residue series solution gives results that are very close to those given by Berry and Daigle's residue series solution with a bilinear profile [Equation (3.2.1)]. Figure 3.5 shows the transmission loss as a function of distance from the source predicted by these two solutions.

For propagation along the surface of a long cylinder, the paths of the creeping wave are *geodesics* and the path connecting two points on the surface is the shortest of all possible paths [3]. Consider a vertical plane, that intercepts the source and receiver, through an angle, ψ, with respect to the circumference of the cylinder, see Figure 3.6. The radius R_c defined in Equation (3.2.2) for a bilinear profile can be replaced by the effective radius of the cylinder [3, 15]

$$R_{eff} = R_c / \cos^2 \psi \,. \tag{3.3.9}$$

The azimuthal angle, ψ, in Equations (3.3.1) to (3.3.7) is identical to that shown in Figure 3.6. Figure 3.7 shows identical predictions in the shadow zone using the residue series solutions with both bilinear and exponential profiles when $\psi = 45°$.

In the penumbra region, the prediction of the series with an exponential profile shows much better agreement with the experimental results [15] than the prediction with a bilinear profile, as shown in Figures 3.8. This figure shows the diffracted sound field above the rigid surface obtained along the line of sight as a function of frequency. The relative

sound pressure level is defined as the excess attenuation minus 6 dB. The excess attenuation is defined as

$$\mathrm{EA} = 20\log(p/p_0), \tag{3.3.10}$$

where p_0 is the sound pressure at an identical field point in the absence of the reflected wave. The two series converge quite rapidly up to a frequency of 10 kHz with no more than 10 terms. In Figure 3.8, the circles represent the experimental results obtained above a smooth cylindrically curved surface with a radius of 5.0 m in the penumbra region by Berry and Daigle. Here, the location of the receiver coincides with the limiting ray. In this figure, the solid line represents the prediction of the series using a bilinear profile, and the dashdot line represents that using an exponential profile.

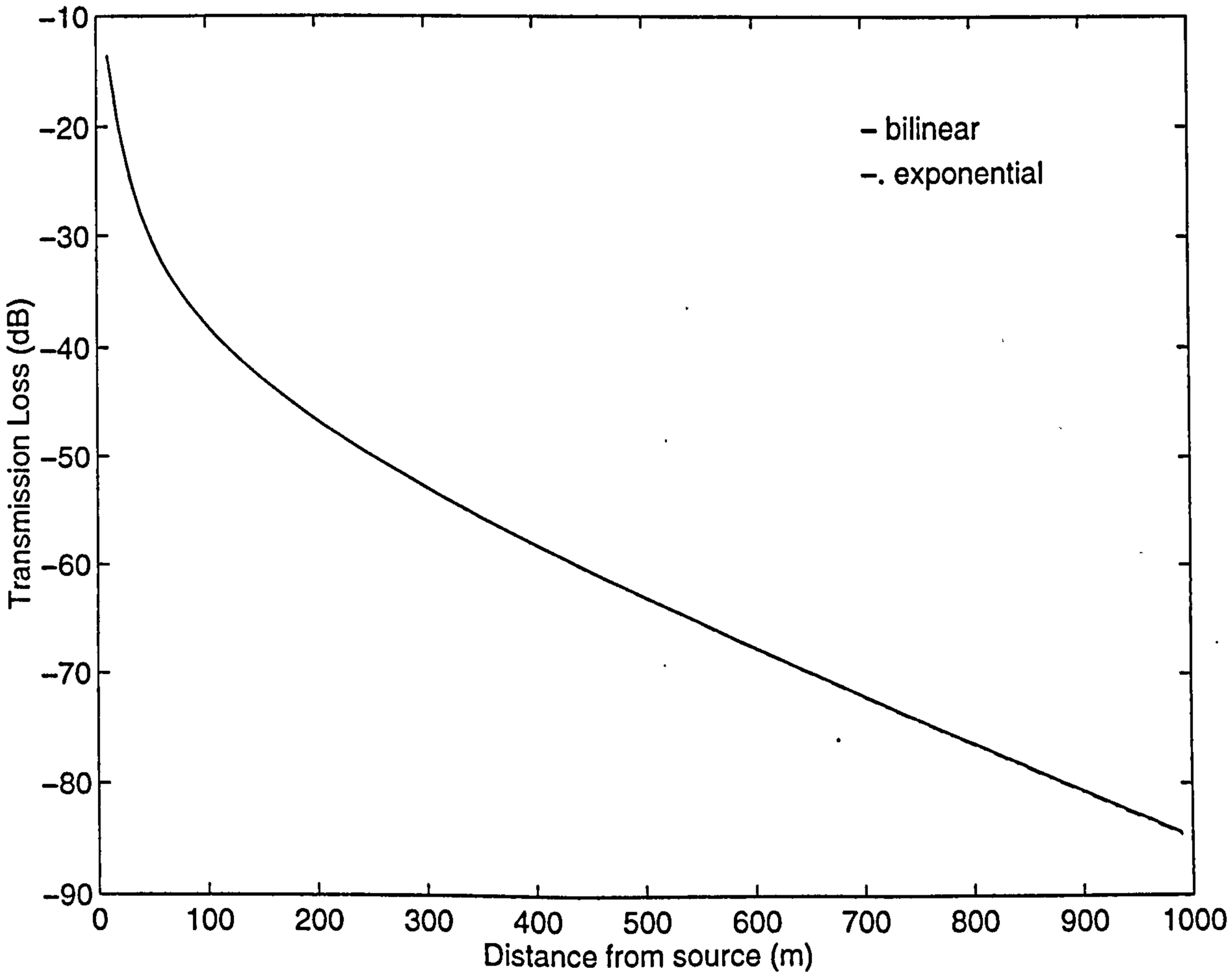

Figure 3.5 Transmission loss calculated at 100 Hz with an exponential profile and with a bilinear profile above an impedance surface. $\beta = 0.0428 - 0.0388i$, $z_s = 1.5$ m, $z = 1.0$ m and $\psi = 0$.

Berthelot [19] suggested that interpreting the source-receiver distance r in Equation (3.2.1) as the shortest path d between the source and receiver improves the predictions of the residue series. However, no rigorous proof has been found for this heuristic modification in the definition of r [19]. The dashed line in Figure 3.8 represents the prediction using d instead of the arc distance r. We note that the dashed line is very close to the dashdot line for the entire frequency range shown in this figure. It is clear that the improvement can be also achieved by the D-G analogy using an exponential profile in the penumbra region behind a cylindrical convex surface. However, there remain discrepancies at higher frequency ranges in the penumbra region that will be discussed in Chapter 4.2.

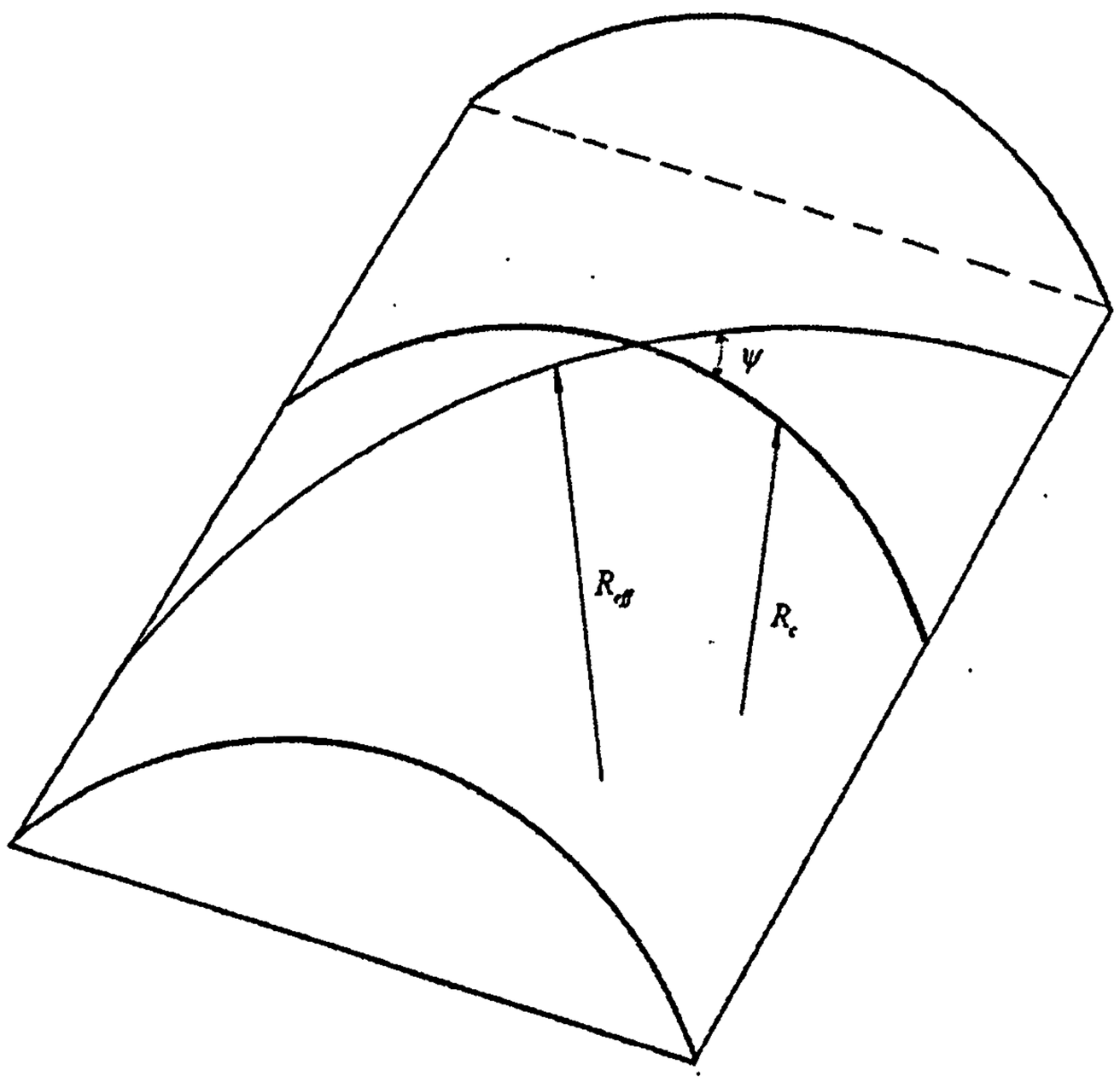

Figure 3.6 Illustration showing the source-receiver plane rotating an angle of ψ with respect to the circumference of the cylinder (radius of curvature R_c) to produce a larger radius of curvature R_{eff}.

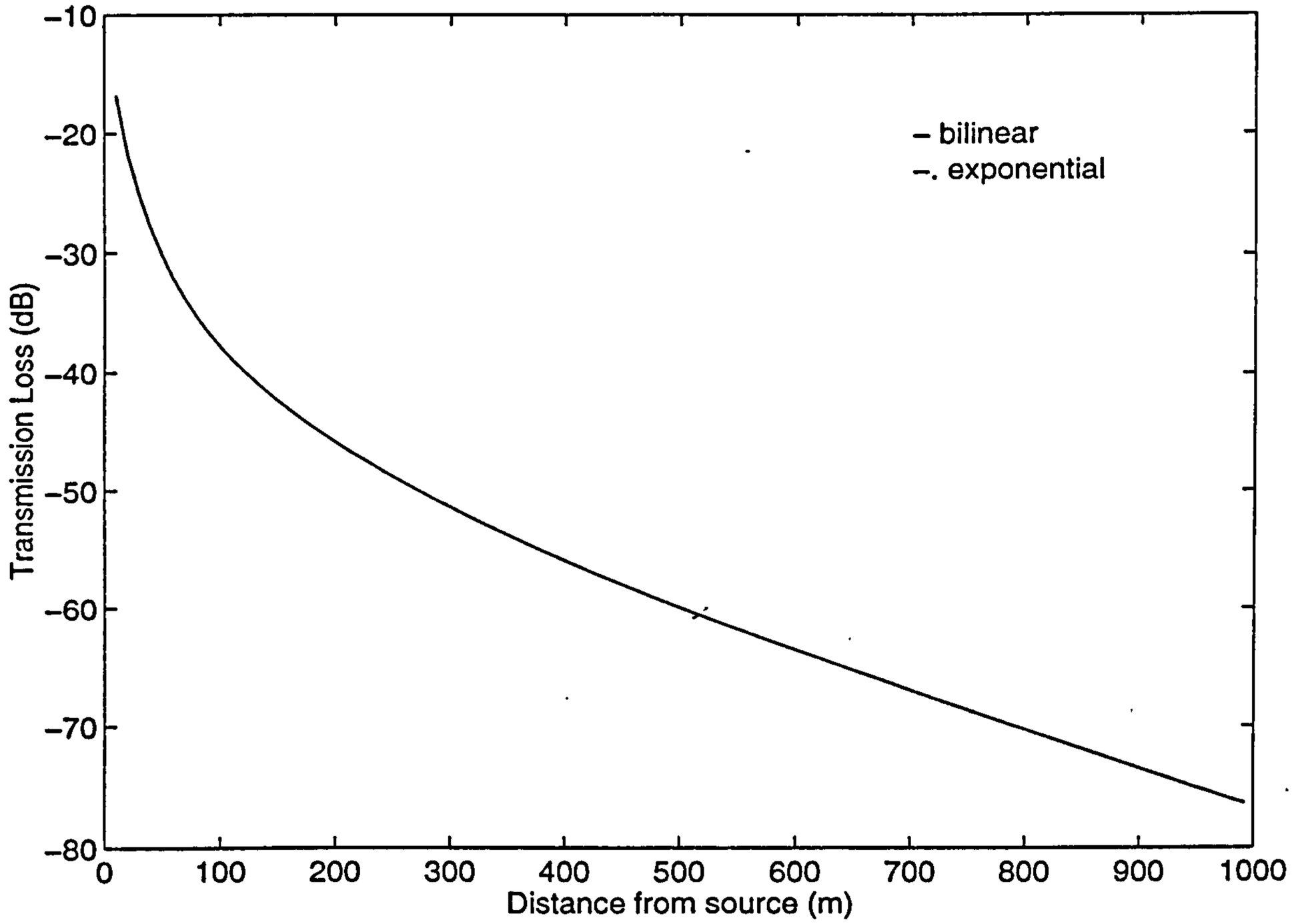

Figure 3.7 Same as **Figure 3.5** except $\psi = 45^{\circ}$.

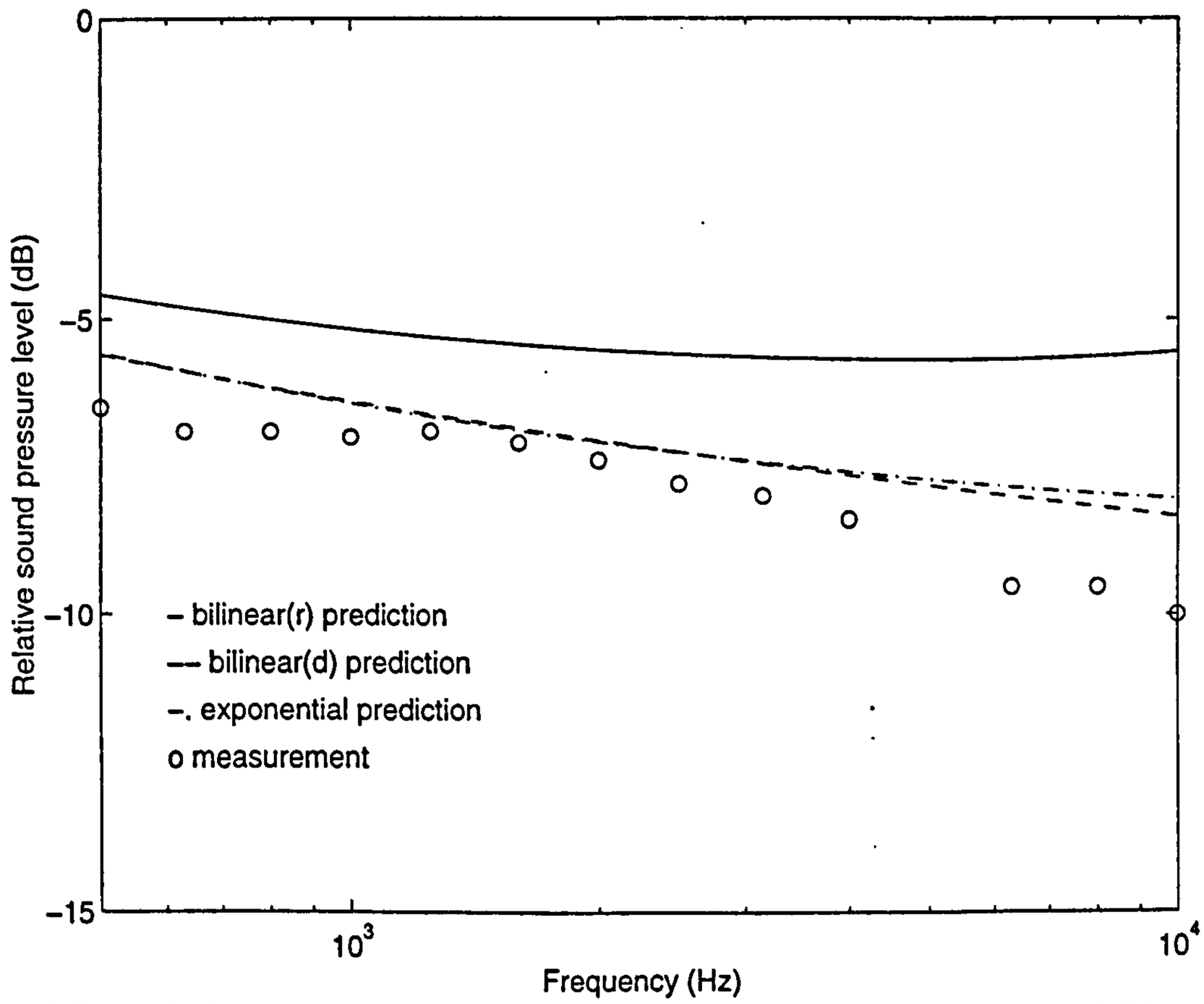

Figure 3.8 Predictions and measurement obtained with the source above a rigid surface, $R_c = 5.0$ m, $z_s = 0.43$ m, $z = 0.38$ m and $r = 3.85$ m.

3.3.2 Comparison to Berthelot and Zhou's data and bilinear profile predictions

To confirm the validity of Equation (3.3.5) for predicting propagation over a cylindrically curved surface, predictions of the residue series solution with a conformal transformation are compared to the experimental results extracted by Berthelot and Zhou [20], and to predictions of the residue series with a bilinear profile along the line of sight in the penumbra of an absorbing cylinder. Figure 3.9 shows the results given in terms of the insertion loss that is defined as $-(\mathrm{EA})$ according to Berthelot and Zhou's notation [19]. The solid line represents the prediction based on Berry and Daigle's residue series solution, the dashed line represents the calculated result of Berthelot [19] using d instead of r, the dashdot line represents the prediction given by Equation (3.3.5), and the circles represent the measured data obtained by Berthelot and Zhou [20]. The impedance is calculated from the Delany-Bazley model [34] with $\sigma = 1600$ kPa s m^{-2} at 10 kHz.

In Figure 3.9, the dimensionless distance $X = (k_0 R_c)^{1/3} x/R_c$ where x is the distance along the limiting ray between the apex of the cylinder and the receiver, and $R_c = 2.5$ m. With regard to the calculation of the residue series, a source height is required. And 0.24 m is found to be the best fit to the dashed line [19]. Again, the prediction of the residue series with the exponential profile shows much better agreement with the experimental results than the prediction with the bilinear profile in the penumbra region. Moreover, it can be seen that there is close agreement between the dashed line and the dashdot line up to a dimensionless distance of 3 from the apex. Beyond this distance, the discrepancies are almost equal between the predictions and the measurements for both dashed line and the dashdot line.

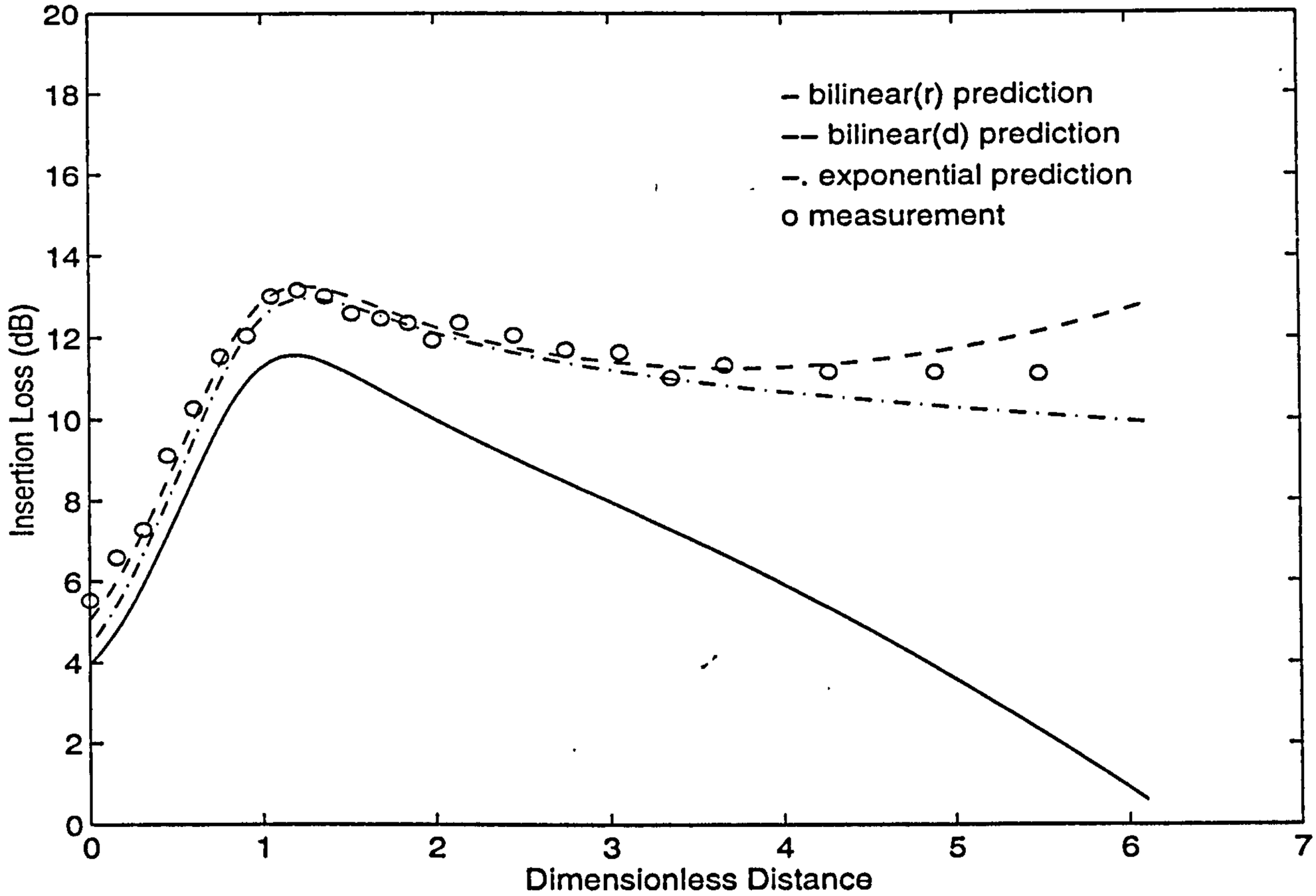

Figure 3.9 Predictions and measurement obtained at 10 kHz with the receiver along the limiting ray behind an impedance surface in the penumbra region with $z_s = 0.24$ m, $R_c = 2.5$ m and $\sigma = 1600$ kPa s m^{-2}.

3.4 Sound field diffracted by a spherical surface

Given a point monopole source placed at $(R_s,\ \theta_s,\ \phi_s)$ in a spherical polar coordinate system, $(R,\ \theta,\ \phi)$, and assuming $R < R_s$, the solution for the scattering of sound by a spherical surface is well known [18, 21, 22]. The direct wave p_i due to a monopole source can be expanded, with the use of Equations (10.1.45) and (10.1.46) of Reference [23], as a series of Legendre polynomials:

$$p_i = S_0 \frac{e^{ik_0 R_d}}{k_0 R_d} = -iS_0 \sum_{n=0}^{\infty} (2n+1) h_n^{(1)}(k_0 R_s) j_n(k_0 R) P_n(\cos\Theta), \tag{3.4.1}$$

where

$$R_d = \sqrt{R^2 + R_s^2 - 2RR_s\cos\Theta}, \tag{3.4.2}$$

and

$$\cos\Theta = \sin\theta \sin\theta_s \cos(\phi - \phi_s) + \cos\theta \cos\theta_s . \tag{3.4.3}$$

In the above, $h_n(\,)$ and $j_n(\,)$ are the nth order spherical Bessel functions and $P_n(\,)$ is the Legendre polynomial of degree n. Similarly, the reflected wave p_r can be expanded into:

$$p_r = -iS_0 \sum_{n=0}^{\infty} V_n (2n+1) h_n^{(1)}(k_0 R_s) h_n^{(1)}(k_0 R) P_n(\cos\Theta), \tag{3.4.4}$$

where V_n are the reflection coefficients to be determined according to the impedance boundary condition given by

$$\frac{\partial p}{\partial R} + ik_0 \beta p = 0 . \tag{3.4.5}$$

The total sound field is then written as

$$p^{(s)} = p_i + p_r$$

$$= -iS_0 \sum_{n=0}^{\infty} (2n+1) \left\{ j_n(k_0 R) + V_n h_n^{(1)}(k_0 R) \right\} h_n^{(1)}(k_0 R_s) P_n(\cos\Theta) . \tag{3.4.6}$$

In the above,

$$V_n = -\frac{j_n'(k_0 R_c) + i\beta j_n(k_0 R_c)}{h_n'^{(1)}(k_0 R_c) + i\beta h_n^{(1)}(k_0 R_c)}, \tag{3.4.7}$$

where the primes denote the derivatives of the spherical Bessel functions with respect to their arguments and the superscript (s) is used to denote the sound field above a spherical surface.

Following the procedures described in Reference [22], and using the asymptotic approximation [23] for Legendre polynomials, Equation (3.4.6) may be approximated by its integral representation as

$$p^{(s)}(r,z) \approx S_0 \frac{\exp\left[i\left(k_0 R_c \Theta + \pi/4\right)\right]}{\sqrt{\frac{1}{2}\pi \sin\Theta}} \times \int_{-\infty}^{\infty} \frac{\left(\varsigma - \frac{1}{2}\right)!}{(\varsigma - 1)!} \exp\left(\frac{1}{2} i k_0 R_c \mu \Theta\right) \left[j_\varsigma(k_0 R) + V_\varsigma h_\varsigma^{(1)}(k_0 R)\right] h_\varsigma^{(1)}(k_0 R_s) d\mu \tag{3.4.8}$$

where

$$\varsigma = k_0 R_c \left(1 + \frac{\mu}{2}\right), \tag{3.4.9}$$

$$R = R_c + z, \qquad R_s = R_c + z_s, \tag{3.4.10}$$

$R_c \gg \max(z, z_s)$, and higher powers of μ are neglected. With the identification of $r = R_c \Theta$, sound propagation near a spherical surface can be approximated by the propagation in a vertically stratified medium with a bilinear sound speed gradient, where the radius of the curvature of ray paths in the medium is R_c. Figure 3.10 illustrates the connection between the parameters for a spherical surface and those for a stratified atmosphere over a plane ground. It is possible to express the connection between the sound field over a spherical surface described by Equation (3.4.8) and the sound field over a cylindrical surface described by Equation (2.4.5) as follows:

$$p^{(s)}(r,z) = \sqrt{\frac{\Theta}{\sin\Theta}} p^{(b)}(r,z), \tag{3.4.11}$$

where $\sqrt{\Theta/\sin\Theta}$ represents a factor that corrects the cylindrical surface field.

Figure 3.11 shows the correction factor as a function of Θ. Clearly, the importance of the correction factor increases as Θ increases. Consequently use of Equation (2.4.5) to predict the sound field above a spherically curved surface, may lead to error especially when the receiver position is deep in the shadow zone.

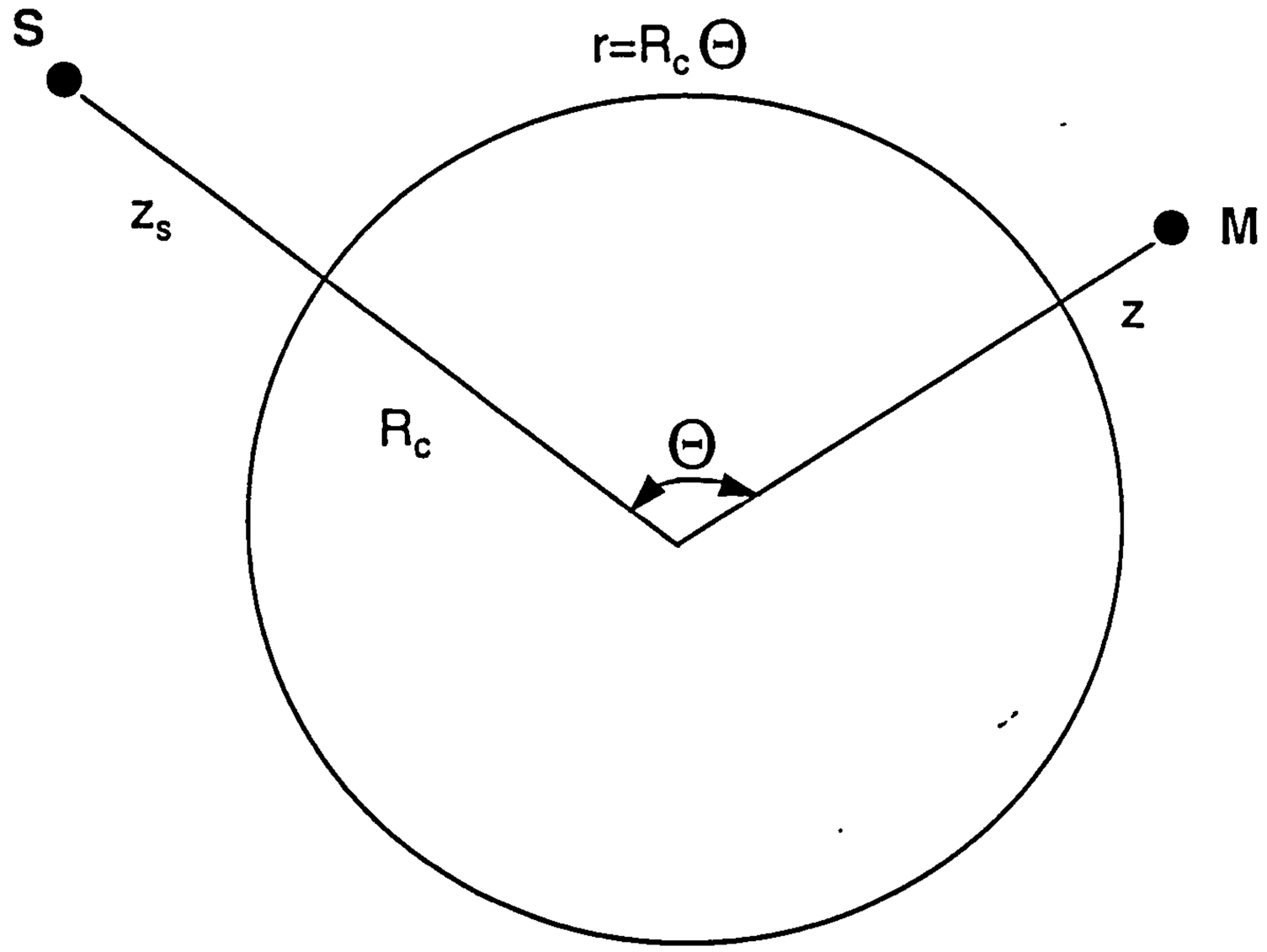

Figure 3.10 Illustration of the connection between the parameters for a spherical surface and those for a stratified atmosphere over a plane boundary.

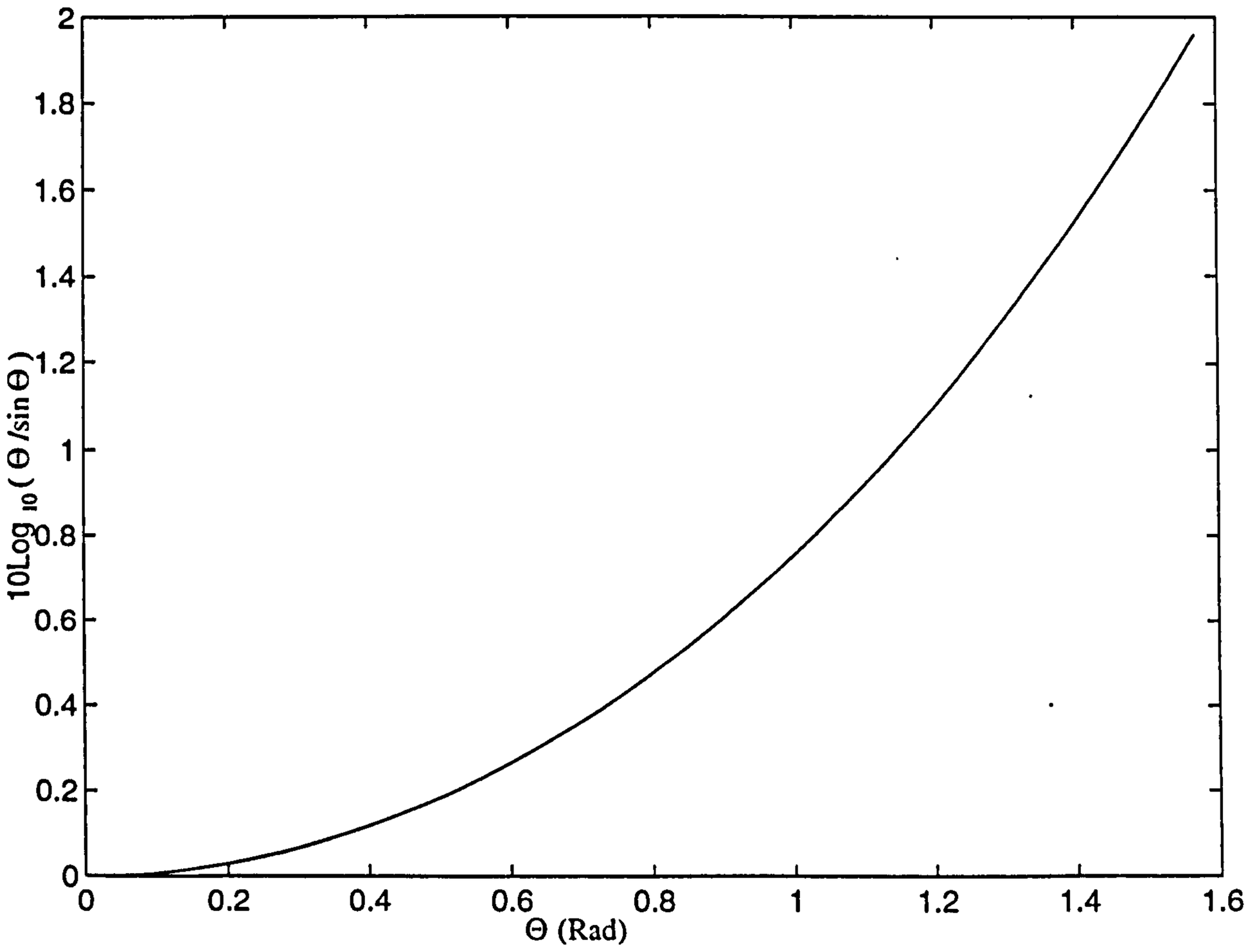

Figure 3.11 The correction factor versus the total angle Θ.

3.5 Comparison with the fast field program

The fast field program (FFP) [10] was developed to predict propagation in a refracting atmospheric above an impedance plane. The atmosphere is assumed to be horizontally stratified and divided into discrete layers, each of which is characterized by its height above the ground and by its sound speed and wind speed. The sound speed gradient within each layer is assumed to be zero. Since there is a useful analogy between propagation along curved ray paths above a flat ground and propagation over a curved surface above which there is no refraction, the fast field program technique can be used to predict the sound field above a convex surface.

In the formulation of the FFP, the sound pressure amplitude $p(r,z)$ is given by the zero-order Hankel transform of the height-dependent Green's function $P(k_r,z)$, and $P(k_r,z)$ is given by the Fourier transform of the function $p(r,z)$. Hence

$$p(r,z) = \int_0^\infty P(k_r,z) J_0(k_r r) k_r dk_r \tag{3.5.1}$$

and

$$P(k_r,z) = \int_0^\infty p(r,z) J_0(k_r r) r dr\,. \tag{3.5.2}$$

It is possible to show that Equation (3.5.2) satisfies

$$\frac{d^2P(k_r,z)}{dz^2} + \left[\frac{\omega^2}{c^2(z)} - k_r^2\right] P(k_r,z) = -2\delta(z-z_s)\,, \tag{3.5.3}$$

where $\delta(\ )$, represents the delta function. Away from the source, $P(k_r,z)$ satisfies the homogeneous equation

$$\frac{d^2P(k_r,z)}{dz^2} + \left[\frac{\omega^2}{c^2(z)} - k_r^2\right] P(k_r,z) = 0\,. \tag{3.5.4}$$

The solution of Equation (3.5.4) is

$$P(k_r,z)=\hat{p}(k_r,z)+A^-(k_r)P^-(k_r,z)+A^+(k_r)P^+(k_r,z), \tag{3.5.5}$$

where $A^-(k_r)$ and $A^+(k_r)$ are arbitrary coefficients to be determined from the boundary conditions, and $\hat{p}(k_r,z)$ is the sound field in the absence of the boundary.

The value of $P(k_r,z)$ at the receiver point must be transformed using Equation (3.5.1) to evaluate the pressure $p(r,z)$ as a function of distance r. The Bessel function in Equation (3.5.1) can be replaced by the sum of two Hankel functions if $k_r r \gg 1$. For numerical computations the infinite integral is replaced by a finite sum over N discrete values of k_r. If the maximum value of k_r in the sum is k_{max}, the wave number intervals are given by $\Delta k = k_{max}/(N-1)$, the corresponding range intervals are $\Delta r = 2\pi/N\Delta k$, and Equation (3.5.1) may be expressed as

$$p(r_m,z)=2(1-i)\sqrt{\frac{\pi}{r_m}}\Delta k\sum_{n=0}^{N-1}P(k_n)\sqrt{k_n}e^{-2i\pi nm/N}, \tag{3.5.6}$$

where $k_n = n\Delta k$ and $r_m = m\Delta r$.

Because of its success in the prediction of outdoor sound propagation, the FFP [101] is compared with our residue series model, which has been described previously in detail, in the cases where the sound speed gradients are assumed to have bilinear, linear and exponential profiles, respectively. Figure 3.12 shows the prediction using the residue series model given by Equation (2.2.17) (the solid line) and the prediction of the FFP (the circles) in the case where a linear profile of the sound speed is assumed. The radius of curvature $R_c = 20.0$ m, the source and receiver heights are 0.8 and 0.05 m, respectively, and the frequency is 500 Hz. The normalized specific admittance of the impedance is $\beta = 0.3512 - 0.3715i$. These parameters are relevant to the laboratory experiments that will be discussed in the next chapter. In Figure 3.13, the two predictions are based on the

assumption of a bilinear sound speed profile. Figure 3.14 shows the two predictions where an exponential profile of the sound speed is assumed. All of the values of parameters used to produce Figures 3.13 and 3.14 are the same as those used to produce Figure 3.12.

Inspection of the above figures shows that the residue series model agrees well with output of the FFP in the shadow zone for all these three profiles. In the illuminated area close to the source, the residue series model is inadequate because that there is no convergence when summing the series.

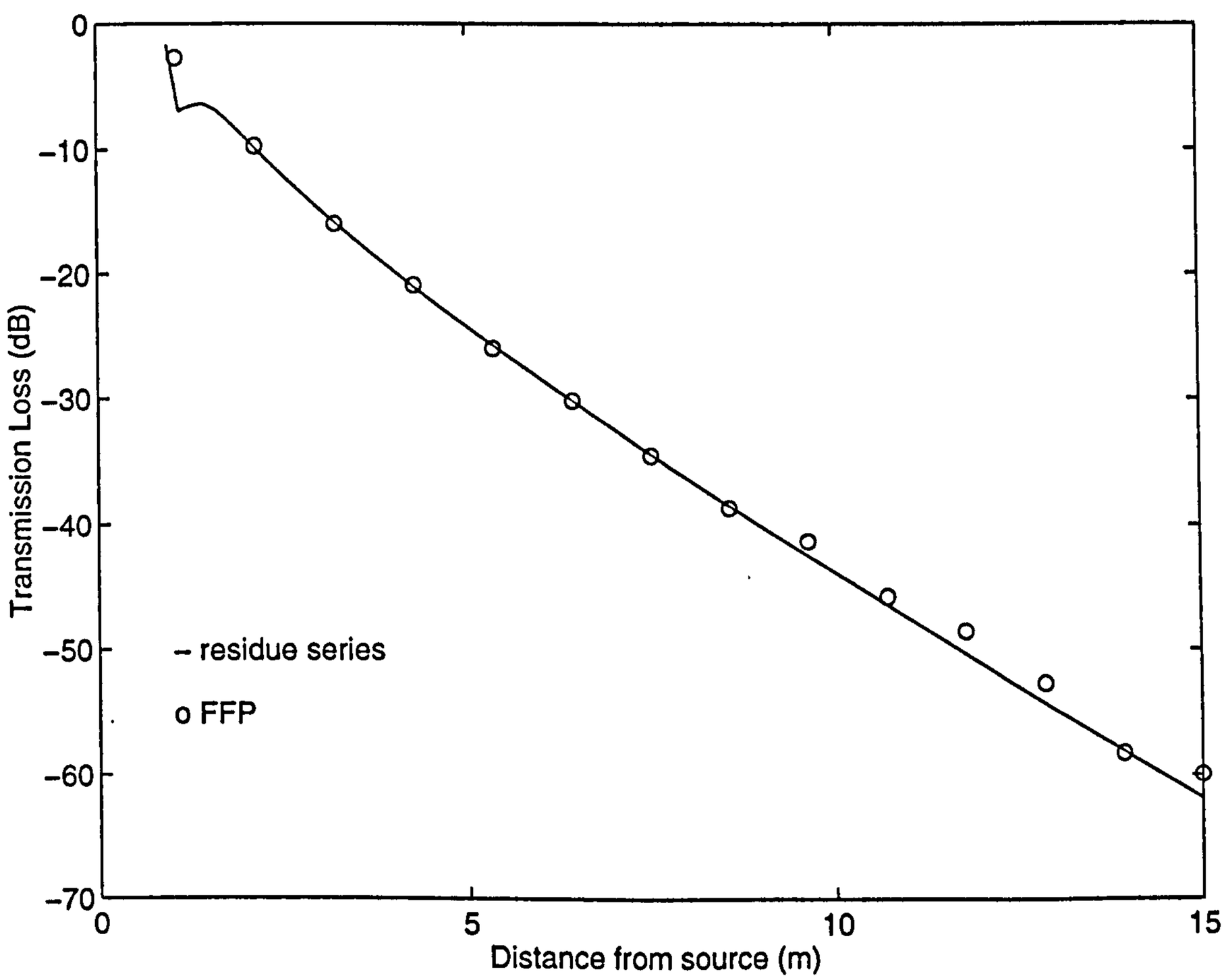

Figure 3.12 Predictions of the residue series and the fast field program obtained with a linear profile of sound speed, $R_c = 20.0$ m, $f = 500$ Hz, $\beta = 0.3512 - 0.3715i$, $z_s = 0.8$ m and $z = 0.05$ m.

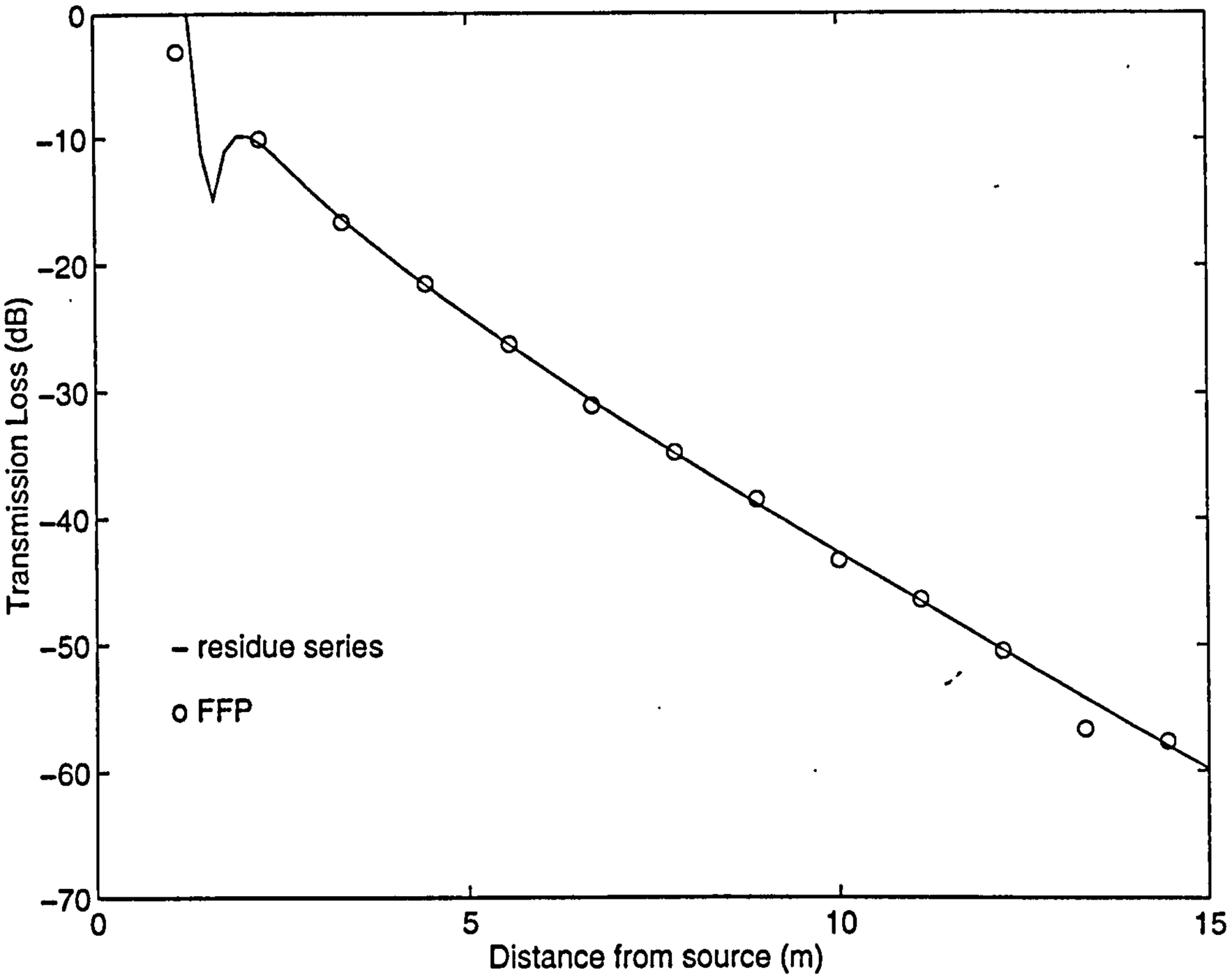

Figure 3.13 Same as **Figure 3.12** except that the sound speed profile varies with height in a bilinear manner.

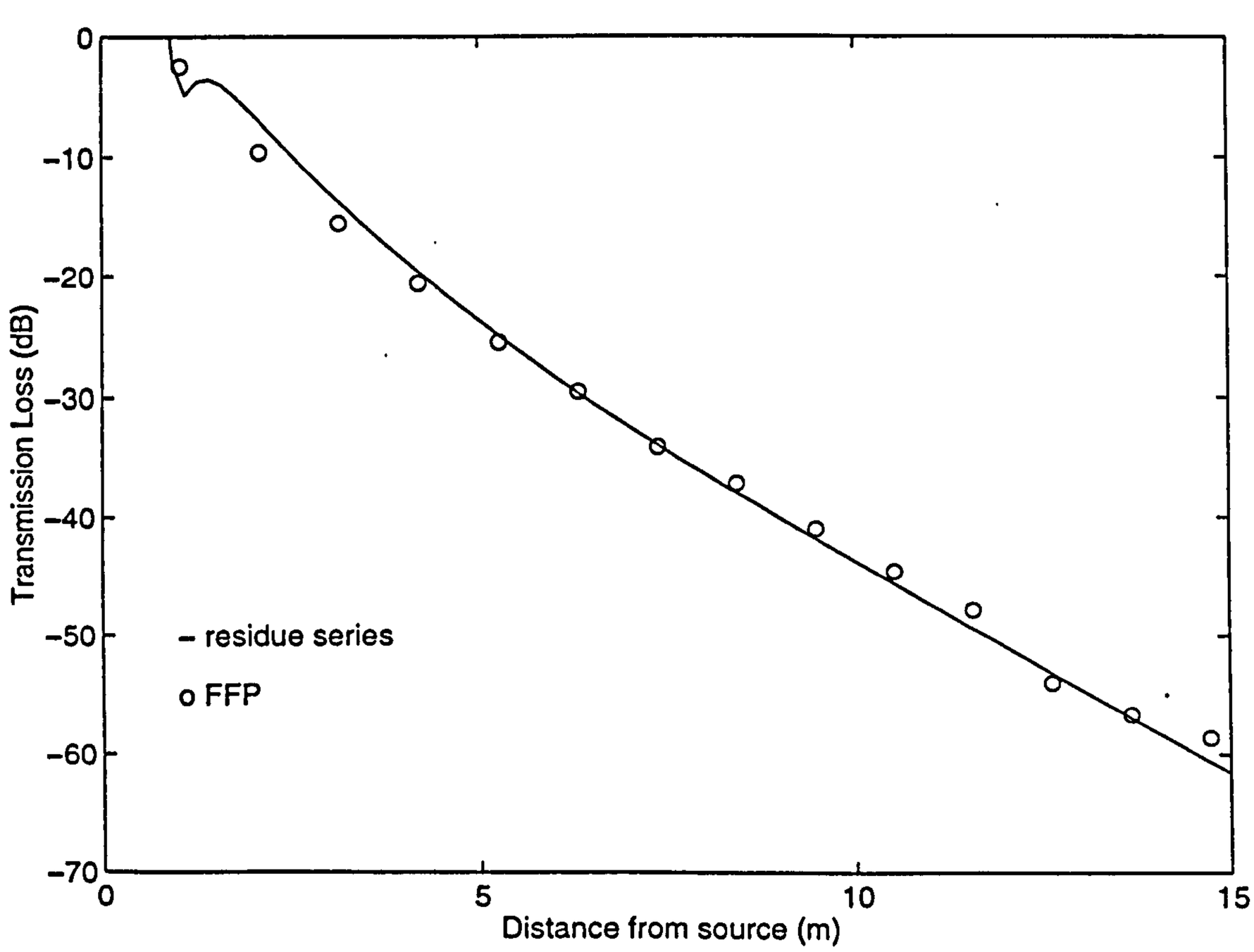

Figure 3.14 Same as **Figure 3.12** except that the sound speed profile varies with height in an exponential manner.

3.6 Comparison with the boundary element method

The boundary element method (BEM) [24] is an alternative approach for dealing with the problem of a sound field diffracted by a curved surface. The problem to be considered is the propagation of sound from a sound source in a quiescent homogeneous medium, above a two-dimensional cylindrically curved surface. The longitudinal axis of the cylinder is aligned with the y-axis. The surface is assumed to be locally reacting with the normalized surface admittance β. By applying Green's second theorem to the Helmholtz equation, impedance boundary condition, and Sommerfeld radiation condition, the acoustic pressure $p(\mathbf{r},\mathbf{r}_0)$ at $\mathbf{r}=(x,z)$ satisfies the following boundary integral equation

$$\upsilon(\mathbf{r})p(\mathbf{r},\mathbf{r}_0)=G_{\beta_c}(\mathbf{r},\mathbf{r}_0)+\int_\gamma\left[\frac{\partial G_{\beta_c}(\mathbf{r}_s,\mathbf{r})}{\partial n(\mathbf{r}_s)}-ik\beta(\mathbf{r}_s)G_{\beta_c}(\mathbf{r}_s,\mathbf{r})\right]p(\mathbf{r}_s,\mathbf{r}_0)ds(\mathbf{r}_s), \qquad (3.6.1)$$

where $\mathbf{r}_0=(x_0,z_0)$ denotes the source position, see Figure 3.15, γ is the curve which is intersection of the convex surface with the vertical plane of the cross-section, $\mathbf{r}_s=(x_s,z_s)$ denotes the position on γ, and $\beta(\mathbf{r}_s)$ is the normalized surface admittance at point $\mathbf{r}_s$. In this equation, $ds(\mathbf{r}_s)$ is the arc-length of an element of γ at $\mathbf{r}_s$, $\partial/\partial n(\mathbf{r}_s)$ is the partial derivative in the direction of the normal to γ at $\mathbf{r}_s$ directed out of the propagating medium, and k is the wave number. If $\mathbf{r}$ lies anywhere in the propagating medium except on γ, $\upsilon(\mathbf{r})=1$; $\upsilon(\mathbf{r})=1/2$ if $\mathbf{r}$ is a point on γ that is not a corner point; if $\mathbf{r}$ is a corner point, $\upsilon(\mathbf{r})=\Omega/(2\pi)$, where Ω is the angle in the medium subtended by the two tangents to the boundary at $\mathbf{r}$. $G_{\beta_c}(\mathbf{r},\mathbf{r}_0)$ is the acoustic pressure at $\mathbf{r}$ due to a source at $\mathbf{r}_0$ above a plane of homogeneous admittance β_c in the absence of the convex surface. $G_{\beta_c}(\mathbf{r},\mathbf{r}_0)$ can be written as

$$G_{\beta_c}(\mathbf{r},\mathbf{r}_0) = -\frac{i}{4}\left[H_0^1(k|\mathbf{r}_0-\mathbf{r}|)+H_0^1(k|\mathbf{r}_0'-\mathbf{r}|)\right]+P_{\beta_c}(\mathbf{r},\mathbf{r}_0), \tag{3.6.2}$$

where $\mathbf{r}_0' = (x_0,-z_0)$ is the image of the source in the straight boundary, and

$$P_{\beta_c}(\mathbf{r},\mathbf{r}_0) = 0 \text{ for } \beta_c = 0 \text{ and} \tag{3.6.3a}$$

$$P_{\beta_c}(\mathbf{r},\mathbf{r}_0) = \frac{i\beta_c}{2\pi}\int_{-\infty}^{+\infty}\frac{\exp\left(ik\left[(z+z_0)\sqrt{1-s^2}-(x-x_0)s\right]\right)}{\sqrt{1-s^2}\left[\sqrt{1-s^2}+\beta_c\right]}ds \text{ for } \mathrm{Re}(\beta_c)>0 \tag{3.6.3b}$$

with $\mathrm{Re}\left(\sqrt{1-s^2}\right)\geq 0$ and $\mathrm{Im}\left(\sqrt{1-s^2}\right)\geq 0$. Equation (3.6.1) must be solved numerically except for very specific geometrical conditions. The solution can be obtained by a boundary element method.

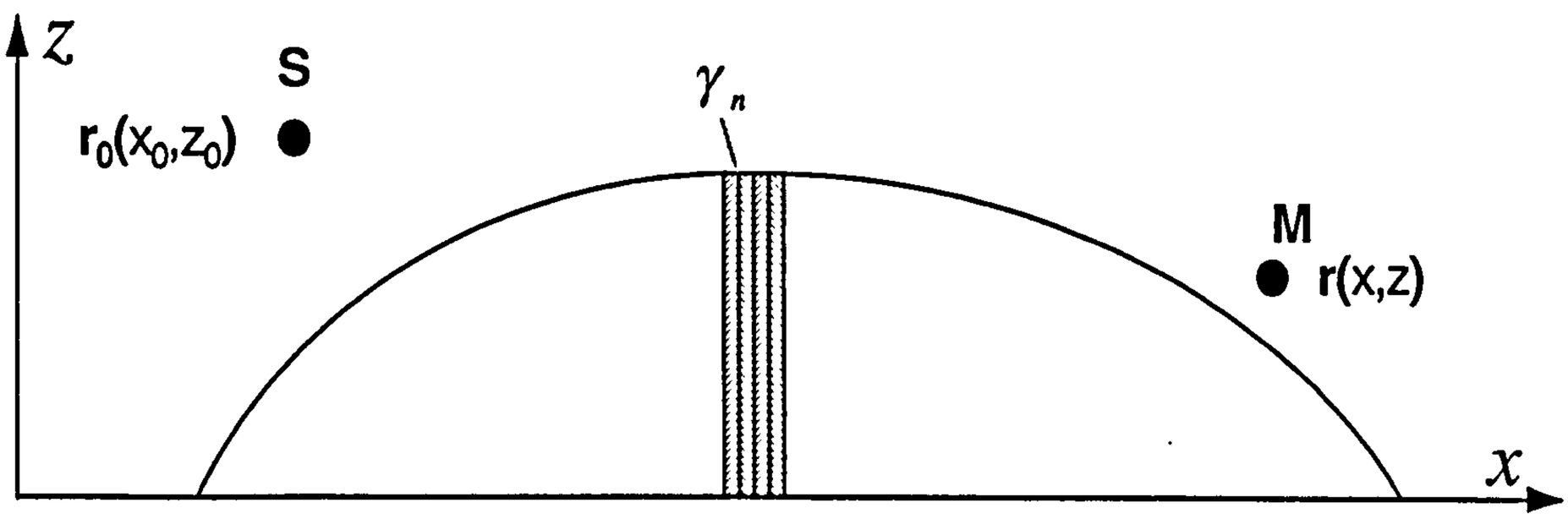

Figure 3.15 Illustration of the BEM for the diffraction problem.

To carry out this BEM, the curve γ is divided into a number of straight line elements γ_1, γ_2, ..., γ_N and approximated by an N-sided polygon. Assuming that, for $n = 1,2,\ldots,N$, $p(\mathbf{r},\mathbf{r}_0) \sim p(\mathbf{r}_n,\mathbf{r}_0)$ for $\mathbf{r}$ on γ_n, where $\mathbf{r}_n$ is the midpoint of γ_n, the integral Equation (3.6.1) becomes

$$\upsilon(\mathbf{r})p(\mathbf{r},\mathbf{r}_0) = G_{\beta_c}(\mathbf{r},\mathbf{r}_0)+\sum_{n=1}^{N}p(\mathbf{r}_s,\mathbf{r}_0)\int_{\gamma_n}\left[\frac{\partial G_{\beta_c}(\mathbf{r}_s,\mathbf{r})}{\partial n(\mathbf{r}_s)}-ik\beta(\mathbf{r}_s)G_{\beta_c}(\mathbf{r}_s,\mathbf{r})\right]ds(\mathbf{r}_s). \tag{3.6.4}$$

By setting $\mathbf{r} = \mathbf{r}_m$ for $m = 1,2, ..., N$ in Equation (3.6.4), a set of N linear equations in the unknowns $p(\mathbf{r}_1, \mathbf{r}_0)$, $p(\mathbf{r}_2, \mathbf{r}_0)$, ..., $p(\mathbf{r}_N, \mathbf{r}_0)$ is obtained. After solving these equations and determining the pressure at the midpoint of each element, Equation (3.6.4) can be used to calculate $p(\mathbf{r}, \mathbf{r}_0)$ at any other point $\mathbf{r}$ in the propagating medium.

In order to obtain a sufficiently accurate solution by the BEM, it is necessary to have a maximum element length of not more than $\lambda/5$, where λ is the wavelength [25].

Having noted that the BEM is successful in modelling sound propagation above an inhomogeneous impedance plane, our residue series model is further compared with output of this method in the case where the sound speed gradient is assumed to have an exponential profile. Using the BEM, the cross section of a cylindrical convex surface is approximated by an 350-sided polygon with impedance faces (*cf.* Figure 3.15). For the purposes of this comparison, excess attenuation, EA, is predicted.

Figure 3.16 shows the prediction of the residue series model (the solid line) and the prediction of BEM (the circles) above an impedance convex surface. The radius of curvature $R_c = 20.0$ m, the source and receiver heights are 0.16 and 0.05 m, respectively. The normalized specific admittance of the impedance is $\beta = 0.3026 - 0.3216i$ at 375 Hz. We shall use these parameters in the following chapter. In Figure 3.17, all the parameters are the same as for Figure 3.16 except that the two predictions are given above a rigid convex surface.

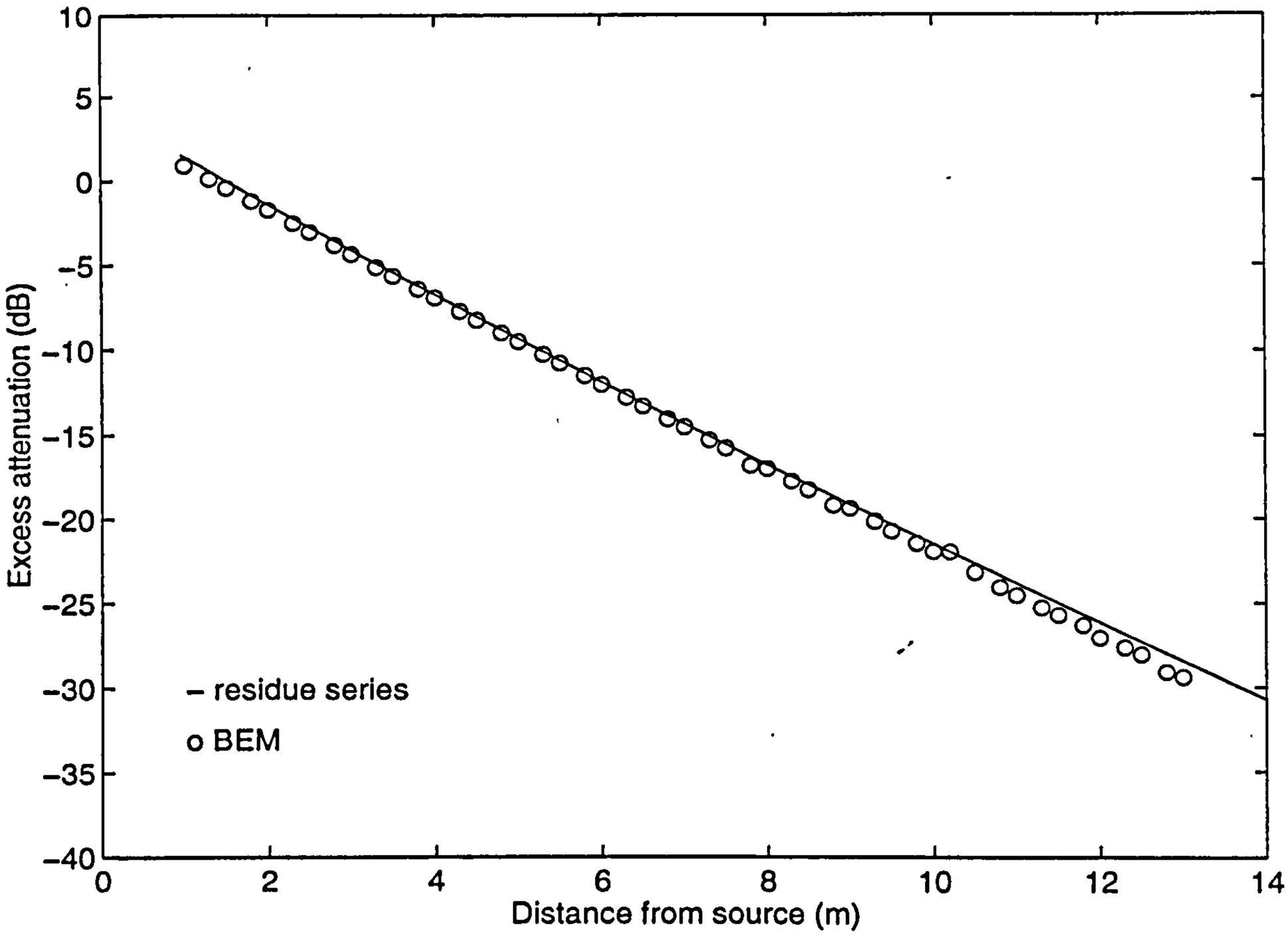

Figure 3.16 Predictions of the residue series and the BEM obtained with a bilinear profile of the sound speed, $R_c = 20.0$ m, $f = 375$ Hz, $z_s = 0.16$ m, $z = 0.05$ m and $\beta = 0.3024 - 0.3216i$.

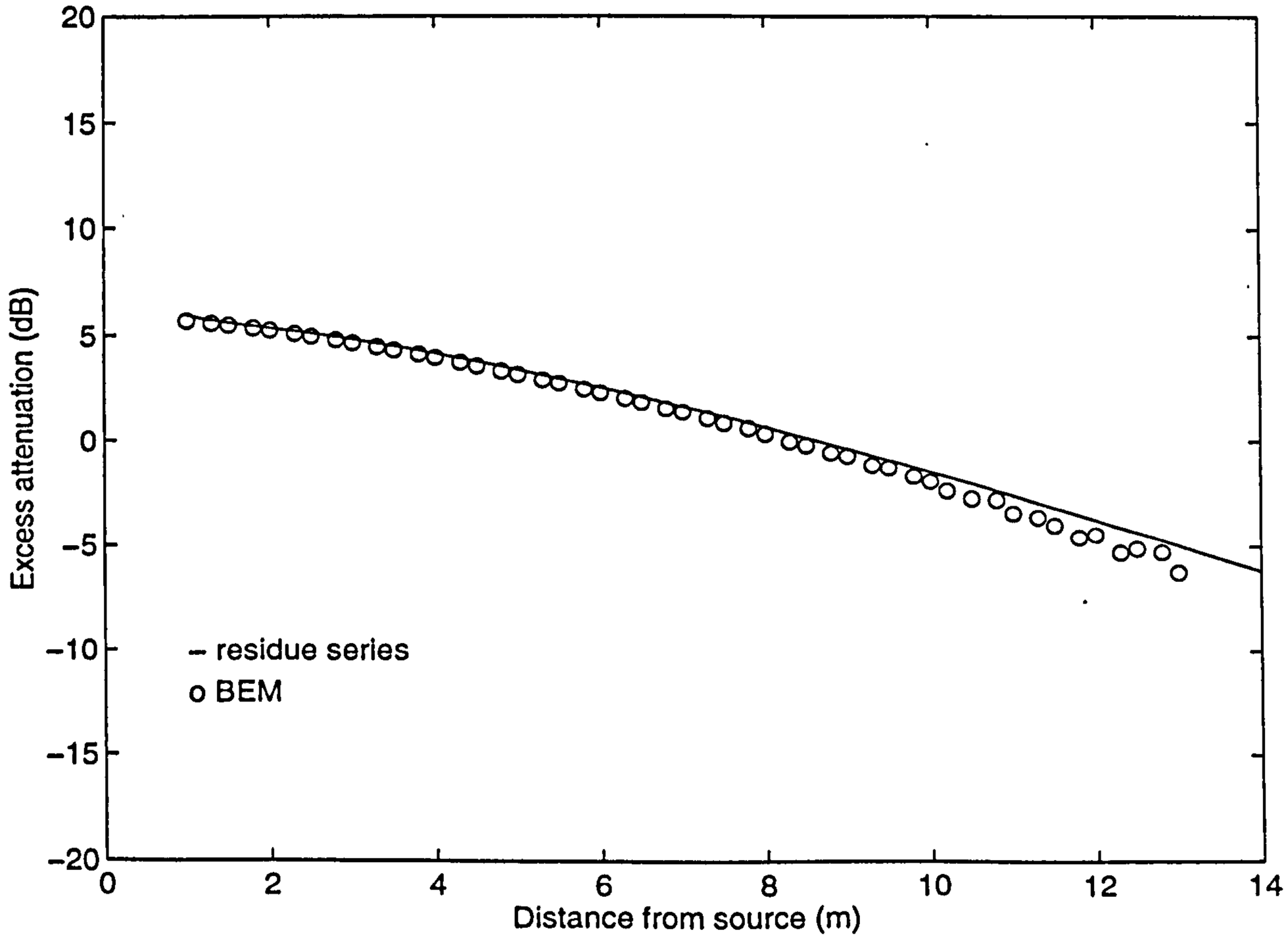

Figure 3.17 Same as **Figure 3.16** except $\beta = 0$.

It can be seen that the predictions resulting from the two prediction schemes are very close. This implies that the BEM may be used to model propagation over absorbing ground surfaces in the presence of a sound speed gradient. The application of the BEM in a more complicated situation, such as in the presence of a thin barrier, will be reported in Chapter 7.

3.7 Discussion of the matched asymptotic expansion theory

As another alternative approach to the residue series, the theory of matched asymptotic expansions (MAE) has been applied to the problem of the diffraction of sound by a convex surface of finite impedance [20, 26]. This work is based on Fock's results concerning the diffraction of electromagnetic waves by conducting curved surfaces. We assume that a plane wave with complex amplitude $P_i e^{ik_0 x}$ is incident upon a locally reacting surface, whose radius of curvature is R_c. A Cartesian coordinate system (x, z) is situated such that its origin is the apex of the convex surface, and the x-axis is coincident with a incident ray, see Figure 3.18. Because the local shape of the surface near the apex can be approximated by the parabola $z = -x^2/2R_c$, a non-dimensional parabolic cylinder coordinate system (ζ, η), is introduced such that the axis $\eta = 0$ defines the curved boundary. The relationship between the two coordinates is defined by

$$\zeta = \frac{1}{2R_c}\left\{\sqrt{\left(2R_c z + R_c^2\right)^2 + 4R_c^2 x^2} - \left(2R_c z + R_c^2\right)\right\}^{1/2}\left(\frac{k_0 R_c}{2}\right)^{1/3}. \tag{3.7.1}$$

and

$$\eta = 2^{1/3}\left(k_0 R_c\right)^{2/3}\left\{\frac{2x}{\left[\sqrt{\left(2R_c z + R_c^2\right)^2 + 4R_c^2 x^2} - \left(2R_c z + R_c^2\right)\right]^{1/2}} - 1\right\}. \tag{3.7.2}$$

The acoustic pressure measured at a field point (ζ,η) is expressed as

$$p(\zeta,\eta) = P_i e^{ik_0 u} e^{i\zeta^{1/3}} G(\zeta,\eta) \tag{3.7.3}$$

where

$$G(\zeta,\eta,q) = \frac{1}{\sqrt{\pi}} \int_{-\infty}^{\infty} \left[v(s-\eta) - \frac{v'(s)-qv(s)}{w_1'(s)-qw_1(s)} w_1(s-\eta) \right] e^{ii\zeta} ds \tag{3.7.4}$$

where the functions v and w_1 are the Fock functions defined as follows

$$v(s) = \sqrt{\pi}\,\mathrm{Ai}(s) \tag{3.7.5}$$

$$w_1(s) = 2\sqrt{\pi} e^{i\pi/6} \mathrm{Ai}\left(e^{i2\pi/3} s\right). \tag{3.7.6}$$

When both ζ and η in Equation (3.7.4) are of the order of unity or smaller, where the field is near the apex, Equation (3.7.4) can be rewritten without approximation as

$$G(\zeta,\eta,q) = \frac{1}{\sqrt{\pi}} \int_0^{\infty} \left[v\left(s-\tilde{\eta}\right) - \frac{v'(s)-\tilde{q}v(s)}{w_2'(s)-\tilde{q}w_2(s)} w_2\left(s-\tilde{\eta}\right) \right] e^{i\zeta} ds$$

$$+ \frac{1}{\sqrt{\pi}} \int_0^{\infty} \left[v(s-\eta) - \frac{v'(s)-qv(s)}{w_1(s)-qw_1(s)} w_1(s-\eta) \right] e^{i\zeta} ds, \tag{3.7.7}$$

where

$$\tilde{\eta} = \eta e^{-i2\pi/3}, \tag{3.7.8a}$$

$$\tilde{q} = q e^{i2\pi/3}, \tag{3.7.8b}$$

$$\tilde{s} = s e^{i2\pi/3} \tag{3.7.8c}$$

and

$$w_2(s) = 2\sqrt{\pi} e^{-i\pi/6} \mathrm{Ai}\left(s e^{-i2\pi/3}\right) \tag{3.7.9}$$

is a third Fock function.

When the acoustic pressure is measured on the convex surface, Equation (3.7.4) can be simplified as follows

$$G(\zeta,0,q)=\frac{1}{\sqrt{\pi}}\int_0^\infty \frac{e^{is\zeta/2}e^{-s\zeta\sqrt{3}/2}}{w_2'(s)-e^{i2\pi/3}qw_2(s)}ds+\frac{1}{\sqrt{\pi}}\int_0^\infty \frac{e^{is\zeta}}{w_1'(s)-qw_1(s)}ds. \tag{3.7.10}$$

In the penumbra region, an approximate expression for G can be derived. This expression can be decomposed into two parts: a knife-edge diffraction Φ_g and a Fock's background Ψ_g. Thus Equation (3.7.4) becomes

$$G=\Phi_g+\Psi_g, \tag{3.7.11}$$

where

$$\Psi_g=-\frac{1}{\sqrt{\pi}}\int_0^\infty e^{is\zeta e^{i2\pi/3}}\frac{v'(s)-qe^{i2\pi/3}v(s)}{w_2'(s)-qe^{i2\pi/3}w_2(s)}w_2\left(s-\eta e^{i2\pi/3}\right)ds$$

$$-\frac{1}{\sqrt{\pi}}\int_0^\infty e^{is\zeta}\frac{v'(s)-qv(s)}{w_1(s)-qw_1(s)}w_1(s-\eta)ds, \tag{3.7.12}$$

and

$$\Phi_g=\frac{1}{2}e^{(2/3)\eta^{3/2}}w\left[-\frac{\sqrt{\pi}}{2}(1+i)Y\right], \tag{3.7.13}$$

where

$$w(z)=\operatorname{erfc}(-iz)e^{-z^2}, \tag{3.7.14}$$

and

$$Y=-\sqrt{\frac{2}{\pi}}\eta^{1/4}\left(\zeta-\sqrt{\eta}\right). \tag{3.7.15}$$

Note that the MAE theory is applicable to the sound field diffracted by a convex surface provided that the incident wave is plane. It is, therefore, not comparable with the residue series solution, in which the spherical wave due to a point source is assumed. However, in a special case where the receiver is located along the line of sight near the apex of the curved surface, Equation (3.7.7) may be used to predict the sound field due to a point source and this will be discussed in Chapter 4.2.

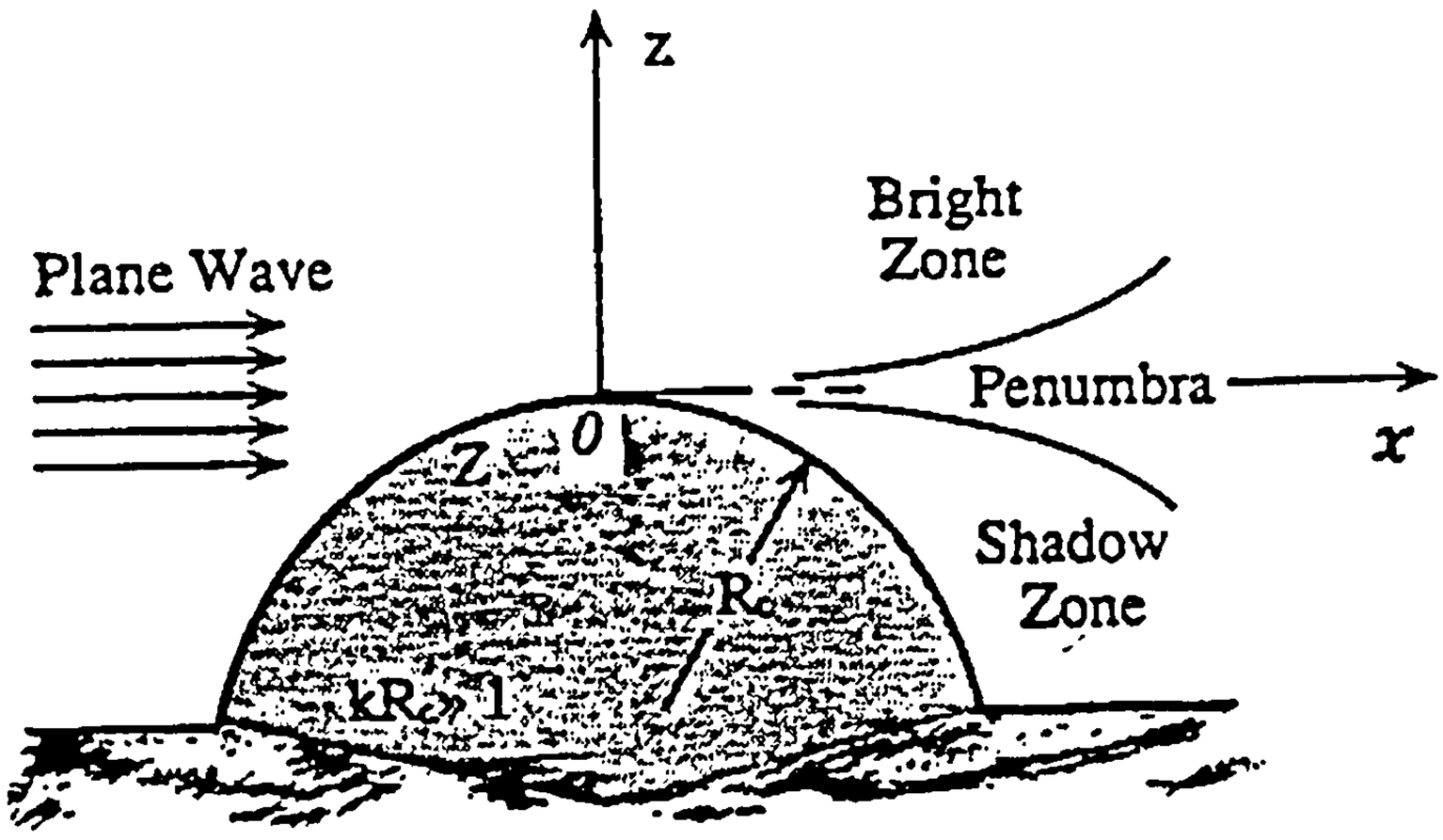

Figure 3.18 Geometry of the diffraction problem.

3.8 Geometrical acoustics solution

If R_c is large compared to the wavelength λ and the receiver is in an insonified region, it is convenient to use a geometrical acoustics solution for the sound field over a convex surface [3, 15]. The insonified regions include the region before the apex of the cylinder close to the source and the region above the limiting ray over the convex surface. The geometric description of the problem is illustrated in Figure 3.19. According to the law of mirrors, the reflected path length is $d_r = d_1 + d_2$ and the point of specular reflection can be obtained from geometrical considerations. However, the effect at the point of reflection must account for the curved surface, *i.e.*, the reflected waves are attenuated by an amount in excess of inverse square law alone because a parallel tube of energy incident on a convex surface is reflected as a divergent energy beam. The solution is a superposition of a reflected and direct ray.

If the convex surface is a cylinder, for a point monopole source, the sound pressure is given by [15]

$$p(r,z) = S_0\left\{\frac{\exp(ik_0 d)}{d} + \frac{Q\exp(ik_0 d_r)}{\sqrt{\frac{d_r^2 R_c \cos\theta_0 + 2d_r d_1 d_2}{R_c\cos\theta_0}}}\right\} \tag{3.8.1}$$

where

$$\theta_0 = \alpha_0 + \beta_0\,, \tag{3.8.2}$$

$$\alpha_0 = \sin^{-1}\left(\frac{R_c \sin\beta_0}{d_1}\right), \tag{3.8.3}$$

$$d_1 = \sqrt{(R_c + z_s)^2 + R_c^2 - 2R_c(R_c + z_s)\cos\beta_0}\,, \tag{3.8.4}$$

$$d_2 = \sqrt{(R_c + z)^2 + R_c^2 - 2R_c(R_c + z)\cos\left(\frac{r}{R_c} - \beta_0\right)}, \tag{3.8.5}$$

$$d = \sqrt{d_1^2 + d_2^2 - 2d_1 d_2\cos(2\theta_0)}, \tag{3.8.6}$$

$$\left[\sin\left(\frac{r}{R_c} - \beta_0\right)\right](\sin\beta_0)^{-1} = \left(\frac{d_2}{d_1}\right)\left(\frac{R_c + z_s}{R_c + z}\right), \tag{3.8.7}$$

and Q is the complex spherical wave reflection coefficient such as

$$Q = R_p + (1 - R_p)F(w), \tag{3.8.8}$$

where $F(w)$ is the boundary loss factor defined by

$$F(w) = 1 + i\sqrt{\pi}w\exp(-w^2)\mathrm{erfc}(-iw)\,. \tag{3.8.9}$$

R_p is the plane wave reflection coefficient. For a locally reacting surface, it is given by

$$R_p = \frac{\cos\theta_0 - \beta}{\cos\theta_0 + \beta}, \tag{3.8.10}$$

and w is defined by [27]

$$w = +\frac{1+i}{2}\sqrt{k_0 d_r(\cos\theta_0 + \beta)}. \qquad (3.8.11)$$

The geometrical acoustics solution is valid for the sound field before the shadow boundary where $r < \sqrt{2z_s R_c}$ as shown by the dotted lines in Figures 3.20 and 3.21. However, it is known [39] that Equation (3.8.1) is not valid at points near the shadow boundary. On the other hand, in the region before the apex in the vicinity of the source, the residue series does not converge, as shown by the solid lines in the above two figures.

L'Esperance *et al* [90] suggested use of the residue series solution in the region $r > \sqrt{2z_s R_c} + \sqrt{2zR_c}$ and the geometrical acoustics solution in the region $r < \sqrt{2z_s R_c} + \sqrt{2zR_c}$. Figures 3.20 and 3.21 show that there is reasonable smooth transition between both the residue series solution and the geometrical acoustics solution in the region $z_s + z > r > \sqrt{2z_s R_c}$ where these two solutions agree to less than 0.5 dB.

Berry and Daigle showed [15] that the predictions given by the geometrical acoustics solution (the solid lines) agree closely with their measurements (the circles) in the region well above the shadow over the entire frequency range of interest, see Figures 3.22 and 3.23. In Figure 3.22, the results shown were obtained above a felt-covered convex surface, the impedance was calculated from Attenborough's four-parameter model [28] with a flow resistivity of 60 kPa s m^{-2}, a porosity of 0.9, a tortusity and a pore shape factor set to unity. The radius of the cylinder was 5.0 m, the source and receiver heights were 0.30 and 1.46 m, respectively, and the range was 3.43 m. In Figure 3.23 , the results shown were obtained above a rigid curved surface. The radius of the cylinder was the same as that relevant to Figure 3.22 but the source and receiver heights were 0.43 and 0.93 m, respectively, and the range was 3.65 m.

In the region above the limiting ray, Berry and Daigle [15] suggested that the geometrical acoustics solution is comparable to the residue series solution with a bilinear profile [15]. However, we find that the series is a poorly convergent sum of many small terms and there are discrepancies between the predictions and the measurements. It can be demonstrated that for the geometry given in Figure 3.22, the series does not converge at 10 kHz even when 300 terms are calculated. In Figure 3.23, the dotted line represents the prediction from the residue series solution using 30 terms. Note that the discrepancy between the two curves becomes larger at higher frequencies.

To investigate this phenomenon, the geometrical acoustics solution will be compared further to both the residue series solution and to results of measurements in the next chapter. It is noted that the number of terms necessary for the convergence of the residue series solution is proportional to the frequency, the height of receiver above the limiting ray increases, and the radius of the cylinder. In addition, the discrepancy between the two prediction schemes increases as the height of receiver above the limiting ray.

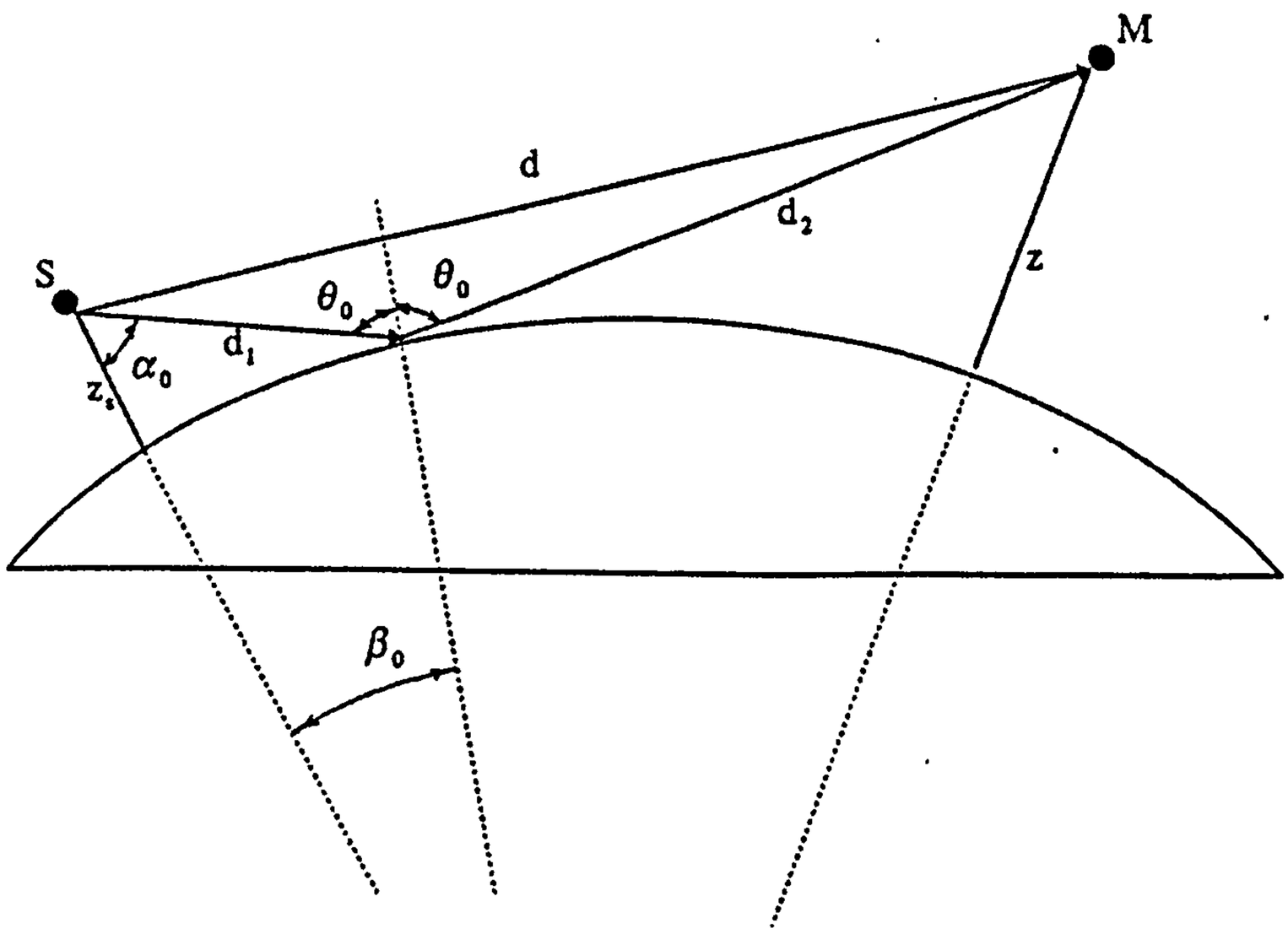

Figure 3.19 Geometrical definitions to obtain the point of specular reflection above the curved surface.

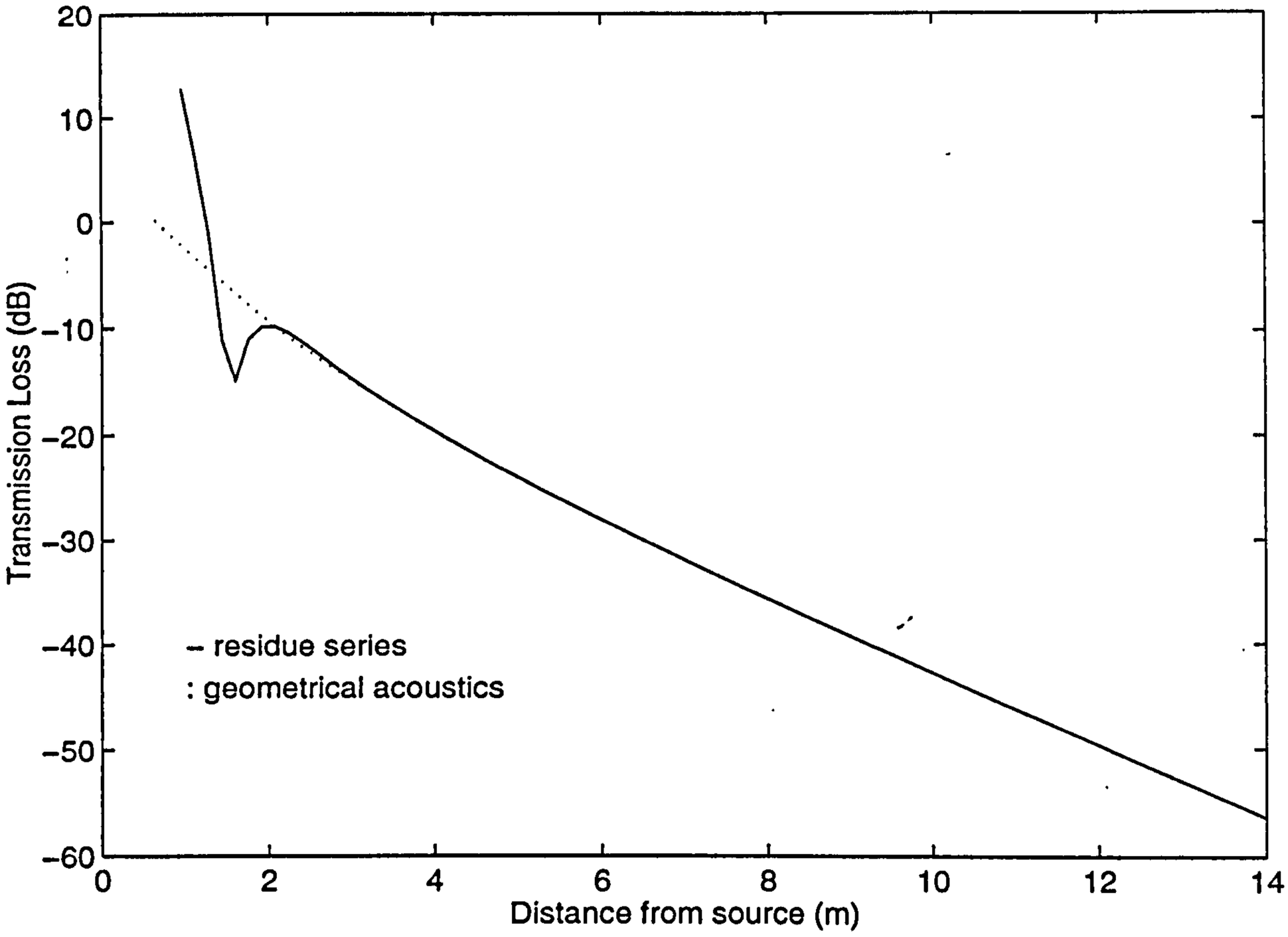

Figure 3.20 Predictions of the residue series and the geometrical acoustics solution obtained above an impedance surface, $R_c = 20.0$ m, $f = 500$ Hz, $\beta = 0.3512 - 0.3715i$, $z_s = 0.8$ m and $z = 0.05$ m.

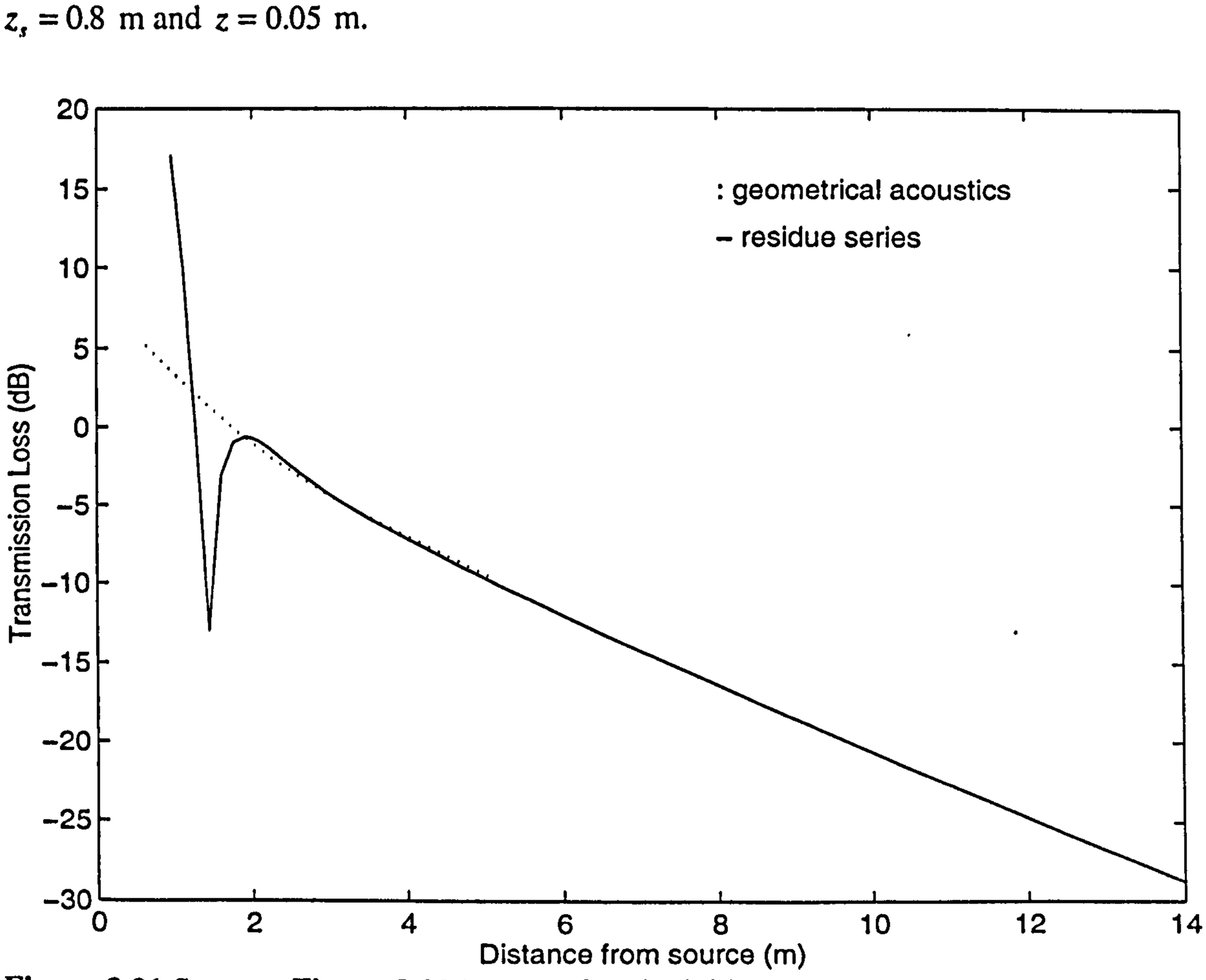

Figure 3.21 Same as **Figure 3.20** but a surface is rigid.

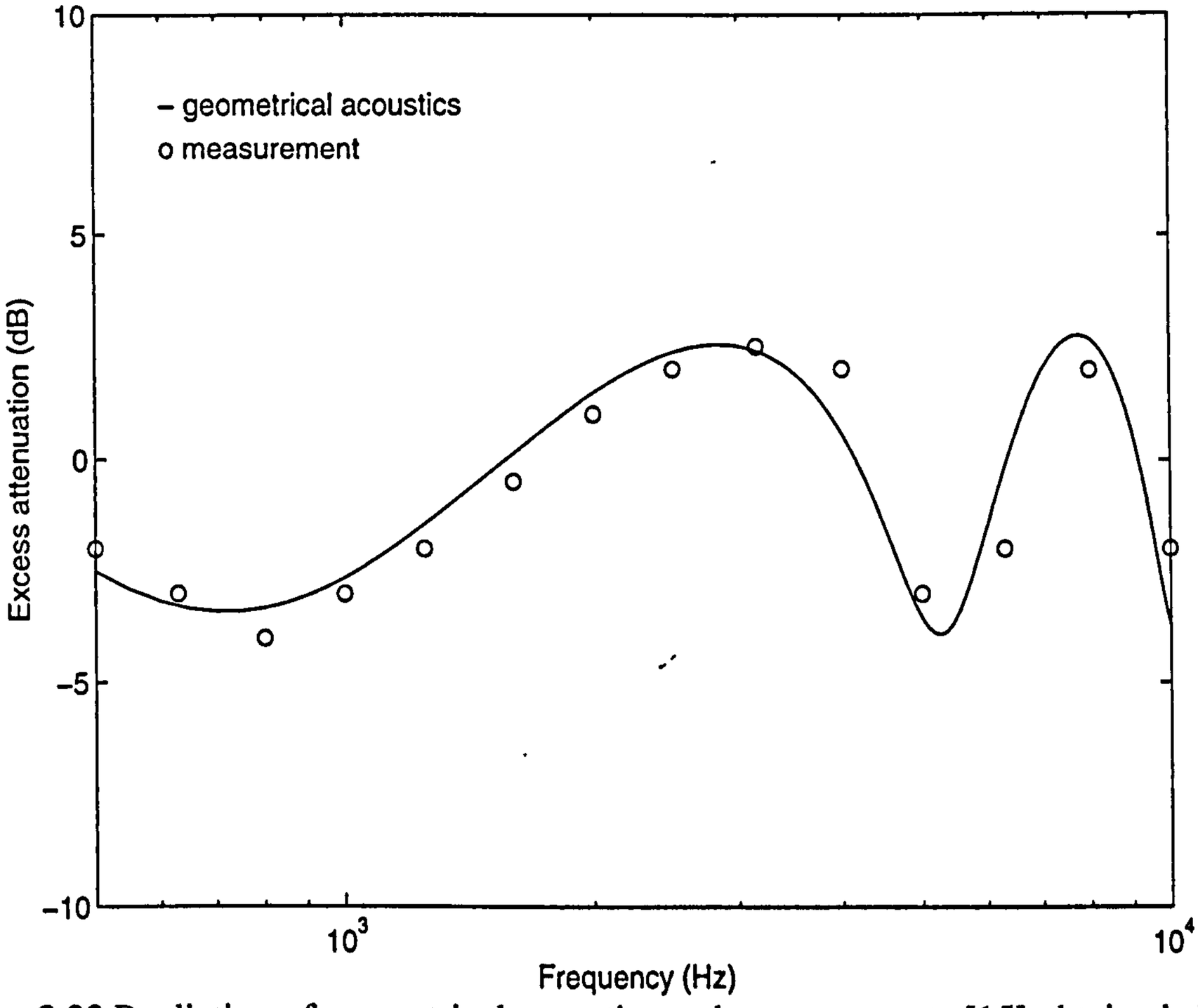

Figure 3.22 Prediction of geometrical acoustics and measurements [15] obtained above an impedance surface, $\sigma = 60$ kPa s m^{-2}, $R_c = 5.0$ m, $z_s = 0.30$ m, $z = 1.46$ m and $r = 3.43$ m.

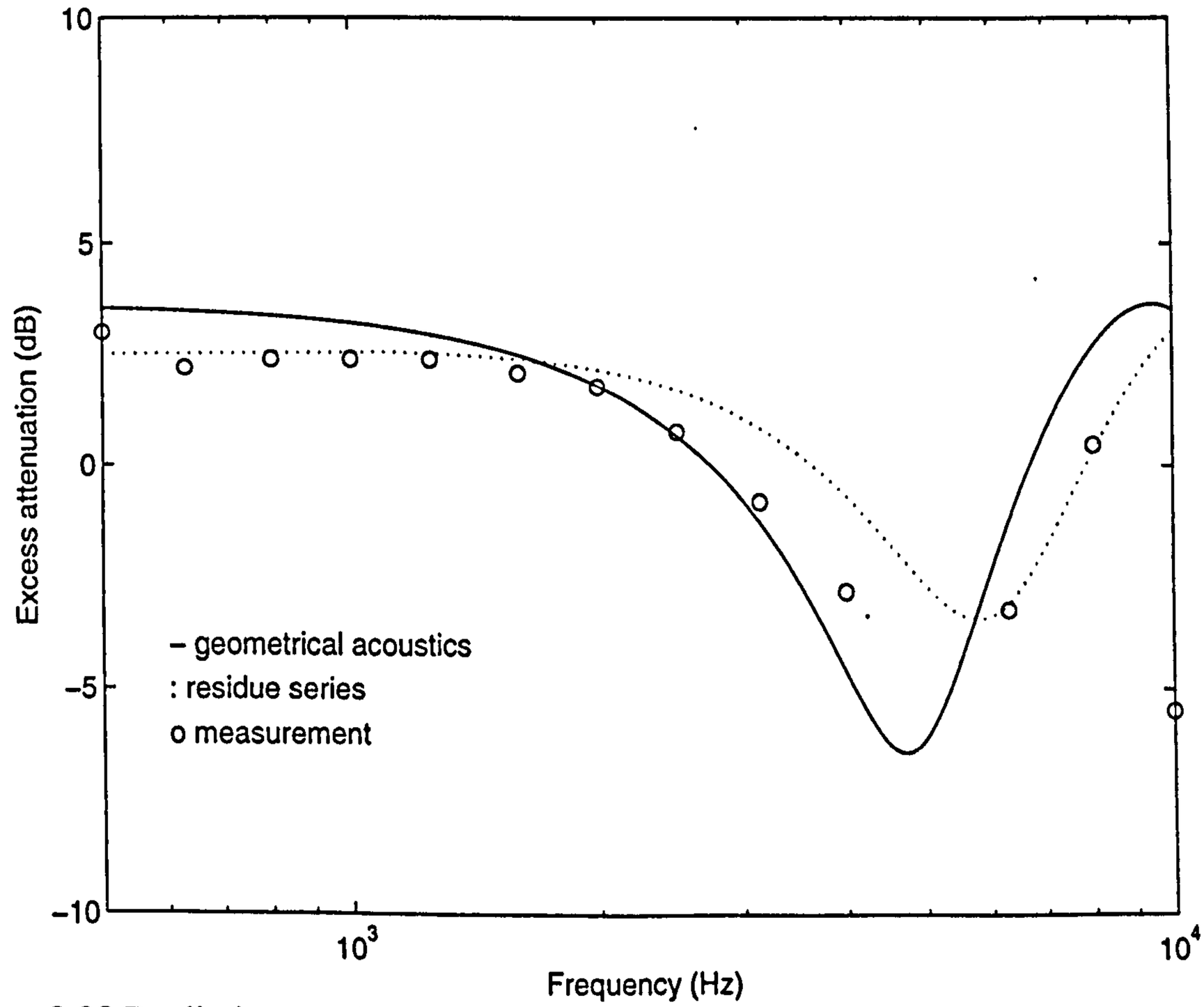

Figure 3.23 Predictions and measurements [15] obtained above the rigid surface, $R_c = 5.0$ m, $z_s = 0.43$ m, $z = 0.93$ m and $r = 3.65$ m.

3.9 Diffraction of a dipole sound field by a convex surface

Theories that have been developed to predict the diffraction of sound over a curved surface have been expressed in terms of sound radiation from point monopole source. However, real noise sources are not always monopolar in character. The theories, therefore, need to be extended for other sources. In the following sections, a dipole source is investigated.

3.9.1 Residue series solution for propagation from a dipole source above an impedance ground

Noting that [30] the horizontal range and the vertical height dependent factors are not coupled in the residue series solution for a monopole source, the dipole field $p_d(r,\psi_r,z)$ can be derived from the monopole field $p(r,z)$ by

$$p_d(r,\psi_r,z)=2\Delta_d S_0\left[\sin\gamma_d\cos(\psi_d-\psi_r)\frac{\partial}{\partial r}p(r,z)+\cos\gamma_d\frac{\partial}{\partial z_s}p(r,z)\right], \qquad (3.9.1)$$

where $2\Delta_d$ is the separation of the components of two out-of-phase monopole components, γ_d and ψ_d are the polar and azimuthal angles of the dipole moment vector, respectively, and ψ_r is the azimuthal angle of the receiver (see Figure 3.24). Substituting Equation (2.4.5) into Equation (3.9.1), the residue series solution with a bilinear profile can be extended for an arbitrarily oriented dipole source

$$p_d^{(h)}(r,\psi_r,z)=p_h^{(b)}(r,\psi_r,z)+p_v^{(b)}(r,\psi_r,z), \qquad (3.9.2)$$

where $p_h^{(b)}(r,\psi_r,z)$ and $p_v^{(b)}(r,\psi_r,z)$ may be regarded, respectively, as the field due to horizontal and vertical dipoles [31]. It is possible to show that

$$p_h^{(b)}(r,\psi_r,z)\approx\frac{e^{-i\pi/12}}{l}\sqrt{\frac{\pi}{2r^3}}S_d\sin\gamma_d\cos(\psi_d-\psi_r)$$

$$\times\sum_n\frac{(2ik_n-1)\mathrm{Ai}\left(-\bar{\xi}_s e^{i2\pi/3}\right)\mathrm{Ai}\left(-\bar{\xi}e^{i2\pi/3}\right)e^{ik_n r}}{\sqrt{k_n}\left\{\left[\mathrm{Ai}'(b_n)\right]^2-b_n\left[\mathrm{Ai}(b_n)\right]^2\right\}}, \qquad (3.9.3)$$

and

$$p_v^{(b)}(r,\psi_r,z) \approx \frac{\pi e^{-i5\pi/12}}{l^2} S_d \cos\gamma_d$$

$$\times \sum_n \sqrt{\frac{2}{\pi k_n r}} \frac{\mathrm{Ai}'\left(-\bar{\xi}_s e^{i2\pi/3}\right)\mathrm{Ai}\left(-\bar{\xi} e^{i2\pi/3}\right) e^{ik_n r}}{\left\{\left[\mathrm{Ai}'(b_n)\right]^2 - b_n\left[\mathrm{Ai}(b_n)\right]^2\right\}}, \tag{3.9.4}$$

where $S_d = 2\Delta_d S_0$ is the dipole source strength.

Similarly, the residue series solution with an exponential profile for an arbitrarily oriented dipole source may be expressed by

$$p_d^{(c)} = p_h^{(c)} + p_v^{(c)}, \tag{3.9.5}$$

where the superscript (c) denotes the sound field above a cylindrically curved surface, and

$$p_h^{(c)} = e^{i\pi/4}\sqrt{\frac{2\pi}{r^3}} S_d \sin\gamma_d \cos(\psi_d - \psi_r) \sum_n \left[\frac{\bar{\xi}_s \bar{\xi}}{\bar{k}_z^2(z_s)\bar{k}_z^2(z)}\right]^{1/4}$$

$$\times \frac{(2ik_n - 1)\sqrt{k_n}\,\mathrm{Ai}\left(-\bar{\xi}_s e^{i2\pi/3}\right)\mathrm{Ai}\left(-\bar{\xi} e^{i2\pi/3}\right) e^{ik_n r}}{e^{-i2\pi/3}\dfrac{\partial\bar{\xi}_0}{\partial k_n}\left\{\left[\mathrm{Ai}'(b_n)\right]^2 - b_n\left[\mathrm{Ai}(b_n)\right]^2\right\} - \dfrac{\partial q_n}{\partial k_n}\left[\mathrm{Ai}(b_n)\right]^2}, \tag{3.9.6}$$

and

$$p_v^{(c)} = e^{i\pi/4} S_d \cos\gamma_d \frac{\partial}{\partial z_s}\left\{\sqrt{\frac{8\pi}{r}} \sum_n \left[\frac{\bar{\xi}_s \bar{\xi}}{\bar{k}_z^2(z_s)\bar{k}_z^2(z)}\right]^{1/4}\right.$$

$$\left. \times \frac{\sqrt{k_n}\,\mathrm{Ai}\left(-\bar{\xi}_s e^{i2\pi/3}\right)\mathrm{Ai}\left(-\bar{\xi} e^{i2\pi/3}\right) e^{ik_n r}}{e^{-i2\pi/3}\dfrac{\partial\bar{\xi}_0}{\partial k_n}\left\{\left[\mathrm{Ai}'(b_n)\right]^2 - b_n\left[\mathrm{Ai}(b_n)\right]^2\right\} - \dfrac{\partial q_n}{\partial k_n}\left[\mathrm{Ai}(b_n)\right]^2}\right\}. \tag{3.9.7}$$

The dispersion equation for dipole sources is given by Equation (2.2.18). This means that if the same geometry is considered, they have the same poles as those of the monopole source. It can be demonstrated that the sound field due to a horizontal dipole source is very similar to the sound field due to a monopole source; also the vertical dipole field follows a similar trend to the monopole field, see Figure 3.25. In the text that follows, the sound

fields due to dipole sources will be calculated as transmission loss and excess attenuation as defined by Equations (2.5.9) and (3.3.10) but for dipole fields.

Figure 3.25 shows the predictions of transmission loss at 100 Hz due to a monopole, a horizontal dipole and a vertical dipole above an impedance convex surface with $R_c = 3430\,\text{m}$, and $\beta = 0.0428 - 0.0388i$. The source and receiver heights are 1 m. The solid line represents the monopole field, the dashed line and the dashdot line are for the horizontal dipole field and vertical dipole field, respectively. The horizontal dipole and monopole fields are indistinguishable on this graph.

3.9.2 Geometrical acoustics solution for a dipole source

It is possible to extend the geometrical acoustics solution to allow for a dipole source above a convex surface. The idea is to replace the monople source shown in Figure 3.19 by two out-of phase monopoles at the source position. For a dipole source, Equation (3.8.1) becomes

$$p_d(r,z) = p_{d+}(r,z) - p_{d-}(r,z), \tag{3.9.8}$$

where

$$p_{d+}(r,z) = \frac{e^{ik_0 d_+}}{d_+} + \frac{e^{ik_0(d_{1+}+d_{2+})}}{d_{1+}}\left[\left(1+\frac{d_{2+}}{d_{1+}}\right)\left(1+\frac{d_{2+}}{d_{1+}}+\frac{2d_{2+}}{R_c\cos\theta_+}\right)\right]^{-1/2}, \tag{3.9.9}$$

and

$$p_{d-}(r,z) = \frac{e^{ik_0 d_-}}{d_-} + \frac{e^{ik_0(d_{1-}+d_{2-})}}{d_{1-}}\left[\left(1+\frac{d_{2-}}{d_{1-}}\right)\left(1+\frac{d_{2-}}{d_{1-}}+\frac{2d_{2-}}{R_c\cos\theta_-}\right)\right]^{-1/2}. \tag{3.9.10}$$

In the above, the subscripts + and - denote the variables due to the two out-of-phase monopoles respectively, and other abbreviations are

$$d_{1+} = \sqrt{\left(R_c + z_s + \Delta_d\cos\theta_d\right)^2 + R_c^2 - 2R_c\left(R_c + z_s + \Delta_d\cos\theta_d\right)\cos\beta_{0+}}\,, \tag{3.9.11}$$

$$d_{1-} = \sqrt{\left(R_c + z_s - \Delta_d \cos\theta_d\right)^2 + R_c^2 - 2R_c\left(R_c + z_s - \Delta_d \cos\theta_d\right)\cos\beta_{0-}}\,,$$

(3.9.12)

$$d_{2+} = \sqrt{\left(R_c + z\right)^2 + R_c^2 - 2R_c\left(R_c + z\right)\cos\left(\frac{r}{R_c} - \beta_{0+}\right)}\,, \tag{3.9.13}$$

$$d_{2-} = \sqrt{\left(R_c + z\right)^2 + R_c^2 - 2R_c\left(R_c + z\right)\cos\left(\frac{r}{R_c} - \beta_{0-}\right)}\,, \tag{3.9.14}$$

$$\left[\sin\left(\frac{r}{R_c} - \beta_{0+}\right)\right]\left(\sin\beta_{0+}\right)^{-1} = \left(\frac{d_{2+}}{d_{1+}}\right)\left(\frac{R_c + z_s + \Delta_d \cos\theta_d}{R_c + z}\right), \tag{3.9.15}$$

$$\left[\sin\left(\frac{r}{R_c} - \beta_{0-}\right)\right]\left(\sin\beta_{0-}\right)^{-1} = \left(\frac{d_{2-}}{d_{1-}}\right)\left(\frac{R_c + z_s - \Delta_d \cos\theta_d}{R_c + z}\right), \tag{3.9.16}$$

$$\theta_{0+} = \alpha_{0+} + \beta_{0+}\,, \tag{3.9.17}$$

$$\theta_{0-} = \alpha_{0-} + \beta_{0-}\,, \tag{3.9.18}$$

$$\alpha_{0+} = \sin^{-1}\left(\frac{R_c \sin\beta_{0+}}{d_{1+}}\right), \tag{3.9.19}$$

$$\alpha_{0-} = \sin^{-1}\left(\frac{R_c \sin\beta_{0-}}{d_{1-}}\right), \tag{3.9.20}$$

$$d_+ = \sqrt{d_{1+}^2 + d_{2+}^2 - 2d_{1+}d_{2+}\cos\left(2\theta_{0+}\right)}\,, \tag{3.9.21}$$

$$d_- = \sqrt{d_{1-}^2 + d_{2-}^2 - 2d_{1-}d_{2-}\cos\left(2\theta_{0-}\right)}\,, \tag{3.9.22}$$

and θ_d is the angle between the dipole moment vector and the plane transverse to the convex surface.

Figure 3.26 shows the predictions given by the residue series solution using Equations (3.9.3) and (3.9.4) for the horizontal dipole and the vertical dipole, respectively (see the solid lines). In the vicinity of the source, the dotted lines show the predictions given by the geometrical acoustics solution using Equation (3.9.7). In this figure, the source and receiver

heights are 1.92 and 0.05 m, respectively, the radius of the convex cylinder R_c is 20.0 m, and the normalized specific admittance of the impedance surface β is $0.3036 - 0.3216i$ at 375 Hz. It can be shown that the predictions given by Equation (3.9.7) agree well with the experimental results, the details will be presented in the next chapter.

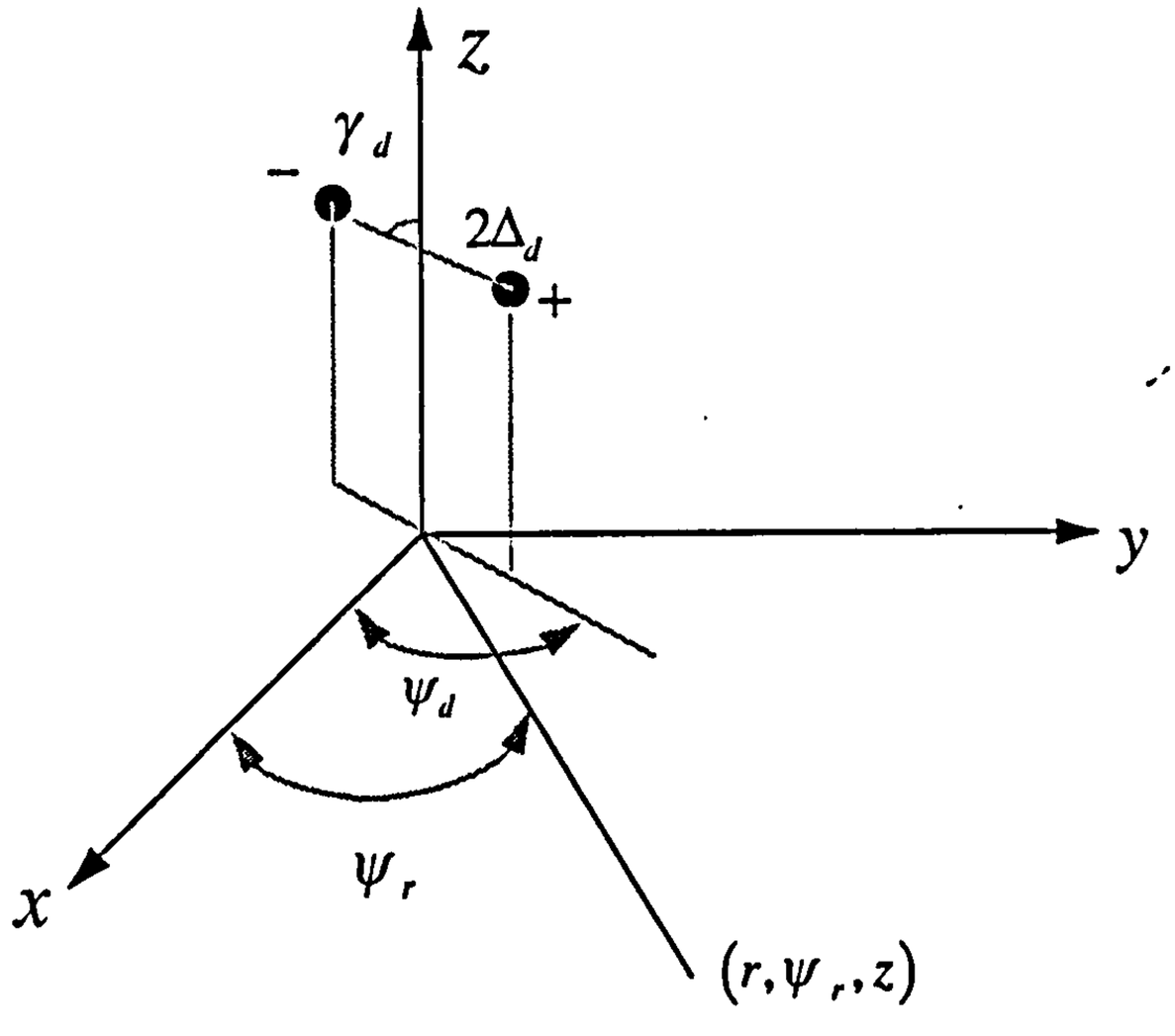

Figure 3.24 Illustration of the dipole location and orientation.

3.10 Summary

In this chapter, the upward sound propagation over a flat ground in the presence of a sound speed gradient caused by a temperature or wind velocity gradient has been studied in the acoustically analogous situations where the sound waves propagate over cylindrically or spherically curved convex surfaces above which there is no refraction.

Where the sound field is diffracted by a cylindrical surface, an analytical expression has been derived for an exponential profile. The output of the solution has been compared to

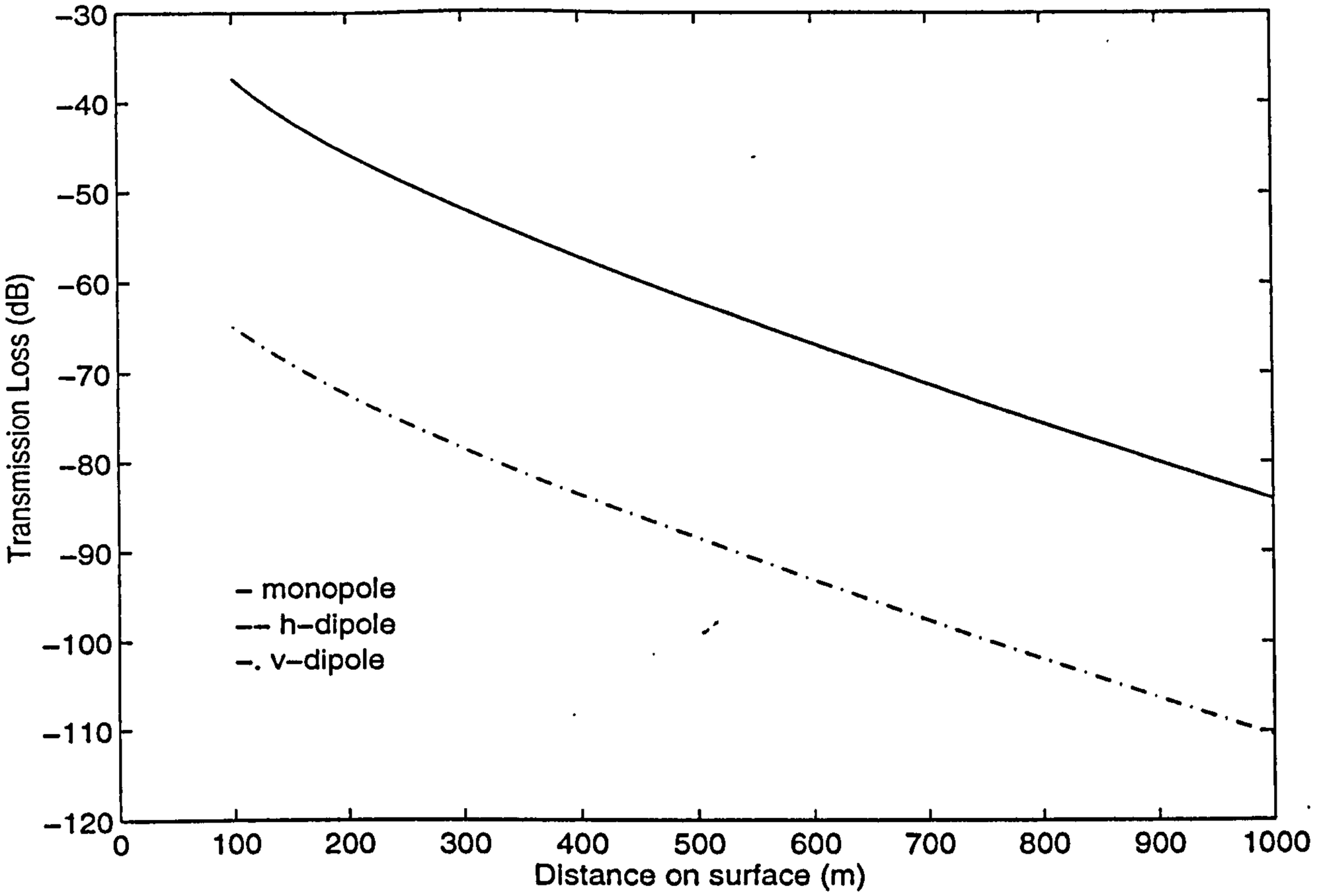

Figure 3.25 Predictions obtained at 100 Hz due to a monopole, a vertical dipole and a horizontal dipole above an impedance surface, $R_c = 3430$ m, $\beta = 0.0428 - 0.0388i$ and $z_s = z = 1.0$ m.

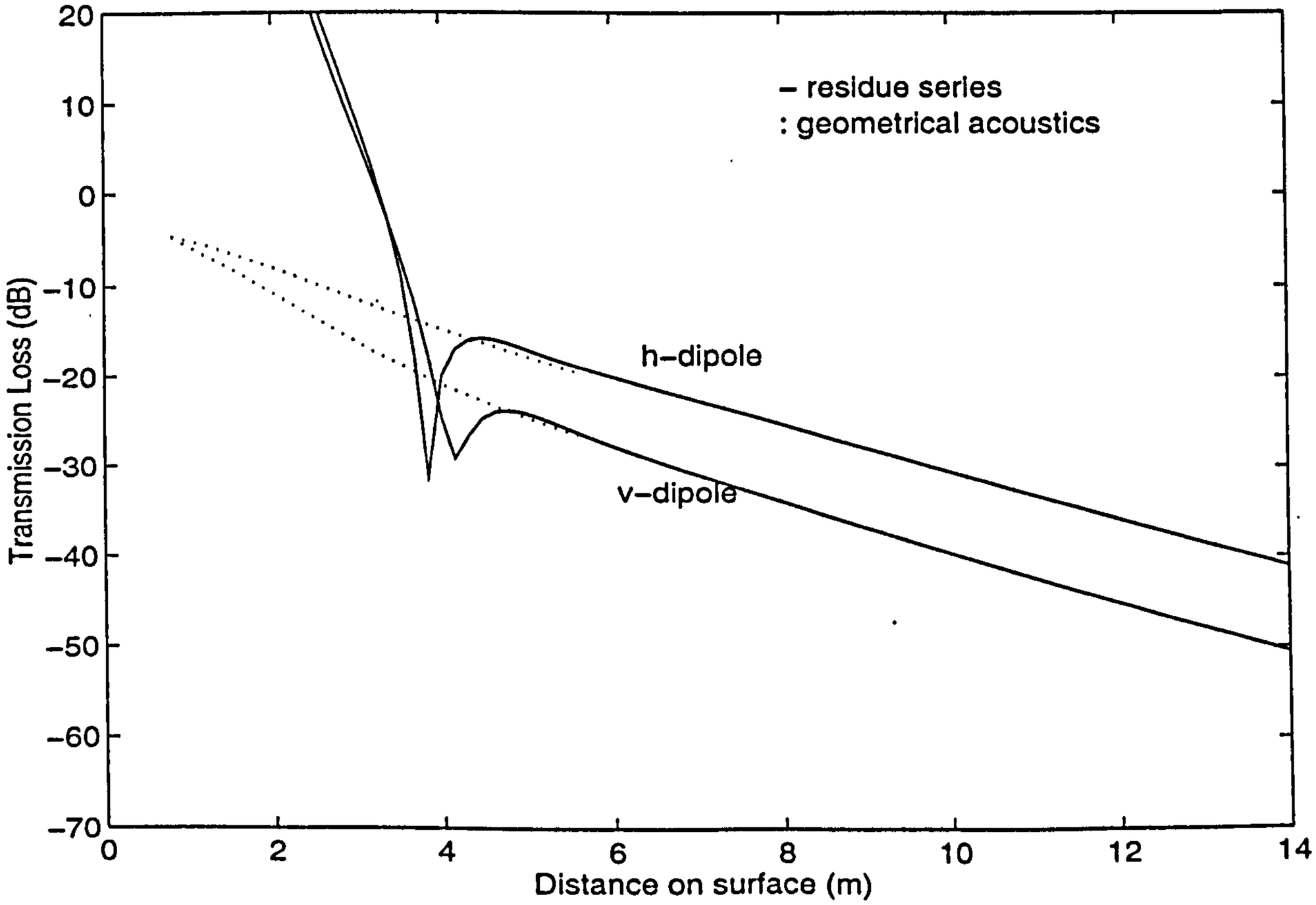

Figure 3.26 Predictions obtained at 375 Hz due to a horizontal dipole and a vertical dipole above an impedance surface, $R_c = 20.0$ m, $z_s = 1.92$ m, $z = 0.05$ m, and $\beta = 0.3036 - 0.3216i$.

Berry and Daigle's experimental data, to Berthelot and Zhou's experimental data, and to bilinear profiles as well. It has been found that the predictions given by the residue series solution for both bilinear and exponential profiles work well deep in the shadow zone, whereas the solution with an exponential profile predicts much better results than that with a bilinear profile in the penumbra region along the line of sight. It has been seen that the predictions obtained from exponential profiles are very similar to those obtained from Berthelot's modification.

Where the sound field is diffracted by a spherical surface, a correction factor of the residue series has been found to be important for predictions of sound field deep in the shadow zone.

The validity of our residue series model has been examined by comparing with the numerical techniques of FFP, BEM and MAE, respectively.

In the insonified region before the apex of the convex surface in the vicinity of a source, the geometrical acoustics solution shows a good agreement with the measurements, whereas the residue series solution does not converge in this region. The geometrical acoustics solution agrees well with the residue series solution in the region $z+z_s < r < \sqrt{2z_sR_c}$. There is reasonably smooth transition between these two solutions. In the region above the shadow boundary, the residue series solution requires much more terms necessary for convergence and shows large discrepancies from the geometrical acoustics solution.

Analytical expressions derived for a monopole source have been extended to predict the sound field for a dipole source. The theoretical study has suggested that the sound field due to a dipole source above a curved convex surface is quite similar to that due to a point monopole source.

Chapter 4

Laboratory experiments of sound propagation over convex surfaces

Problems in predicting the sound field from a point monopole source in the acoustic penumbra behind a convex surface have been noted in the last decade. Although Berry and Daigle [15] achieved generally good agreement between the residue series solutions for bilinear profiles and their experimental data obtained above a rigid convex surface and a convex surface of finite impedance, they reported considerable discrepancies in the penumbra region along the limiting ray. Berry and Daigle [15] suggested that the residue series solution is valid in the insonified region above the shadow boundary, however, they did not obtain convergent results at high frequencies. In the vicinity of the shadow boundary predictions from the residue series solution were found to differ from their measurements by 2-5 dB. Berthelot and Zhou [20] observed dips in the measurements of excess attenuation as a function of range in the penumbra region along the limiting ray above a carpet-covered convex surface and suggested that the cause of this phenomenon is not well understood.

In this chapter, these problems are investigated by comparing the residues series predictions (*cf.* Chapter 3) with laboratory measurements conducted above convex surfaces. Previous experimental studies above a convex surface have been restricted to the sound field due to a point monopole source. The experimental investigations described

here test the validity not only of solutions for a monopole source but also of the theoretical expressions derived in Chapter 3 for dipole fields diffracted by a convex surface.

4.1 Measurement techniques and configurations

First, descriptions of the experimental measurement techniques and surfaces used to examine the diffraction of sound by convex surfaces are given.

4.1.1 The convex surfaces

Convex surfaces were constructed to behave as a rigid surface and as a surface of finite impedance respectively. The rigid convex surface was constructed by attaching sheets of masonite to a curved wooden frame, this is illustrated in Figure A-1. The frame was in the form of a semi-cylinder that had a radius of curvature of 2.5 m. It was built to have a length of 2.5 m with a span of 1.8 m and a height of 0.45 m. To ensure that the model surface behaved as a rigid reflector, particular care was taken when fastening the sheets to the frame. To obtain the surface of finite impedance, a commercialized felt with a thickness of 16 mm was used, see Figure A-2. The felt was secured to the rigid surface by using double sided tapes to eliminate any transmission path between the surface and the felt.

4.1.2 Impedance estimation

To estimate the impedance of the surfaces, a flat rigid board was constructed by attaching sheets of masonite to a flat wooden frame. It was 2.5 m long, 1.8 m wide and 0.2 m deep.

Figures 4.1 and 4.2 show the excess attenuation, which has been defined in Equation (3.3.10), measured (the solid lines) above this surface with a point source and receiver 2.0 m apart and at heights of 0.15 m and 1.0 m, respectively. The theoretical predictions (the dotted lines) were given by Equation (3.3.10) where the sound pressure was obtained from

$$p = \frac{e^{ik_0 d}}{d} + Q\frac{e^{ik_0 d_r}}{d_r}, \qquad (4.1.1)$$

where Q is the spherical wave reflection coefficient [55]. For the rigid surface, the sound field is calculated by assuming that $Q = 1$. It can be seen from these figures that the predictions fit the experimental results well except at frequencies near the interference minima. The results support the assumption that the bare masonite surface closely approximates a rigid surface.

The dotted lines in Figures 4.3a and 4.3b represent predictions calculated from Equation (4.1.1) considering the felt-covered surface to be locally reacting, and using Equation (2.5.15), *i.e.* the Attenborough two-parameter model [33], to predict the impedance. In these two figures, the solid lines represent measurements obtained above the flat board covered by the felt. The best agreement was found with $\sigma_e = 38$ kPa s m^{-2} and $\alpha_e = 15$ m^{-1} in the predictions. In Figure 4.3a, the source and receiver were at 0.05 m above the surface, and 2.0m apart, corresponding to an incident angle of 87.1°. In Figure 4.3b, the source height and the separation were the same as in Figure 4.3a but the receiver height was 0.15 m, so the angle of incidence was 84.3°. The measurements over the flat surface agree with predictions according to local reaction.

4.1.3 Instrumentation and procedure

The model was placed in an anechoic chamber, which has an effective volume of $3\,\text{m} \times 3\,\text{m} \times 3\,\text{m}$ and is housed within a large workshop at the Silsoe Research Institute.

A B&K 4311 quarter-inch condenser microphone fitted with a preamplifier was used for making the sound pressure measurements. The microphone was connected to a B&K 2608 measuring amplifier via the preamplifier.

A tannoy speaker fitted with a 3 cm internal diameter tube 90 cm long was used as the point monopole source, see Figure A-4. Two piezo-ceramic transducer discs with resonance frequencies of 2915 and 4350 Hz were found to be adequate as the dipole sources [35], these are shown in Figure A-5. When the disc plane is vertical, it acts as a horizontal dipole source and when it is horizontal, it acts as a vertical dipole source.

A PC-based system analyzer, Maximum Length Sequence System Analyzer (MLSSA), was used both as the signal generator for the speakers and as the analyzer for subsequent signal processing. The signal was analyzed using a half Blackman-Harris window and Fourier Transformed [56]. Figure 4.4 is a schematic diagram of the experiments.

The experimental procedure was similar for all of the experiments reported in this dissertation. A measurement in the absence of the boundary serves as the direct field, *i.e.* reference field and subsequent measurements were divided by the reference field to obtain either the transmission loss [*cf.* Equation (2.5.9)] or the excess attenuation [*cf.* Equation (3.3.10)]. Most of the experiments were conducted with both the source and receiver in the plane transverse to the centerline of the cylinder, *i.e.* $\psi = 0$ (*cf.* Figure 3.6). Data was taken along the surface, along a vertical across the illuminated region and shadow zone, along the line of sight, and above the limiting ray. Figure 4.5 shows a detailed sketch of the experimental configurations. In this figure, r represents the *distance from source* measured from source to receiver; x represents the *distance from apex* measured along the line of sight starting at the apex of a curved surface and z_v represents the *vertical distance* above the surface starting at an arc distance $r = r_0$ from the source.

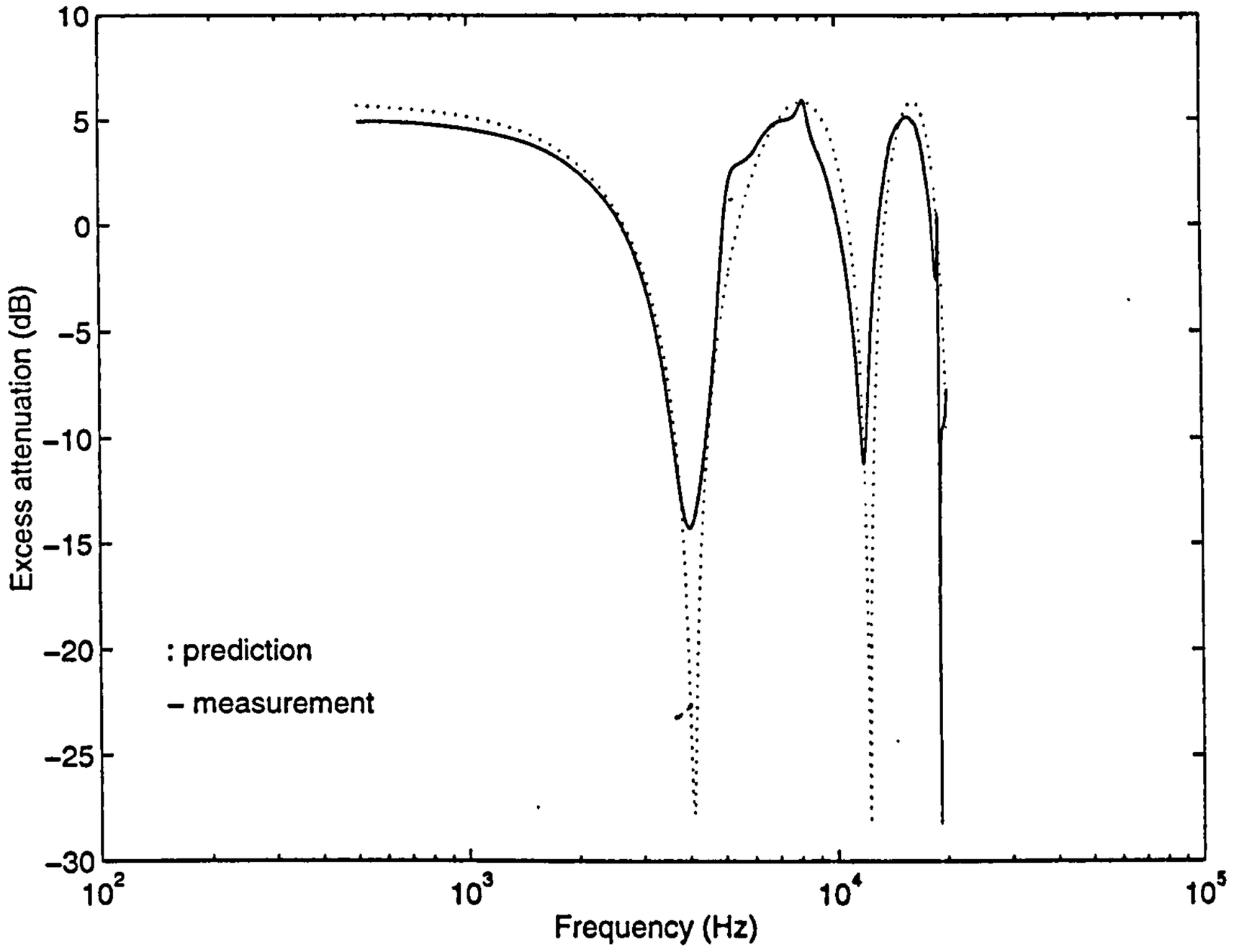

Figure 4.1 Excess attenuation obtained above a flat rigid surface, with $z_s = z = 0.15$ m, and $r = 1.0$ m. Solid curve: measurements and dotted line: prediction.

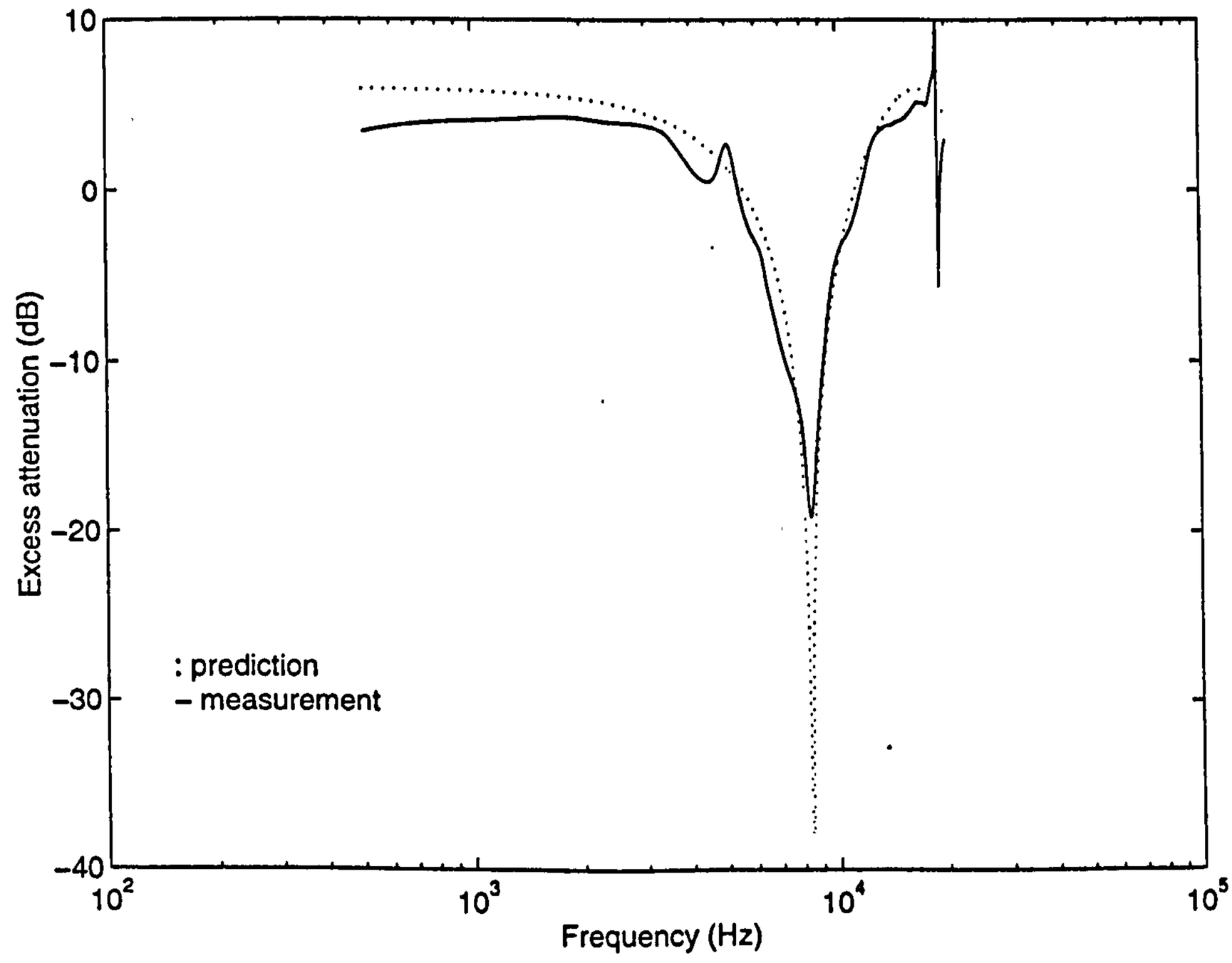

Figure 4.2 Excess attenuation obtained above a flat rigid surface, with $z_s = z = 0.15$ m, and $r = 2.0$ m. Solid curve: measurement and dotted line: prediction.

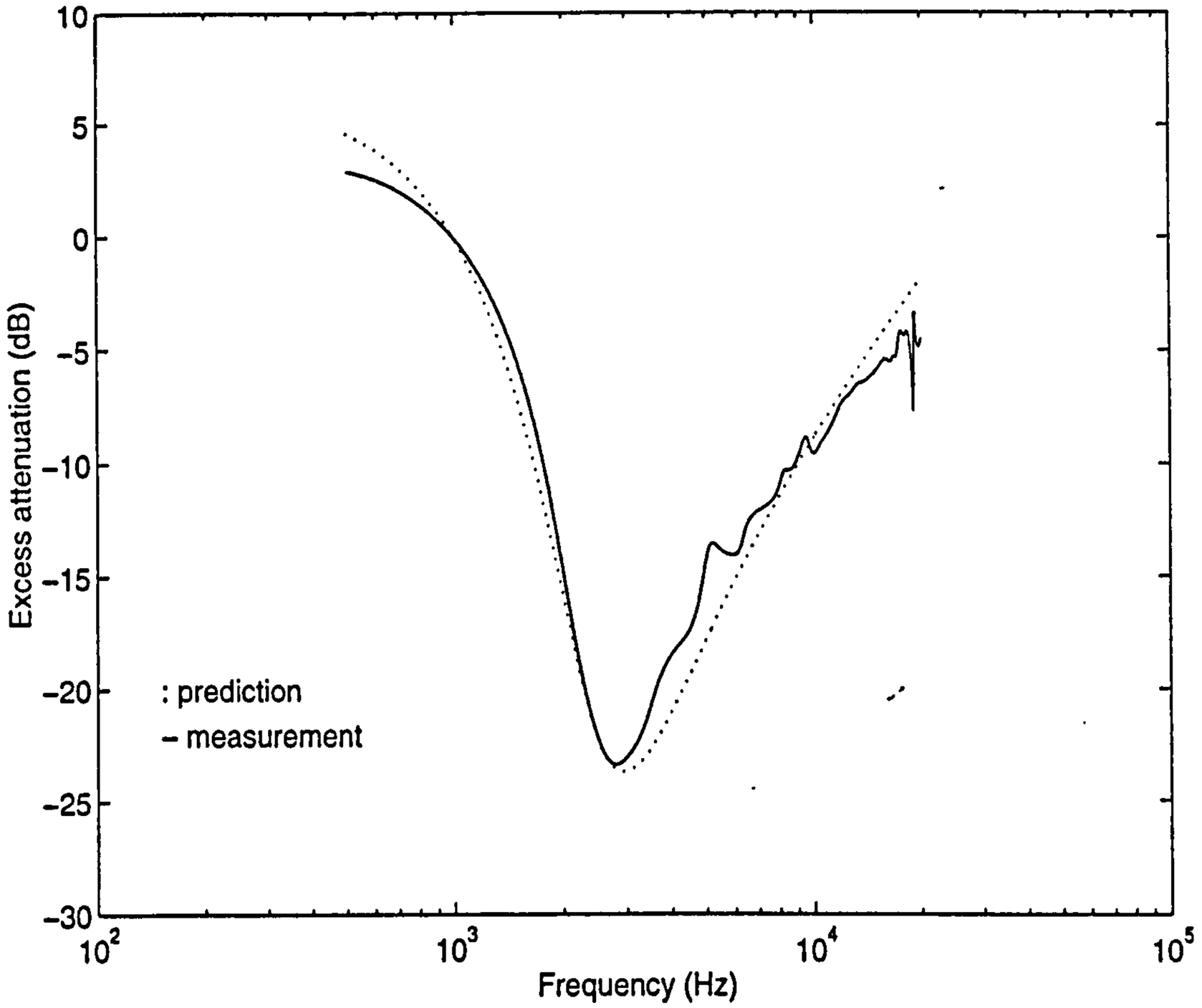

Figure 4.3a Excess attenuation obtained above a flat felt-covered surface, with $z_s = z = 0.15$ m , and $r = 2.0$ m . Solid curve: measurement and dotted line: prediction with $\sigma_e = 38$ kPa s m^{-2} and $\alpha_e = 15$ m^{-1} .

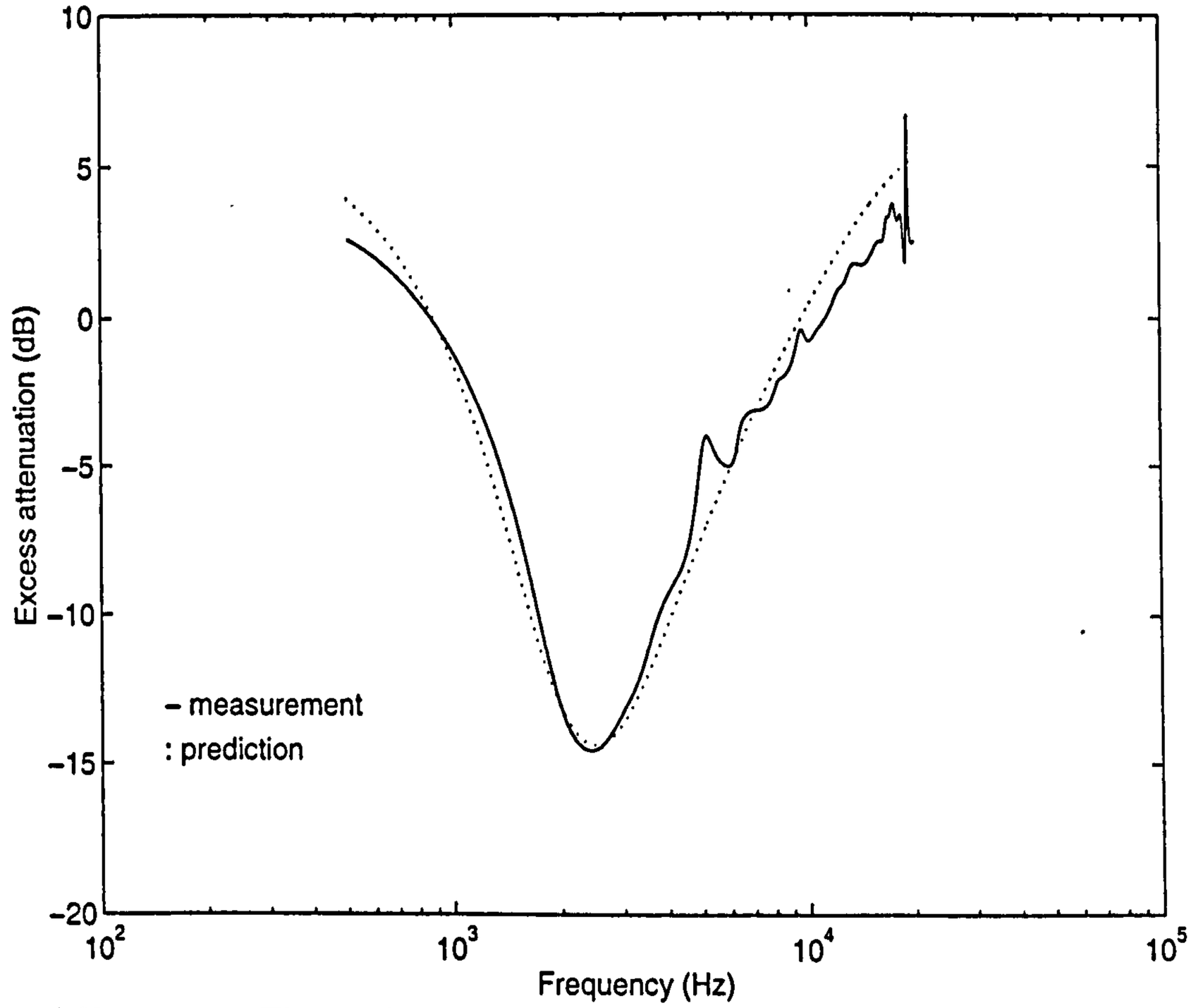

Figure 4.3b Same as **Figure 4.3a** but $z_s = 0.15$ m and $z = 0.05$ m .

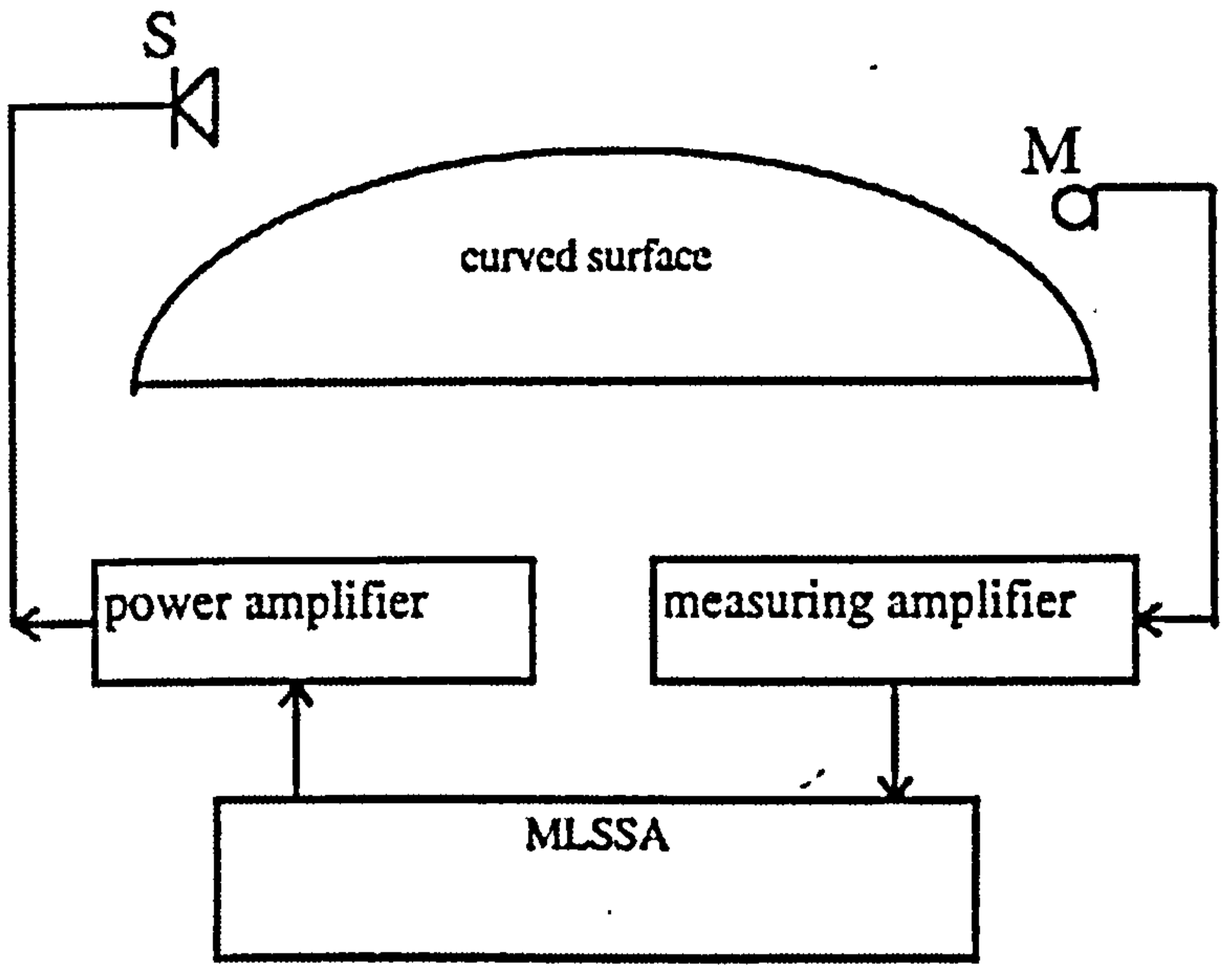

Figure 4.4 Schematic diagram of the experiments.

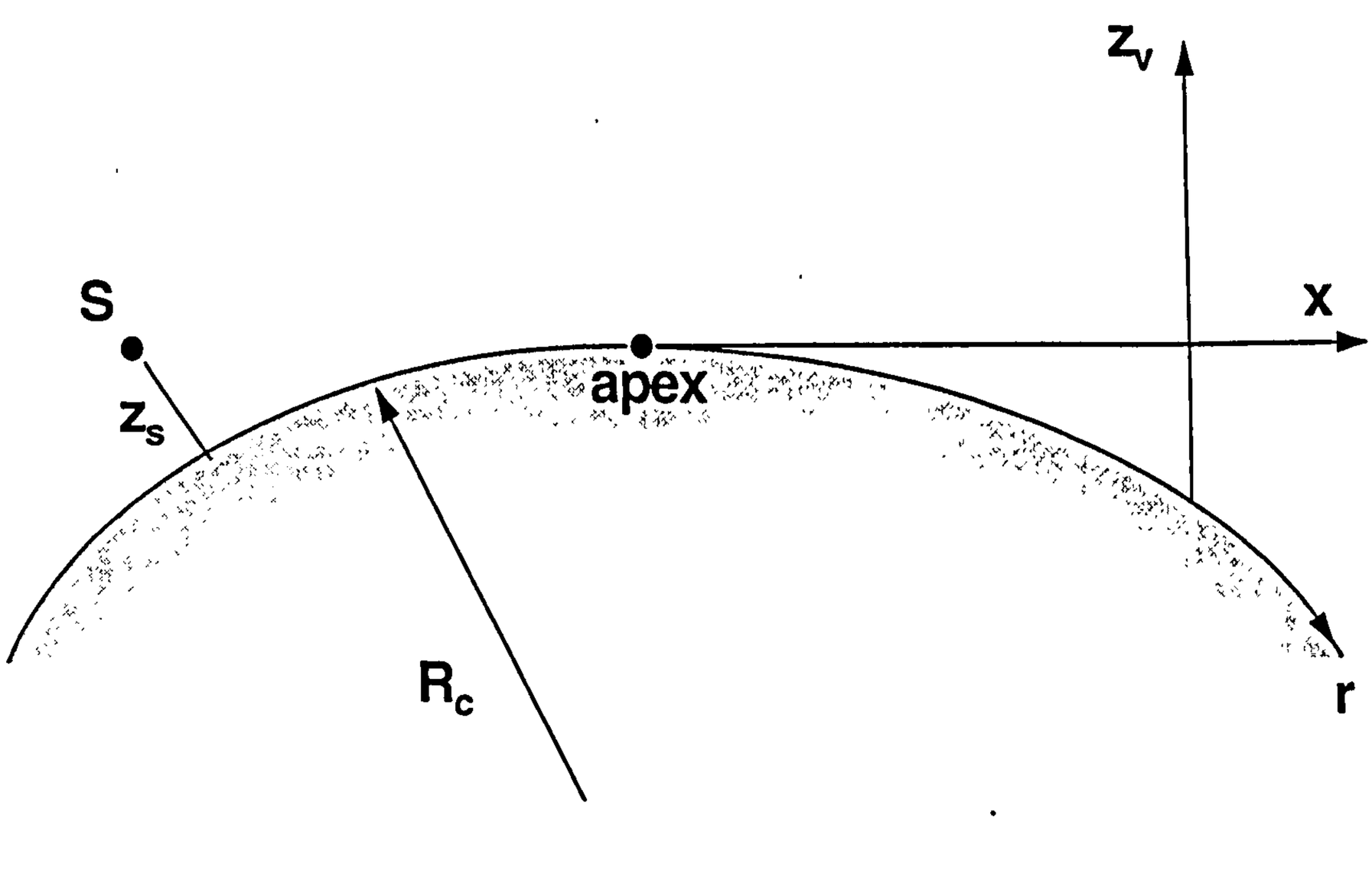

Figure 4.5 A sketch of the experimental configurations (*cf.* **Figure 3.1**). r represents *distance from source*, that is the arc length measured from source. x represents *distance from apex*, that is the length measured from the apex along the line of sight. z_v represents *vertical distance*, that is the length coordinate vertically above the surface with an initial position at an arc distance $r = r_0$ from the source.

4.2 The sound field due to a monopole

As a prelude to experiments using dipole sources above the convex surfaces, experiments were undertaken with the monopole source. Although these experiments duplicate the work of Berry and Daigle [15] and Berthelot and Zhou [20], the discrepancies they reported between the theoretical predictions and the measurements in the penumbra region warrant further investigation. In the region above the shadow boundary, both the residue series solution and the geometrical acoustics solution were suggested to be valid [15]; however, the theoretical predictions show discrepancies which have been described in Chapter 3.8. To examine this problem, this section also reports the comparison results between the two solutions and the measurement data.

4.2.1 Experimental results

Typical results for the rigid and felt-covered convex surfaces are presented in Figures 4.6, 4.7 and 4.8 for three different receiver locations, where the source was 0.115 m above the curved surface and at a source frequency of 1.5 kHz. The circles represent experimental data obtained above the rigid surface while the plus signs represent experimental data obtained above the felt-covered surface. The solid lines are the predictions of the residue series solution for a bilinear profile. Figure 4.6 shows the results obtained as the receiver was moved along the surface. Figure 4.7 shows the results obtained as the receiver was moved along the vertical distance to a height of 0.40 m above the surface starting on the surface at an arc distance of 1.65 m from the source. Figure 4.8 shows results obtained as the receiver was moved along the line of sight out to a distance of 1.20 m from the apex.

It has been demonstrated in Chapter 3.3.1 that the predictions given by the residue series solution for a bilinear profile are adequate in the shadow zone. However, where the

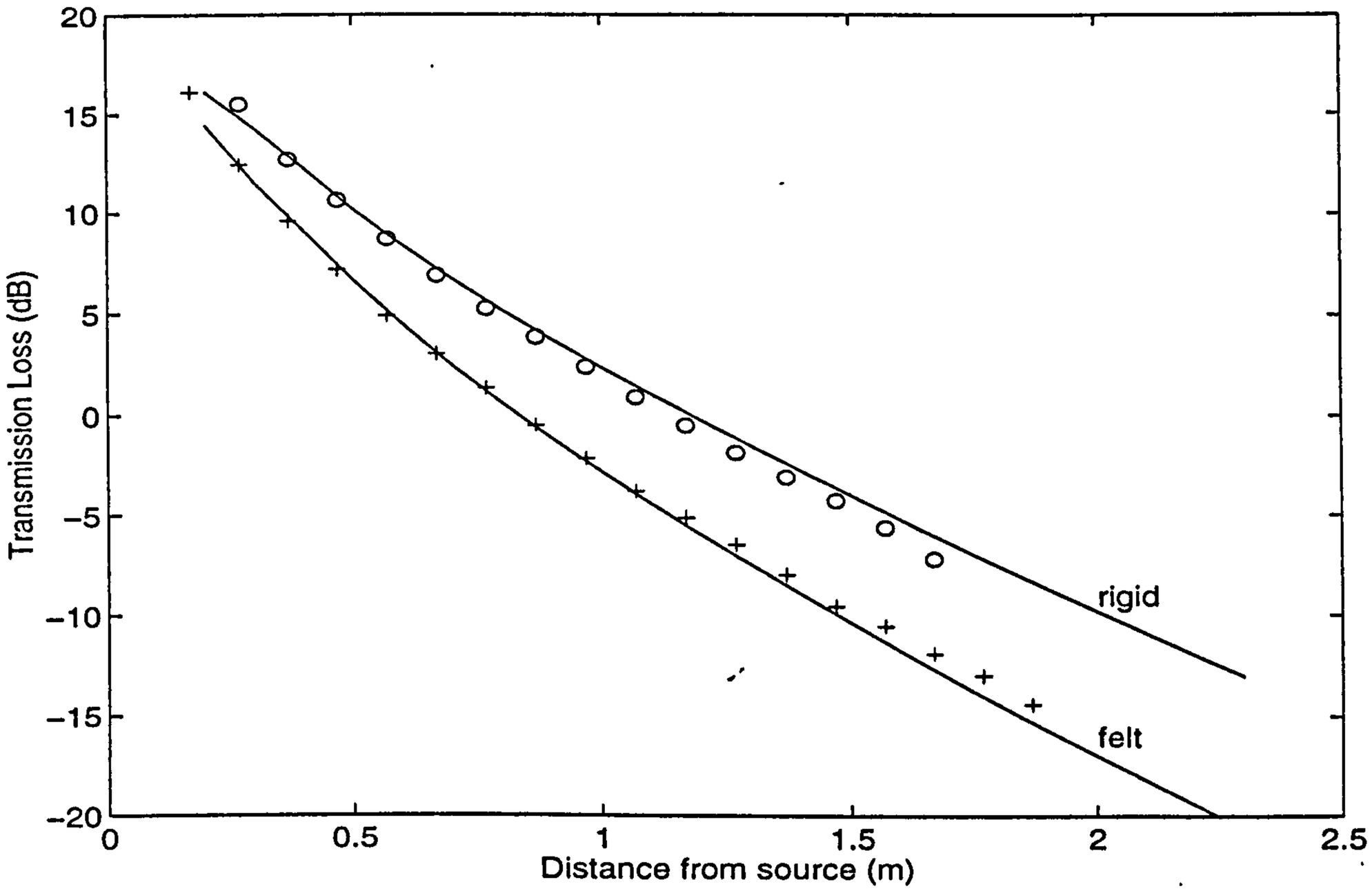

Figure 4.6 Transmission loss from a monopole source at 1.5 kHz measured along a convex surface, $R_c = 2.5$ m, $z_s = 0.115$ m and $z \sim 0.00$ m. Circles and plus signs: measurement data obtained above a rigid surface and a felt-covered surface, respectively. Solid lines: predictions.

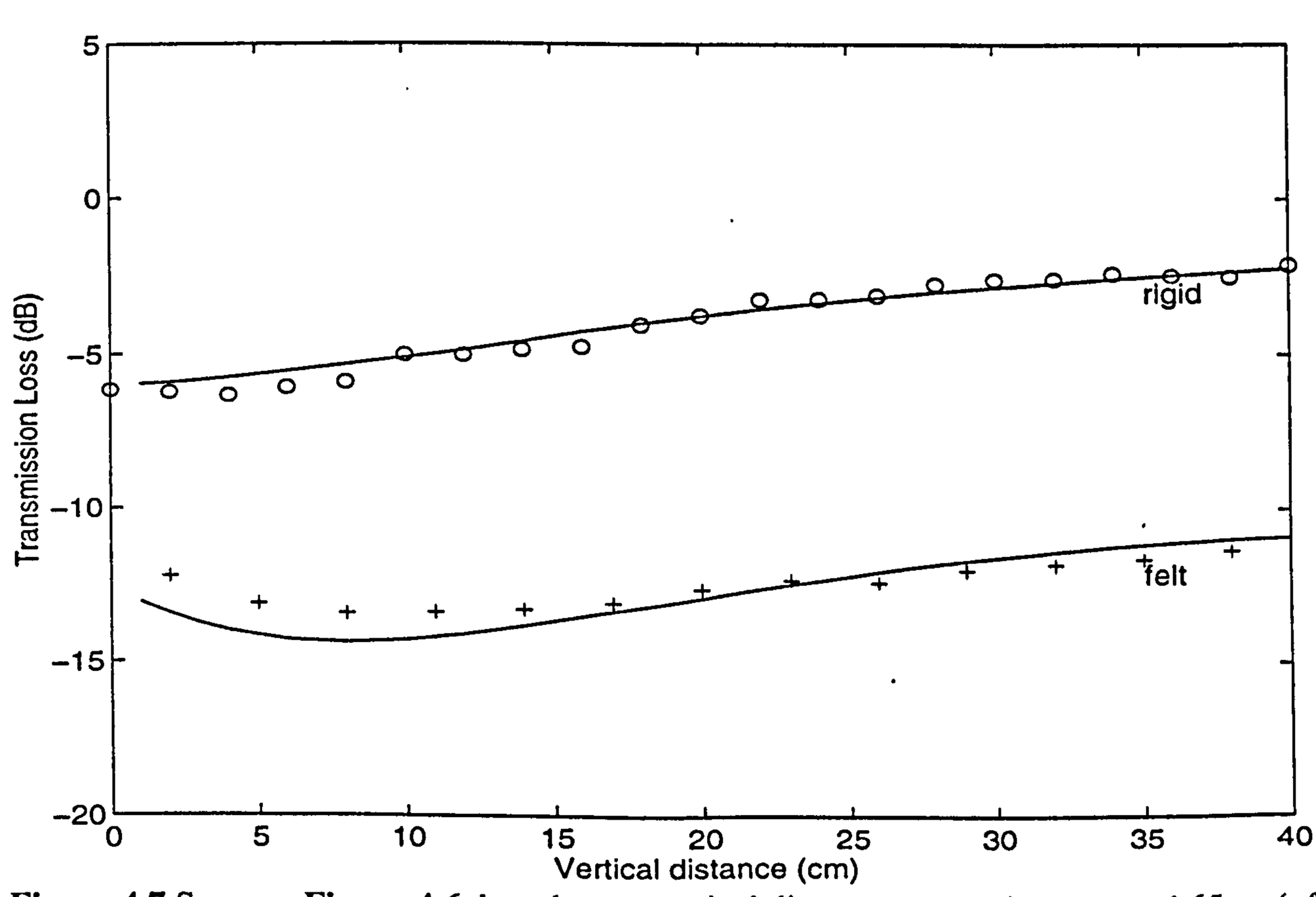

Figure 4.7 Same as **Figure 4.6**, but along a vertical distance z_v starting at $r_0 = 1.65$ m (*cf.* **Figure 4.5**).

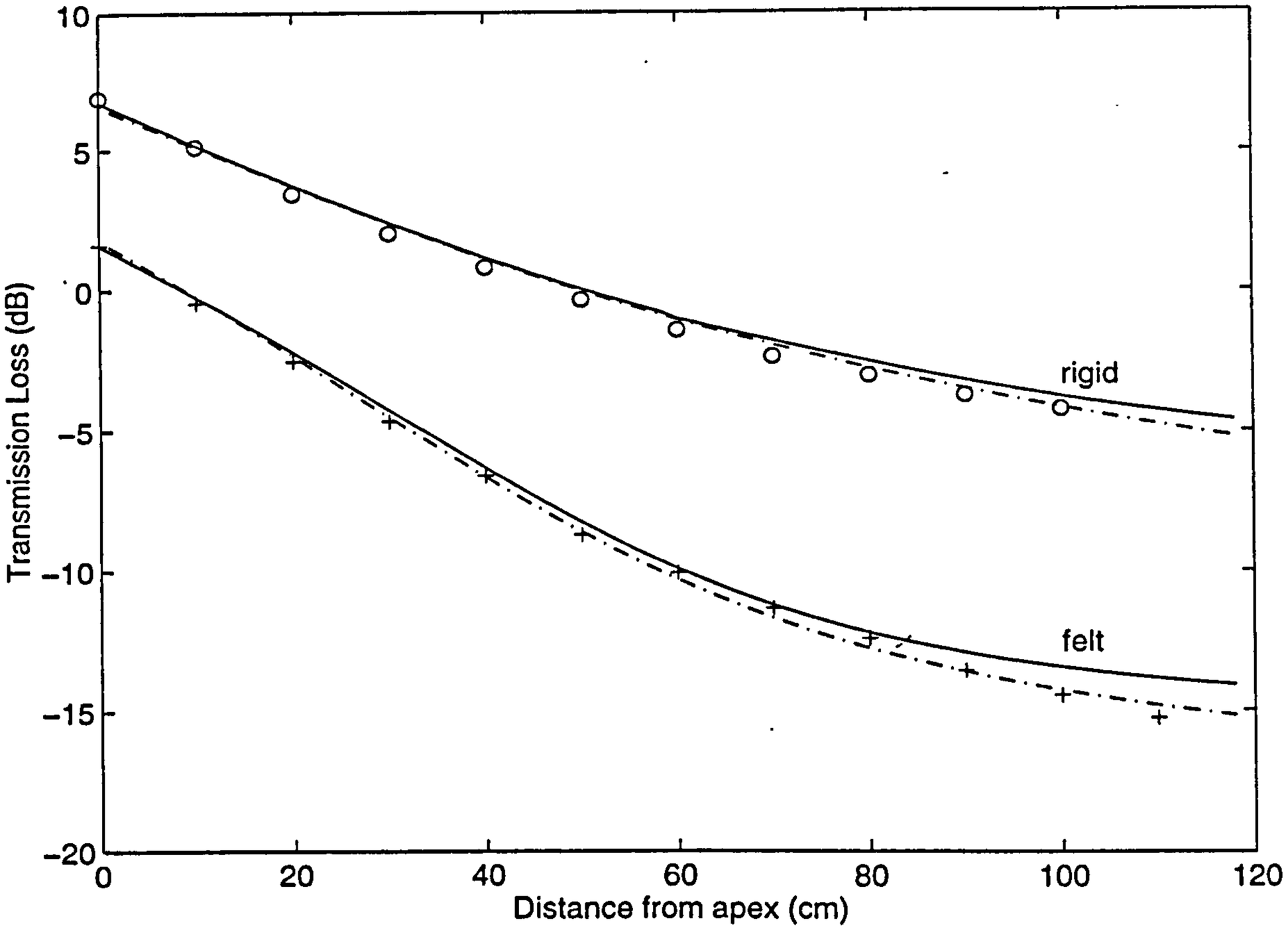

Figure 4.8 Same as **Figure 4.6**, but along the line of sight.

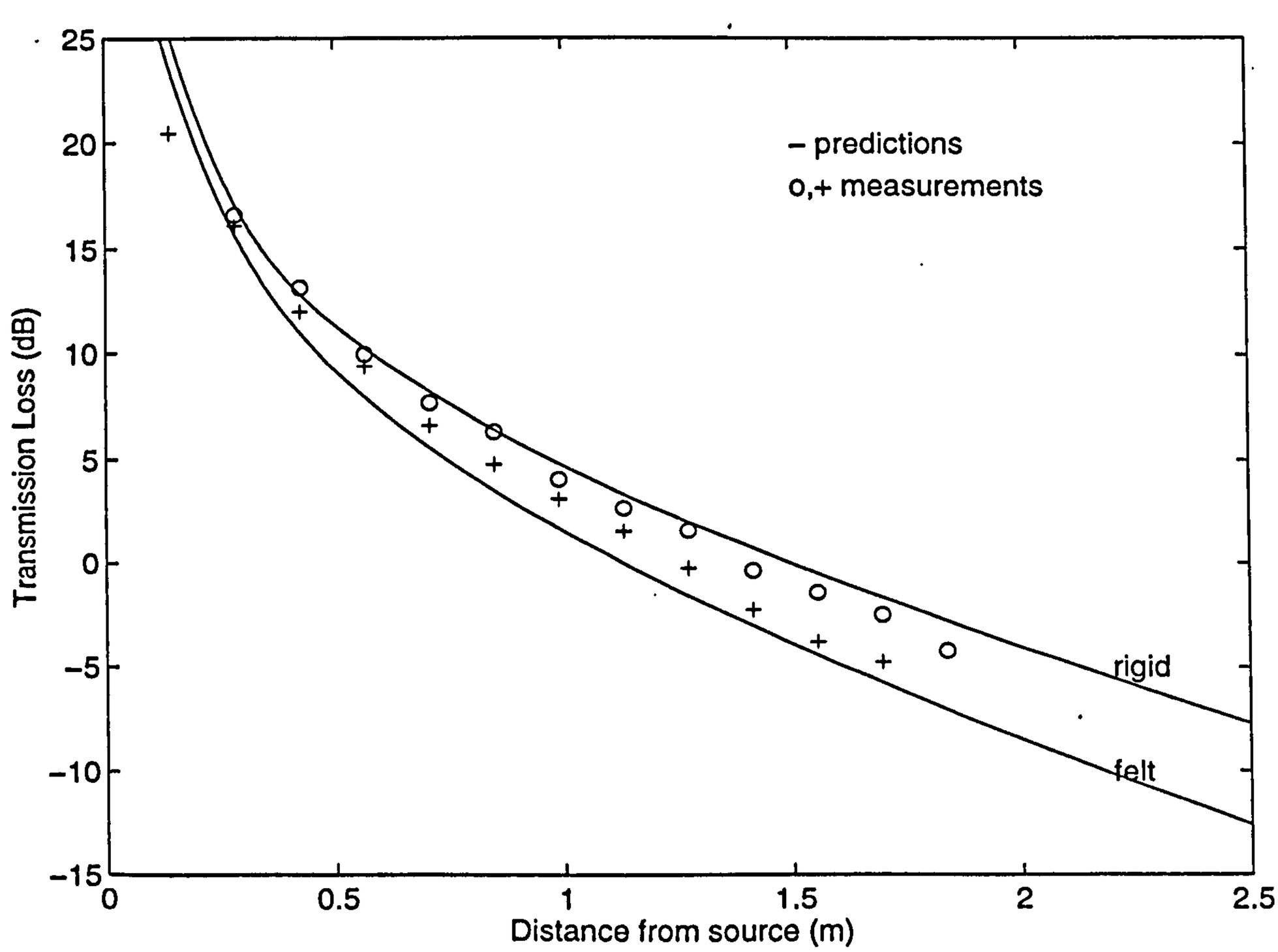

Figure 4.9 Same as **Figure 4.6**, but results obtained with $\psi = \pi/4$, and source frequency at 1 kHz.

receiver was moved along the line of sight, the predictions using an exponential profile show better agreement (the dashdot lines in Figure 4.8). The agreement between the predictions and the experimental data shown in these three figures is good.

If we rotate the vertical plane, that intercepts the source and receiver, through an angle of ψ with respect to the circumference of the cylinder the resulting effective radius of curvature is R_{eff} (*cf.* Figure 3.6). The circles and plus signs in Figure 4.9 represent measured data at an angle $\psi = \pi/4$ above the rigid and felt-covered cylinder, respectively. In this figure, the discrepancy between measurements and predictions calculated from Equation (3.3.5) is less than 1 dB.

4.2.2 Results above the shadow boundary

Measurements with a monopole source were also made above the shadow boundary over the rigid and felt-covered convex surfaces to examine the residue series solution and the geometrical acoustics solution in this region. In Figure 4.10, the source and receiver heights were 0.165 m and the distance between them was 1.0 m. The receiver position was 0.16 m above the limiting ray over a rigid curved surface. The residue series converges for frequencies up to 20 kHz when 40 terms are calculated and the curves agree to within 0.5 dB. When the receiver was moved higher above the limiting ray, more terms were necessary in the summation and a larger discrepancy was observed, see Figures 4.11 and 4.12. In Figure 4.11, the receiver was raised to 0.41 m above the limiting ray over a rigid curved surface, and 55 terms have been used in computing the residue series solution. Figure 4.12 shows data obtained with the receiver 0.53 m above the limiting ray over a felt-covered convex surface. For this case the residue series converges up to 20 kHz if 76 terms are included in the summation. In these figures, the solid lines represent the measured results, the dashdot lines represent the predictions given by the geometrical acoustics

solutions, and the dotted lines represent the predictions given by the residue series solution assuming bilinear effective sound speed profiles. It is found that the geometrical acoustics solutions (dashdot lines) are consistent with the measurements (solid lines) over the entire frequency range of interest, whereas the discrepancies become apparent at higher frequencies between the residue series results (dotted lines) and the measurements (solid lines).

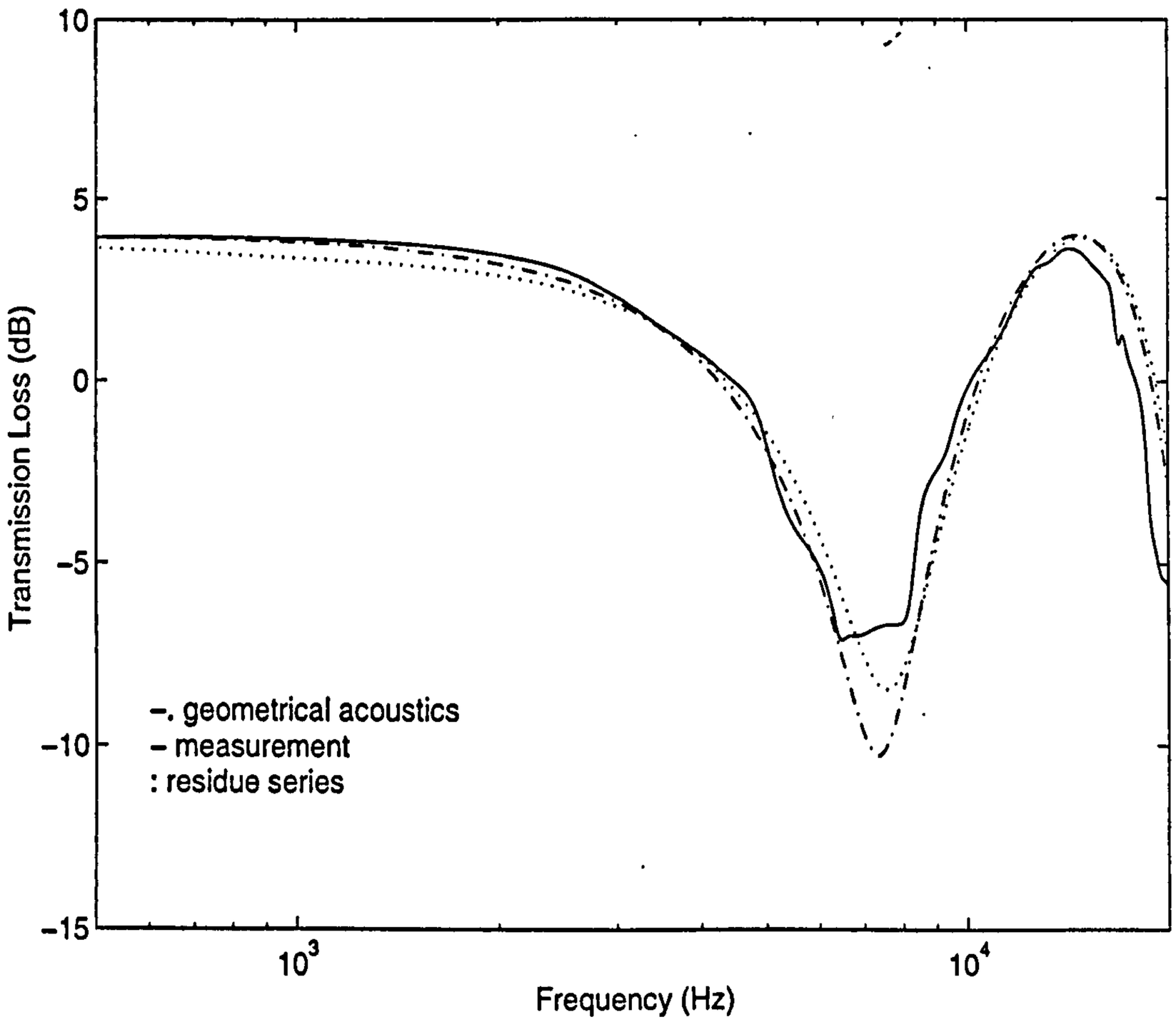

Figure 4.10 Predictions and measurements obtained above the rigid surface, $R_c = 2.5$ m, $z_s = z = 0.165$ m and $r = 1.0$ m.

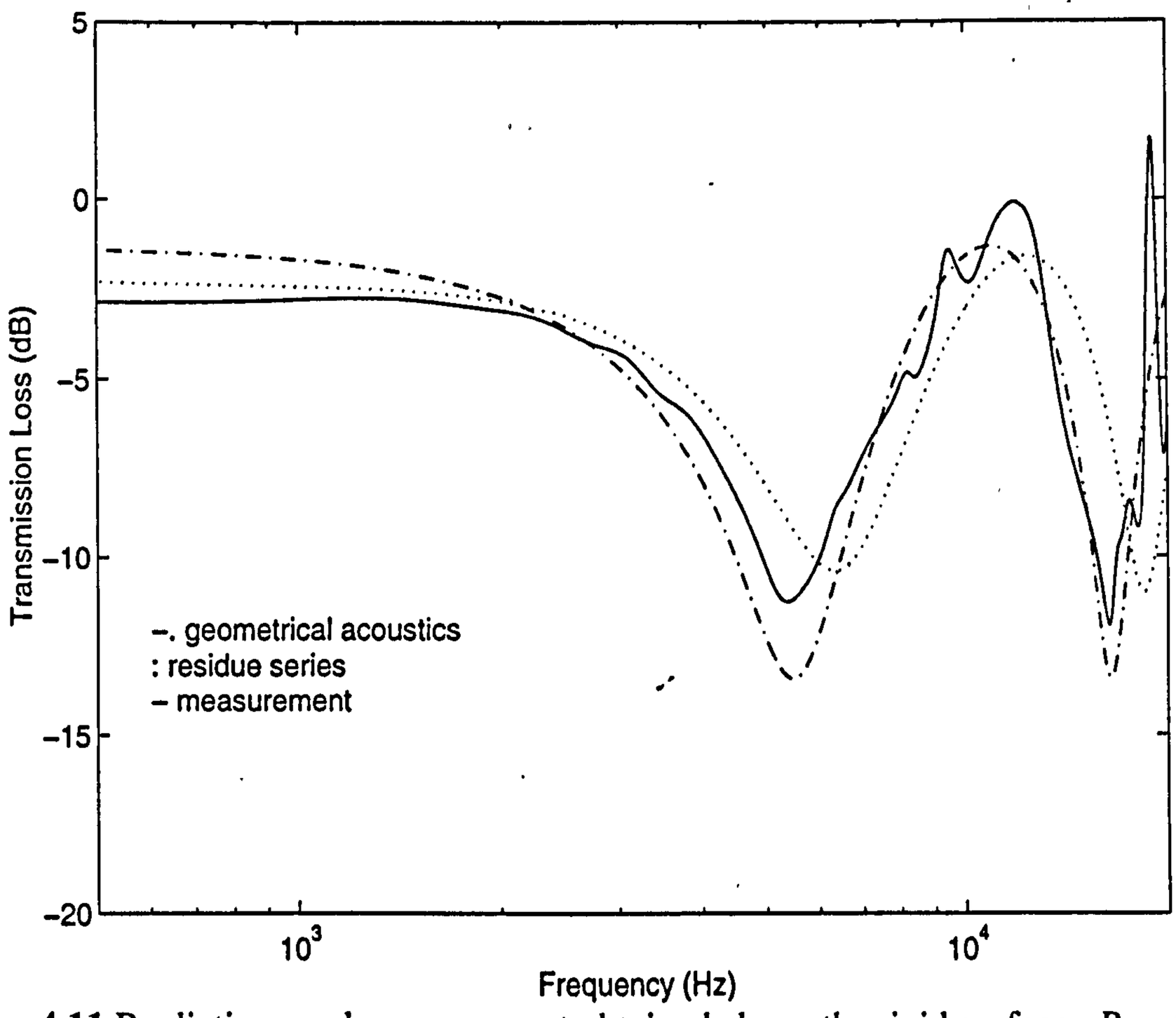

Figure 4.11 Predictions and measurement obtained above the rigid surface, $R_c = 2.5$ m, $z_s = 0.20$ m, $z = 0.50$ m and $r = 1.65$ m.

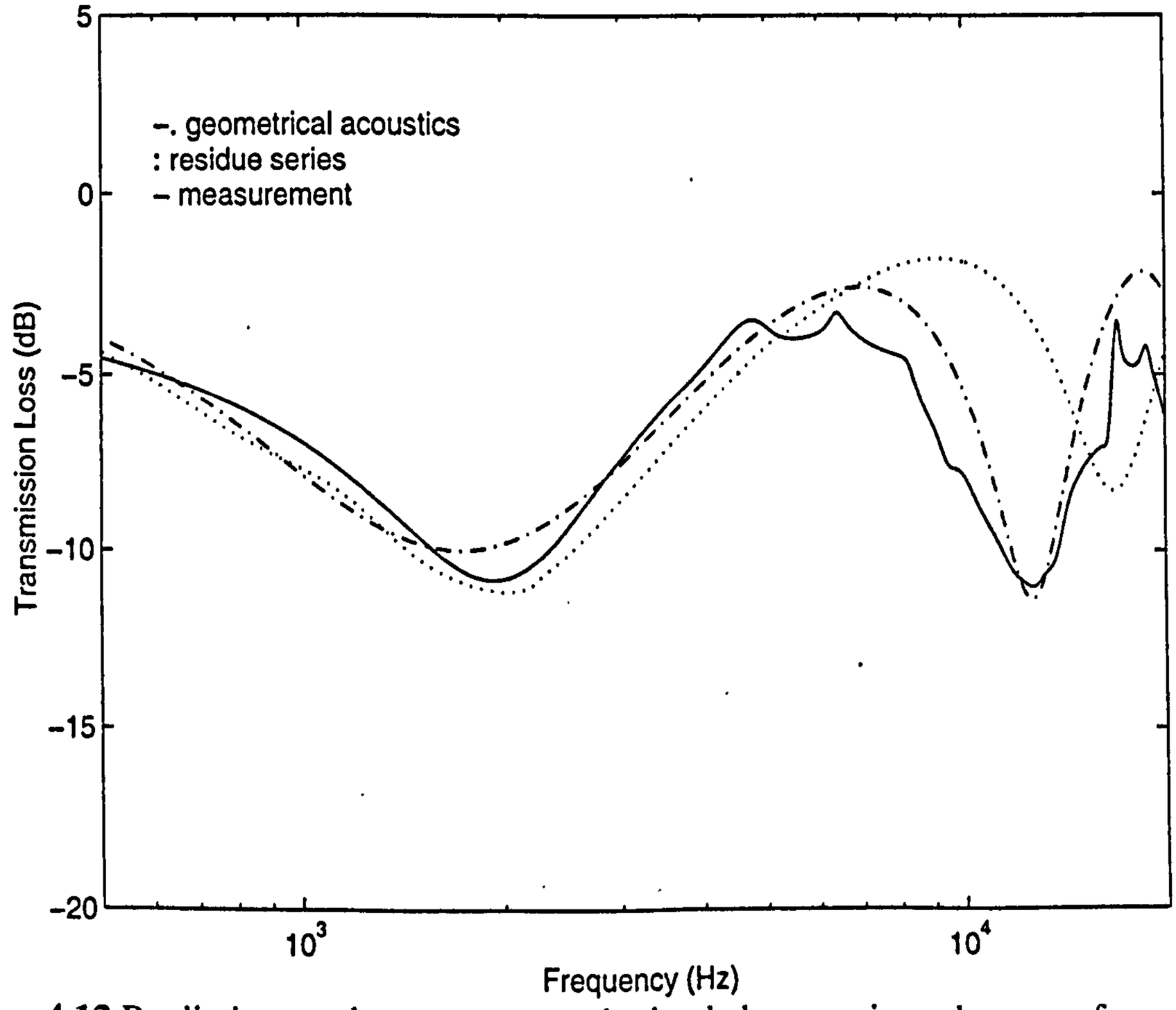

Figure 4.12 Predictions and measurement obtained above an impedance surface, $\sigma_e = 38$ kPa s m^{-2}, $\alpha_e = 15$ m^{-1}, $R_c = 2.5$ m, $z_s = 0.68$ m, $z = 0.12$ m and $r = 1.65$ m.

4.2.3 Failure of predictions in the penumbra region

Note that the curves of sound pressure predicted above the felt-covered surface become dissimilar to those above the rigid surface. This is particularly the case when the scaled and nondimensionalized admittance q (described in Chapter 2 and Chapter 3) is large and the receiver is located in the penumbra region along the line of sight. Furthermore, the transmission loss (or the excess attenuation) will show dips when the magnitude of q is greater than a certain value, depending on the phase angle and geometrical factors. The curves in Figures 4.13 and 4.14 were plotted with various $|q|$ with $\varphi = \pi/4$ and $\pi/3$ respectively. We note that the depth of the dips is enlarged as $|q|$ increases, and that the curves with a phase angle of $\pi/4$ show greater dips than those with a phase angle of $\pi/3$. This implies that the impedance parameters are important in determining the dips. However, the measured variations with range at frequencies of 3 kHz and 4 kHz differ from those predicted by the theory, as shown in Figure 4.15. In Figure 4.15, the solid lines and the dashdot lines represent the predictions given by using the residue series solution with a bilinear profile and an exponential profile respectively. The predictions are presented at 1 kHz, 2 kHz, 3 kHz and 4 kHz, and the corresponding magnitudes of q are 1.02, 1.28, 1.81 and 2.31. The measured results are displayed by the points in the form of crosses, stars, circles and plus signs, respectively.

In their measurements, Berthelot and Zhou [19] observed the phenomenon of dips [or peaks in their case (see Figure 3.9)] where $|q| = 1.35$. They reported that the cause of the phenomenon was not well understood but the discrepancies between the predictions and measurement data were small. However, this is not the case for large $|q|$. It can be demonstrated, see Figure 4.16, that the dips become greater and the discrepancies between

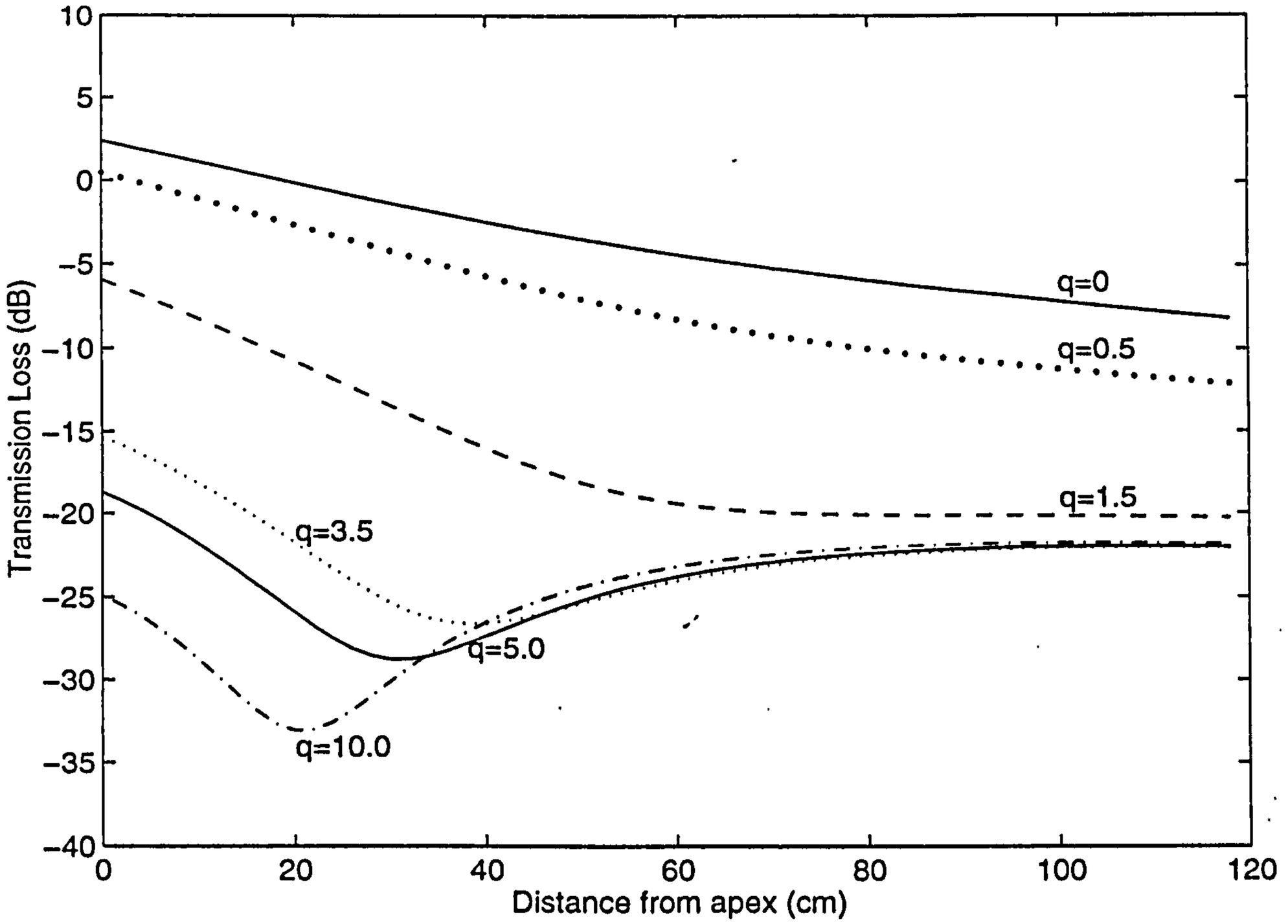

Figure 4.13 Transmission loss predicted along the line of sight above a convex impedance surface with source frequency at 2 kHz. $R_c = 2.5$ m, $z_s = 0.24$ m and $\varphi = \pi/4$.

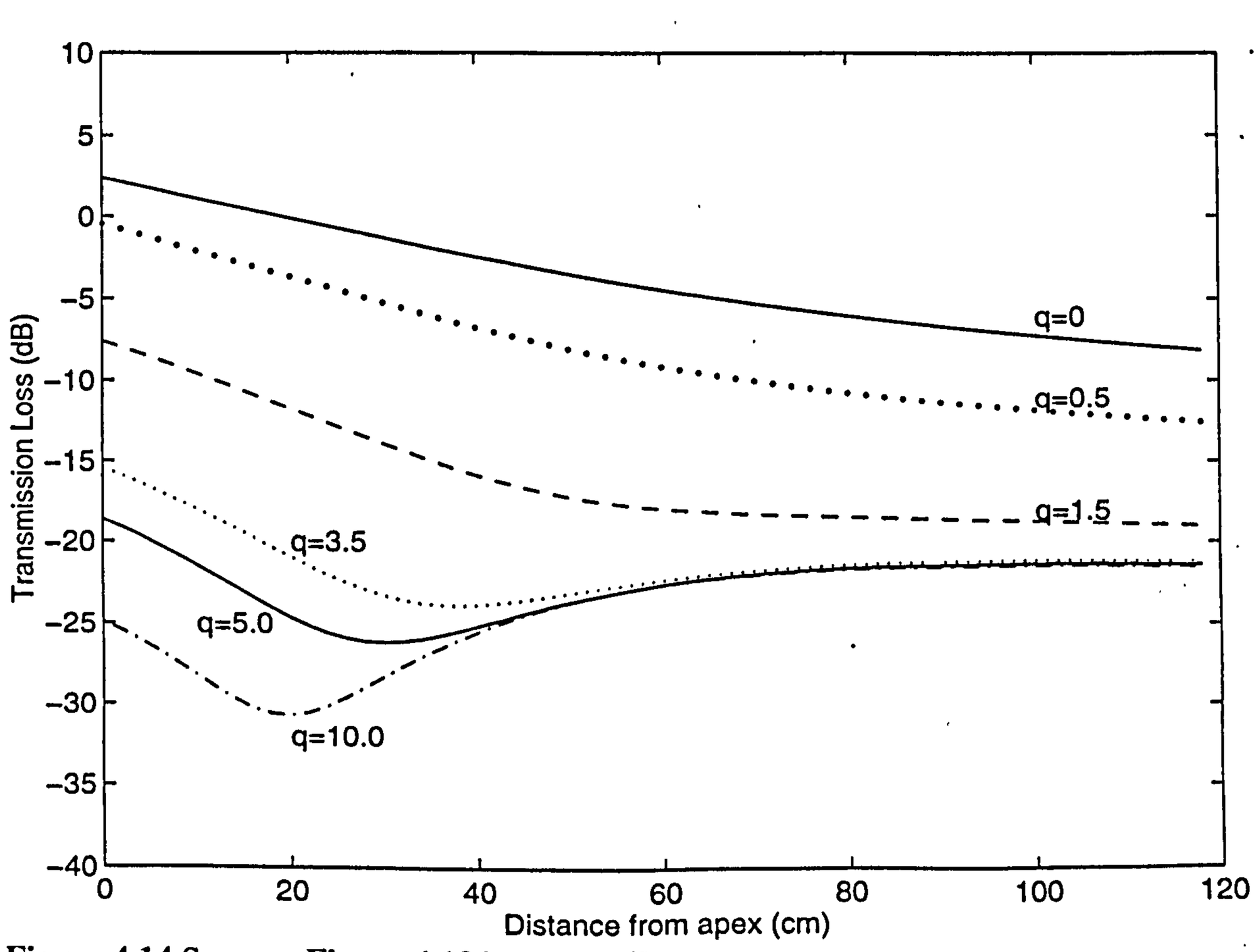

Figure 4.14 Same as **Figure 4.13** but $\varphi = \pi/3$.

the theory and the measurements become larger as $|q| > 1.35$. The measured data consistently shows shallower dips than the predictions.

In order to understand the problem, the measured data obtained at 4.35 kHz behind the felt-covered surface, where $|q|$ is 2.48, is compared with other versions of theory in terms of excess attenuation. Figure 4.16 shows the measured results compared with the theoretical predictions from the residue series solution assuming a bilinear sound speed profile with both interpretations of r and d (*cf.* Chapter 3), and the residue series solution for an exponential profile in this particular region. In this figure, the dips appeared in the measured results are 2-4 dB shallower than the predictions and there are discrepancies apparently in the vicinity of the apex. In the region beyond 80 cm from the apex along the line of sight, the prediction calculated from the bilinear profile with Berthelot and Zhou's interpretation [19] of d is very close to that calculated from the exponential profile. Furthermore, they agree well with the measurements.

By performing the measurement several times and identifying similar trends in the data it has been confirmed that there are persistent discrepancies between predictions and measurements in the penumbra region. An example is shown in Figure 4.17, where these measured data were obtained from a different experiment. In this experiment, a more powerful speaker was used to increase the signal-to-noise ratio. Clearly, the result is in accord with that shown in Figure 4.16.

In Figure 4.18, the measurements are further compared with the predictions calculated from the fast field program (FFP) for the exponential sound speed profile. As was stated earlier, the prediction is consistent with the residue series solution for the same profile used in Figure 4.17.

Figure 4.19 compares the measurements with predictions obtained by the boundary element method (BEM). The prediction from the BEM is very similar to the predictions presented in Figures 4.16, 4.17 and 4.18 in the region beyond 80 cm from the apex along the limiting ray. In the region between 10 to 80 cm from the apex, the prediction follows the trends of the measured dips, but again over-predicts the dips by up to 2 dB. When the receiver was on the apex, the predicted sound field was about 3 dB lower than the measured results, this is in contrast to the previous predictions.

In the penumbra region along the line of sight, the matched asymptotic expansions (MAE) theory has been applied to the problem [29]. These measured data are compared with predictions calculated according to Equation (3.7.7) in Figure 4.20. There is good agreement between the measurements and the prediction in the region beyond 20 cm from the apex. However, the agreement is less satisfactory in the region near the apex.

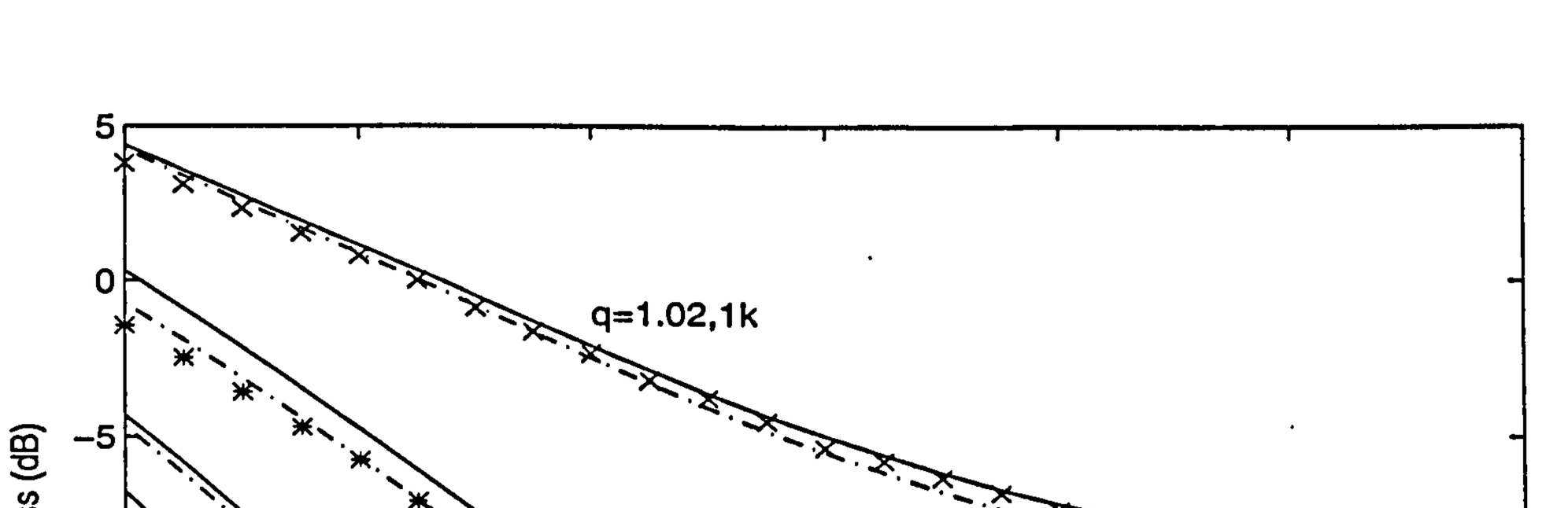

Figure 4.15 Transmission loss due to a monopole source obtained along the line of sight above a felt-covered convex surface. Measured results given by crosses: 1 kHz, stars: 2 kHz, circles: 3 kHz, and plus signs: 4 kHz. Corresponding predictions given by solid lines: for a bilinear profile, dotted lines: for an exponential profile. $R_c = 2.5$ m and $z_s = 0.115$ m.

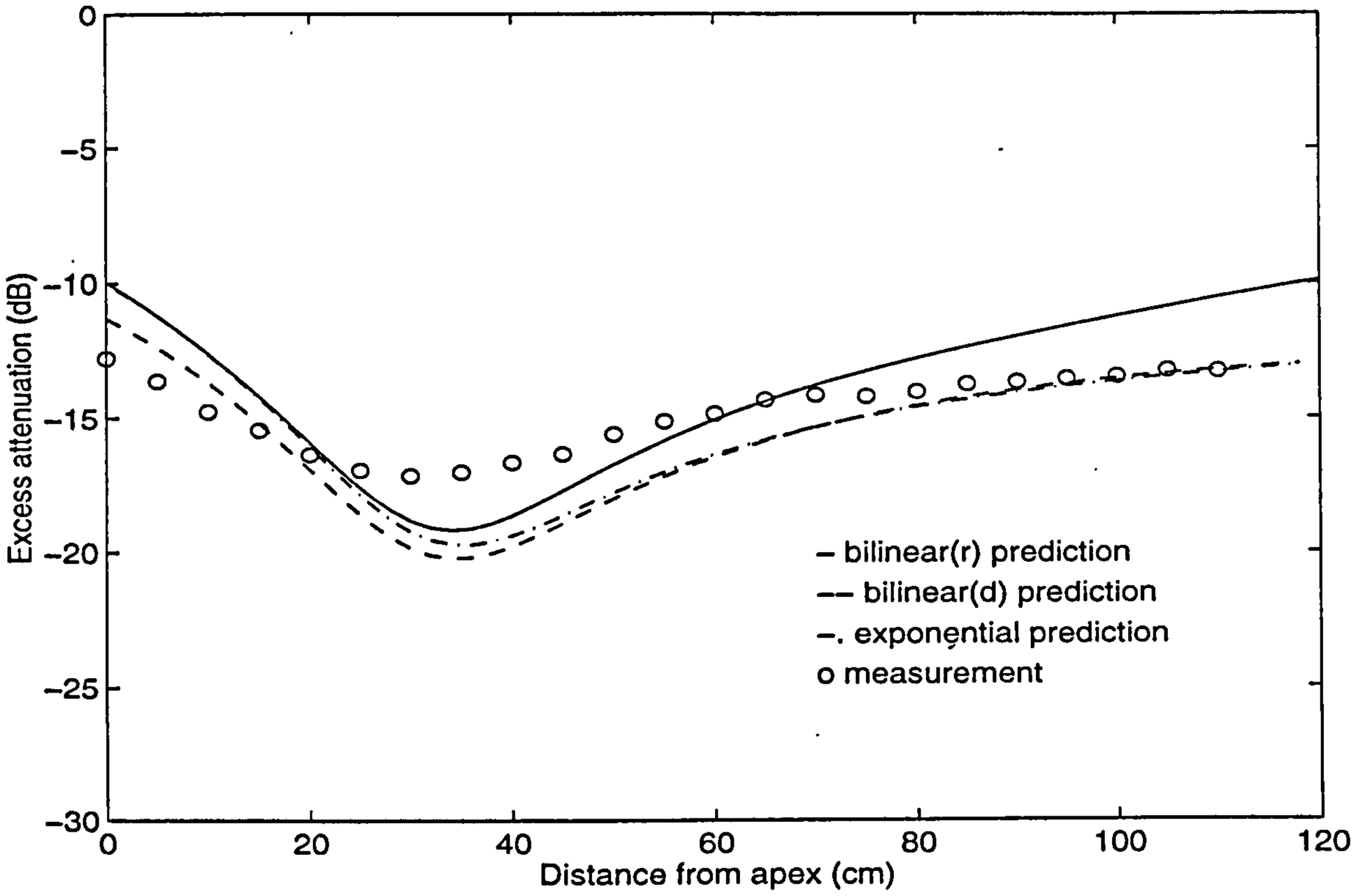

Figure 4.16 Excess attenuation obtained at 4350 Hz along the line of sight above a felt-covered convex surface. $R_c = 2.5$ m and $z_s = 0.24$ m.

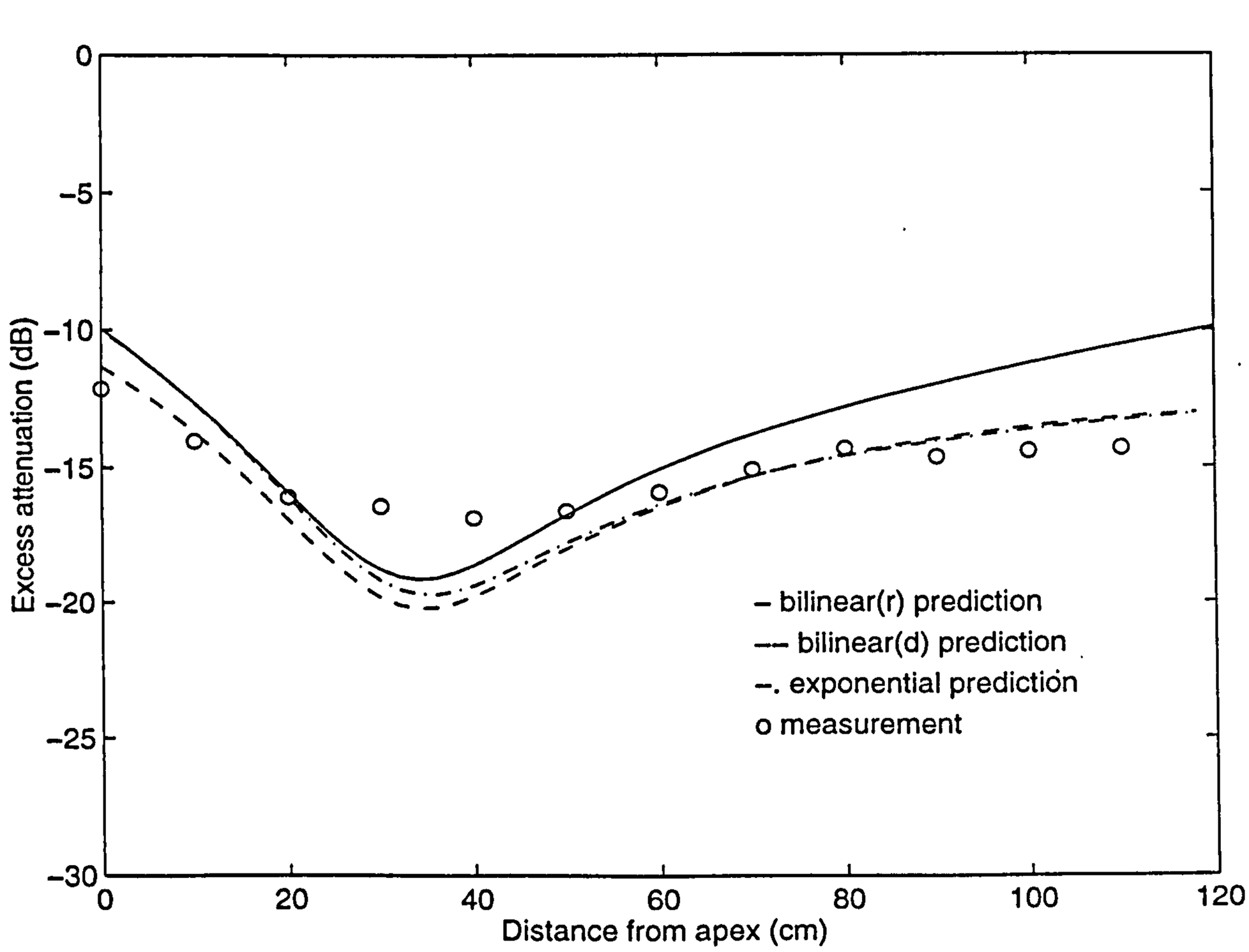

Figure 4.17 Same as **Figure 4.16** but measurement results obtained from different experiment.

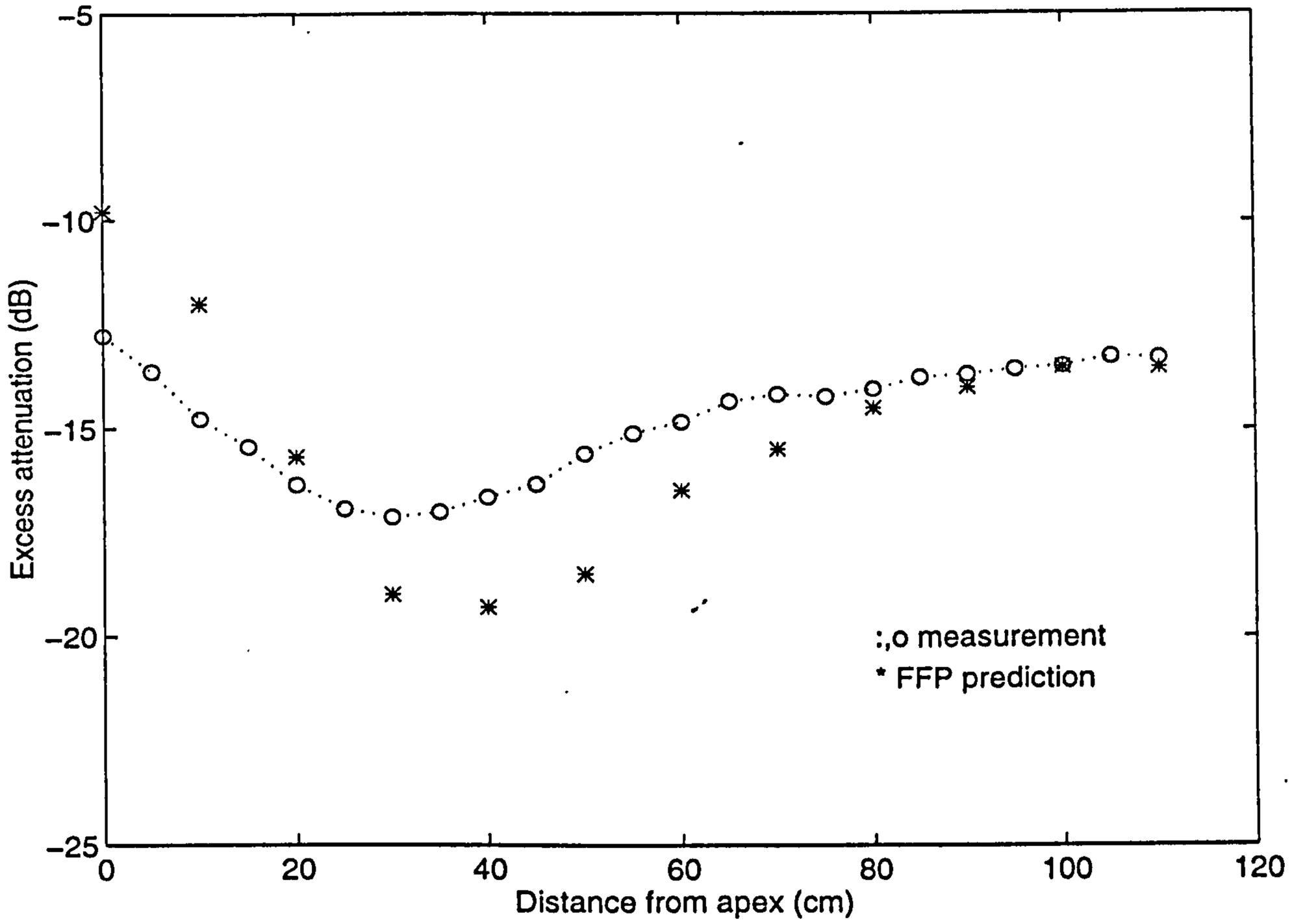

Figure 4.18 Same as **Figure 4.16** but prediction calculated using the fast field program (FFP) represented by the stars.

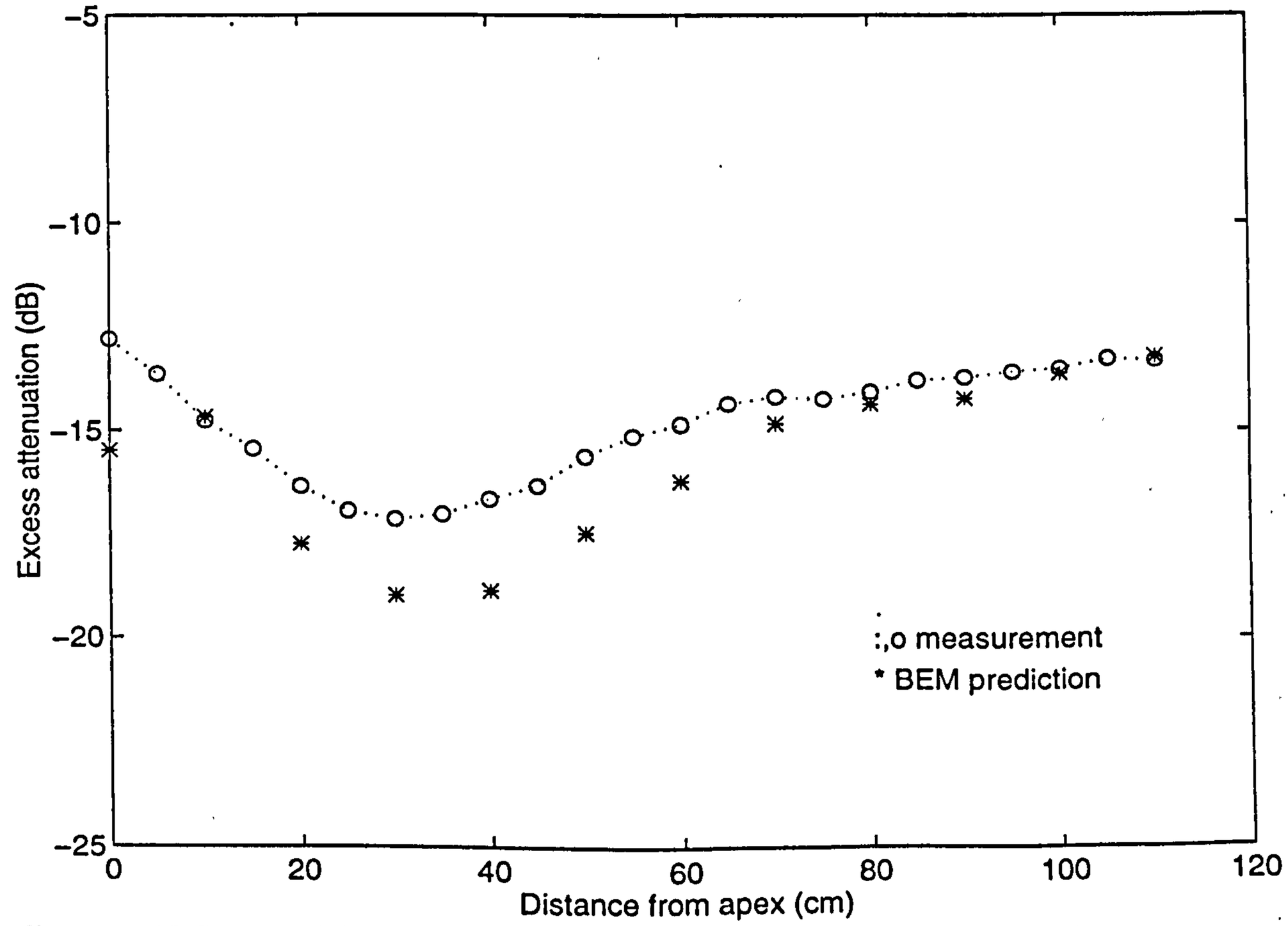

Figure 4.19 Same as **Figure 4.16** but prediction calculated using the boundary element method (BEM), represented by the stars.

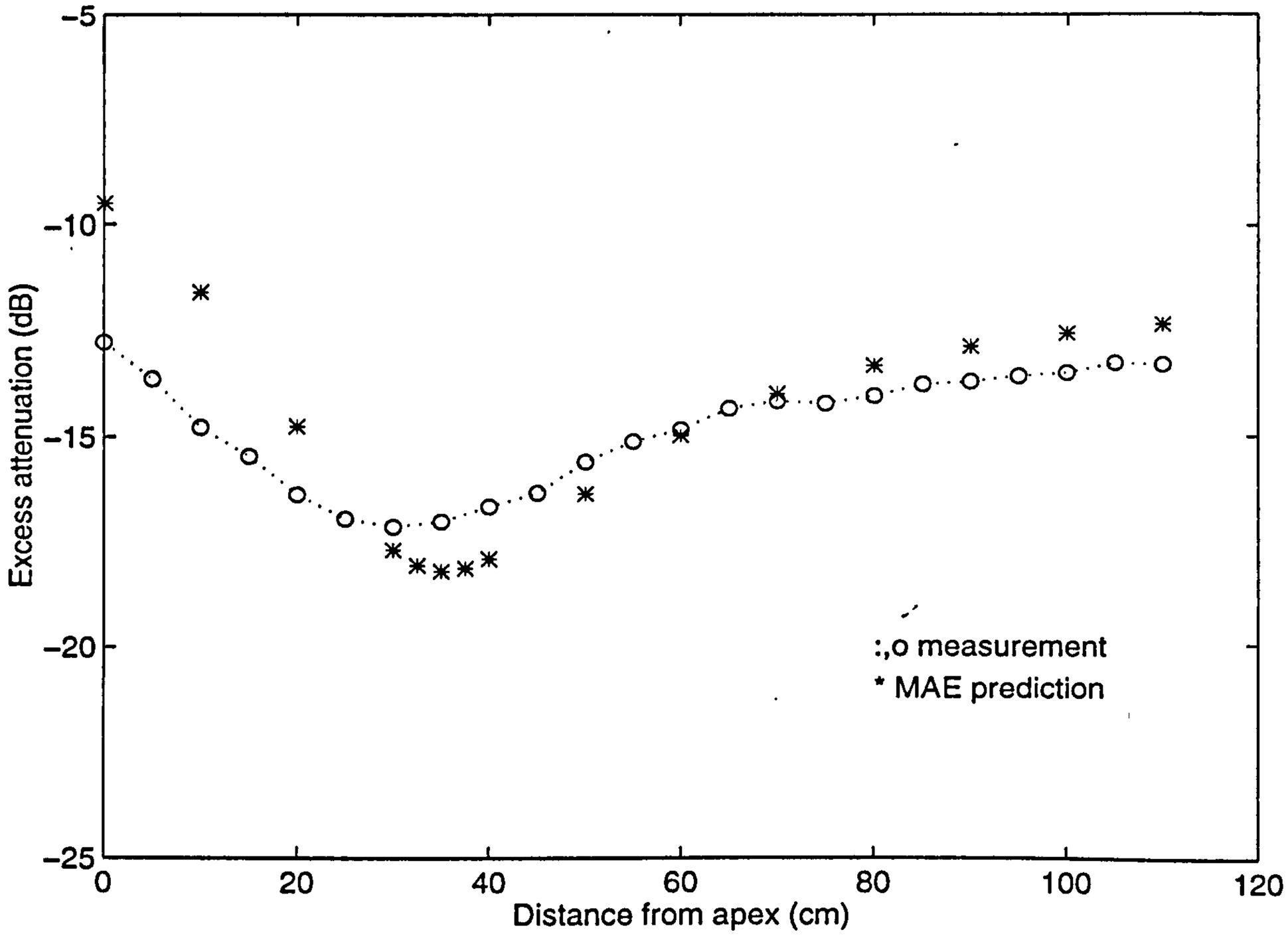

Figure 4.20 Same as **Figure 4.16** but prediction calculated using the matched asymptotic expansions (MAE), represented by the stars.

It is seen that none of the predictions match the measurements for the entire range of interest.

4.3 The sound field due to a horizontal dipole

This section compares experimental results with predictions for the sound field due to a horizontal dipole above convex surfaces. The section ends with a brief comparison of the horizontal dipole sound field and a monopole sound field.

4.3.1 Experimental results

To enable comparison, a series of measurements was conducted using the horizontal dipole source under the same conditions as those using the monopole source. Data obtained by the transducer disc with resonance frequency of 2915 Hz are presented for three receiver configurations. The experimental results are presented according to the following sequence.

I. Along the surface

The experimental data shown in Figure 4.21 were obtained with the horizontal dipole source at a height of 0.24 m above the rigid and felt-covered surfaces. The receiver was moved along the surfaces ($z \sim 0.00$ m), (*cf.* Figure 4.5). The circles represent measurements made above the rigid surface, while the plus signs represent data obtained above the felt-covered surface. The predictions were calculated from Equation (3.9.3) and are represented by the solid lines. In the region near the source, Equation (3.9.3) is invalid and the predictions were calculated instead by Equation (3.9.6), the geometrical acoustics solution (the dotted lines). In general, there is good agreement between the measurements and the predictions in this region.

II. Along the line of sight

In Figure 4.22, the transmission loss is shown as a function of distance from the apex along the line of sight (*cf.* Figure 4.5). The horizontal dipole source remained at a height of 0.24 m, while the receiver height varied with distance. Similarly, the circles represent data measured above the rigid surface while the plus signs represent data obtained above the felt-covered surface. The predictions were calculated from Equation (3.9.3) and are represented by the solid lines. In this configuration, there is good agreement between predictions and data only above the rigid surface. Above the felt-covered surface, discrepancies are found near the dips in the penumbra region where $|q|$ is 1.77. These are consistent with the discrepancies described in Chapter 4.2.2 for a monopole sound field.

III. Across the shadow zone

Figure 4.23 shows the results obtained when the receiver was moved along the vertical starting at an arc distance of 1.95 m from the source (*cf.* Figure 4.5), while the source was at 0.24 m above the surfaces. As in Figure 4.21, the circles represent data measured above

the rigid surface, whereas the plus signs represent data obtained above the felt-covered surface. The predictions were calculated from Equation (3.9.3) and are represented by the solid lines. The discrepancies between the measured results and the theory are no more than 1 dB for both the rigid and the felt-covered surfaces in this region.

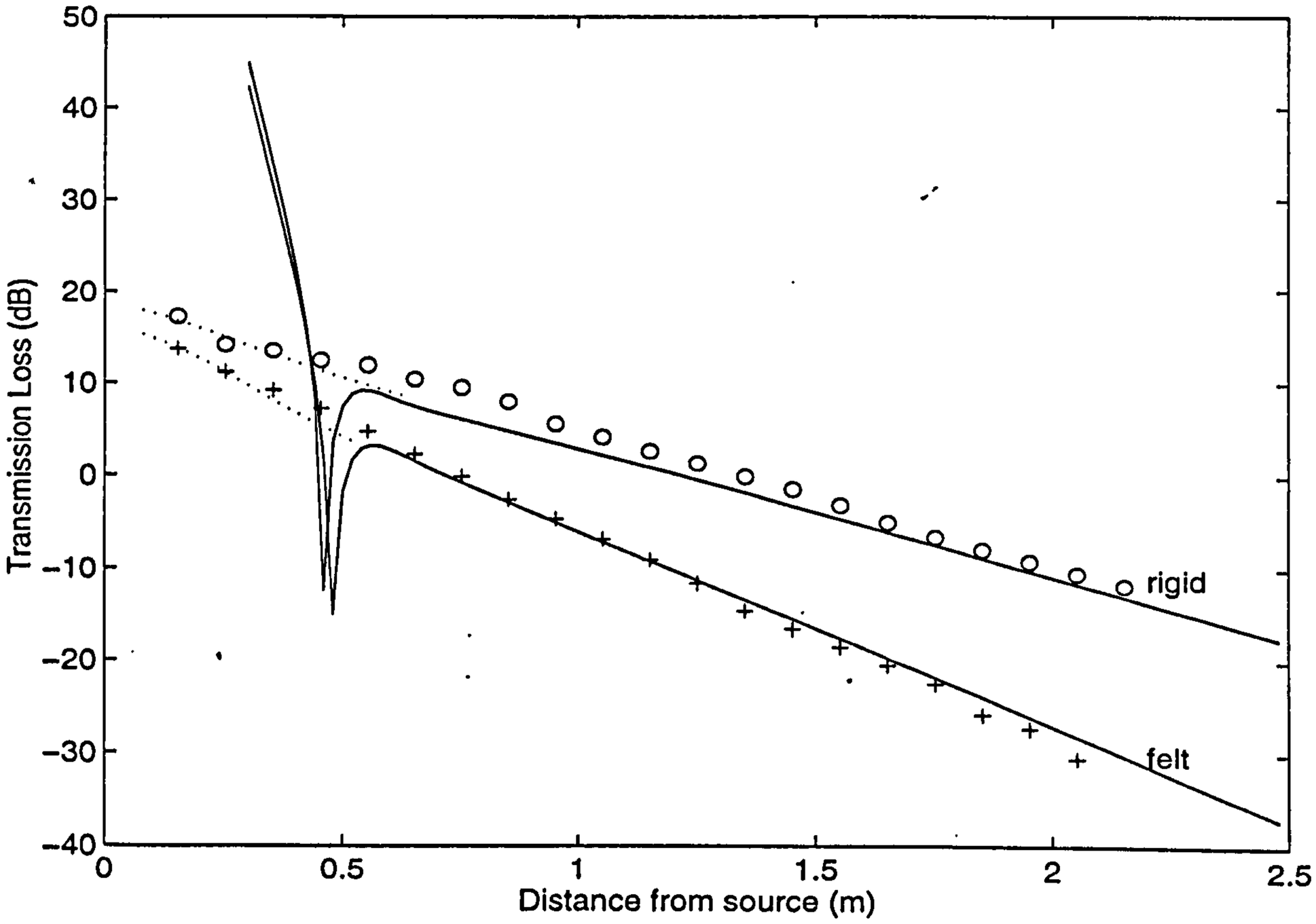

Figure 4.21 Transmission loss due to a horizontal dipole obtained along the rigid and felt-covered surfaces respectively , with source frequency at 2915 Hz. $R_c = 2.5$ m and $z \sim 0.00$ m, $z_s = 0.24$ m. Circles and plus signs: measurement results, solid lines: the residue series predictions and dotted lines: predictions of the geometrical acoustics solution for a dipole.

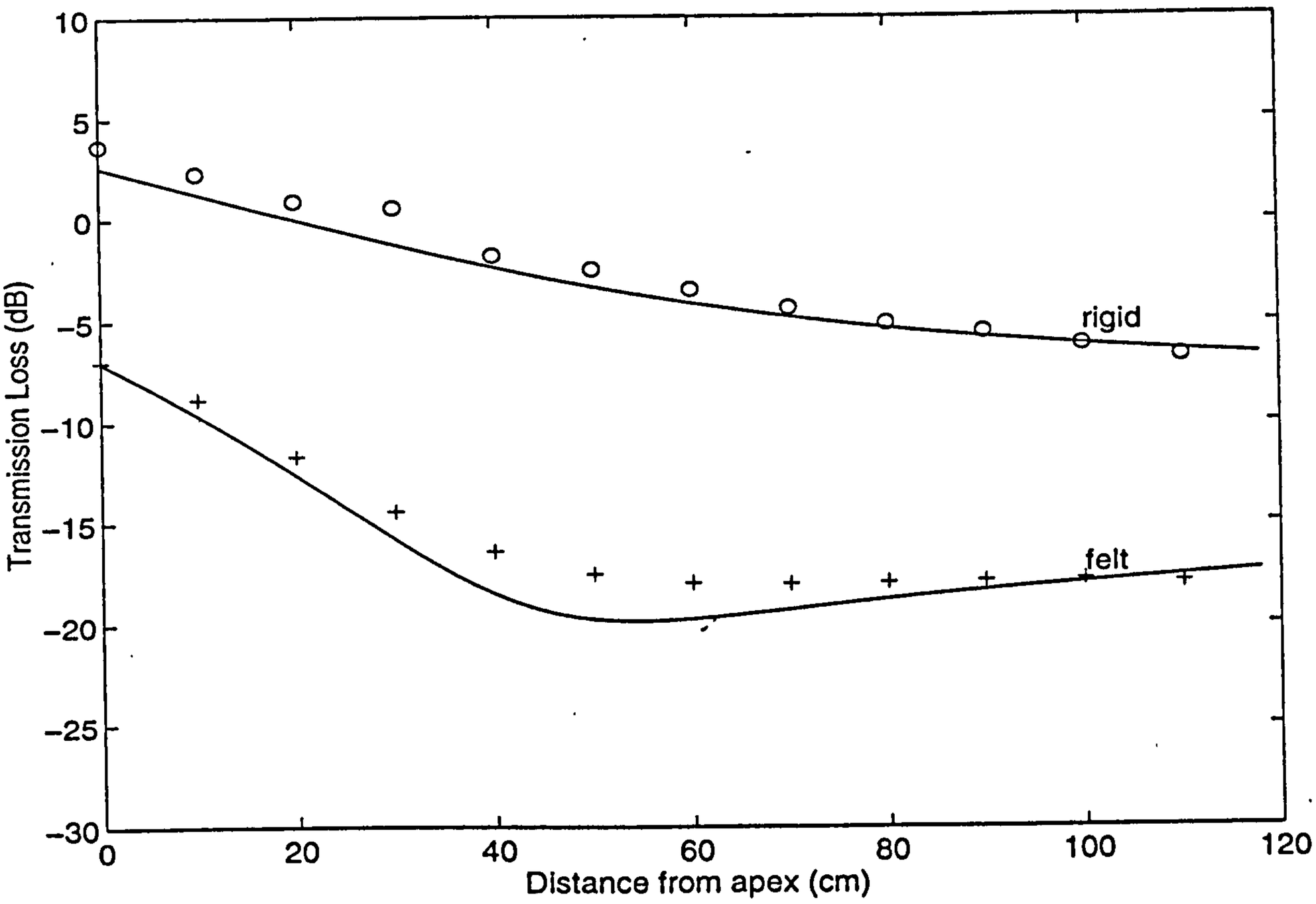

Figure 4.22 Same as **Figure 4.21**, but along the line of sight.

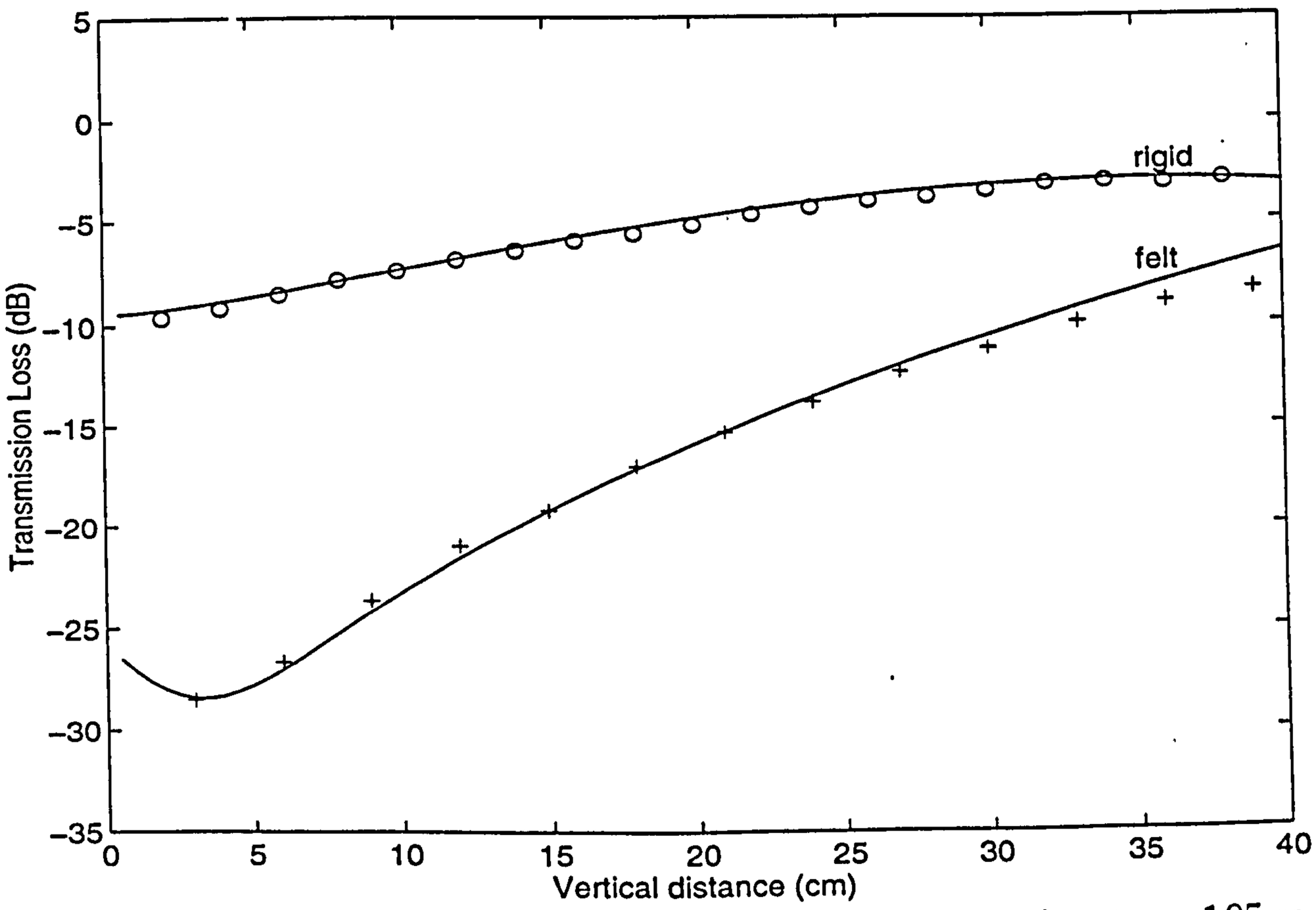

Figure 4.23 Same as **Figure 4.21**, but along a vertical distance z_v starting at $r_0 = 1.95$ m (*cf.* **Figure 4.5**).

4.3.2 Comparisons with monopole data

In the following comparisons, the circles represent data measured from the monopole source at the same geometry as that used for the horizontal dipole source, which has been described earlier. The plus signs represent data measured from the horizontal dipole source. The theoretical predictions for the monopole and horizontal dipole sources were calculated from Equation (2.4.5) and Equation (3.9.3), and are represented by the solid and dotted lines respectively.

Figures 4.24 and 4.25 display the dipole results, which have been shown in Figure 4.19, compared with the monopole field along the rigid and felt-covered surfaces, respectively.

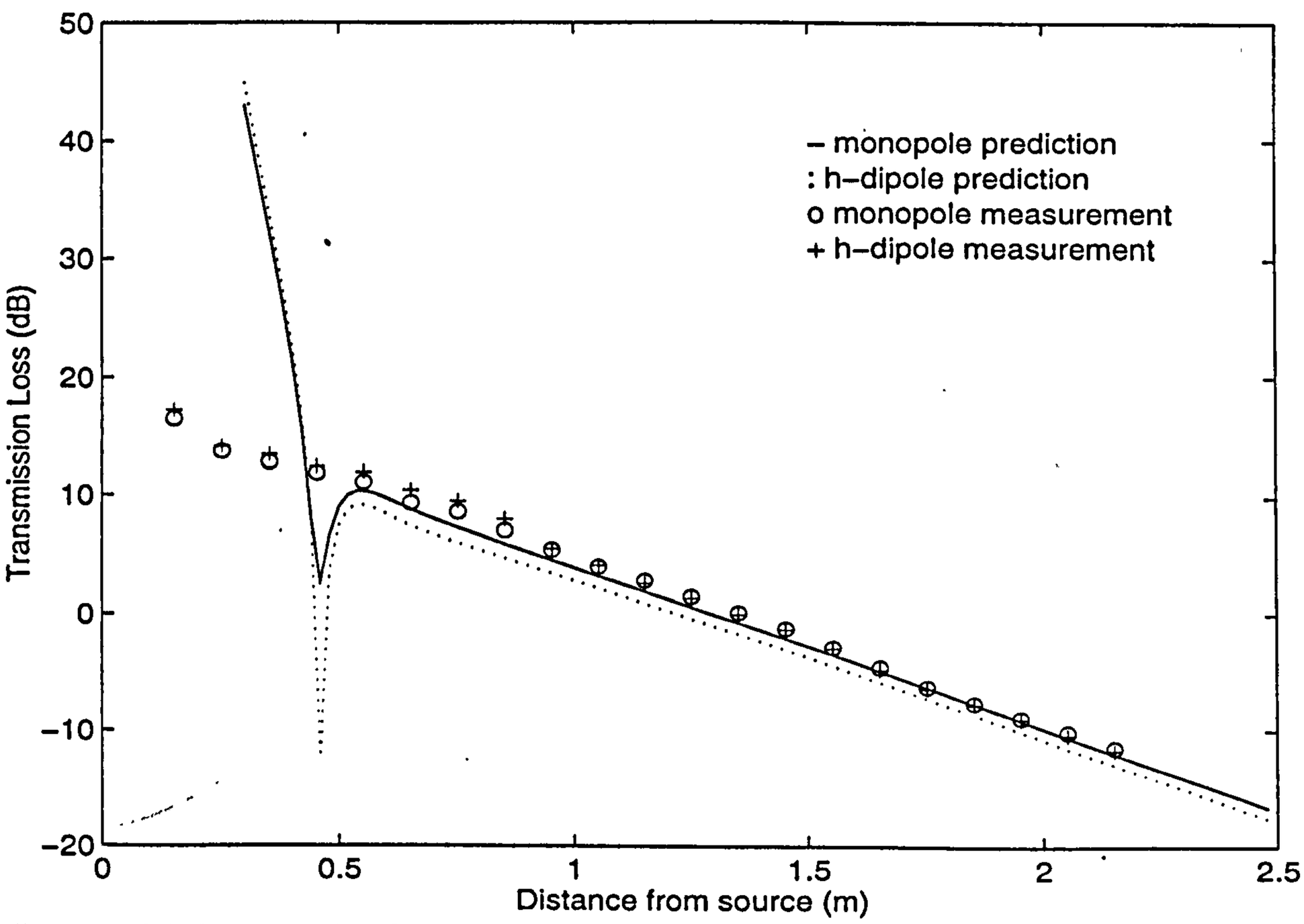

Figure 4.24 Transmission loss due to a monopole source and a horizontal dipole source obtained along a rigid surface, and with source frequency at 2915 Hz. $R_c = 2.5$ m, $z \sim 0.00$ m and $z_s = 0.24$ m.

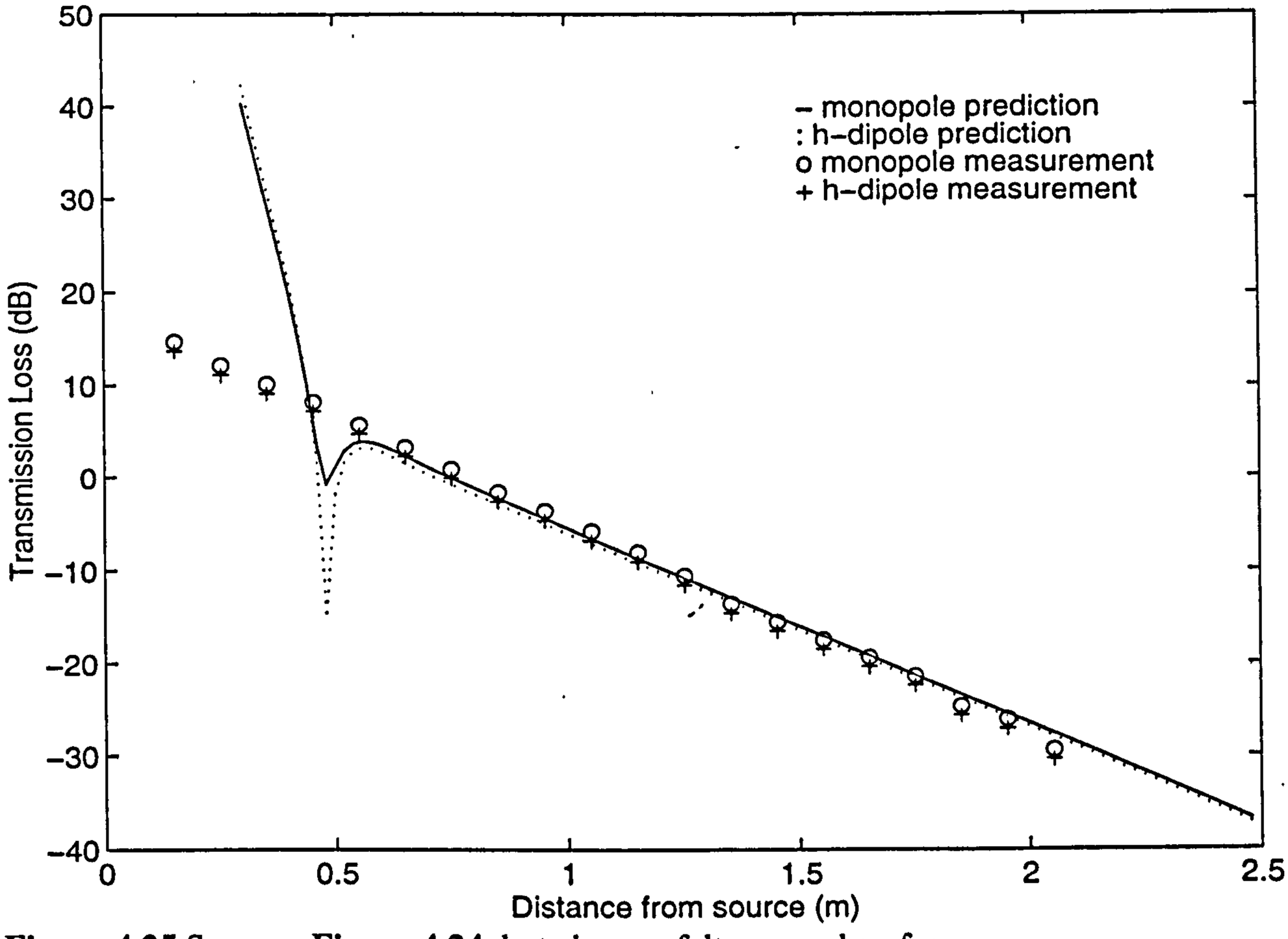

Figure 4.25 Same as **Figure 4.24**, but above a felt-covered surface.

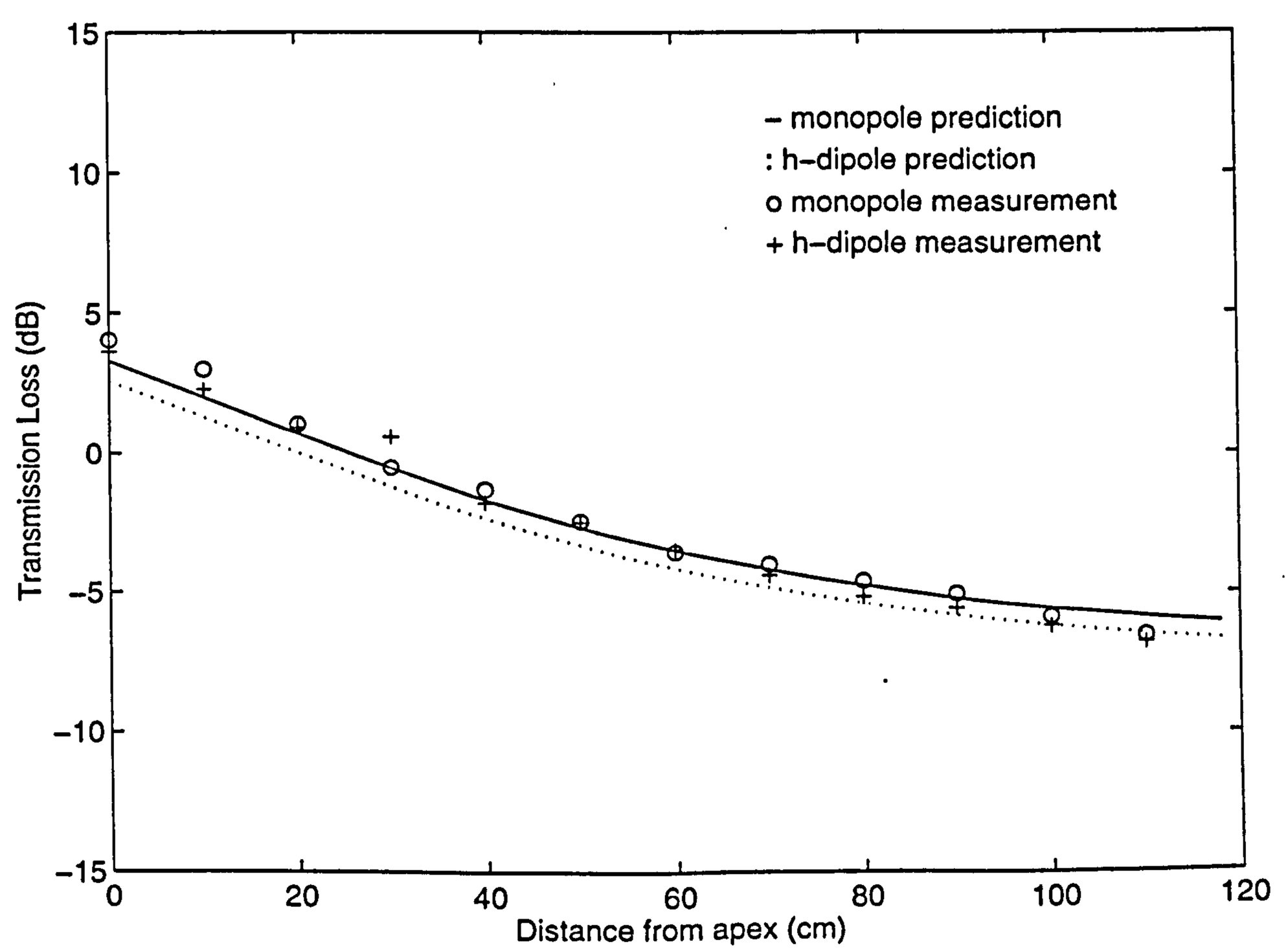

Figure 4.26 Same as **Figure 4.24**, but along the line of sight.

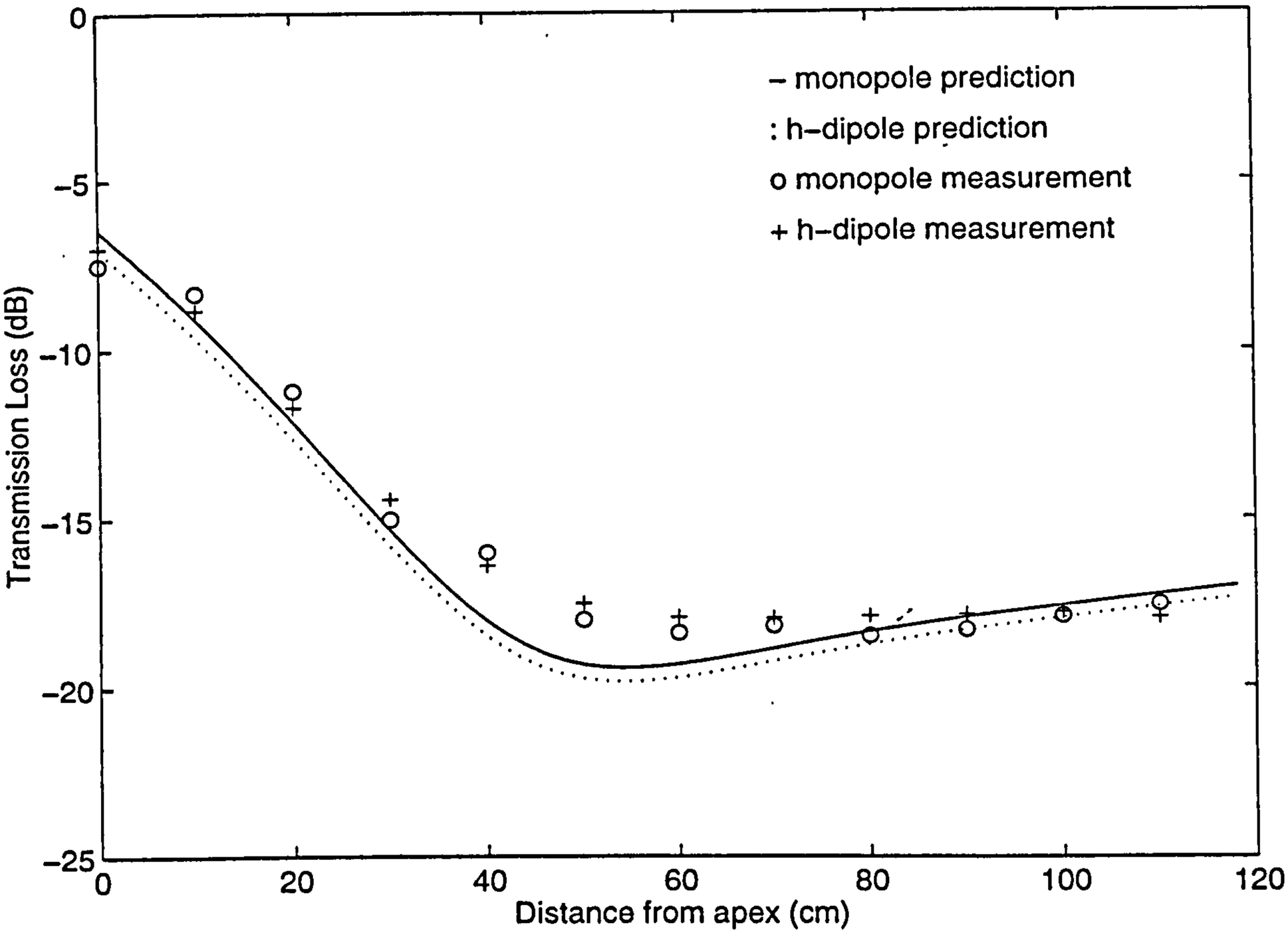

Figure 4.27 Same as **Figure 4.26**, but above a felt-covered surface.

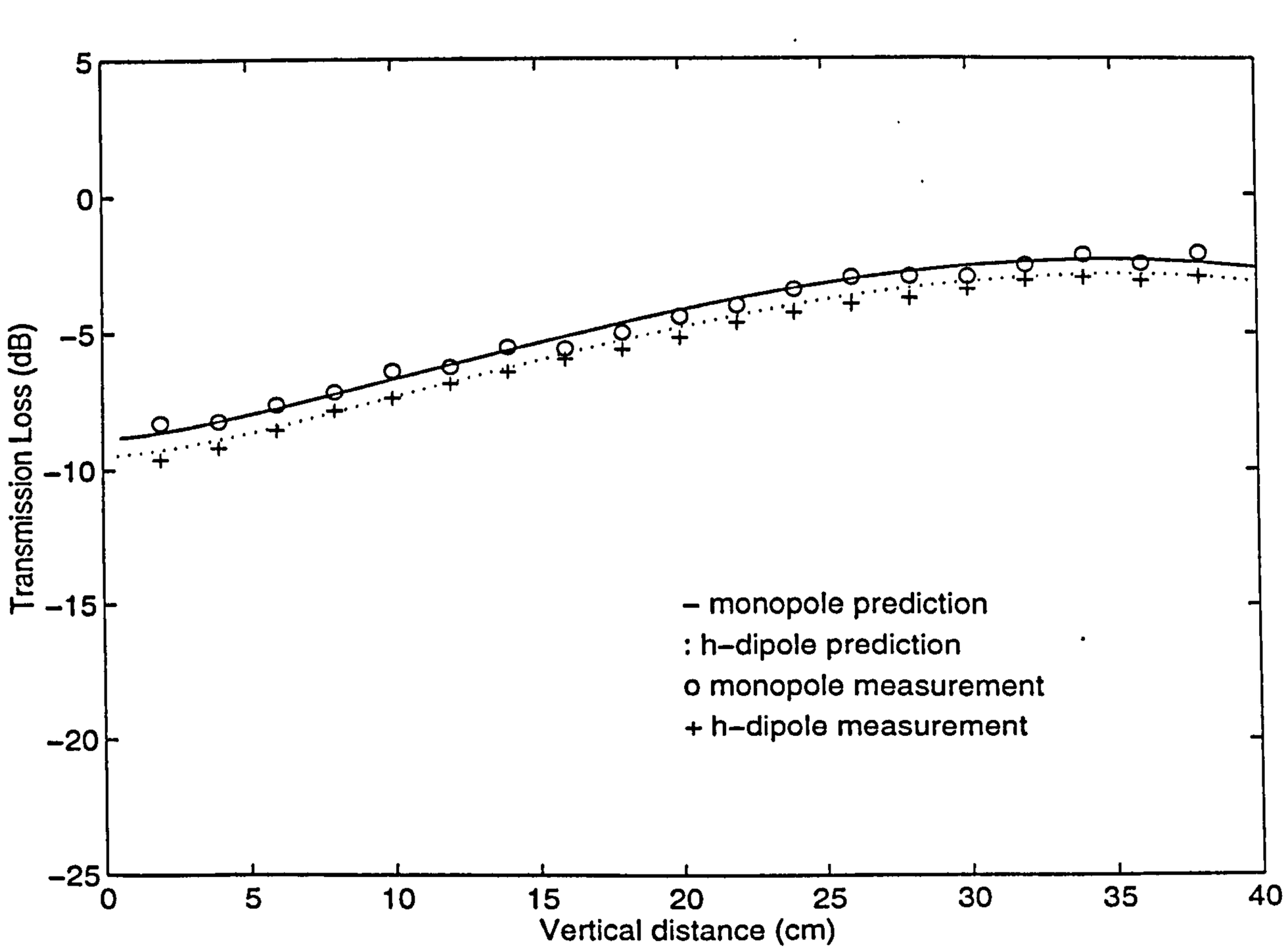

Figure 4.28 Same as **Figure 4.24**, but along a vertical distance z_v at $r_0 = 1.95$ m (*cf.* **Figure 4.5**).

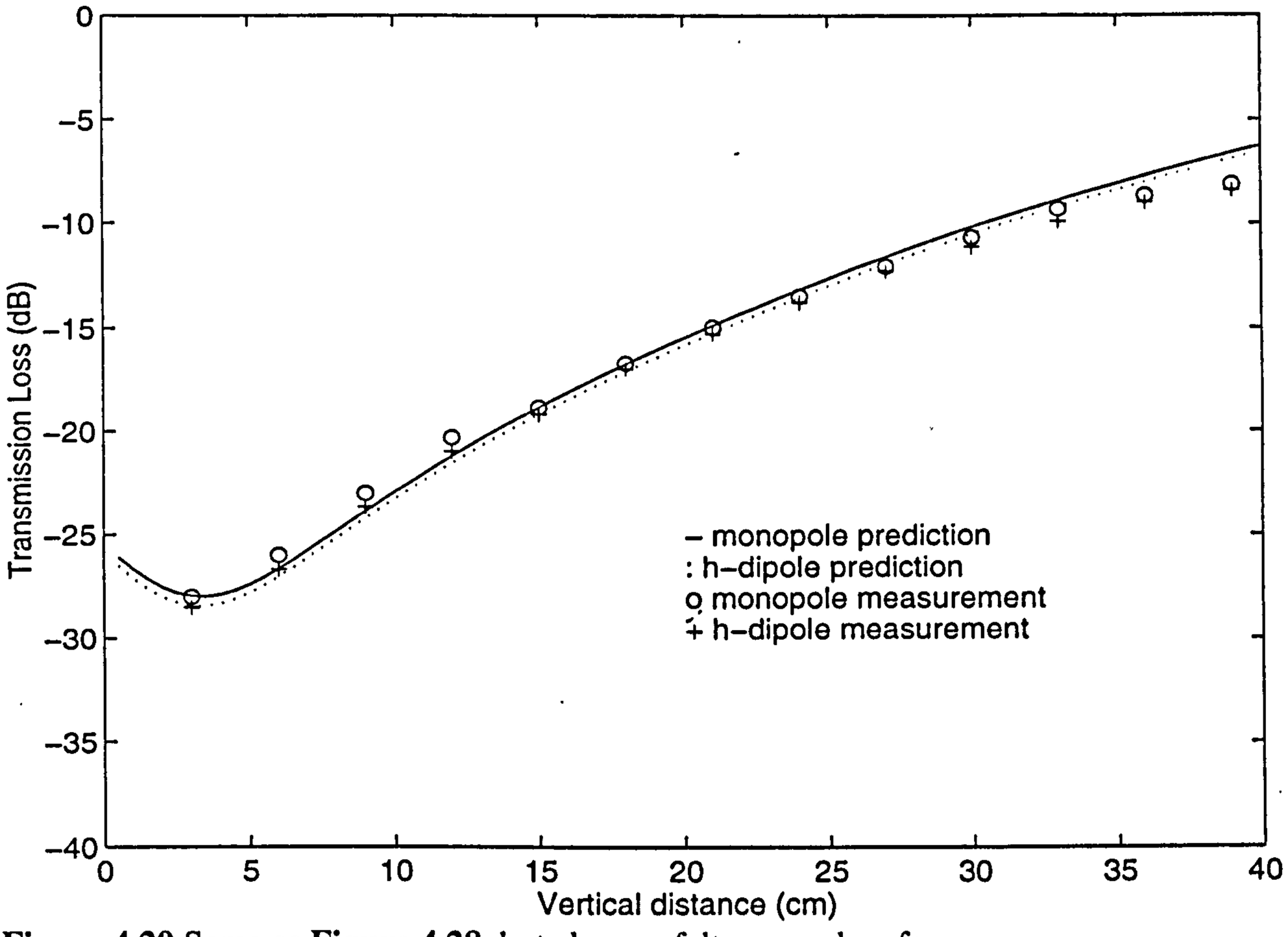

Figure 4.29 Same as **Figure 4.28**, but above a felt-covered surface.

Figures 4.26 and 4.27 display the dipole results, which have been shown in Figure 4.22, compared with the monopole field along the line of sight above the rigid and felt-covered surfaces, respectively.

Figures 4.28 and 4.29 include the monopole field results, which have been already shown in Figure 4.23, and enable comparison of the horizontal dipole and monopole fields across the shadow zone above the rigid and felt-covered surfaces, respectively.

It is clear that the horizontal dipole sound field is very similar to the monopole sound field for these three configurations. The two independent sets of measurements using the monopole source and the horizontal dipole source show almost identical results. In general, the differences in the amplitude of transmission loss between them are predicted and measured to be less than 1 dB.

4.4 The sound field due to a vertical dipole

This section compares experimental results with theoretical predictions for the sound field due to a vertical dipole over convex surfaces. The section ends with a brief comparison of the vertical dipole sound field and a monopole sound field.

4.4.1 Experimental results

A series of measurements has been conducted using a vertical dipole source under the same conditions as those using the monopole source. Data obtained by the transducer disc with resonance frequency of 2915 Hz and in vertical dipole orientation are presented for the three receiver configurations. The presentation of the experimental results follows the previous sequence.

I. Along the surface

The experimental data shown in Figure 4.30 were obtained with the vertical dipole source at a height of 0.24 m above the rigid and felt-covered convex surfaces. The receiver was moved along the surfaces ($z \sim 0.00$ m), (*cf.* Figure 4.5). The circles in this figure represent data measured above the rigid surface, while the plus signs represent data obtained above the felt-covered surface. The predictions were calculated from Equation (3.9.4) and are represented by the solid lines. In the regions near the source, Equation (3.9.4) is invalid and the predictions were calculated by Equation (3.9.7) corresponding to the geometrical acoustics solution (dotted lines). In general, there is good agreement between the measurements and the predictions.

II. Along the line of sight

In Figure 4.31, the transmission loss is shown as a function of distance from the apex along the line of sight (*cf.* Figure 4.5). The vertical dipole source remained at a height of 0.24 m, while the receiver height varied with distance. The circles represent data measured above

the rigid surface while the plus signs represent data obtained above the felt-covered surface, the predictions were calculated from Equation (3.9.4) and are represented by the solid lines. For this configuration, the discrepancies between data and predictions described in the previous chapter are repeated. Agreement is found to be good above the rigid surface only. Above the felt-covered surface, where $|q|$ is 1.77, with a characteristic vertical dipole source, there are obvious discrepancies near the dips.

III. Across the shadow zone

Figure 4.32 shows the results obtained as the receiver was moved along the vertical starting at an arc distance of 1.95 m from the source [*cf.* Figure 4.5], while the receiver was at 0.24 m above the surfaces. As in Figure 4.30 the circles represent data measured above the rigid surface, whereas the plus signs represent data obtained above the felt-covered surface, the predictions were calculated from Equation (3.9.4) and are represented by the solid lines. The discrepancies between the measured results and the theory are no more than 1 dB for both the rigid and the felt-covered surfaces in this region.

4.4.2 Comparisons with monopole data

In the following comparisons, the circles represent data measured for the monopole source at the same geometry as that for the vertical dipole source, which has been described earlier. The plus signs represent data measured for the vertical dipole source. The theoretical predictions for the monopole and vertical dipole sources were calculated from Equation (2.4.5) and Equation (3.9.4), and are represented by the solid and dotted lines respectively.

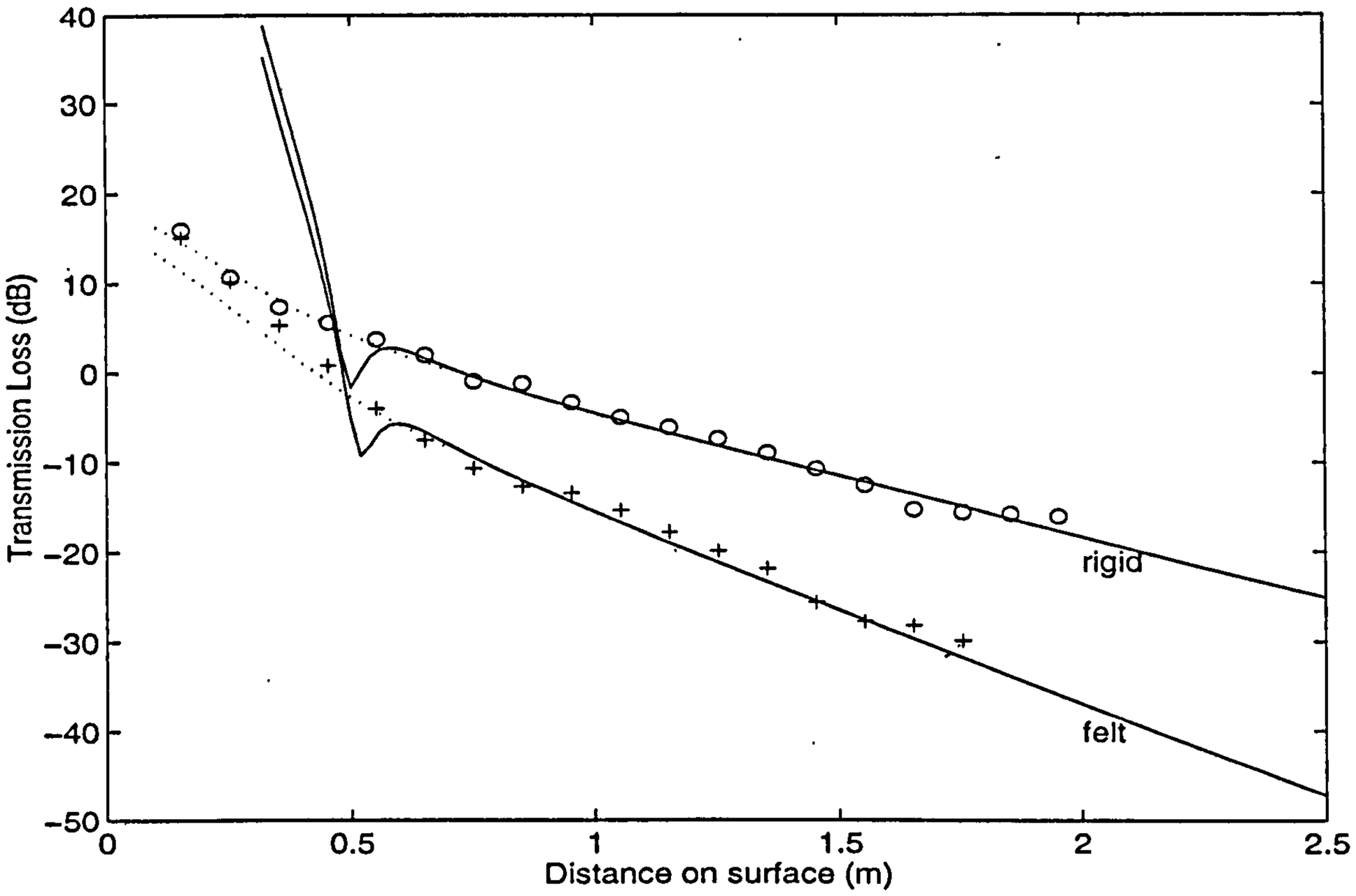

Figure 4.30 Transmission loss due to a vertical dipole obtained along the rigid and felt covered convex surfaces respectively, and with source frequency 2.9 kHz. $R_c = 2.5$ m, $z \sim 0.00$ m and $z_s = 0.24$ m. Circles and plus signs: measurement results, solid lines: the residue series predictions and dotted lines: predictions of the geometrical acoustics solution for a dipole.

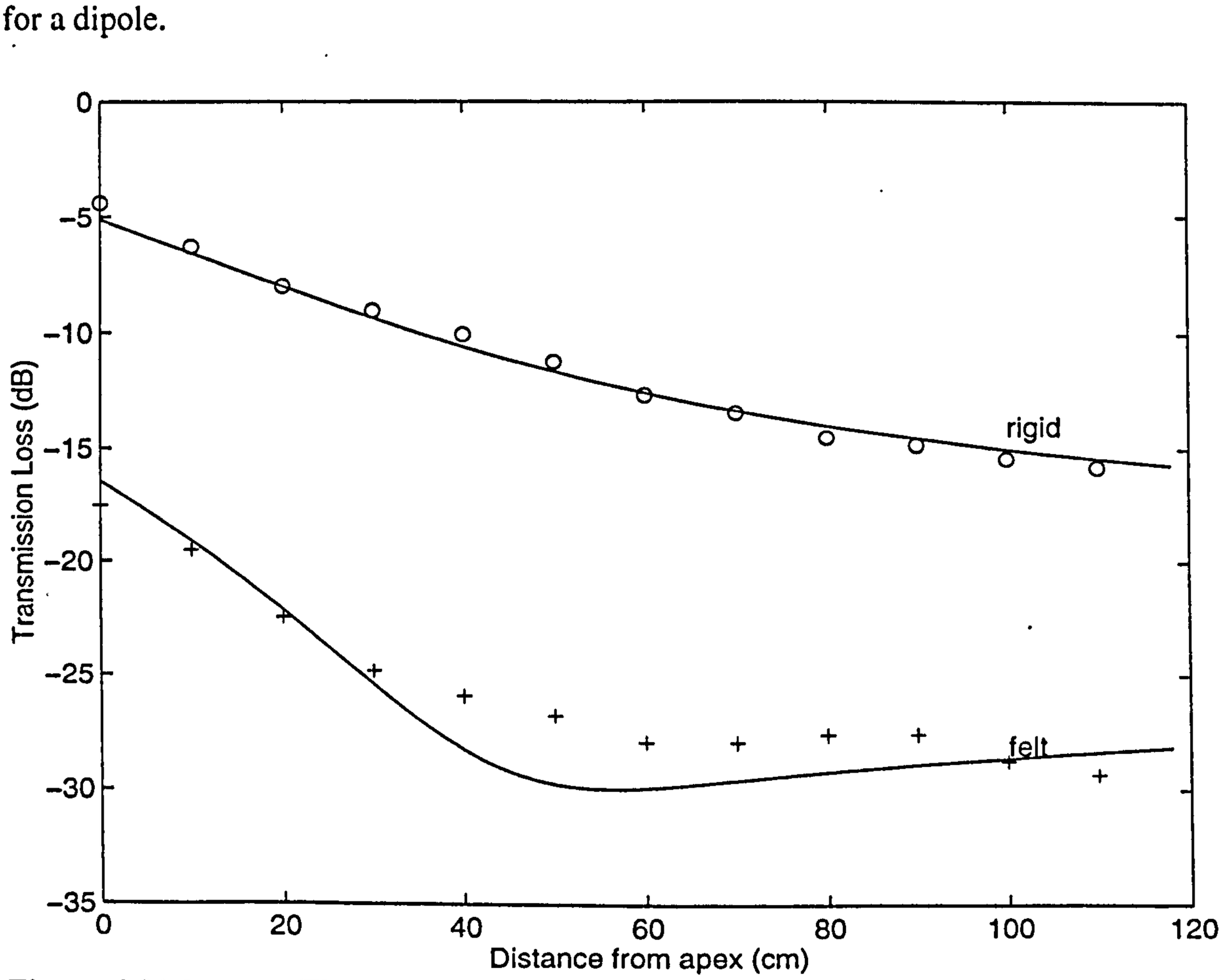

Figure 4.31 Same as **Figure 4.30**, but along the line of sight.

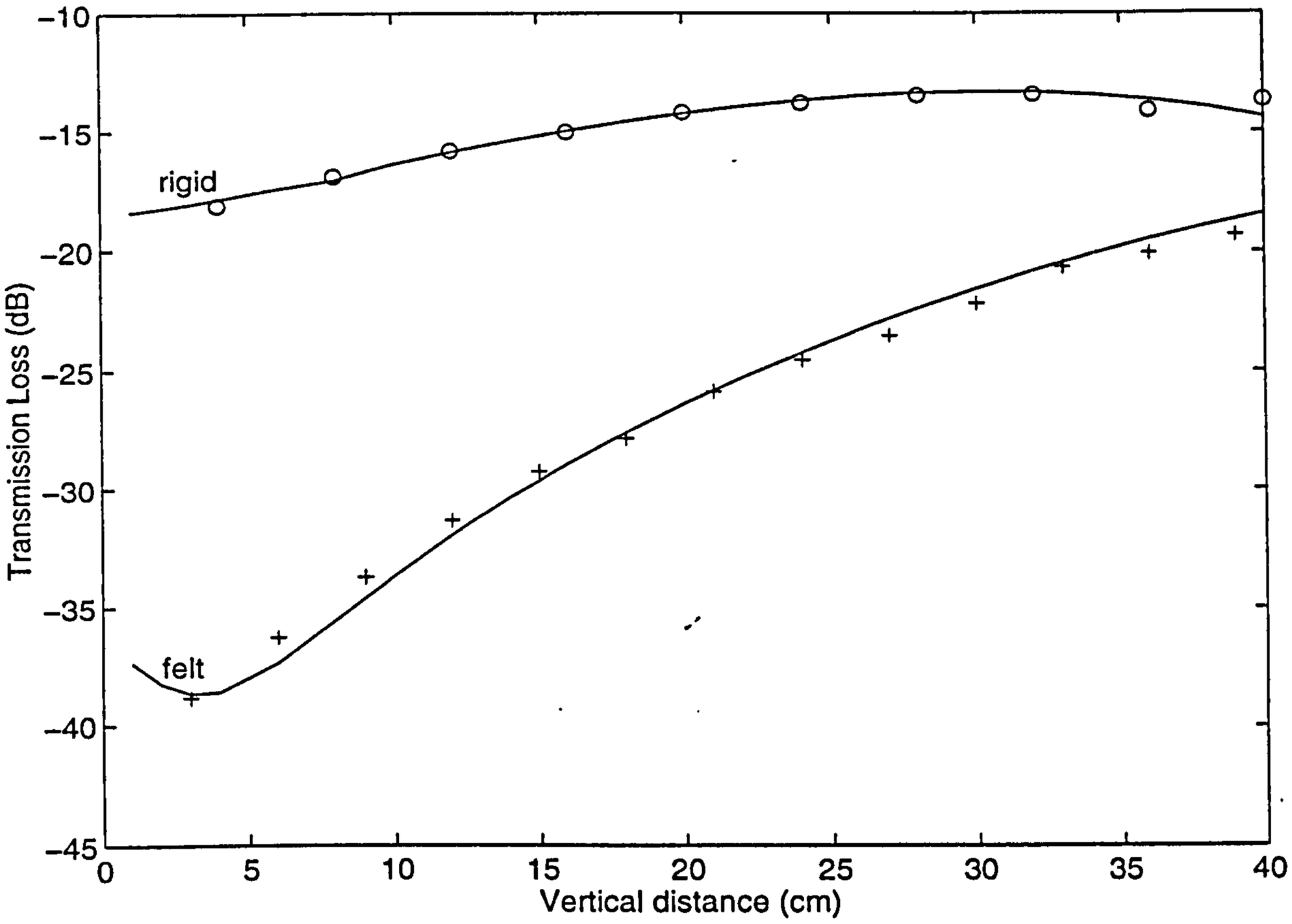

Figure 4.32 Same as **Figure 4.30**, but along a vertical distance z_v starting at $r_0 = 1.95$ m (*cf.* **Figure 4.5**).

Figures 4.33 and 4.34 include the results which have been shown already in Figure 4.30 and enable comparison between the vertical dipole and the monopole fields along the rigid and felt-covered surfaces, respectively.

Figures 4.35 and 4.36 include the results which have been shown already in Figure 4.31 and enable comparison between the vertical dipole and the monopole fields along the line of sight above the rigid and felt-covered surfaces, respectively.

Figures 4.37 and 4.38 include the results which have been shown already in Figure 4.31 and enable comparison between the vertical dipole and the monopole fields across the shadow zone above the rigid and felt-covered surfaces, respectively.

It is seen that the vertical dipole sound field varies with range in a similar way to the monopole sound field for these three configurations. The two independent sets of

measurements using the monopole source and the vertical dipole source show similar trends which are, however, of different magnitude. The differences in the amplitude of transmission loss are predicted and measured to be around 10 dB in this region.

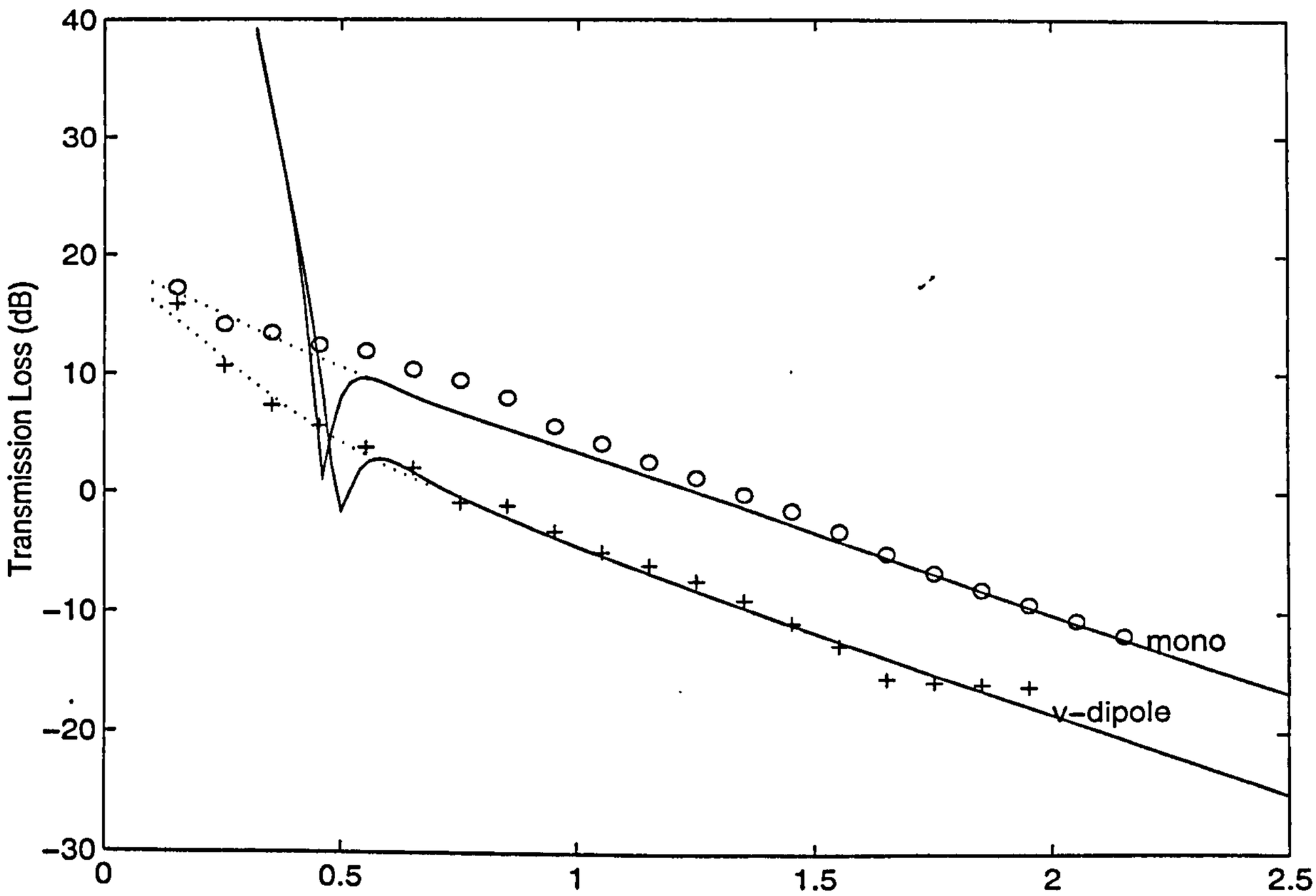

Figure 4.33 Transmission loss due to a monopole source and a vertical dipole obtained along a rigid surface, and with source frequency 2915 Hz. $R_c = 2.5$ m, $z \sim 0.00$ m and $z_s = 0.24$ m. Circles and plus signs: measurement results, solid lines: the residue series predictions and dotted lines: predictions of the geometrical acoustics solution for a dipole.

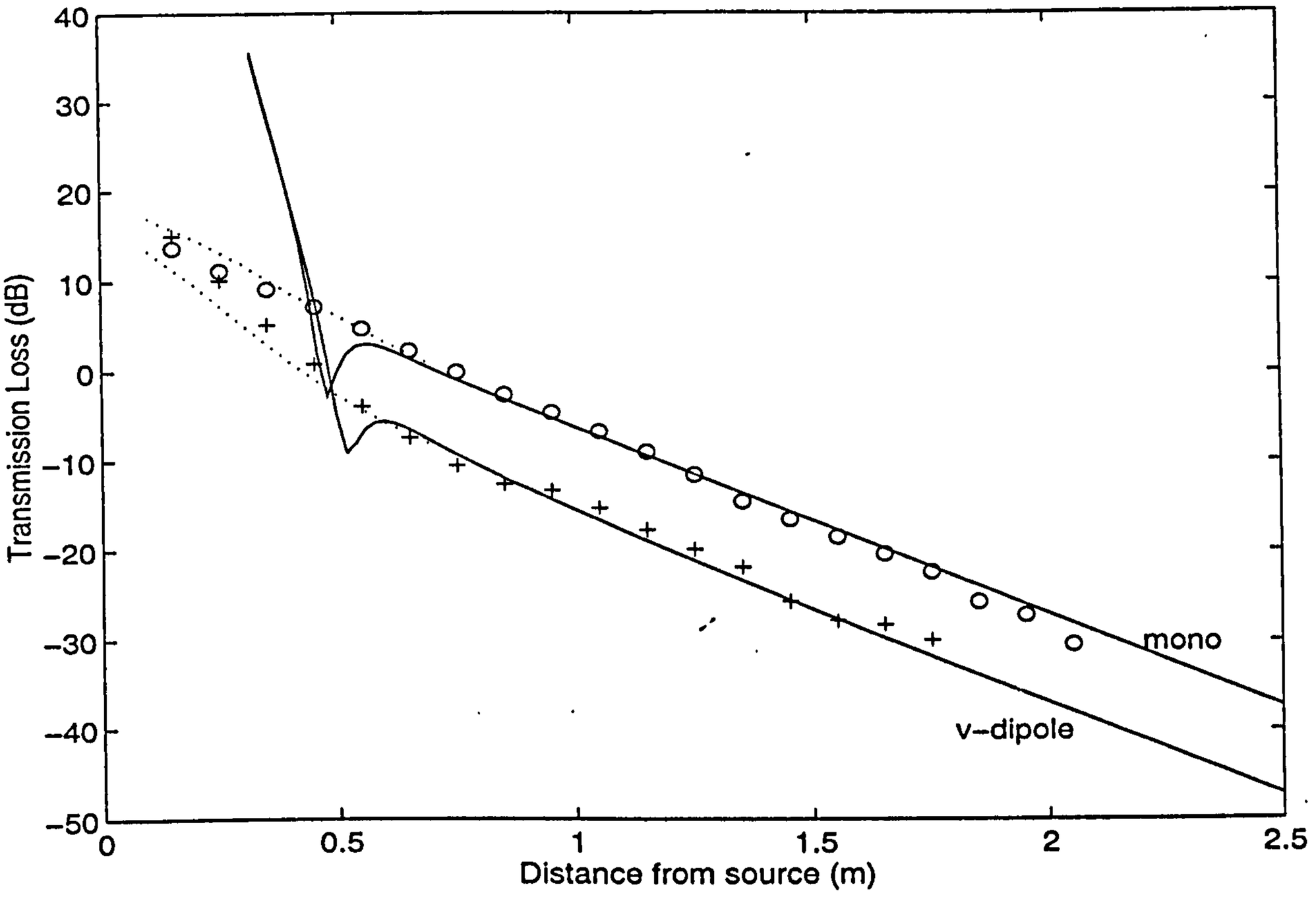

Figure 4.34 Same as **Figure 4.33**, but above a felt-covered surface.

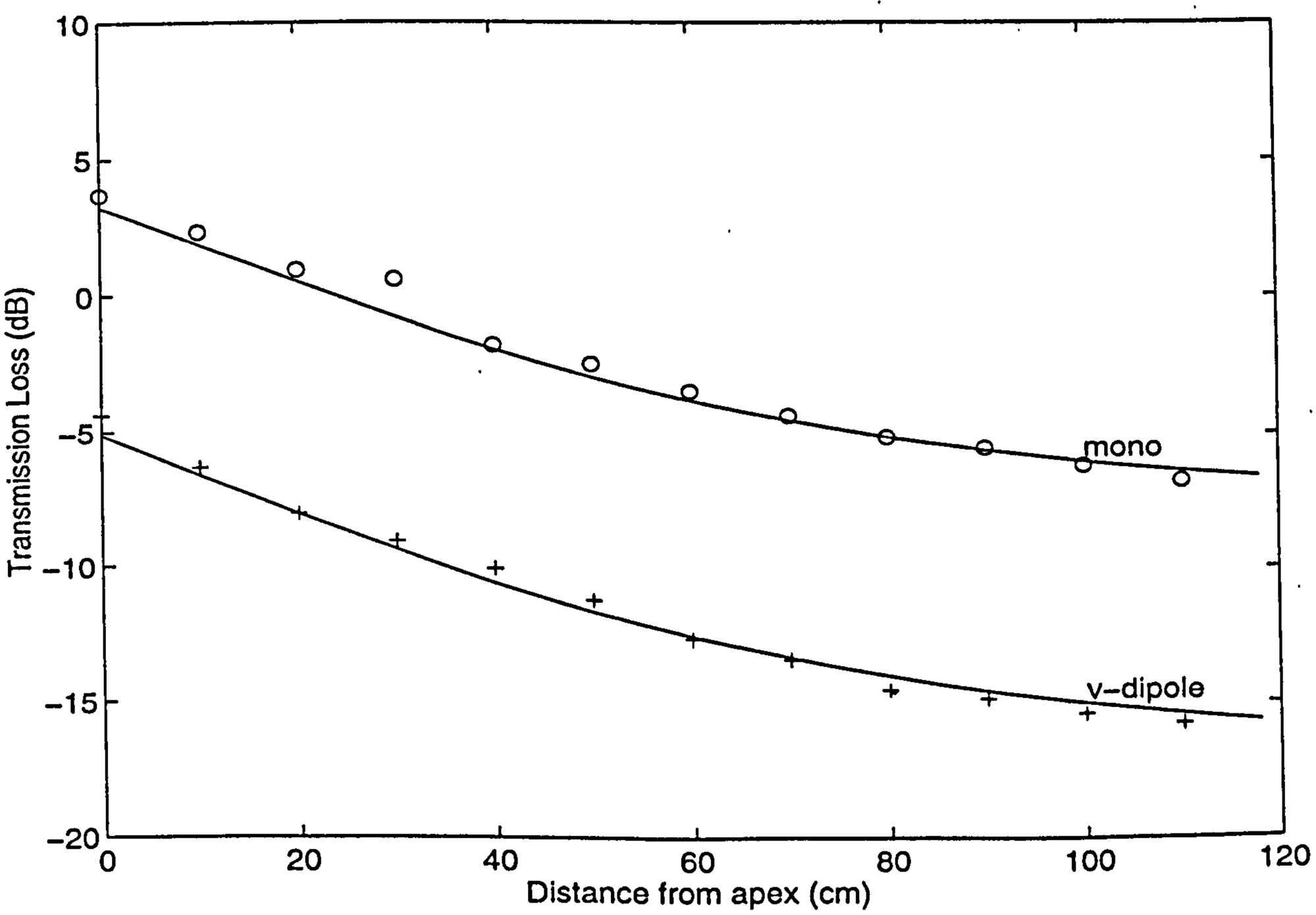

Figure 4.35 Same as **Figure 4.33**, but along the line of sight.

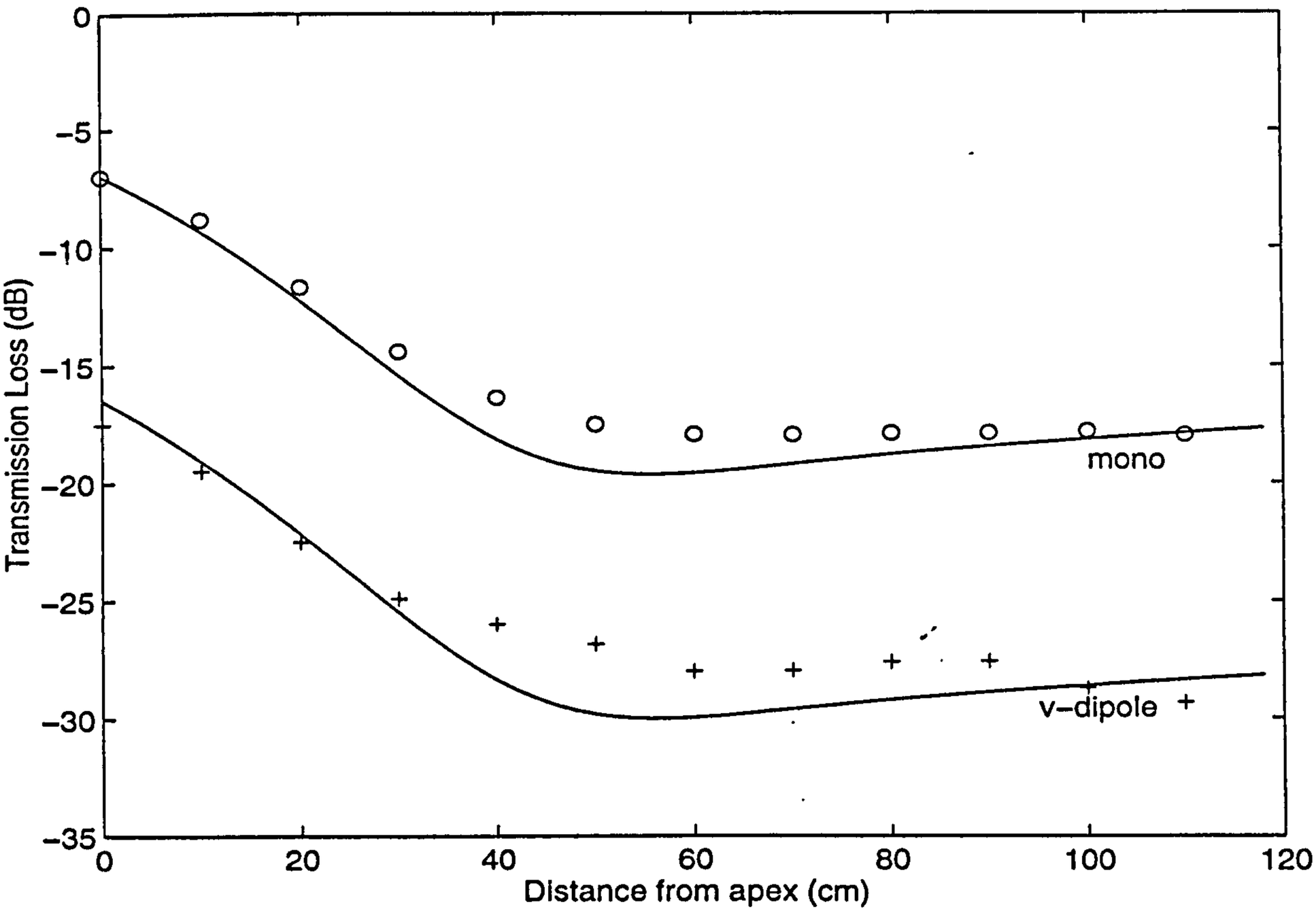

Figure 4.36 Same as **Figure 4.35**, but above a felt-covered surface.

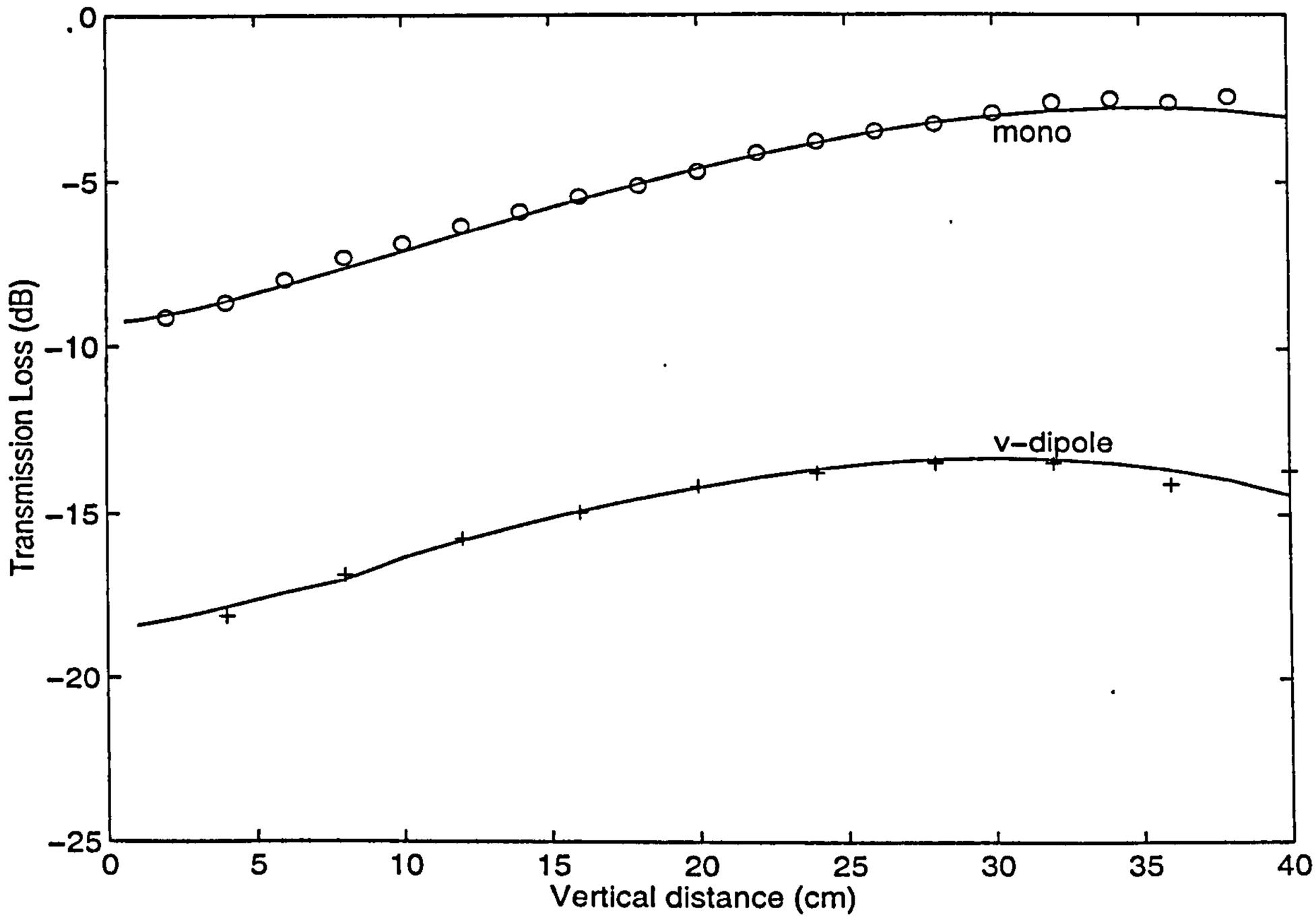

Figure 4.37 Same as **Figure 4.33**, but along a vertical distance z_v starting at $r_0 = 1.95$ m (*cf.* **Figure 4.5**).

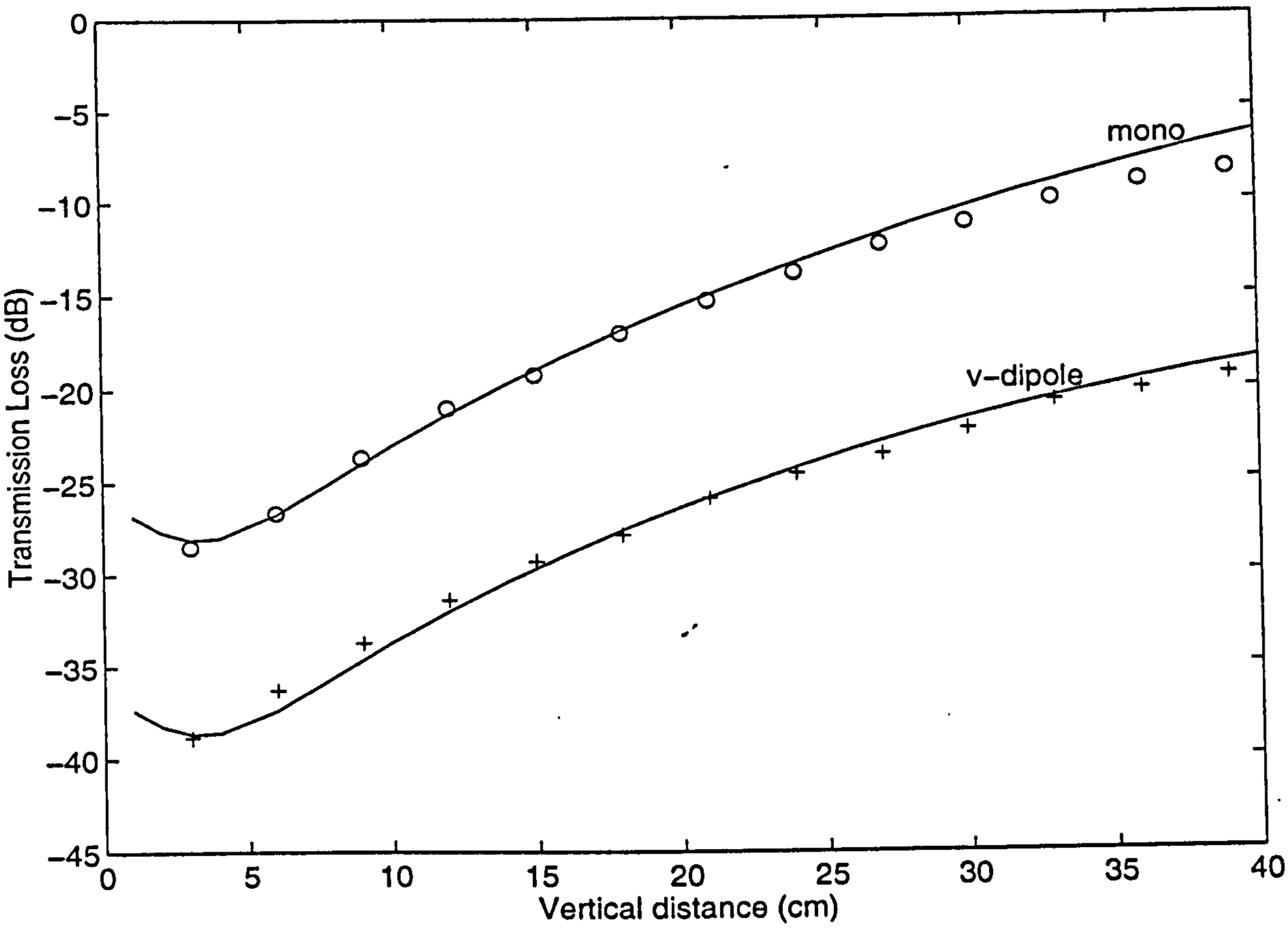

Figure 4.38 Same as **Figure 4.37**, but above a felt-covered surface.

4.5 Summary

Experimental investigations have been conducted indoors to validate the theoretical studies presented in the previous chapters. The experiments were carried out in an anechoic chamber above a rigid convex surface with and without a felt covering. The measurements have been made using a monopole source, a horizontal dipole source and a vertical dipole source above convex surfaces. The receiver has been moved along the curved surface, the line of sight and vertically across the shadow zone. In general, the experimental measurements agree well with the theoretical predictions.

In the vicinity of a source, predictions from the geometrical acoustics solution have shown good agreement with the measurements, whereas the residue series solution does not converge in this region. The geometrical acoustics solution agrees well with the residue series solution in the region where $z + z_s < r < \sqrt{2 z_s R_c}$. There is reasonably smooth

transition between these two solutions. In the insonified region well above the shadow boundary, the geometrical acoustics solution agrees well with the measurements, whereas the residue series solution requires many more terms to achieve convergence and shows significant discrepancies from the measurements.

A persistent discrepancy between predictions and experimental data has been found in the penumbra region along the line of sight above the felt-covered convex surface as the magnitude of q, the scaled and non-dimensionalized admittance, defined in Equation (2.2.6), is large. Although this discrepancy has been exhibited in a set of repeatable experimental results, there is yet no satisfactory explanation.

It has been shown that above a convex surface, the sound field of a horizontal dipole behaves like that of a monopole point source, and the sound field due to a vertical dipole is quite similar in range dependence to that due to a monopole point source, but at a more or less constant amplitude difference.

Chapter 5

Sound propagation over concave surfaces†

This chapter is concerned with the diffraction of sound by concave surfaces, which is analogous to sound propagation in downward refracting media.

The diffraction of sound by convex surfaces has been studied in great detail since the initial work of Fock [48] for electromagnetic waves and subsequent works in acoustics by Pierce [3] and others [15, 20]. However, much less work has been conducted on the diffraction by concave surfaces, and has been concerned only with monopole sources [32, 46]. Almgren [32] measured the sound field above a rigid concave curved surface. He reported that the measurements agree reasonably well with the sound fields calculated by using the theories of Pridmore-Brown [77, 117], Pierce [3], and Rasmussen [49] for propagation over a flat rigid ground in a downward refracting medium. He suggested that further work can be related to a finite impedance surface.

Gabillet *et al* [46] have conducted similar indoor experiments above a concave surface to simulate propagation under downward refraction over both rigid and finite impedance surfaces. The experimental results were compared to the Gaussian beam solution. They found that for propagation over a rigid concave surface, there was good agreement between theory and measurement only beyond 2000 Hz; for propagation over a concave surface of

† Parts of the work reported here have been published [152].

finite impedance, the agreement was only satisfactory for frequencies higher than 6000 Hz.

In this chapter, diffraction of sound by concave surfaces is investigated theoretically and experimentally for both monopole and dipole sources. The theories developed for the sound propagation in the presence of positive sound speed gradients due to temperature or wind velocity variations outlined in previous chapters are adapted to problems of diffraction of sound by concave surfaces in the absence of refraction. The residue series solution for sound propagation in an exponential sound speed profile, derived from the sound field diffracted by a cylindrical convex surface, is extended to enable calculation of the sound field diffracted by a cylindrical concave surface. Analytical expressions developed for a monopole source are used straightforwardly to predict the sound field for dipole sources. Measurement results using a point monopole source, a horizontal dipole source and a vertical dipole source over cylindrical concave surfaces are reported and compared with theoretical predictions.

5.1 The normal mode solution

It has been found [45] that the acoustic analogy described in Chapter 3 also exists between downwardly curving ray paths over flat ground and propagation over a concave surface in a neutral atmosphere. The analogy is illustrated in Figure 5.1. Almgren [32] has shown that it is valid to use a concave surface to simulate the effect of refraction due to a positive sound speed gradient on outdoor sound propagation.

Inversion of the B-D analogy (*cf.* Chapter 3) suggests that sound propagation above a cylindrical concave surface in a homogeneous medium with no refraction is analogous to the downwardly curving ray paths above a plane boundary due to a bilinear profile of sound speed. The sound speed profile is given by

$$c(z) = \frac{c_0}{\sqrt{1-2z/R_c}} \approx c_0\left(1+\frac{z}{R_c}-\frac{2z^2}{3R_c^2}+\cdots\right). \qquad (5.1.1)$$

Raspet *et al* [9] developed a normal mode solution for sound propagation in a downward refracting medium above a complex impedance ground surface. The solution was found when the sound speed variation with height was approximated by Equation (5.1.1). It may be expressed by

$$p^{(b)}(r,z) = \frac{i\pi}{l}\sum_n H_0^1(k_n,r)\frac{\mathrm{Ai}(\tau_n + z_s/l)\mathrm{Ai}(\tau_n + z/l)}{\left\{\tau_n\left[\mathrm{Ai}(\tau_n)\right]^2 - \left[\mathrm{Ai}'(\tau_n)\right]^2\right\}}, \qquad (5.1.2)$$

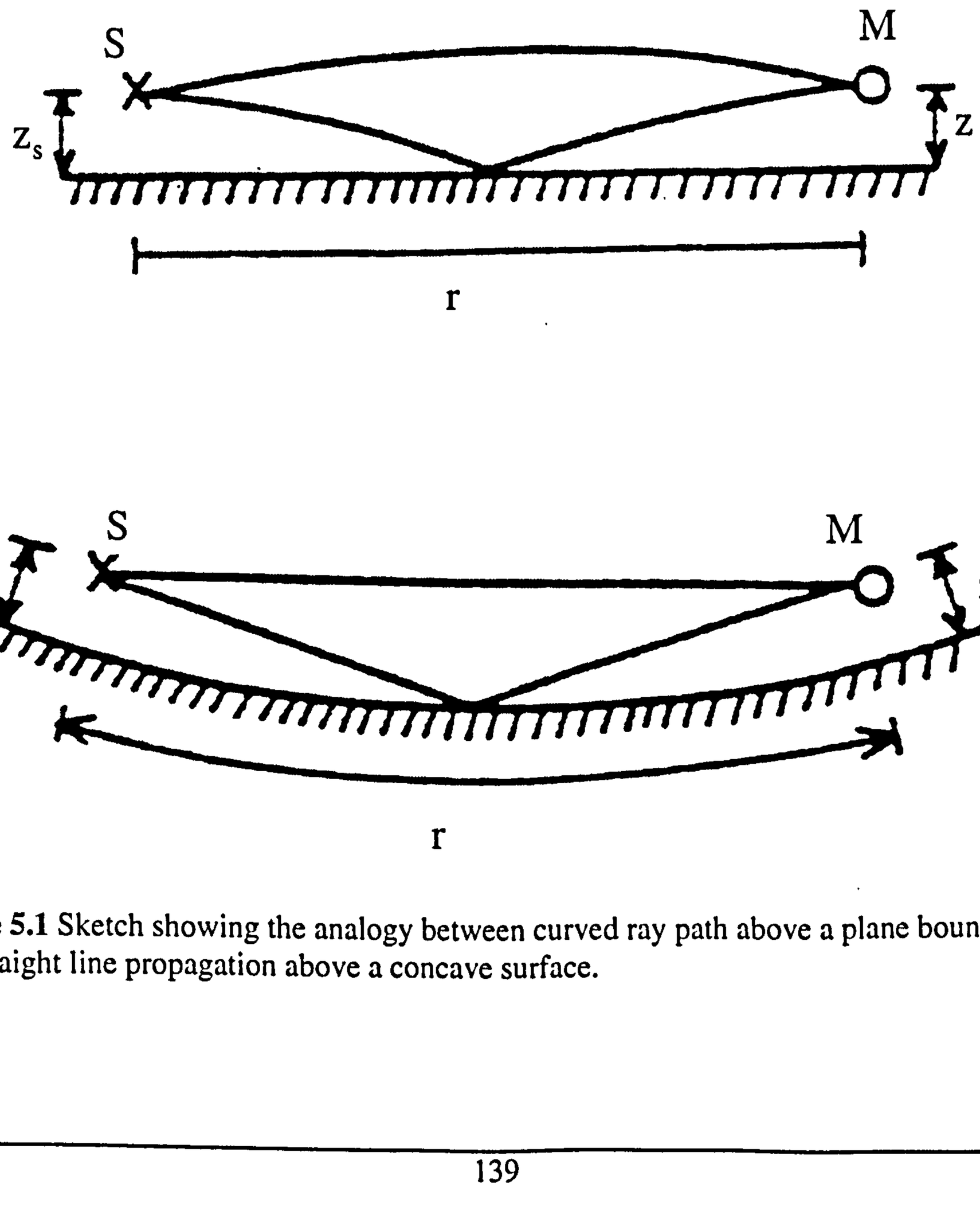

Figure 5.1 Sketch showing the analogy between curved ray path above a plane boundary and straight line propagation above a concave surface.

where τ_n are the zeros of

$$\mathrm{Ai}'(\tau_n)+q\mathrm{Ai}(\tau_n)=0\,. \tag{5.1.3}$$

For large arguments, the Hankel function in Equation (5.1.2) can be approximated by its asymptotic form and Equation (5.1.2) then becomes

$$p^{(b)}(r,z)=\frac{i\pi e^{-i\pi/4}}{l}\sum_n\sqrt{\frac{2}{\pi k_n r}}\frac{\mathrm{Ai}(\tau_n+z_s/l)\mathrm{Ai}(\tau_n+z/l)e^{ik_n r}}{\left\{\tau_n\left[\mathrm{Ai}(\tau_n)\right]^2-\left[\mathrm{Ai}'(\tau_n)\right]^2\right\}}, \tag{5.1.4}$$

which is identical to Equation (2.4.8).

Inversion of the D-G analogy and the associated conformal transformation (*cf.* Chapter 3) suggests that the residue series solution derived for the sound pressure behind a long cylinder can be developed for the sound pressure over a cylindrical concave surface. The solution is found in the form

$$p^{(c)}(r,\psi,z)=e^{i\pi/4}\sqrt{\frac{8\pi}{r}}\times$$

$$\sum_n\left[\frac{\bar{\xi}_s\bar{\xi}}{\bar{k}_z^2(z_s)\bar{k}_z^2(z)}\right]^{1/4}\frac{\sqrt{k_n}\,\mathrm{Ai}(-\bar{\xi}_s)\mathrm{Ai}(-\bar{\xi})e^{ik_n r}}{\frac{\partial\bar{\xi}_0}{\partial k_n}\left\{\left[\mathrm{Ai}'(\tau_n)\right]^2-\tau_n\left[\mathrm{Ai}(\tau_n)\right]^2\right\}+\frac{\partial q_n}{\partial k_n}\left[\mathrm{Ai}(\tau_n)\right]^2}, \tag{5.1.5}$$

when the sound speed variation with height is approximated by an exponential profile

$$c(z)=c_0\exp(z/R_c)\approx c_0\left(1+\frac{z}{R_c}-\frac{z^2}{2R_c^2}+\cdots\right), \tag{5.1.6}$$

where $\tau_n=-\bar{\xi}_0$ are the zeros of Equation (5.1.3), and

$$\bar{k}_z(z)=+\sqrt{\left(k_0^2-k_n^2\sin^2\psi\right)\exp(-2z/R_c)-k_n^2\cos^2\psi}\,. \tag{5.1.7}$$

In Equation (5.1.5) the variables $\bar{\xi}(z)$, $\bar{\xi}_0$ and $\partial\bar{\xi}_0/\partial k_n$ are the same as in the case of convex surface, and they have been defined in Equations (3.3.6) to (3.3.8). The values of τ_n, q_n and k_n can be determined using the numerical method described in Chapter 2.3.2.

5.2 Theoretical comparisons

In this section the validity of the normal mode solution for an exponential profile is investigated by means of numerical comparisons. Two frequencies 2915 Hz and 4350 Hz, at which experiments have been made, are presented for the numerical comparisons.

5.2.1 Comparison of predictions of the normal mode solution and the fast field program

The normal mode solution for an exponential profile should agree with the fast field program (FFP) [10] solution for the same sound speed gradient. In particular the fast field program and the normal mode predictions for transmission loss versus the distance from source are compared. Figure 5.2 shows the results of the normal mode calculation (solid lines) compared with the FFP calculation (circles) for the sound speed profile varying exponentially with height. In Figure 5.2(a), the propagation above the felt-covered concave surface was predicted at a frequency of 2915 Hz in a gradient with $R_c = 2.5$ m when the gradient was truncated at 1.24 m altitude [*cf.* Equation (2.3.10)]. A good approximation for the truncated gradient may be obtained by using 14 modes. This number of modes is the so-called full solution that can be determined from Equation (2.3.9). The complex impedance surface was calculated using Equation (2.5.15), *i.e.* Attenborough's two-parameter model with $\sigma_e = 38$ kPa s m^{-2} and $\alpha_e = 15$ m^{-1}. The chosen parameters (R_c, σ_e and α_e reflect the radius and the impedance of the curved surfaces used in our subsequent laboratory measurements. The source height was 0.1 m, and the receiver height was 0.15 m. Figures 5.2(b) and 5.2(c) show the comparison for the propagation due to a horizontal dipole source and a vertical dipole source respectively. The agreement between the two numerical schemes for monopole and horizontal dipole sources is excellent.

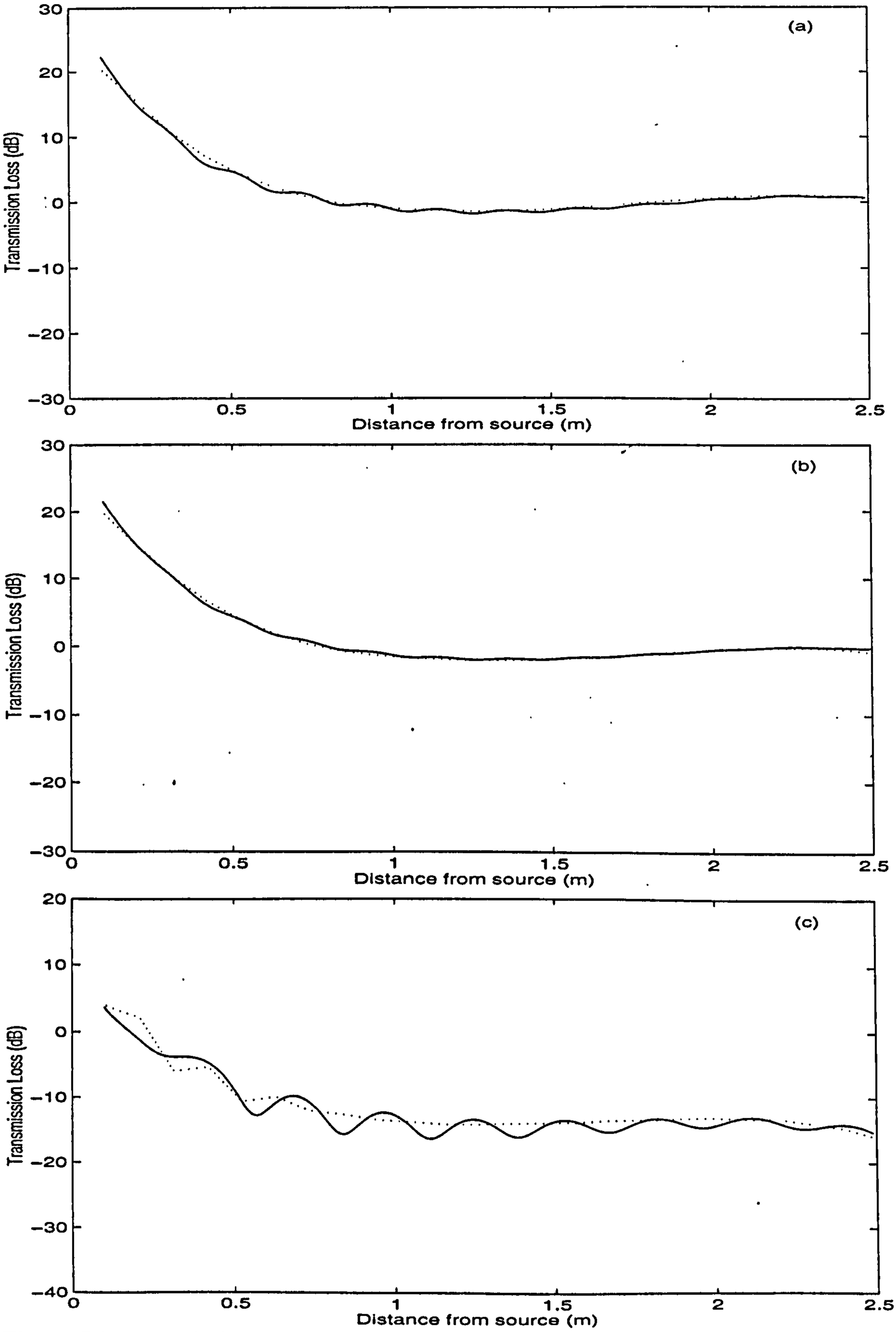

Figure 5.2 Transmission loss predicted over a felt-covered concave surface with $R_c = 2.5$ m and $z_s = z = 0.10$ m at a frequency of 2915 Hz. Dotted curves: FFP calculations and solid curves: the normal mode calculations for exponential profiles for (a) monopole, (b) horizontal dipole and (c) vertical dipole sources.

However, for the vertical dipole source, the agreement between the FFP and the normal predictions is less satisfactory. There are considerable oscillations in the magnitudes of the TL for the normal mode predictions. This is largely due to the fact that the contribution due to a branch-line integral, which is beyond the scope of the present study, has been ignored in the normal mode solution [153]. The inadequacy of the approximation is only apparent for the case of a vertical dipole because the solution involves the spatial differentiation with respect to the vertical height. In view of the acoustic analogy, the normal mode solution may be used to predict the sound propagation above a curved surface in an exponential sound speed profile.

5.2.2 Comparison of the normal mode predictions for two profiles

In this section, typical comparisons of the normal mode predictions between bilinear and exponential profiles are displayed. Figure 5.3 shows the predictions above the felt-covered concave surface in a gradient with $R_c = 2.5$ m, at frequencies of (a) 2915 and (b) 4350 Hz, for both profiles. The solid curves were calculated from Equation (5.1.5), while the dotted curves were calculated from Equation (5.1.4). The source and receiver heights were 0.10 and 0.02 m, respectively.

If the vertical plane that intercepts the source and receiver is rotated through an angle, ψ (*cf.* Figure 3.6), with respect to the circumference of the concave cylinder, prediction of the normal mode solution for an exponential profile can be calculated using Equation (5.1.5) straightforwardly. For the inversion of the B-D analogy, the radius of curvature R_c will be replaced by the effective radius defined in Equation (3.3.9).

Figure 5.4 shows similar predictions to Figure 5.3 with $\psi = \pi/4$ instead of $\psi = 0$ for both profiles. In this figure, the effective radius of curvature increases up to 5.0 m. With a

weaker gradient, the two profiles show closer sound speed variations with height, the differences between the two profiles become smaller.

Over a rigid concave surface, the differences are similar to those over the felt-covered concave surface. Figure 5.5 shows the predictions for both profiles over a rigid surface with the source and receiver heights of 0.05 and 0.02 m respectively.

It is noted that the calculations for an exponential profile and a bilinear profile are similar only at short ranges. The differences between the two profiles appear larger at long ranges. To examine the validity of the calculations for both profiles over a cylindrical concave surface, the normal mode solutions will be compared to the boundary element method calculation in the next section.

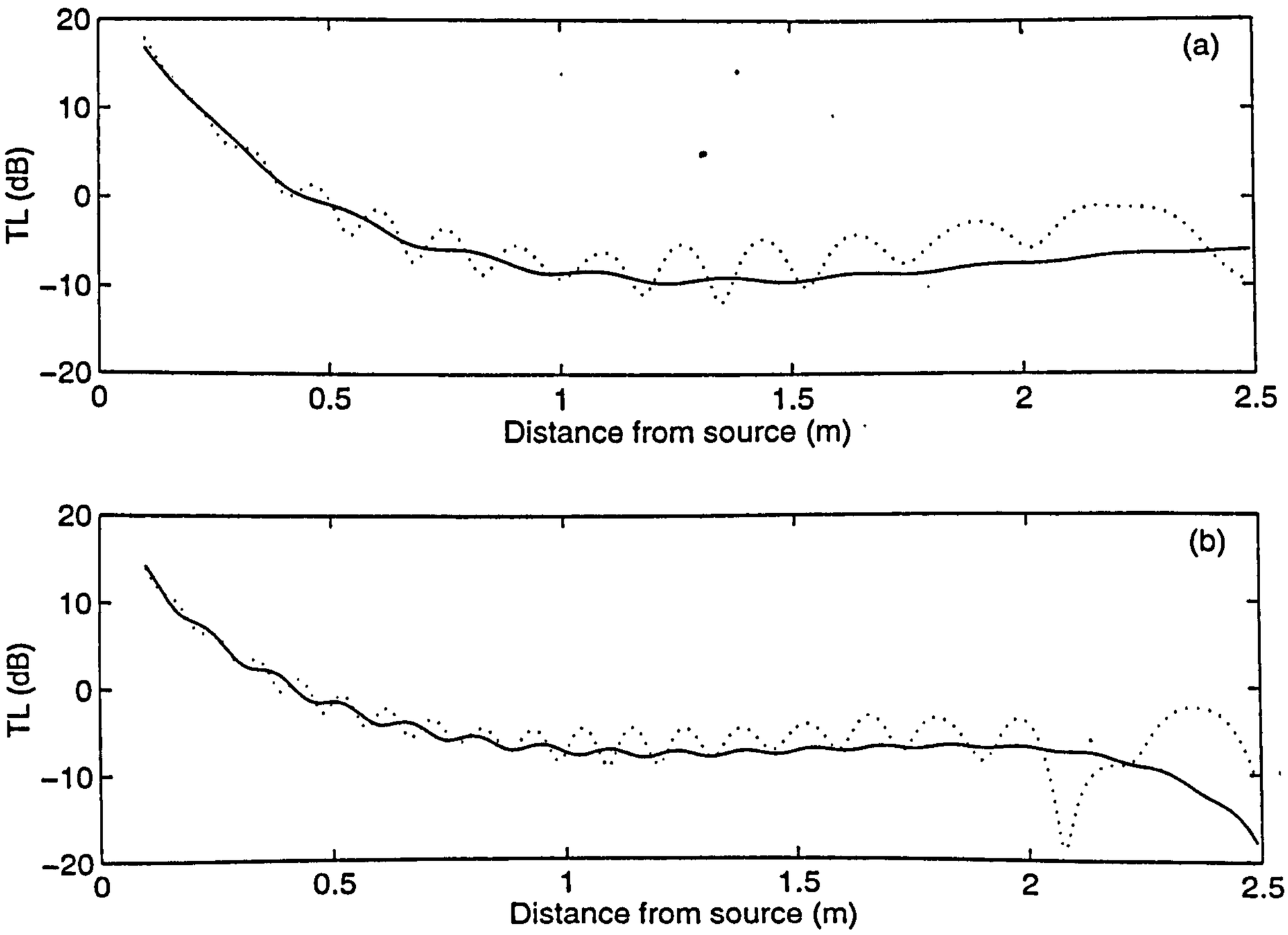

Figure 5.3 Transmission loss predicted over a felt-covered concave surface with $R_c = 2.5$ m, $z_s = 0.10$ m and $z = 0.02$ m, at frequencies of (a) 2915 Hz and (b) 4350 Hz. Solid curves: the normal mode calculations for exponential profiles, dotted curves: for bilinear profiles.

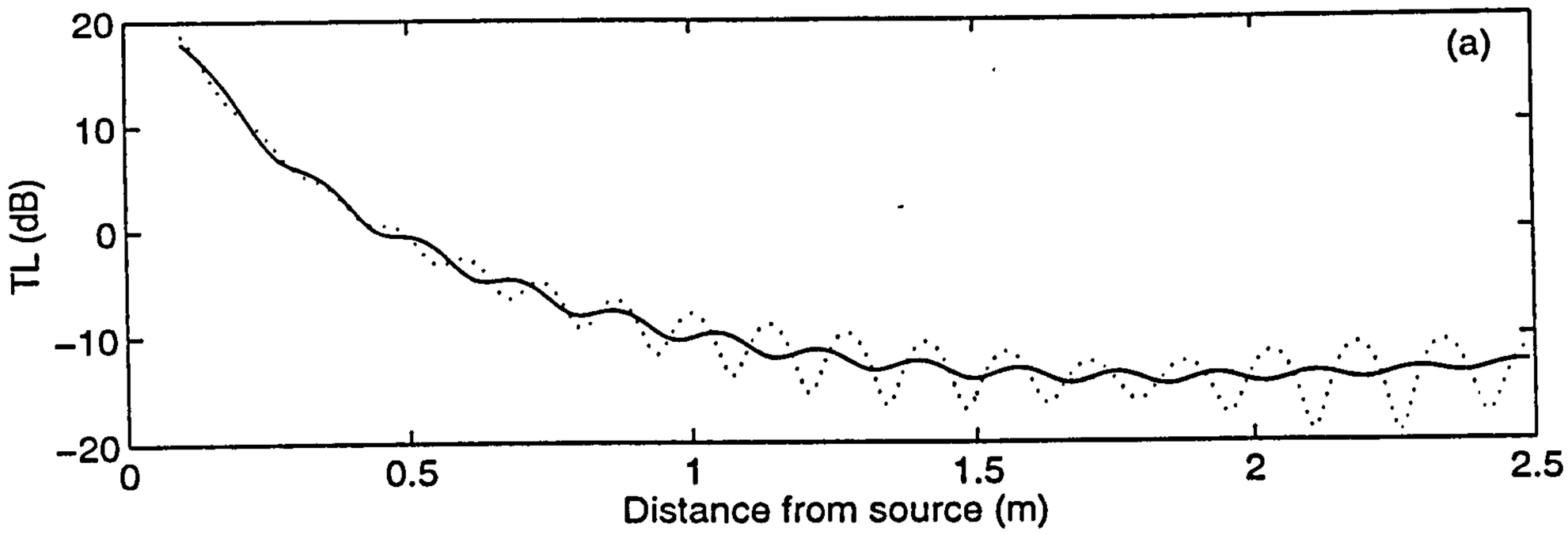

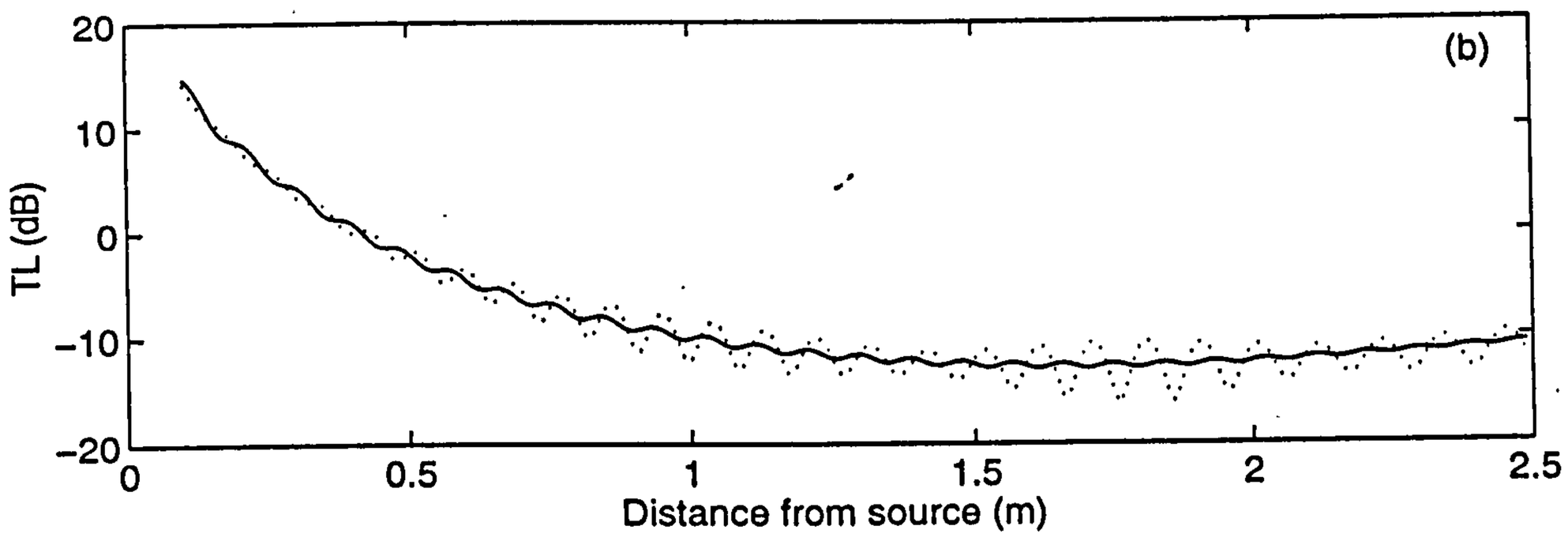

Figure 5.4 Same as **Figure 5.3**, but $\psi = \pi/4$.

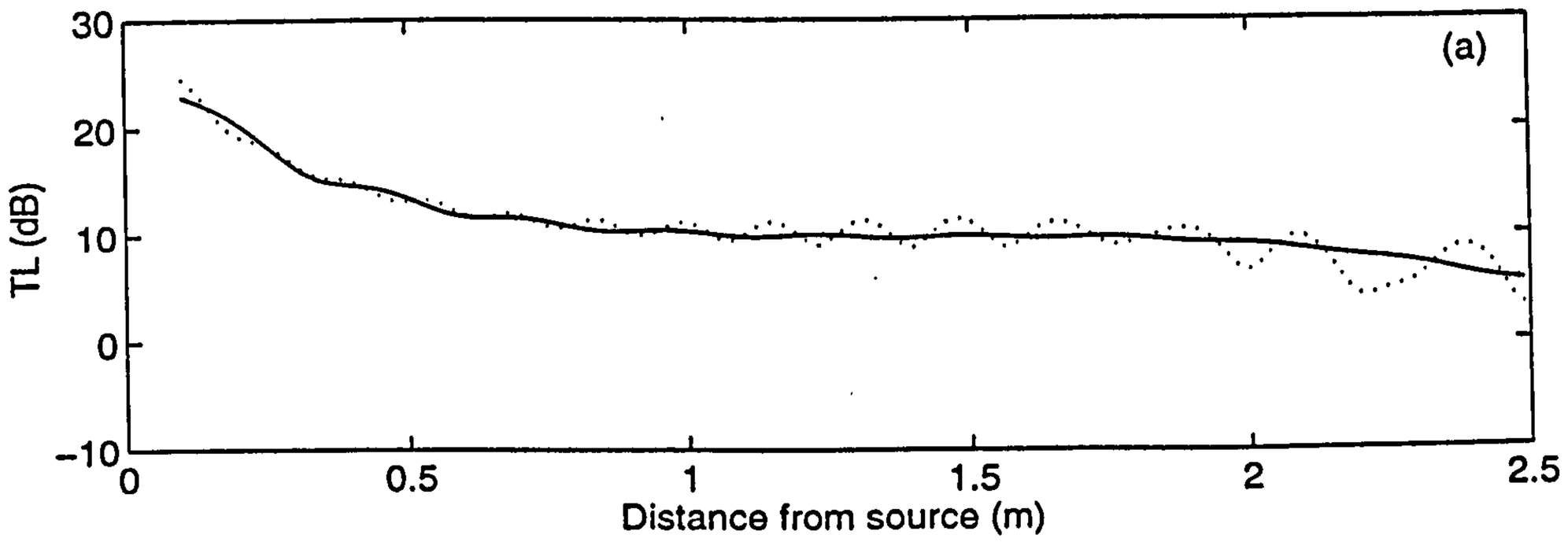

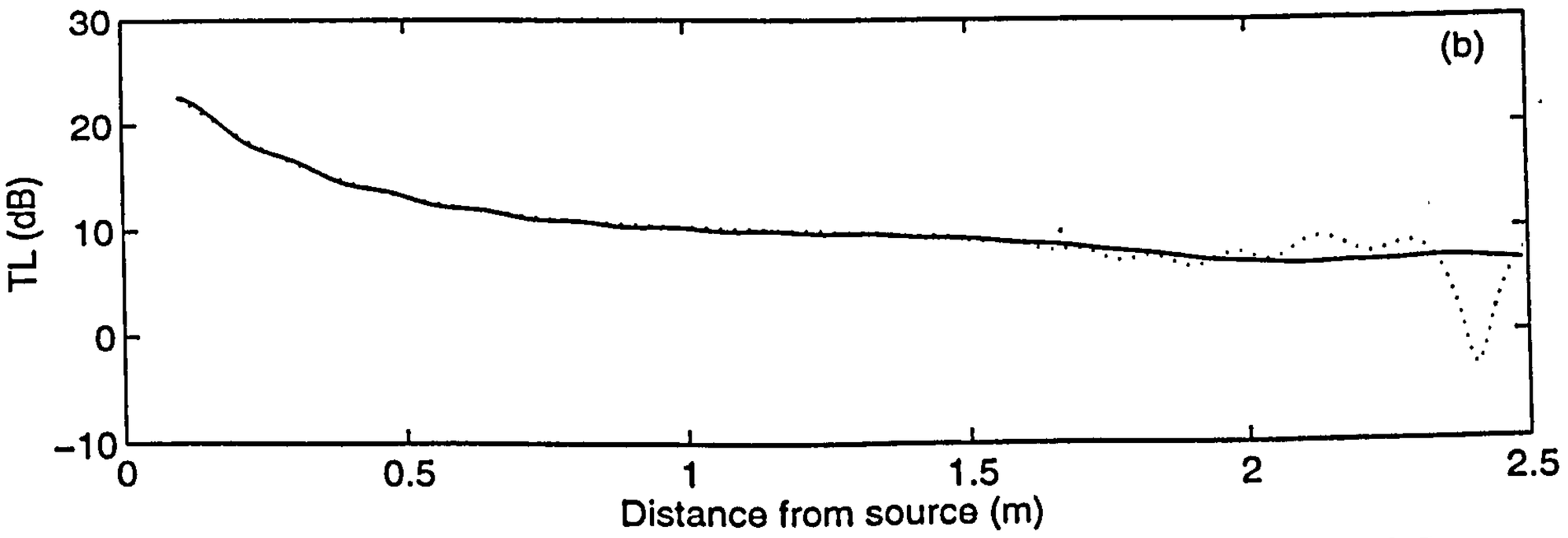

Figure 5.5 Transmission loss predicted over a rigid concave surface with $R_c = 2.5$ m, $z_s = 0.05$ m and $z = 0.02$ m, at frequencies of (a) 2915 Hz and (b) 4350 Hz. Solid curves: calculations for exponential profiles, dotted curves: for bilinear profiles.

5.2.3 Comparison with the boundary element method

It is possible to model sound propagation over a cylindrical concave surface by the boundary element method (BEM) [24]. Using the boundary element method, the cross section of the cylindrical concave surface is modelled as a series of adjacent elements with impedance surfaces. The normal mode predictions for both exponential and bilinear profiles are further compared with the BEM prediction over concave surfaces in a gradient with $R_c = 2.5$ m. Figure 5.6 shows two typical examples of prediction over (a) the felt-covered surface and (b), a rigid surface. The solid lines represent the predictions for the exponential profile, while the dotted lines represent those for the bilinear profile. The circles represent the calculations from the BEM.

There are considerable discrepancies between the normal mode predictions for the bilinear profile and predictions calculated from the BEM, especially at longer ranges. At short ranges, the discrepancies are small except for oscillations in magnitude. As the receiver is moved away from the source, the differences become greater.

Contrary to the bilinear sound speed profile, the normal mode predictions for the exponential profile accord generally with the boundary element method calculations over the concave surfaces. This implies that the equivalent sound speed increases exponentially rather than bilinearly with height over a cylindrical concave surface. This implication is in agreement with the conclusion obtained in the case of a cylindrical convex surface. In a later section, the data extracted from measurements over cylindrical concave surfaces will be compared with the normal mode predictions for both sound speed profiles to test the performance of the theoretical models.

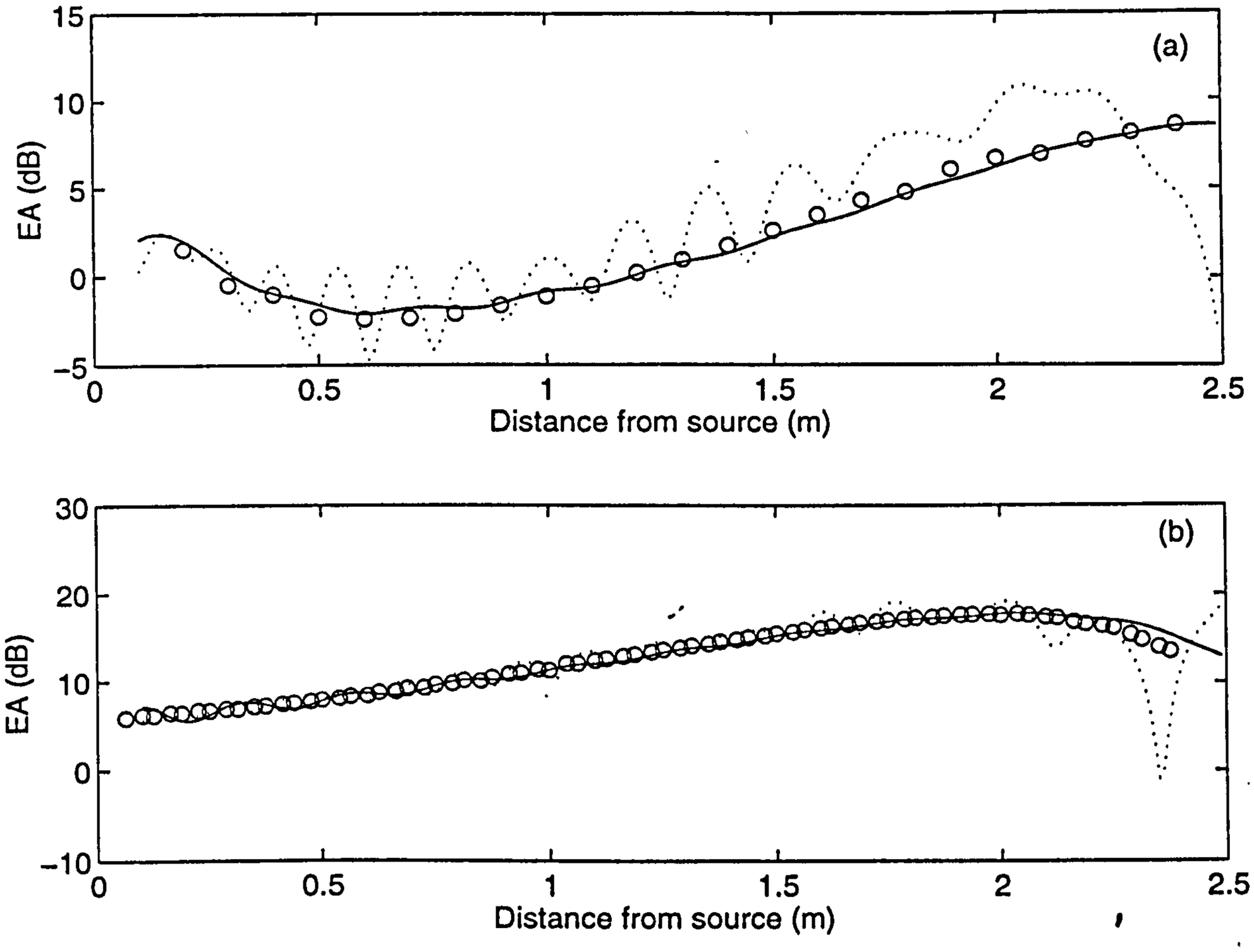

Figure 5.6 Excess attenuation predicted at a frequency of 2915 Hz in a gradient with $R_c = 2.5$ m, (a) over the felt-covered concave surface with $z_s = z = 0.10$ m and (b) over a rigid surface with $z_s = 0.02$ m, $z \sim 0.00$ m. Circles: BEM calculations, solid curves: the normal mode calculations for exponential profiles, dotted curves: the normal mode calculations for bilinear profiles.

5.3 The normal mode solution for a dipole source

Substituting Equation (2.4.8) into Equation (3.9.1), the normal mode solution for a bilinear profile can be extended for an arbitrarily oriented dipole source over a concave surface, *i.e.*

$$p_d^{(b)}(r,\psi_r,z) = p_h^{(b)}(r,\psi_r,z) + p_v^{(b)}(r,\psi_r,z), \tag{5.3.1}$$

where $p_h^{(b)}$ and $p_v^{(b)}$ are, respectively, the horizontal component and the vertical component of a dipole, and the superscript (b) denotes the sound field due to a bilinear sound speed profile (*cf.* Chapter 2). They are determined according to

$$p_h^{(b)}(r,\psi_r,z) \approx \frac{e^{i\pi/4}}{l}\sqrt{\frac{\pi}{2r^3}}S_d \sin\gamma_d \cos(\psi_d - \psi_r)$$

$$\times\sum_n \frac{(2ik_n - 1)\mathrm{Ai}(-\bar{\xi}_s)\mathrm{Ai}(-\bar{\xi})e^{ik_n r}}{\sqrt{k_n}\left\{\tau_n\left[\mathrm{Ai}(\tau_n)\right]^2 - \left[\mathrm{Ai}'(\tau_n)\right]^2\right\}}, \qquad (5.3.2)$$

and

$$p_v^{(b)}(r,\psi_r,z) \approx \frac{\pi e^{i\pi/4}}{l^2} S_d \cos\gamma_d$$

$$\times\sum_n \sqrt{\frac{2}{\pi k_n r}} \frac{\mathrm{Ai}'(-\bar{\xi}_s)\mathrm{Ai}(-\bar{\xi})e^{ik_n r}}{\left\{\tau_n\left[\mathrm{Ai}(\tau_n)\right]^2 - \left[\mathrm{Ai}'(\tau_n)\right]^2\right\}}. \qquad (5.3.3)$$

The normal mode solution for an exponential profile for an arbitrarily oriented dipole source may be expressed by

$$p_d^{(c)} = p_h^{(c)} + p_v^{(c)}, \qquad (5.3.4)$$

where the superscript (c) denotes the sound field above a cylindrical curved surface, and

$$p_h^{(c)} \approx e^{i\pi/4} S_d \sin\gamma_d \cos(\psi_d - \psi_r)\sqrt{\frac{2\pi}{r^3}}$$

$$\times\sum_n \left[\frac{\bar{\xi}_s\bar{\xi}}{\bar{k}_z^2(z_s)\bar{k}_z^2(z)}\right]^{1/4} \frac{(2ik_n - 1)\sqrt{k_n}\mathrm{Ai}(-\bar{\xi}_s)\mathrm{Ai}(-\bar{\xi})e^{ik_n r}}{\frac{\partial\bar{\xi}_0}{\partial k_n}\left\{\left[\mathrm{Ai}'(\tau_n)\right]^2 - \tau_n\left[\mathrm{Ai}(\tau_n)\right]^2\right\} + \frac{\partial q_n}{\partial k_n}\left[\mathrm{Ai}(\tau_n)\right]^2}, \qquad (5.3.5)$$

and

$$p_v^{(c)} \approx e^{i\pi/4} S_d \cos\gamma_d \sqrt{\frac{8\pi}{r}}$$

$$\times\sum_n \left[\frac{\bar{k}_z^2(z_s)\bar{\xi}}{\bar{k}_z^2(z)\bar{\xi}_s}\right]^{1/4} \frac{\sqrt{k_n}\mathrm{Ai}'(-\bar{\xi}_s)\mathrm{Ai}(-\bar{\xi})e^{ik_n r}}{\frac{\partial\bar{\xi}_0}{\partial k_n}\left\{\left[\mathrm{Ai}'(\tau_n)\right]^2 - \tau_n\left[\mathrm{Ai}(\tau_n)\right]^2\right\} + \frac{\partial q_n}{\partial k_n}\left[\mathrm{Ai}(\tau_n)\right]^2}. \qquad (5.3.6)$$

The poles for dipole sources are the same as those for a monopole source and are described by Equation (5.1.3).

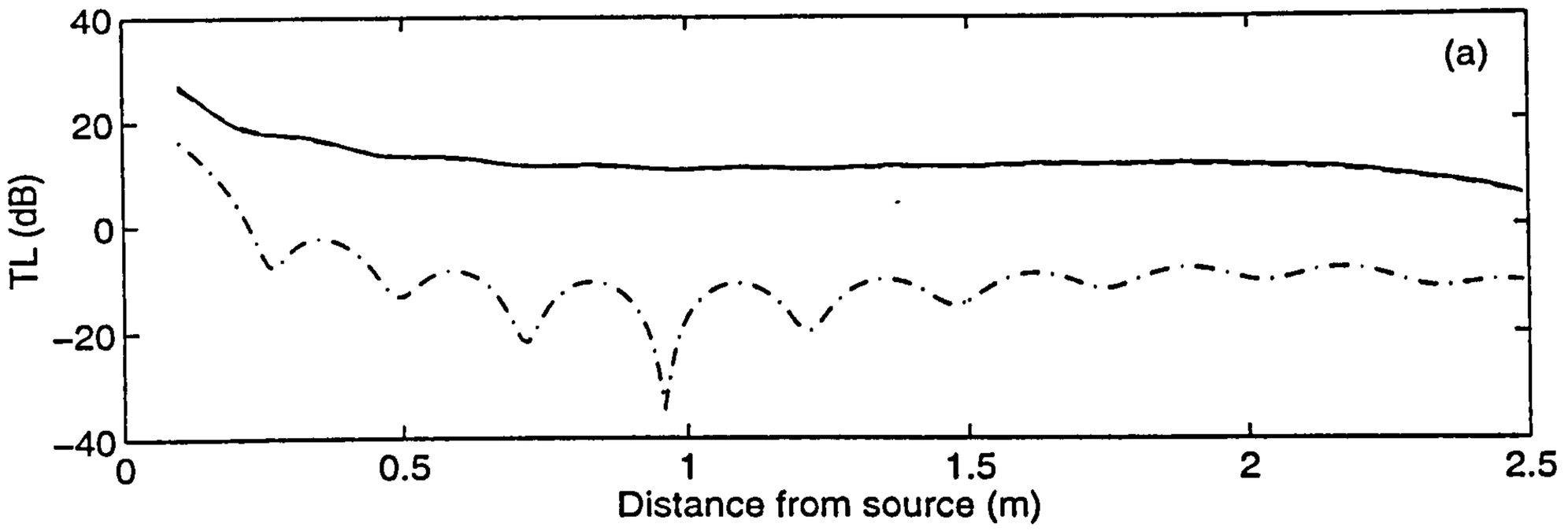

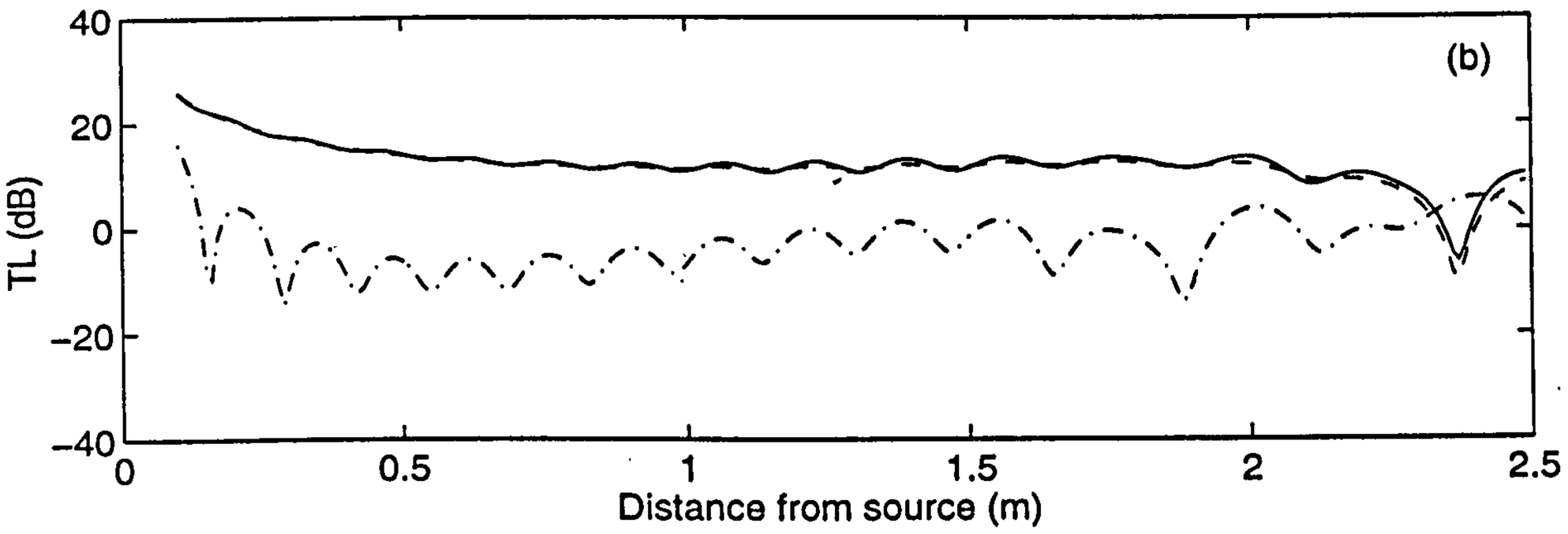

Figure 5.7 Transmission loss due to a monopole source (solid lines), a horizontal dipole source (dashed lines) and a vertical dipole source (dashdot lines) predicted at 2915 Hz, over a rigid concave surface with $R_c = 2.5$ m, $z_s = 0.02$ m and $z \sim 0.00$ m, for (a) an exponential profile and (b) a bilinear profile.

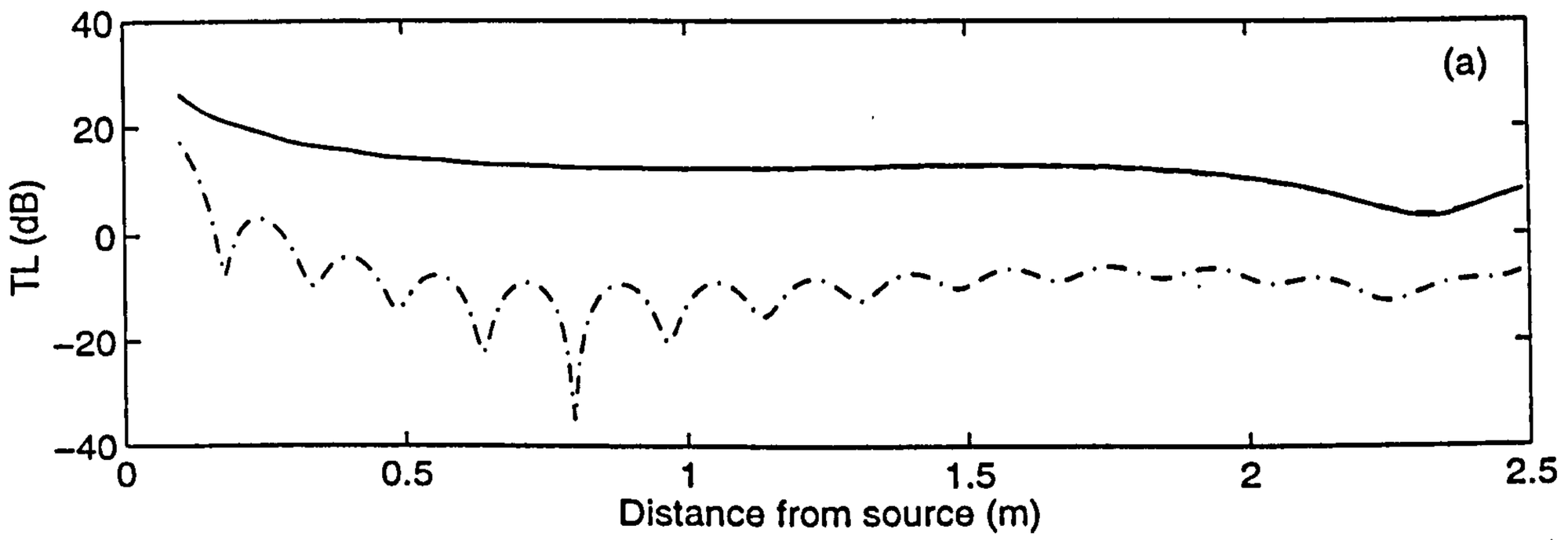

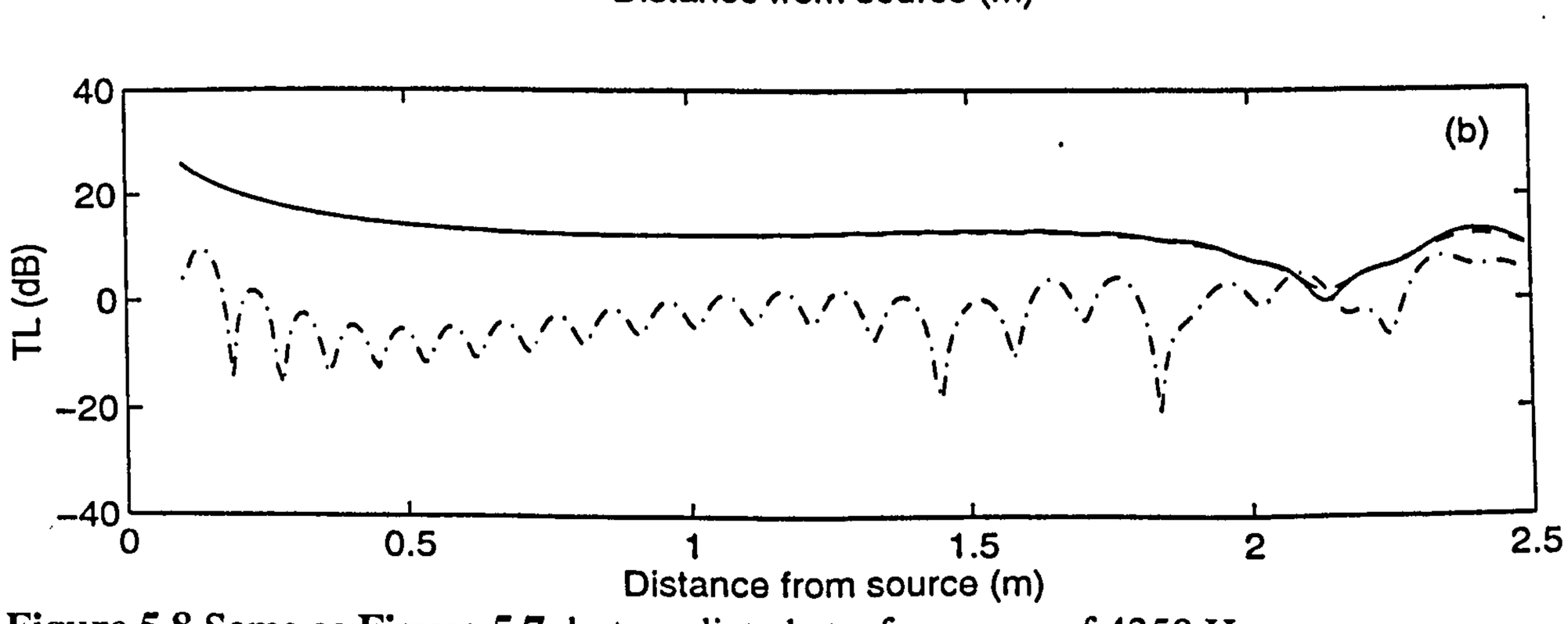

Figure 5.8 Same as **Figure 5.7**, but predicted at a frequency of 4350 Hz.

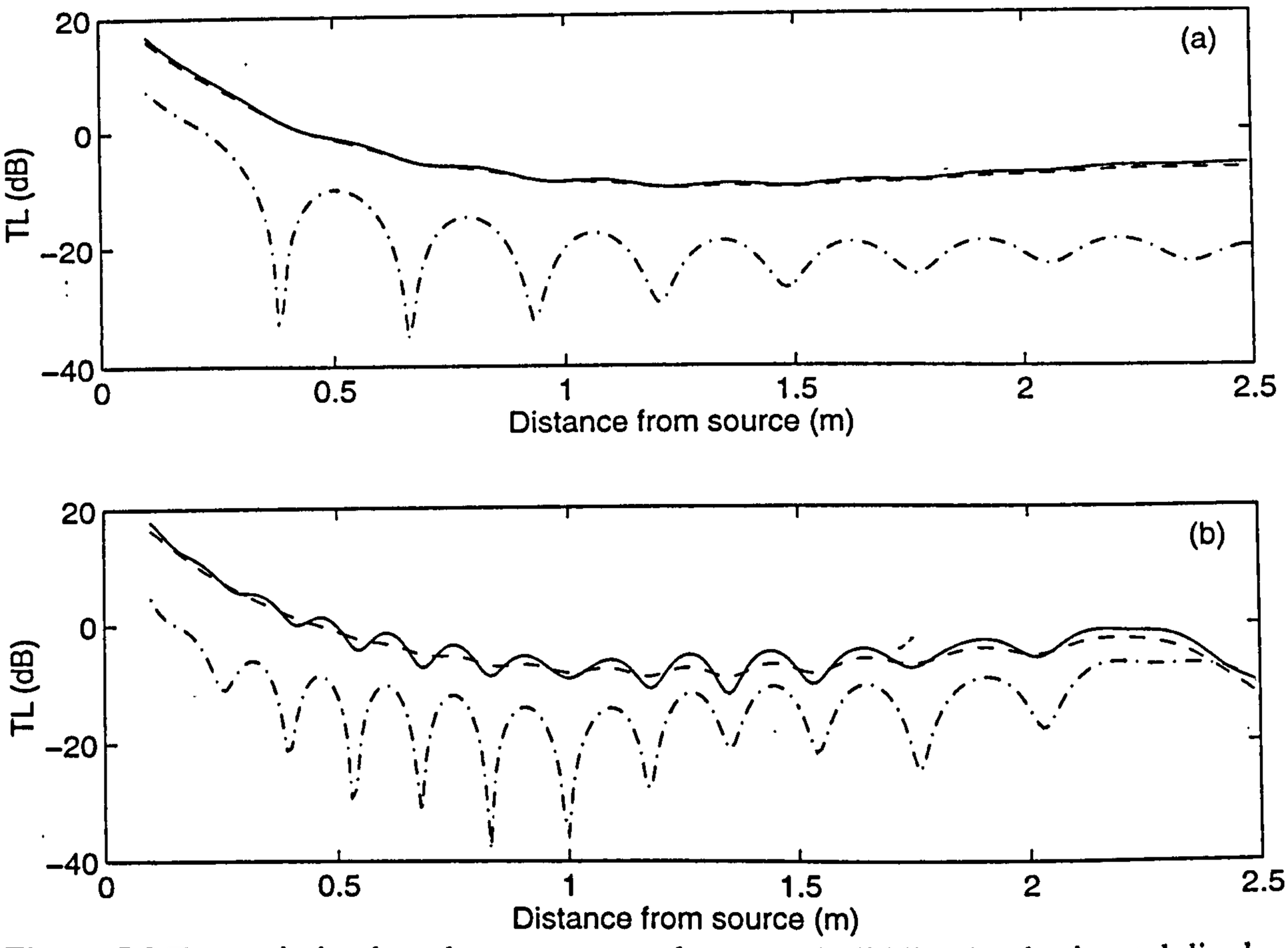

Figure 5.9 Transmission loss due to a monopole source (solid lines), a horizontal dipole source (dashed lines), and a vertical dipole source (dashdot lines) predicted at 2915 Hz, over a felt-covered concave surface with $R_c = 2.5$ m, $z_s = 0.10$ m and $z = 0.02$ m, for (a) an exponential profile and (b) a bilinear profile.

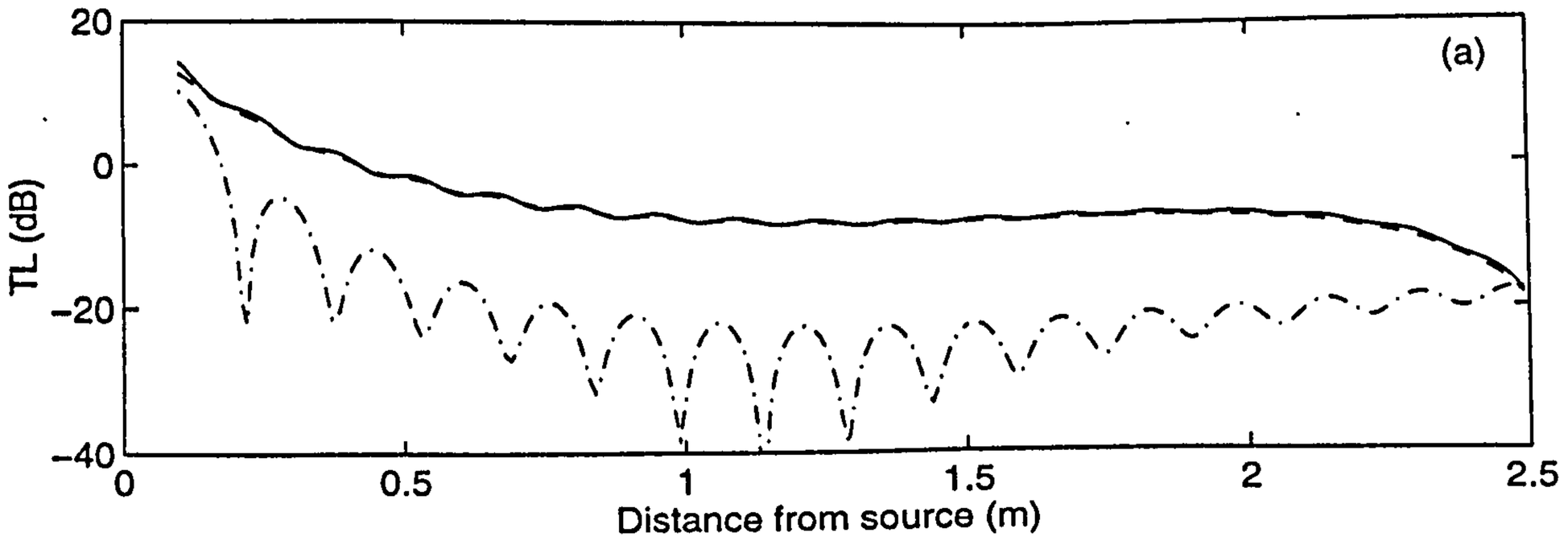

Figure 5.10 Same as **Figure 5.9**, but predicted at a frequency of 4350 Hz.

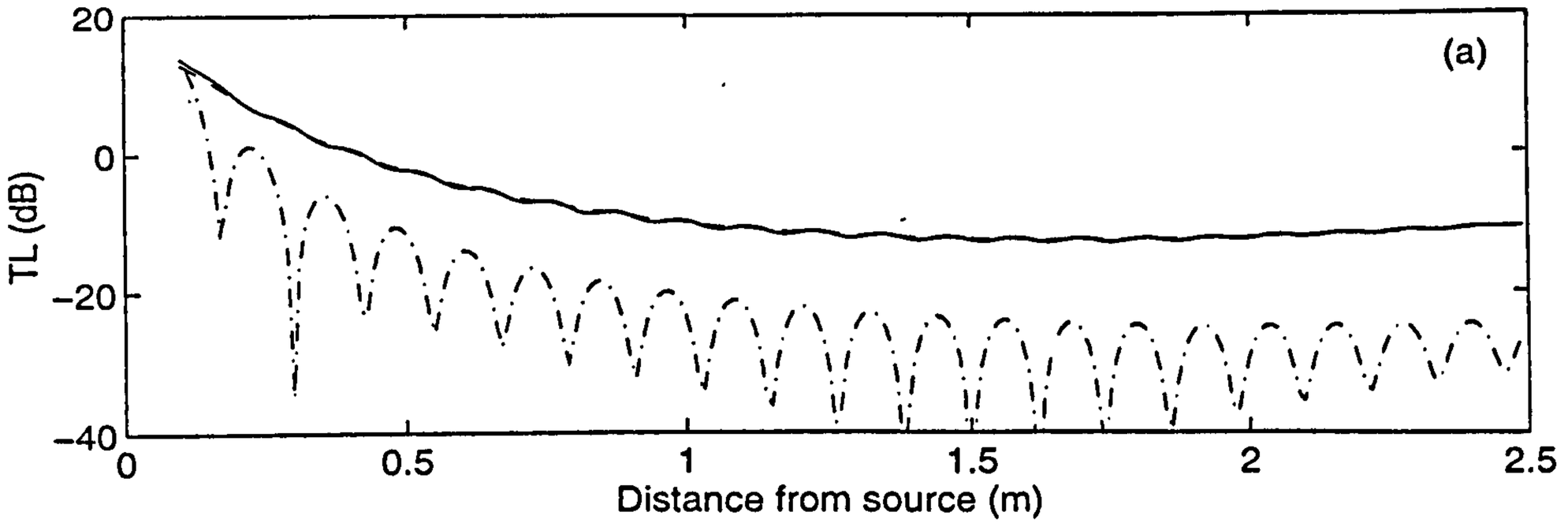

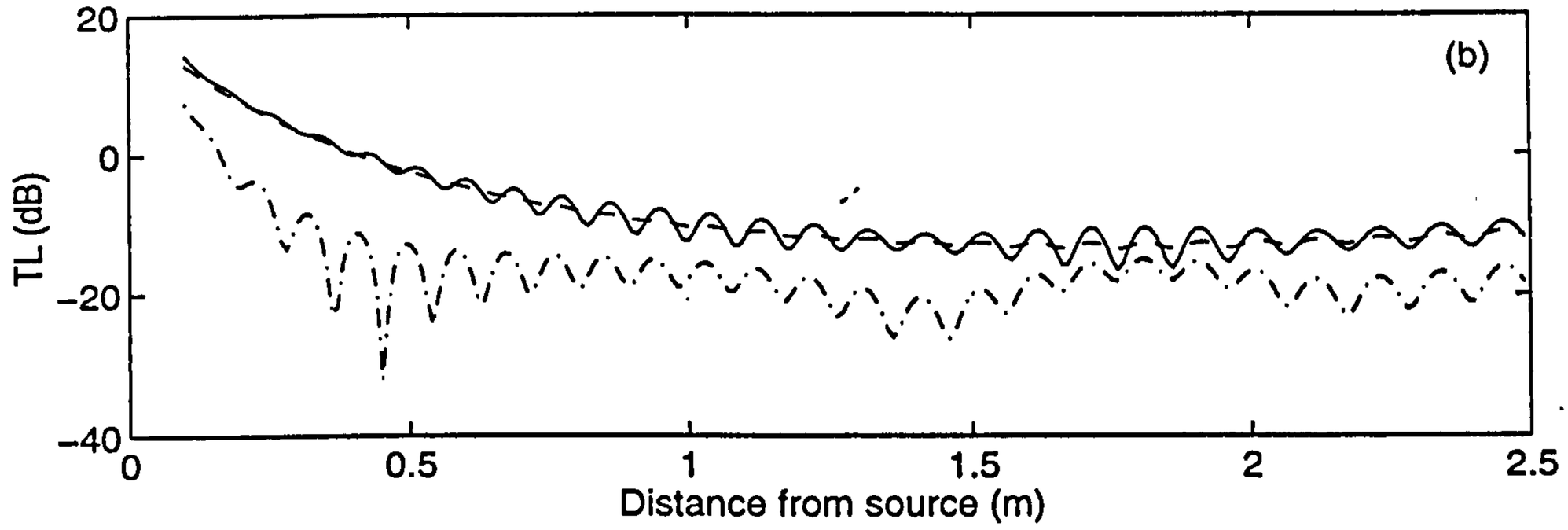

Figure 5.11 Same as **Figure 5.10**, but $\psi = \pi/4$.

It can be demonstrated that, over a concave surface, the variation of transmission loss with range, due to a horizontal dipole source is similar to that due to a monopole source, but the sound field due to a vertical dipole is quite different from that due to a monopole. Figures 5.7 to 5.11 show the calculated range dependence of the sound fields of a monopole source (solid lines), a horizontal dipole source (dashed lines) and a vertical dipole source (dashdot lines) for (a) exponential profiles and (b) bilinear profiles. The curves shown in Figures 5.7 and 5.8 are predicted for a rigid concave surface with $R_c = 2.5$ m, $z_s = 0.02$ m, and $z \sim 0.00$ m and for frequencies of 2915 and 4350 Hz, respectively. Figures 5.9 and 5.10 show the predictions for the felt-covered concave surface with $R_c = 2.5$ m, $z_s = 0.10$ m and $z = 0.02$ m and for frequencies of 2915 and 4350 Hz, respectively. Figure 5.11 shows similar predictions to those of Figure 5.10 but $\psi = \pi/4$ instead $\psi = 0$ (*cf.* Figure 3.6). It is seen that there are clear differences between the predictions for these two profiles for both monopole and dipole sources.

5.4 Experimental investigations

This section is devoted to measurements of the sound field over concave surfaces. The experimental data is analyzed and compared to predictions of the normal mode solutions for both an exponential profile [Equation (5.1.5)] and a bilinear profile [Equation (5.1.4)].

5.4.1 Measurement techniques

The measurement techniques for investigations of the sound fields over concave surfaces are similar to those used above convex surfaces and reported in Chapter 4. The concave surfaces were constructed to behave either as rigid surfaces or as surfaces of finite impedance. The rigid concave surface was constructed by attaching sheets of masonite to a series of curved ribbed structures, as shown in Figure A-6. The resulting surface was that of a long cylinder with a radius of curvature 2.5 m. It was built to have a centerline of 2.5 m with a span of 1.8 m and a depth of 0.45 m. To ensure that the surface acted as a rigid reflector, particular care was paid in fastening the masonite sheets to the structures. To obtain a surface of finite impedance, felt was secured to the rigid surface using double sided tape to eliminate the possible transmission path between the sheets and the felt, see Figure A-7. The surfaces allow sound propagation distances of up to 2.5 m. Propagation above this concave surface simulates propagation in the presence of a positive constant sound speed gradient with $R_c = 2.5$ m.

Measurements were made separately with the source and receiver in the plane transverse to the centerline of the concave surfaces, *i.e.* $\psi = 0$, and in the plane rotated by an angle, $\psi = \pi/4$ (*cf.* Figure 3.6), with respect to the circumference of the surfaces.

5.4.2 The sound field due to a monopole source over concave surfaces

Gabillet *et al* [46] reported that there are up to 5 dB discrepancies between the calculations from the Gaussian beam solution and the measurements obtained from a monopole source above a concave surface of finite impedance below a frequency of 6000 Hz. They found good agreement between predictions and measurements above a rigid concave surface only for frequencies higher than 2000 Hz. To investigate this problem, a series of laboratory measurements have been conducted, using a point monopole source, above both rigid and felt-covered concave surfaces.

The circles in Figures 5.12(a) and (b) represent measurements for frequencies of 2915 and 4350 Hz, respectively, with the receiver moved along the rigid surface ($z \sim 0.00$ m) and the source at a height of 0.02 m. The solid curves represent predictions of the normal mode solution for the exponential profile, while the dotted curves represent predictions for the bilinear profile. The agreement between the circles and the two curves is excellent out to 2.0 m from the source. Beyond this distance, there is no data.

The circles in Figures 5.13(a) and (b) represent measurements at 2915 and 4350 Hz, respectively, over the felt-covered concave surface with both the source and receiver at heights of 0.10 m. Good agreement is found between measurements and predictions for the exponential profile (solid curves). However, there are considerable discrepancies between the measured data and the calculations for the bilinear profile (dotted curves) at longer ranges.

The circles in Figures 5.14(a) and (b) represent measurements at 2915 and 4350 Hz, respectively, with the source and receiver in the plane $\psi = \pi/4$, over the felt-covered surface. The source height was 0.10 m and the receiver height was 0.02 m. The predictions

for both profiles agree with the measurements except that there are oscillations in the magnitude of the predictions for the bilinear profiles.

It is found that the predictions given by Equation (5.1.5) for the exponential profiles agree with the experimental results obtained over the cylindrical concave surfaces. The agreement is better than that with the predictions given by Equation (5.1.4) for the bilinear profiles. This accords with the conclusion from the sound field refracted by an exponential sound speed profile that is analogous to propagation over cylindrical convex surfaces.

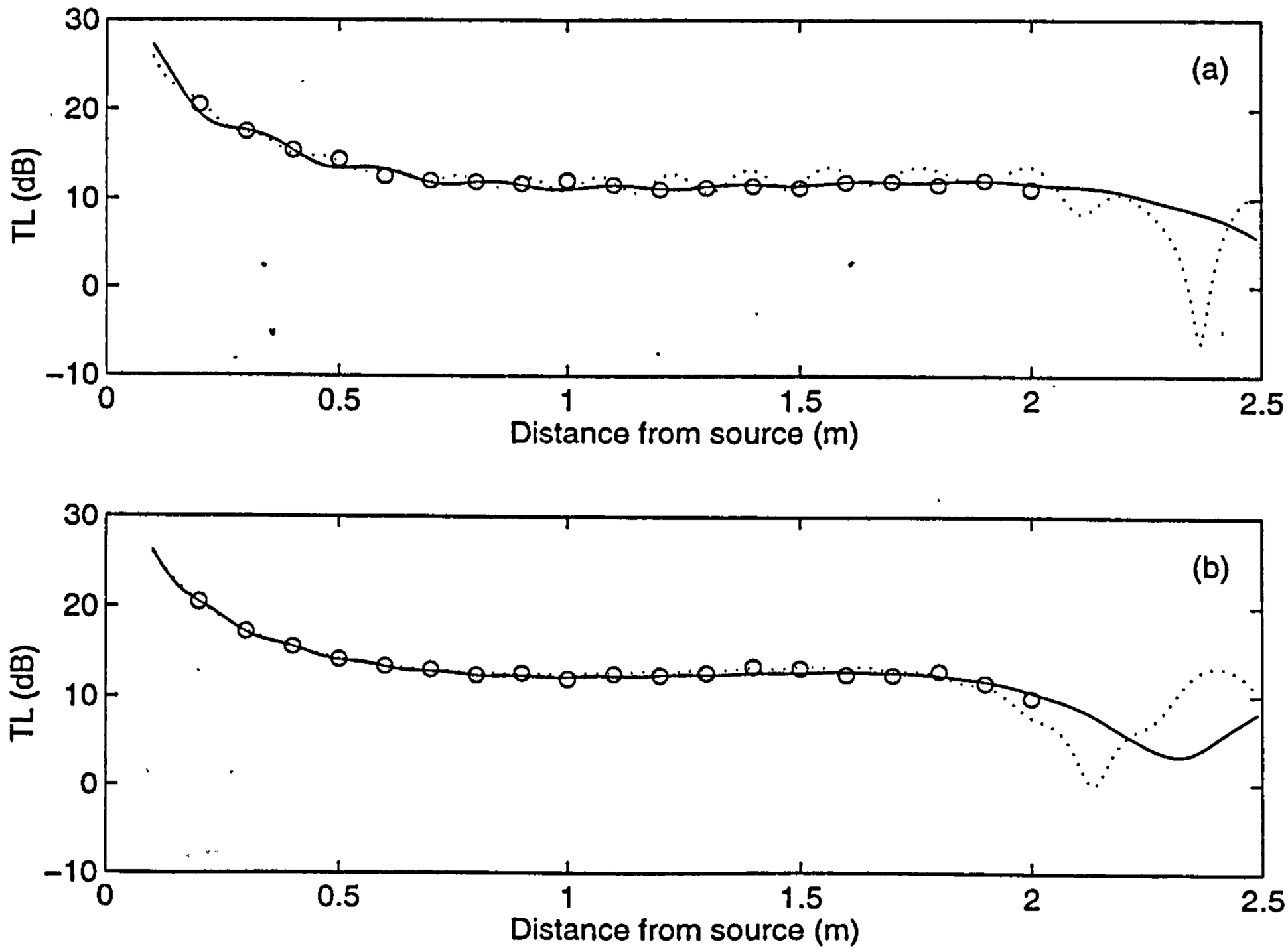

Figure 5.12 Transmission loss due to a monopole source obtained over a rigid concave surface with $R_c = 2.5$ m, $z_s = 0.02$ m and $z \sim 0.00$ m, at frequencies of (a) 2915 Hz and (b) 4350 Hz. Circles: measurements, solid curves: predictions for exponential profiles, dotted curves: predictions for bilinear profiles.

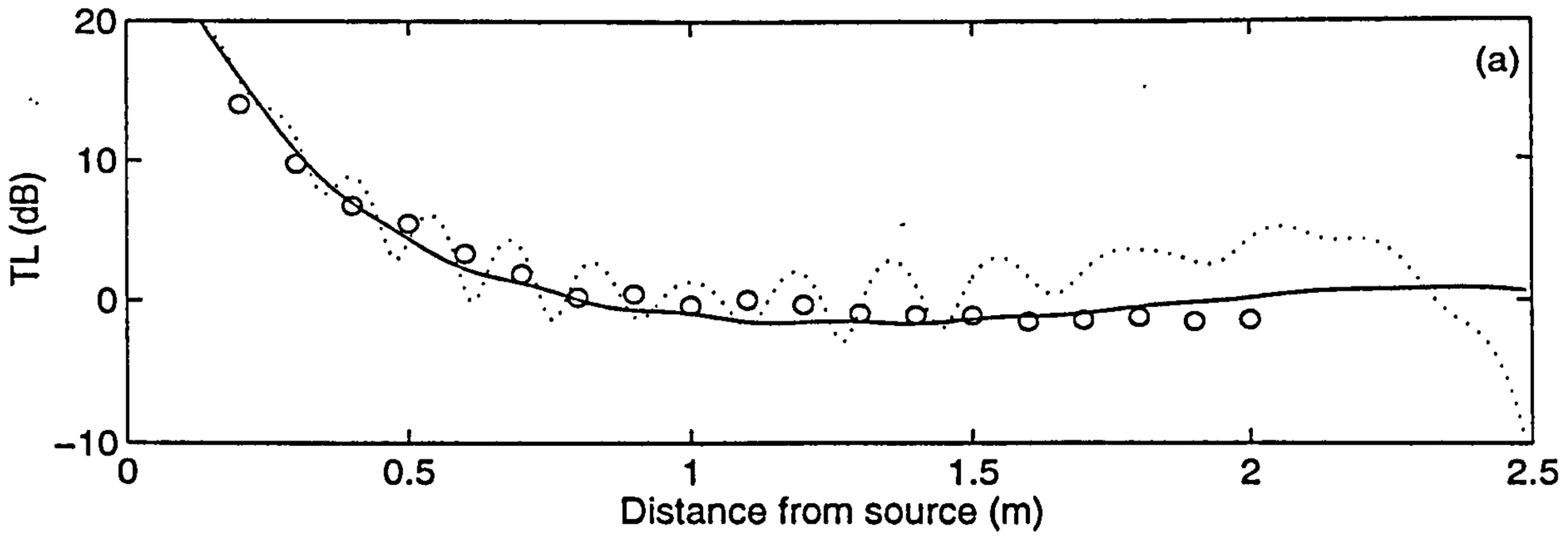

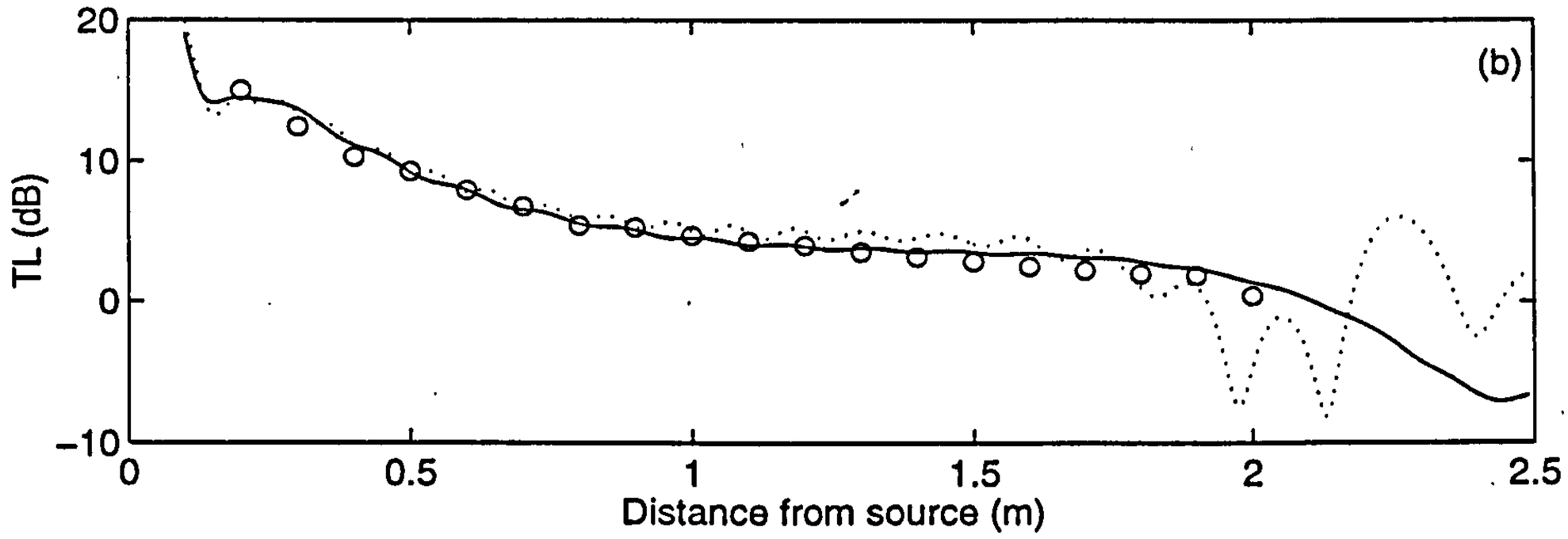

Figure 5.13 Same as **Figure 5.12,** but over a felt-covered concave surface with $z_s = z = 0.10$ m.

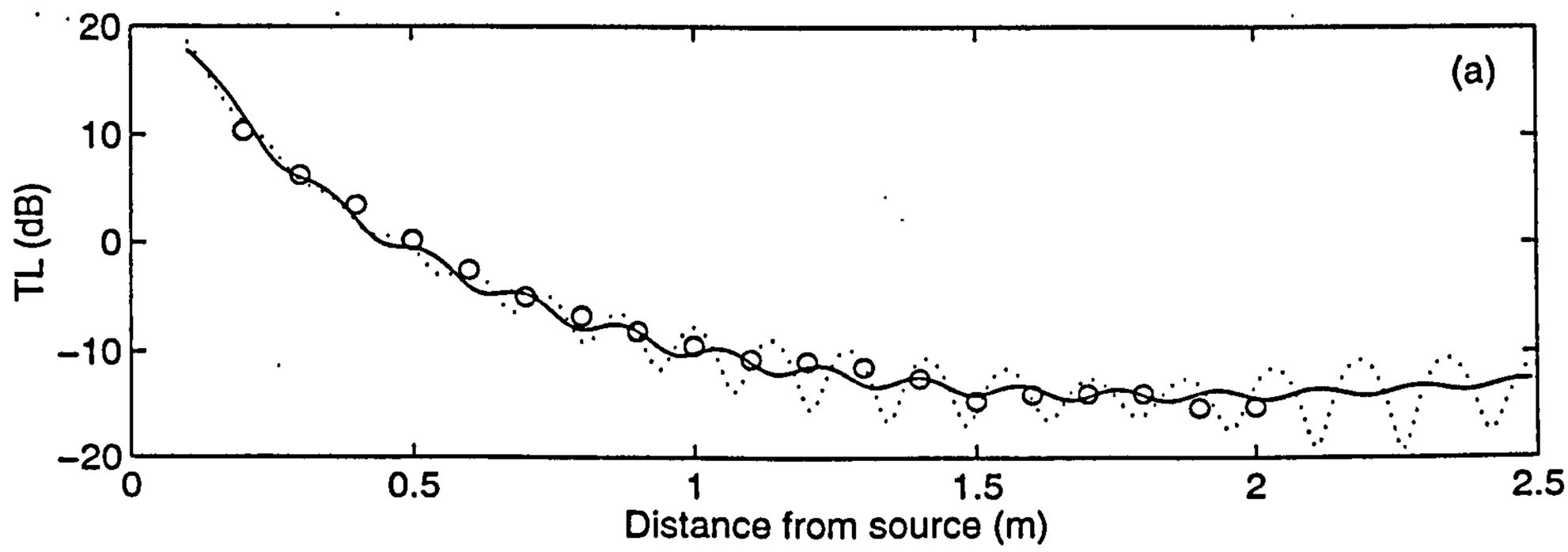

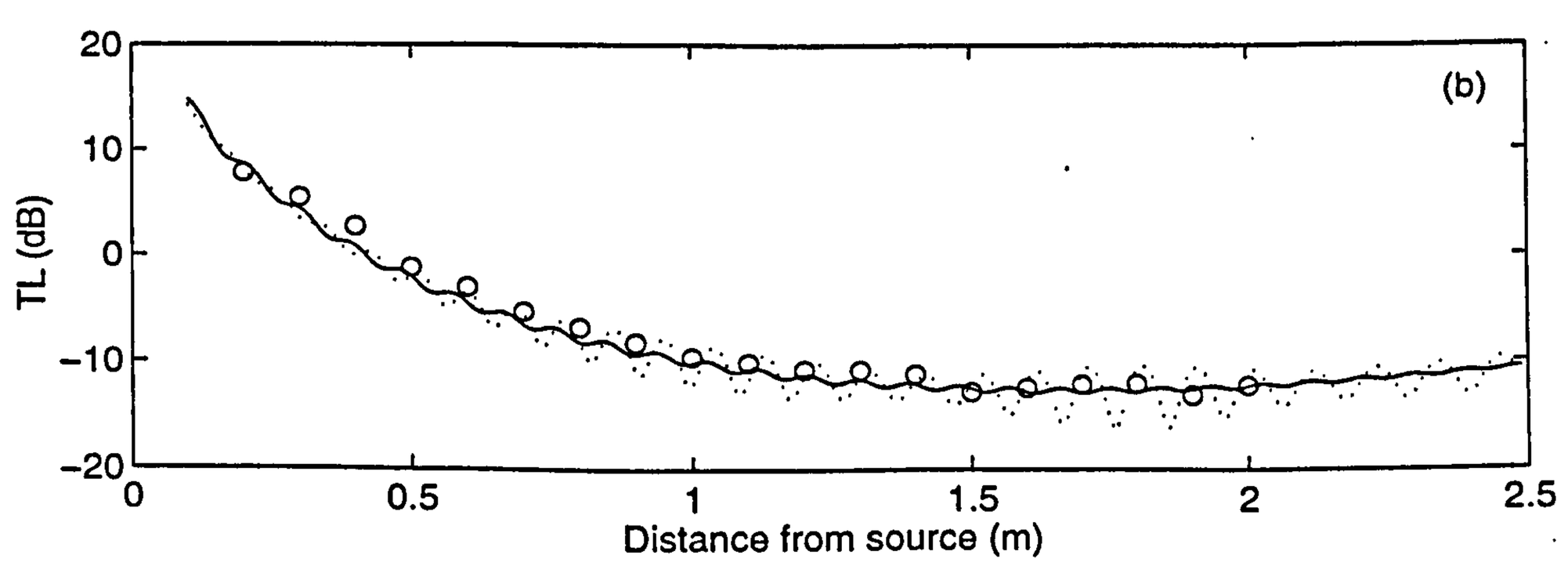

Figure 5.14 Similar to **Figure 5.13**, but with $\psi = \pi/4$, $z_s = 0.10$ m and $z = 0.02$ m.

5.4.3 The sound field due to a horizontal dipole source over concave surfaces

The circles in Figures 5.15(a) and (b) represent measurements at 2915 and 4350 Hz, respectively, with the receiver moved along the rigid surface ($z \sim 0.00$ m) and the source at a height of 0.02 m. The solid curves represent predictions from Equation (5.3.5) for the exponential profile, while the dotted curves represent predictions from Equation (5.3.2) for the bilinear profile. The agreement between the measurements and the calculations for both profiles is very good out to 2.0 m from the source.

The circles in Figures 5.16(a) and (b) represent measurements at 2915 and 4350 Hz, respectively, over the felt-covered concave surface with both the source and receiver at heights of 0.10 m. The agreement between the measurements and the calculations for the exponential profile (solid curves) remains good. However, there are considerable discrepancies between the measurements and the calculations for the bilinear profile (dotted curves) at longer ranges.

The circles in Figures 5.17(a) and (b) represent measurements at 2915 and 4350 Hz, respectively, with the source and receiver in the plane $\psi = \pi/4$ over the felt-covered surface. The source height was 0.10 m, and the receiver height was 0.02 m. The predictions for both profiles agree with the measurements.

It is noted that over concave surfaces, the sound field due to a horizontal dipole source is very similar to that due to a monopole source. This is consistent with what has been found in the case of convex surfaces. Moreover, as was the case with a monopole source, where the diffraction is by a cylindrical concave surface, the normal mode solution for an exponential sound speed profile is better able to describe the sound field than that for a bilinear profile.

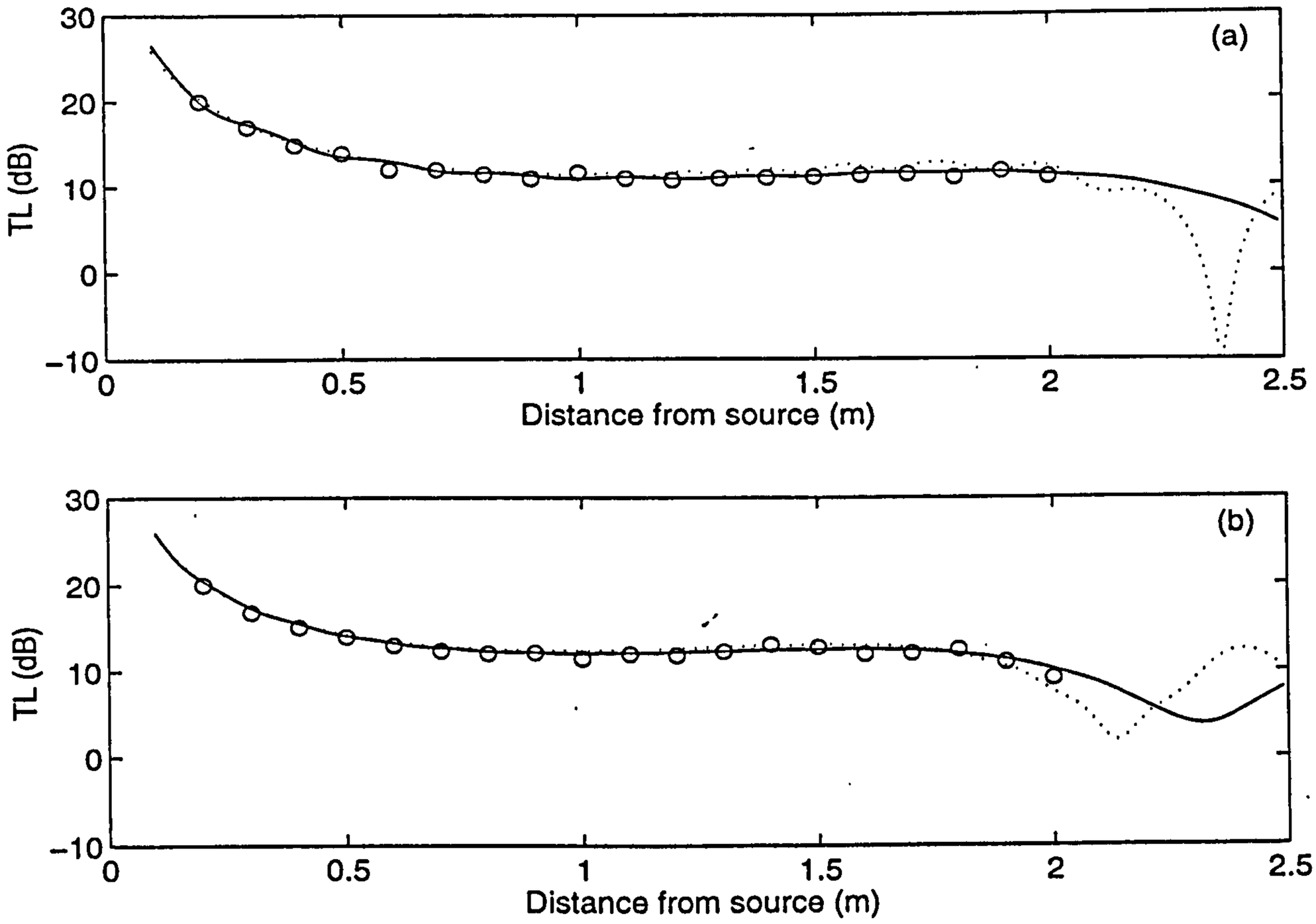

Figure 5.15 Transmission loss due to a horizontal dipole source obtained over a rigid concave surface with $R_c = 2.5$ m, $z_s = 0.02$ m and $z \sim 0.00$ m, at frequencies of (a) 2915 Hz and (b) 4350 Hz. Circles: measurements, solid curves: predictions for exponential profiles, dotted curves: predictions for bilinear profiles.

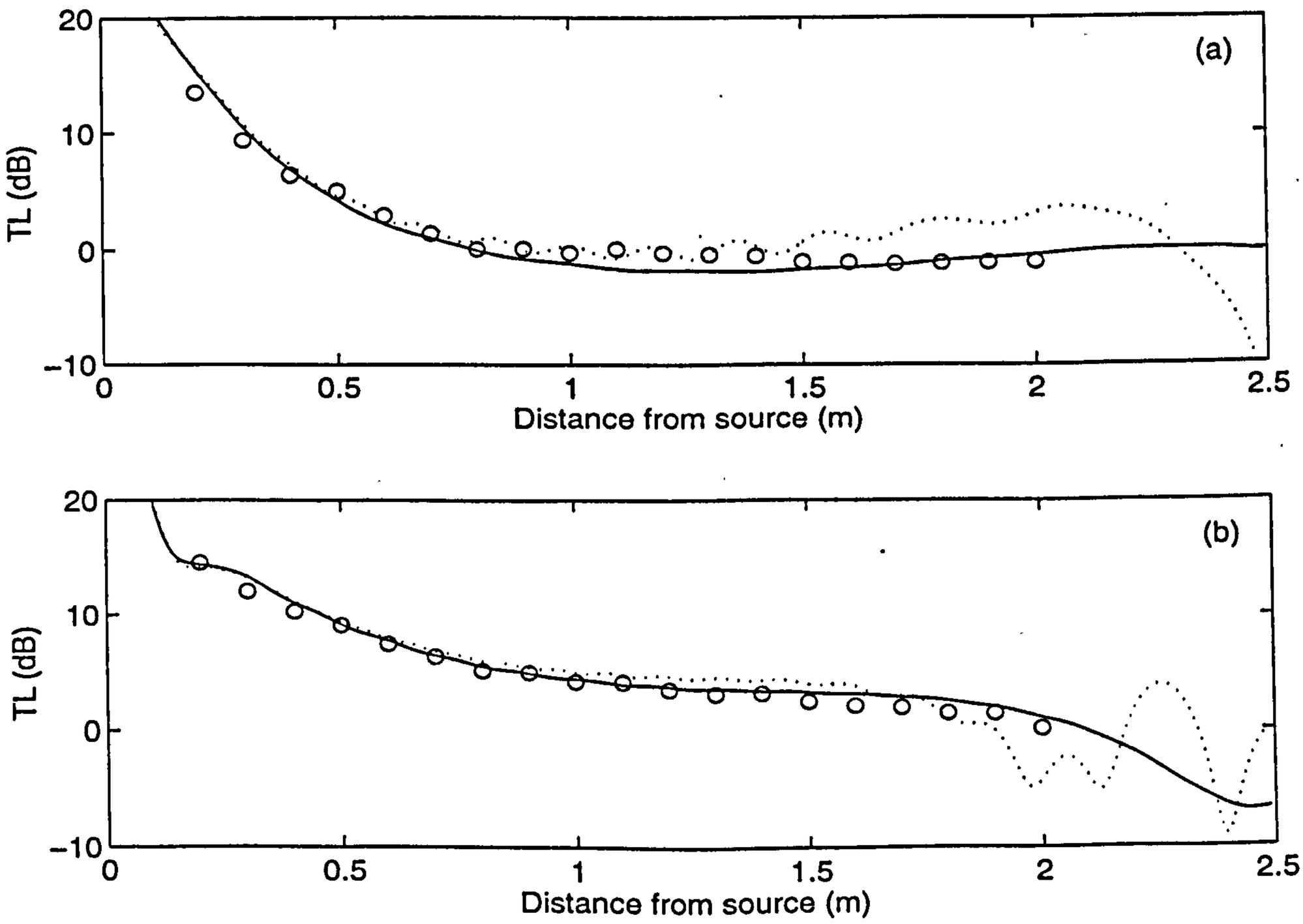

Figure 5.16 Same as **Figure 5.15**, but over a felt-covered concave surface with $z_s = z = 0.10$ m.

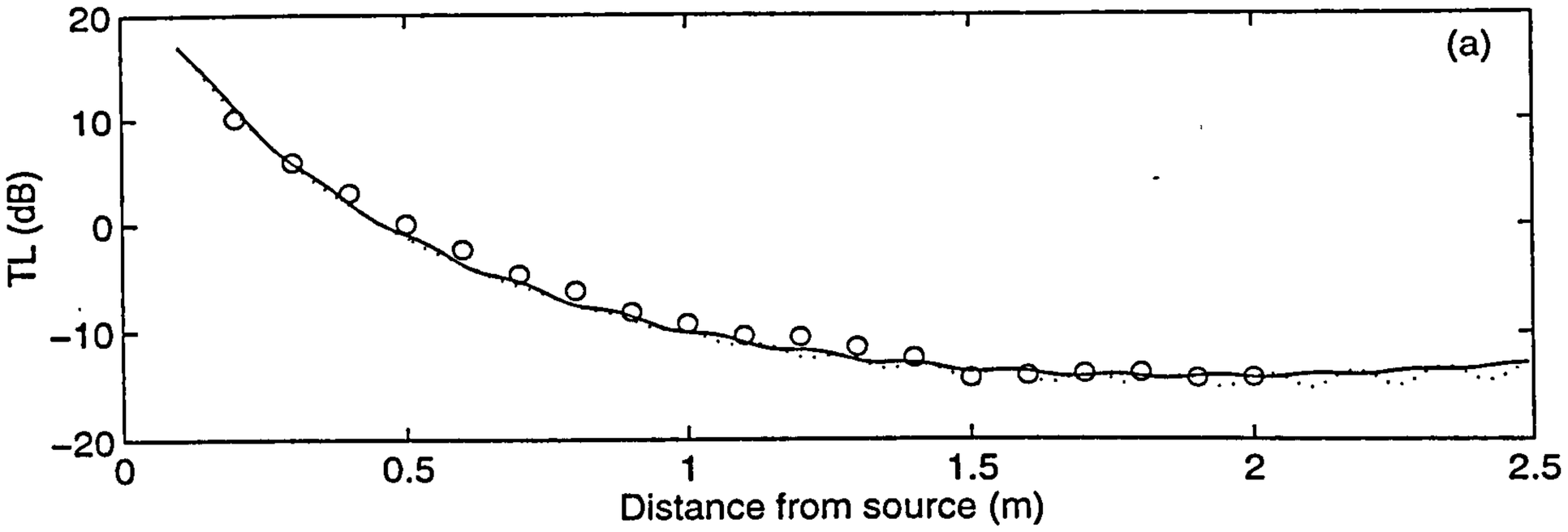

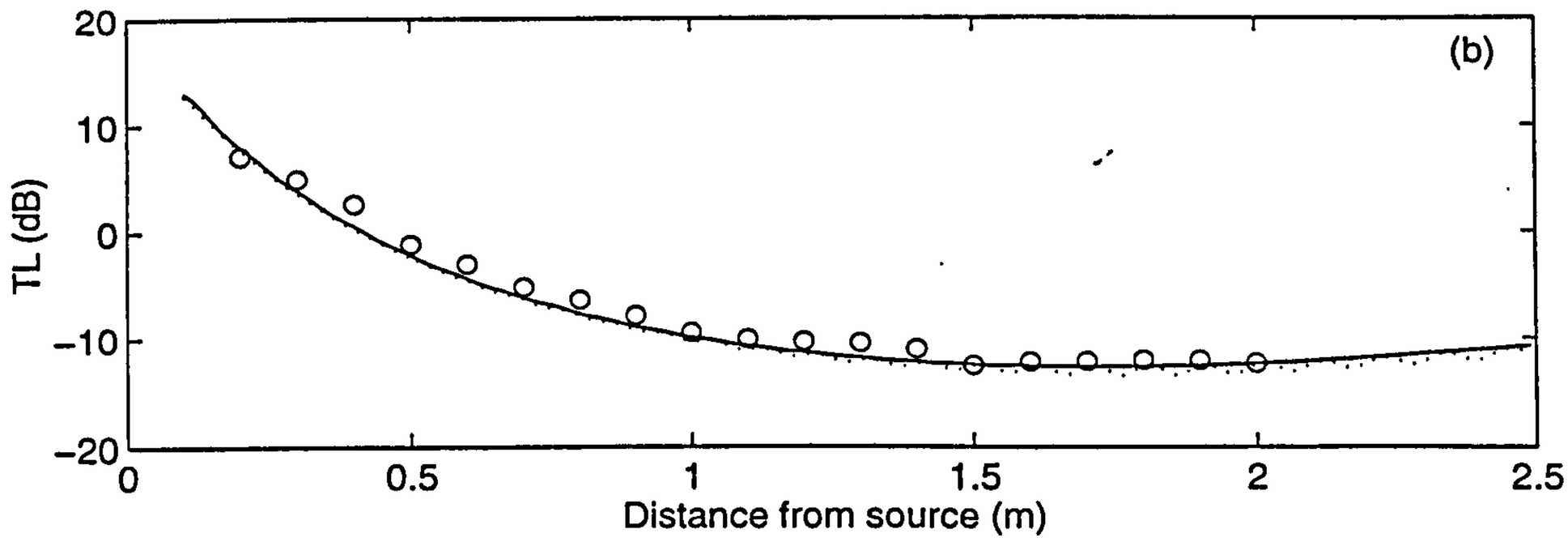

Figure 5.17 Same as **Figure 5.16**, but with $\psi = \pi/4$, $z_s = 0.10$ m and $z = 0.02$ m.

5.4.4 The sound field due to a vertical dipole source over concave surfaces

The circles in Figure 5.18(a) and (b) represent measurements at 2915 and 4350 Hz, respectively, with the receiver moved along the rigid surface ($z \sim 0.00$ m) and the source at a height of 0.02 m. The solid curves represent predictions from Equation (5.3.6) for the exponential profile, while the dotted curves represent predictions from Equation (5.3.3) for the bilinear profile. In contrast to the theoretical predictions, the experimental results lie on smooth curves (the dashed curves), which show similar trends to predictions of the monopole sound fields (*cf.* Figures 5.7 and 5.8).

Similar results have been obtained over the felt-covered concave surface. The circles in Figures 5.19(a) and (b) represent data at 2915 and 4350 Hz, respectively, with both the source and receiver at heights of 0.10 m, over the felt-covered surface. Figure 5.21 shows

the results obtained with the source and receiver in the plane $\psi = \pi/4$, and at heights of 0.10 and 0.02 m, respectively.

It would appear that, for a vertical dipole source over a cylindrical concave surface, the agreement between the measurements and the normal mode predictions for both profiles is not satisfactory due to the branch-line integral problem mentioned earlier in this chapter. Nevertheless, relatively speaking, there is better agreement with predictions for an exponential profile, within the experimental ranges.

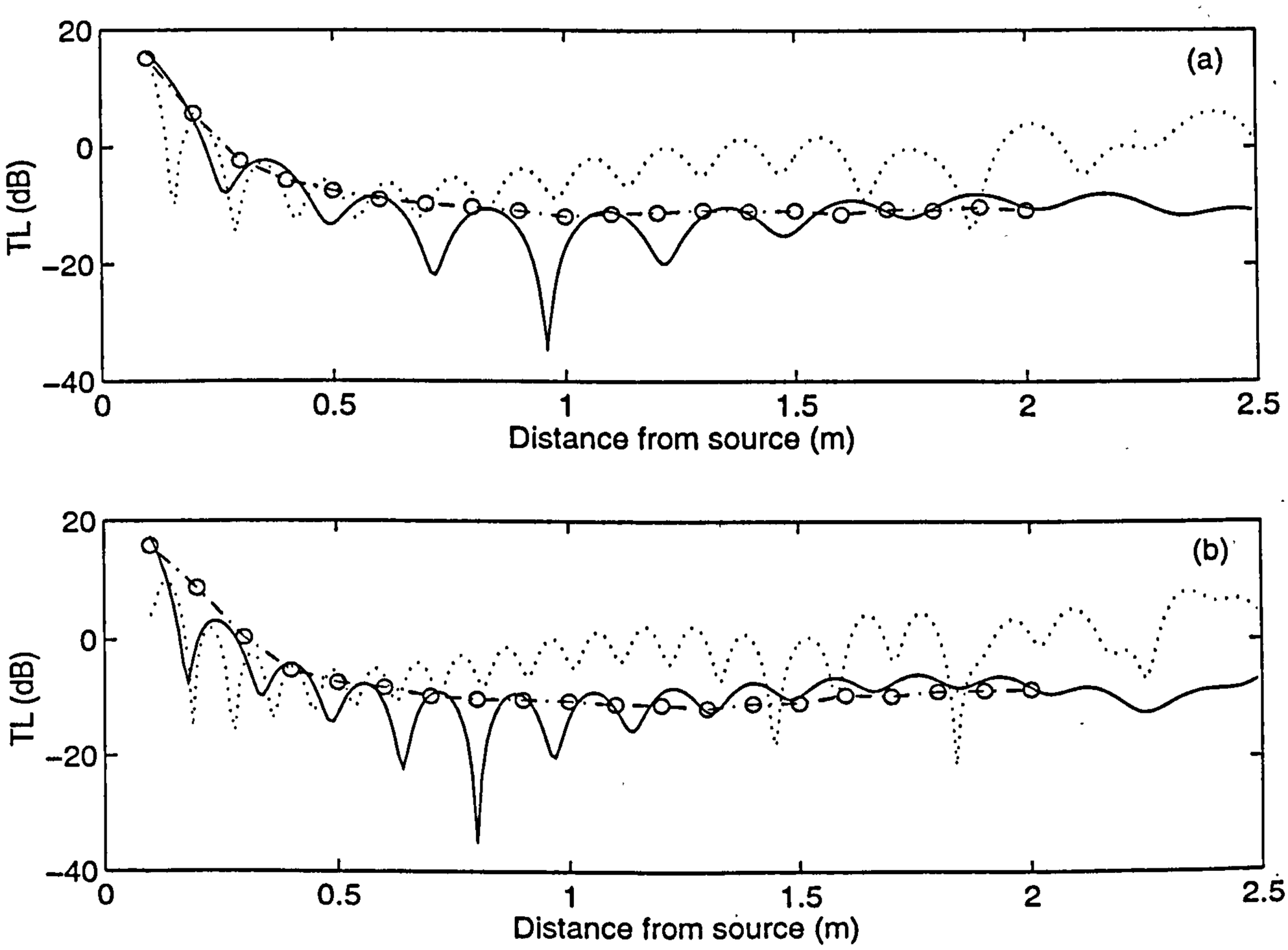

Figure 5.18 Transmission loss due to a vertical dipole source obtained over a rigid concave surface with $R_c = 2.5$ m, $z_s = 0.02$ m and $z \sim 0.00$ m, at frequencies of (a) 2915 Hz and (b) 4350 Hz. Circles & dashed curves: measurements, solid curves: predictions for exponential profiles, dotted curves: predictions for bilinear profiles.

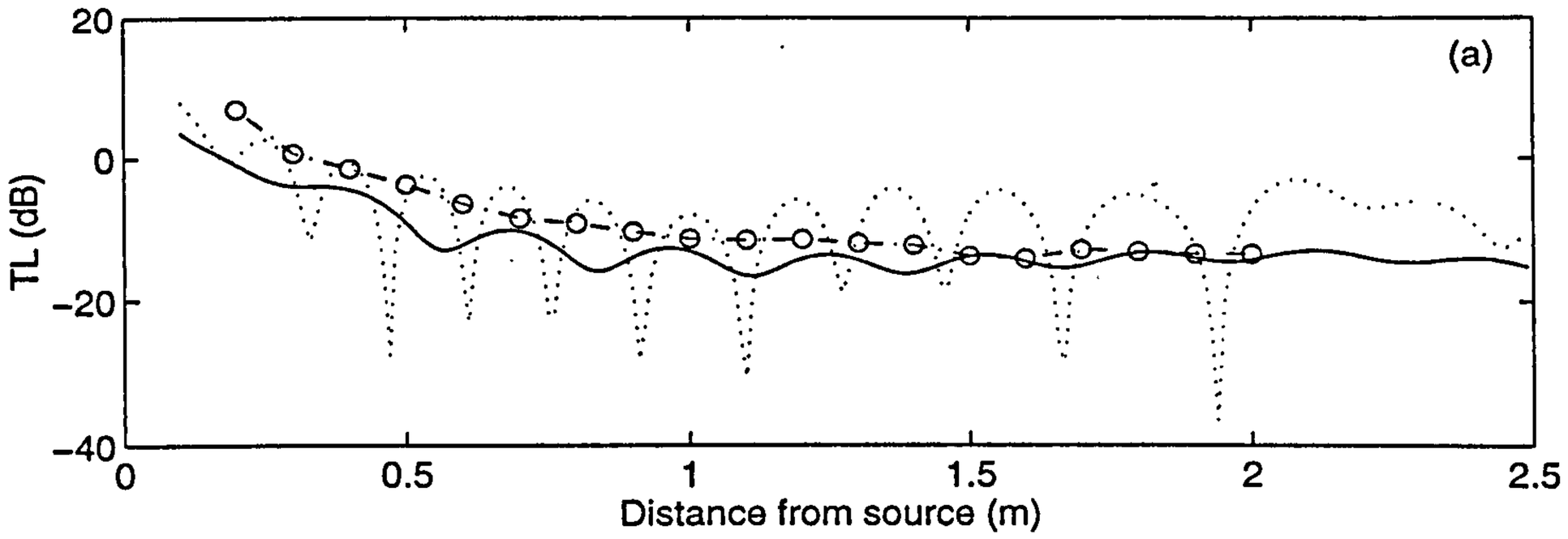

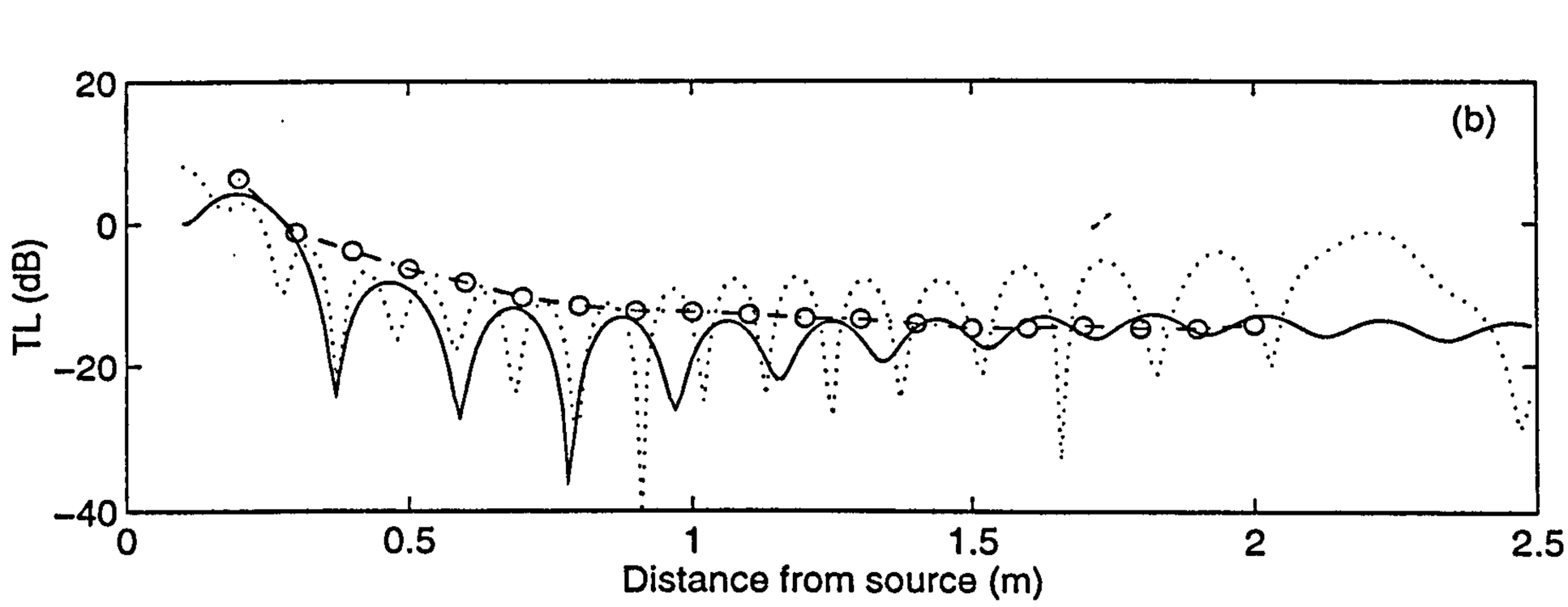

Figure 5.19 Same as **Figure 5.18**, but over a felt-covered concave surface with $z_s = z = 0.10$ m.

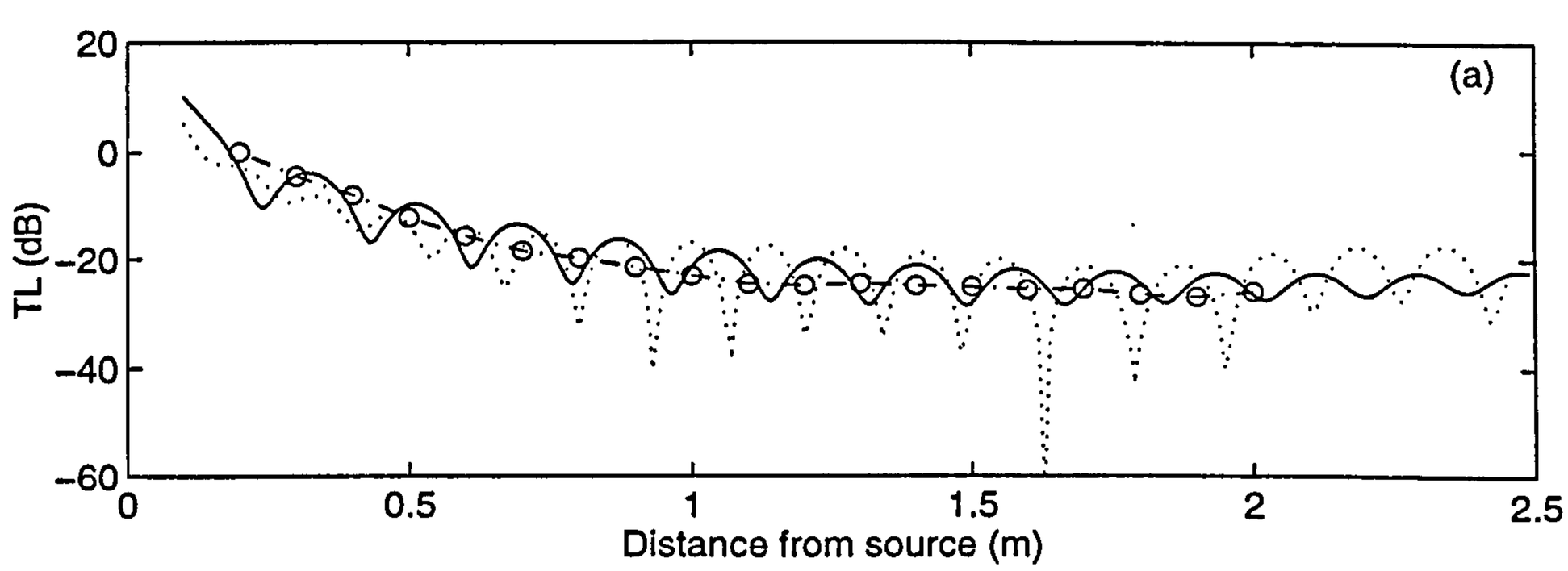

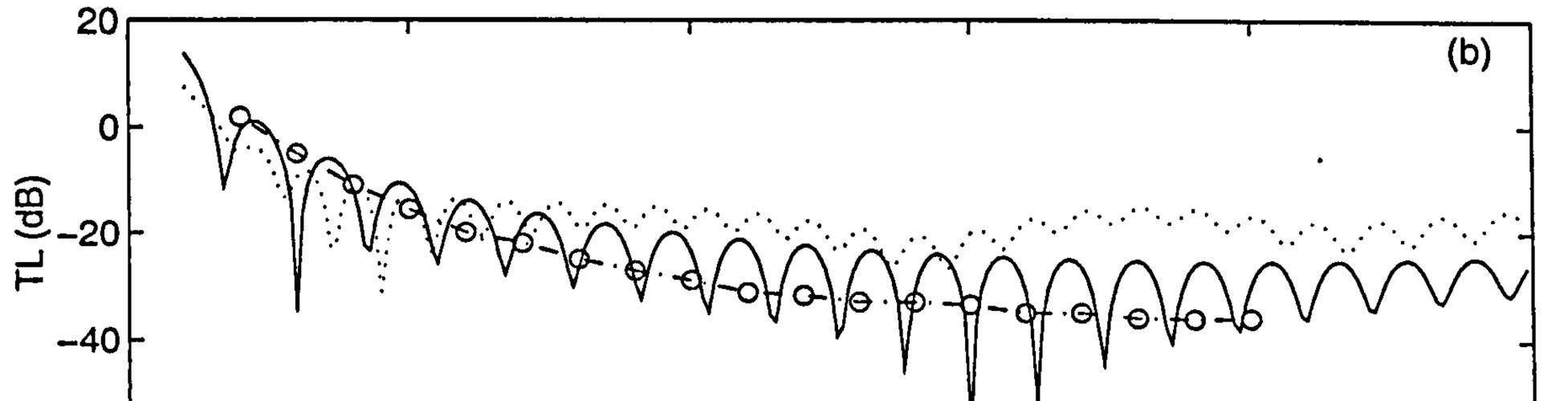

Figure 5.20 Similar to **Figure 5.19**, but with $z_s = 0.10$ m, $z = 0.02$ m and $\psi = \pi/4$.

5.5 Summary

A normal mode solution has been developed for propagation in an exponential sound speed profile and used to predict the sound field diffracted by a cylindrical concave surface. Analytical expressions for dipole sources have been deduced directly from those for a monopole source.

A series of laboratory experiments have been conducted using a monopole source, horizontal and vertical dipole sources over cylindrical concave surfaces.

The measurement results have been compared with normal mode predictions for both an exponential profile and a bilinear profile. The comparison of the measurements with the predictions was limited to ranges of less than 2.0 m. Good agreement has been found between measurements and normal mode predictions for an exponential profile where the sound field was due to a monopole source or horizontal dipole sources, but the agreement is less satisfactory where the sound field is due to vertical dipole sources. The solution for a bilinear profile showed considerable disagreement with measurements at long ranges in both monopole and horizontal dipole sound fields, and significant differences from measurements in vertical dipole sound fields.

The predicted and measured transmission loss due to a horizontal dipole source, as a function of range, have been found to be close to those predicted for a monopole source. However, the predicted transmission loss due to a vertical dipole source shows serious oscillations resulting from possible omissions in the normal mode calculations.

Chapter 6

Surface waves over a convex porous surface

Many of the essential features associated with surface wave propagation near a complex impedance plane have been clarified by a number of theoretical and experimental studies [40-44]. The existence of the surface wave above an impedance plane in a homogeneous atmosphere is now generally accepted.

Theoretical studies [40, 41, 63, 65] have revealed that surface waves propagate horizontally above porous ground, decaying exponentially with height, at a phase velocity less than the sound speed in the air. Laboratory measurements have detected these surface waves using both continuous and pulse sources [40, 44, 65-69] above lighting diffuser lattices mounted on flat rigid boards. It has been verified [43, 70] that a true surface wave exists independently in spherical wave propagation above such an impedance ground. Daigle *et al* [44] and Hutchinson-Howorth and Attenborough [69, 71] have demonstrated that a surface wave may be identified, in pulse experiments, as a separate arrival from that of a body wave arriving earlier.

The technique of pole searching in an upward refracting medium suggested by Pierce [3] works well for phase angles of the scaled and nondimensionalized admittance, $q = |q|e^{i\varphi}$, greater than $\pi/6$, *i.e.* $\varphi > \pi/6$ [*cf.* Equation (3.2.6)], but Raspet *et al* [8] indicated that this technique would not work for moderately large $|q|$ if $\varphi < \pi/6$. Instead they have developed

a numerical scheme of pole searching (*cf.* Chapter 3.2) that can avoid missing the pole related to the surface wave for $\varphi < \pi/6$. However, the Raspet *et al*'s scheme has not yet been confirmed by experimental evidence.

For complex impedance with phase angles, $\varphi_z > \pi/3$ ($\varphi_z = \pi/2 - \varphi$), Raspet *et al* [8] have pointed out that the surface wave pole identified in the analytical solution for sound propagation in a homogeneous atmosphere is present also in the solution for the sound field in an upward refracting medium. They stated that this surface wave pole arises from the residue series which contains an independent contribution from the surface wave. However, the surface wave has not yet been observed outdoors, and there is little experimental evidence as to whether and how the surface wave exists over a curved porous surface.

Previous studies suggest that the nature of the surface waves can be investigated from controlled experiments above appropriate model surfaces. On the basis of the acoustic analogy described earlier (*cf.* Chapter 3 and Chapter 4), it is possible to study the surface waves that would occur over an impedance plane in an upward refracting medium by making measurements above a convex porous surface. In this chapter, we shall examine the surface wave pole locations, wave contributions and sound field above a convex impedance surface, and present experimental evidence for the existence of the surface waves over the convex surface. Measurements of the sound fields due to horizontal and vertical dipole sources including the surface wave contributions above this convex surface are reported also in this chapter.

6.1 Surface waves from a monopole source

In a stationary upward refracting medium, with a bilinear sound speed profile given by

$$c(z) = \frac{c_0}{\sqrt{1+2z/R_c}}, \tag{6.1.1}$$

the solution for the acoustic pressure wave equation can expressed as [72]

$$p(r,z) = -\int_{-\infty}^{\infty} H_0^1(k_r r) P(z,k_r) k_r dk_r, \tag{6.1.2}$$

where

$$P(z,k_r) = -2\pi l e^{i\pi/6} \mathrm{Ai}\left(-\xi_> e^{i2p/3}\right)\left[\mathrm{Ai}\left(-\xi_<\right) - \Gamma \mathrm{Ai}\left(-\xi_< e^{i2p/3}\right)\right], \tag{6.1.3}$$

$$l = \left(R_c/2k_0^2\right)^{1/3}, \tag{6.1.4}$$

$$\xi = \left(k_0^2 - k_r^2\right) l^2 - \frac{z}{l}, \tag{6.1.5}$$

$$q = ik_0 \beta l, \tag{6.1.6}$$

and

$$\Gamma = \frac{\mathrm{Ai}'\left(-\xi_0\right) - q\mathrm{Ai}\left(-\xi_0\right)}{e^{i2\pi/3}\mathrm{Ai}\left(-\xi_0 e^{i2\pi/3}\right) - q\mathrm{Ai}'\left(-\xi_0 e^{i2\pi/3}\right)}. \tag{6.1.7}$$

The remaining parameters are the same as identified in previous chapters. The residue of Equation (6.1.3) can be evaluated at each pole of Equation (6.1.2), and the results summed to form the total solution. The condition for a pole is

$$e^{i2\pi/3}\mathrm{Ai}\left(-\xi_0 e^{i2\pi/3}\right) - q\mathrm{Ai}'\left(-\xi_0 e^{i2\pi/3}\right) = 0. \tag{6.1.8}$$

Evaluating the residue at each pole $\tau_n = -\overline{\xi}_0$ gives

$$p(r,z) = \frac{\pi e^{i\pi/6}}{l} \sum_n H_0^1(k_n r) \frac{\mathrm{Ai}\left(-\overline{\xi}_s e^{i2\pi/3}\right)\mathrm{Ai}\left(-\overline{\xi} e^{i2\pi/3}\right)}{\left[\mathrm{Ai}'\left(-\overline{\xi}_0 e^{i2\pi/3}\right)\right]^2 + \overline{\xi}_0 e^{i2\pi/3}\left[\mathrm{Ai}\left(-\overline{\xi}_0 e^{i2\pi/3}\right)\right]^2}. \tag{6.1.9}$$

Raspet *et al* investigated the behavior of the residue series solution in an upward refracting medium as the radius of curvature becomes large [8]. They found that the integrand, Equation (6.1.3), in Equation (6.1.2) can be written as

$$P(z,k_r)=\left[-i/2\sqrt{k_0^2-k_r^2}\right] \times\left[\exp\left(\sqrt{k_0^2-k_r^2}\right)(z_<+z_>)+R_p\exp\left(\sqrt{k_0^2-k_r^2}\right)(z_<+z_>)\right], \tag{6.1.10}$$

where

$$R_p=\frac{\cos\theta_0-\beta}{\cos\theta_0+\beta} \tag{6.1.11}$$

is the plane wave reflection coefficient, and θ_0 is the incidence angle. The properties of this integrand for acoustic propagation in an upward refracting medium have been found to have the features of a surface wave [8] if $\varphi_z > \pi/3$ (or $\varphi < \pi/6$).

6.1.1 Pole locations

Raspet *et al* [8] have indicated that, for a sufficiently large $|q|$ with $0 < \varphi < \pi/6$, there is always a solution for the so-called surface wave pole [8] in an upward refracting medium. Figure 6.1 shows the variation of τ_n as $|q|$ increases and for φ = 30°, 25°, 20° and 15° using Raspet *et al*'s numerical technique described in Chapter 2. In Figure 6.1(a), $\varphi = 30°$, all the poles are located between the zeros of the Airy function derivative, marked by the circles and the zeros of the Airy function, marked by the plus signs. In Figures 6.1(b)-(d), there are surface wave poles. The surface wave poles are those that originate from the zeros of the Airy function derivative but their trajectories in the complex plane do not end at the zeros of the Airy function. For the residue series solution, if $\varphi < 20°$, the pole including the surface wave contribution may arise from the first zero of the derivative of the Airy function.

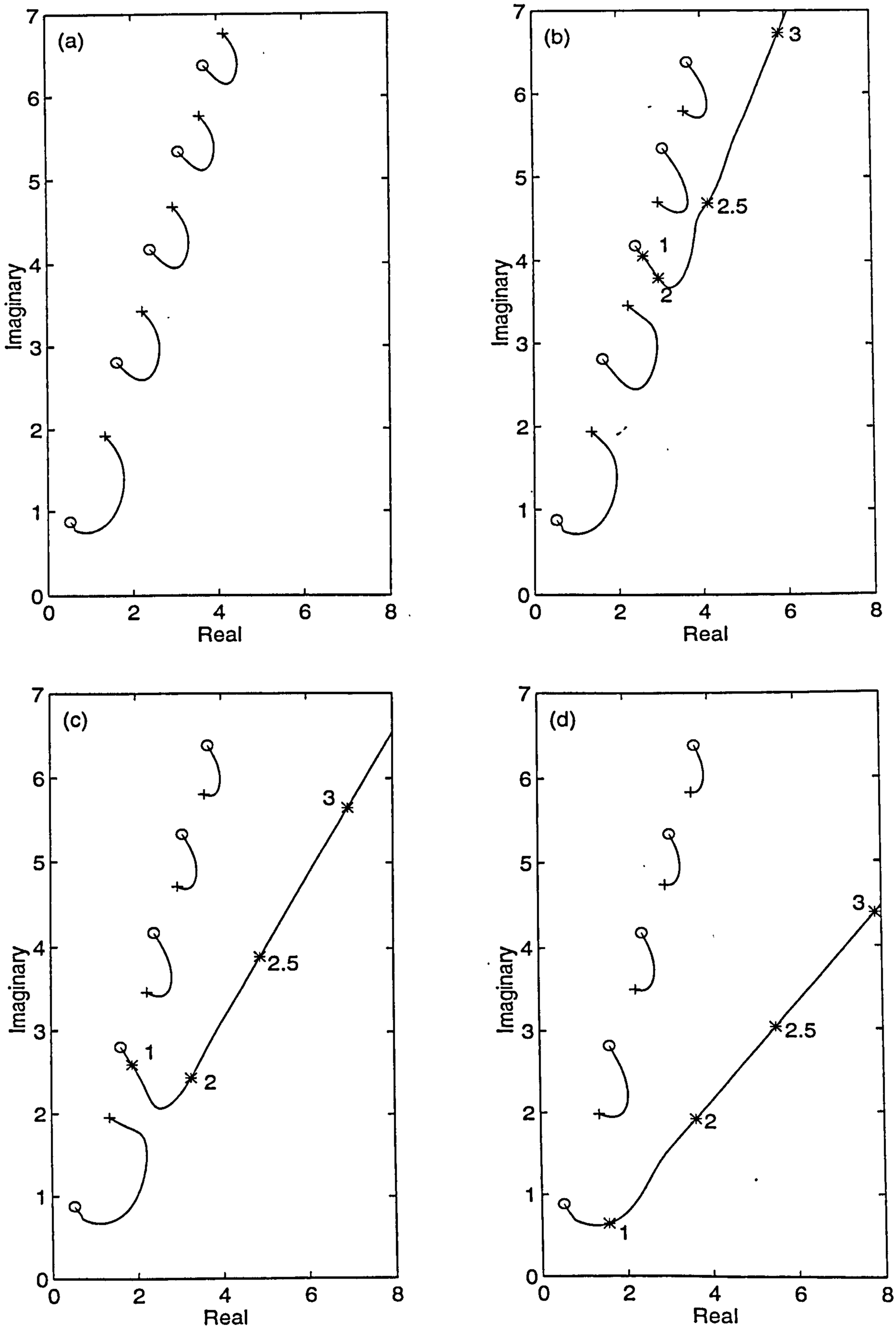

Figure 6.1 The behavior of the zeros of τ_n with increasing $|q|$ for φ = (a) 30°, (b) 25°, (c) 20° and (d) 15°. o: the zeros of Ai; +: the zeros of Ai′. The position of the zeros for $|q| = 1.0, 2.0\ 2.5$ and 3.0 marked by * in (b) to (d).

However, we shall demonstrate that the so-called surface wave poles may not be pure surface wave poles. They include the contributions of both the creeping wave and the surface wave. Detailed discussions can be found later in this chapter.

6.1.2 Wave contributions

Above a convex surface, the wave contributions are different as q is varied. In Figures 6.2(a), 6.3(a) and 6.4(a) the nature of the wave contributions is investigated at a frequency of 500 Hz, for admittance magnitude $|\beta| = 1/3.0$; and a source height z_s and receiver height z at 0.10 m. The variation of the first three residue series terms, with $|q|$ having values of 1.5, 2.0, 2.5 and 3.0 with $\varphi = 25°$, is shown in Figure 6.2(a), Figure 6.3(a) and

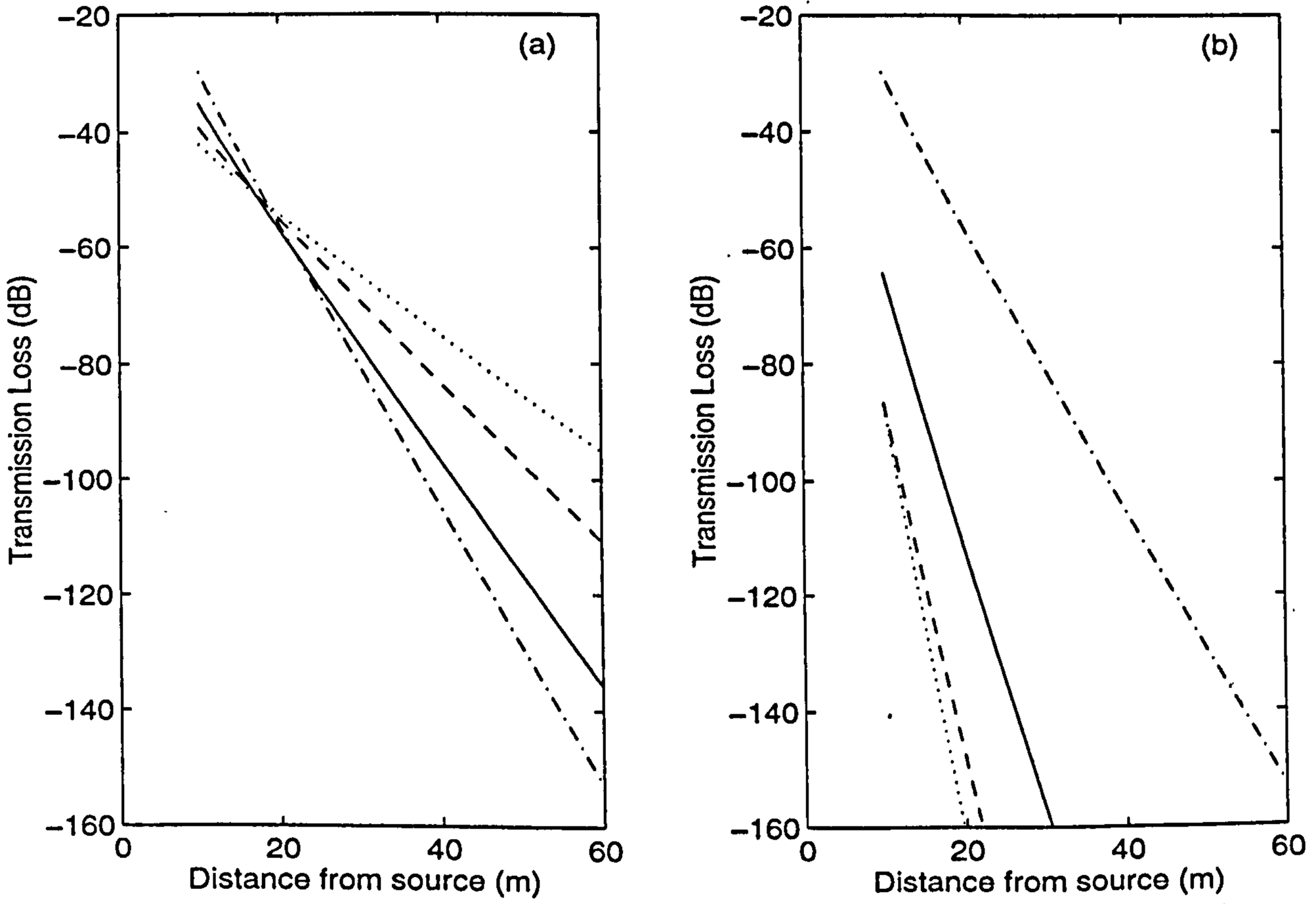

Figure 6.2 The behavior of the wave contribution with q varying for the first term, for a phase angle $\varphi = 25°$. $z_s = z = 0.1$ m, and $|\beta| = 1/3.0$. Dashdot line: $|q| = 1.5$, solid line: $|q| = 2.0$, dashed line: $|q| = 2.5$, and dotted line: $|q| = 3.0$. (a) $f = 500$ Hz, $|q|$ varying with R_c, and (b) $R_c = 20$ m, $|q|$ varying with f.

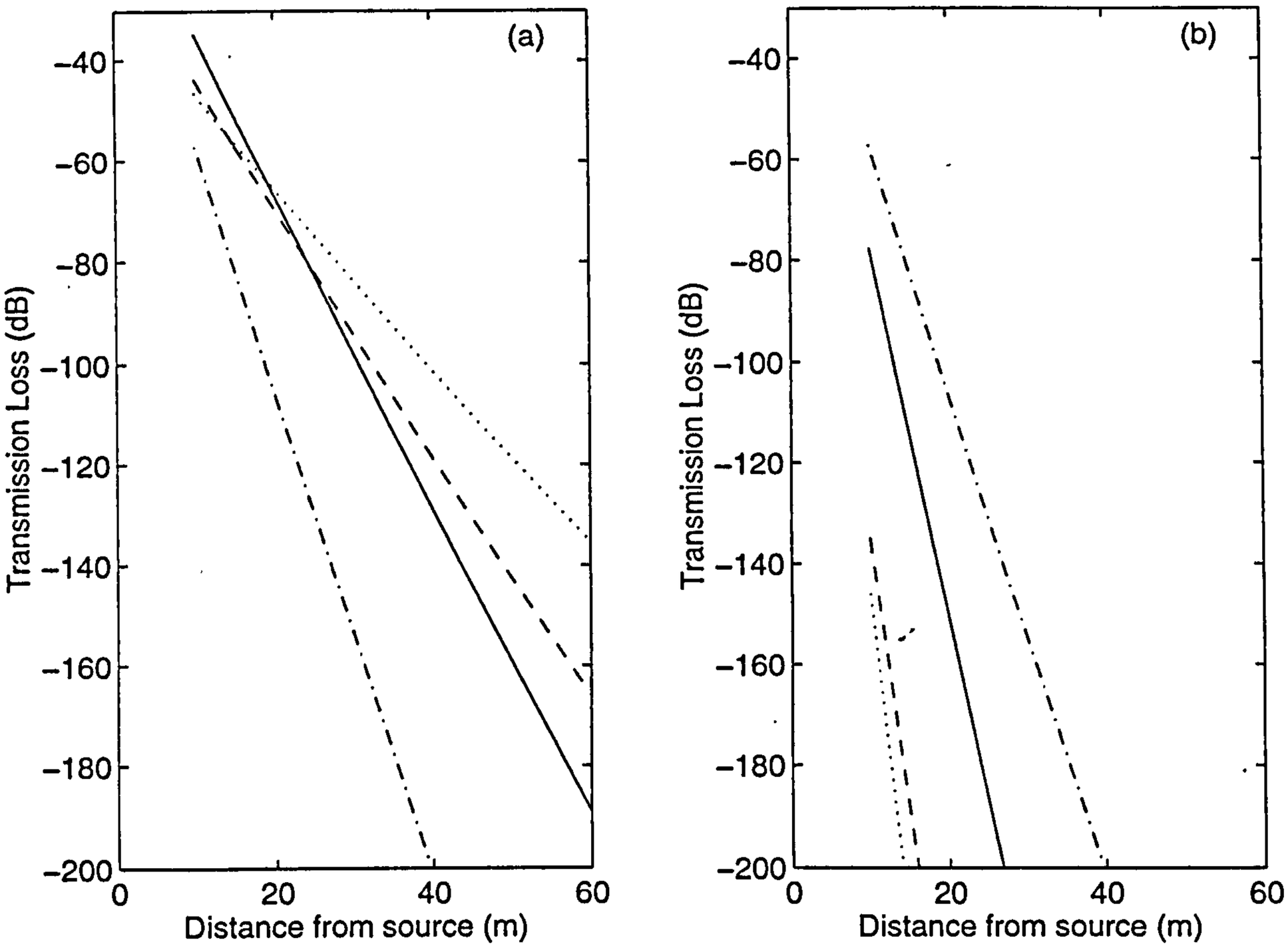

Figure 6.3 Same as **Figure 6.2,** but for the second term.

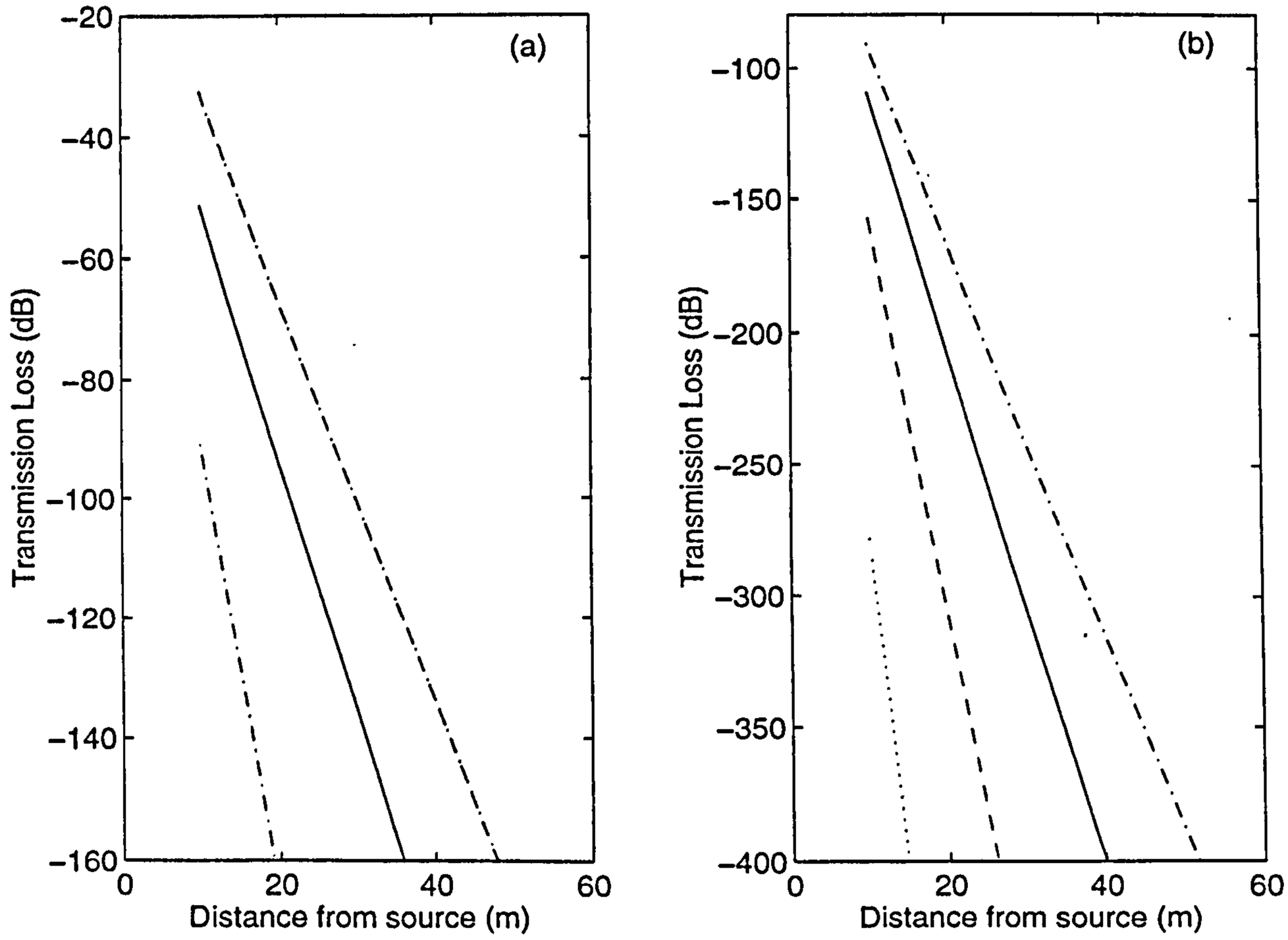

Figure 6.4 Same as **Figure 6.2**, but for the third term. In (a), the right-hand dash-dot line includes both the dashed line ($|q| = 2.5$) and dotted line ($|q| = 3.0$).

Figure 6.4(a), respectively. $|q|$ increases as the radius of curvature R_c takes successive values of 20, 47.6, 92.6 and 160.8 m, corresponding to sound speed gradients of -17.15, -7.2, -3.7 and $-2.1\ s^{-1}$, respectively.

Figure 6.2(a) shows the variation of the first term in the residue series as $|q|$ is varied, while Figure 6.3(a) shows that of the second term. In the ranges where $r > 20$ m, the wave contributions due to the first two terms increase as $|q|$ increases.

The variation of the third term, as $|q|$ is varied, is displayed in Figure 6.4(a). This term contains the surface wave pole that is shown in Figure 6.1(b). It behaves in a different manner from the first two terms. The wave contribution increases rapidly, as $|q|$ increases, to a limit when $|q|$ is approximately 2.5. The $|q| = 3.0$ results cannot be distinguished from the $|q| = 2.5$ results, the dotted line ($|q| = 3.0$) and the dashed line ($|q| = 2.5$) are coincident and appear as the right-hand dash-dot line.

Calculations for a radius of curvature $R_c = 20$ m corresponding to a sound speed gradient of $-17.15\ s^{-1}$, source height z_s and receiver height z at 0.10 m, the variation of the first terms, with the amplitude of $|q| = 1.5$ 2.0, 2.5 and 3.0 and $\varphi = 25°$, are shown in Figure 6.2(b), Figure 6.3(b), and Figure 6.4(b), respectively. The amplitude of $|q|$ increases as frequency increases from 500 Hz, taking the values 1.2 kHz, 2.3 kHz, and 4 kHz.

Figure 6.2(b) shows the variation of the first term in the residue series as q is varied, while Figure 6.3(b) shows that of the second term. The wave contributions decrease to a limit as $|q|$ increases. The behavior of the third term, as shown in Figure 6.4(b), is different from the first two terms, it decreases at an accelerated rate as $|q|$ becomes larger.

In an upward refracting medium over an impedance ground, it is common that $|q|$ increases with increasing frequency. If $\varphi < 30°$, the surface wave contribution will decrease as f increases. Figure 6.5 shows the wave contributions due to the first four terms above a convex surface of finite impedance with a curvature of 2.5 m (corresponding to a sound speed gradient of $-137.2\ s^{-1}$) at frequencies of (a) 1.8 kHz, (b) 4.2 kHz, (c) 5.5 kHz, and (d) 7.4 kHz. The impedance is calculated from the Attenborough's two-parameter model [*cf.* Equation (2.5.15)] with $\sigma_e = 4$ kPa s m^{-2} , and $\alpha_e = 570\ m^{-1}$. It is found that the surface wave contribution, which is included in the first residue series term, decreases with increasing frequency to a very low level. At a frequency of 1.8 kHz, where $|q|$ is 0.5, the first term dominates over almost the entire range. At frequencies of 4.2 kHz and 5.5 kHz, where $|q|$ is 1.5 and 2.0 respectively, the first term becomes weaker and there are interference patterns in the total sound field caused by the first three terms. At a frequency of 7.4 kHz, where $|q|$ is 3.0, the total sound field is dominated by the second term deep within the shadow zone, and the surface wave makes no contribution to the total sound field.

Figure 6.6(a) shows the wave contributions calculated at 3.9 kHz above the same convex impedance surface as was appropriate to Figure 6.5. The transmission loss is plotted as a function of distance from the apex along the line of sight, with a source height of 0.21 m. Figure 6.6(b) is similar to (a) but the transmission loss is plotted as a function of vertical distance across the shadow zone. The vertical distance starts at an arc length of 1.9 m from the source (*cf.* Figure 4.5).

It is interesting to find from Figure 6.6(a) that the surface wave creeps into the penumbra region and erases the dips, which would be produced by the remaining other residue series

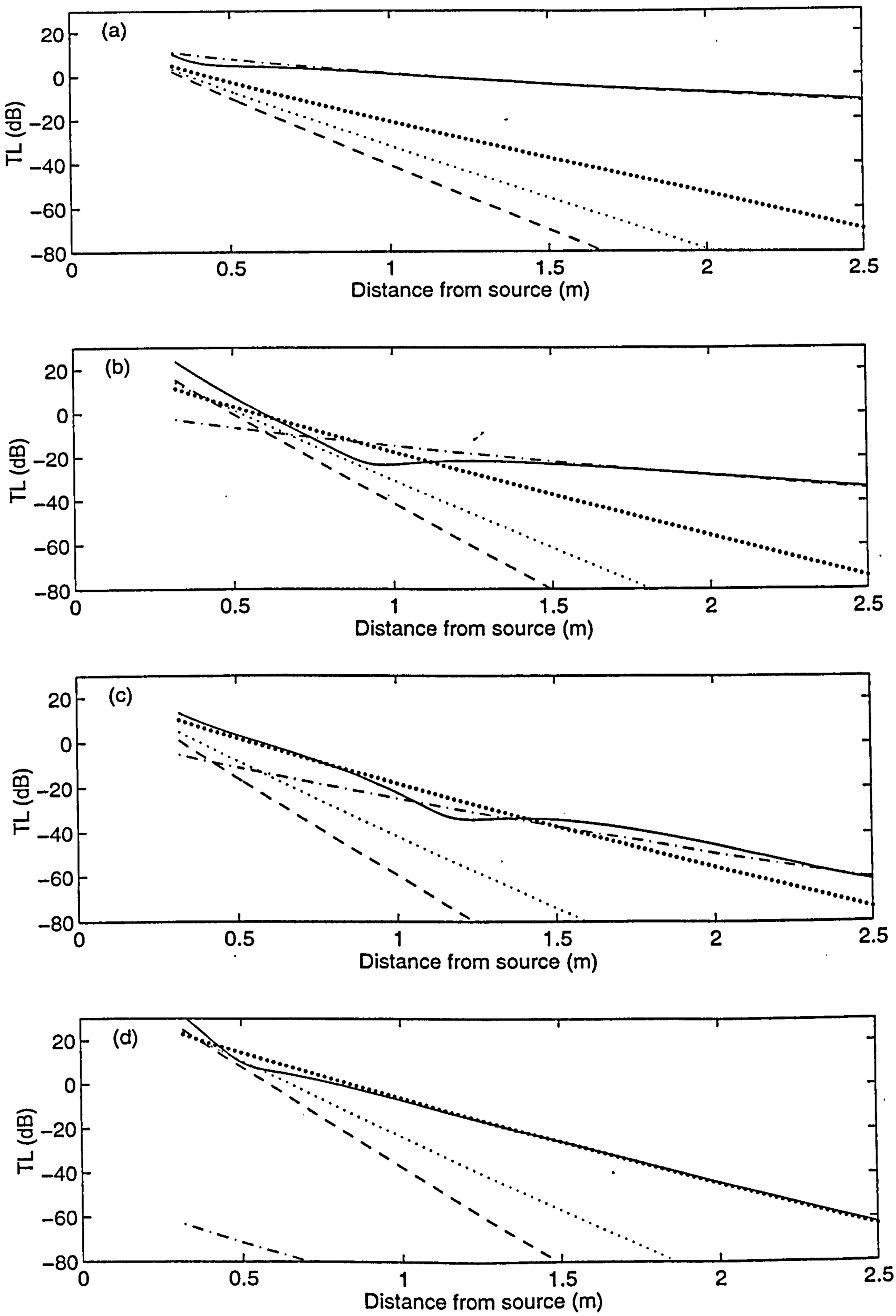

Figure 6.5 The wave contributions and total sound field above an impedance convex surface with $\sigma_e = 4$ kPa s m^{-2} and $\alpha_e = 570$ m^{-1} for (a) $|q| = 0.5$, (b) $|q| = 1.5$, (c) $|q| = 2.0$ and (d) $|q| = 3.0$. Solid lines: total wave, dashdot lines: 1st term, points: 2nd term; dotted lines: 3rd term and dashed lines: 4th term.

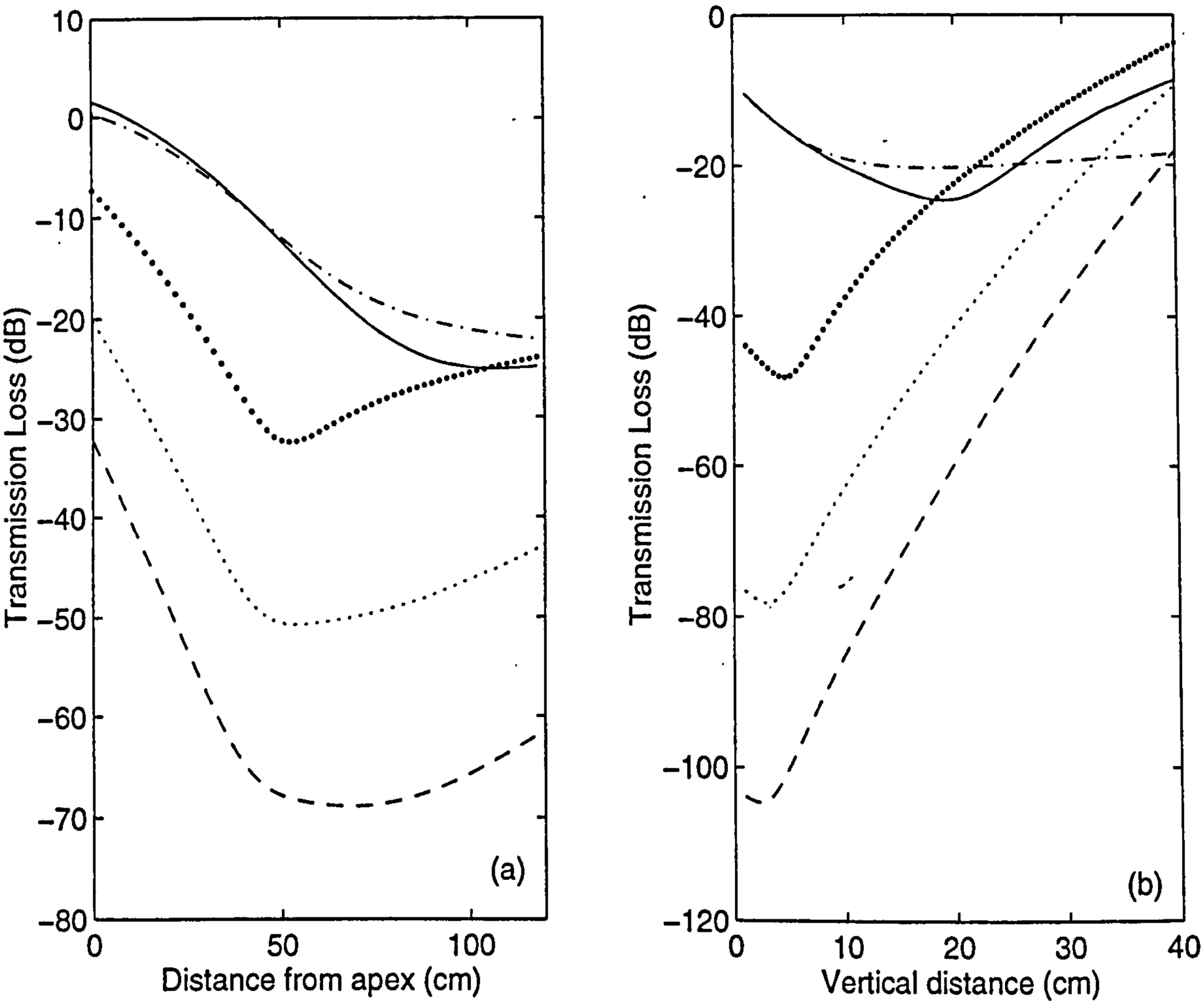

Figure 6.6 Same as **Figure 6.5**, but for a frequency of 3.9 kHz, $z_s = 0.21$ m, (a) along the line of sight and (b) along a vertical distance z_v starting with at $r_0 = 1.90$ m (*cf.* **Figure 4.5**).

terms. The first term including the surface wave contribution dominates out to a distance of 1.5 m from the source.

In the region behind the apex vertically across the shadow zone, see Figure 6.6(b), the first term only dominates at short ranges where the receiver height is close the surface. As the receiver height increases, the surface wave contribution becomes smaller, and the first term has decayed to a lower level than even the fourth term at a vertical distance of 40 cm.

6.1.3 Impedance of a mat-on-masonite surface

The lighting diffuser lattice that has been used as the model surface to produce a surface wave by previous researchers cannot be attached to a curved surface because it is inflexible. To obtain a surface with an impedance in which the imaginary part is larger than the real part and $\varphi_z > \pi/3$, a suitable comb-like structure has to be found to cover the curved surface. The material must be sufficiently flexible to follow the contour of the surface uniformly and behave as a locally reacting medium. A commercial mat was found to be the most suited for this purpose. The mat is open meshed with a hole size of 22 mm square and a depth of 12 mm. It was sealed with double-sided tape to the rigid convex surface model that has been described in Chapter 4, to produce a convex mat-on-masonite surface ($R_c \sim 2.5$ m), see Figure A-3.

The measurement techniques employed here are similar to those used above a convex surface and with a monopole source which are described in Chapter 4.

The application of the residue series solution to the prediction of the sound propagation above the mat-on-masonite surface requires knowledge of the impedance of the surface. Therefore, a series of measurements was performed to examine the acoustical behavior of the mat-on-masonite surface structure. Figure 6.7 shows the excess attenuation measured above a flat mat-on-masonite surface with a point source and a receiver 1.0 m apart at heights of (a) 0.08 m, (b) 0.10 m and (c) 0.15 m. The solid curves were calculated from Equation (4.1.1). The impedance was evaluated using Equation (2.5.15), *i.e.* the Attenborough two-parameter model [33]. The best agreement between the predictions and the measurements was found with $\sigma_e = 4$ kPa s m^{-2}, and $\alpha_e = 570$ m^{-1}. In these figures, the angles of incidence are 81.0°, 78.7° and 73.3°, respectively. The measurements are in

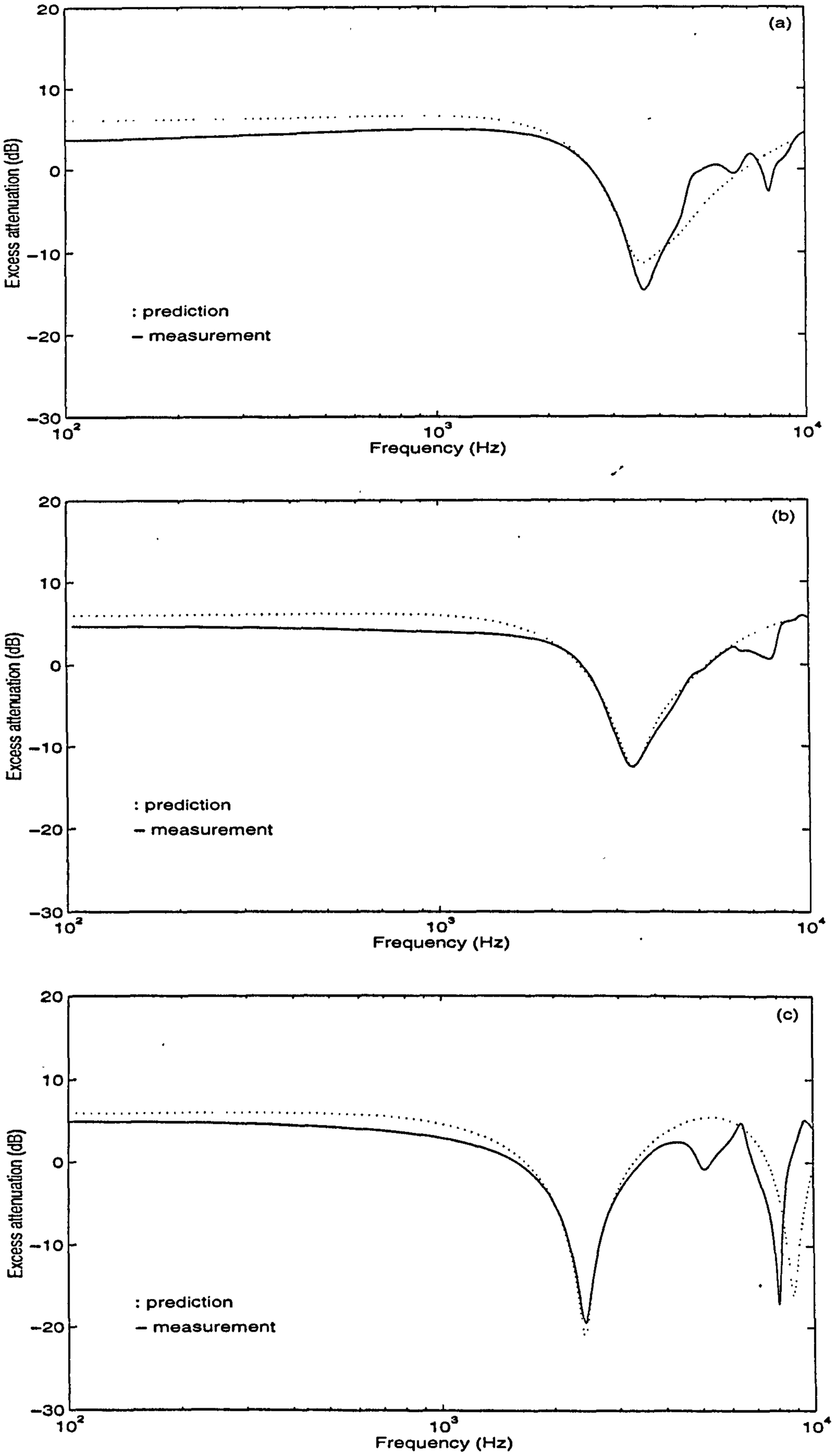

Figure 6.7 Excess attenuation obtained above a flat mat-on-masonite surface, with $\sigma_e = 4$ kPa s m^{-2}, $\alpha_e = 570$ m^{-1}, $r = 1.0$ m and $z_s = z =$ (a) 0.08 m, (b) 0.10 m and (c) 0.15 m.

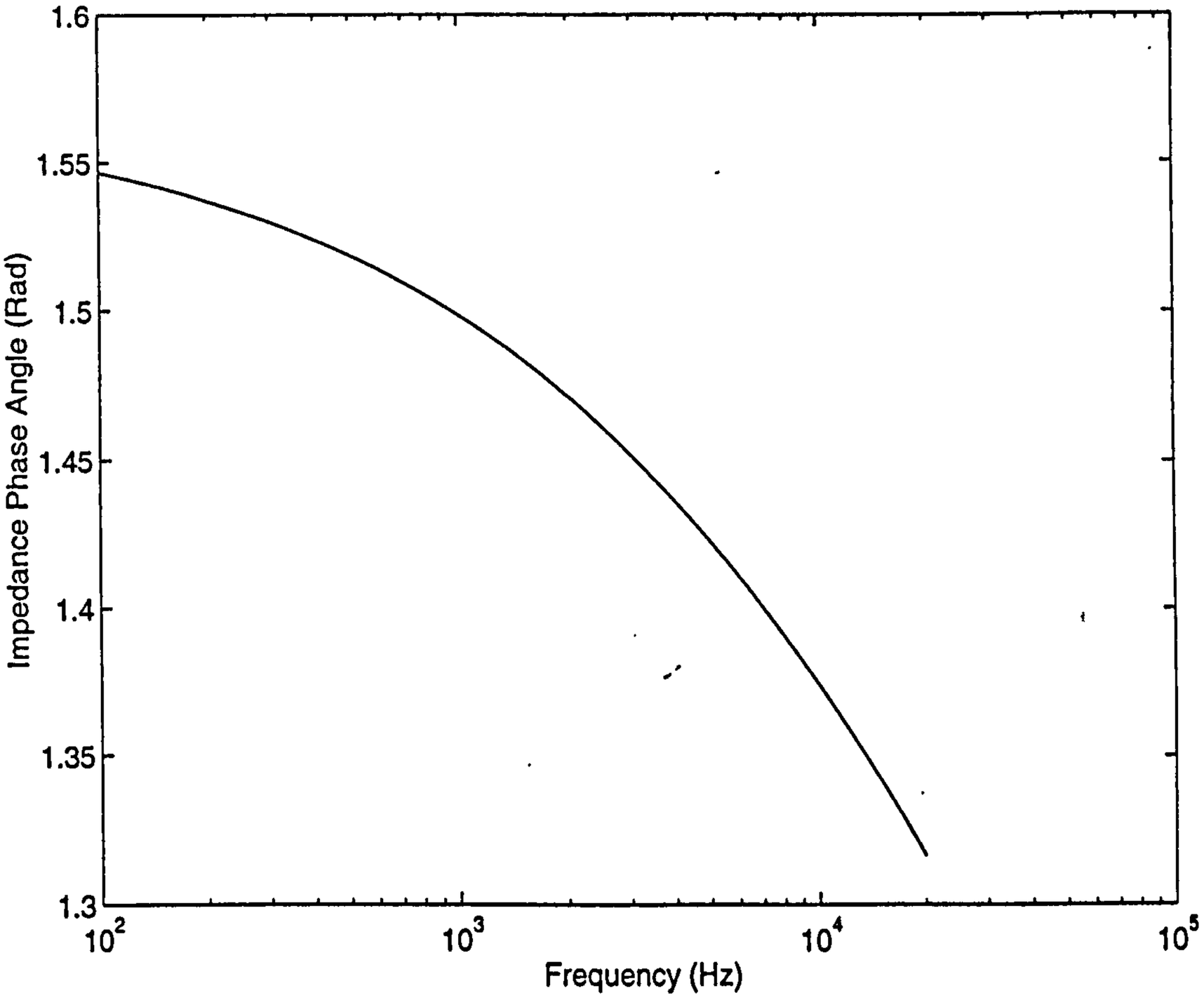

Figure 6.8 Predicted impedance phase angle, φ_z, of the mat-on-masonite surface versus frequency showing $\varphi_z > \pi/3$.

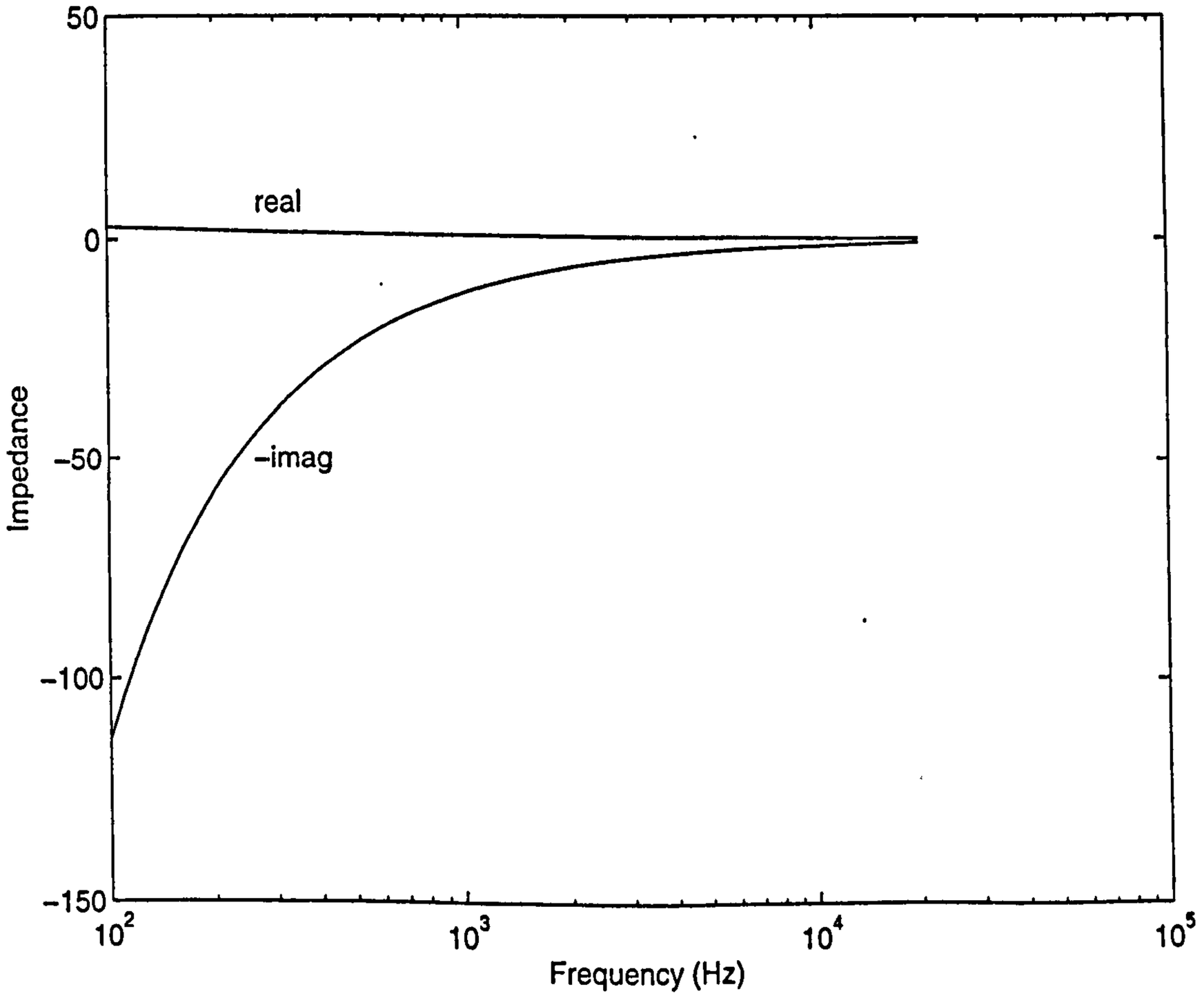

Figure 6.9 Predicted imaginary part and real part of the impedance of the mat-on-masonite surface versus frequency.

accord with predictions assuming local reaction and using the two parameter impedance model. Figure 6.8 shows the impedance phase angle of the mat-on-masonite surface as a function of frequency. The imaginary part and the real part of the impedance versus frequency are plotted in Figure 6.9. It is seen that the impedance of the mat-on-masonite surface satisfies $\varphi_z > \pi/3$. The imaginary component produces a decreasing amplitude above the surface with positive values larger than those of the real component.

6.1.4 The sound field above a convex mat-on-masonite surface

To investigate the surface wave contribution to the total sound field above a convex surface of finite impedance for $\varphi_z > \pi/3$, we performed a series of anechoic laboratory measurements above the mat-on-masonite convex surface ($dc/dz \sim -137.2$ s^{-1}) for three configurations (*cf.* Figure 4.5), *i.e.* along the surface, along the line of sight, and along a vertical distance across the bright and shadow zones in the frequency domain. The measurement results are presented as functions of range.

Pierce [3] suggested a technique for pole searching (*cf.* Chapter 3). Raspet *et al* [8] have improved this technique and proposed a numerical scheme (*cf.* Chapter 3). In order to examine these two techniques, the residue series calculations evaluated at the poles searched by these two techniques are compared with the measurement results. At lower frequencies where $|q|$ is small, the two techniques give similar results which are shown as the solid curves in Figure 6.10 to Figure 6.12 for the receiver placed along the surface, along the line of sight and along a vertical distance across the bright and shadow zones, respectively. In each figure, the results were plotted at frequencies of 1.0, 2.0 and 3.0 kHz, corresponding to $|q| = 0.24$, 0.58 and 0.97. The calculations agree with the measurements in each region.

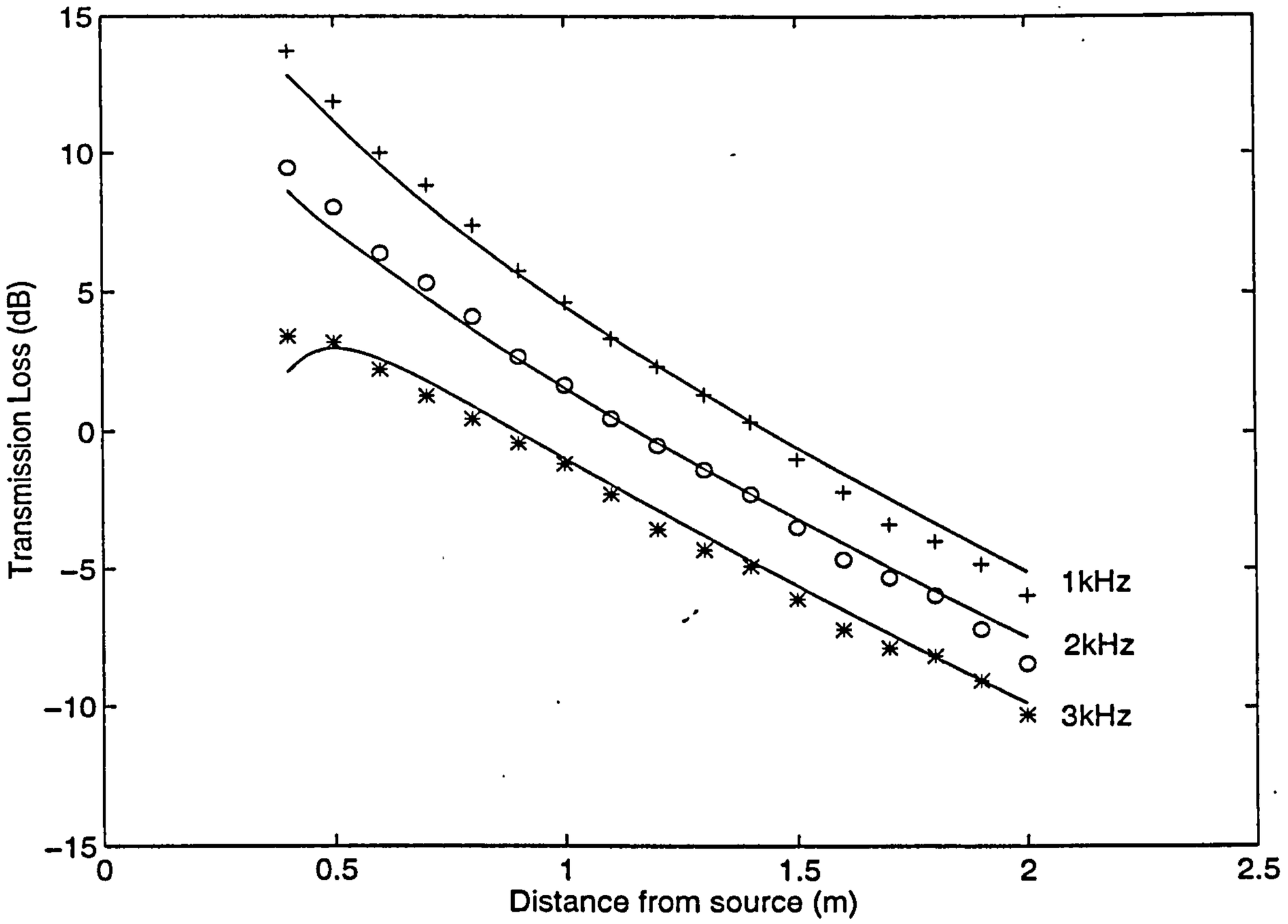

Figure 6.10 Transmission loss from a monopole source measured above a convex mat-on-masonite surface for the plus signs: 1.0 kHz, circles: 2.0 kHz and stars: 3.0 kHz. $\sigma_e = 4$ kPa s m^{-2}, $\alpha_e = 570$ m^{-1}, $z_s = 0.1$ m and $z = 0.06$ m. Solid curves: predictions.

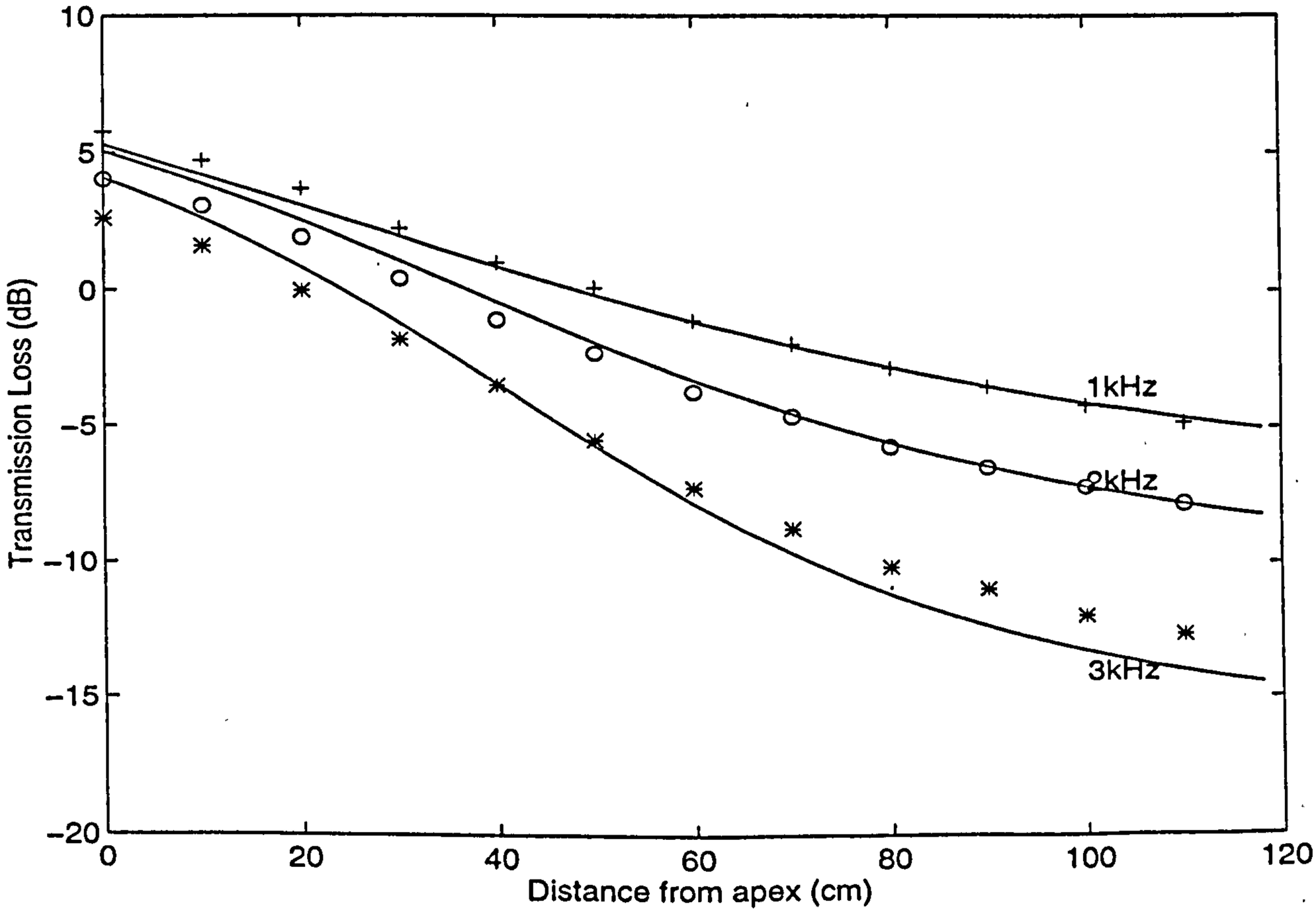

Figure 6.11 Same as **Figure 6.10**, but along the line of sight and $z_s = 0.21$ m.

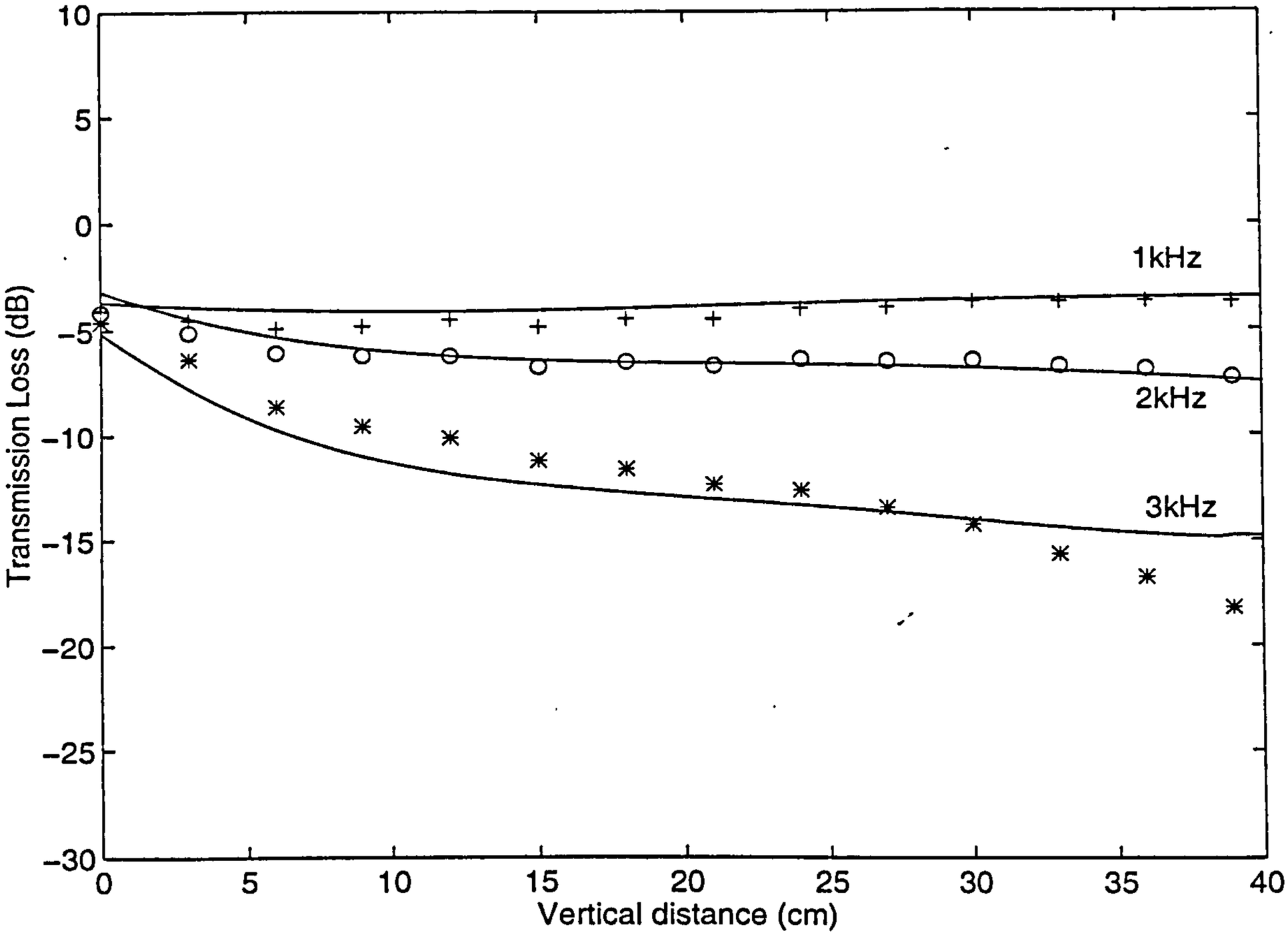

Figure 6.12 Same as **Figure 6.11**, but along a vertical distance z_v starting at $r_0 = 1.90$ m (*cf.* **Figure 4.5**).

As $|q|$ increases, however, the sum of the poles calculated by Pierce's technique, which failed to trace the pole related to the surface wave, diverges significantly from the experimental measurements as shown in Figure 6.13. The circles represent measurement results, while the solid curves represent predictions from the residue series solution evaluated at the poles that were calculated by Raspet *et al*'s technique, and the dashdot lines represent predictions from the solution evaluated at the poles calculated by Pierce's technique. Figure 6.13(a) shows the results along the convex mat-on-masonite surface for a frequency of 3.9 kHz ($|q| = 1.34$, $\varphi = 8°$), with a source height of 0.1 m and a receiver height of 0.08 m. The transmission loss shows a dip in the transition area and high levels in the shadow zone resulting from the contributions of the surface wave and the creeping

wave in the shadow zone, it is dominated by the first term, which includes the surface wave.

Figure 6.13(b) shows the results along the line of sight for the same frequency as Figure 6.13(a), with a source height of 0.21 m above the surface. The first term, which contains the surface wave contribution, dominates out to a distance of 1.5 m from the source along the limiting ray. As the receiver is moved further away from the source, the height of the receiver becomes higher above the surface, consequently the surface wave contribution becomes weaker and the second residue series term becomes the dominant term.

Figure 6.13(c) shows the results along a vertical distance starting with an arc length 1.90 m from the source for a frequency of 3.7 kHz ($|q| = 1.29$, $\varphi = 7.5°$). The source height is 0.21 m. The term with contribution from the surface wave only dominates at short ranges where the receiver is close to the surface. As the receiver height is increased, the surface wave contribution becomes smaller than other residue series terms. At a vertical distance of 40 cm, the surface wave contribution has decayed such that it is weaker than even the fourth residue series term.

It should be noted that the good agreement between experimental data and predictions in Figures 6.10 to 6.13 has been obtained with a somewhat simpler model for the surface impedance than was found necessary by Daigle *et al* [44].

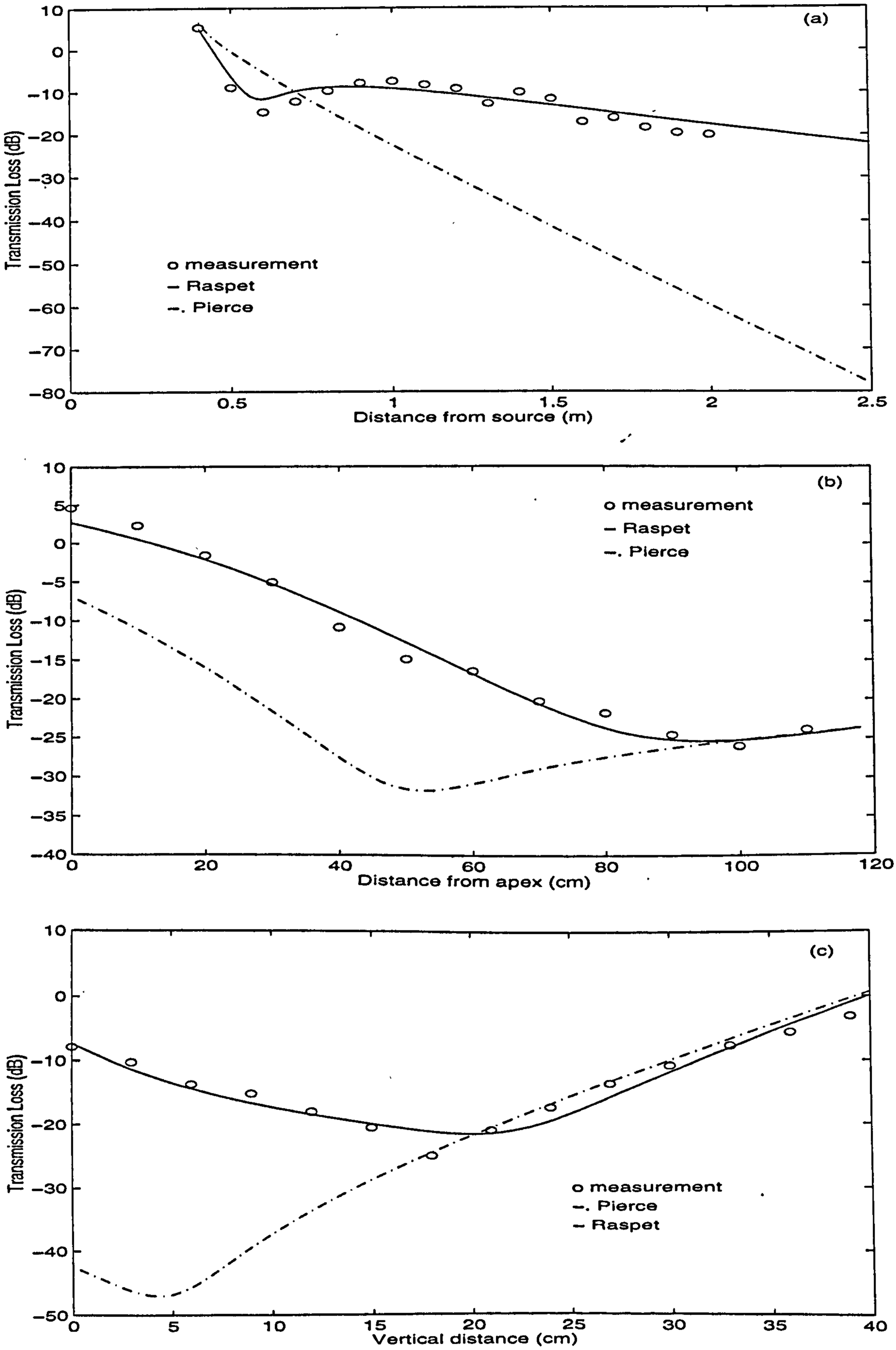

Figure 6.13 Transmission loss obtained above the convex mat-on-masonite surface for (a) along the surface, $f = 3.9$ kHz, $z_s = 0.10$ m and $z = 0.08$ m, (b) along the line of sight $f = 3.9$ kHz and $z_s = 0.21$ m, (c) along the vertical distance, $f = 3.7$ kHz, $z_s = 0.21$ m, z_v starting at $r_0 = 1.90$ m (*cf.* **Figure 4.5**).

6.2 The sound field due to a dipole source above a convex mat-on-masonite surface

For an impedance convex surface, the pole locations in the analytical expression for the sound field due to a dipole source are same as those in the analytical expression of the field due to a monopole source (*cf.* Chapter 3). The techniques of zero searching described above can be also used for calculating the field due to a dipole source. Similarly, if $\varphi_z > \pi/3$, there is a surface wave contribution for dipole sources as well. Figure 6.14 shows the contributions of the first four residue series terms as functions of distance from the sources due to (a) a horizontal dipole source and (b) a vertical dipole source above the mat-on-masonite convex surface with $\varphi_z = 80°$ at a frequency of 5.5 kHz. In each case, the first term contains the surface wave contribution. For both a horizontal and vertical dipole sources, there are interference patterns between the wave contributions of the first few terms. Figure 6.15 and Figure 6.16 are similar to Figure 6.14, except that the contributions are predicted for a frequency of 3.9 kHz, along the line of sight and along the vertical distance starting at 1.90 m from the source, respectively. In these figures, the pole contributions for the horizontal dipole source cannot be distinguished from those for the monopole source, while the pole contributions from the vertical dipole source have similar trends with range to those for the monopole source.

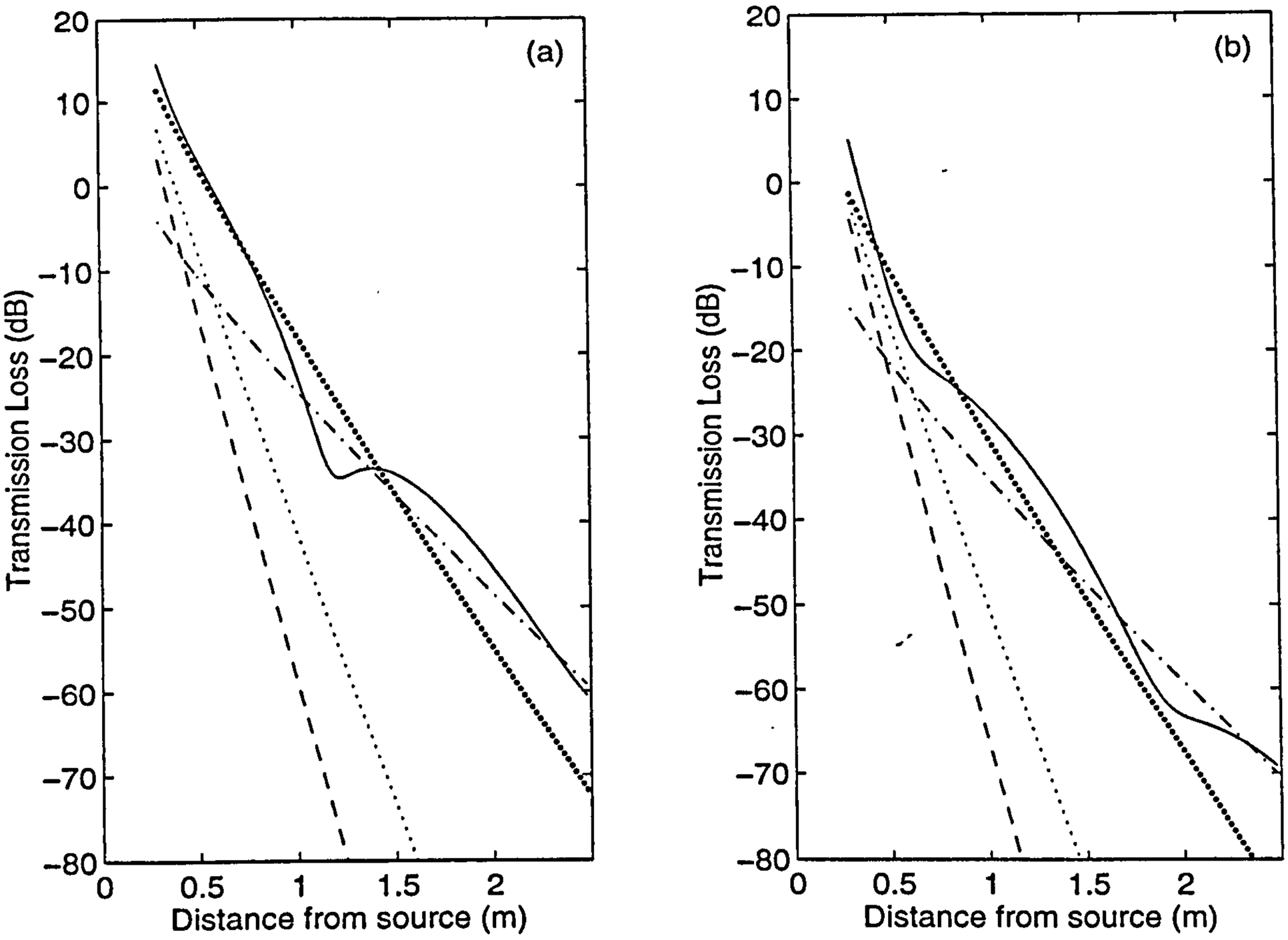

Figure 6.14 Pole contributions and total sound field along an impedance convex surface with $\sigma_e = 4$ kPa s m^{-2}, and $\alpha_e = 570$ m^{-1} for a frequency of 5.5 kHz, $z_s = 0.1$ m and $z \sim 0.00$ m. (a) horizontal dipole source and (b) vertical dipole source.

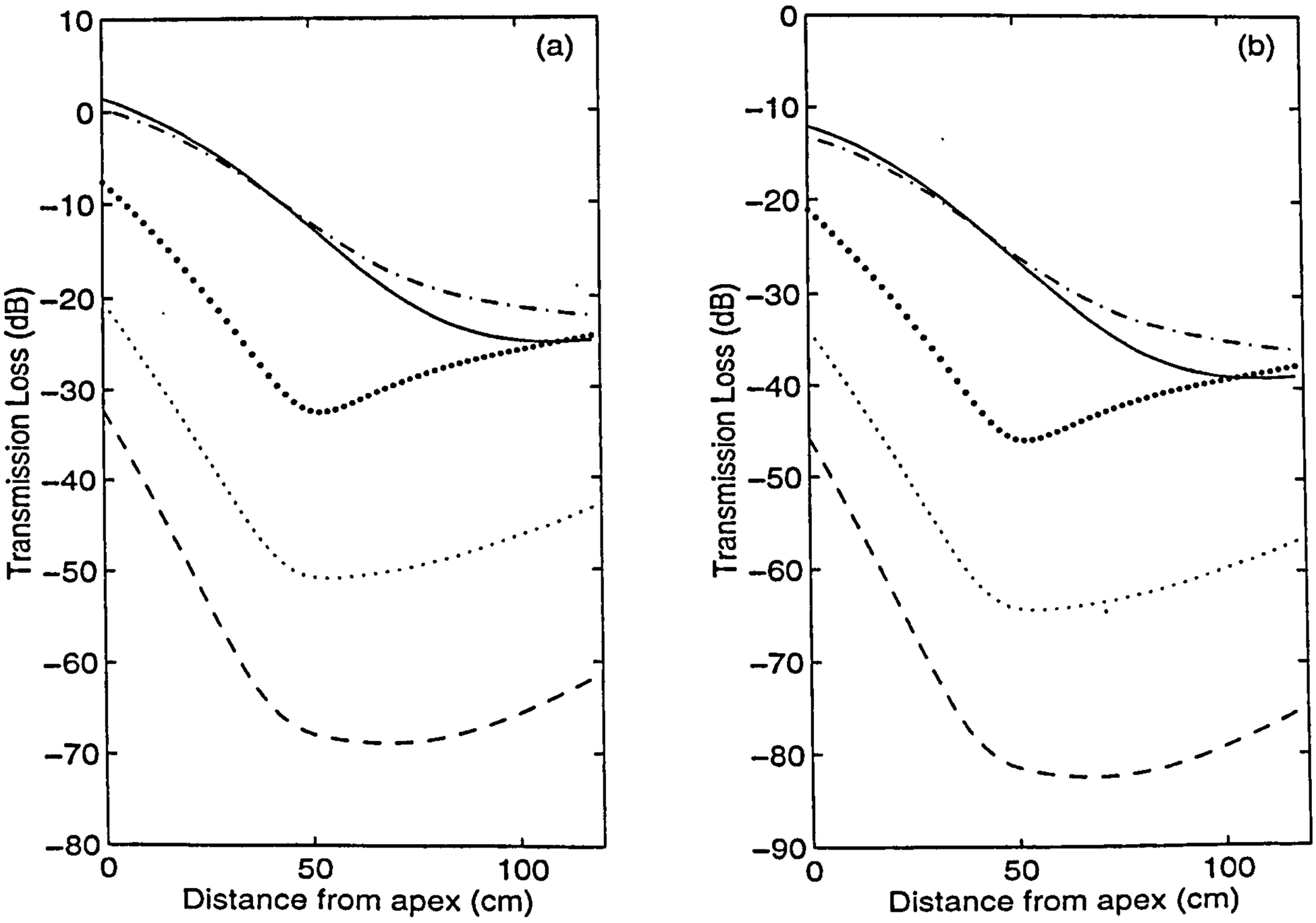

Figure 6.15 Same as **Figure 6.14**, but for a frequency of 3.9 kHz, $z_s = 0.21$ m and along the line of sight.

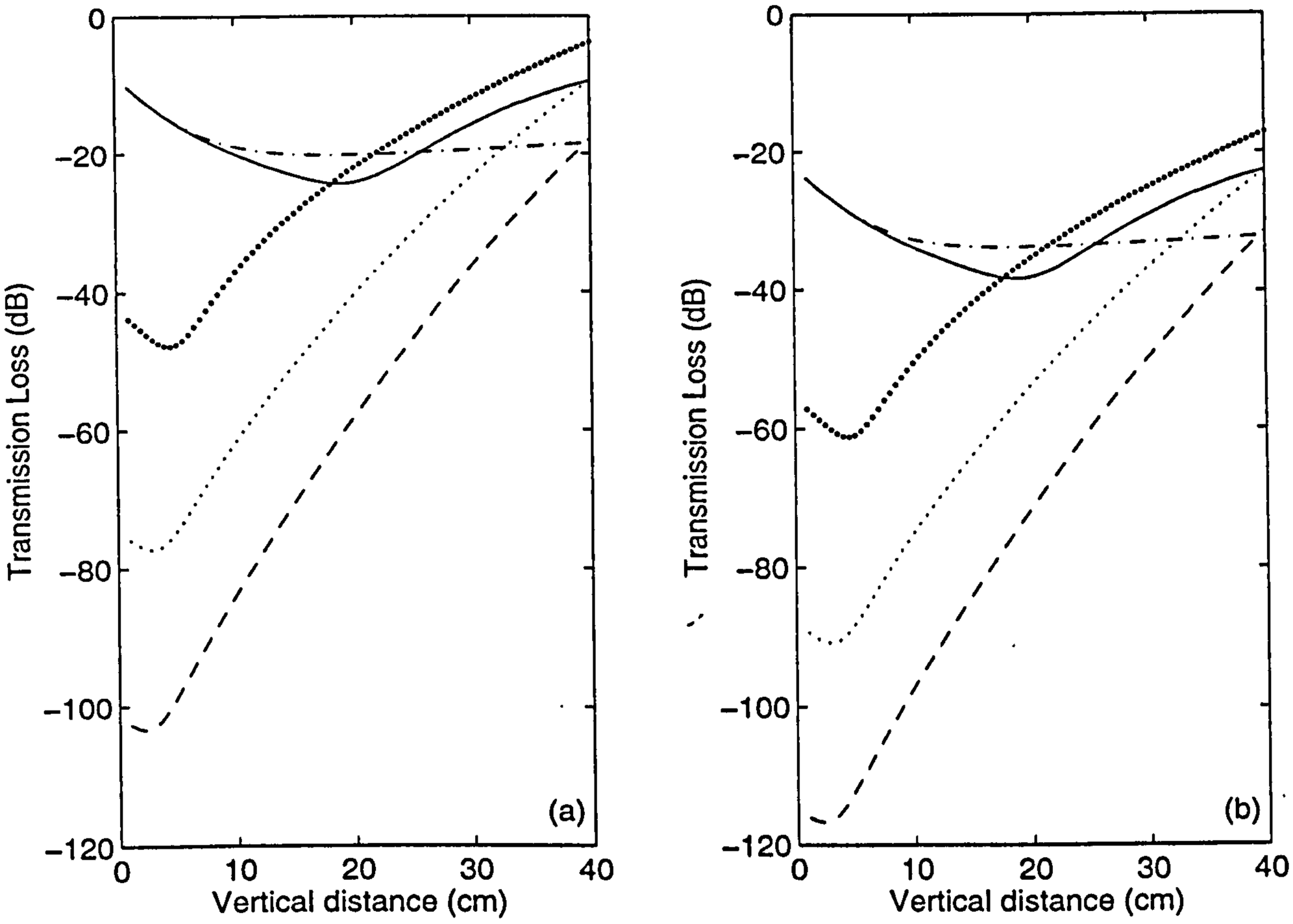

Figure 6.16 Same as **Figure 6.15**, but along a vertical distance z_v starting at $r_0 = 1.90$ m (*cf.* **Figure 4.5**).

Figure 6.17(a) shows measurements as a function of range, from a vertical dipole source, compared with predictions from the residue series solution evaluated at the poles calculated by Raspet *et al*'s technique and Pierce's technique. The measurements were made above the convex mat-on-masonite surface by using the vertical dipole source that has been described in Chapter 4. The data were taken at a frequency of 3.6 kHz ($|q| = 1.25$, $\varphi = 7.5^\circ$, or $\varphi_z = 82.5^\circ$), with a source height of 0.1 m and the receiver on the surface.

Figure 6.17(b) shows the results along the line of sight with a source height of 0.10 m and various receiver heights. Figure 6.17(c) shows the results along a vertical distance z_v starting at a distance of 1.90 m from the source (*cf.* Figure 4.5).

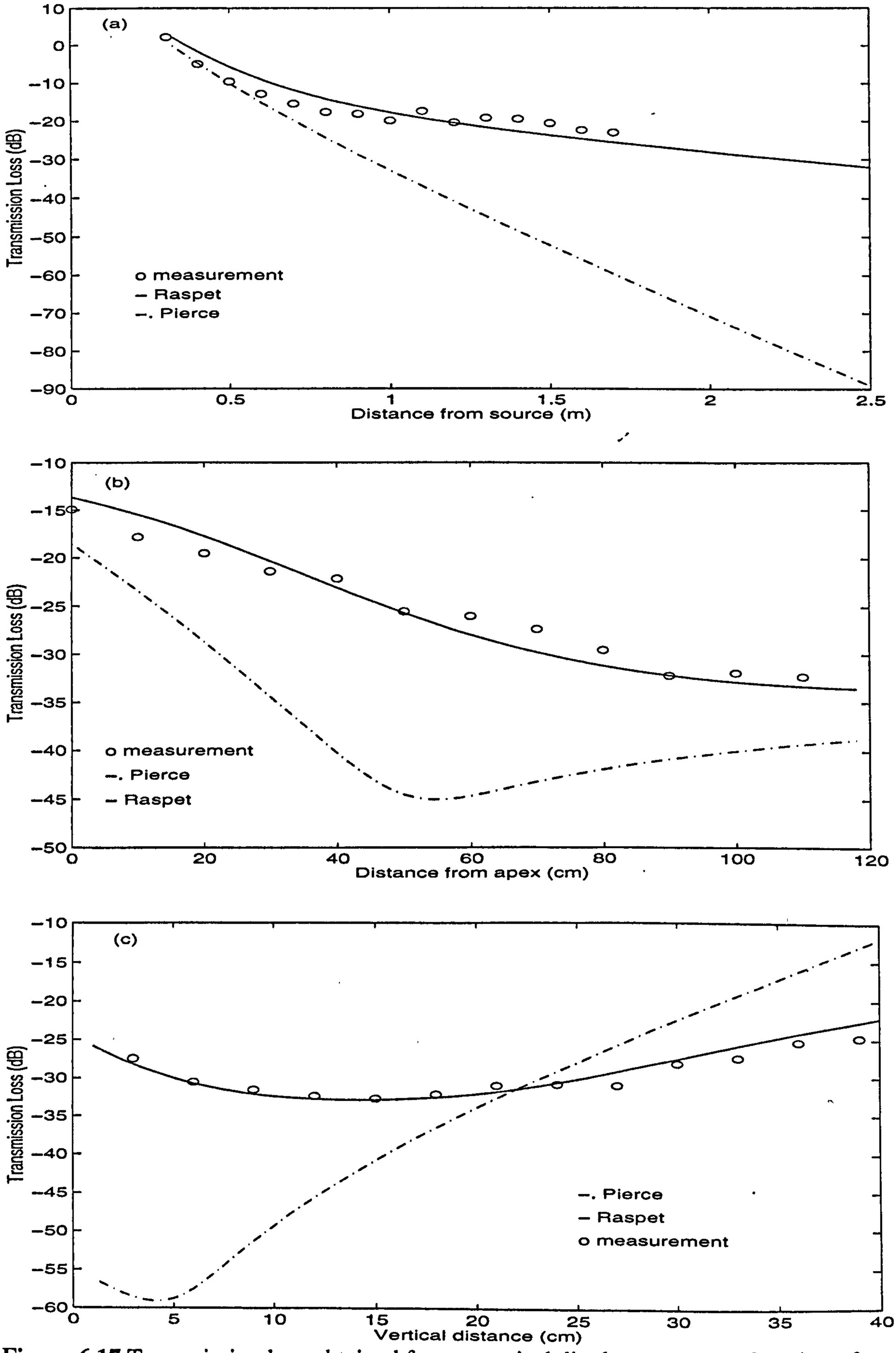

Figure 6.17 Transmission loss obtained from a vertical dipole source, as a function of range along the convex mat-on-masonite surface for a frequency of 3.6 kHz. $z_s = 0.10$ m, (a) along the surface and $z \sim 0.00$ m, (b) along the line of sight and (c) along a vertical distance z_v starting at $r_0 = 1.65$ m (*cf.* **Figure 4.5**).

The dashdot curves in Figure 6.17 represent the residue series predictions from poles evaluated by using Pierce's technique, while the solid curves represent the predictions from poles evaluated by using Raspet *et al*'s technique. The measured data are indicated by the circles. It is seen that the agreement between the circles and the solid curves is much better than that between the circles and the dashdot curves.

6.3 Observations of surface waves in the time domain

In pulse experiments above a lighting diffuser lattice mounted on a flat rigid surface, the surface wave has been observed as a separate arrival from the body wave [44, 71]. So far there have been no reports of similar experiments for propagation over a curved surface of finite impedance.

Figure 6.18 to Figure 6.22 show the results of measurements obtained above the convex mat-on-masonite surface, where the source height was approximately 4.0 cm and the receiver heights were 1.0 cm, 5.0 cm, 10.0 cm, 15.0 cm, and 20.0 cm above the surface at a constant range of 1.5 m. In these configurations, all receiver positions were below the line of sight. For comparison, the measurement results obtained above a flat mat-on-masonite surface, where the source and receiver were located at the same heights as those above the convex surface, are also shown in the upper parts of these figures. The signal was detected in a 1/3 octave band centred at 4 kHz. At this frequency, there was a sufficient arrival time difference between the surface wave and the remainder of the field beyond a horizontal range of 1.5 m. That surface wave appears as a separate arrival above both the flat and the convex surfaces. The velocity of the surface wave appears less than the velocity of that of the remaining field, which in the case of a convex surface may be identified as the creeping wave. As the receiver was moved closer to the surface, the surface wave amplitude became

much larger than that of the creeping wave. However, the surface wave component of the pulse decayed quickly with increasing receiver height. At a height of 20.0 cm above the convex surface, the surface wave amplitude was much smaller than the creeping wave amplitude. This satisfies a standard property of a true surface wave [41]. Similar results can be observed over the flat mat-on-masonite surface.

Figure 6.23 compares the pulse in a 1/3 octave band centred at a frequency of 4 kHz measured over the convex surface, where the source and receiver were 2.0 m apart and at heights of 4.0 and 5.0 cm, with the reference pulse that was generated by the point source and measured in a free field at an identical distance between the source and the receiver to the measured pulse. The second arrival in the reference pulse indicates an unwanted reflection, which has been noticed to be caused by the tannoy speaker. This unwanted reflection can be filtered out by appropriate signal processing techniques so that it does not affect the measurements of sound pressure levels.

Figure 6.24 and Figure 6.25 show that the measured pulses deform with increasing range. The pulse was measured at a carrier frequency of 4 kHz. At shorter ranges (< 1.0 m), the creeping wave and surface wave overlap in time, with the surface wave arrival delayed with respect to that of the creeping wave. As the range was increased, beyond a horizontal range of 1.0 m, for source and receiver heights of 4.0 and 2.0 cm, respectively, the two waves started to separate.

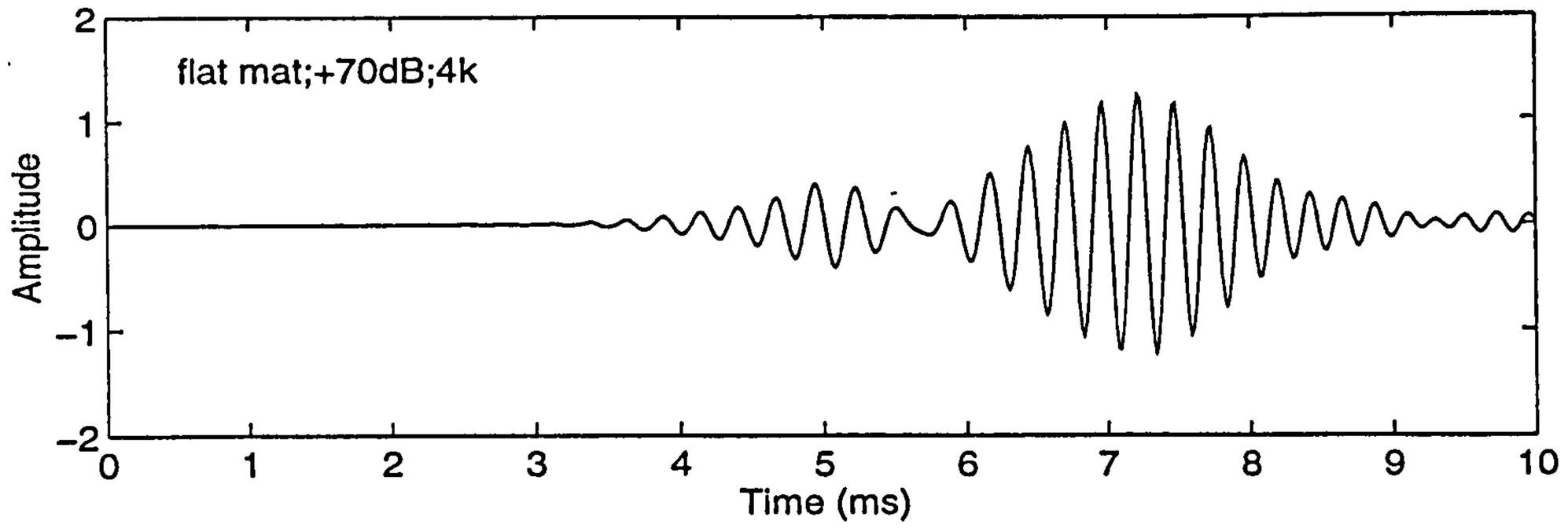

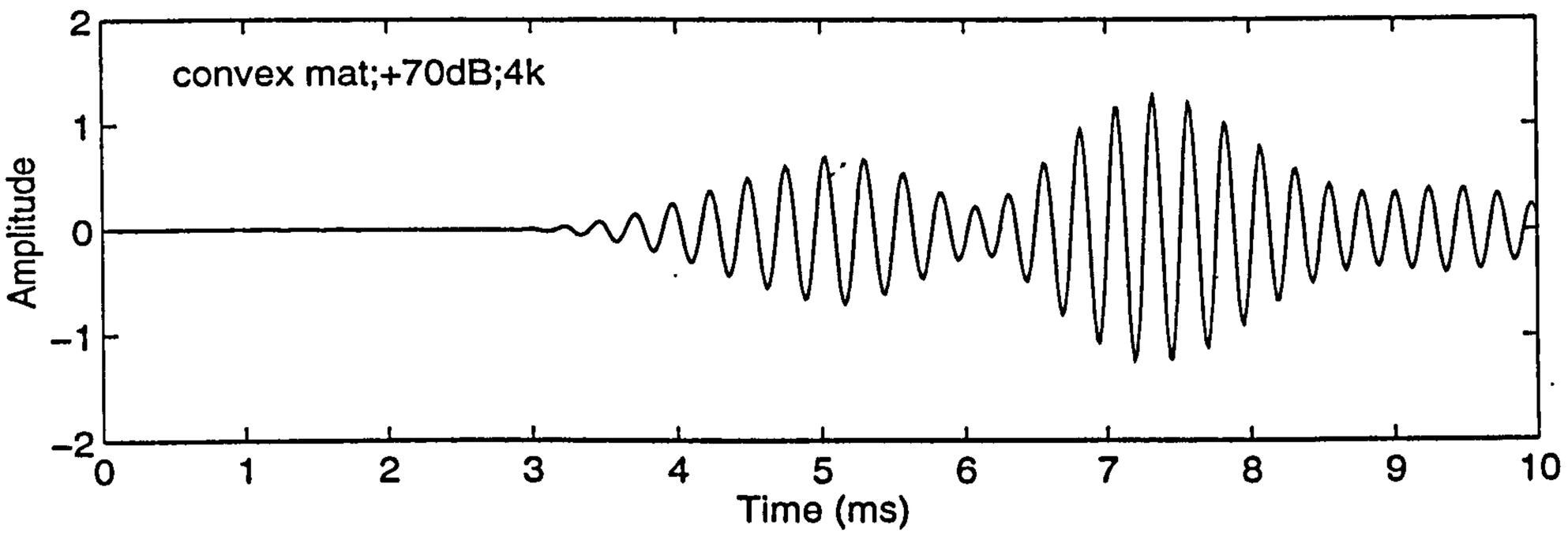

Figure 6.18 Pulses measured above the convex mat-on-masonite surface at a frequency of 4 kHz, for $z_s = 4.0$ cm, $z = 1.0$ cm and $r = 1.5$ m.

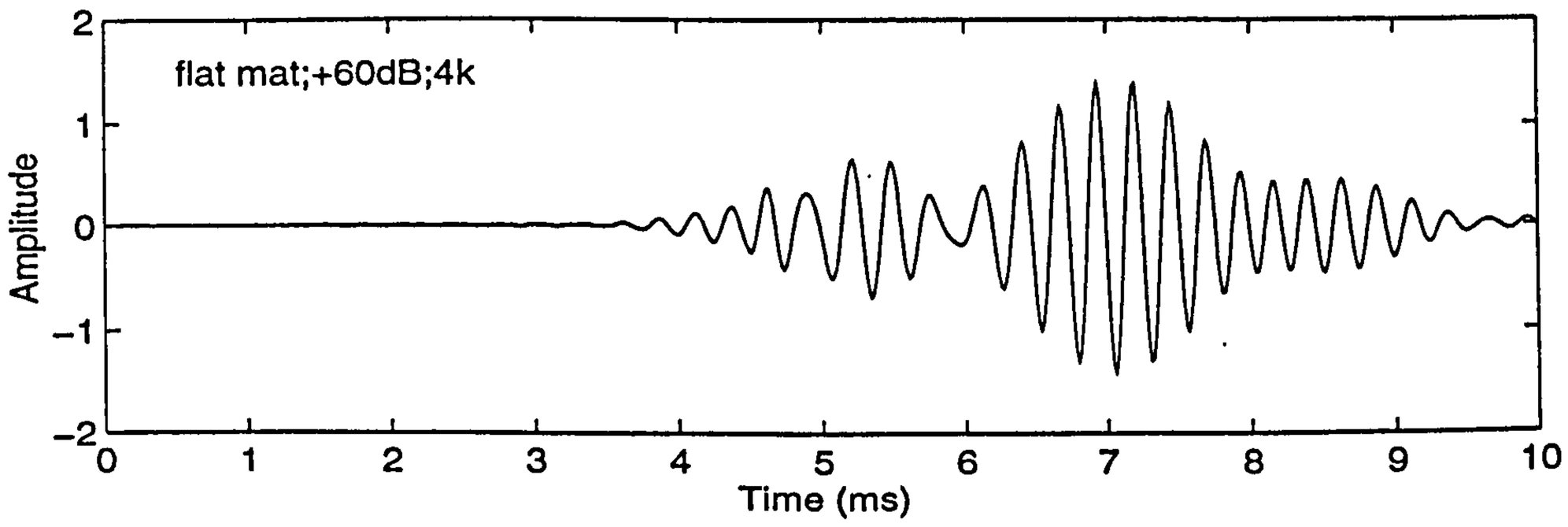

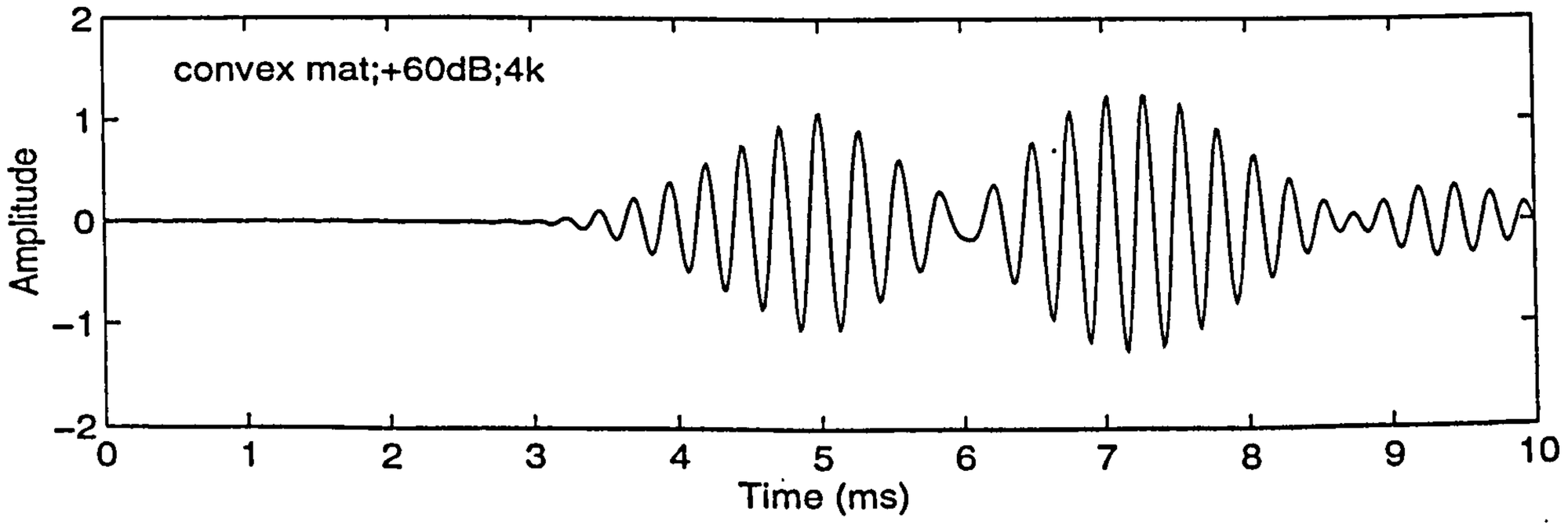

Figure 6.19 Same as **Figure 6.18**, but $z = 5.0$ cm.

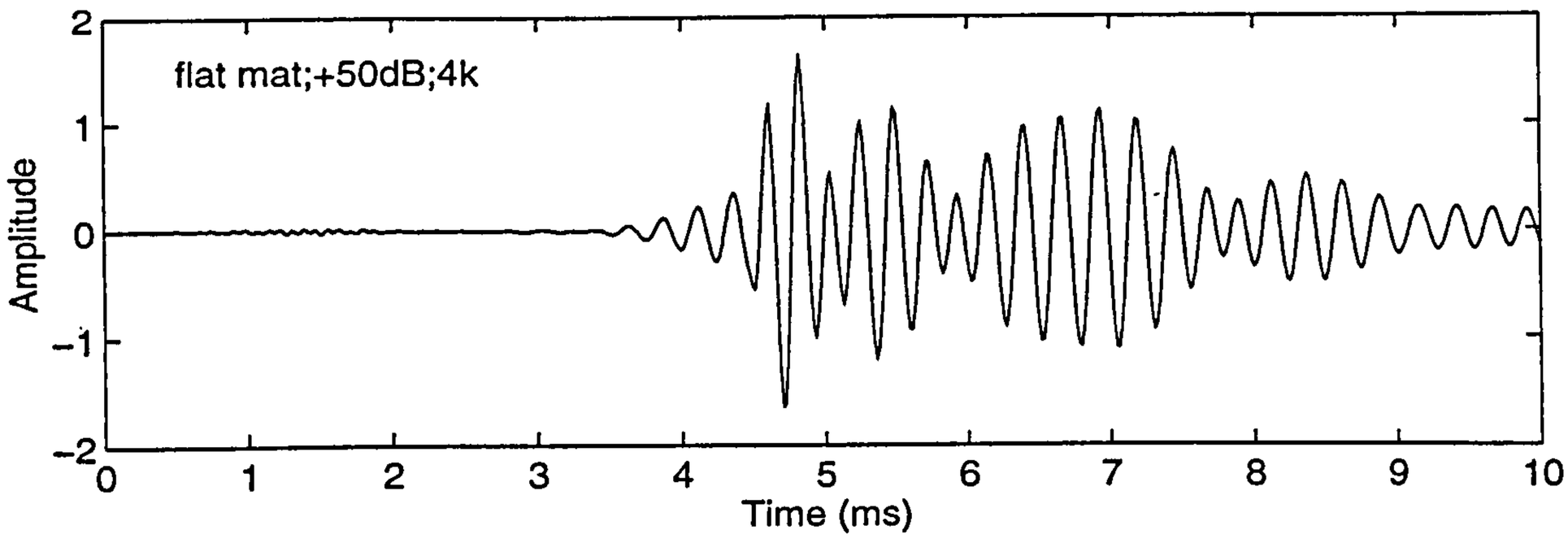

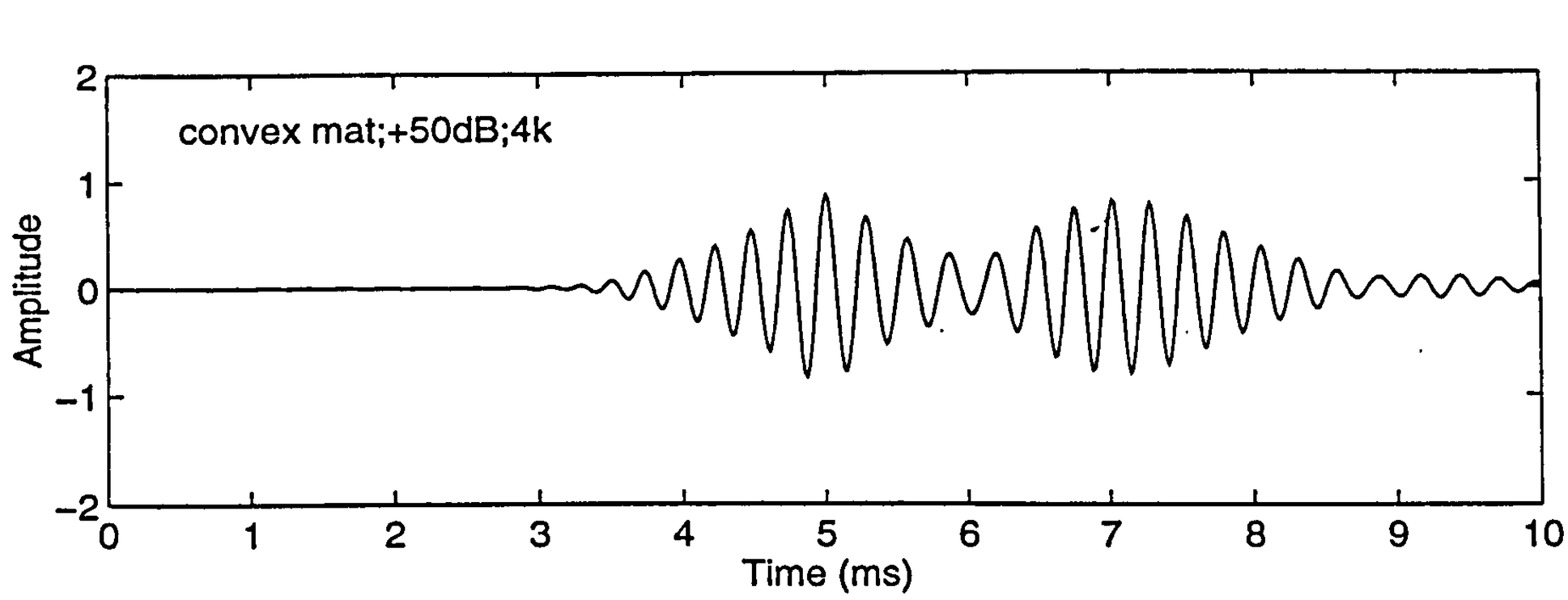

Figure 6.20 Same as **Figure 6.18**, but $z = 10.0$ cm.

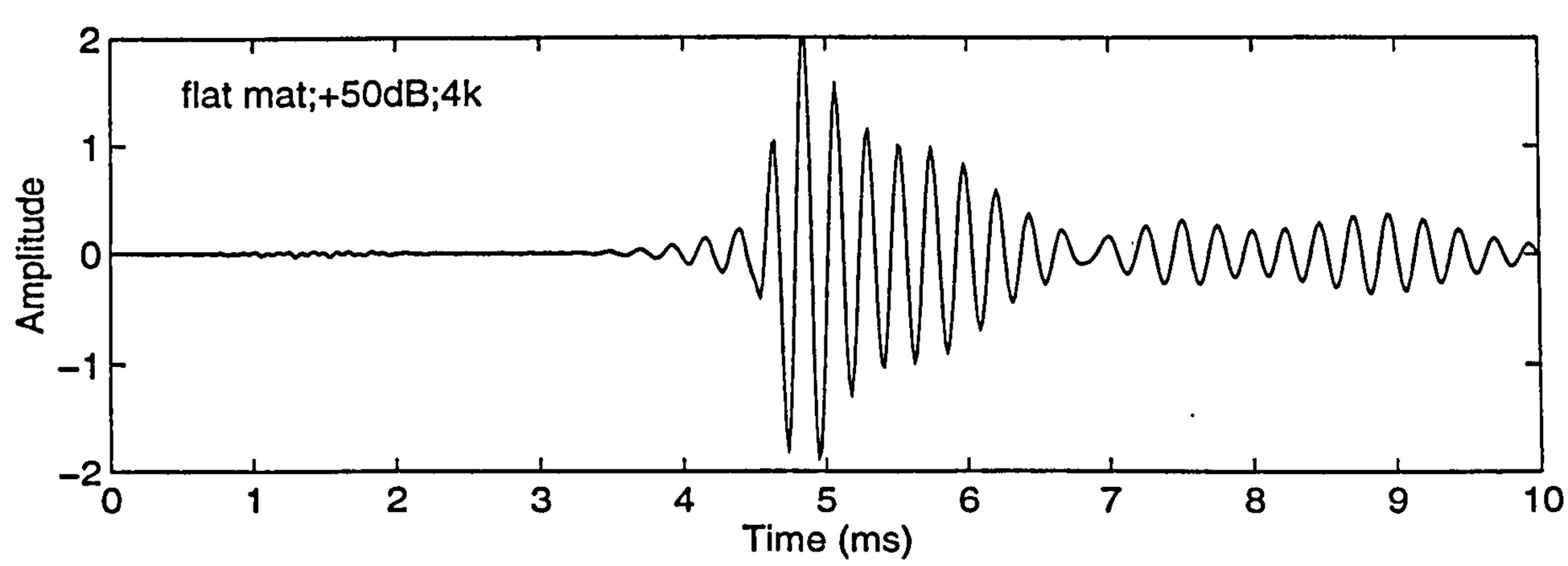

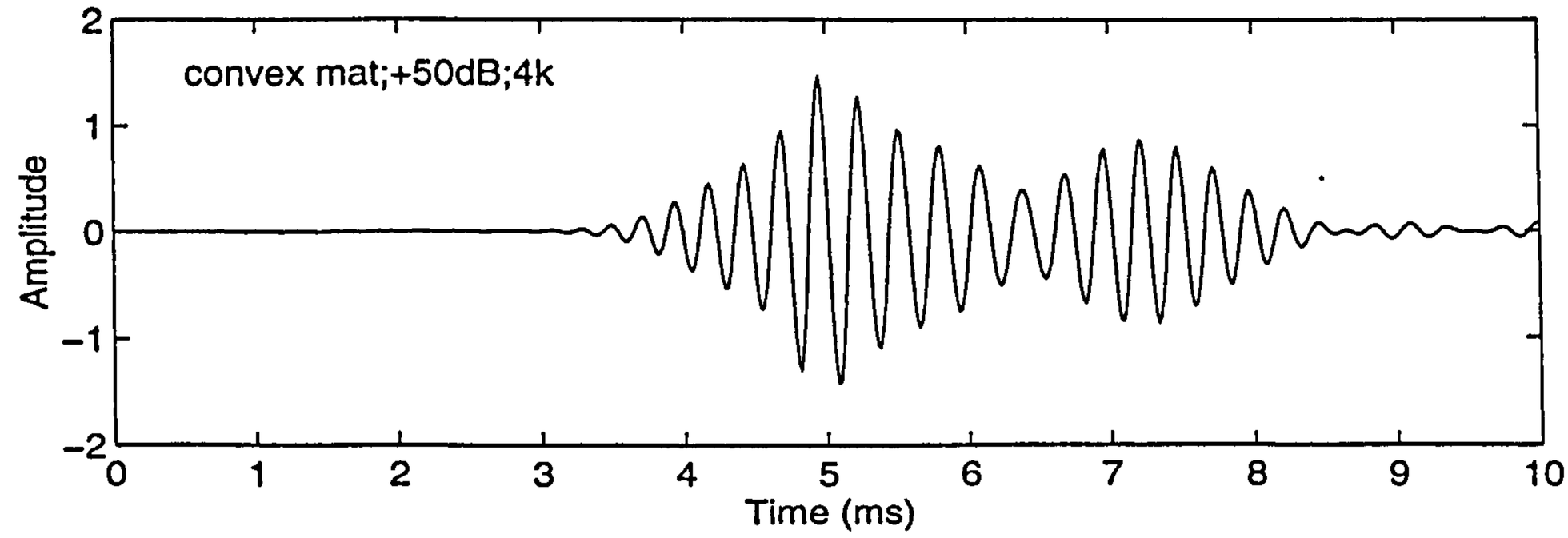

Figure 6.21 Same as **Figure 6.18**, but $z = 15.0$ cm.

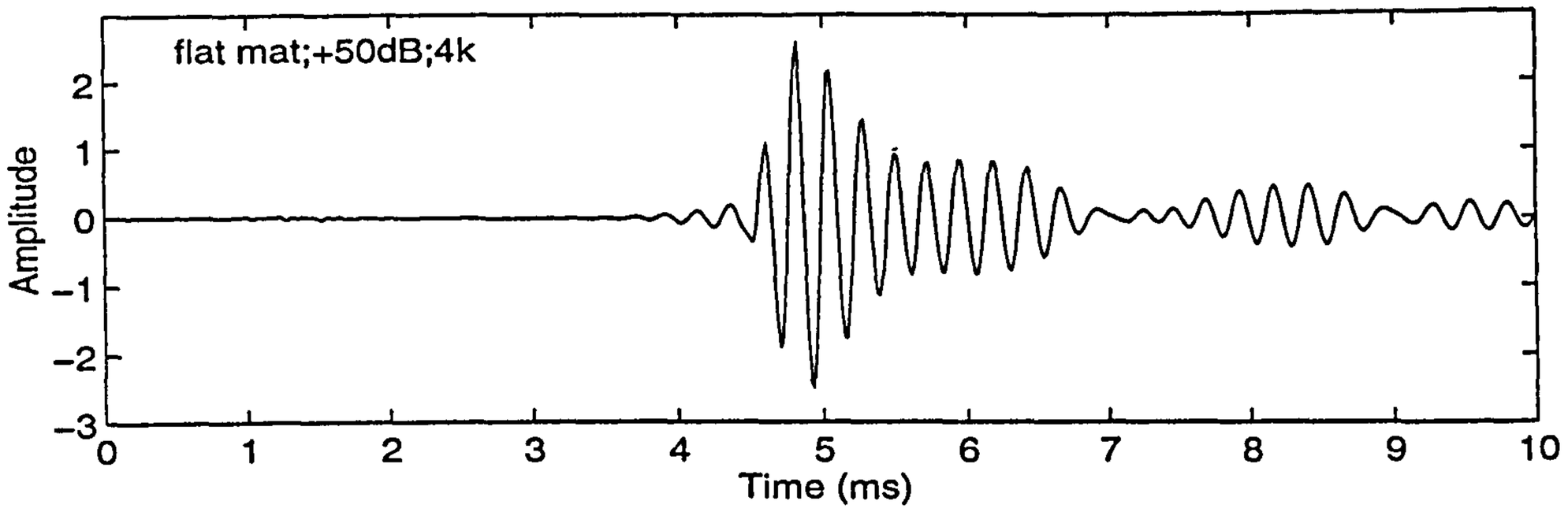

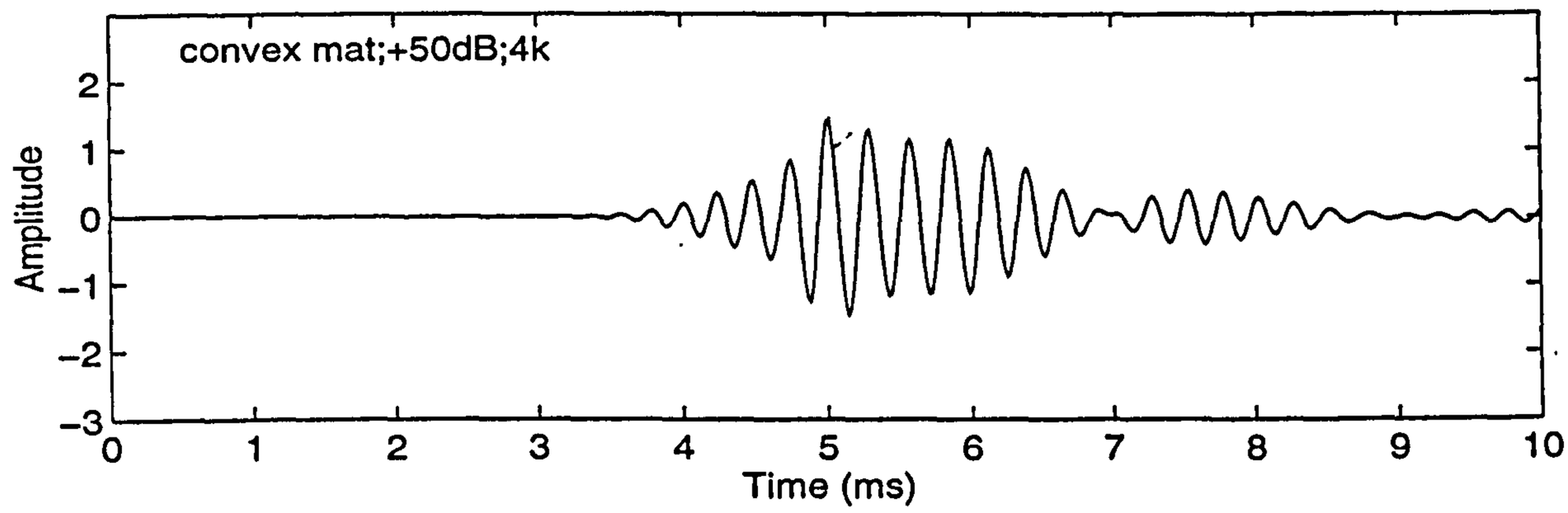

Figure 6.22 Same as **Figure 6.18**, but $z = 20.0$ cm.

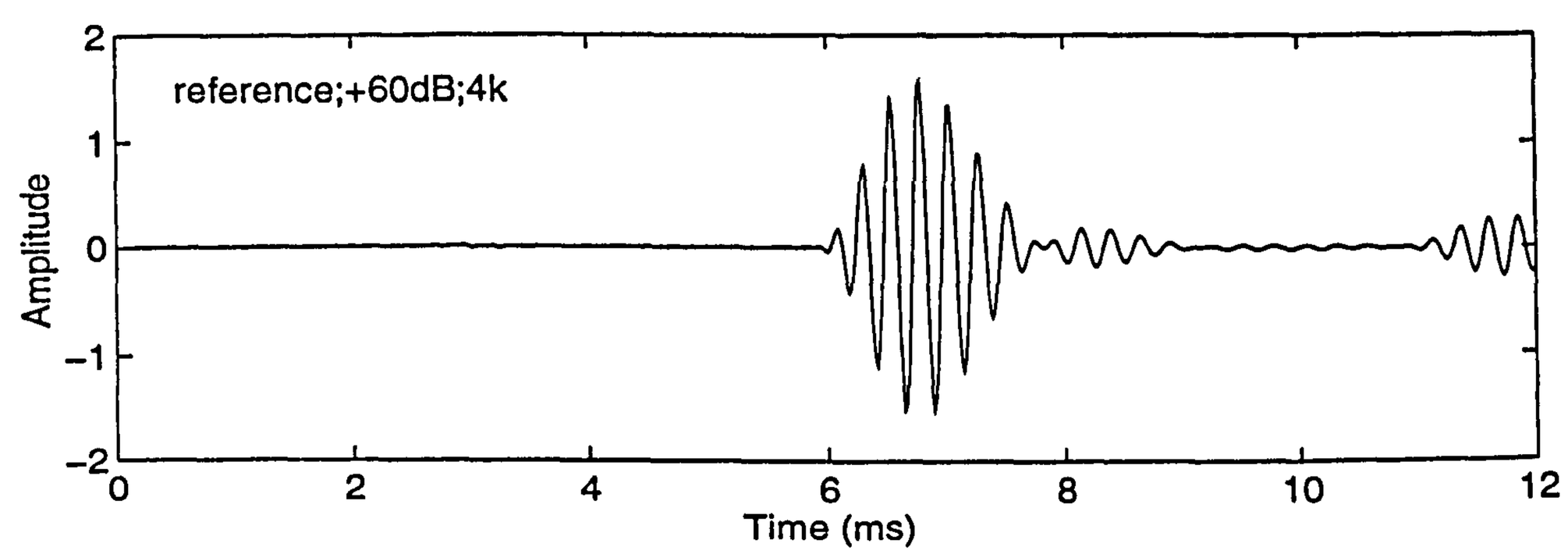

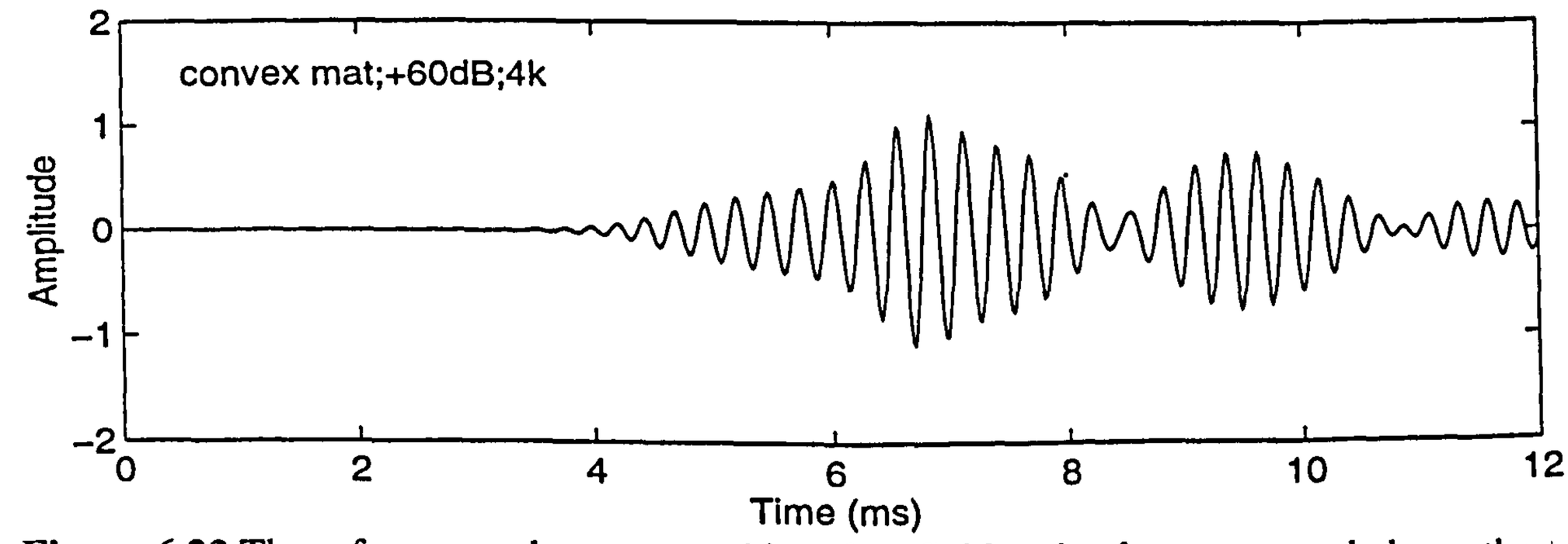

Figure 6.23 The reference pulse measured in a free field and pulses measured above the convex mat-on-masonite surface at a frequency of 4 kHz, for $z_s = 4.0$ cm, $z = 5.0$ cm and $r = 2.0$ m.

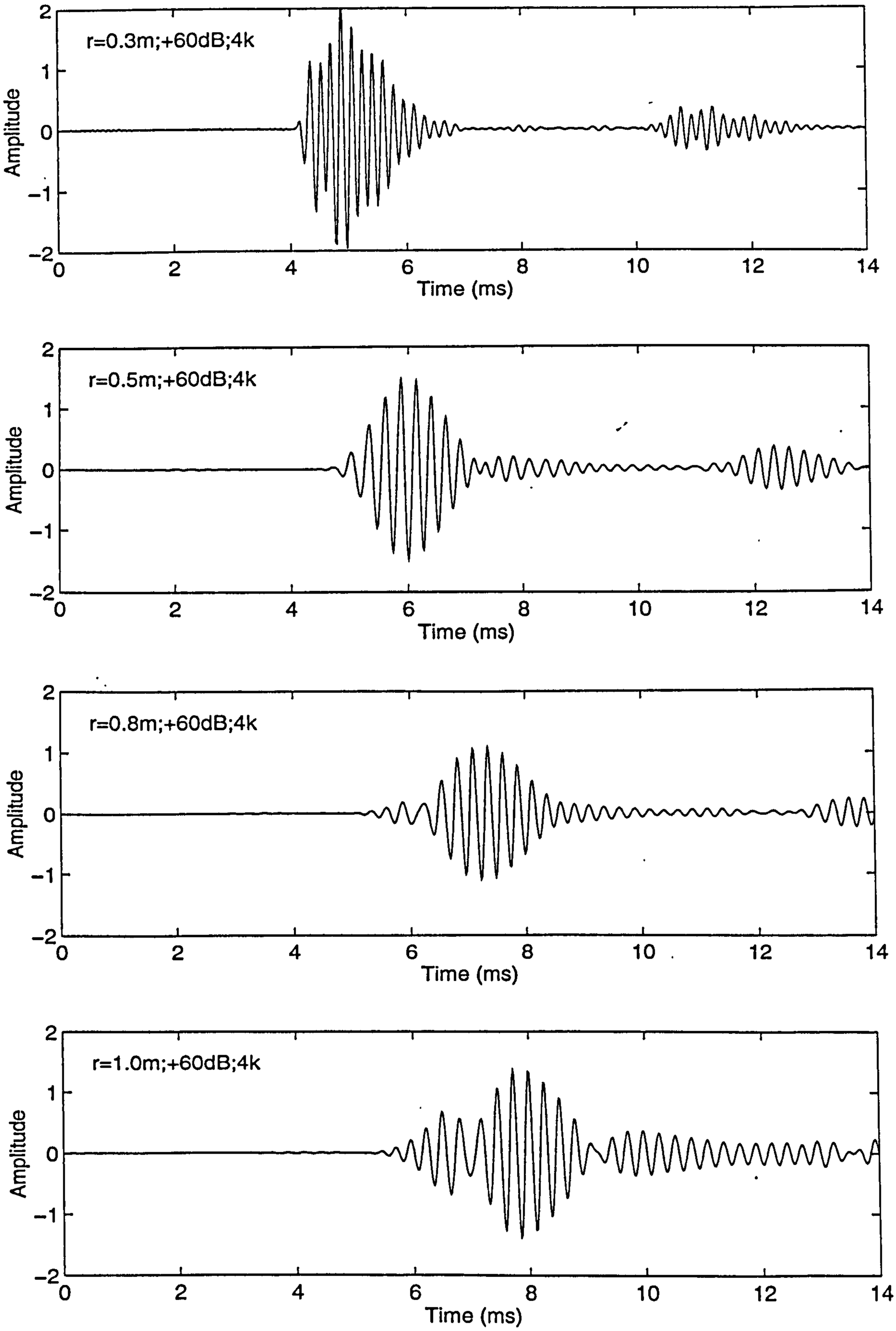

Figure 6.24 Pulses measured above the convex mat-on-masonite surface at a frequency of 4 kHz, for $z_s = 4.0$ cm, $z = 2.0$ cm and various ranges.

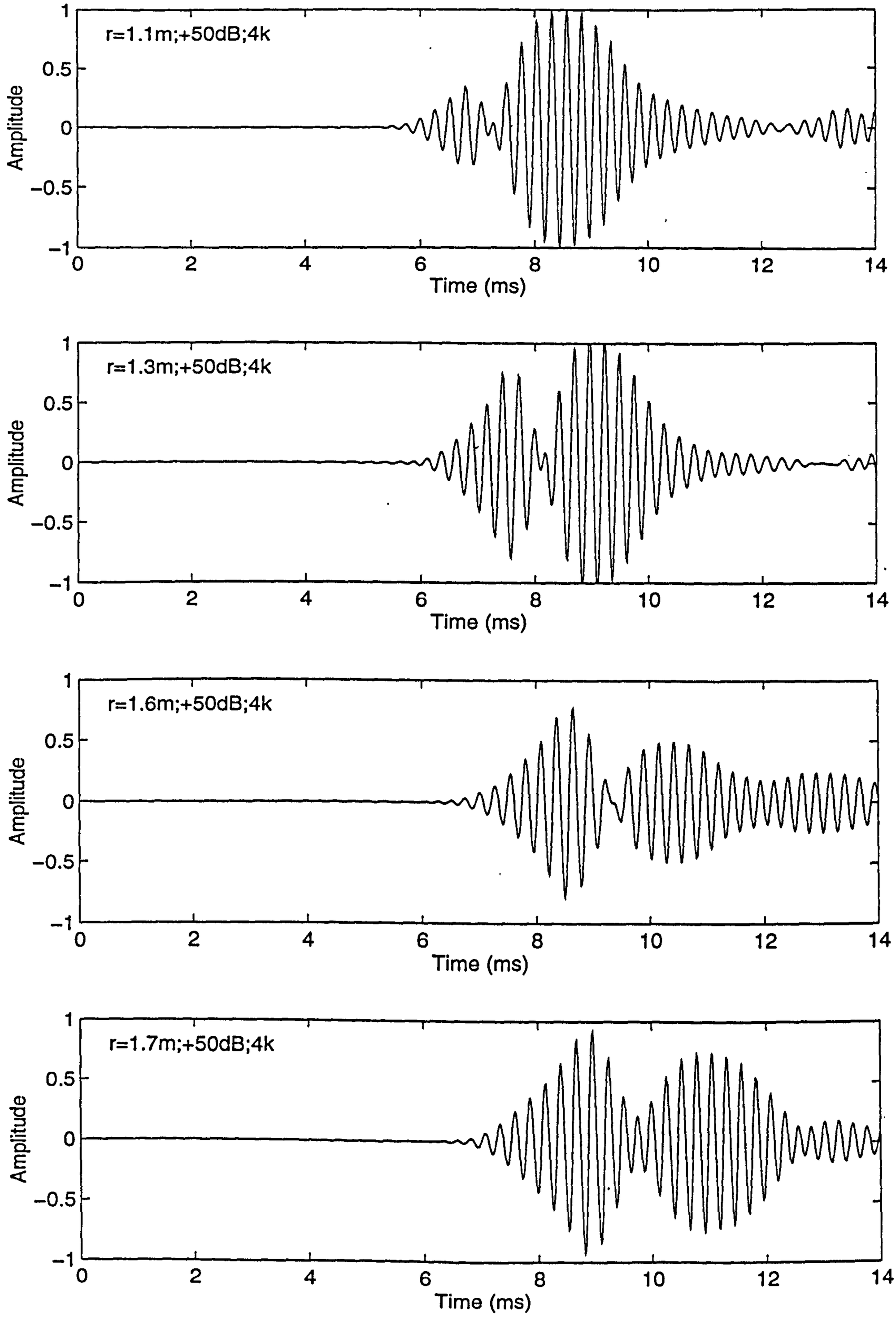

Figure 6.25 Same as **Figure 6.24**.

6.4 Surface wave pole

In Figure 6.25, two separate arrivals for the creeping wave and the surface wave are apparent beyond a distance of 1.3 m. It is, therefore, possible to measure the surface wave and the creeping wave contributions to the total sound field by means of appropriate signal processing technique, the Maximum Length Sequence (MLS) technique. In this signal processing technique, the sound propagation path may be considered as a system with one input and one output, which extends from the source to the receiver. In a time domain such a system can be identified as an impulse response. The MLS technique offers that the travel time of the arrival is known for each pulse sequences, as shown in Figure 6.26. Using a time window, we can taper [151] the framed time data to analyze any separate wave contribution in a frequency domain. For example, we can taper the framed time data between t_1 and t_2 for the creeping wave analysis, the framed time data between t_2 and t_3 for the surface wave analysis, and the framed time data between t_1 and t_3 for the total sound field analysis. The unwanted reflection can be therefore cut out by this technique.

Figure 6.27 shows the transmission loss plotted for a frequency of 3.9 kHz, as a function of distance from the source to the receiver for the framed time data of the surface wave, the creeping wave and the total sound field, respectively. The source and receiver heights were 4.0 and 5.0 cm, respectively. The dotted line represents the sound field predicted by using the first pole, while the dashdot line represents the sound field predicted by using the remaining poles between the second pole and the twentieth pole, which should represent the corresponding wave contributions. The total sound field was predicted by using all these twenty poles. The plus signs represent the measured surface wave contribution, whereas the stars represent the measured creeping wave contribution. It is noted that there may be no clear separation between the creeping wave and the surface wave in some cases. However, the wave amplitude at the overlapped region is much less than that in the region

of either the creeping wave or surface wave. In addition, the overlapped region occupies a relatively small time interval. Consequently the contribution of this overlapped wave is negligible. Raspet *et al* [8] suggested that the first pole is the surface wave pole and the remaining poles are the ordinary residue series poles. If this suggestion is correct, the plus signs should agree with the dotted line and the solid line within the shadow zone, while the stars should agree with the dashdot line. However, the results presented in Figure 6.27 are different. The levels represented by the plus signs are several decibels lower than the levels represented by the dotted line. This means that the dotted line (the prediction using the first pole) over-predicts the surface wave contribution. The levels represented by the stars are at much higher levels, up to 50 dB, higher than the levels represented by the dashdot line. In other words, the dashdot line (the prediction using the poles between the second pole and the twentieth pole) under-predicts the creeping wave contribution significantly. The contribution from the first term of the residue series, represented by the dotted line, which dominates the total sound field deep in the shadow zone, appears to be the sum of both the surface wave and creeping wave. This implies that the first pole includes *both* the surface wave contribution *and* the main part of the creeping wave contribution. Hence, it is somewhat misleading to refer this pole as the surface wave pole [8].

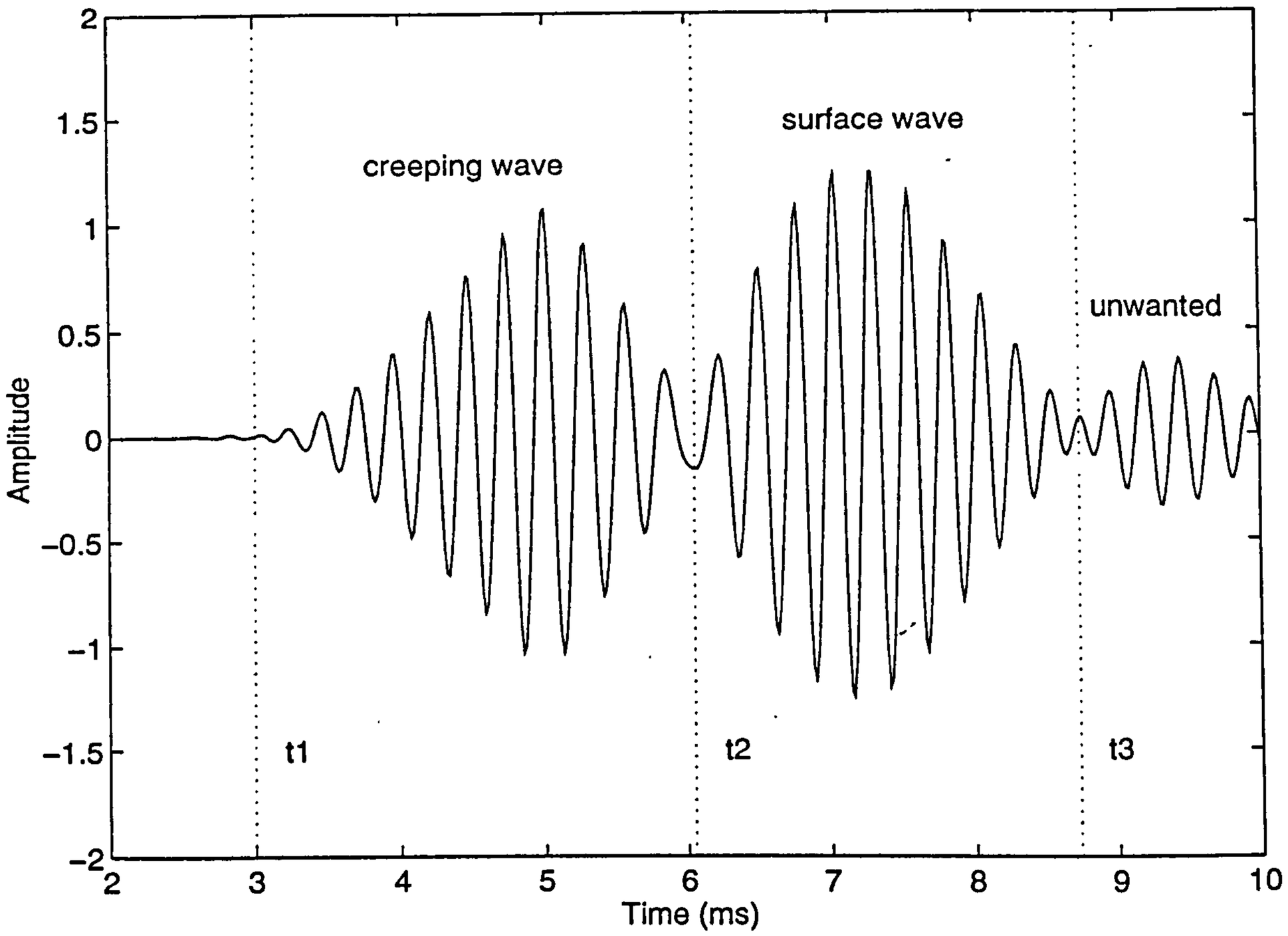

Figure 6.26 Pulses measured above the mat-on-masonite convex surface at a frequency of 4 kHz, for $z_s = 0.04$ m, $z = 0.05$ m and $r = 1.5$ m.

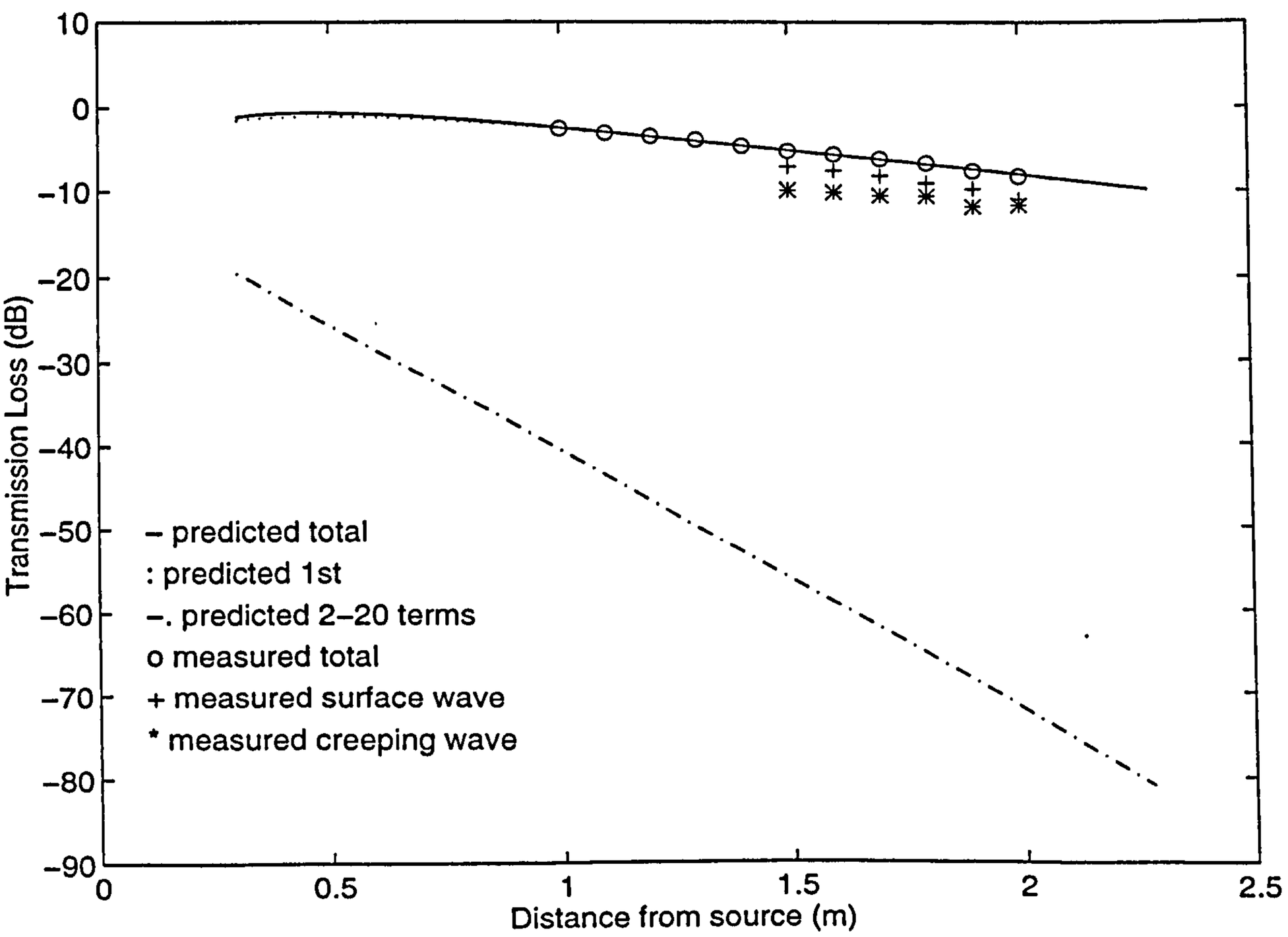

Figure 6.27 Transmission loss obtained as a function of range above the convex mat-on-masonite surface for a frequency of 3.9 kHz. $z_s = 0.04$ m, $z = 0.05$ m.

6.5 Summary

A series of laboratory experiments has been conducted to study the sound field above a convex mat-on-masonite surface with an impedance in which the imaginary part is greater than the real part and where $\varphi_z > \pi/3$. Monopole, horizontal dipole and vertical dipole sources have been used in these experiments. There is generally good agreement between the measurements and the residue series predictions from poles evaluated by using Raspet *et al*'s technique rather than by using Pierce's technique. However, it appears that Raspet *et al*'s so-called surface wave poles may not be pure surface wave poles. They appear to include contributions from *both* the surface waves *and* the creeping waves.

Surface waves have been observed in the experiments over a convex mat-on-masonite surface, which may be considered to simulate propagation over an impedance plane under an upward refracting atmosphere. This phenomenon may be explained using the theory of Raspet *et al* [8]. The results of this study have shown that near the convex mat-on-masonite surface, there are wave contributions that arrive later than the creeping waves. These later arriving waves that propagate along the surface and decay with height transverse to the surface may be identified as surface waves.

Chapter 7

Sound propagation over barriers on curved surfaces†

The performance of a barrier on the ground in the presence of wind and temperature gradients is an important problem. However, theoretical and experimental studies of this problem are difficult. In an upward or a downward refracting medium, ignoring the influence of atmospheric turbulence, the effectiveness of a barrier is in question because of the possibility of curved ray paths passing over the top of the barrier.

De Jong and Stusnick [57] performed scale model experiments in a low-speed wind tunnel to study the effect of the wind on the barrier reduction that was characterized as the mean sound pressure level with no wind minus the mean level with a wind. They reported that the barrier reduction fluctuated due to the effects of turbulent scattering around the barrier. Their conclusion, therefore, is beyond the scope of this chapter.

Seznec [52] used the boundary element method (BEM) to study the diffraction of sound by barriers of different shapes on a flat surface in a homogeneous atmosphere. Hothersall *et al* [24] used this method to predict the insertion loss over flat surfaces of finite impedance for various barrier configurations. As an numerical alternative approach to the residue series solution or the normal mode solution, the BEM has been applied to the particular

† Parts of the work reported in this chapter were presented in Reference [51].

problem of the diffraction of sound from a convex surface or a concave surface of finite impedance (*cf.* Chapter 4 and Chapter 5). For investigating complicated boundaries that diffract sound, the BEM has important advantages over the methods based on a geometrical theory of diffraction approach [24], and is probably the most useful numerical tool available at present.

Salomons [53] has presented a numerical model for long-range sound propagation over a barrier in a refracting atmosphere. The model agrees with predictions based on the parabolic equation method (PE). He defined the insertion loss of a barrier as the sound pressure in a homogeneous medium without a barrier minus the sound pressure behind the barrier in a refracting atmosphere. Salomons found that for downward propagation over a barrier on absorbing ground, the so-called total insertion loss of a barrier (*cf.* Chapter 1.5) decreases with increasing distance behind the barrier, whereas it remains approximately constant over a barrier on reflecting ground.

As indicated in previous chapters, it is possible to solve many outdoor problems by making laboratory measurements. Gabillet *et al* [46] made indoor measurements above a concave surface with a thin barrier installed between the source and receiver, to simulate sound propagation in a downward refracting medium in the presence of a barrier. They found that downward refraction does not necessarily reduce the effectiveness of a barrier.

Rasmussen [54] used a wind tunnel to investigate a barrier on an absorbing ground under upwind and downwind conditions. He presented the results as excess attenuation (or the sound pressure level *re* free field in his notation) rather than studying the effectiveness of the barrier.

Nevertheless, the effectiveness of a barrier in the presence of positive or negative sound speed gradients remains an interesting problem.

This chapter describes a series of laboratory measurements to investigate the diffraction of sound by a barrier on the top of a convex or concave surface, and the effectiveness of a barrier under negative and positive sound speed gradients. The experiments simulate sound propagation in an upward or downward refracting atmosphere in the presence of a rigid barrier. Numerical predictions using the BEM are compared with the experimental measurements. The BEM is then used to extrapolate predictions of the effectiveness of a noise barrier in both upward and downward refracting media, up to a range over 100 m, in comparison with that in a homogeneous atmosphere.

7.1 Application of the boundary element method

In order to predict the sound field behind a barrier with the BEM, we make the following assumptions: the source and receiver are separated by an infinitely long, straight barrier, of uniform cross-section and impedance along its length, sitting on a cylindrical convex or concave surface of finite impedance, the source is a point monopole source, and the receiver positions lie in the vertical plane which passes through the source and perpendicular to the barrier (see Figure 7.1). Hothersall *et al* [24] have tested the performance of the BEM for a similar problem with a plane boundary. We shall examine the performance of the BEM when modelling propagation over a barrier on curved surfaces. To present the results, excess attenuation (EA) is considered the most convenient indication of the diffraction of sound from a curved surface in the presence of a barrier. Here EA is defined as the sound pressure behind a barrier on a curved surface relative to its free-field level.

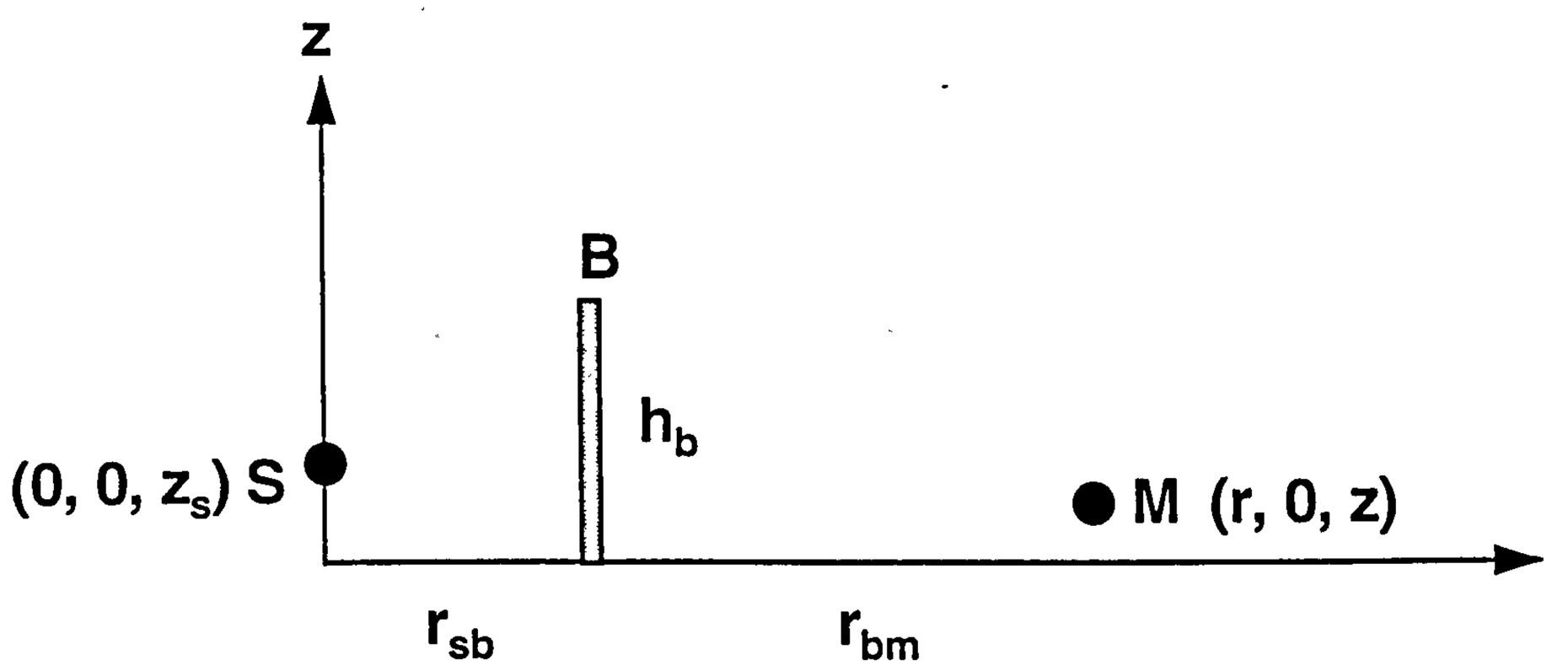

Figure 7.1 Sketch illustrating a barrier with uniform cross-section along its length inserted between a source and receiver.

7.1.1 Acoustic analogy

As described earlier, there is an acoustic analogy between sound propagation following straight lines above a curved surface and propagation following curved ray paths due to a constant sound speed gradient above a flat boundary. To simulate upward or downward refraction of sound outdoors, the use of a convex or a concave surface has been established. It is also possible to investigate upward or downward refraction in the presence of a barrier by adding a thin screen to the curved surface. Therefore, the diffraction of sound from a barrier on the ground in the presence of negative or positive sound speed gradients can be studied indoors.

The analogy may be explained by reference to Figures 7.2 and 7.3. Figure 7.2(a) illustrates sound propagation in an upward refracting atmosphere whose sound speed decreases constantly with height at lower altitudes in the presence of a barrier. This decrease causes the rays initially leaving the source in nearly horizontal directions to bend upward with a curvature radius of $R_c = c/|dc/dz|$. Similarly, assuming that there is a secondary source

located on the top of the barrier, we can describe sound propagation from the top of the barrier to the receiver by curved rays. The grey lines in this figure represent the ray paths in the absence of sound speed gradients. Figure 7.2(b) is analogous to Figure 7.2(a), which shows straight line propagation above a convex surface in the presence of a barrier. Figure 7.3(a) illustrates sound propagation in a downward refracting atmosphere where the sound speed increases constantly with height at lower altitudes in the presence of a barrier. This increase causes the rays initially leaving the source in nearly horizontal directions to bend downward with a curvature radius of $R_c = c/|dc/dz|$. The grey lines in this figure represent the ray paths in a homogeneous medium. Similarly, assuming that there is a secondary source located on the top of the barrier, we can describe sound propagation from the top of the barrier to the receiver by curved rays.

According to this analogy, the BEM is valid for curved ray paths above a plane ground in the presence of a barrier, with approximations consistent with those applicable to homogeneous medium above a curved surface.

(a)

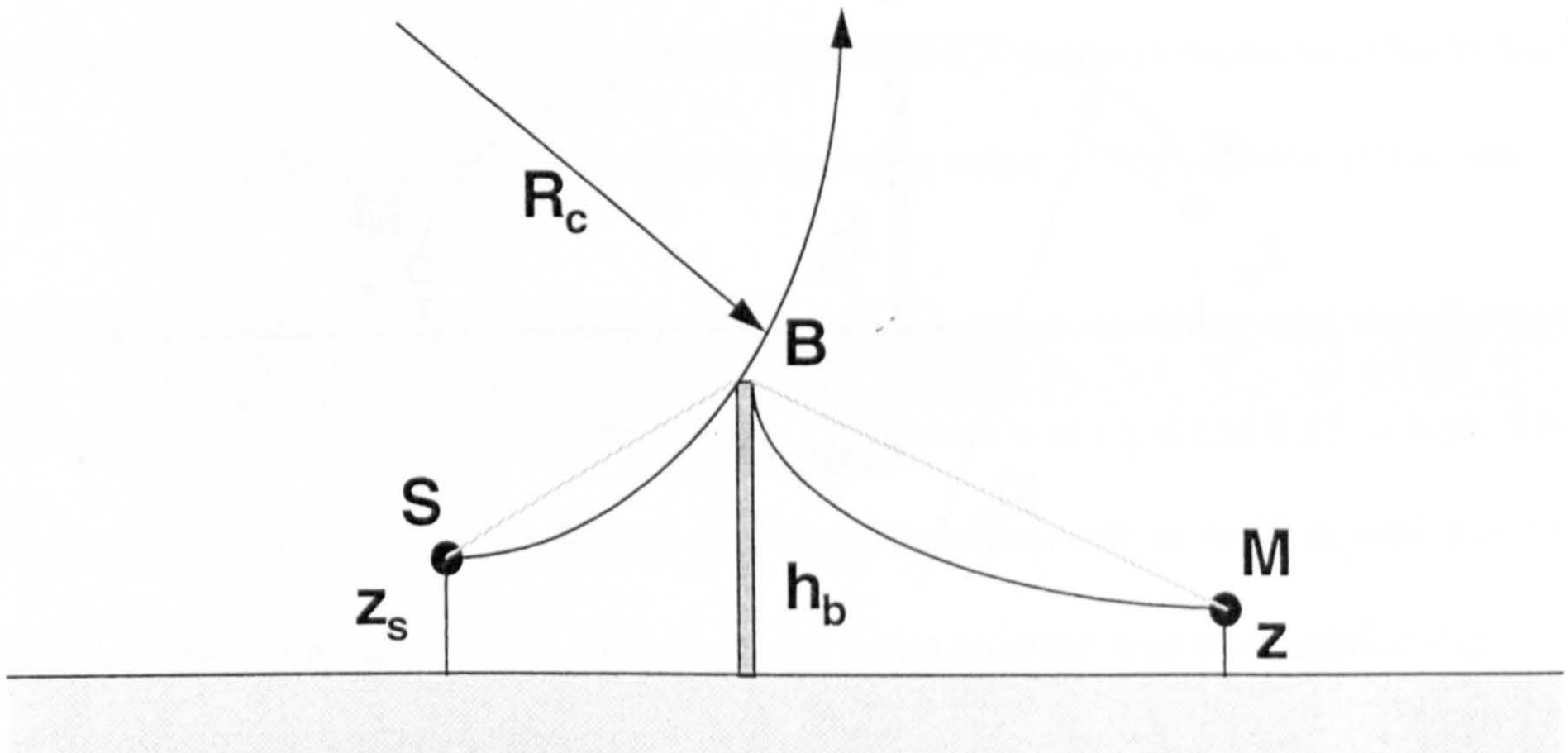

(b)

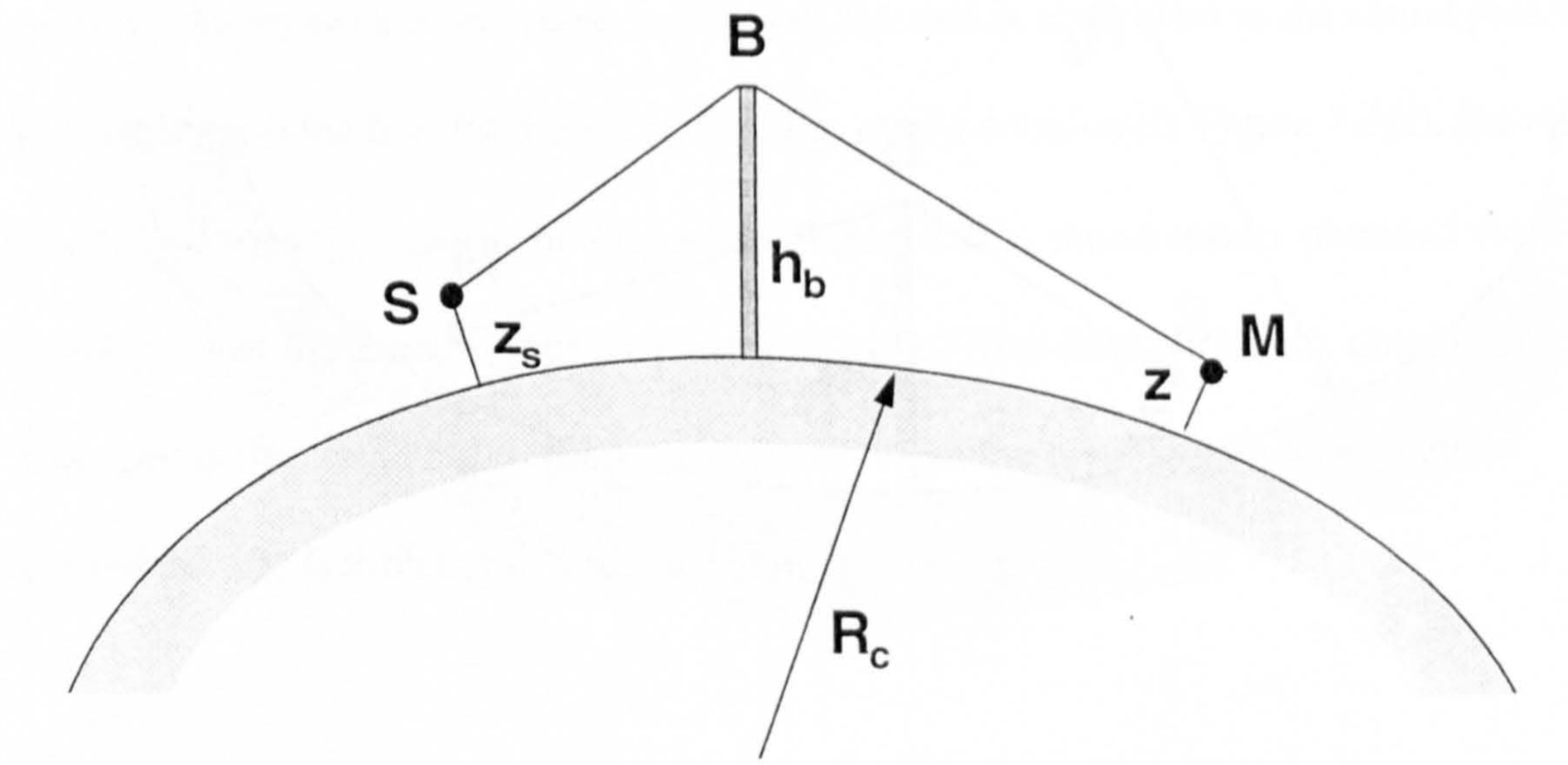

Figure 7.2 Sketch illustrating the analogy between upwardly curved ray paths above a flat boundary and straight line propagation above a convex surface in the presence of a barrier (reflected waves not shown).

(a)

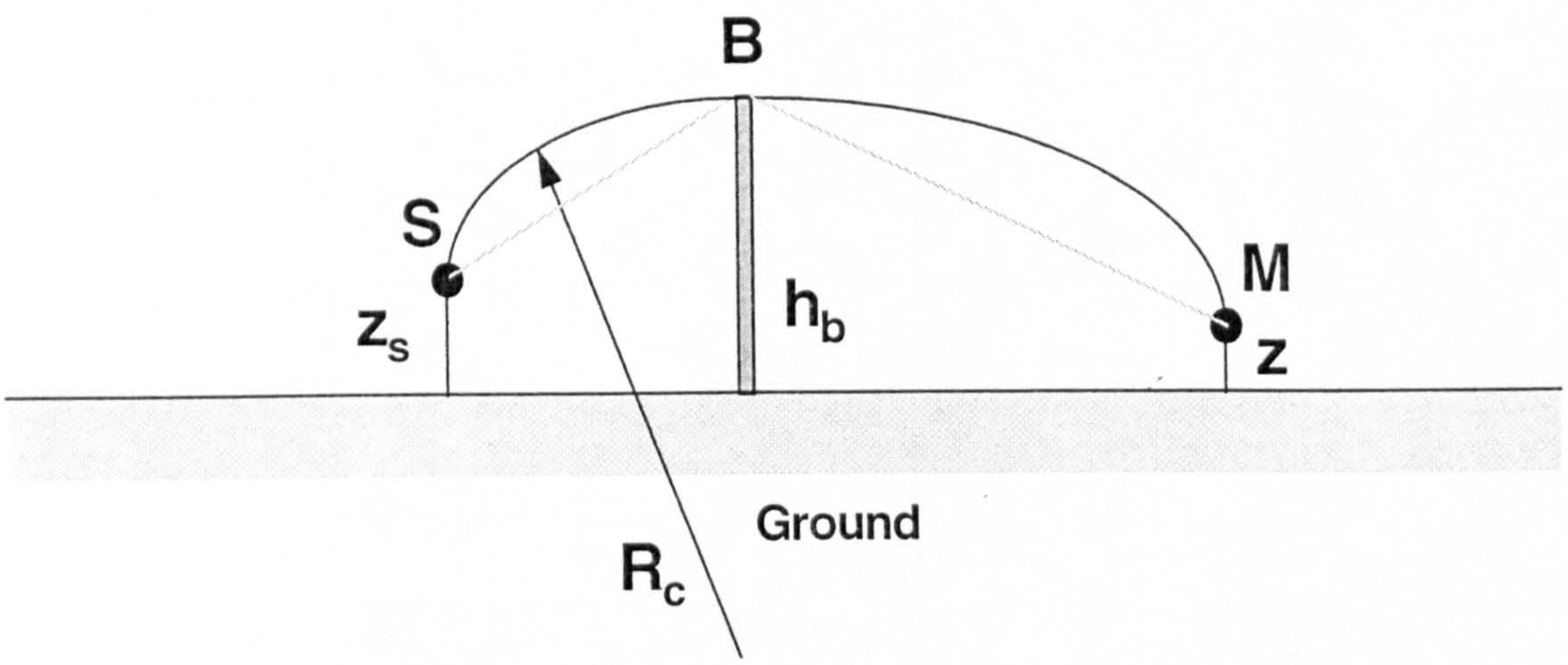

(b)

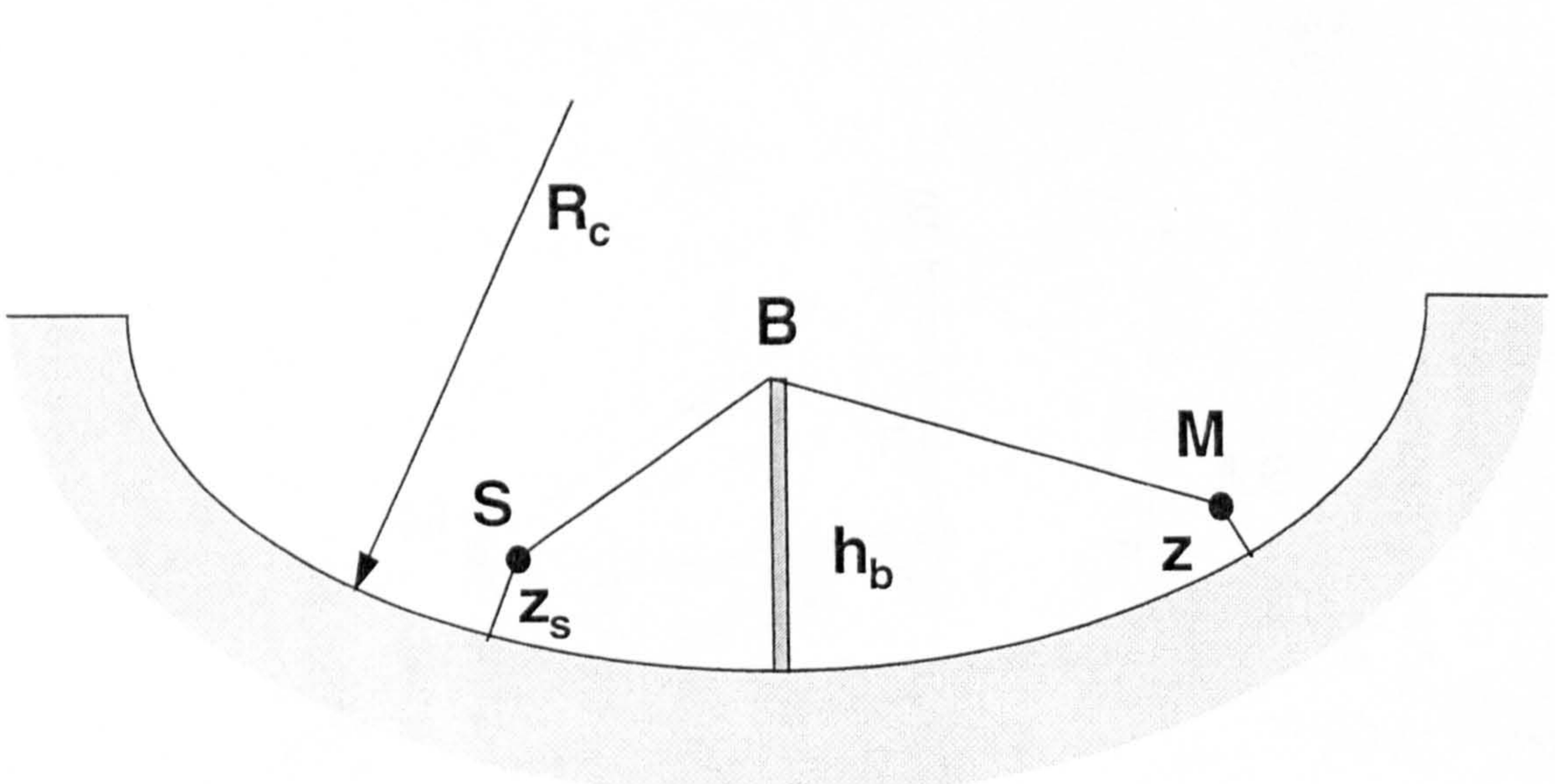

Figure 7.3 Sketch illustrating the analogy between downwardly curved ray paths above a flat boundary and straight line propagation above a concave surface in the presence of a barrier (reflected waves not shown).

7.1.2 Comparison with Gabillet *et al*

Firstly, we present numerical results calculated from the BEM for a barrier on a rigid concave surface which simulates sound propagation over a flat rigid surface with barrier in the presence of a positive sound speed gradient. By comparison with the data obtained by Gabillet *et al* [46], we show that the BEM is a valid and accurate numerical tool to study the acoustic performance of a noise barrier in the presence of atmospheric refraction.

Gabillet *et al* [46] made measurements above a rigid concave surface after installing a thin barrier at a distance of 4 m from the source. The barrier was rigid and 0.15 m high. The extent of the concave surface allowed propagation distances of up to 10 m with a resulting radius of curvature $R_c = 20$ m . The Gaussian beam solution was compared to the measurements, and a good agreement was found between them. The dotted curves in Figure 7.4 represent their measured results which are taken directly from Figure 15 in Reference [46]. The circles represent predictions calculated from the boundary element method. The results are presented in terms of EA that is equivalent to the sound pressure level relative to the free-field level in Gabillet *et* al's notation. In Figure 7.4(a), the receiver was deep within the shadow of the barrier. Figure 7.4(b) shows results obtained close to the limiting ray of the shadow boundary, while Figure 7.4(c) displays results obtained farther from the barrier. In all cases, the agreement between the boundary element method predictions and Gabillet *et al*'s measurements is very good.

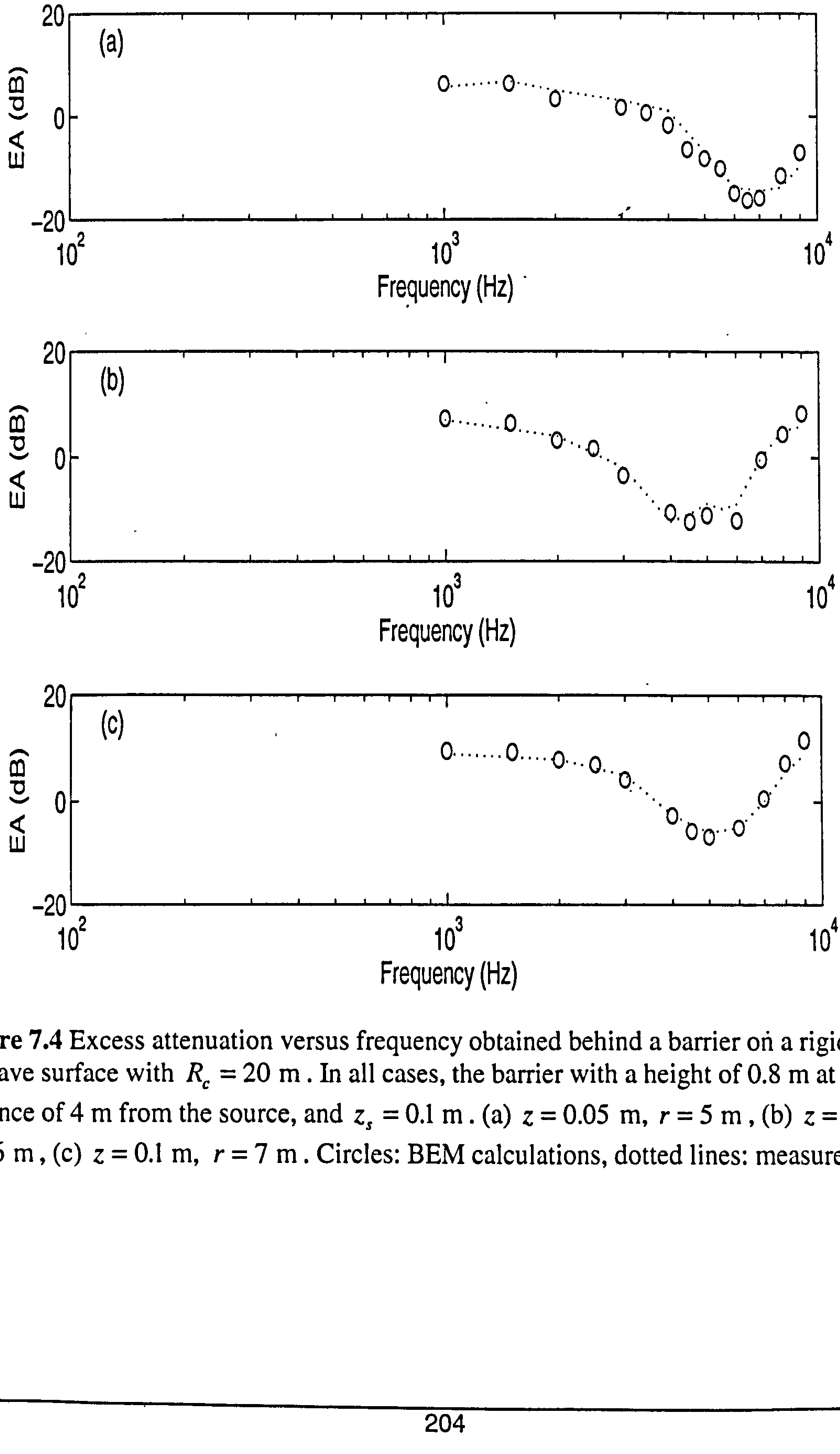

Figure 7.4 Excess attenuation versus frequency obtained behind a barrier on a rigid concave surface with $R_c = 20$ m. In all cases, the barrier with a height of 0.8 m at a distance of 4 m from the source, and $z_s = 0.1$ m. (a) $z = 0.05$ m, $r = 5$ m, (b) $z = 0.15$ m, $r = 6$ m, (c) $z = 0.1$ m, $r = 7$ m. Circles: BEM calculations, dotted lines: measurements.

7.1.2 Comparison with Rasmussen

Next, we present numerical results calculated from the BEM for a barrier on absorbing convex and concave surfaces which simulate sound propagation over a barrier on an absorbing plane in an upward and a downward refracting atmosphere, respectively. The numerical results are compared with Rasmussen's experimental measurements conducted in a wind tunnel, where the wind velocity can be described by a set of linear profiles [54]. In our numerical calculations, the sound speed profiles are approximated by constant gradients of $\mp 1.0\ ms^{-1}$. We can demonstrate that it is reasonable to make such an approximation near the ground.

Figure 7.5 shows the comparisons between the numerical predictions and Rasmussen's measurements. The dotted curves in Figures 7.5(a) and (b) represent his measurement results directly extracted from Figs. 9 and 11 in References [54] for upwind and downwind conditions, respectively. The circles represent the corresponding numerical results obtained from the BEM calculations. The results are presented as excess attenuation which is equivalent to the sound pressure level relative to the free field level, as described by Rasmussen. The agreement, in spite of the use of the approximate constant sound speed gradient, is very good for both upwind and downwind conditions. This implies that a cylindrically curved surface may be used as an alternative to the use of a wind tunnel and the BEM is valid and useful tool to study the acoustic performance of noise barriers in the presence of wind velocity gradients.

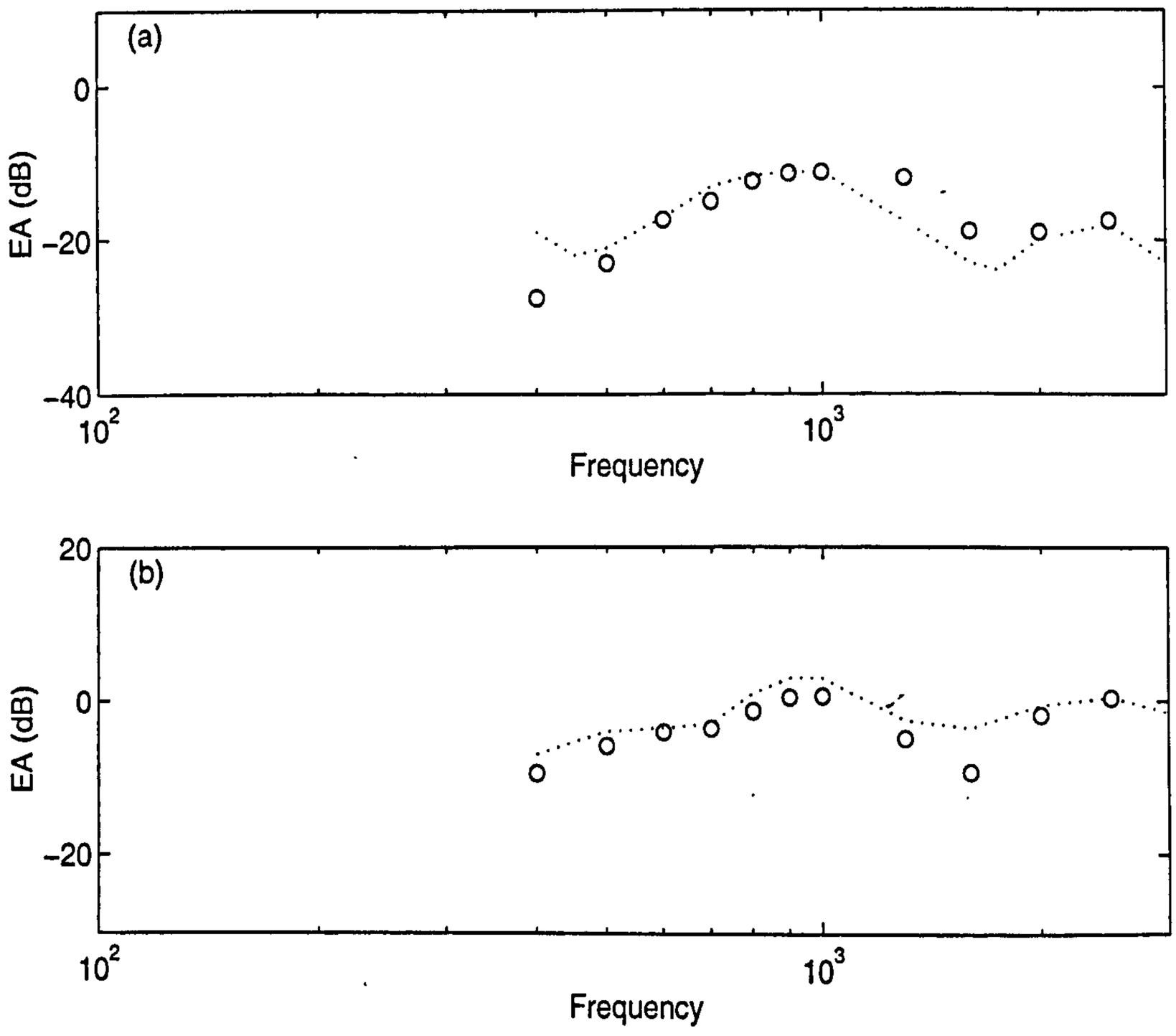

Figure 7.5 Excess attenuation versus frequency obtained behind a barrier on an absorbing ground, with $\sigma_e = 20$ kPa s m^{-2}, $\alpha_e = 60$ m^{-1}, $z_s = 2$ m, $z = 1$ m, and $h_b = 2.5$ m. (a) upwind condition, $r_{sb} = 40$ m, $r_{bm} = 20$ m and (b) downwind condition, $r_{sb} = 20$ m, $r_{bm} = 40$ m. Circles: BEM calculations, dotted curves: measurements.

7.2 Measurement techniques and configurations

The experimental techniques employed in this chapter are similar to those described in Chapter 4 and Chapter 5.

7.2.1 Scale model simulation

Almgren reported [14] that it is reasonable to use a convex or concave surface scale model to simulate the effect of refraction due to a negative or a positive sound speed gradient in the atmosphere. He found that the errors introduced by the scale model experiments in comparison with those of outdoor full-scale measurements are negligible.

The basic assumption of the scale model simulation [50] is that the EA of the system at the full-scale frequencies is the same as the EA of the scale model simulation at the model-scale frequencies. The results obtained from the scale model experiments are independent of the scale factor, as can been seen if all length dimensions are divided by the scale factor and all frequencies are multiplied by it. Hence, with the curved model surface, we can use the scale modelling technique to investigate the refraction of sound for various sound speed gradients.

The experimental investigation may be limited by the geometrical parameters of the scale model. The radius of curvature is always small in the scale model experiments, this is equivalent to a very strong sound speed gradient. However, it has been shown [49] that it is possible to achieve good agreement between full-scale measurements and predictions deduced from the scale model experimental results with an appropriate gradient.

A long thin edge barrier was installed on the top of the convex or concave surfaces which have been described in detail in the previous chapters (*cf.* Chapter 4 and Chapter 5). The barrier consisted of a stainless-steel sheet with a height $h_b = 0.10$ m, and a thickness of 0.003 m. It was installed perpendicular to the centreline of the curved surfaces. To ensure adequate transmission loss through the barrier, the barrier was sealed to the surface by using blu-tack. To compare with the barrier performance in a homogeneous medium, the barrier was installed also on the flat board with or without the felt covering described in Chapter 4 and Chapter 5.

Since the diffraction of sound depends strongly upon the source and receiver geometry and relative position of the barrier [50], the source and receiver heights were kept constant, such that $z_s = 0.02$ m, and $z = 0.0064$ m. Measurements were made after inserting the

barrier at distances $r_{sb} = 0.125$ m, 0.25 m, 0.375 m, and 0.5 m from the source. The measured data were collected as a function of the distance from the source to the receiver at scaled frequencies of 3 kHz and 4 kHz.

The model dimensions and geometries were arranged to give a scale factor of 1:8. With this scale factor, full-scale results correspond to all length dimensions being multiplied by it, when all frequencies are divided by it. Thus, the equivalent full-scale geometry is given by $z_s = 0.16$ m , $z = 0.05$ m , $h_b = 0.80$ m , and $r_{sb} = 1.0$, 2.0, 3.0 and 4.0 m, and the equivalent full-scale source frequencies are at 375 Hz and 500 Hz. In the experiments reported here, all measurement results are presented in full-scale and no attempt has been made to model a particular outdoor surface. The felt-covered surface represents an absorbing surface that has the same specific normalized admittance β at the measurement frequencies as the felt-covered surface at full-scale frequencies. In fact, the full-scale equivalent of the felt impedance used in these experiments would correspond to a relatively soft surface at representative outdoor geometries.

7.2.2 Instrumentation and procedure

The experimental facility and procedure used here are similar to those described in Chapter 4 and Chapter 5. The curved surfaces were placed in the anechoic chamber, and the tannoy speaker was used as the point monopole source. The MLSSA analyzer acted as both the signal generator for the speaker and as the analyzer for subsequent signal processing.

In the measurements, the source and receiver were placed in the plane transverse to the barrier. Data were taken along the curved surfaces as a function of arc distance from the source.

7.3 Measurement results and analysis

In this section, numerical results predicted by the BEM calculation are compared with the results of measurements. Comparison of theoretical predictions and measurements are made for both rigid surfaces and surfaces of finite impedance. The configurations are presented for the equivalent full-scale geometries rather than the measurement geometries.

7.3.1 Barriers on flat surfaces

First, the predictions of the BEM in the absence of the barrier are compared with those of Equation (4.1.1).

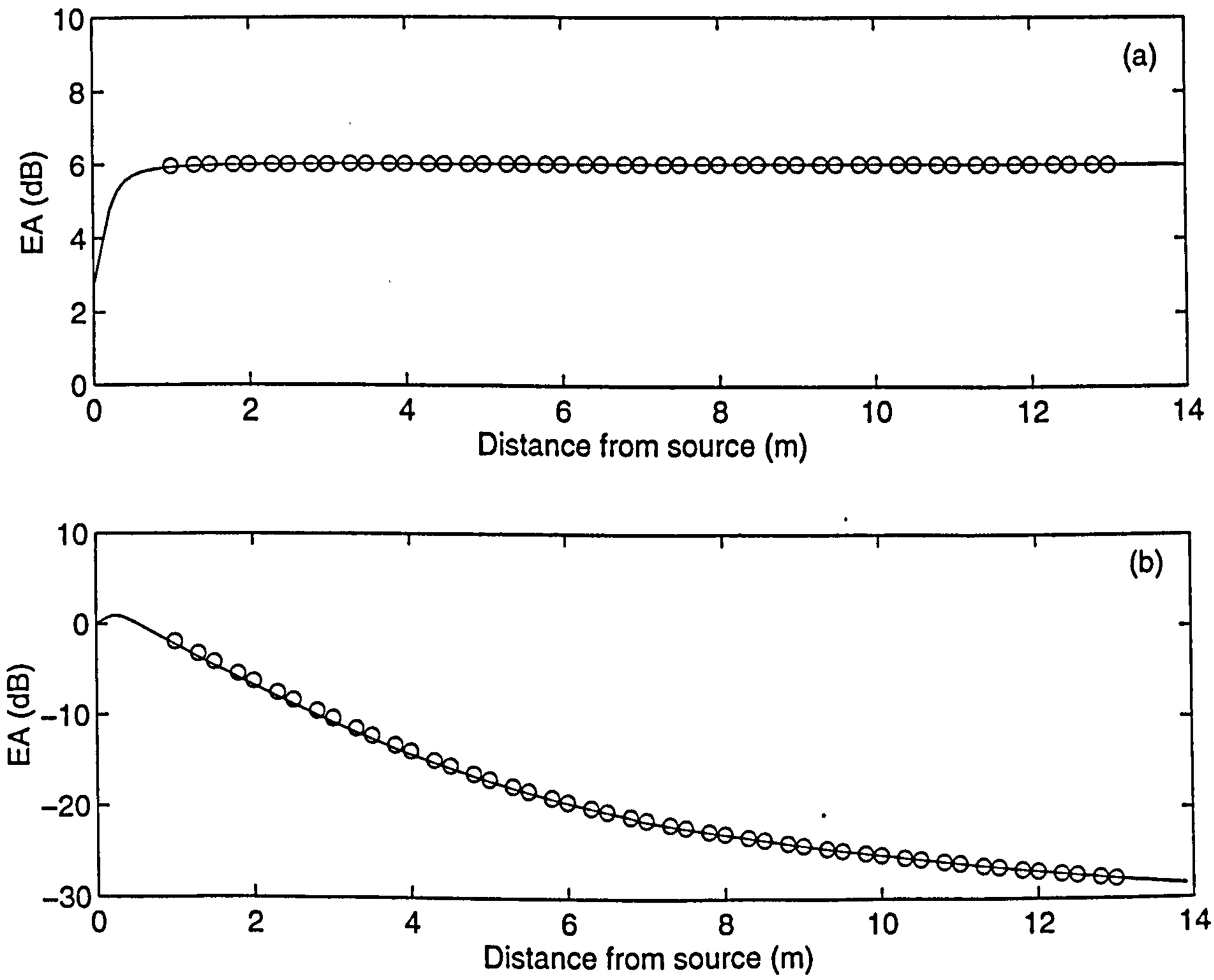

Figure 7.6 Excess attenuation predicted for a frequency of 500 Hz over (a) a rigid and (b) an absorbing flat surfaces in the absence of a barrier. Circles: the BEM calculations, solid lines: the calculations from Equation (4.1.1). $z_s = 0.16$ m , $z = 0.05$ m .

Figure 7.6 shows comparisons of the results obtained from Equation (4.1.1) and the BEM calculation above flat surfaces in the absence of a barrier. Figure 7:6(a) shows the results above the rigid flat surface, while Figure 7.6(b) shows those above the absorbing flat surface. The results are presented as functions of a distance along surface from the source. The agreement is excellent between these two predictions for each case.

Next, BEM predictions are compared with data obtained over the flat surfaces described in Chapter 4. In the subsequent figures, the points represent the results of the BEM calculations, while the plus signs represent the measurement data obtained over the rigid surface and the circles represent the data obtained over the absorbing surface. Figure 7.7 shows the results obtained for a full-scale source frequency of 500 Hz, in terms of the excess attenuation, as a function of the distance from source above the flat surfaces after inserting a barrier. In Figure 7.7(a), the barrier was inserted at a full-scale distance of 1.0 m from the source. This barrier location gives the most effective attenuation in comparison with the other cases. Figure 7.7(b) to Figure 7.7(d) show the results obtained as the barrier at equivalent full-scale distances of 2.0, 3.0 and 4.0 m from the source, respectively. In general the agreement between the experimental measurements and the BEM calculation is very good.

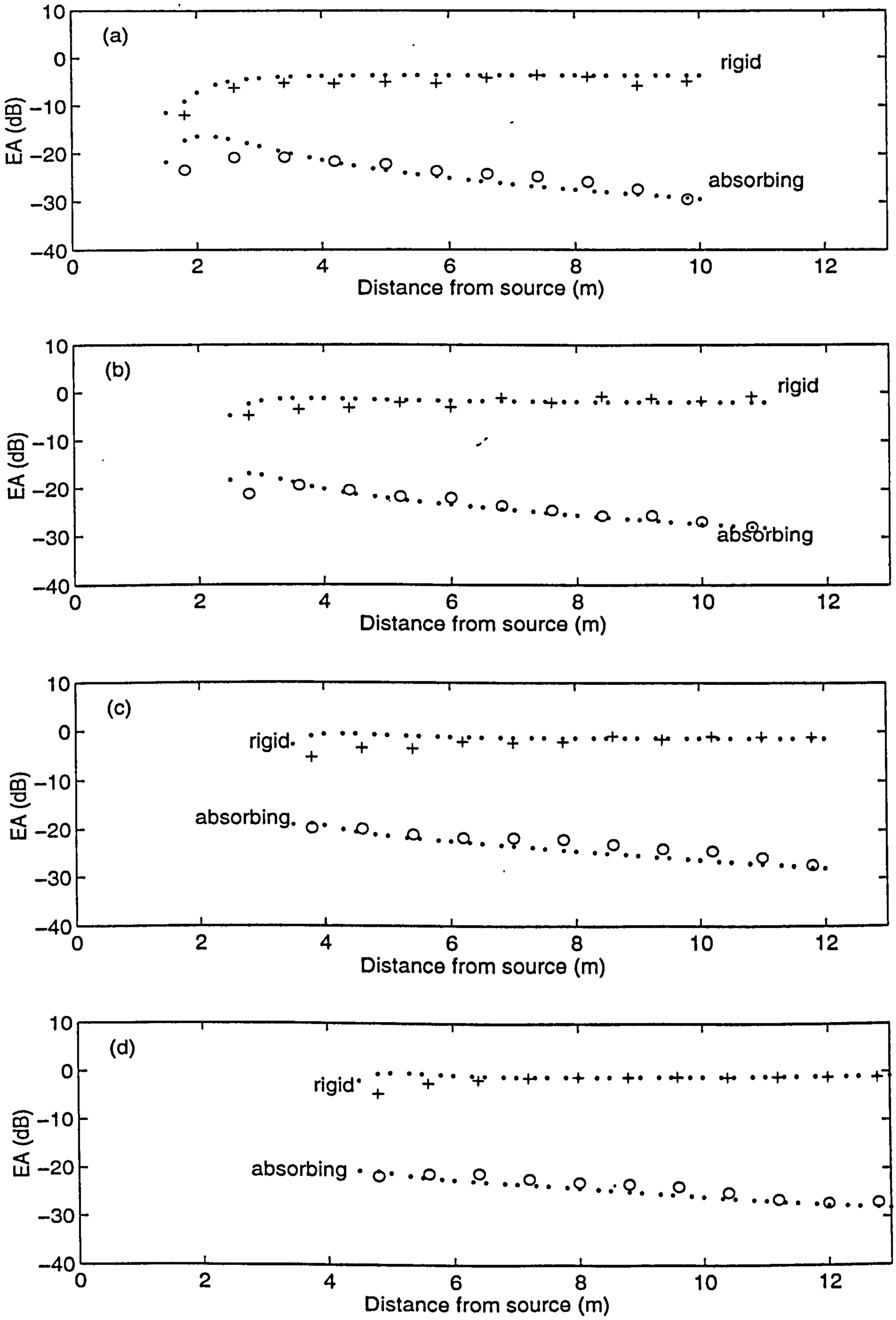

Figure 7.7 Excess attenuation obtained for a frequency of 500 Hz over flat surfaces in the presence of a barrier. Points: the BEM calculations, circles and plus signs: the experimental measurements. $z_s = 0.16$ m , $z = 0.05$ m , $h_b = 0.80$ m , r_{sb} = (a) 1.0 m, (b) 2.0 m, (c) 3.0 m and (d) 4.0m.

7.3.2 Barriers on convex surfaces

In this section, the diffraction of sound from barriers on convex surfaces is discussed. Measurements have been conducted in an anechoic chamber after installing the thin barrier on the top of the convex surfaces. The measurements simulate sound propagation over flat ground in an upward refracting medium in the presence of a barrier.

In the following figures, the points represent results from the BEM calculations, while the plus signs represent the measurement data obtained over the rigid convex surface and the circles represent the data obtained over the absorbing convex surface. Figure 7.8 shows the results obtained in terms of the excess attenuation as a function of distance from source above the rigid convex surface for a full-scale source frequency of 500 Hz, and the absorbing surface for a full-scale source frequency of 375 Hz. The analogous sound speed gradient to this convex surface is $-17.15\ ms^{-1}$. In Figure 7.8(a), the barrier was installed at a full-scale distance of 1.0 m from the source. Similar to the case on the flat surface, this location of the barrier gives rise to the most attenuation in comparison with the other cases. Figure 7.8(b) to Figure 7.8(d) show results obtained when the barrier was at equivalent full-scale distances of 2.0, 3.0 and 4.0 m from the source respectively. It is possible to generalize that the closer the barrier is located to the source, the larger the barrier attenuation that is obtained. In general, the agreement between the BEM predictions and the scale measurements is very good.

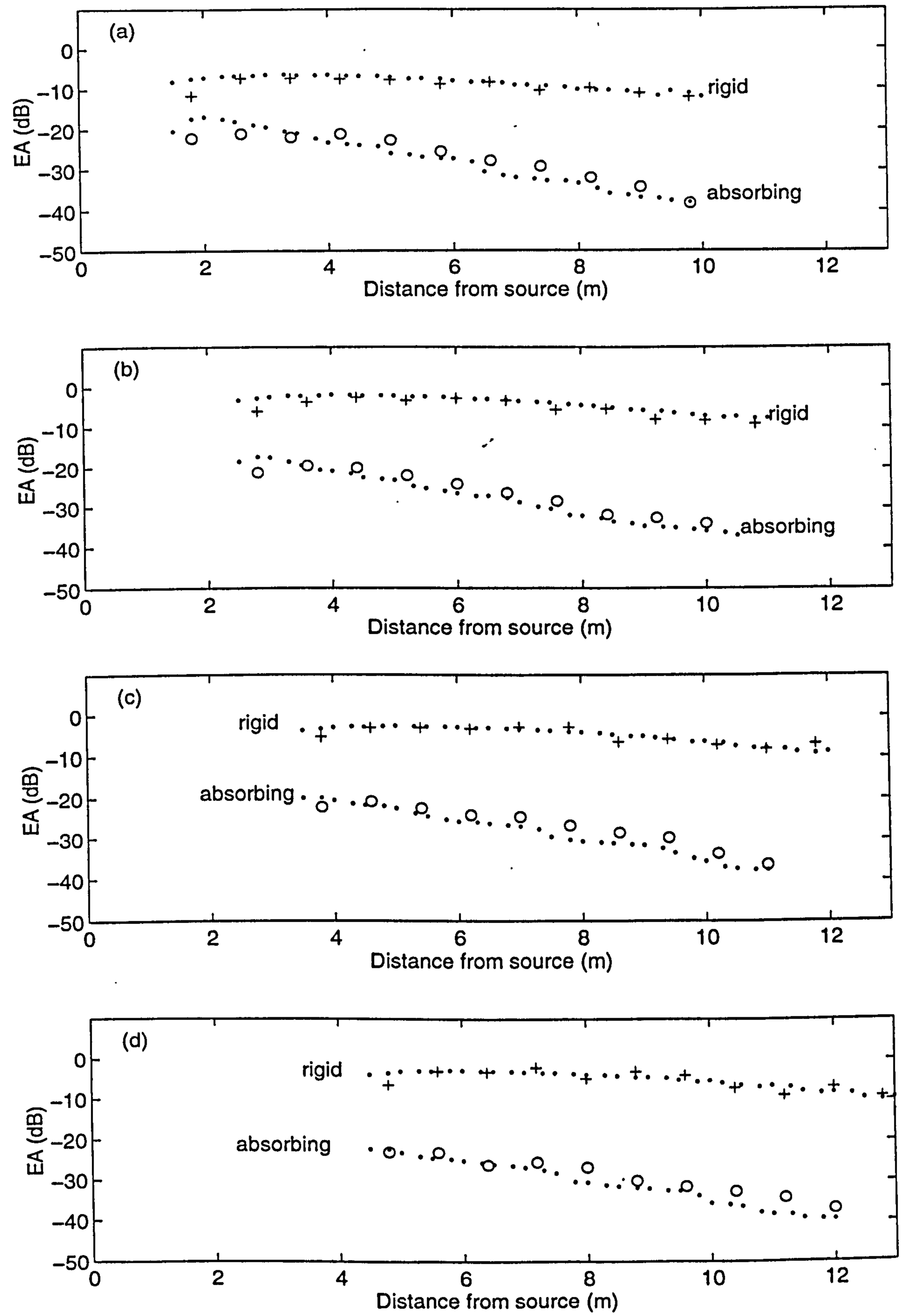

Figure 7.8 Excess attenuation obtained for a frequency of 500 Hz over convex surfaces in the presence of a barrier. Points: the BEM calculations, circles and plus signs: the experimental measurements. $z_s = 0.16$ m , $z = 0.05$ m , $h_b = 0.80$ m , r_{sb} = (a) 1.0 m, (b) 2.0 m, (c) 3.0 m and (d) 4.0m.

7.3.3 Barriers on concave surfaces

In this section, the diffraction of sound from barriers on concave surfaces is discussed. Measurements were conducted above in an anechoic chamber with a thin barrier placed on the concave surfaces. The measurements simulate sound propagation in an downward refracting medium in the presence of a barrier on flat ground.

In the following figures, the points represent the boundary element method calculations, while the plus signs represent the measurement data obtained over the rigid concave surface and the circles represent the data obtained over the absorbing concave surface. Figure 7.9 shows the results obtained for a full-scale source frequency of 500 Hz in terms of the excess attenuation as a function of distance from the source above a rigid concave surface. The analogous sound speed gradient to this convex surface is $+17.15\ ms^{-1}$. In Figure 7.9(a), the barrier was installed at an equivalent distance of 1.0 m from the source. As noted with the flat surface, this location of the barrier gives rise to the most efficient attenuation in comparison with the other cases. Figure 7.8(b) to Figure 7.8(d) show results obtained when the barrier was at equivalent full-scale distances of 2.0, 3.0 and 4.0 m from the source respectively. In general, the agreement between the BEM calculations and the experimental measurements over both rigid and absorbing concave surfaces is very good.

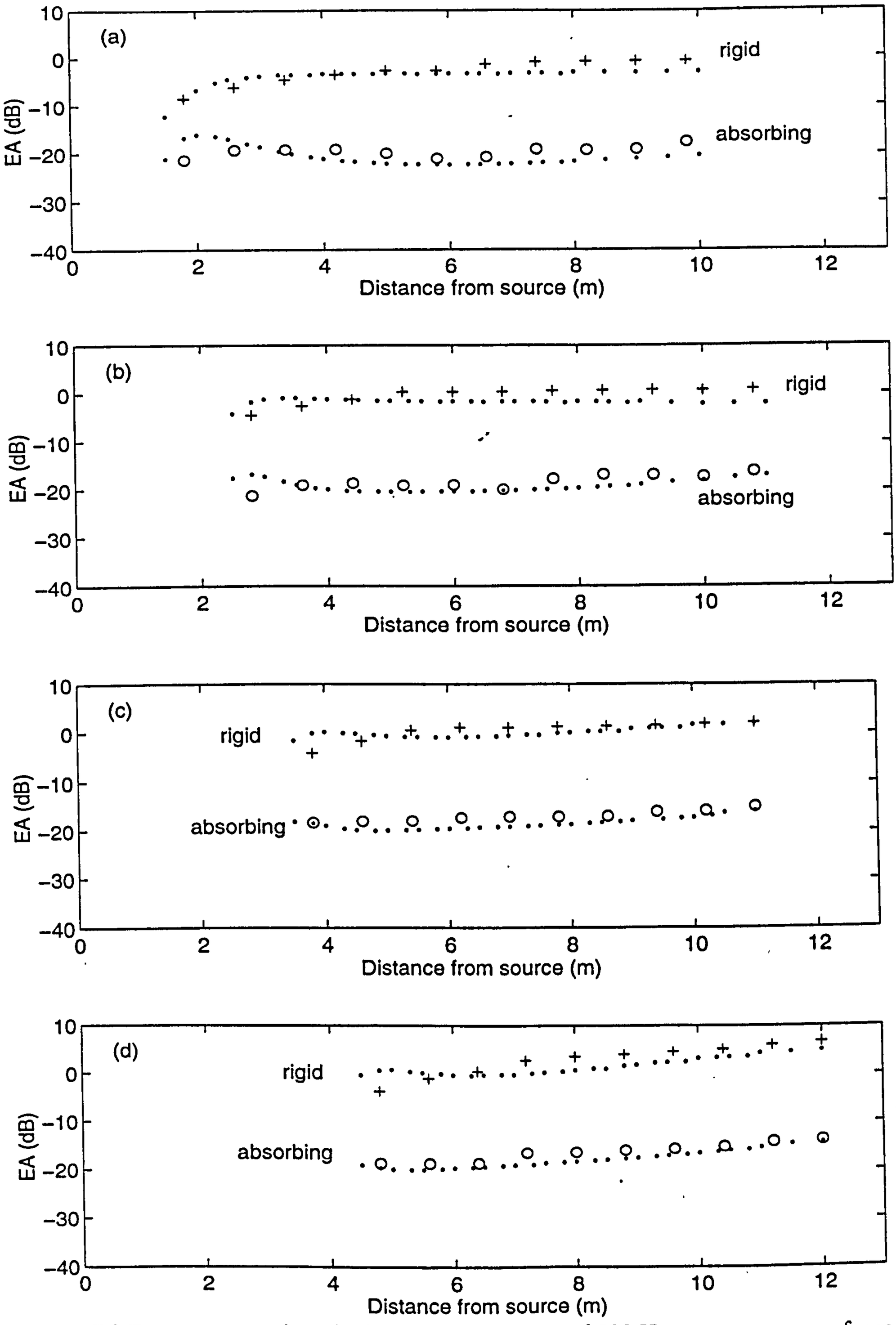

Figure 7.9 Excess attenuation obtained for a frequency of 500 Hz over concave surfaces in the presence of a barrier. Points: the BEM calculations, circles and plus signs: the experimental measurements. $z_s = 0.16$ m, $z = 0.05$ m, $h_b = 0.80$ m, r_{sb} = (a) 1.0 m, (b) 2.0 m, (c) 3.0 m and (d) 4.0m.

7.3.4 Total insertion loss of a barrier

The total insertion loss of a barrier, IL_{total}, which is equivalent to Salomons' so-called insertion loss of a barrier [53], is defined as the sound pressure in a homogeneous medium minus the sound pressure behind the barrier in a refracting medium. With the acoustic analogy, IL_{total} for curved surfaces is defined by

$$IL_{total} = -20\log_{10}\left(\frac{p}{p_{f0}}\right), \qquad (7.3.1)$$

where p is the total sound pressure behind the barrier over a surface, and p_{f0} is the sound pressure in the absence of the barrier over a flat ground with the same impedance surface. There is a common belief that IL_{total} is increased under upward refraction and decreased under downward refraction [46, 54].

Figure 7.10 shows IL_{total} for an equivalent full-scale source frequency of 500 Hz as a function of distance from source over the flat, convex and concave surfaces. The barrier was inserted at an equivalent full-scale distance of 1.0 m from the source. The measured results (the circles for flat surfaces, the stars for convex surfaces, and the plus signs for concave surfaces) are compared with the BEM predictions (the solid lines for flat surfaces, the points for convex surfaces, and the dotted lines for concave surfaces). Figure 7.10(a) shows the results over the rigid surfaces, while Figure 7.10(b) shows the results over the absorbing surfaces. There is, in general, good agreement between the measurements and the BEM predictions.

In Figure 7.10(a), IL_{total} decreases and then remains approximately constant with increasing distance between the source and receiver in the case where the barrier was installed on the rigid flat surface. Similar trends to this have been found in the case of the

barrier on the rigid concave surface. In the case of the barrier on the rigid convex surface, IL_{total} increases gradually with increasing distance behind the barrier.

In Figure 7.10(b), IL_{total} decreases slightly with increasing distance between the source and receiver in the case where the barrier was located on the absorbing flat surface. In the case of the barrier on the absorbing concave surface, IL_{total} is in accord with that due to the barrier on the flat surface at short ranges, and then decreases quickly with increasing distance behind the barrier at longer ranges. For the barrier on the absorbing convex surface, however, IL_{total} increases at longer ranges, in comparison with that in the situation of the flat absorbing surface.

These cases simulate sound propagation in a homogeneous, an upward refracting, and a downward refracting media, over a barrier on reflecting and absorbing surfaces. The results obtained here agree with PE predictions and Salomons' numerical calculations for a downward refraction with a logarithmic sound speed profile [53]. The experimental and numerical results indicate that IL_{total} is improved under upward refraction and destroyed under downward refraction. Consequently these results are consistent with the common belief [46, 54] described earlier.

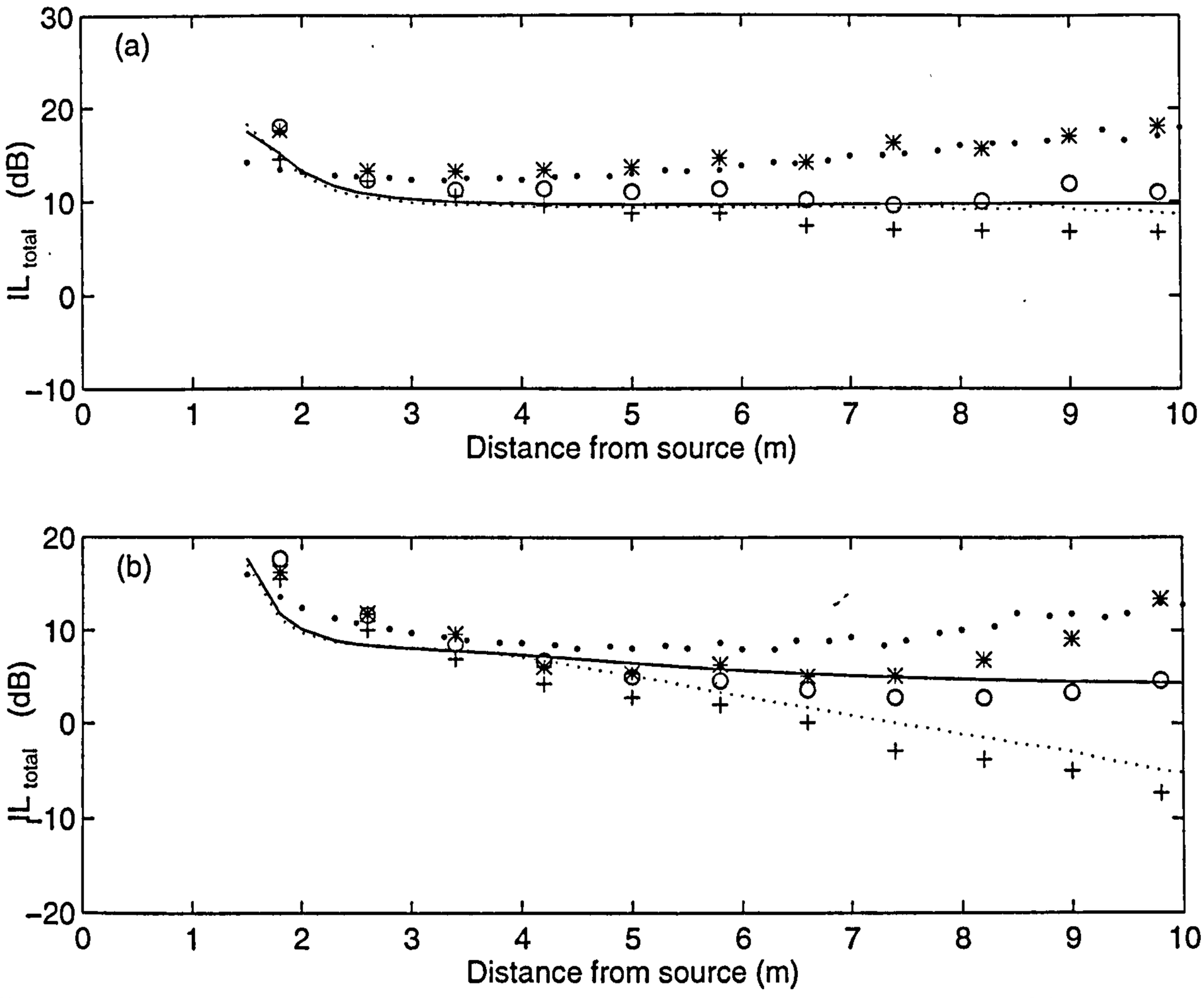

Figure 7.10 IL_{total} obtained for an equivalent source frequency of 500 Hz, with $z_s = 0.16$ m , $z = 0.05$ m , $h_b = 0.80$ m , $r_{sb} = 1.0$ m. Solid line: the BEM predictions for flat surfaces; circles: measurements over flat surfaces; points: the BEM predictions for convex surfaces; stars: measurements over convex surfaces; dotted lines: the BEM predictions for concave surfaces; plus signs: measurements over concave surfaces. (a) rigid surfaces and (b) absorbing surfaces.

7.4 Effectiveness of a barrier

On the basis of the success reported above, we may extrapolate the BEM result to predict the effectiveness of a barrier. The total insertion loss of a barrier, IL_{total} , is not a clear measure for the effectiveness of a barrier in a refracting atmosphere because it includes the effects of atmospheric refraction due to temperature or wind velocity gradients over the barrier. To assess the effectiveness of a barrier, we use the barrier insertion loss, $IL_{barrier}$ instead. It is defined as the sound field above an impedance ground without a barrier to that the sound field with a barrier and related to IL_{total} by

$$IL_{total} = IL_{barrier} + IL_{geom}, \tag{7.4.1}$$

where IL_{geom} is the insertion loss due to the effect of refraction and defined as the sound field above an impedance ground in a homogeneous medium relative to the sound field in the refracting atmosphere.

Analogously, $IL_{barrier}$ for curved surfaces is defined by

$$IL_{barrier} = -20\log_{10}\left(\frac{p}{p_{s0}}\right), \tag{7.4.2}$$

where p is the total sound pressure behind the barrier over a surface and p_{s0} is the sound pressure in the absence of a barrier over the corresponding surface..

In a situation without a barrier, there is a shadow region behind a convex surface. The sound pressure inside the shadow region may be determined by the creeping wave analysis [3]. A barrier is therefore expected to be less effective in the shadow region [53]. Gabillet *et al* [46] found that $IL_{barrier}$ may be improved by the concave surface. The reason for their improvement may be that the rays with multiple reflections near the surface that produce caustics, cause increased levels in the absence of the barrier, but are blocked when the barrier is inserted [46].

$IL_{barrier}$ can be obtained directly from Figure 7.7 to Figure 7.9 with knowledge of the excess attenuation of the surfaces without the barrier. Figure 7.11 shows $IL_{barrier}$ for the barrier on the flat, convex and concave surfaces in a typical case where the barrier was inserted at an equivalent distance of 1.0 m from the source, *i.e.* $r_{sb} = 1.0$ m . For the rest three cases where the barriers were inserted at equivalent distances of 2.0, 3.0 and 4.0 m from the source, $IL_{barrier}$ can be deduced by the same method. The solid lines, points and dotted lines represent the BEM predictions for the barrier on the flat, convex and concave

surfaces, respectively, while the circles, stars and plus signs represent the measurement results. Figure 7.11(a) shows the results over the rigid surfaces, and Figure 7.11(b) shows those over the absorbing surfaces. The BEM predictions agree well with the measurement results in the situations of the absorbing surfaces. For the rigid surfaces, there is good agreement between the BEM calculations and the measurements in the cases of the flat and convex surfaces. In the case of concave surface, however, the agreement is not as good as the flat and convex surfaces. The theory over-estimates $IL_{barrier}$ when the receiver is at longer ranges from the source.

It is noted that for a barrier on absorbing surfaces, $IL_{barrier}$ is not necessarily destroyed by concave surfaces, whereas it is not significantly improved by convex surfaces, in comparison with $IL_{barrier}$ over flat surfaces.

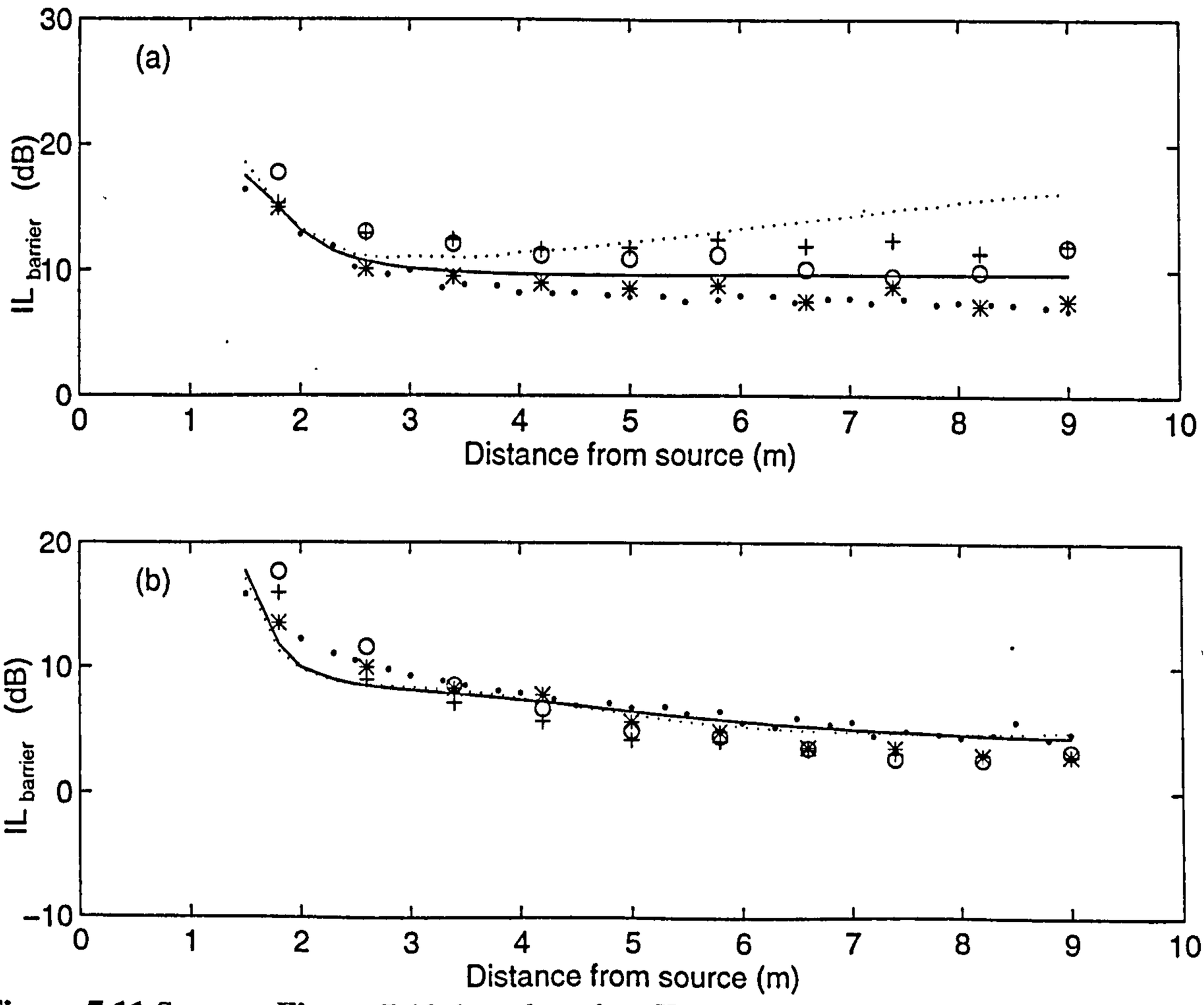

Figure 7.11 Same as **Figure 7.10**, but plotted as $IL_{barrier}$.

We may predict the effectiveness of a noise barrier, in terms of $IL_{barrier}$, in more realistic situations using the BEM. We consider a noise barrier with a height of 2.5 m on an impedance ground ($\sigma_e = 100$ kPa s m^{-2}, $\alpha_e = 100$ m^{-1}). The source height is 1.0 m and the receiver height is 1.5 m. Figures 7.12 shows the calculated $IL_{barrier}$ as a function of range for a source frequency of 1 kHz. The results are presented in a upward refracting medium (stars and dotted lines), a downward refracting medium (plus signs and dashdot lines), and a homogeneous medium (circles and solid lines). The sound speed gradients in the upward and downward refracting media are ∓ 0.1 ms^{-1}, respectively. Figure 7.12 (a) shows the results for the barrier inserted at a distance of 10 m from the source, this location of the barrier gives rise to the most effective $IL_{barrier}$ in comparison with the other cases. Figure 7.12(b) and Figure 7.12(c) show the corresponding results for the barrier inserted at distances of 15 m and 20 m from the source. It is found that $IL_{barrier}$ under the upward and downward refracting conditions is approximately at the same levels as $IL_{barrier}$ under the no refraction conditions. The maximum difference between these three conditions is less than 3 dB.

Then, we consider the barrier located on a softer impedance ground with $\sigma_e = 20$ kPa s m^{-2}, $\alpha_e = 60$ m^{-1} for a steeper sound speed gradients of ∓ 1.0 ms^{-1}. Figure 7.13(a) shows the calculated $IL_{barrier}$ for a source frequency of 500 Hz, with a different geometry to that of Figure 7.12. The barrier is installed at a distance of 20 m from the source, with the source and receiver heights of 2.0 m. It is seen that $IL_{barrier}$ increases in the downward refracting medium, whereas it decreases in the upward refracting medium, in comparison with $IL_{barrier}$ under no refraction conditions.

However, this may not be the case if the barrier is installed on a harder impedance ground with a weaker sound speed gradient, for the same source frequency and geometry of the source and receiver. Figure 7.13(b) shows the calculated $IL_{barrier}$ for an impedance ground with $\sigma_e = 100$ kPa s m^{-2} and $\alpha_e = 100$ m^{-1}, and a sound speed gradient of ∓ 0.1 ms^{-1}. $IL_{barrier}$ increases in the upward refracting medium, whereas it decreases in the downward refracting medium, in comparison with $IL_{barrier}$ under no refraction conditions.

Figures 7.12(a)-(c) show that $IL_{barrier}$ decreases as the distance between source and barrier, r_{sb}, increases from 10 m to 20 m. In the conditions of $r_{sb} = 20$ m [*cf.* Figures 7.12(c), 7.13(a) and (b)], $IL_{barrier}$ is degraded by the effects of the ground reflection even to negative values when the receiver is at longer distances from the source. The situation of a degraded insertion loss is analogous to the case where a barrier is installed in a homogenous medium. It is of interest to note that, according to the numerical predictions, $IL_{barrier}$ is optimized by placing the barrier as close to the source as possible. This conclusion is similar to that of Reference [150] in which Hothersall *et al* ignore the effect of atmospheric refraction.

The results shown in these figures indicate that $IL_{barrier}$ is not affected significantly by either upward or downward refraction in comparison with $IL_{barrier}$ in a homogeneous medium. Negative sound speed gradients may not improve the performance of a barrier, while positive sound speed gradients do not necessarily destroy the effectiveness of a barrier. It appears difficult to find a simple conclusion for $IL_{barrier}$ in a refracting medium over an impedance ground. The barrier insertion loss, $IL_{barrier}$ varies with sound speed gradient, source frequency, source-barrier-receiver geometry, and ground impedance.

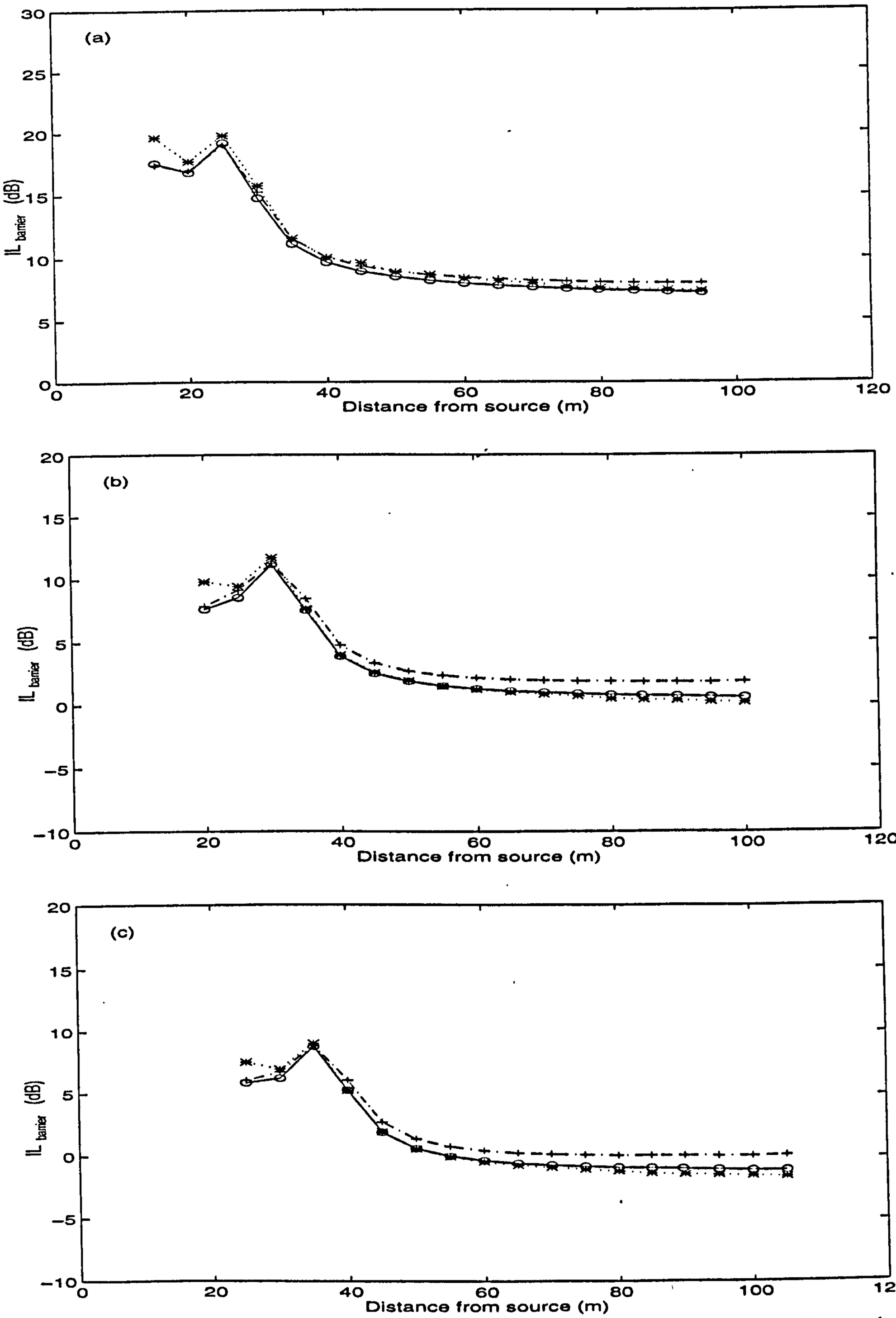

Figure 7.12 $\mathrm{IL}_{\mathrm{barrier}}$ predicted by the BEM for a source frequency of 1 kHz, with $z_s = 1$ m, $z = 1.5$ m and $h_b = 2.5$ m. Solid line and circles: no refraction; dotted lines and stars: upward refraction with a gradient of $-0.1\ \mathrm{ms}^{-1}$; dashdot lines and plus signs: downward refraction with a gradient of $+0.1\ \mathrm{ms}^{-1}$; $\sigma_e = 100$ kPa s m^{-2} and $\alpha_e = 100\ \mathrm{m}^{-1}$. (a) $r_{sb} = 10$ m, (b) $r_{sb} = 15$ m and (c) $r_{sb} = 20$ m.

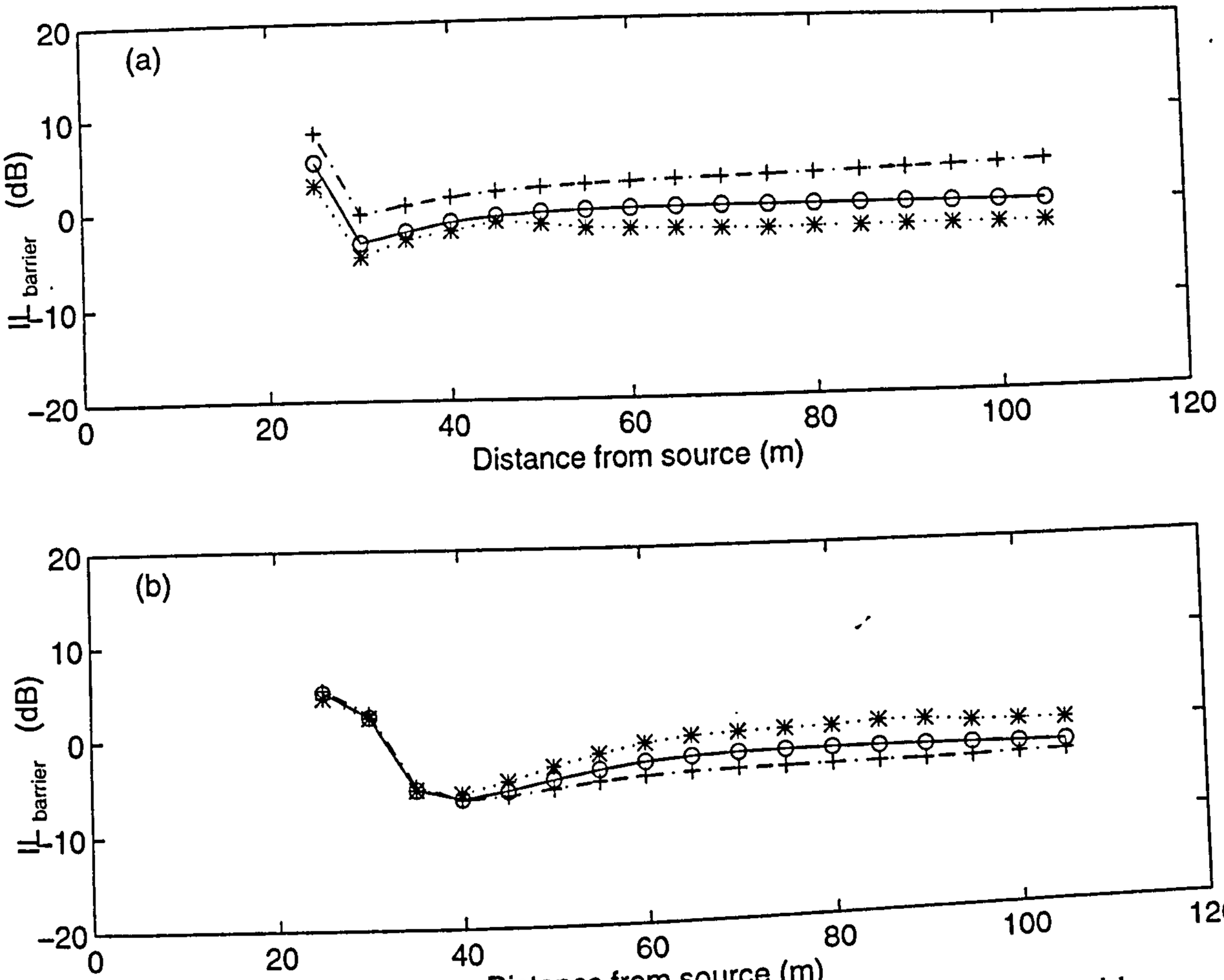

Figure 7.13 $IL_{barrier}$ predicted by the BEM for a source frequency of 500 Hz, with $z_s = z = 2.0$ m, $h_b = 2.5$ m and $r_{sb} = 20$ m. Solid line and circles: no refraction; dotted lines and stars: upward refraction; dashdot lines and plus signs: downward refraction. (a) $\sigma_e = 20$ kPa s m^{-2} and $\alpha_e = 60$ m^{-1} with gradients of ∓ 1.0 ms^{-1} and (b) $\sigma_e = 100$ kPa s m^{-2}, $\alpha_e = 100$ m^{-1} with gradients of ∓ 0.1 ms^{-1}.

7.5 Summary

In this chapter, laboratory measurements of the sound field from a point source above flat surfaces, convex surfaces and concave surfaces in the presence of barriers, which were used to simulate sound propagation in a homogeneous medium, in an upward refracting medium and in a downward refracting medium, in the presence of a barrier on flat ground surfaces, have been reported. Numerical predictions of the BEM have been used to compare with the experimental measurements in the cases of both rigid surfaces and

surfaces of finite impedance. In general, the agreement between the BEM calculations and the experimental measurements is very good.

The total insertion loss of a barrier, IL_{total}, has been used to characterize the effects of curved surfaces on acoustic barrier performance, which simulate the effects of temperature or wind velocity gradients on barrier performance in refracting media. Conclusions from the laboratory measurements and numerical calculations are in agreement with the general belief [54, 57] that IL_{total} is degraded in a downward refracting medium and enhanced in an upward refracting medium. However, these apparent changes in IL_{total} are largely the results of meteorological influences on sound propagation outdoors.

The barrier insertion loss, $IL_{barrier}$, has been used to study the effectiveness of a barrier on curved surfaces, simulating the effectiveness of a barrier on plane ground beneath refracting media. It has been suggested that $IL_{barrier}$ depends on a number of factors including the source -barrier-receiver geometry, the effective sound speed gradient, the source frequency, and the impedance of the ground surface. There are no consistent trends to show a degraded $IL_{barrier}$ in a downward refracting medium or an enhanced $IL_{barrier}$ in an upward refracting medium.

Chapter 8

Conclusions and suggestions

In this chapter, the main results of this work are summarized and some suggestions for further work are presented.

8.1 Conclusions

The main objectives of this work have been to investigate theories on sound propagation in a refracting atmosphere above an impedance plane and to derive theories and to make measurements of sound propagation over curved surfaces of finite impedance from monopole and dipole sources. Chapter 2 has examined numerical models for propagation of sound in the presence of temperature and wind velocity gradients. Analytical expressions have been derived for a stratified upward or downward refracting medium with arbitrary vector wind and temperature profiles. The approach used here has considered wind and temperature effects separately and the resulting predictions have been compared with those of the conventional studies in which the effect of wind is replaced by the use of an effective sound speed gradient. The results show that in an upward refracting medium, the use of an effective sound speed gradient is adequate for predicting the sound field at most practical ranges of interest. On the other hand, in a downward refracting medium, this method is adequate only for short distances, low frequencies and weak gradients.

Chapter 3 and Chapter 4 have studied upward refraction over flat impedance ground and the acoustically analogous situations where the sound waves propagate over cylindrically or spherically curved convex surfaces above which there is no refraction. Chapter 3 emphasizes the theoretical studies while Chapter 4 is concerned mainly with experimental investigations.

An analytical expression has been derived for propagation over flat impedance ground beneath an exponential sound speed profile and has been used to predict the diffraction of sound by a cylindrical surface in a homogeneous atmosphere. The output of this solution has been compared to Berry and Daigle's experimental data [15], to Berthelot and Zhou's experimental data [20], and to predictions based on the assumption of a bilinear profile as well. It has been found that the predictions given by the residue series solution for both bilinear and exponential profiles work well deep in the shadow region, whereas the residue series solution based on an exponential profile predicts much better results than those obtained by using a bilinear profile in the penumbra region along the line of sight. It has been shown that the predictions obtained from exponential profiles are very similar to those obtained from Berthelot's heuristic modification [19].

A factor that corrects the residue series solution has been found to be important for predicting the sound field deep in the shadow zone over a spherical surface.

The validity of our residue series model has been examined by comparing its predictions with those of the numerical techniques FFP, BEM and MAE, respectively, and with results of the experiments carried out in an anechoic chamber above a rigid convex surface with and without a felt covering. A persistent discrepancy between predictions and measured data has been found in the penumbra region along the shadow boundary above the felt-covered convex surface when q, the scaled nondimensionalized admittance defined in

Equation (2.2.6), is large. This discrepancy between predictions and data has been exhibited repeatedly with dipole as well as point monopole sources and no satisfactory explanation has been found.

In the vicinity of a source over a convex surface, predictions from the geometrical acoustics solution have shown good agreement with the measurements, whereas the residue series solution does not converge in this region. In the region where $z+z_s < r < \sqrt{2z_sR_c}$, the geometrical acoustics solution agrees well with the residue series solution. There is reasonably smooth transition between these two solutions. In the insonified region well above the shadow boundary, the geometrical acoustics solution agrees well with the measurements, whereas the residue series solution requires many more terms to achieve convergence and shows significant discrepancies from the measurements.

Analytical expressions derived for a monopole source have been extended to predict the sound field for a dipole source above convex impedance boundaries. The resulting predictions, in general, agree well with measured data. Both theoretical and experimental results have shown that the sound field above a convex surface, due to a horizontal dipole source behaves like that of a monopole point source. The sound field of a vertical dipole is quite similar, in range dependence, to that exhibited by the field due to a monopole source.

In Chapter 5, the normal mode solution has been developed for propagation in an exponential sound speed profile and used to predict the sound field diffracted by a concave surface. Analytical expressions for dipole sources have been deduced directly from those for a monopole source. Predictions from these expressions have been compared with the results of a series of laboratory experiments using a monopole source, a horizontal dipole source, and a vertical dipole source over cylindrical concave surfaces. Good agreement has been found between the measurements and the normal mode predictions for an exponential

profile where the sound field is due to a monopole source or a horizontal dipole source, but the agreement is less satisfactory where the sound field is due to a vertical dipole source. The prediction for a bilinear profile shows considerable disagreement with measurements at long ranges in both monopole and horizontal dipole sound fields, and significant differences from measurements in a vertical dipole sound field.

The predicted and measured transmission losses due to a horizontal dipole source, as a function of range, have been found to be close to those predicted and measured for a monopole source. In the case of a vertical dipole source, however, the predicted transmission loss shows oscillations due to the omission of the branch-line integral in the normal mode calculations, which is beyond the scope of the present thesis.

Chapter 6 describes studies and laboratory experiments on the sound field due to both monopole, horizontal dipoles and vertical dipoles above a convex mat-on-masonite surface with an impedance in which the imaginary part is greater than the real part and the phase angles $\varphi_z > \pi/3$. There is generally good agreement between the experimental data and the residue series predictions from poles evaluated by using Raspet *et al*'s technique [8] rather than by using Pierce's technique [3]. However, it appears that Raspet *et al*'s so-called surface wave poles are not pure surface wave poles. They include contributions from both the surface wave and the creeping wave.

The surface waves have been observed from the experiments above the convex mat-on-masonite surface that may be considered to simulate propagation over an impedance plane under an upward refraction. This phenomenon may be explained using the theory of Raspet *et al* [8]. The results show that near the convex mat-on-masonite surface, there are surface waves which propagate along the surface, decaying with height transverse to the surface, as separate arrivals from the earlier arriving creeping waves.

Laboratory measurements of the sound field from a point monopole source above flat, convex and concave surfaces, in the presence of barriers, have been reported in Chapter 7. In general, the agreement between the boundary element method (BEM) calculations and the experimental data is very good.

The total insertion loss of a barrier, IL_{total}, has been used to characterize the effects of curved surfaces on acoustic barrier performance which simulate the effects of temperature or wind velocity gradients on barrier performance in refracting media. The laboratory measurements and numerical calculations are in agreement with the general belief [54, 57] that IL_{total} is degraded in the downward refracting medium and enhanced in the upward refracting medium. However, these apparent changes in IL_{total} are largely the results of meteorological influences on sound propagation outdoors.

The barrier insertion loss, $IL_{barrier}$, has been used to study the effectiveness of a barrier on curved surfaces, simulating the effectiveness of a barrier on plane ground beneath refracting media. It has been suggested that $IL_{barrier}$ depend on a number of factors including the source-receiver-barrier geometry, the effective sound speed gradient, the source frequency, and the impedance of the ground surface. There are no consistent trends that show a degraded $IL_{barrier}$ in a downward refracting medium or an enhanced $IL_{barrier}$ in an upward refracting medium.

8.2 Suggestions for further work

The theories and experimental methods developed in this work can be extended in many ways. Five suggestions for further related work are presented as follows:

8.2.1 Surfaces with extended reaction

The residue series solution derived for a stratified refracting medium with an arbitrary sound speed profile above a locally-reacting impedance surface (*cf.* Chapter 2 and Chapter 3) may be extended to predict the sound field above surfaces exhibiting extended reaction. Analytical expressions may be found for both monopole and dipole sources. The resulting scaled and nondimensionalized admittance, q, would involve Airy functions of complex argument. Consequently much more complicated numerical techniques would be required to find the pole locations.

To validate the analytical expressions, experiments could be attempted using the present convex and concave surfaces with the monopole and dipole sources. Surfaces with extended reaction may be obtained by covering the rigid surfaces with materials such as fibre glass. A lateral wave [155] may be expected to be captured above such surfaces.

8.2.2 Studies on surface waves

Further studies are expected to be concerned with propagation velocities of the surface waves and the creeping waves over a convex impedance surface. Pierce [3] suggested that the creeping wave phase velocity, v_c, can be approximated by

$$v_c = \frac{c_0}{1+\dfrac{\mathrm{Im}\left(\tau_1 e^{i\pi/2}\right)}{\left(2k_0^2 R_c^2\right)^{1/3}}}, \tag{8.2.1}$$

where τ_1 is the first pole in Equation (6.1.8). However, this expression may not work if the first pole contains the surface wave contribution. The surface wave phase velocity, v_s, and group velocity, v_g, were suggested [69] to be

$$v_s = \frac{c_0}{\sqrt{1+\beta^2}}, \tag{8.2.2}$$

and

$$v_g = v_s + k_0 \frac{\partial v_s}{\partial k}. \qquad (8.2.3)$$

Surface curvature has been shown to enhance the existence of surface waves. Given the analogy between propagation over curved surfaces and refraction over plane ground, the existence of surface waves in a refracting atmosphere may be verified by outdoor measurements above a seasonal snow covered ground in the presence of temperature or wind velocity gradients.

8.2.3 Diffraction of sound by an elliptical surface

If the sound speed, $c = c(z,r)$, varies with both vertical and horizontal directions, an elliptically curved surface may be used to simulate sound propagation in such a 2-D refracting medium. A cross section of an elliptical cylinder could be used to simulate an upward refracting medium, while a cross section of a concavely elliptical cylinder could be used to simulate a downward refracting medium.

8.2.4 Effect of turbulence on sound propagation

Calculation of average turbulence effects on sound propagation based on the residue theorem may be pursued. The effects of decorrelation in amplitude and phase of sound due to turbulent scattering, and the interference of the horizontal wave number components would be incorporated into the spectral calculation of sound pressure levels in a refracting atmosphere above a complex impedance plane. The result of the turbulent residue series solution could be compared with the turbulent FFP [147] and measurements of sound propagation in a turbulent atmosphere [104]. The turbulent residue series solution may be extended further to evaluate the sound fields due to dipole sources in a turbulent atmosphere.

8.2.5 Effect of turbulence on barrier performance

Theoretical investigations on a barrier in a refracting turbulent atmosphere are of practical interest. Calculation would be of average turbulence effects on sound propagation over a noise barrier in an upward and a downward refracting atmosphere. A combination of the theory of Pierce for diffraction by a wedge in a homogeneous atmosphere and the residue series solution for refraction in an inhomogeneous atmosphere may be developed. This approach could be extended to include the effect of turbulence, if the turbulent residue series solution mentioned in Chapter 8.2.4 is developed. Various barrier profiles may be modelled in this way.

References

[1] D K Wilson, "Sound field computations in a stratified, moving medium," J. Acoust. Soc. Am. **94** (1), 400-407 (1993).

[2] Y L Li, M J White, and S J Franke, "New fast field programs for anisotropic sound propagation through an atmosphere with velocity profile," J. Acoust. Soc. Am. **95** (2), 718-726 (1994).

[3] A D Pierce, *Acoustics: An Introduction to Its Physical Principles and Applications*, (Acoustical Society of America, New York, 1989).

[4] L Nijs and C P A Wapenaar, "The influence of wind and temperature gradients on sound propagation, calculated with the two-way wave equation," J. Acoust. Soc. Am. **87** (5), 1987-1998 (1990).

[5] M West, F Walkden and R A Sack, "The acoustic shadow produced by wind speed and temperature gradients close to the ground," Appl. Acoust. **27**, 239-260 (1989).

[6] K B Rasmussen, "Outdoor sound propagation under the influence of wind and temperature gradients," J. Sound Vib. **104** (2), 321-335 (1986).

[7] B De Jong, "The influence of wind and temperature gradients on outdoor sound propagation," PhD thesis, Deft University Press (1983).

[8] R Raspet, G E Baird and W Wu, "The relationship between upward refraction above a complex impedance plane and the spherical wave evaluation for a homogeneous medium," J. Acoust. Soc. Am. **89**, 107-114 (1991).

[9] R Raspet, G E Baird and W Wu, "Normal mode solution for low frequency sound propagation in a downward refracting atmosphere above a complex impedance plane," J Acoust. Soc. Am. **91**, 1341-1352 (1992).

[10] K Attenborough, S Taherzadeh, H E Bass, X Di, R Raspet, G R Becker, A Gudesen, A Chrestman, G A Daigle, A L'Esperance, Y Gabillet, K E Gilbert, Y L Li, M J White, P Naz, J M Noble, and H A J M van Hoof, "Benchmark cases for outdoor sound propagation models," J. Acoust. Soc. Am. **97**(1), 173-191 (1995).

[11] K Attenborough, "Ground parameter information for propagation models," J. Acoust. Soc. Am. **92**, 418-427 (1992).

[12] K M Li, K Attenborough and N W Heap, "Source height determination by ground effect inversion in the presence of a sound velocity," J. Sound Vib. **145**, 111-128 (1991).

[13] T F Embleton, "Analogies between nonflat ground and nonuniform meteorological profiles in outdoor sound propagation," J. Acoust. Soc. Am. Suppl. 1 **78**, S86 (1985)

[14] M Almgren, "Scale model simulation of outdoor sound propagation considering a sound speed gradient," Proc. INTER-NOISE **86**, 1301-1306 (1986).

[15] A Berry and G A Daigle, "Controlled experiments of the diffraction of sound by a curved surface," J. Acoust. Soc. Am. **83**(6), 2047-2058 (1988).

[16] P A Stark, *Introduction to Numerical Methods* (Macmillan, London, 1970).

[17] A Berry, "Etude de la propagation du son sur les surfaces courbees," M.sc. thesis, University de Sherbrook (1987).

[18] K M Li, Q Wang and K Attenborough, "Analytical approximations for the 3-D sound fields due to monopole and dipole sources over convex impedance surfaces," Submitted to J. Acoust. Soc. Am.

[19] Y H Berthelot, "A note on the acoustic penumbra behind a curved surface," J. Acoust. Soc. Am. **99**(4), 2428-2429 (1996).

[20] Y H Berthelot and J.-X. Zhou, " Scale model experiments on the validity of the matched asymptopic expansions theory for sound diffraction by curved surfaces of finite impedance," J. Acoust. Soc. Am. **93**(2), 605-608 (1993).

[21] R E Langer (Ed.), *Electronmagnetic Waves*, (The University of Wisconsin Press, Madison, 1962).

[22] D S Jones, *Acoustics and Electronmagnetic Waves*, (Vlaredon Press, Oxford, 1986).

[23] M Abramowitz and I Stegun, *Handbook of Mathematical Functions*, (Dover Publications, New York, 1970).

[24] D C Hothersall, S N Chandler-Wilde and M N Hajmirzae, " Efficiency of single noise barriers," J. Sound Vib. **146**(2), 303-322 (1991).

[25] S N Chandler-Wilde and D C Hothersall, " Sound propagation above an inhomogeneous impedance plane," J. Sound Vib. **98**(4), 475-491 (1985).

[26] A D Pierce and G L Main, "Computational algorithms for the matched asympototic expansion solution of high frequency acoustic wave diffraction by curved surfaces of finite impedance," in *Advances in Computer Methods for Partial Differential Equations-6*, edited by R Vichnevetsky and R Stepleman (IMACS, Rutgers University, New Brunswick, NJ, 1987), 187-194.

[27] M R Stinson, "A note on the use of an approximate formula to predict sound fields above an impedance plane due to a point source," J. Acoust. Soc.Am. **98**(3), 1810-1812 (1995).

[28] K Attenborough, "Acoustical impedance models for outdoor ground surfaces," J. Sound Vib. **99**, 521-544 (1985).

[29] J A Kearns, "An investigation of the diffraction of an acoustic plane wave by a curved surface of finite impedance," Ph.D. thesis, Georgia Institute of Technology (1989).

[30] A P Dowling and J E F Williams, *Sound and Sources of Sound*, (Ellis Horwood Ltd., Chichester, 1983) pp. 152.

[31] Z Hu and J S Bolton, "Sound propagation from an arbitrarily oriented multi-pole placed near a plane, finite impedance surface," J. Sound Vib. **170**(5), 637-669 (1994).

[32] M Almgren, "Simulation by using a curved ground scale model of outdoor sound propagation under the influence of a constant sound speed gradient," J. Sound Vib. **118**(2), 353-370 (1987).

[33] K Attenborough, J M Lawther and S I Hayek, "Propagation of sound above a porous half-space," J. Acoust. Soc.Am. **68**(5), 1493-1501 (1980).

[34] M E Delany and E N Bazley, "Acoustical properties of fibrous absorbent materials," Appl. Acoust. **3**, 105-116 (1970).

[35] K M Li and Q Wang, " Analytical solution for outdoor sound propagation in the presence of wind," J. Acoust.Soc.Am. **102**(4), 2040-2049 (1997).

[36] V E Ostashev, "Waveguide propagation of a high-frequency scoustic field in a stratified moving medium near an impedance boundary," Izv. Atmos. Oceanic Phys. **22**, 936-941 (1986).

[37] *Handbook of Mathematical Functions*, edited by M Abramowitz and I A Stegun (Dover, New York, 1970), pp 448-449.

[38] Q Wang and K M Li, "The prediction of sound field above a curved surface," Proceedings of The Seventh International Symposium on Long Range Sound Propagation, July 1996, pp 95-109.

[39] A D Pierce, "Wave equation for sound in fluids with unsteady inhomogeneous flow," J. Acoust. Soc. Am. **87** (6), 2292-2299 (1990).

[40] A R Wenzel, "Propagation of waves along an impedance boundary," J. Acoust. Soc. Am. **55**(5), 956-963 (1974).

[41] R J Donato, "Propagation of a spherical wave near a plane boundary with a complex impedance," J. Acoust. Soc. Am. **60**(1), 34-39 (1976).

[42] R J Donato, "Model experiments on surface waves," J. Acoust. Soc. Am. **63**(3), 700-703 (1978).

[43] R Raspet and G E Baird, "The acoustic surface wave above a complex impedance ground surface," J. Acoust. Soc. Am. **85**(2), 638-640 (1989).

[44] G A Daigle, M R Stinson and D I Havelock, "Experiments on surface waves over a model impedance plane using acoustical pulses," J. Acoust. Soc. Am. **99**(4), 1993-2005 (1996).

[45] A Berry, "Propagation of sound above a curved surface," J. Acoust. Soc.Am. Suppl. 1 **81**, PP8 (1987).

[46] Y Gabillet, H Schroeder, G A Daigle, and A L'Esperance, "Application of the Gaussian beam approach to sound propagation in the atmosphere: Theory and experiments," J. Acoust. Soc. Am. **93**(6), 3105-3116 (1993).

[47] K Attenborough and K M Li, "Ground effect for A-weighted noise in the presence of turbulence and refraction," Proceeding of The Seventh International Symposium on Long Range Sound Propagation, July 1996, pp 49-62.

[48] V A Fock, *Electromagnetic Diffraction and Propagation Problems*, (Pergamon Press, Oxford London Edinburgh NewYork Paris Frankfurt, 1965).

[49] K B Rasmussen, "Outdoor sound propagation under the influence of wind and temperature gradients," J. Sound Vib. **104**, 321-336 (1986).

[50] M Almgren, "Scale model simulation of outdoor sound propagation," Chalmers Univ. of Technology, Goteborg, Sweden, 1983.

[51] K M Li and Q Wang, "A BEM approach to assess the acoustic performance of noise barriers in the refracting atmosphere," accepted by J. Sound Vib..

[52] R Seznec, "Diffraction of sound around barriers: use of the boundary element technique," J. Sound Vib. **73**, 195-209 (1980).

[53] E M Salomons, "Noise barriers in a refracting atmosphere," Appl. Acoust. **47**(3), 217-238 (1996).

[54] K B Rasmussen, "Sound propagation over screened ground under upwind conditions," J. Acoust. Soc. Am. 100(6), 3581-3586 (1996).

[55] K Attenborough, "Review of ground effects on outdoor sound propagtion from continuous broadband sources," Appl. Acoust. **24**, 289-319 (1988).

[56] D D Rife and J Vanderkooy, "Transfer-function measurement with Maximum-Length Sequences," J. Audio Eng. Soc. **37**, 419 (1989).

[57] R De Jong and E Stusnick, "Scale model studies of the effects of wind on acoustic barrier performance," Noise Control Engineering **6**(3), 101-109 (1976).

[58] P M Morse and H Feshbach, "Methods of theoretical physics," (McGraw-Hill, New York, 1953), Vol. 1, 408-410.

[59] B D Seckler and J B Keller, "Asymptotic theory of diffraction in inhomogeneous media," J Acoust. Soc. Am. **31**, 206-216 (1959).

[60] A D Pierce, "Wave equation for sound in fluids with unsteady in inhomogeneous flow," J. Acoust. Soc. Am. **87**, 2292-2299 (1990).

[61] K M Li, "A high-frequency approximation of sound propagation in a stratified moving atmosphere above a porous ground surface," J. Acoust. Soc. Am. **95**(4), 1840-1852 (1994).

[62] L B Felsen and N Marcuvitz, *Radiation and scattering of waves*, pp. 339-341, (IEEE press, Inc., New York, 1994).

[63] L M Brekhovskikh, "Surface wave in acoustics," Sov. Phys. Acoust., **5(1)**, 3-12, (1959).

[64] K M Ivanov-Shits and F V Rozhin, "Investigation of surface waves in air," Sov. Phys. Acoust., **5**(4), 510-512 (1959).

[65] S I Thomasson, "Sound propagation above a layer with a large refraction index," J. Acoust. Soc. Am. **61**(3), 659-674 (1977).

[66] M R Stinson, G A Daigle, and D I Havelock, "The formation of surface waves over a model surface," *Proc. of the 5th International Symposium on Long Range Sound Propagation* (Milton Keynes, U.K., 1992), pp17-28.

[67] G A Daigle, "Surface waves above porous ground surfaces," J. Acoust. Soc.Am. Suppl. 1 **85**, S82 (1989).

[68] G A Daigle and T F W Embleton, "Surface waves and surface wave devices in atmospheric acoustics," J. Acoust. Soc. Am. Suppl. 1 **88**, S190 (1990).

[69] C H Howorth and K Attenborough, "Model experiments on air-coupled surface waves," J. Acoust. Soc. Am. **92**(4), 2431(A) (1992).

[70] I Tolstoy, *Wave Propagation* (McGraw-Hill, New York, 1973).

[71] C H Howorth, "Sound propagation over rigid porous layers," PhD Thesis, The Open University (1991).

[72] A D Pierce, "Creeping waves, shadow zones, and acoustic energy conservation," J. Acoust. Soc. Am. Suppl. 1 **65**, S129 (1979).

[73] T L Richard and K Attenborough, "Accurate FFT-based Hankel transforms for predictions of outdoor sound propagation," J. Sound Vib. **109**, 157-167 (1980).

[74] K Attenborough, S I Hayek, and J M Lawther, "Propagation of sound above a porous half-space," J. Acoust. Soc. Am. **68**(5), 1493-1501 (1980).

[75] G A Daigle, "Role of surface waves in outdoor noise propagation," Proc. INTER-NOISE 91 **I**, 455-458 (1991).

[76] C L Pekeris, "Theory of propagation of sound in a half-space of variable sound velocity under conditions of formation of a shadow zone," J. Acoust. Soc. Am. **18**, 295-315 (1946).

[77] D C Pridmore-Brown and U Ingard, "Sound propagation into the shadow zone in a temperature-stratified atmosphere above a plane boundary," J. Acoust. Soc. Am. **27**, 36-42 (1955).

[78] H Bateman, Monthly Weather Rev. **42**, 258 (1914).

[79] L Rayleigh, Phil. Mag. **6**, 289, (1903).

[80] L Rayleigh, *Theory of Sound* (Dover Publications, New York, 1945), Vol. II, pp. 130.

[81] L V King, Trans. Roy. Soc. (London) **A218**, 211 (1919).

[82] W Derham, "Experimenta et observationes de soni motu," Philos. Trans. Roy. Soc. **5**, 380 (1708).

[83] V M Babic and V S Buldyrev, "Asymptotic theory of diffraction in inhomogeneous media," J. Acoust. Soc. Am. **31**, 206-216 (1959).

[84] P M Morse and H Fesbach, *Methods of Theoretical Physics*, Pt. I, (McGraw-Hill Book Company, New York, 1963), pp. 502-504.

[85] X Di and K E Gilbert, "The effect of turbulence and irregular terrain on outdoor sound propagation," Proc. of 6th International Symposium on Long Range Sound Propagation, 315-333 (1994).

[86] J P Chambers, R Raspet, Y H Berthelot and M J White, "Use of the fast field program for predicting diffraction of sound by curved surfaces," J. Acoust. Soc. Am. **102**(1), 646-649 (1997).

[87] U Ingard, "A review of the influence of meteorological conditions on sound propagation," J. Acoust. Soc. Am. **25**(3), 405-411 (1953).

[88] M E Delany, "Sound propagation in the atmosphere: A historical review," Acustica **38**, 201-223 (1977).

[89] J E Piercy, T F W Embleton and L C Sutherland, "Review of noise propagation in the atmosphere," J. Acoust. Soc. Am. **61**(6), 1403-1418 (1977).

[90] A L'Esperance, P Herzog, G A Daigle and J R Nicolas, "Heuristic model for outdoor sound propagation based on an extension of the geometrical ray theory in the case of a linear sound speed profile," Appl. Acoust. **37**, 111-139 (1992).

[91] T F W Embleton, "Tutorial on sound propagation outdoors," J. Acoust. Soc. Am. **100**(1), 31-48 (1996).

[92] A L'Esperance, J Nicolas, D K Wilson, D W Thomson, Y Gabillet and G A Daigle, "Sound propagation in the atmospheric surface layer, Comparison of experiments with FFP predictions," Appl. Acoust. **40**, 325-346 (1993).

[93] Y L Li, S J Franke and C H Liu, "Numerical implementation of an adaptive fast-field program for sound propagation in layered media using the chirp z-transform," J. Acoust. Soc. Am. **89**, 2068-2075 (1991).

[94] R Raspet, L Yao, S J Franke and M J White, "Comments on 'The influence of wind and temperature gradients on sound propagation, calculated with two way equations' [J. Acoust. Soc. Am. 87, 1987-1998 (1990)]," J. Acoust. Soc. Am. **91(1)**, 498-500 (1992).

[95] L Nijis and C P A Wapenaar, "Reply to: 'Comments on the influence of wind and temperature gradients on sound propagation calculated with the two-way wave equation' [J. Acoust. Soc. Am. 91, 498-500 (1992)]," J. Acoust. Soc. Am. **91**(1), 501-504 (1992).

[96] R J Thompson, "Ray-acoustic intensity in a moving medium. I," J. Acoust. Soc. Am. **55**(4), 729-732 (1974).

[97] R J Thompson, "Ray-acoustic intensity in a moving medium. II. A stratified medium," J. Acoust. Soc. Am. **55**(4), 733-737 (1974).

[98] J S Lamancusa, "Ray tracing in a moving medium with two dimensional sound-speed variation and application to sound propagation over terrain discontinuities," J. Acoust. Soc. Am. **93**(4), 1716-1726 (1993).

[99] V E Ostashev, "High-frequency acoustic field of a point source lying above an impedance surface in a stratified moving medium," Izv. Atmos. Oceanic Phys. **23**(5), 370-377 (1987).

[100] F R DiNapoli and R L Deavenport, "Theoretical and numerical Green's function solution in aplane layered medium," J. Acoust. Soc. Am. **67**, 92-105 (1980).

[101] S W Lee, N Bong, W F Richards, and R Raspet, "Impedance formulation of the fast field program for acoustic wave propagation in the atmosphere," J. Acoust. Soc. Am. **79**, 628-634 (1986).

[102] Y L Li, M J White and S J Franke, "New fast field programs for anisotropic sound propagation through an atmosphere with a wind velocity profile," J. Acoust. Soc. Am. **95**, 718-726 (1994).

[103] P H Parkin and W E Scholes, "The horizontal propagation of sound from a jet engine close to the ground, at Radlett," J. Sound Vib. **1**, 1-13 (1964).

[104] P H Parkin and W E Scholes, "The horizontal propagation of sound from a jet engine close to the ground, at Hatfield," J. Sound Vib. **2**(4), 353-374 (1965).

[105] J B Keller, "Diffraction by a convex cylinder," IEEE Trans. Antennas Propagat., **AP-24**, 312-321 (1956).

[106] N A Logan and K S Yee, "A mathematical model for diffraction by convex surfaces," in References [21], pp. 139-180.

[107] V M Babic and V S Buldyrev, *Short-Wavelength Diffraction Theory*, (Springer-Verlag, Berlin Heidelberg, 1991).

[108] P J Filippi, D Habault and P Gaitan, "Sound propagation above grounds," in Proc. INTER-NOISE **86**, 433-446 (1986).

[109] R Raspet, S W Lee, E Kuester, D C Chang, W F Richards, R Gilbert, and N Bong, "A fast field program for sound propagation in a layered atmosphere above an impedance ground," J. Acoust. Soc. Am. **77**, 345-352 (1985).

[110] S J Franke, R Raspet, and C H Liu, "Numerical prediction of atmospheric sound pressure levels in shadow zones," J. Acoust. Soc. Am. **83**, 816-820 (1988).

[111] M west, R A Sack, and F Walkden, "The fast field program (FFP). A second tutorial : Application to long range sound propagation in the atmosphere," Appl. Acoust. **33**, 199-228 (1991).

[112] L Nijis and C P A Wapenaar, " The influence of wind and temperature gradients on sound propagation, calculated with the two-way wave equation," J. Acoust. Soc. Am. **87**, 1987-1998 (1990).

[113] J P Chambers, "Scale model experiments on the diffraction and scattering of sound by geometrical step discontinuities and curved rough surfaces," Ph.D Dissertation, Georgia Institute of Technology (1994).

[114] G A Daigle and R Raspet, "Dispersion of impulse sound above a curved surface," J. Acoust. Soc. Am. **89**(1), 101-106 (1991).

[115] M Almgren, "Effect of the acoustic boundary layer on scale model simulation of outdoor sound propagation," Chalmers Univ. of Tech., Dept. of Building Acoust., Report **F85-03** (1985).

[116] B Hallberg, C Larsson, and S Israelsson, "Measurements of meteorological effects on long-range sound propagation using m-sequence correlation," J. Acoust. Soc. Am. **78**, 1038-1044 (1985).

[117] D C Pridmore-Brown, "Sound propagation in a temperature- and wind-stratified medium," J. Acoust. Soc. Am. **34**, 438-443 (1962).

[118] F R DiNapoli, "A fast field program for multilayered media," Naval Underwater Systems Centre, Tech. Rep. 4103 (1971).

[119] H W Kutschale, "The integral solution of the sound field in a multilayered liquid-solid half-space with numerical computation for low-frequency propagation in the Arctic Ocean," Tech. Rep. No. 1 (CU-1-70, ONR Contract N00014-67-A-0108-0016), Lamont-Doherty Geological Observatory, Columbia University, Palisades, New York (1970).

[120] H W Kutschale, "Rapid computation by wave theory of the propagation loss in the Arctic Ocean," Tech. Rep. No. 8, Lamont-Doherty Geological Observatory, Columbia University, Palisades, New York (1981).

[121] I P Chunchuzov, "Field of a low frequency point source of sound in an atmosphere with non-uniform wind-height distribution." Sov. Phy. Acoust. **30,** 323-327 (1984).

[122] W E Zorumski and W L Willshire, Jr., "Downward sound propagation in an atmospheric boundary layer," AIAA J. **27**, 515-523 (1989).

[123] C H Harrison, "Ocean propagation models," Appl. Acoust. **27**, 163-201 (1989).

[124] T F W Embleton and G A Daigle, "Experiments with surface waves," INTER-NOISE **90**, (1990).

[125] R Raspet, H E Bass, and J Ezell, "Effect of finite ground impedance on the propagation of acoustic pulses," J. Acoust. Soc. Am. **74**(1), 267-274 (1983).

[126] R Raspet, J Ezell, and H E Bass, "Additional comments on and erratum for 'Effect of finite ground impedance on the propagation of acoustic pulses' [J. Acoust. Soc. Am. 74, 267-274 (1983)]," J. Acoust. Soc. Am. **77**(5), 1955-1958 (1985).

[127] Z Maekawa, "Noise reduction by screens," Appl. Acoust. **1**, 157-173 (1968).

[128] M Born and E Wolf, *Principles of Opitics*, Pergamon, Oxford, 1959.

[129] A D Pierce, "Diffraction of sound around corners and over wide barriers," J. Acoust. Soc. Am. **55**(5), 941-955 (1974).

[130] U J Kurze, "Noise reduction by barriers," J. Acoust. Soc. Am. **55**(3), 504-518 (1974).

[131] T Isei, T F W Embleton, and J E Piercy, "Noise reduction by barriers on finite impedance ground," J. Acoust. Soc. Am. **67**(1), 46-58 (1980).

[132] J Nicolas and G A Daigle, "Experimental study of a slow-waveguide barrier on finite impedance ground," J. Acoust. Soc. Am. **80**(3), 869-876 (1986).

[133] C G Don, "Application of a hard truncated wedge theory of diffraction to wide barriers," J. Acoust. Soc. Am. **90**(2), 1005-1010 (1991).

[134] A I Papadopoulos and C G Don, "A study of barrier attenuation by using acoustic impulses," J. Acoust. Soc. Am. **90**(2), 1011-1018 (1991).

[135] Y W Lam and S C Roberts, "A simple method for accuate prediction of finite barrier insertion loss," J. Acoust. Soc. Am. **93**(3), 1445-1452 (1993).

[136] D J Saunders and R D Ford, "A study of the reduction of explosive impulses by finite sized barriers," J. Acoust. Soc. Am. **94**(5), 2859-2875 (1993).

[137] K Takagi, R Hotta, and K Yamamoto," A simple method for the calculation of noise attenuation by a finite length barrier," Appl. Acoust. **43**, 353-365 (1994).

[138] Y W Lam, "Using Maekawa's chart to calculate finite length barrier insertion loss," Appl. Acoust. **42**, 29-40 (1994).

[139] Y W Lam, "On the modelling of the effect of ground terrain profile in environmental noise calculations," Appl. Acoust. **42**, 99-123 (1994).

[140] R G De Jong, "A model study of the effects of wind on the sound attenuation of barriers," Master's thesis (Massachusetts Institute of Technology, May 1974).

[141] E M Salomons, "Diffraction by a screen in downwind sound propagation: A parabolic-equation approach," J. Acoust. Soc. Am. **95**(6), 3109-3117 (1994).

[142] E M Salomons, "Downwind propagation of sound in an atmosphere with a realistic sound-speed profile: a semianalytical ray model," J. Acoust. Soc. Am. **95**, 2425-2436 (194).

[143] K G Kouyoumjian and P H Pathak, "A uniform geometrical theory of diffraction for an edge in a perfectly conducting surface," Proc. IEEE **62**, 1448-1461 (1974).

[144] K B Rasmussen, "On the effect of terrain profile on sound propagation outdoors," J. Sound Vib. **98**, 35-44 (1985).

[145] K B Rasmussen, "Sound propagation over ground under the influence of a sound speed profile in the atmosphere," J Sound Vib. **139**, 71-81 (1990).

[146] K B Rasmussen, Computer simulation of sound propagation over ground under the influence of atmospheric effects. Letter to the editor," J Sound Vib. **141**, 347-354 (1990).

[147] R Raspet and W Wu, "Calculation of average turbulence effects on sound propagation based on the fast field program formulation," J. Acoust. Soc. Am. **97**(1), 147-153 (1995).

[148] K M Li, S Taherzadeh, and K Attenborough, "Sound propagation from a dipole source near an impedance plane," J. Acoust. Soc. Am. **101**(6), 3343-3352 (1997).

[149] K M Li, S Taherzadeh, and K Attenborough, "The ground effect for a dipole source," Acustica **82**(S1), 126 (1996).

[150] D C Hothersall and S A Tomlinson, "Effects of high-sided vehicles on the performance of noise barriers," J. Acoust. Soc. Am. **102**(2), 998-100 (1997).

[151] Douglas D Rife, "MLSSA Maximum-Length Sequence System Analyzer reference manual," DRA Laboratories, 1992.

[152] Q Wang and K M Li, "Sound propagation over concave surfaces," submitted to J. Acoust. Soc. Am..

[153] D C Strickler, "Normal mode program with both discrete and branch line contributions," J. Acoust. Soc. Am. **61**, 856-861 (1974).

[154] K M Li, S Taherzadeh and K Attenborough, "Sound propagation from a dipole source near an impedance plane," J. Acoust. Soc. Am. **101**(6), 2006-2012 (1997).

[155] L M Brekhovskikh, *Waves in Layered Media*, (Harcourt Brace Jovanovich, London, 1980).

Appendix

Photographic section

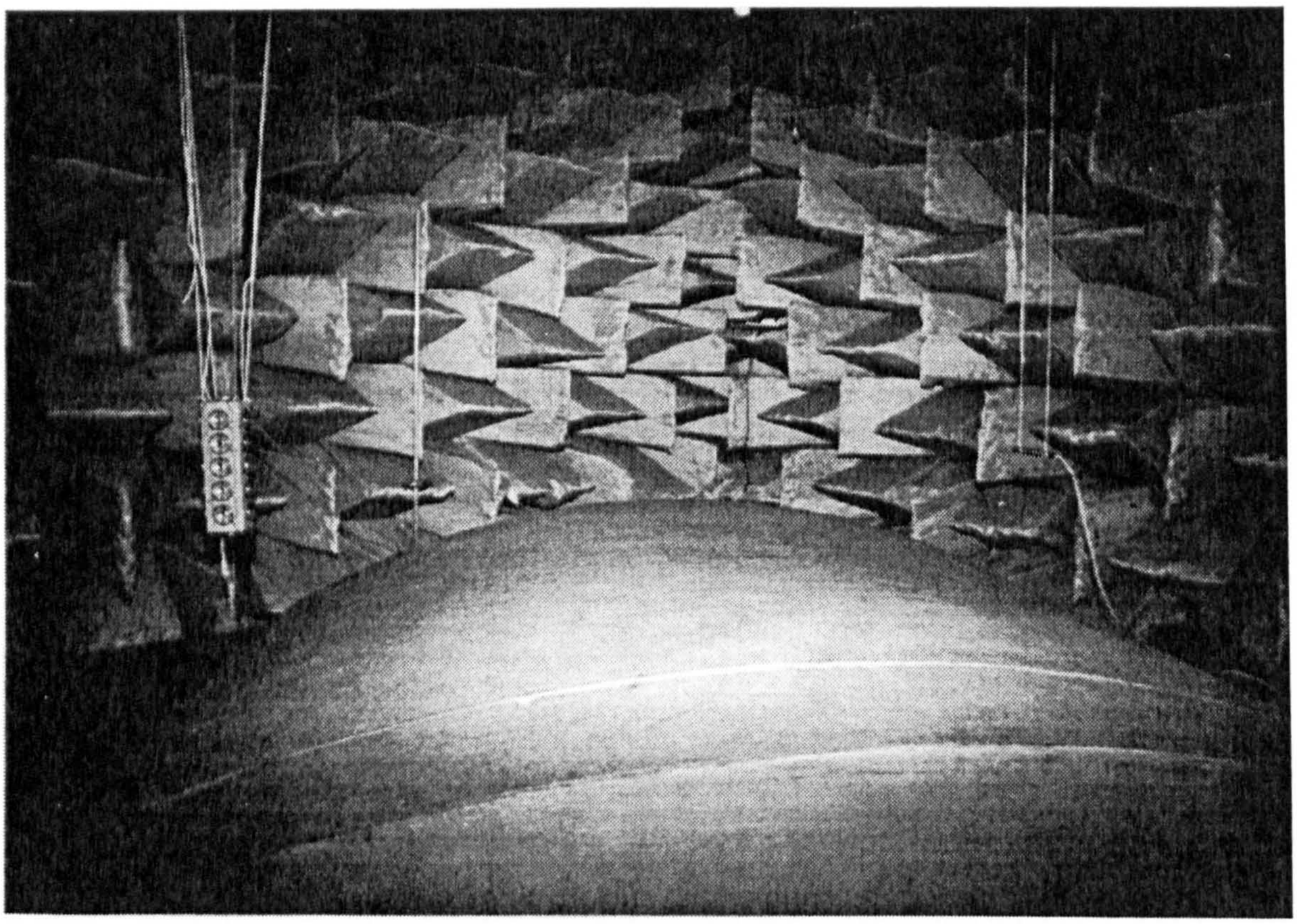

Figure A-1 Photograph showing the rigid convex surface.

Figure A-2 Photograph showing the felt-covered convex surface.

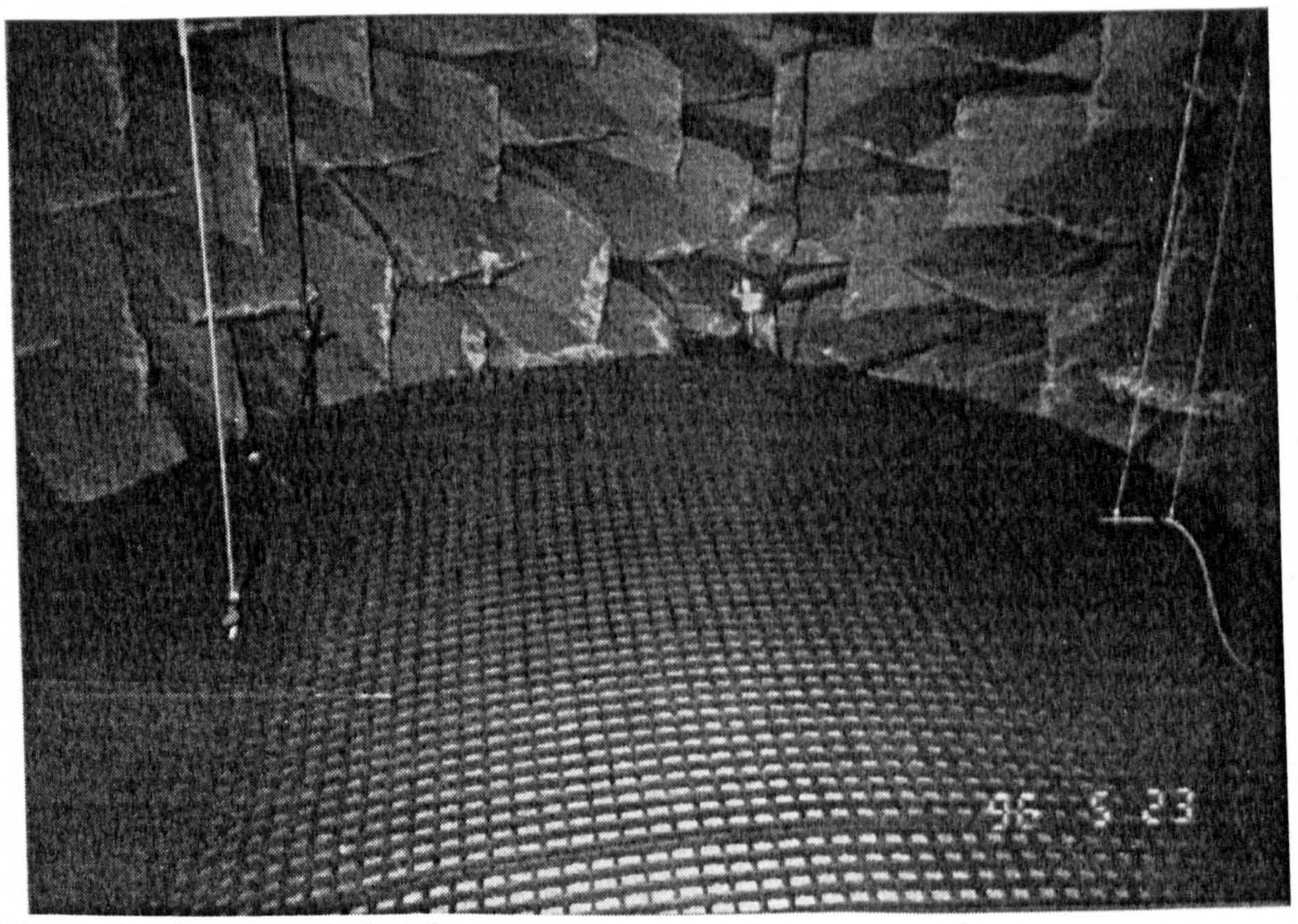

Figure A-3 Photograph showing the mat-on-masonite convex surface.

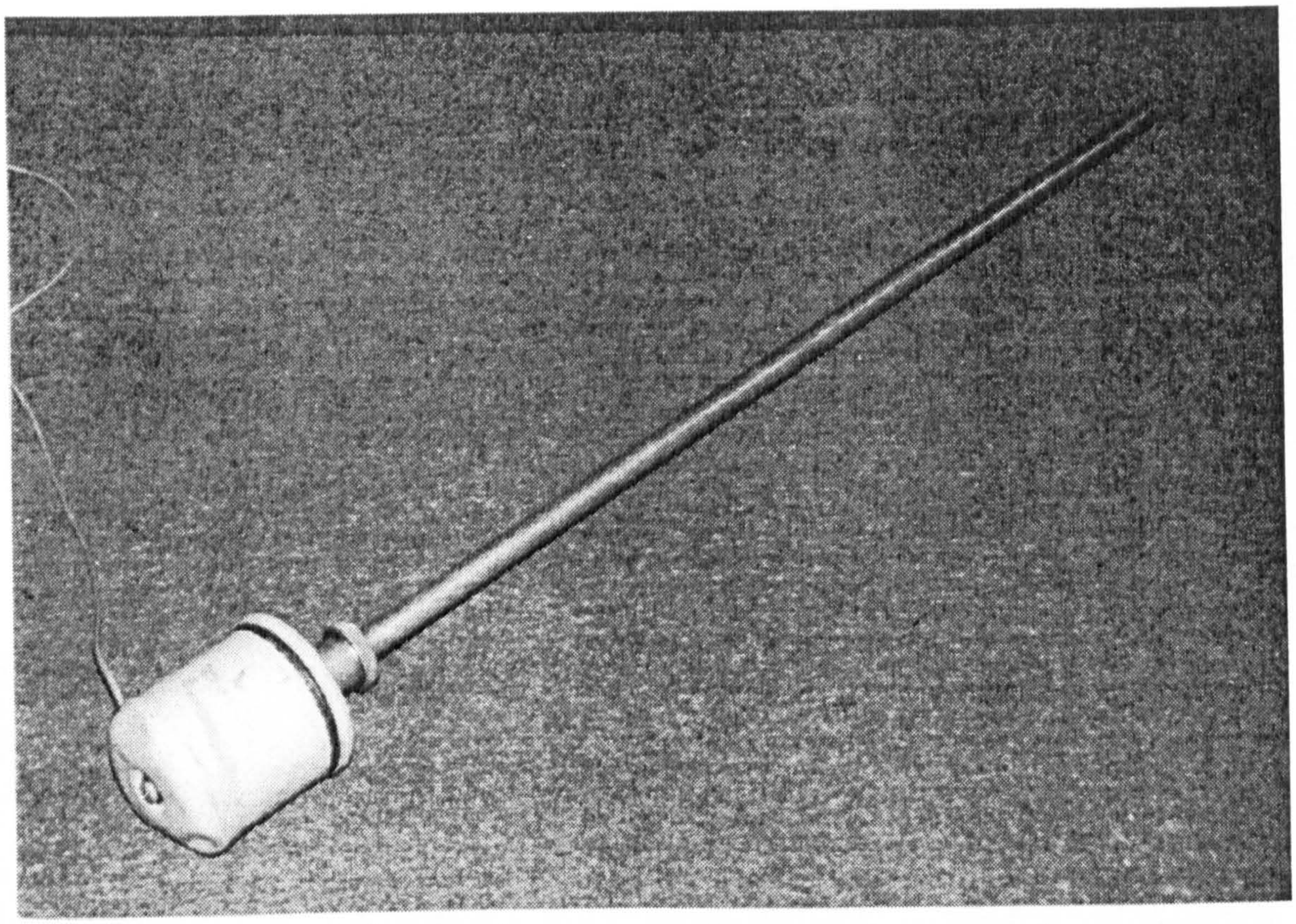

Figure A-4 Photograph showing the tannoy speaker as a point monopole source.

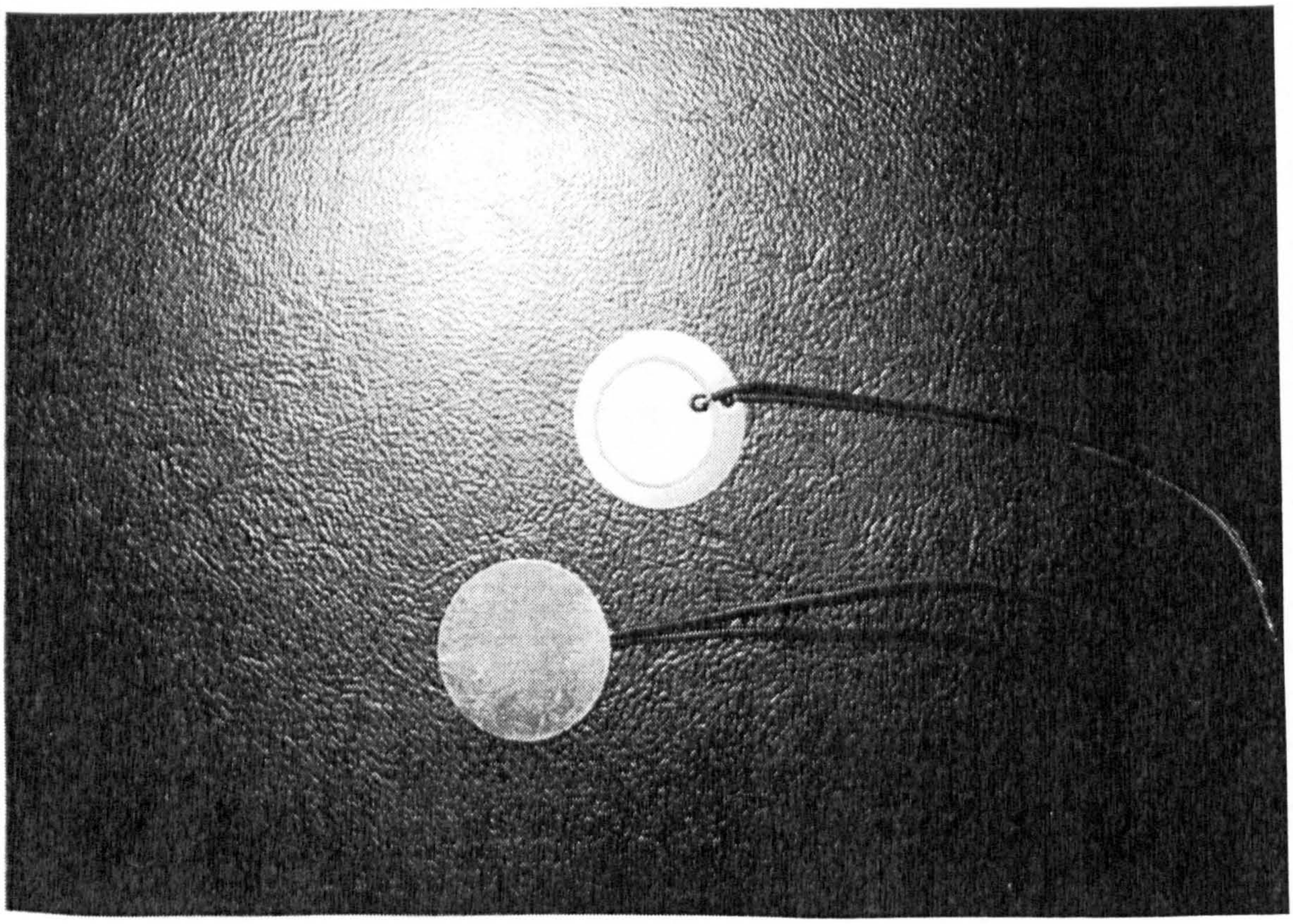

Figure A-5 Photograph showing the piezo-ceramic transducer dics as dipole sources.

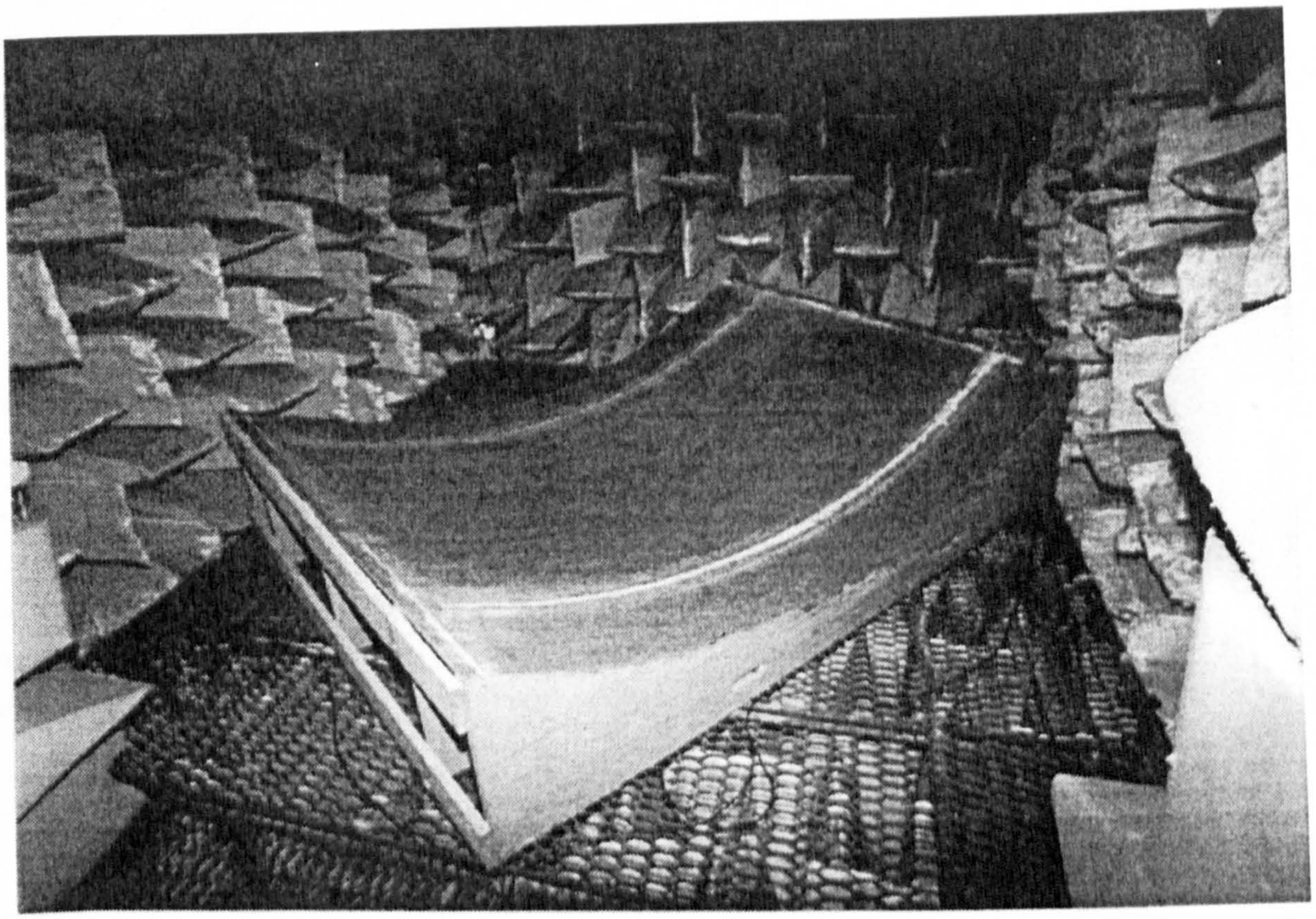

Figure A-6 Photograph showing the rigid concave surface.

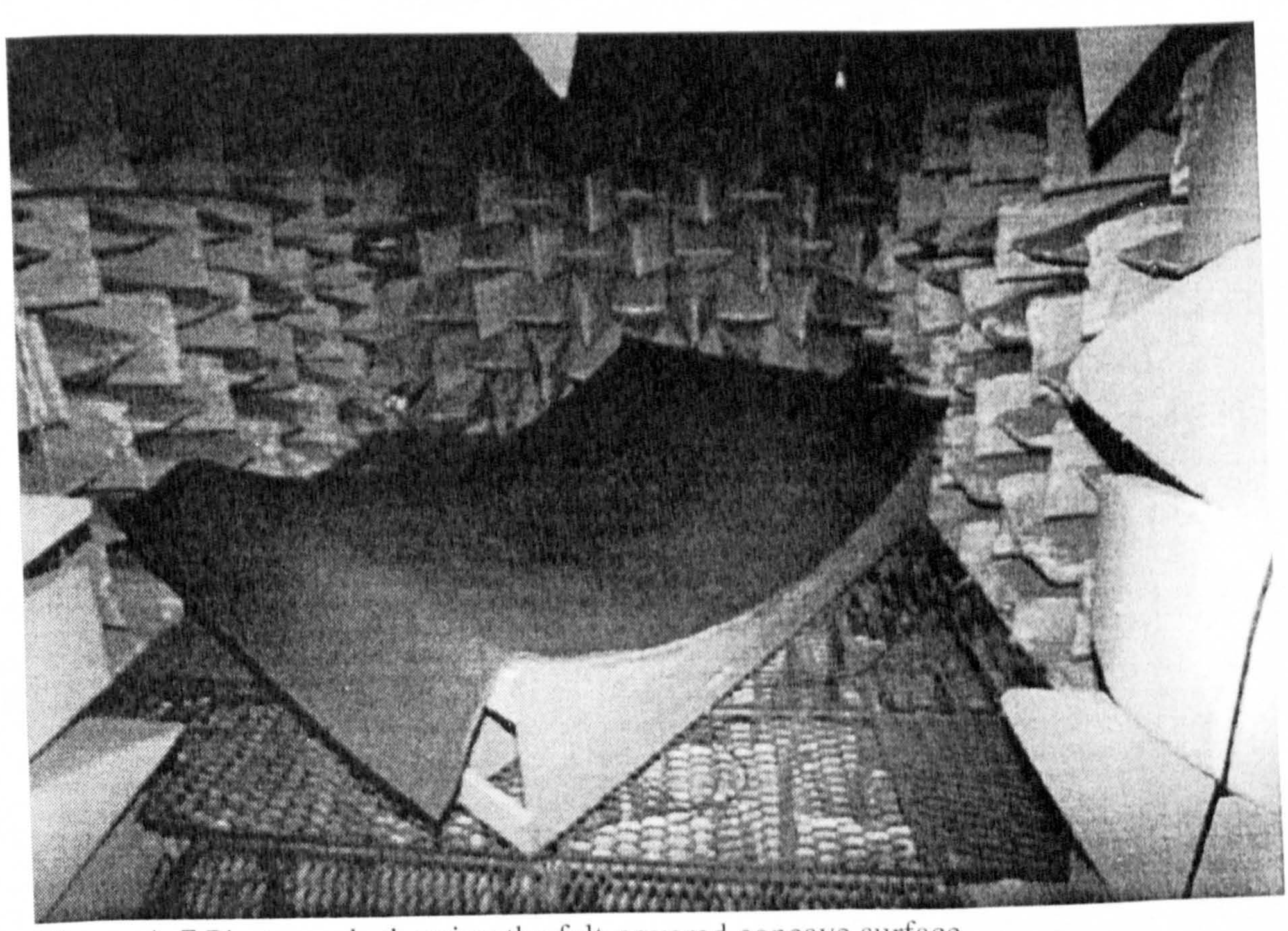

Figure A-7 Photograph showing the felt-covered concave surface.